Pertanika Journal of

SCIENCE & TECHNOLOGY

JST

VOL. 33 (4) JUL. 2025

PERTANIKA JOURNALS

A scientific journal published by Universiti Putra Malaysia Press

Pertanika Journal of Science & Technology
Pertanika Journal of Science & Technology

PERTANIKA JOURNAL OF SCIENCE & TECHNOLOGY

About the Journal

Overview

Pertanika Journal of Science & Technology is an official journal of Universiti Putra Malaysia. It is an open-access online scientific journal. It publishes original scientific outputs. It neither accepts nor commissions third party content.

Recognised internationally as the leading peer-reviewed interdisciplinary journal devoted to the publication of original papers, it serves as a forum for practical approaches to improve quality on issues pertaining to science and engineering and its related fields.

Pertanika Journal of Science & Technology currently publishes 6 issues a year (*January, March, April*, *July, August,* and *October*). It is considered for publication of original articles as per its scope. The journal publishes in **English** and it is open for submission by authors from all over the world.

The journal is available world-wide.

Aims and scope

Pertanika Journal of Science & Technology aims to provide a forum for high quality research related to science and engineering research. Areas relevant to the scope of the journal include: bioinformatics, bioscience, biotechnology and bio-molecular sciences, chemistry, computer science, ecology, engineering, engineering design, environmental control and management, mathematics and statistics, medicine and health sciences, nanotechnology, physics, safety and emergency management, and related fields of study.

History

Pertanika Journal of Science & Technology was founded in 1993 and focuses on research in science and engineering and its related fields.

Vision

To publish a journal of international repute.

Mission

Our goal is to bring the highest quality research to the widest possible audience.

Quality

We aim for excellence, sustained by a responsible and professional approach to journal publishing. Submissions can expect to receive a decision within 90 days. The elapsed time from submission to publication for the articles averages 180 days. We are working towards decreasing the processing time with the help of our editors and the reviewers.

Abstracting and indexing of Pertanika

Pertanika Journal of Science & Technology is now over 33 years old; this accumulated knowledge and experience has resulted the journal being abstracted and indexed in SCOPUS (Elsevier), Journal Citation Reports (JCR-Clarivate), EBSCO, ASEAN CITATION INDEX, Microsoft Academic, Google Scholar, and MyCite.

Citing journal articles

The abbreviation for Pertanika Journal of Science & Technology is *Pertanika J. Sci. & Technol.*

Publication policy

Pertanika policy prohibits an author from submitting the same manuscript for concurrent consideration by two or more publications. It prohibits as well publication of any manuscript that has already been published either in whole or substantial part elsewhere. It also does not permit publication of manuscript that has been published in full in proceedings.

Code of Ethics

The *Pertanika* journals and Universiti Putra Malaysia take seriously the responsibility of all of its journal publications to reflect the highest in publication ethics. Thus, all journals and journal editors are expected to abide by the journal's codes of ethics. Refer to *Pertanika*'s **Code of Ethics** for full details, or visit the journal's web link at http://www.pertanika.upm.edu.my/code_of_ethics.php

Originality

The author must ensure that when a manuscript is submitted to *Pertanika*, the manuscript must be an original work. The author should check the manuscript for any possible plagiarism using any program such as Turn-It-In or any other software before submitting the manuscripts to the *Pertanika* Editorial Office, Journal Division.

All submitted manuscripts must be in the journal's acceptable similarity index range:

≤ 20% – PASS; > 20% – REJECT.

International Standard Serial Number (ISSN)

An ISSN is an 8-digit code used to identify periodicals such as journals of all kinds and on all media–print and electronic.

Pertanika Journal of Science & Technology: e-ISSN 2231-8526 (Online).

Lag time

A decision on acceptance or rejection of a manuscript is reached in 90 days (average). The elapsed time from submission to publication for the articles averages 180 days.

Authorship

Authors are not permitted to add or remove any names from the authorship provided at the time of initial submission without the consent of the journal's Chief Executive Editor.

Manuscript preparation

For manuscript preparation, authors may refer to Pertanika's **INSTRUCTION TO AUTHORS**, available on the official website of *Pertanika*.

Editorial process

Authors who complete any submission are notified with an acknowledgement containing a manuscript ID on receipt of a manuscript, and upon the editorial decision regarding publication.

Pertanika follows a **double-blind peer-review** process. Manuscripts deemed suitable for publication are sent to reviewers. Authors are encouraged to suggest names of at least 3 potential reviewers at the time of submission of their manuscripts to *Pertanika*, but the editors will make the final selection and are not, however, bound by these suggestions.

Notification of the editorial decision is usually provided within 90 days from the receipt of manuscript. Publication of solicited manuscripts is not guaranteed. In most cases, manuscripts are accepted conditionally, pending an author's revision of the material.

The journal's peer review

In the peer-review process, 2 to 3 referees independently evaluate the scientific quality of the submitted manuscripts. At least 2 referee reports are required to help make a decision.

Peer reviewers are experts chosen by journal editors to provide written assessment of the **strengths** and **weaknesses** of written research, with the aim of improving the reporting of research and identifying the most appropriate and highest quality material for the journal.

Operating and review process

What happens to a manuscript once it is submitted to *Pertanika*? Typically, there are 7 steps to the editorial review process:

1. The journal's Chief Executive Editor and the Editor-in-Chief examine the paper to determine whether it is relevance to journal needs in terms of novelty, impact, design, procedure, language as well as presentation and allow it to proceed to the reviewing process. If not appropriate, the manuscript is rejected outright and the author is informed.

2. The Chief Executive Editor sends the article-identifying information having been removed, to 2 to 3 reviewers. They are specialists in the subject matter of the article. The Chief Executive Editor requests that they complete the review within 3 weeks.

   Comments to authors are about the appropriateness and adequacy of the theoretical or conceptual framework, literature review, method, results and discussion, and conclusions. Reviewers often include suggestions for strengthening of the manuscript. Comments to the editor are in the nature of the significance of the work and its potential contribution to the research field.

Pertanika Journal of Science & Technology
Pertanika Journal of Science & Technology

Pertanika Journal of Science & Technology
Pertanika Journal of Science & Technology

3. The Editor-in-Chief examines the review reports and decides whether to accept or reject the manuscript, invite the authors to revise and resubmit the manuscript, or seek additional review reports. In rare instances, the manuscript is accepted with almost no revision. Almost without exception, reviewers' comments (to the authors) are forwarded to the authors. If a revision is indicated, the editor provides guidelines for attending to the reviewers' suggestions and perhaps additional advice about revising the manuscript.

4. The authors decide whether and how to address the reviewers' comments and criticisms and the editor's concerns. The authors return a revised version of the paper to the Chief Executive Editor along with specific information describing how they have addressed' the concerns of the reviewers and the editor, usually in a tabular form. The authors may also submit a rebuttal if there is a need especially when the authors disagree with certain comments provided by reviewers.

5. The Chief Executive Editor sends the revised manuscript out for re-review. Typically, at least 1 of the original reviewers will be asked to examine the article.

6. When the reviewers have completed their work, the Editor-in-Chief examines their comments and decides whether the manuscript is ready to be published, needs another round of revisions, or should be rejected. If the decision is to accept, the Chief Executive Editor is notified.

7. The Chief Executive Editor reserves the final right to accept or reject any material for publication, if the processing of a particular manuscript is deemed not to be in compliance with the S.O.P. of *Pertanika*. An acceptance letter is sent to all the authors.

   The editorial office ensures that the manuscript adheres to the correct style (in-text citations, the reference list, and tables are typical areas of concern, clarity, and grammar). The authors are asked to respond to any minor queries by the editorial office. Following these corrections, page proofs are mailed to the corresponding authors for their final approval. At this point, **only essential changes are accepted**. Finally, the manuscript appears in the pages of the journal and is posted on-line.

Pertanika Journal of

SCIENCE & TECHNOLOGY

Vol. 33 (4) Jul. 2025

PERTANIKA JOURNALS

A scientific journal published by Universiti Putra Malaysia Press

PJST
Pertanika Journal of Science & Technology
AN INTERNATIONAL PEER-REVIEWED JOURNAL

UNIVERSITY PUBLICATIONS COMMITTEE

CHAIRMAN
Zamberi Sekawi

EDITOR-IN-CHIEF
Luqman Chuah Abdullah
Chemical Engineering

EDITORIAL STAFF
Journal Officers:
Navaneetha Krishna Chandran
Siti Zuhaila Abd Wahid
Tee Syin Ying
Yavinaash Naidu Saravanakumar

Editorial Assistants:
Zulinaardawati Kamarudin

English Editor:
Norhanizah Ismail

PRODUCTION STAFF
Pre-press Officers:
Ku Ida Mastura Ku Baharom
Nur Farrah Dila Ismail

WEBMASTER
IT Officer:
Kiran Raj Kaneswaran

EDITORIAL OFFICE
JOURNAL DIVISION
Putra Science Park
1st Floor, IDEA Tower II
UPM-MTDC Technology Centre
Universiti Putra Malaysia
43400 Serdang, Selangor Malaysia.

General Enquiry
Tel. No: +603 9769 1622
E-mail:
executive_editor.pertanika@upm.edu.my
URL: http://www.pertanika.upm.edu.my

PUBLISHER
UPM Press
Universiti Putra Malaysia
43400 UPM, Serdang, Selangor, Malaysia.
Tel: +603 9769 8855
E-mail: dir.penerbit@upm.edu.my
URL: http://penerbit.upm.edu.my

ASSOCIATE EDITOR
2024-2026

Miss Laiha Mat Kiah
Security Services Sn: Digital Forensic, Steganography, Network Security, Information Security, Communication Protocols, Security Protocols
Universiti Malaya, Malaysia

Saidur Rahman
Renewable Energy, Nanofluids, Energy Efficiency, Heat Transfer, Energy Policy
Sunway University, Malaysia

EDITORIAL BOARD
2024-2026

Abdul Latif Ahmad
Chemical Engineering
Universiti Sains Malaysia, Malaysia

Hsiu-Po Kuo
Chemical Engineering
National Taiwan University, Taiwan

Mohd. Ali Hassan
Bioprocess Engineering, Environmental Biotehnology
Universiti Putra Malaysia, Malaysia

Ahmad Zaharin Aris
Hydrochemistry, Environmental Chemistry, Environmental Forensics, Heavy Metals
Universiti Putra Malaysia, Malaysia

Ivan D. Rukhlenko
Nonliner Optics, Silicon Photonics, Plasmonics and Nanotechnology
The University of Sydney, Australia

Nor Azah Yusof
Biosensors, Chemical Sensor, Functional Material
Universiti Putra Malaysia, Malaysia

Azlina Harun@ Kamaruddin
Enzyme Technology, Fermentation Technology
Universiti Sains Malaysia, Malaysia

Lee Keat Teong
Energy Environment, Reaction Engineering, Waste Utilization, Renewable Energy
Universiti Sains Malaysia, Malaysia

Norbahiah Misran
Communication Engineering
Universiti Kebangsaan Malaysia, Malaysia

Bassim H. Hameed
Chemical Engineering: Reaction Engineering, Environmental Catalysis & Adsorption
Qatar University, Qatar

Mohamed Othman
Communication Technology and Network, Scientific Computing
Universiti Putra Malaysia, Malaysia

Roslan Abd-Shukor
Physics & Materials Physics, Superconducting Materials
Universiti Kebangsaan Malaysia, Malaysia

Biswajeet Pradhan
Digital image processing, Geographical Information System (GIS), Remote Sensing
University of Technology Sydney, Australia

Mohd Shukry Abdul Majid
Polymer Composites, Composite Pipes, Natural Fibre Composites, Biodegradable Composites, Bio-Composites
Universiti Malaysia Perlis, Malaysia

Sodeifian Gholamhossein
Supercritical technology, Optimization, nanoparticles, Polymer nanocomposites
University of Kashan, Iran

Ho Yuh-Shan
Water research, Chemical Engineering and Environmental Studies
Asia University, Taiwan

Mohd Zulkifly Abdullah
Fluid Mechanics, Heat Transfer, Computational Fluid Dynamics (CFD)
Universiti Sains Malaysia, Malaysia

Wing Keong Ng
Aquaculture, Aquatic Animal Nutrition, Aqua Feed Technology
Universiti Sains Malaysia, Malaysia

INTERNATIONAL ADVISORY BOARD
2024-2027

Hiroshi Uyama
Polymer Chemistry, Organic Compounds, Coating, Chemical Engineering
Osaka University, Japan

Mohini Sain
Material Science, Biocomposites,Biomaterials
University of Toronto, Canada

Mohamed Pourkashanian
Mechanical Engineering, Energy, CFD and Combustion Processes
Sheffield University, United Kingdom

Yulong Ding
Particle Science & Thermal Engineering
University of Birmingham, United Kingdom

ABSTRACTING AND INDEXING OF PERTANIKA JOURNALS

Pertanika Journal of Science & Technology is indexed in Journal Citation Reports (JCR-Clarivate), SCOPUS (Elsevier), EBSCO, ASEAN Citation Index, Microsoft Academic, Google Scholar and MyCite.

The publisher of Pertanika will not be responsible for the statements made by the authors in any articles published in the journal. Under no circumstances will the publisher of this publication be liable for any loss or damage caused by your reliance on the advice, opinion or information obtained either explicitly or implied through the contents of this publication.
All rights of reproduction are reserved in respect of all papers, articles, illustrations, etc., published in Pertanika. Pertanika provides free access to the full text of research articles for anyone, web-wide. It does not charge either its authors or author-institution for refereeing/publishing outgoing articles or user-institution for accessing incoming articles.
No material published in Pertanika may be reproduced or stored on microfilm or in electronic, optical or magnetic form without the written authorization of the Publisher.
Copyright ©2021 Universiti Putra Malaysia Press. All Rights Reserved.

Pertanika Journal of Science & Technology
Vol. 33 (4) Jul. 2025

Contents

Foreword i
Luqman Chuah Abdullah

Efficiency of Self-Healing Microcapsules in Concrete Slabs Subjected to Low Velocity Impact Force 1683
Salima Al Badi, Zarina Itam, Wong Leong Sing, Muhammad Imran Najeeb, Nazirul Mubin Zahari, Afeeq Haiqal Mohd Hafiez, Shaikh Muhammad Mubin Shaik Ahmad Fadzil, Mohd Meer Saddiq Mohd Sabee and Zuratul Ain Abdul Hamid

Review Article 1707
MXene as a Microstructural Modifier in Solar Thermal Absorber: A Review
Mannir Ibrahim Tarno, Azmah Hanim Mohamed Ariff, Suraya Mohd Tahir and Che Nor Aiza Jaafar

Tailored Cognitive Interventions for Aging Populations: Development and Analysis of a Machine Learning-Driven Web Platform 1743
Mario Macea-Anaya, Rubén Baena-Navarro, Yulieth Carriazo-Regino, Ober Primera-Correa and Juan Pérez-Díaz

Influence of Pyrolysis Temperature on the Composition of Bio-Oil Derived from *Cerbera odollam* as a Raw Material 1765
Muhammad Fathuddin Noor, Sumardi Hadi Sumarlan, Bambang Dwi Argo and Yusuf Hendrawan

Development of Machine Learning Wildlife Camera Using ESP32 CAM for Small Mammals 1783
Leu Mei Xin and Nik Fadzly N Rosely

Analysis and Simulation of Temperature Reduction and Cooling Rate in Precooling Process Using Compressive Force Plate Cooler 1809
Surya Abdul Muttalib, Nursigit Bintoro, Joko Nugroho Wahyu Karyadi and Arifin Dwi Saputro

A Novel Multifaceted Approach to the Detection and Analysis of Formalin's Effect on Enhancing the Shelf Life of Apples 1829
Shahed Alam, Md Saif Kabir, Md. Minhazul Islam Royel and Md. Rakibul Islam

Morphological and Genetic Relationship of Ancient Shan Tea Tree *(Camellia sinensis* var. *assamica)* from Ecogeographical Regions in Northern Vietnam 1849
Lien Thuy Bui, Phong Xuan Ong, Thiep Van Nguyen, Khang Tan Do, Huy Gia Tran, Phi Bang Cao, Ha Duc Chu, Dung Phuong Le and Hong Viet La

Growth and Productivity of Maize *(Zea mays)* Using Gibberellic Acid 3 (GA3) with Different Planting Distances in a Clay Condition at Cabagan, Isabela, Philippines 1869
Darwin Marzan Cacal, Janet Paday-os Pablo, Leila Mary Alipio Ayban, Esther Josephine Daoal Sagalla and Darwin Aldas Basquial

Analysis of Phased Array Corrosion Mapping Data Using Probabilistic Detection (POD) Method 1887
Jan Lean Tai, Mohamed Thariq Hameed Sultan and Farah Syazwani Shahar

Stochastic Distribution of Channel Allocation Algorithm for 5G and Future Generation Ultra-Dense Networks Applications 1907
Joseph Sunday Ojo, Olalekan Lawrence Ojo and Stephen Adebayo Olu-Ojo

Distribution and Population Abundance of Odonates in Relation to Abiotic Factors in an Urbanized Freshwater Ecosystem: A Case Study from Universiti Sains Malaysia 1923
Nur Aina Alisa Adnan, Azimah Abd Rahman, Nur Faeza Abu Kassim and Nurhafizul Abu Seri

A Comparative Study of Gradient Descent Methods in Deep Learning Using Body Motion Dataset 1943
Zulfikar Sembiring, Khairul Najmy Abdul Rani and Amiza Amir

Reduction of Transport Carbon Emissions of India by the Implementation of Strategies Based on IoT-Enabled Intelligent Transportation System: A System Dynamics Approach 1971
Aditi Rajput and Madhuri Jai

Comparison of Crystal Structure, Surface Morphology Structure, and Energy Band Gap of Thin Films of Zinc Oxide, Tin(IV) Oxide, and Titanium Dioxide 2001
Teguh Ardianto, Aris Doyan, Susilawati, Dedi Riyan Rizaldi, Ziadatul Fatimah, Muhammad Ikhsan and Nuraini Rachma Ardianti

Foreword

Welcome to the fourth issue of 2025 for the Pertanika Journal of Science and Technology (PJST)!

PJST is an open-access journal for studies in Science and Technology published by Universiti Putra Malaysia Press. It is independently owned and managed by the university for the benefit of the world-wide science community.

This issue contains 15 articles: one review article; and the rest are regular articles. The authors of these articles come from different countries namely Bangladesh, Colombia, India, Indonesia, Malaysia, Nigeria, Philippines and Vietnam.

The regular article entitled "MXene as A Microstructural Modifier in Solar Thermal Absorber: A Review" explores the latest microstructural modifications of solar thermal absorbers using MXene as a microstructural modifier, along with their effects on thermal conductivity, strength, photothermal conversion, and corrosion resistance. The research aims to identify the core challenges in solar thermal systems (STSs) and to create opportunities for their integration, processing, and manufacturing. MXene has shown promising results in enhancing the thermal and corrosion properties of solar thermal energy systems, reinforced nanofluids, phase change materials, coatings, carbon nanotubes, and nanocapsules. Additionally, MXene used as the backing for metallic absorbers and in coatings has demonstrated significant improvements in the thermal and corrosion performance of STSs. Further details of this study can be found on page 1707.

Muhammad Fathuddin Noor and his teammates from Universitas Brawijaya have studied how pyrolysis temperature affects the composition of bio-oil derived from *Cerbera odollam* as a raw material. Pyrolysis was conducted in a fixed-bed reactor at temperatures of 350, 450, and 550°C. The higher the pyrolysis temperature, the more gas products are produced, and the less char product is formed. Conversely, lower pyrolysis temperatures result in greater char production and fewer gas products. The optimal temperature for producing bio-oil from the pyrolysis of *C. odollam* is 550°C, as this yields the most chemical components analysed using GC-MS to identify the compounds present. The pyrolysis of *C. odollam* biomass shows distinct product distributions at different temperatures. Further detailed information can be found on page 1765.

A selected article titled "A Novel Multifaceted Approach to the Detection and Analysis of Formalin's Effect on Enhancing the Shelf Life of Apples" examined the impact of formalin on the shelf life of apples. Three different concentrations of formalin (20, 30, and 40%)

were applied to apples, which were analysed using three methods: (1) spectrophotometry, (2) a formalin test kit developed by the Bangladesh Council of Scientific and Industrial Research, and (3) a MS1100 gas sensor functioning as an E-nose. The results indicated that formalin emissions reverted to their natural or pure form after approximately 30 hours. Formalin does not extend the shelf life of apples and, in fact, appears to make them look less fresh. Full details of this study are available on page 1829.

We anticipate that you will find the evidence presented in this issue to be intriguing, thought-provoking and useful in reaching new milestones in your own research. Please recommend the journal to your colleagues and students to make this endeavour meaningful.

All the papers published in this edition underwent Pertanika's stringent peer-review process involving a minimum of two reviewers comprising internal as well as external referees. This was to ensure that the quality of the papers justified the high ranking of the journal, which is renowned as a heavily-cited journal not only by authors and researchers in Malaysia but by those in other countries around the world as well.

We would also like to express our gratitude to all the contributors, namely the authors, reviewers and Editorial Board Members of PJST, who have made this issue possible.

PJST is currently accepting manuscripts for upcoming issues based on original qualitative or quantitative research that opens new areas of inquiry and investigation.

Editor-in-Chief
Luqman Chuah Abdullah

Pertanika J. Sci. & Technol. 33 (4): 1683 - 1706 (2025)

PERTANIKA JOURNALS

SCIENCE & TECHNOLOGY

Journal homepage: http://www.pertanika.upm.edu.my/

Efficiency of Self-Healing Microcapsules in Concrete Slabs Subjected to Low Velocity Impact Force

Salima Al Badi[1], Zarina Itam[2]*, Wong Leong Sing[2], Muhammad Imran Najeeb[3], Nazirul Mubin Zahari[2], Afeeq Haiqal Mohd Hafiez[4], Shaikh Muhammad Mubin Shaik Ahmad Fadzil[2], Mohd Meer Saddiq Mohd Sabee[5] and Zuratul Ain Abdul Hamid[5]

[1]College of Graduate School, Universiti Tenaga Nasional, Jalan IKRAM - UNITEN, 43000 Kajang, Selangor, Malaysia
[2]Institute of Energy Infrastructure, Universiti Tenaga Nasional, Jalan IKRAM - UNITEN, 43000 Kajang, Selangor, Malaysia
[3]Department of Engineering Education, Faculty of Engineering and Built Environment, Universiti Kebangsaan Malaysia, 43600 Bangi, Selangor, Malaysia
[4]Department of Civil Engineering, Universiti Tenaga Nasional, Jalan IKRAM - UNITEN, 43000 Kajang, Selangor, Malaysia
[5]Biomaterials Research Niche Group, School of Materials and Mineral Resources Engineering, Universiti Sains Malaysia, 14300 Nibong Tebal, Pulau Pinang, Malaysia

ABSTRACT

Plentiful modern buildings in urban and rural zones, especially buildings constructed from reinforced concrete (RC) materials, were exposed to severe defects such as spalling and delamination as the years progressed. The most used method to repair damages on existing RC is through the use of shotcrete cement grout or heavy-duty structure tape retrofits. These methods involved multiple manpower, modern equipment and a longer time of structural healing, which led to a higher cost of maintenance. Therefore, the application of self-healing microcapsules within the RC structures is one of the solutions to support the rehabilitation of cementitious-based products by developing a building with self-healing properties. This research investigates the concrete's self-healing performances subjected to low velocity impact using large (L) and small (S) self-healing microcapsules measured at 70 mm × 10 mm and 70 mm × 5 mm. The positions (Point 1, 2 and 3) of the microcapsule in the concrete were placed based on the simulated results of severe cracks on the impacted control concrete sample from the ANSYS explicit dynamics. Post impact results

ARTICLE INFO

Article history:
Received: 23 May 2024
Accepted: 24 December 2024
Published: 11 June 2025

DOI: https://doi.org/10.47836/pjst.33.4.01

E-mail addresses:
Salimaroyalpalac2023@gmail.com (Salima Al Badi)
imran.najeeb@ukm.edu.my (Muhammad Imran Najeeb)
iZarina@uniten.edu.my (Zarina Itam)
WongLS@uniten.edu.my (Wong Leong Sing)
Nazirul@uniten.edu.my (Nazirul Mubin Zahari)
afeeq.nikon@gmail.com (Afeeq Haiqal Mohd Hafiez)
smmubin27@gmail.com (Shaikh Muhammad Mubin Shaik Ahmad Fadzil)
meersaddiq@gmail.com (Mohd Meer Saddiq Mohd Sabee)
srzuratulain@usm.my (Zuratul Ain Abdul Hamid)
* Corresponding author

© Universiti Putra Malaysia Press

show that the concrete with L microcapsules had 68.2% more self-healing efficiency compared to S microcapsules, showing it had better damage recovery.

Keywords: Crack reduction, drop weight test, energy efficiency, reinforced concrete slabs, self-healing microcapsules

INTRODUCTION

Reinforced concrete (RC) has become one of the most broadly applied components in construction, in addition to steel structures. RC is proven as a very strong structural element for an infrastructure's column, beam, wall, and slab, but it deteriorates as the years progress. This, in return, degrades the materials bonded within the building (Lv et al., 2022). Generally, concrete has low tensile strength and durability, but the implementation of steel reinforcement bars boosts the toughness of the concrete. The steel reinforcement bars are protected from the damage caused by the alkaline environment formed in the RC, yet due to defects in the structure that are prone to breaking down from outside mechanical stress, it forms problems such as drying or self-shrinking (Muhammad et al., 2016). Thus, through the fissures, the reinforcement becomes exposed to acidic ions, which causes it to corrode and ultimately weaken the concrete. In an attempt to improve the mechanical properties of RC, concrete mix design or proportions went through plenty of changes in terms of material choices throughout the years (Muhammad et al., 2016).

Numerous researchers are currently conducting a comprehensive study on the moderated environmental impact of RC, especially studies on repairing and rehabilitating RC structures from early production (Hilloulin et al., 2015). The studies are an initiative to reduce the repair and maintenance costs of the structures. Recently, the frequently used method to repair damage on existing RC is through shotcrete cement grout or heavy-duty structure tape retrofits (Vijay et al., 2017). The actions to repair the RC with these methods will involve multiple man-hours, modern equipment, and a longer time for structural healing, which leads to a higher cost of maintenance. The application of self-healing microcapsules within the RC structures is one of the latest types of research to support the rehabilitation of cementitious-based products by developing a building with self-healing properties (Mir et al., 2023). Concrete is susceptible to cracking due to various factors such as shrinkage, temperature changes, and external loads. Normal concrete is brittle, causing it to fail without warning. The traditional repair methods for concrete structures are costly and labour-intensive. However, the reports show that concrete repairs are performed inconsistently and failure rates are high, and it was estimated that nearly half of the traditional concrete repairs fail in the field. Additionally, the replacement and repair activity with new concrete often has a substantial environmental impact due to the production and disposal of waste materials (Yıldırım et al., 2018). Self-healing microcapsules release healing agents that can fill these cracks, effectively repairing the

damage and restoring the concrete's strength and durability. Therefore, a self-healing system that treats internal defects without human intervention is one of the most desired properties in material science and engineering.

Concrete is one of the most widely used construction materials globally, but its production has a considerable environmental impact due to the extraction of raw materials and high energy consumption. By enhancing the durability of concrete structures, self-healing technology reduces the need for new concrete production and promotes a more sustainable approach to construction. The self-healing microcapsules' utilisation in RC slabs supports several UNESCO Sustainable Development Goals (SDGS). SDG 9 promotes resilient infrastructure, inclusive industrialization, and innovation. Using self-healing microcapsules in concrete falls under innovation in construction materials and techniques. These microcapsules contain healing agents released when cracks form in the concrete, effectively repairing the damage independently. This innovation can enhance the durability and lifespan of concrete structures, reducing the need for frequent repairs or replacements, and ultimately promoting more sustainable infrastructure development.

Additionally, self-healing concrete contributes to the United Nations initiative in the SDGs by improving the sustainability and resilience of infrastructure. This aligns with SDG 9, which promotes resilient infrastructure through innovative materials. Besides that, self-healing concrete improves the longevity and durability of the structure, minimising the waste of material due to frequent replacements/damages. These attributes align with and support SDG 11 (sustainable cities and communities) and SDG 12 (responsible consumption and production).

By automatically repairing cracks as they occur, self-healing concrete can extend the lifespan of structures. This reduces the need for frequent repairs or replacements, saving time, money, and resources in the long run. Cracks in concrete can lead to water infiltration, which can cause corrosion of the embedded reinforcement, compromising the structure's overall safety. Self-healing concrete minimises the potential for further damage and ensures the safety of the infrastructure. Hence, the capability of self-healing capsules to repair concrete initial and severe cracks is anticipated as a further environmentally friendly building practice (Van Tittelboom et al., 2011).

Previous research by Zhang et al. (2020) discovered that concrete's capacity for self-healing is an autogenous process where numerous chemicals and materials were experimented with in order to identify the optimum potentials and efficiency in self-healing agents (Zhang et al., 2020). Variation of healing agents that consisted of sodium silicate, polyurethane, epoxy, cyanoacrylates, and bacterial spores has been studied to effectively rehabilitate RC components (Zhang et al., 2020). However, fewer articles in engineering describe the efficiency and validations of using the various healing agents to reduce the width of the cracks on the RC surfaces. The authors formed three types of self-healing processes: natural self-healing, chemical self-healing, and biological self-healing processes

(Althoey et al., 2023; Zhang et al., 2020). The natural self-healing process is a process that partially heals cracks in RC naturally with the formation of $CaCO_3$ or CaOH from the self-healing agents, such as calcium nitrate and sodium silicate (Althoey et al., 2023). The agents react with the impurities during water transport as well as the hydration of unreacted ordinary Portland cement. Hydrated cement patterns like calcium silicate hydrate gel are then formed at the crack zones, which will repair the cracks on the RC surfaces (Jogi & Lakshmi, 2021).

The creation of calcium carbonate and calcium hydroxide is among the important factors for the natural repair of concrete. The initial phase of the healing process by the self-healing agent is carbon dioxide, which dissolves in water as shown in Equation 1 (Rosewitz et al., 2021).

$$H_2O + CO_2 \rightarrow HCO_3^- + H^+ \quad [1]$$

Then, a reaction occurred between pH7.5 to pH8 in the cement, which led to the development of calcium carbonate crystals after the loss of calcium ions into the RC as a system of cement hydration, as shown in Equation 2 (Rosewitz et al., 2021).

$$Ca^{2+} + 2HCO_3^- \rightarrow CaCO_3 \text{ and } Ca^{2+} + HCO_3^- \rightarrow CaCO_3 + H^+ \quad [2]$$

Universally, the chemical process of self-healing is known as a chemical healing technique that is supported by chemical compounds. Self-healing RC is made through the injection of liquid chemical reagents into small containers of fresh RC structure (Restuccia et al., 2017). The chemical self-healing process is performed through the passive method, where the chemicals are stored in a capsule or other materials of hollow shapes and applied into the structure during the construction process. The liquid within the capsules is transferred throughout the fractures and repaired the cracks in due course (Restuccia et al., 2017). Furthermore, a detailed study that was accomplished proved the capsules fractured after bending test released adhesive at 20% of its weight (Jakubovskis et al., 2020). According to Homma et al. (2009), specimens of self-healing RC can recover 26% of the RC's initial strength compared to restrained specimens that recovered by 10%. Thus, the increase in the quantity of self-healing agents inside the capsules increased the strength of the repair rate of the RC structures.

From the perspective of the biological self-healing process, the use of microorganisms in RC is considered a biological application for self-healing, as the microorganism can cover the crack in any condition, including cold or warm, water and soil (Jakubovskis et al., 2020). The researcher of self-healing properties mentioned that polymorphic ferro-aluminium silicate and calcium carbonate are necessary for precipitation to produce a self-healing reaction on RC structures. The microbial broth of the microorganisms is alternatively encapsulated inside microbial encapsulation before implementation into the

fresh RC mix to improve the condition of structures. Strong self-healing by employing a microencapsulation approach depends on how the healing agent works alongside the concrete to create healing after cracks occur.

The autogenous process of self-healing is influenced by the increment degree of hydration of the concrete and the calcium hydroxide carbonisation (Gupta et al., 2017). The solution of sodium silicate is one of the self-healing agents that produces carbonisation through RC hydration to heal the cracks over time and is preferred due to its hydration-enhancing characteristics, ready availability, and low cost in the engineering industry. The self-healing agents are labelled as monomer liquid in a plastic-based material, microcapsules. The microcapsules are capable of microcracking, which can lead to the liquid to release in an instant if a crack occurs within the structures (Durga et al., 2021). The model of microcapsules is created from pure polymers and a polymer layer which has a tensile strength of 0.73MPa to 1.2MPa, respectively (Khaliq & Ehsan, 2016). The literature indicates that self-healing microcapsules are engineered to release healing agents via various triggers, including mechanical stress, temperature, light, pH changes, and ion interactions, as shown in Table 1 (Gao et al., 2022; Lv et al., 2020; Ren et al., 2021; Xiong et al., 2015). However, research on the low-velocity impact of concrete remains insufficiently explored. In real-world applications, concrete is also susceptible to impact damage, resulting in sudden failure, a critical concern distinct from flexural and compressive stress.

This research aims to determine the performance of 70 × 10 mm (large) and 70 × 5 mm (small) polymeric microcapsules filled with sodium silicate liquid to heal ultimate cracks in the concrete slab specimens subjected to a 200 mm height of low velocity impact. Furthermore, investigation of the efficiency rate of microcapsules in terms of the rehabilitation process or crack reduction analysis on the specimens was also conducted. The healing mechanism will determine current self-healing limitations such as reliance on environmental conditions, microcapsule dosage, and crack width. For these reasons,

Table 1
Summary of past work on the development of self-healing microcapsules

Trigger type	Mechanism of trigger	Description	Material of capsule/core
Physical	Mechanical fracture	Mechanism of rupture under stress (flexural and compressive)	sodium carbonate (Na_2CO_3) and calcium acetate ($Ca(CH_3COO)_2$)
	Temperature	At a certain temperature, the microcapsule activated	polymethylmethacrylate-methacrylate shell and magnesium oxide core
	Light	Activate when there is light exposure	Epoxy acrylate-based free radical-cationic UV curable adhesive, A331
Chemical	pH	Responsive to pH change	Acrylate-based microcapsules
	ion	Release inhibitors to prevent corrosion of steel in concrete	Ag-alginate capsules with oil cores

research into healing mechanisms is critical, as results of the study may allow for the optimisation of a self-healing method as well as the establishment of conditions for proper implementation in the future of RC maintenance (Dixit et al., 2021).

MATERIALS AND FABRICATION

The self-healing microcapsules' efficiency in RC slab subjected to low velocity impact force was conducted according to the flowchart as presented in Figure 1. Prior to testing, the location of the self-healing microcapsule was determined using simulation software based on the results of severe crack formation on the impacted control RC. Two types of self-healing microcapsules (small and large) are prepared and embedded in three spots

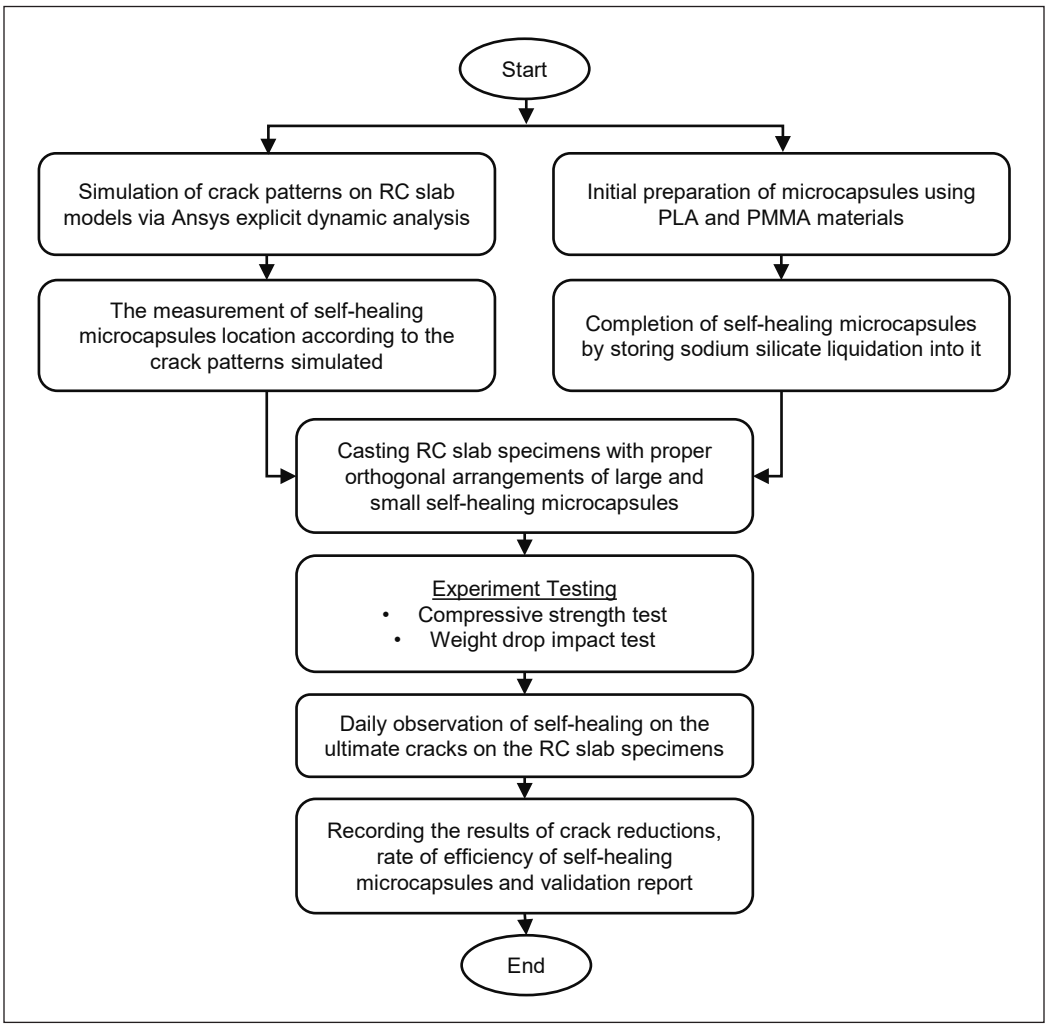

Figure 1. Flowchart of the research work

on RC slabs. Low-velocity impact tests were conducted on RC slabs with small and large self-healing microcapsules, with three repetitions for each type. The crack gap around the microcapsule was recorded and compared for both RC slabs for 28 days.

Types and Preparation of Self-Healing Microcapsules

The microcapsules were prepared from the use of polylactic acid (PLA) and polymethyl methacrylate (PMMA) materials that resemble transparent thermoplastic or acrylic glass components (Khaliq & Ehsan, 2016). A thermal printing machine moulded PLA and PMMA into a hollow cylinder. Then, the elongated hollow cylindrical shapes were cut into an equivalent length of 70 mm. The thickness between the inner and outer circles of the microcapsules is 2 mm. The microcapsules were moulded into two different diameters, which are 10 × 70 mm (large) and 5 × 70 mm (small), as shown in Figure 2.

The microcapsules were created to encapsulate the chemically pure (C.P.) sodium silicate liquid as a self-healing agent in order to repair the RC slab specimens internally after the occurrence of ultimate cracks (Khaliq & Ehsan, 2016; Durga et al., 2021). A strong waterproof silicone sealant sealed one end of the self-healing microcapsule. Sodium silicate liquidation was then injected into the self-healing microcapsules. The microcapsules were sealed again on the other end to secure the agent. The chosen self-healing material is because it has shown success in healing properties reported in several studies (Irico et al., 2017; Li & Guan, 2023; Mokhtar & Hassan, 2021). This method is particularly advantageous because it offers a good response to crack formation, enhances the durability and longevity of concrete structures, and requires minimal intervention once applied. To extend the work on this material, the author investigates the concrete healing performance with two different sizes of self-healing microcapsules subjected to low-velocity impact.

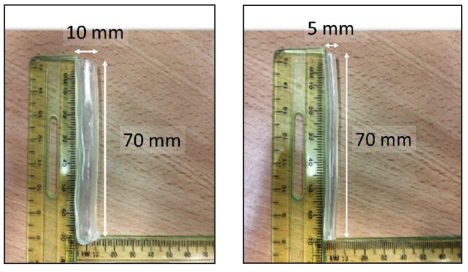

(a) (b)

Figure 2. (a) Large self-healing microcapsules; and (b) Small self-healing microcapsules

Arrangement of Self-Healing Microcapsules

Following the preparations of the self-healing microcapsules, a numerical simulation for explicit dynamic analysis of the concrete slab specimen was performed via ANSYS analysis software. The material properties of the concrete slab and stainless-steel ball impactor used are as per Table 2 (Ferrara et al., 2018).

The concrete slab was developed with a size of 305 mm × 305 mm × 50 mm, with a steel ball for impact loading at a diameter of 110 mm. The boundary conditions of the concrete model were set as a four-sided fixed support. The explicit dynamic analysis was performed,

and the results demonstrated that the cracks were formed in a critical orthogonal crack pattern with crack initiation and orientation at the middle of each side of the slab. The critical zones of the cracks on the model were presented in Figure 3(a).

The crack patterns from the low-velocity impact result obtained from the numerical simulation were used to determine the number of self-healing microcapsules as well as the distance or location of each self-healing microcapsules within the concrete slab specimens. The length of 305 mm was divided into two (152.5 mm) to identify the centre of the slab specimens as seen in Figure 3(b). Ten self-healing microcapsules, either large or small in size, were then placed in the slab specimens, where the distance

Table 2
Material properties form explicit dynamic analysis

Materials	Bulk Modulus, MPa	Density, kg/m^3
Structural steel (Steel ball)	25	7850
CONC-30MPA (Plain concrete)	30	2314

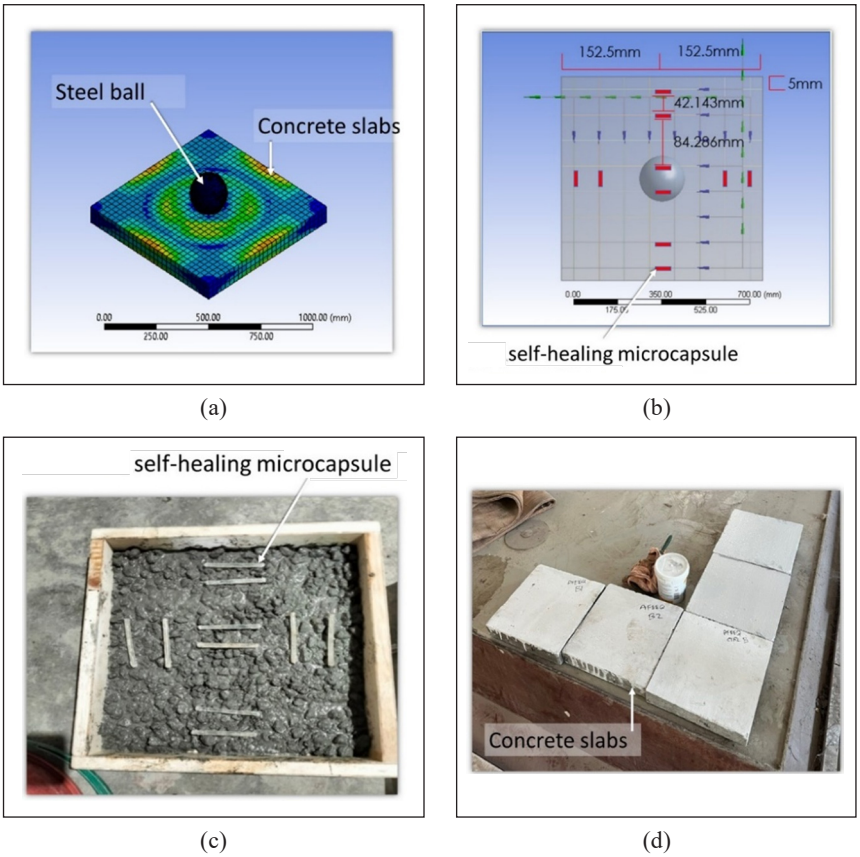

Figure 3. (a) The explicit dynamic analysis on the concrete slab model; (b) Schematic diagram of the microcapsule position; (c) Experimental arrangement layouts of self-healing microcapsules inside concrete slab specimens; and (d) Concrete slab specimens with white bottom surfaces

between each two microcapsules at the centre and each side of the specimens was 42.14 mm, excluding the 5mm concrete covers as seen in Figure 3(c). The distance between each segment location of self-healing microcapsules was 84.29 mm.

Mix Proportion Design of Concrete Slabs

The specimens of concrete slabs were prepared at the laboratory of the University Tenaga Nasional. The size of the concrete slab specimens prepared for the impact test is 305 mm × 305 mm × 50 mm, with specific arrangements of self-healing microcapsules. The mix proportion ofw the specimens was determined through the measurements in the Department of Environment (DOE) method and according to the BS 8500 standards (Azman et al., 2023; Jang et al., 2017). The mix ratio of the specimens is 1:1.7:2.9, which is designed to surpass the compressive strength at 30 MPa. The water/cement ratio of the concrete slab is 0.4. The weight of each material used to prepare a concrete slab is presented in Table 3. The curing condition for the prepared specimens is inside plain water at ambient temperature.

Table 3
Mix proportion of concrete slab specimens

OPC, kg	Fine Agg., kg	Coarse Agg., kg	Water, kg
1.86	3.14	5.42	0.82

Eight concrete slab specimens were cast, consisting of two controlled specimens (LC and SC), one large self-healing microcapsule with three repetitions denoted as L1, L2, and L3. On the other hand, one small self-healing microcapsule with three repetitions is denoted as S1, S2 and S3. The materials used are ordinary Portland cement (OPC), fine aggregates of sand, coarse aggregates of gravel, and a sufficient amount of water. The fine and coarse aggregates were sieved below 5 mm and between 9 and 12 mm, respectively (Jang et al., 2017).

The slump result achieved from the fresh concrete was 10 mm, which, according to the BS EN 12350–2 standards, proved to be a true slump with good workability (Zheng & Qian, 2020). The fresh concrete was then added into the formwork with a size of 305 mm × 305 mm × 50 mm, in the form of three layers and vibrated using the vibration machine to prevent air voids and specimen bleeding (Amran et al., 2022). A total of ten each for large and small microcapsules were added into the fresh mix at the first layer in an orthogonal arrangement, which replicated the crack pattern of the concrete slab in the simulation. Then, the second and third layers of fresh mix were poured consequently and left to harden for 24 hours. After the specimens were cured for 28 days, it was painted white on the bottom surface for ease of visibility of cracks as seen in Figure 3(d) (Huang & Zhou, 2022).

METHODOLOGY

Compressive Strength

The compressive strength was conducted to show that the formulation of the RC slab used in this study had the minimum compressive strength required according to BS EN 12390-3 standards (Hu et al., 2018). The compressive strength test was performed for all eight concrete cube specimens after 28 days of curing. The sizes of the cube specimens were prepared at 100 mm × 100 mm × 100 mm to surpass the compressive strength of 30 MPa, tested after 28 days of curing. A universal testing machine (UTM) conducted the compressive strength test. The dimensions and weight of the specimens were inserted into the UTM software, and the specimens were labelled. Then, the specimens were placed at the centre of the UTM machine, pushed and compressed with two opposite forces until they reached failure (Hu et al., 2018). Afterwards, the result of compressive strength of the specimens was recorded, as presented in Figure 4.

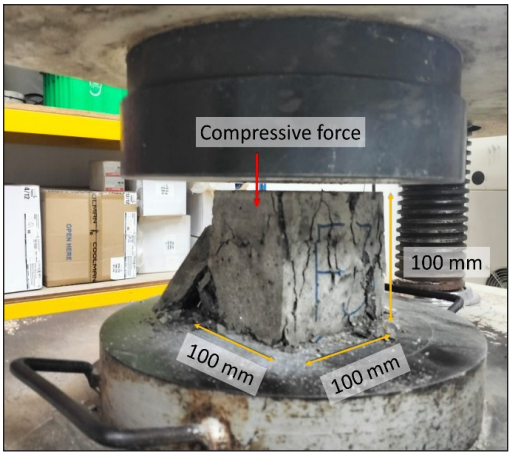

Figure 4. Cube compression test on a concrete cube specimen

Drop Weight

The drop weight test is a low-velocity impact test to measure the impact energy or impact resistance of an RC structure, especially the concrete slab specimens. The test is performed according to the BS EN 1621–1:1998 standards. Initially, 305 mm × 305 mm × 50 mm concrete specimens were placed on a flat stand and clamped at four-sided fixed supports using G-clamps. The stainless-steel ball impactor with a weight of 4 kg and a diameter of 110 mm was placed on top of the steel slide to free fall by gravity to hit the top surface of the concrete slab specimens. The height of the impactor from the top surface of the concrete slab was determined by using the formula of impact energy as presented in Equation 3.

$$E = N mgh \quad [3]$$

The energy, E, of the impact is obtained through the number of hits of the impactor, N, combined with mass, gravity and height, which are m, g and h, respectively. However, the calculation of the height, h, can be made by exclusion of the number of hits, N, as it is only used to evaluate the initial and ultimate cracks of the specimens while dividing it with the dimension of the specimens at 305 mm × 305 mm × 50 mm to create a correlation

measurement. The height of the impactor from the top surface of the concrete slab was approximately 175.24 mm. Later, the impactor was released once at a time, and the bottom surfaces of the specimens were observed for initial cracking until ultimate cracking occurred. The reduction of cracks in the specimens due to the efficiency rate of the self-healing microcapsules was observed and recorded day-to-day. The setup of the drop weight test is presented in Figure 5. Using a single impact location may not provide a comprehensive understanding of concrete self-healing performance as reflected in the real-life scenario. However, it offers valuable insights into how the concrete self-healing mechanism works when subjected to impact in this specific study.

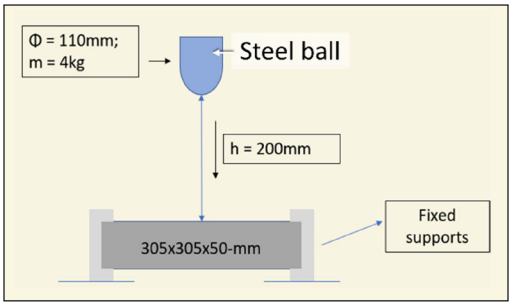

(a)

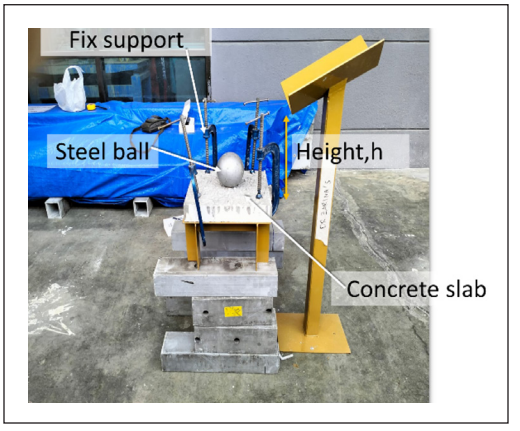

(b)

Figure 5. (a) The schematic; and (b) The setup of the drop weight test

RESULTS AND DISCUSSION

Compressive Strength

The compressive strength results demonstrated by eight concrete cube specimens were adequate for the industry's concrete structure, as they achieved results within the range of the compressive strength at 30 MPa. The failure patterns of the concrete cube specimens formed prism shapes, which followed the BS EN 12390-3 standards (Hu et al., 2018). Furthermore, the compressive strength obtained from the cube specimens was identical to the strength of the concrete slab specimens, as their fresh concrete mixture was cast together during the experiment (Qureshi & Al-Tabbaa, 2020; Wang et al., 2014). The compressive strength results were 33.68 MPa (S=5.23).

Low Velocity Impact of Concrete Slab with Self-Healing Microcapsules

The drop weight test was performed on two controlled concrete slabs, three with large self-healing microcapsules, and three with small self-healing microcapsules according to the BS EN 1621–1:1998 standards. The number of hits, N, from the stainless-steel ball impactor to the top surface of the concrete slab specimens was below twenty hits to obtain the ultimate cracks. Furthermore, the ultimate cracks obtained by eight concrete slab specimens do not exceed 2.5 mm, which is suitable for self-healing agents to seep

through the gaps and reduce the crack widths (Maddalena et al., 2021). The results of the impact test on the specimens, LC, L1, L2, L3, SC, S1, S2 and S3 are recorded in Tables 4, 5, 6 and 7, respectively.

Based on Tables 3 to 6, there were three points of crack widths on concrete slab specimens parallel to the location of the self-healing microcapsule that were recorded after each hit from the impactor in a weight drop test. The test results demonstrated that the concrete slab specimens with microcapsules can withstand more impact hits compared to the controlled concrete slab specimens. The maximum number of impact hits, N, obtained by the controlled concrete slabs, LC and SC, was nine hits. At the same time, the specimens with large and small self-healing microcapsules, L1, L2, L3 and S1, S2 and S3, received ultimate cracks after 19 hits, 16 hits, 11 hits and 14 hits, 10 hits and 12 hits, respectively. Furthermore, the average crack width displayed by the specimens LC, L1, L2, L3, SC, S1, S2 and S3 was 2.19 mm, 1.21 mm, 1.5 mm, 1.97 mm, 1.99 mm, 1.02 mm, 1.13 mm and 1.28 mm, respectively. The increment and comparison of the number of impacts on the specimens subjected to the drop weight test are presented in Figure 6.

Table 4
The low-velocity impact results of controlled concrete slab LC and L1 with large self-healing microcapsules

Weight drop test	**Controlled RC slab, LC**			**RC slabs with large self-healing microcapsules, L1**		
Points	**Point 1**	**Point 2**	**Point 3**	**Point 1**	**Point 2**	**Point 3**
No. of Impact, N	**Crack width, mm**	**Crack width, mm**	**Crack width, mm**	**Crack width, mm**	**Crack width, mm**	**Crack width, mm**
1	0	0	0	0	0	0
2	0	0	0	0	0	0
3	0	0	0	0	0	0
4	0	0	0	0	0	0
5	0	0	0	0	0	0
6	0.76	0.53	0.59	0	0	0
7	1.57	0.93	1.34	0	0	0
8	1.88	1.65	1.43	0	0	0
9	2.32	2.08	2.18	0	0	0
10				0	0	0
11				0.16	0.21	0.27
12				0.3	0.5	0.37
13				0.45	0.61	0.53
14				0.62	0.70	0.65
15				0.73	0.72	0.84
16				0.81	0.84	0.87
17				0.92	1.02	0.96
18				1.13	1.10	1.15
19				1.24	1.18	1.20

Table 5
The low-velocity impact results of concrete slabs L2 and L3 with large self-healing microcapsules

Weight drop test	RC slabs with large self-healing microcapsules, L2			RC slabs with large self-healing microcapsules, L3		
Points	Point 1	Point 2	Point 3	Point 1	Point 2	Point 3
No. of Impact, N	Crack width, mm	Crack width, mm	Crack width, mm	Crack width, mm	Crack width, mm	Crack width, mm
1	0	0	0	0	0	0
2	0	0	0	0	0	0
3	0	0	0	0	0	0
4	0	0	0	0	0	0
5	0	0	0	0	0	0
6	0	0	0	0	0	0
7	0	0	0	0.18	0.21	0.15
8	0	0	0	0.35	0.41	0.47
9	0	0	0	0.59	0.63	0.62
10	0.23	0.21	0.21	1.78	1.19	1.65
11	0.46	0.44	0.43	2	1.94	1.98
12	0.51	0.55	0.52			
13	0.66	0.70	0.64			
14	0.75	0.75	0.70			
15	1.03	0.97	0.99			
16	1.6	1.4	1.5			

Table 6
The low-velocity impact results of controlled concrete slabs SC and S1 with small self-healing microcapsules

Weight drop test	Controlled RC slab, SC			RC slabs with small self-healing microcapsules, S1		
Points	Point 1	Point 2	Point 3	Point 1	Point 2	Point 3
No. of Impact, N	Crack width, mm	Crack width, mm	Crack width, mm	Crack width, mm	Crack width, mm	Crack width, mm
1	0	0	0	0	0	0
2	0	0	0	0	0	0
3	0	0	0	0	0	0
4	0	0	0	0	0	0
5	0.14	0.13	0.17	0	0	0
6	0.36	0.23	0.31	0	0	0
7	0.75	0.71	0.72	0	0	0
8	1.69	1.43	1.6	0	0	0
9	2	2.04	1.93	0	0	0
10				0	0	0
11				0.14	0.09	0.11
12				0.43	0.38	0.42
13				0.76	0.74	0.68
14				1.07	0.97	1.03

Table 7
The low-velocity impact results of concrete slabs S2 and S3 with small self-healing microcapsules

Weight drop test	RC slabs with small self-healing microcapsules, S2			RC slabs with small self-healing microcapsules, S3		
Points	Point 1	Point 2	Point 3	Point 1	Point 2	Point 3
No. of Impact, N	Crack width, mm	Crack width, mm	Crack width, mm	Crack width, mm	Crack width, mm	Crack width, mm
1	0	0	0	0	0	0
2	0	0	0	0	0	0
3	0	0	0	0	0	0
4	0	0	0	0	0	0
5	0	0	0	0	0	0
6	0	0	0	0	0	0
7	0.29	0.23	0.25	0	0	0
8	0.57	0.62	0.6	0.36	0.37	0.32
9	0.75	0.83	0.86	0.6	0.43	0.5
10	1.17	1.09	1.12	0.84	0.79	0.91
11				1.19	1.02	1.14
12				1.32	1.21	1.31

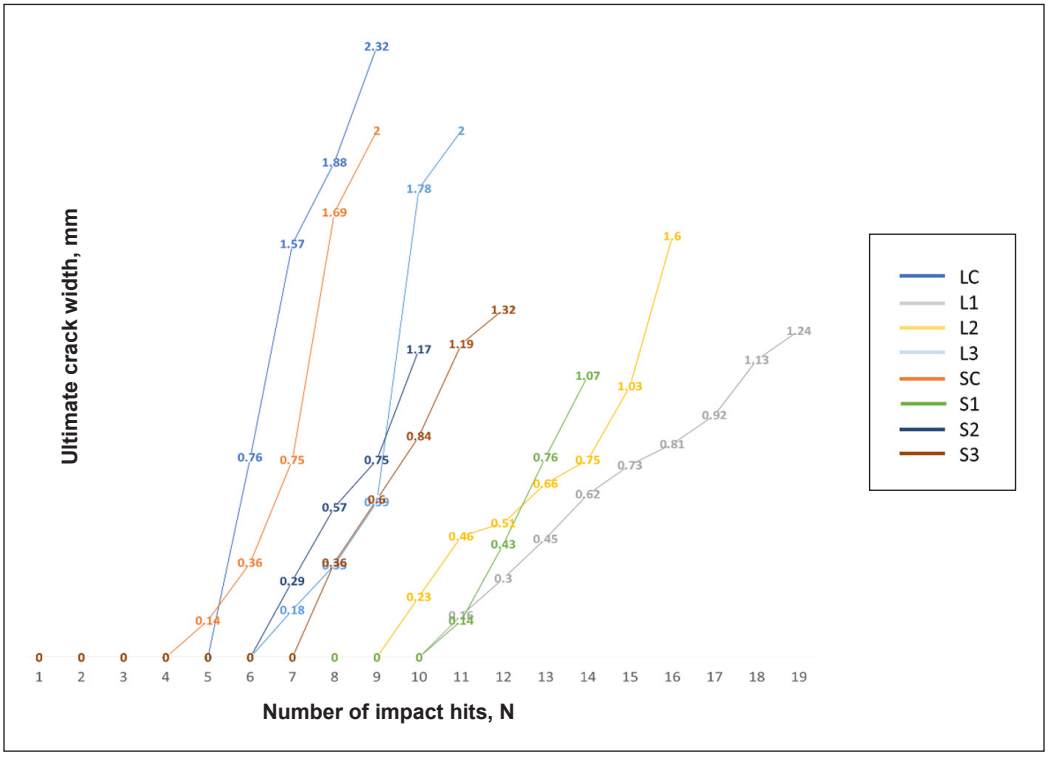

Figure 6. The number of impact hits on the concrete slab specimens

Based on Figure 6, the overall number of impact hits, N, received by the concrete slab specimens were systematic as its maximum hits was below the 50 hits which led to the structure prevented from obtained any severe defects such as spalling or delamination of steel reinforcement bars as according to BS EN 1992-2 standards (Frigo et al., 2017). The impact on specimen L1 was 10 hits more compared to specimen LC. Meanwhile, in terms of the highest number of impacts on the large and small self-healing microcapsules inside concrete slab specimens, the specimen L1 achieved more impact by five hits compared to the specimen S1. Though the specimens were similar in size, curing days and mix design, the hit numbers still varied, resulting from the small air voids or improper distribution of materials in the specimens (Raza et al., 2023).

The Efficiency of Crack Size Reductions on Concrete Slabs with Self-Healing Microcapsules

The ultimate crack widths that occurred on eight concrete slab specimens consisted of two controlled RC slabs, three R concrete slabs with large self-healing microcapsules and three concrete slabs with small self-healing microcapsules were varied in general due to the difference in number of low velocity impact hits, N. Overall, all specimens obtained self-healing process after the self-healing microcapsules that contained sodium silicate liquidation were released resulted from the breaking of the encapsulation from impact (Maddalena et al., 2021; Kahar et al., 2021). All specimens displayed an orthogonal crack pattern of length 152.5 mm from the centre of the specimens. The average reduction in the size of the crack width of specimens is presented in Table 8.

Based on Table 7, there are three main points of ultimate crack on specimens that displayed self-healing process, where the crack was above the location of the large and small self-healing microcapsules. The reduction of cracks at the three points mentioned for the specimens was measured and recorded as an average crack reduction in 28 days. The average crack reductions of specimens LC, L1, L2, L3, SC, S1, S2 and S3 were 2.19 mm, 0.28 mm, 0.36 mm, 0.42 mm, 1.99 mm, 0.99 mm, 1.07 mm and 1.25 mm, respectively. The average crack of specimens, L1, L2, L3, S1, S2 and S3 were reduced by 0.93 mm, 1.14 mm, 1.55 mm, 0.03 mm, 0.06 mm, and 0.03 mm from its original crack width of 1.21 mm, 1.5 mm, 1.97 mm, 1.02 mm, 1.13 mm and 1.28 mm, correspondingly. However, both the ultimate cracks on the controlled concrete slab specimens, LC and SC, have no self-healing process because of the absence of the large and small self-healing microcapsules. The visible crack reductions on the specimens L1, L2, L3, S1, S2, and S3 in 28 days were consistently fast due to the efficiency of the volume of sodium silicate liquidation reaction with the cementitious-based chemical inside the specimens, as presented in Table 9. The healing process is monitored from day one by circling the area of the crack. The circled area of the crack is checked daily, and the width of the crack is recorded using a microscope

Table 8
The size reduction of cracks on concrete slab specimens

Weight drop test		**The process of self-healing in days**									**Crack reduction, mm**
Specimens	**Points**	**1**	**3**	**5**	**7**	**11**	**14**	**18**	**21**	**28**	**Average**
Controlled, LC	Point 1	2.32	2.32	2.32	2.32	2.32	2.32	2.32	2.32	2.32	2.19
	Point 2	2.08	2.08	2.08	2.08	2.08	2.08	2.08	2.08	2.08	
	Point 3	2.18	2.18	2.18	2.18	2.18	2.18	2.18	2.18	2.18	
L1	Point 1	1.24	0.72	0.59	0.32	0.28	0.28	0.28	0.28	0.28	0.28
	Point 2	1.18	0.8	0.74	0.30	0.28	0.26	0.26	0.26	0.26	
	Point 3	1.20	0.7	0.62	0.36	0.31	0.31	0.31	0.31	0.31	
L2	Point 1	1.6	1.26	0.7	0.61	0.53	0.38	0.38	0.38	0.38	0.36
	Point 2	1.4	1.27	0.4	0.39	0.37	0.36	0.36	0.35	0.35	
	Point 3	1.5	1.19	0.68	0.61	0.43	0.43	0.43	0.38	0.37	
L3	Point 1	2	1.52	0.83	0.58	0.47	0.45	0.45	0.45	0.45	0.42
	Point 2	1.94	0.99	0.82	0.7	0.65	0.53	0.44	0.42	0.42	
	Point 3	1.98	1.65	1.25	1.03	1.03	0.74	0.53	0.41	0.4	
Controlled, SC	Point 1	2	2	2	2	2	2	2	2	2	1.99
	Point 2	2.04	2.04	2.04	2.04	2.04	2.04	2.04	2.04	2.04	
	Point 3	1.93	1.93	1.93	1.93	1.93	1.93	1.93	1.93	1.93	
S1	Point 1	1.07	1.07	1.05	1.05	1.04	1.04	1.04	1.04	1.04	0.99
	Point 2	0.97	0.96	0.95	0.95	0.95	0.94	0.94	0.94	0.94	
	Point 3	1.03	1.02	1.02	1	1	1	1	1	1	
S2	Point 1	1.17	1.15	1.15	1.14	1.14	1.14	1.14	1.14	1.14	1.07
	Point 2	1.09	1.07	1.07	1.07	1.07	1.06	1.06	1.06	1.06	
	Point 3	1.12	1.1	1.1	1.1	1.09	1.09	1.09	1.09	1.09	
S3	Point 1	1.32	1.32	1.3	1.3	1.3	1.3	1.3	1.3	1.3	1.25
	Point 2	1.21	1.20	1.19	1.17	1.17	1.17	1.17	1.17	1.17	
	Point 3	1.31	1.30	1.29	1.29	1.29	1.29	1.28	1.28	1.28	

at the laboratory. The width of the crack reduction from day one until the end of the 28th day is recorded.

Based on Table 8, all specimens besides the controlled specimens, LC and SC, obtained self-healing effectively and reduced the original ultimate cracks up to a certain width. The efficiency in the healing process was increased by 87.2%, 83.6% and 80.8% for the Specimens L1, L2 and L3 with the large self-healing microcapsules compared to their controlled specimens. Moreover, in comparison to the controlled specimen, the specimens S1, S2, and S3 with the small self-healing microcapsules displayed an increment in healing efficiency of 50.3%, 46.2%, and 37.2%, respectively. Hence, the efficiency difference between the specimens with large self-healing microcapsules and small self-healing microcapsules was 68.2%, where the large microcapsules contributed more to the self-healing of specimens compared to the small microcapsules.

Table 9
Concrete slab specimens with large and small self-healing microcapsules before and after the 28-day self-healing process

Specimens	Point 1	Point 2	Point 3
Specimen L1	Before: 1.24 mm	Before: 1.18 mm	Before: 1.20 mm
	After: 0.28 mm	After: 0.26 mm	After: 0.31 mm
Specimen L2	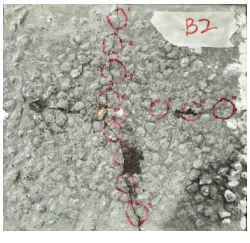 Before: 1.6 mm	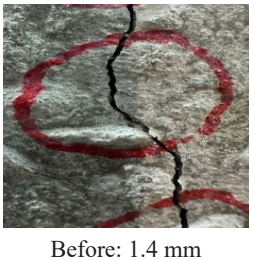 Before: 1.4 mm	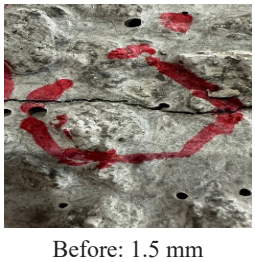 Before: 1.5 mm
	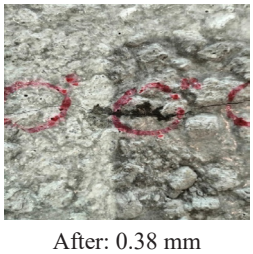 After: 0.38 mm	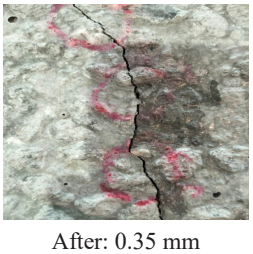 After: 0.35 mm	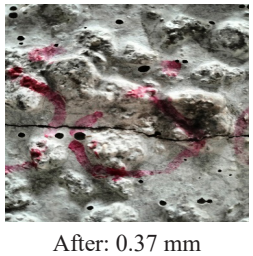 After: 0.37 mm
Specimen L3	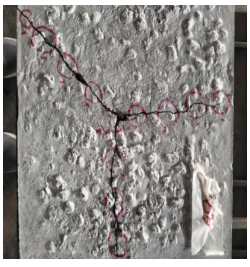 Before: 2 mm	Before: 1.94mm	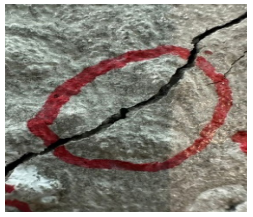 Before: 1.98 mm

Table 9 *(continue)*

Specimens	Point 1	Point 2	Point 3
	After: 0.45 mm	After: 0.42 mm	After: 0.4 mm
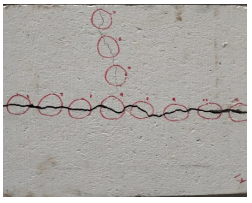 Specimen S1		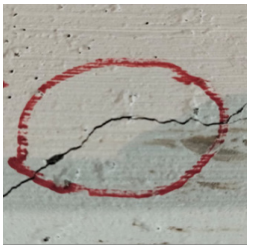	
	Before: 1.07 mm	Before: 0.97 mm	Before: 1.03 mm
	After: 1.04 mm	After: 0.94 mm	After: 1 mm
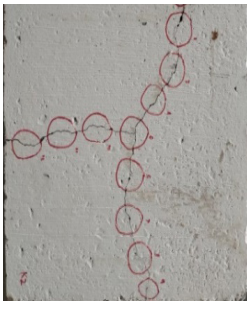 Specimen S2		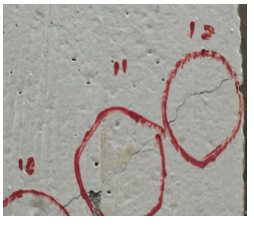	
	Before: 1.17 mm	Before: 1.09 mm	Before: 1.12 mm
	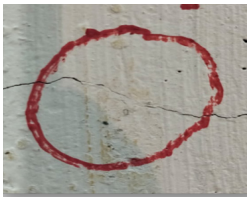	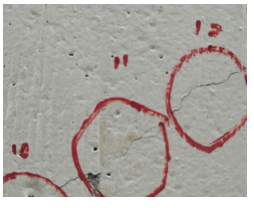	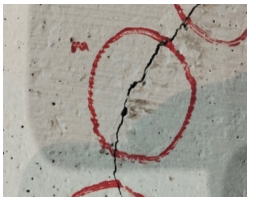
	After: 1.14 mm	After: 1.06 mm	After: 1.09 mm

Table 9 *(continue)*

Specimens	Point 1	Point 2	Point 3
Specimen S3	Before: 1.32 mm	Before: 1.21 mm	Before: 1.31 mm
	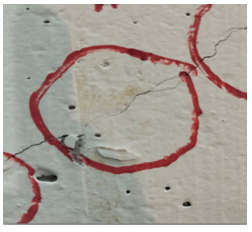 After: 1.3 mm	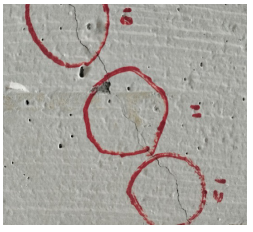 After: 1.17 mm	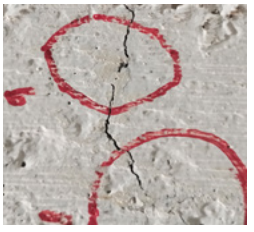 After: 1.28 mm

The crack widths dominant at specimens L1, L2 and L3, demonstrated that the larger size of the self-healing microcapsules resulted in the RC slab becoming slightly fragile due to the volume of PLA and PMMA materials consuming space in the specimens, with their low tensile break points (Ridwan et al., 2017). However, the sodium silicate liquidation inside the self-healing microcapsules compromised the strength loss and managed to repair the cracks from inside to outside of the ultimate cracks on the specimens, as the volume and spread radius of the liquidation were within the critical zones of the specimens (Sabee et al., 2022). Furthermore, the process of self-healing in specimens S1, S2 and S3 was slow and less so due to the volume of sodium silicate liquidation in the small self-healing microcapsules, which can only occupy a small range of crack gaps from their encapsulation sources (Muda et al., 2016; Kahar et al., 2021).

CONCLUSION

The research on the efficiency of the self-healing microcapsules in concrete slab specimens subjected to low velocity impact force was successful in 28 days. The maximum number of impact hits, N, obtained by the controlled concrete slabs, LC and SC, was nine hits. At the same time, the specimens with large and small self-healing microcapsules, L1, L2, L3 and S1, S2 and S3, received ultimate cracks after 19 hits, 16 hits, 11 hits and 14 hits,

10 hits and 12 hits, respectively. The highest and lowest impact hits for specimens with self-healing microcapsules were obtained by specimens L1 and S2, with 19 hits and 10 hits, respectively. Furthermore, the average crack width displayed by the specimens LC, L1, L2, L3, SC, S1, S2 and S3 was 2.19 mm, 1.21 mm, 1.5 mm, 1.97 mm, 1.99 mm, 1.02 mm, 1.13 mm and 1.28 mm, respectively. The results demonstrated that the concrete slab specimens with microcapsules can endure more impact hits compared to the controlled concrete slab specimens. Though the specimens were similar in size, curing days and mix design, the hit numbers still varied, resulting from the small air voids or improper distribution of materials in the specimens.

In terms of the reduction of crack width, the average crack of specimens, L1, L2, L3, S1, S2 and S3 were reduced by 0.93 mm, 1.14 mm, 1.55 mm, 0.03 mm, 0.06 mm and 0.03 mm from its original crack width of 1.21 mm, 1.5 mm, 1.97 mm, 1.02 mm, 1.13 mm and 1.28 mm, correspondingly. Moreover, the ultimate cracks of eight concrete slab specimens do not exceed 2.5 mm, which is suitable for self-healing agents, such as sodium silicate liquidation, to seep through the crack gaps and reduce their width. The efficiency in the healing process was increased by 87.2%, 83.6% and 80.8% for specimens L1, L2, and L3 with the large self-healing microcapsules compared to their controlled specimens. In comparison to the controlled specimen, the specimens S1, S2, and S3 with the small self-healing microcapsules displayed an increment in healing efficiency of 50.3%, 46.2%, and 37.2%, respectively. As a whole, the materials of PLA and PMMA with low tensile properties to break point dominated the concrete slab specimens' volume, thus leading to the crack widths on specimens like specimen LC to be larger than the ultimate crack. The larger size of the self-healing microcapsules led to a slight fragility in specimens. Nevertheless, self-healing microcapsules containing sodium silicate liquidation dealt with the strength loss and repaired the overall ultimate cracks on the specimens.

FUTURE RESEARCH DIRECTION

The future research direction of the work could explore the development of a hybrid triggering mechanism (e.g., mechanical/thermal) of self-healing concrete subjected to high-velocity impact. Besides that, looking into the performance of recycled/reused concrete material promotes sustainable construction practices (Ahmad & Shokouhian, 2024; Akor et al., 2023; Gao, 2023). Machine learning models (e.g., gene expression programming) can help broaden the parameters of the investigation, reducing the cost and time of the investigation and resulting in better data accuracy (Inqiad et al., 2023).

ACKNOWLEDGEMENT

The authors express gratitude to the Innovation & Research Management Centre of Universiti Tenaga Nasional for supporting this research through Project No: BOLD 2022

J510050002/2022024, facilities support from Universiti Sains Malaysia, UNITEN Civil Engineering Laboratory, J510050002/HICOE05 for the journal publication fees and BOLD Refresh Postdoctoral Fellowships under Grant J510050002-IC-6 BOLDREFRESH2025-Centre of Excellence.

REFERENCES

Ahmad, I., & Shokouhian, M. (2024). Promoting sustainable green infrastructure: Experimental and numerical investigation of concrete reinforced with recycled steel fibers. *Archives of Advanced Engineering Science, 3*(1), 1-13. https://doi.org/10.47852/bonviewAAES42022837

Akor, J., Onjefu, L., Edeh, J., & Olubambi, A. (2023). Suitability of crushed sandcrete block (CSB) as a partial replacement for fine aggregate in concrete structures. *Archives of Advanced Engineering Science, 3*(1), 1-9. https://doi.org/10.47852/bonviewAAES32021741

Althoey, F., Zaid, O., Arbili, M. M., Martínez-García, R., Alhamami, A., Shah, H. A., & Yosri, A. M. (2023). Physical, strength, durability and microstructural analysis of self-healing concrete: A systematic review. *Case Studies in Construction Materials*, *18*, Article e01730. https://doi.org/10.1016/j.cscm.2022.e01730

Amran, M., Onaizi, A. M., Fediuk, R., Vatin, N. I., Rashid, R. S. M., Abdelgader, H., & Ozbakkaloglu, T. (2022). Self-healing concrete as a prospective construction material: A review. *Materials*, *15*(9), Article 3214. https://doi.org/10.3390/ma15093214

Azman, N. A., Syamsir, A., Bakar, M. S. A., Rizal, M. A. M., Sanusi, K. A., & Abdullah, M. J. (2023). The characteristics of polymer concrete reinforced with polypropylene fibres under axial and lateral compression loads. *Pertanika Journal of Science and Technology*, *31*(3), 1535 - 1554. https://doi.org/10.47836/pjst.31.3.23

Dixit, A. C., Achutha, M. V., & Sridhara, B. K. (2021). Elastic properties of aluminum boron carbide metal matrix composites. *Materials Today: Proceedings*, *43*, 1253–1257. https://doi.org/10.1016/j.matpr.2020.08.766

Durga, C. S. S., Ruben, N., Chand, M. S. R., Indira, M., & Venkatesh, C. (2021). Comprehensive microbiological studies on screening bacteria for self-healing concrete. *Materialia*, *15*, Article 101051. https://doi.org/10.1016/j.mtla.2021.101051

Ferrara, L., Van Mullem, T., Alonso, M. C., Antonaci, P., Borg, R. P., Cuenca, E., Jefferson, A., Ng, P. L., Peled, A., Roig-Flores, M., Sanchez, M., Schroefl, C., Serna, P., Snoeck, D., Tulliani, J. M., & De Belie, N. (2018). Experimental characterization of the self-healing capacity of cement-based materials and its effects on the material performance: A state of the art report by COST Action SARCOS WG2. *Construction and Building Materials*, *167*, 115–142. https://doi.org/10.1016/j.conbuildmat.2018.01.143

Frigo, B., Fantilli, A. P., & Chiaia, B. (2017). Size effect on fracture toughness of snow. *Procedia Structural Integrity*, *3*, 261–268. https://doi.org/10.1016/j.prostr.2017.04.028

Gao, J., Jin, P., Zhang, Y., Dong, H., & Wang, R. (2022). Fast-responsive capsule based on two soluble components for self-healing concrete. *Cement and Concrete Composites*, *133*, Article 104711. https://doi.org/10.1016/j.cemconcomp.2022.104711

Gao, X. (2023). Review: Development trends in the reuse of waste materials in concrete production. *Academic Journal of Science and Technology*, *8*(2), 26–30. https://doi.org/10.54097/ajst.v8i2.14714

Gupta, S., Pang, S. D., & Kua, H. W. (2017). Autonomous healing in concrete by bio-based healing agents – A review. *Construction and Building Materials*, *146*, 419–428. https://doi.org/10.1016/j.conbuildmat.2017.04.111

Hilloulin, B., Van Tittelboom, K., Gruyaert, E., De Belie, N., & Loukili, A. (2015). Design of polymeric capsules for self-healing concrete. *Cement and Concrete Composites*, *55*, 298–307. https://doi.org/10.1016/j.cemconcomp.2014.09.022

Homma, D., Mihashi, H., & Nishiwaki, T. (2009). Self-healing capability of fibre reinforced cementitious composites. *Journal of Advanced Concrete Technology, 7*(2), 217–228. https://doi.org/10.3151/jact.7.217

Hu, Z. X., Hu, X. M., Cheng, W. M., Zhao, Y. Y., & Wu, M. Y. (2018). Performance optimization of one-component polyurethane healing agent for self-healing concrete. *Construction and Building Materials*, *179*, 151–159. https://doi.org/10.1016/j.conbuildmat.2018.05.199

Huang, F., & Zhou, S. (2022). A review of lightweight self-healing concrete. *Materials*, *15*(21), Article 7572. https://doi.org/10.3390/ma15217572

Inqiad, W., Raza, M. A., & Asim, M. (2023). Predicting 28-day compressive strength of self-compacting concrete (SCC) using gene expression programming (GEP). *Archives of Advanced Engineering Science, 3*(1), 1-13. https://doi.org/10.47852/bonviewAAES32021606

Irico, S., Bovio, A. G., Paul, G., Boccaleri, E., Gastaldi, D., Marchese, L., Buzzi, L., & Canonico, F. (2017). A solid-state NMR and X-ray powder diffraction investigation of the binding mechanism for self-healing cementitious materials design: The assessment of the reactivity of sodium silicate based systems. *Cement and Concrete Composites*, *76*, 57–63. https://doi.org/10.1016/j.cemconcomp.2016.11.006

Jakubovskis, R., Jankutė, A., Urbonavičius, J., & Gribniak, V. (2020). Analysis of mechanical performance and durability of self-healing biological concrete. *Construction and Building Materials*, *260*, Article 119822. https://doi.org/10.1016/j.conbuildmat.2020.119822

Jang, H. O., Lee, H. S., Cho, K., & Kim, J. (2017). Experimental study on shear performance of plain construction joints integrated with ultra-high performance concrete (UHPC). *Construction and Building Materials*, *152*, 16–23. https://doi.org/10.1016/j.conbuildmat.2017.06.156

Jogi, P. K., & Lakshmi, T. V. S. V. (2021). Self healing concrete based on different bacteria: A review. *Materials Today: Proceedings*, *43*, 1246–1252. https://doi.org/10.1016/j.matpr.2020.08.765

Kahar, N. N. F. N. M. N., Osman, A. F., Alosime, E., Arsat, N., Azman, N. A. M., Syamsir, A., Itam, Z., & Hamid, Z. A. A. (2021). The versatility of polymeric materials as self-healing agents for various types of applications: A review. *Polymers*, *13*(8), Article 1194. https://doi.org/10.3390/polym13081194

Khaliq, W., & Ehsan, M. B. (2016). Crack healing in concrete using various bio influenced self-healing techniques. *Construction and Building Materials*, *102*, 349–357. https://doi.org/10.1016/j.conbuildmat.2015.11.006

Li, J., & Guan, X. (2023). Pretreated lightweight aggregates for self-healing concrete exposed to calcium hydroxide-rich sewage. *Construction and Building Materials*, *365*, Article 130117. https://doi.org/10.1016/j.conbuildmat.2022.130117

Lv, L., Guo, P., Liu, G., Han, N., & Xing, F. (2020). Light induced self-healing in concrete using novel cementitious capsules containing UV curable adhesive. *Cement and Concrete Composites*, *105*, Article 103445. https://doi.org/10.1016/j.cemconcomp.2019.103445

Lv, Z., Yao, J., Cui, G., & Chen, H. (2022). Geometrical probability of a capsule hitting irregular crack networks: Application to capsule-based self-healing materials. *Applied Mathematical Modelling*, *101*, 406–419. https://doi.org/10.1016/j.apm.2021.08.031

Maddalena, R., Taha, H., & Gardner, D. (2021). Self-healing potential of supplementary cementitious materials in cement mortars: Sorptivity and pore structure. *Developments in the Built Environment*, *6*, Article 100044. https://doi.org/10.1016/j.dibe.2021.100044

Mir, N., Khan, S. A., Kul, A., Sahin, O., Ozcelikci, E., Sahmaran, M., & Koc, M. (2023). Construction and demolition waste-based self-healing geopolymer composites for the built environment: An environmental profile assessment and optimization. *Construction and Building Materials*, *369*, Article 130520. https://doi.org/10.1016/j.conbuildmat.2023.130520

Mokhtar, N., & Hassan, M. F. M. (2021). Performance of sodium silicate as self-healing agent on concrete properties: A review. *IOP Conference Series: Materials Science and Engineering*, *1144*(1), Article 012024. https://doi.org/10.1088/1757-899X/1144/1/012024

Muda, Z. C., Kamal, N. L. M., Syamsir, A., Sheng, C. Y., Beddu, S., Mustapha, K. N., Thiruchelvam, S., Usman, F., Alam, M. A., Birima, A. H., & Zaroog, O. S. (2016). Impact resistance performance of kenaf fibre reinforced concrete. *IOP Conference Series: Earth and Environmental Science*, *32*, Article 012019. https://doi.org/10.1088/1755-1315/32/1/012019

Muhammad, N. Z., Shafaghat, A., Keyvanfar, A., Majid, M. Z. A., Ghoshal, S. K., Yasouj, S. E. M., Ganiyu, A. A., Kouchaksaraei, M. S., Kamyab, H., Taheri, M. M., Shirdar, M. R., & McCaffer, R. (2016). Tests and methods of evaluating the self-healing efficiency of concrete: A review. *Construction and Building Materials*, *112*, 1123–1132. https://doi.org/10.1016/j.conbuildmat.2016.03.017

Qureshi, T., & Al-Tabbaa, A. (2020). Self-healing concrete and cementitious materials. In N. Tasaltin, P. S. Nnamchi & S. Saud (Eds.), *Advanced Functional Materials* (pp. 191-214). IntechOpen. https://doi.org/10.5772/intechopen.92349

Raza, A., El Ouni, M. H., uz Zaman Khan, Q., Azab, M., Khan, D., Elhadi, K. M., & Alashker, Y. (2023). Sustainability assessment, structural performance and challenges of self-healing bio-mineralized concrete: A systematic review for built environment applications. *Journal of Building Engineering*, *66*, Article 105839. https://doi.org/10.1016/j.jobe.2023.105839

Ren, J., Wang, X., Li, D., Han, N., Dong, B., & Xing, F. (2021). Temperature adaptive microcapsules for self-healing cementitious materials. *Composites Part B: Engineering*, *223*, Article 109138. https://doi.org/10.1016/j.compositesb.2021.109138

Restuccia, L., Reggio, A., Ferro, G. A., & Tulliani, J. M. (2017). New self-healing techniques for cement-based materials. *Procedia Structural Integrity*, *3*, 253–260. https://doi.org/10.1016/j.prostr.2017.04.016

Ridwan, M., Yoshitake, I., & Nassif, A. Y. (2017). Two-dimensional fictitious truss method for estimation of out-of-plane strength of masonry walls. *Construction and Building Materials*, *152*, 24–38. https://doi.org/10.1016/j.conbuildmat.2017.06.138

Rosewitz, J. A., Wang, S., Scarlata, S. F., & Rahbar, N. (2021). An enzymatic self-healing cementitious material. *Applied Materials Today*, *23*, Article 101035. https://doi.org/10.1016/j.apmt.2021.101035

Sabee, M. M. S. M., Itam, Z., Beddu, S., Zahari, N. M., Kamal, N. L. M., Mohamad, D., Zulkepli, N. A., Shafiq, M. D., & Hamid, Z. A. A. (2022). Flame retardant coatings: Additives, binders, and fillers. *Polymers*, *14*(14), Article 2911. https://doi.org/10.3390/polym14142911

Van Tittelboom, K., De Belie, N., Van Loo, D., & Jacobs, P. (2011). Self-healing efficiency of cementitious materials containing tubular capsules filled with healing agent. *Cement and Concrete Composites*, *33*(4), 497–505. https://doi.org/10.1016/j.cemconcomp.2011.01.004

Vijay, K., Murmu, M., & Deo, S. V. (2017). Bacteria based self healing concrete – A review. *Construction and Building Materials*, *152*, 1008–1014. https://doi.org/10.1016/j.conbuildmat.2017.07.040

Wang, J. Y., Soens, H., Verstraete, W., & De Belie, N. (2014). Self-healing concrete by use of microencapsulated bacterial spores. *Cement and Concrete Research*, *56*, 139–152. https://doi.org/10.1016/j.cemconres.2013.11.009

Xiong, W., Tang, J., Zhu, G., Han, N., Schlangen, E., Dong, B., Wang, X., & Xing, F. (2015). A novel capsule-based self-recovery system with a chloride ion trigger. *Scientific Reports*, *5*(1), Article 10866. https://doi.org/10.1038/srep10866

Yıldırım, G., Şahmaran, M., & Anıl, Ö. (2018). Engineered cementitious composites-based concrete. In F. Pacheco-Torgal, R. E. Melchers, X. Shi, N. De Belie, K. Van Tittelboom & A. Sáez (Eds.), *Eco-Efficient Repair and Rehabilitation of Concrete Infrastructures* (pp. 387–427). Elsevier. https://doi.org/10.1016/B978-0-08-102181-1.00015-0

Zhang, W., Zheng, Q., Ashour, A., & Han, B. (2020). Self-healing cement concrete composites for resilient infrastructures: A review. *Composites Part B: Engineering*, *189*, Article 107892. https://doi.org/10.1016/j.compositesb.2020.107892

Zheng, T., & Qian, C. (2020). Influencing factors and formation mechanism of $CaCO_3$ precipitation induced by microbial carbonic anhydrase. *Process Biochemistry*, *91*, 271–281. https://doi.org/10.1016/j.procbio.2019.12.018

Pertanika J. Sci. & Technol. 33 (4): 1707 - 1741 (2025)

PERTANIKA JOURNALS

SCIENCE & TECHNOLOGY

Journal homepage: http://www.pertanika.upm.edu.my/

Review Article

MXene as a Microstructural Modifier in Solar Thermal Absorber: A Review

Mannir Ibrahim Tarno[1,2], Azmah Hanim Mohamed Ariff[1,3]*, Suraya Mohd Tahir[1] and Che Nor Aiza Jaafar[1]

[1]*Department of Mechanical and Manufacturing Engineering, Faculty of Engineering, Universiti Putra Malaysia, 43400 UPM Serdang, Selangor, Malaysia*

[2]*Department of Mechanical Engineering, Faculty of Engineering, Usmanu Danfodiyo University, Sokoto, Sokoto State, Nigeria*

[3]*Advanced Engineering Materials and Composites Research Center, (AEMC), Faculty of Engineering, Universiti Putra Malaysia, 43400 UPM Serdang, Selangor, Malaysia*

ABSTRACT

Solar thermal systems enhance wastewater treatment efficiency, preservation, and processing of agricultural produce, facilitating industrial/domestic heating and cooling. They provide cost-effective, green energy harvesting, storage, and conversion. However, the efficiency and durability of those devices largely depend on the quality of their absorbing medium. Hence, researchers channeled their focus toward enhancing their performance. This prompted the use of MXene for microstructural modification of solar thermal absorbers. MXene has shown outstanding photothermal conversion characteristics and excellent stability in strong alkaline and acidic solutions. Yet, recent literature reported lower efficiency in solar thermal systems. This review focuses on the latest microstructural modifications of the solar thermal absorber with MXene as a microstructural modifier, as well as their influence on thermal conductivity, strength, photothermal conversion, and corrosion characteristics. The study aims to find the root of the basic challenges in solar thermal systems (STSs) and to create opportunities for integration, processing, and manufacturing of a large and rapidly expanding family of STSs with improved characteristics and reliability in service. Previous studies reveal that the integration of 0.1 wt.%–7.5 wt.% MXene as a microstructural modifier significantly improved the thermal and corrosion properties in solar thermal systems employing nanofluids, phase-changing materials, and coatings. However, it is worth mentioning that there is no significant literature on the fabrication of MXene-reinforced metal matrix composites for solar thermal

ARTICLE INFO

Article history:
Received: 08 August 2024
Accepted: 07 March 2025
Published: 11 June 2025

DOI: https://doi.org/10.47836/pjst.33.4.02

E-mail addresses:
mannir.ibrahim@udusok.edu.ng; gs66745@student.upm.my (Mannir Ibrahim Tarno)
azmah@upm.edu.my (Azmah Hanim Mohamed Ariff)
su_mtahir@upm.edu.my (Suraya Mohd Tahir)
cnaiza@upm.edu.my (Che Nor Aiza Jaafar)
* Corresponding author

e-ISSN: 2231-8526

© Universiti Putra Malaysia Press

absorbers. The study highlights the benefits of powder metallurgy in fabricating MXene-reinforced metallic solar thermal absorbers and suggests exploring the potential of MXene in this previously unexplored area.

Keywords: Corrosion behavior, mechanical properties, microstructural modification, MXene, photothermal conversion, solar thermal absorber, solar thermal systems, thermal conductivity

INTRODUCTION

Solar thermal systems (STSs) increase energy efficiency and help in improving environmental factors that impact human health. They are basic for both life and environmental sustenance. STSs' affordability, sustainability, and pollution-free sources of energy make them novel and renewable solutions for agricultural, domestic, and industrial heating and cooling applications. Al-Mamun et al. (2023) emphasized that one of the most practical uses of solar energy, which is a readily available, affordable, and ecologically harmless energy source to meet global energy demands, is the solar thermal system. However, recent studies of STSs revealed lower efficiency (Bogdanovics et al., 2024; Goel et al., 2023). According to García-Segura et al. (2021), erosion and corrosion were recognized as the main issues in solar stills. The study further identified 16 types of degradation in solar reflectors for Concentrated Solar Thermal (CST) systems and attributed the defects to the synergistic relationship with their environmental agents. Tarno, Masuri, Ariff and Musa (2024) reported that during their operational sequences, solar absorbers were confronted with many challenges, such as the risk of atmospheric attack, thermal fatigue, and cracks resulting in failure (Figure 1).

Xu et al., (2025) studied a novel solar absorber design using a three-layer periodic structure of T_i-Al_2O_3-T_i circular composites on a T_i-Al_2O_3 substrate, achieving the highest solar absorption (average >97.8%, minimum >90%) across a broad spectrum (240 nm to 3354 nm) with high thermal stability, However, while the design demonstrates significant potential for solar energy applications, its reliance on precise periodic structures may pose fabrication complexity and material cost, which could impact large-scale manufacturing. Ali et al. (2024) investigated graphene-based solar absorber structure and concluded that it can be efficiently used for harvesting solar energy. Dumka et al. (2024) enhanced solar still performance by integrating wax-filled rods and reported a 6.3% reduction in distillate production costs. Bady et al. (2024) modified and investigated solar distillers that utilize copper tubes filled with PCM are highly beneficial. Nie et al. (2024) improved the mechanical properties of Al by introducing Cu reinforcement. The study revealed that Copper (Cu) atoms diffuse into aluminum (Al) particles during the PM process, filling the gaps in the Al particles and strengthening their interfacial bond. The improvement of the alloy's mechanical characteristics is another benefit of the $CuAl_2$ phase's development. The materials were recommended for applications in the aerospace industry as well as in the automotive industry. Suraparaju et

Figure 1. (a) Corroded absorber in a solar dryer; (b) Corroded solar dryer; (c) Corroded absorber in a solar still; and (d) Corroded absorber solar still. Pictures taken from Sokoto Energy Research Centre, Usmanu Danfodiyo University, Sokoto, Nigeria

al. (2025) investigate the combination of nanoparticle-infused composite energy storage materials with a unique double-finned absorber in a single-slope solar still. The finding reveals that coal nanoparticles combined with paraffin wax increase thermal conductivity by 52.61% at optimal concentration. The double-finned absorber improves thermal distribution by increasing surface area for heat absorption, resulting in a 123% increase in distillate yield, peak absorber temperatures of 68°C, and thermal efficiency rising to 51.38%.

The systems continue to face challenges of low efficiency (Fayaz, et al., 2022; Thakur et al., 2022). These challenges prompted the integration of MXene as a microstructural modifier in solar thermal absorbers (Alhamada et al., 2022; Aslfattahi et al., 2020, 2021; El Hadi Attia et al., 2023; Mao et al., 2022; Panda et al., 2024; Singh et al., 2023; Solangi et al., 2022; Thakur et al., 2022; Zhao et al., 2023; Y. Zhou et al., 2024). This was due to MXene's transparency, plasmonic behavior, and the nature of its high surface and tunable area due to its layered structure, strong chemical bonding, and tunable surface chemistry. MXene, as a family member of the two-dimensional (2D) materials, mainly carbides, nitrides, and carbonatites of transition metal, has shown outstanding photothermal conversion characteristics and demonstrated excellent stability in both strong alkaline and acidic solutions.

This study has been conducted through a comprehensive review of academic literature and presents a review of the latest microstructural modifications of the absorbers in STSs

with MXene as an absorber modifier, as well as their influence on thermal conductivity, photothermal conversion, corrosion characteristics, and behaviors under the action of mechanical loading. This paper identifies the most suitable types of materials for solar thermal absorbers and their manufacturing processes and discusses their disadvantages and implications. Scientific contributions to the development of MXene-reinforced aluminum solar-thermal absorbers with the optimal microstructure were offered to promote the efficiency of STSs and unlock the potential of MXene that had hitherto remained closed. Thus, the need for a better and wider understanding of the impact of MXene on the basic qualities of solar thermal absorbers in STSs at certain mechanical and thermal loadings, as well as its corrosive and atmospheric stabilities, prompted this study.

TYPES OF SOLAR THERMAL SYSTEMS

STSs absorb and convert electromagnetic radiation released from the sun into heat, which is regarded as solar thermal energy, and are used to directly heat fluid (Tarno, Masuri, Ariff, & Musa, 2024). Another option is to cause the movement of electrons in a conducting material, which is referred to as a photovoltaic system (Kalidasan et al., 2024). Absorber is the fundamental component of STSs that directly absorbs the electromagnetic radiation from the sun and converts it to thermal energy. In solar thermal systems, the principles lie in exposing the surface of a dark thermal conducting material to the electromagnetic radiation of sunlight. This resulted in the absorption of radiation and its conversion into thermal energy. The energy is transferred to a medium, usually water or air, for utilization. Figure 2 demonstrates common solar energy utilization.

STSs may be active systems or passive types. Active solar systems have moving parts or sophisticated electronic packages, such as automatic sun tracking systems attached. The solar thermal absorber is the specific part of the collector that directly absorbs solar energy and produces heat, frequently using an absorber plate with a unique coating. Passive solar systems use thermal mass as a heat-preserving substance in conjunction with natural absorption techniques to reduce solar radiation. When no optical concentration design is incorporated in an STS, the system is a non-concentrating solar thermal collector (STC) and can achieve a temperature range of 60°C to 80°C. When temperatures higher than 80°C are needed, the radiation should be concentrated (Vahidhosseini et al., 2024). Figure 3 shows a solar still incorporated with mirror solar radiation concentration (Figure 3a) and a non-concentrating solar dryer (Figure 3b).

The absorber, the central component of all solar collectors, captures sunlight, converts it into heat as efficiently as possible, and transfers it to a circulating fluid with the least heat loss. The efficiency of every solar thermal system depends on the quality of its absorbing unit. However, geometrical qualities such as thickness, surface area exposed to the sun, density, material type, manufacturing, and finishing processes of the absorber all affect

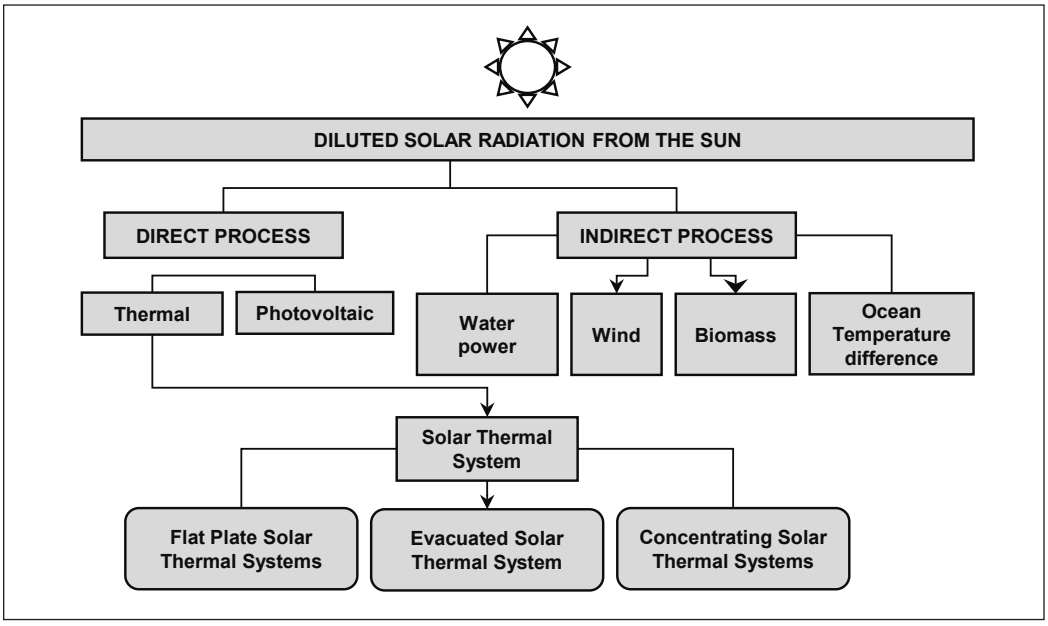

Figure 2. Solar thermal energy for major industrial, agricultural, and domestic utilizations

Figure 3. Concentrating and non-concentrating STSs (a) Concentrating solar still; (b) non-concentrating solar dryer; (c) hybrid solar dryer, and (d) non-concentrating evacuated solar water heater. Pictures taken from Sokoto Energy Research Centre, Usmanu Danfodiyo University, Sokoto, Nigeria

absorbance. Solar energy concentrators employ accessories such as mirrors, lenses, or parabolic surface reflectors to direct and concentrate sunlight into the absorbing material. Typically, the working fluid, such as water, air, nano-enriched water, or synthetic oil, is passed through the receiver tube. To reduce heat losses and achieve higher temperatures than a non-concentrating collector. An image concentrator concentrates STSs to focus and direct sunlight onto a small absorbing area. A hybrid STS, as shown in Figure 3(c), comprises a solar panel performing two functions: an external thermal absorber and a direct current electricity source for supplying an electric inverter, which provides current to a circuit containing a resistor for heat generation and to an electric motor for air blowing. Evacuated STSs, as shown in Figure 3(d), have highly efficient insulation due to their vacuum.

This vacuum significantly reduces heat loss, enabling these collectors to effectively capture and retain solar energy. The evacuated collectors utilize an inner metallic heat pipe or U-tube, as shown in Figure 3(d). The heat pipe absorbs and transfers the heat to a heat exchanger, which converts it to energy and transfers it to a working fluid circulating throughout the solar system. They consist of glass tubes with double walls coated with a unique substance with a low thermal emittance and a high solar absorbance. The vacuum created serves as a better insulator. Thermal applications are based on the constructional features, working principles, and operational sequences of thermal systems. Figure 4 depicts the major applications of STSs.

However, being exposed to an atmosphere, evacuated tubes (STSs) could be affected by weather cycles such as seasons and day-night frequencies. El-Fakharany et al. (2024)

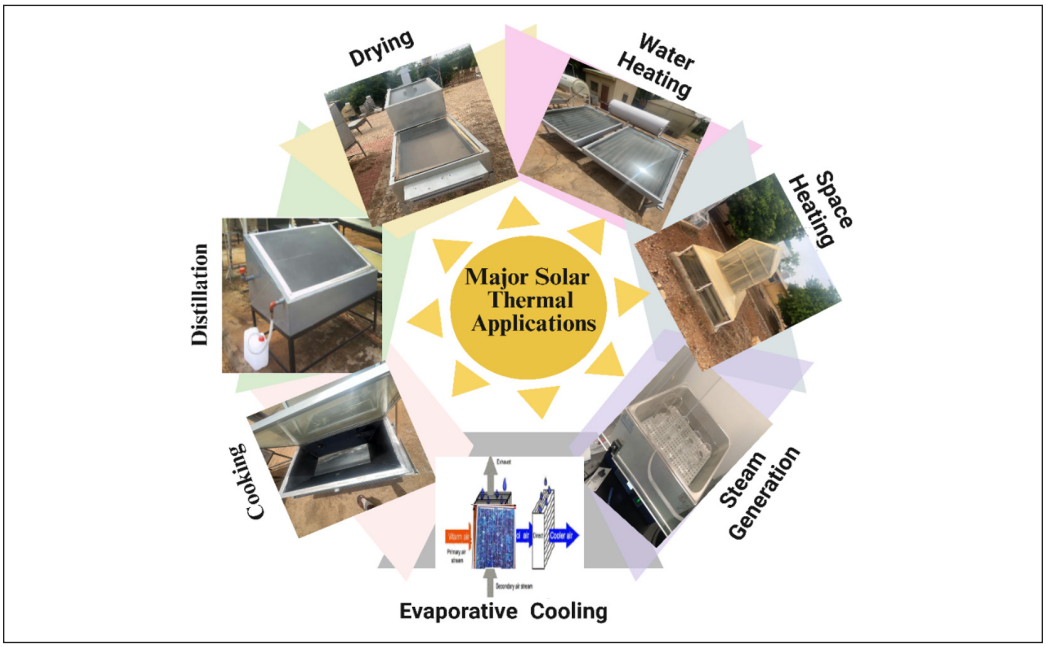

Figure 4. STSs basic applications

attempted to improve the performance of evacuated STSs by placing a PCM (paraffin C20–C33) as a backing bar for the absorber. The highest air outlet temperature measured was 106°C at 0.015 kg/s, and the highest thermal efficiency measured was 64.5% at 0.03 kg/s. Evacuated tube solar receivers are more expensive but effective than non-evacuated ones. Nonetheless, the benefits of a non-evacuated solar receiver include its affordable price, ease of assembly, and superior thermal and optical properties.

MATERIALS FOR SOLAR THERMAL ABSORBER

Solar thermal systems require good strength. They must also have efficient heat conduction, corrosion resistance, and photo-thermal qualities (Kalidasan et al., 2024; Samylingam et al., 2021; Zhao et al., 2023). The incoming radiation, thickness, refractive index, and extinction coefficient of the material all influence its transmittance, reflectance, and absorbance. Metallic materials are widely used as absorbers due to their structural makeup. A sea of electrons surrounds the matrix of electrons in metals. The sea facilitates conductivity and corrosion resistance. The coating deposited on the surface of the absorber enhances the STC absorber's photothermal characteristics (Sethi et al., 2024). A material composed of stannic selenide ($SnSe_2$), aluminum (Al), and titanium (Ti) with graphene was developed. The contribution of this design has been investigated in 4-atm regimes, with 0.22, 0.8, 2.46, and 2.85 being the optimal four wavelengths (micrometers). In the 2.4–3 micrometer bandwidth, the current absorption exceeds 97% (97.4%), surpasses 95% from 0.2–1 micrometer, and extracts 90.3% for the 2800 nanometer band between 0.2 and 3.0 wavelength regimes. A heat treatment process was used by Tarno, Masuri, Ariff, Daura et al. (2024), where mild steel was carburized for enhanced mechanical and corrosion characteristics. With the formation of a corrosion phase, the material was recommended for STS applications. Additionally, many studies have attempted to enhance the absorber's thermal conductivity and corrosion behavior through one or more approaches created by advanced engineering materials and composites (Alhamada et al., 2022; Tarno, Masuri, Ariff & Musa, 2024; Zhao et al., 2023). Other studies employ coating on the surface of the absorber (Sethi et al., 2024).

The literature may indicate that MXene, a family of two-dimensional (2D) transition metal nitrides, carbides, and carbonates, has shown outstanding photothermal conversion characteristics and excellent stability in strong alkaline and acidic solutions. However, the application of MXene as a reinforcement in a metal matrix for modifying microstructures of metallic solar thermal absorbers was not reported.

MXENE AS MICROSTRUCTURAL MODIFIER

Microstructural modification in solar thermal absorbers is critical for developing or transforming inherited structures into an improved structure with new phases that can withstand oxidation at high temperatures. By optimizing the material's structure at the

microscopic level, the basic qualities of the absorber, such as photothermal conversion, thermal conductivity, and strength, can be significantly enhanced. These modifications enable better tribology, reduce heat losses, and increase the lifespan of the STSs under high and fluctuating temperatures.

According to Fan et al. (2022), $Ti_3C_2T_x$ MXenes, known for their higher conductivity ranging from 6000 to 8000 S cm^{-1}, offer a highly promising composite for improved solar energy capture. Figure 5 presents images produced by scanning electron microscope with (a) MAX and multilayered MXene in (b), (c) MXene nanosheet and MXene colloid solution, and (d) X-ray diffraction patterns of MXene and MAX with their common peaks and h-k-l values (Wu et al., 2023). Figure 6 demonstrates images from SEM with a thin-layered material in (a) and an accordion-like multilayered material in (b)–(d). Figure 7. Compared with Ti_3AlC_2, $Ti_3C_2T_x$ missed an intensity peak at $2\theta \approx 39°$, attributed to the elimination of Al. Hence, such properties allow MXene to be used in solar thermal absorbers of various STSs. The study by Fayaz et al. (2022) attempts to improve the temperature of the absorber plate in a solar still using titanium particles. The study reported that integrating titanium particles improved the thermal behavior of the absorber plate.

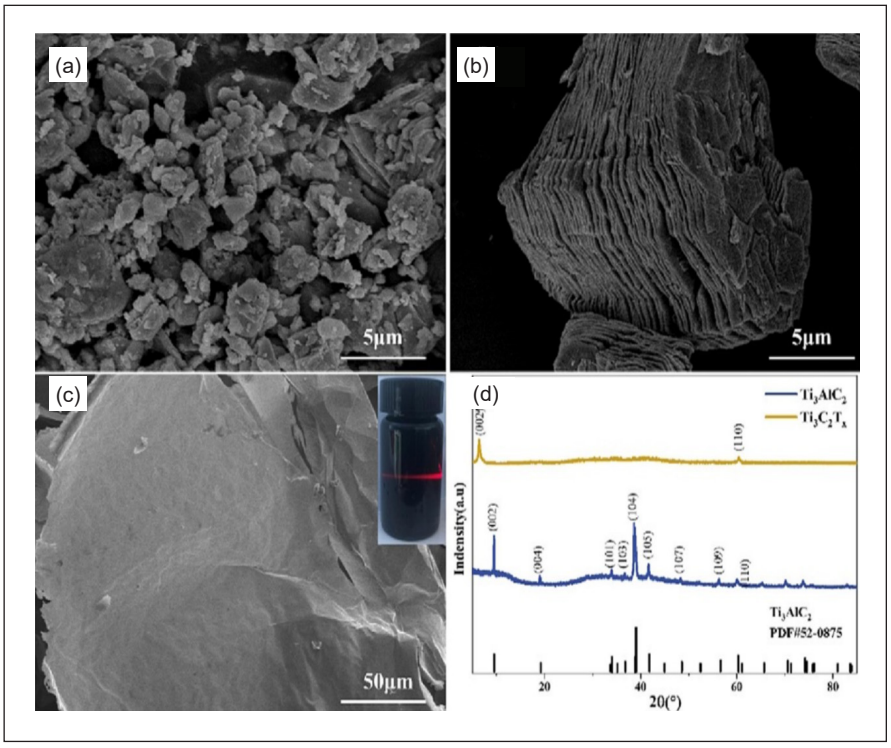

Figure 5. Images produced by scanning electron microscope with: (a) MAX; (b) multilayered MXene; (c) MXene nanosheet and MXene colloid solution; and (d) X-ray diffraction patterns of MXene and MAX (Bai & Wang, 2023)

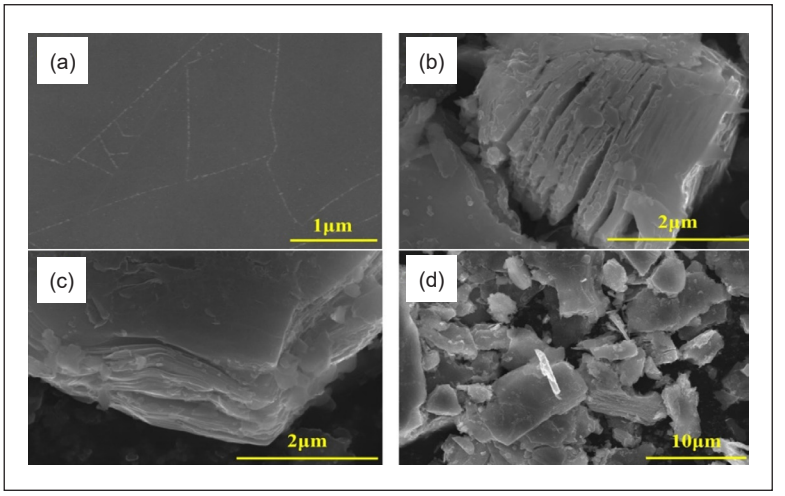

Figure 6. Images captured by SEM with: (a) thin and multi-layered materials (a); (b-d) with an accordion-like multilayered material (Wu et al., 2023)

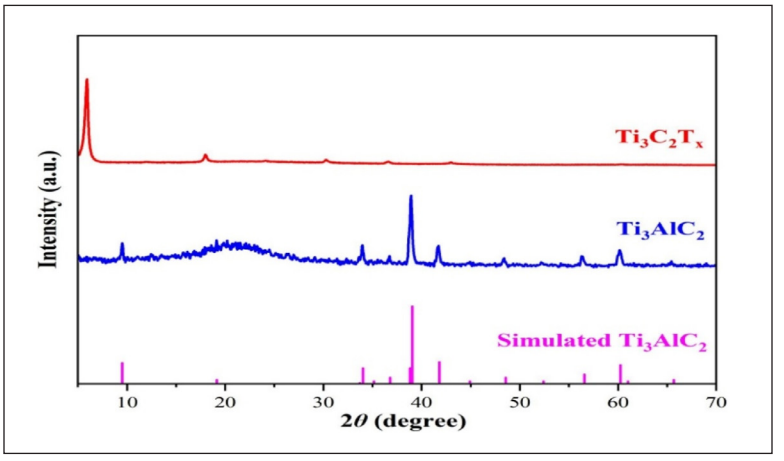

Figure 7. X-ray diffraction spectra (XRD) of intrinsic $Ti_3C_2T_x$ (red), Ti_3AlC_2 (indicated in blue), and standard Ti_3AlC_2 (represented in pink color) (Wu et al., 2023)

According to Kumar et al. (2023), MXenes have a unique nanostructure, which is planar, that exhibits superior optical and thermophysical qualities. The structure makes them qualify for a variety of applications in STSs. Panda et al. (2024), while describing the basic structure of MXene, stressed that they were stacked in several stable layers that featured an irregular exfoliated morphology made up of two-dimensional nanosheets that were transitional carbides. Aluminum is separated from layered MAX phases by chemically treating the material with hydrofluoric acid to create this exfoliated structure. The layered exfoliated assemblage of MXene nanosheets, featuring pore walls attached in the form of carbides of transition metal, Ti_3C_2, V_2C, Mo_2C, and Nb_2C, the' strong thermal conductivity

of transitional carbides facilitates the liquidus and solidus phenomenon of phase-change material inside the 2D nanosheet structure without any leakage.

This suggests the presence of a eutectic phase change material (PCM), a long molecular chain compound, between these MXene's exfoliated layers. Blocks are stacked tightly, exposing a rough surface in the MAX phase, Figure 8(a). The dense structure of MAX was changed into the multilayer structure of MXene by etching the layers of aluminum elements Figure 8(b). The X-ray diffraction phase patterns of the MAX phase and MXene are displayed in Figure 8(c). It is possible to identify the distinctive MAX phase signals at 8.5° (002), 33.9° (101), 39.0° (104), and 41.6° (105) (Xu et al., 2023). In contrast, MXene's (002) peak widens and moves from 9.5° to 6.2°. In the meantime, the peaks in the MXene XRD pattern that corresponded to the (101), (104), and (105) faces nearly vanished. Moreover, the Al element is symbolized by the (104) peak disappearing.

XPS was used to examine the components of MXene, as shown in Figure 8(d). Orbitals F 1s, Ti 2p, C 1s, and O 1s are responsible for the four distinctive signals detected at 685 electron Volt, 530 electron Volt, 459 electron Volt, and 285 eV, respectively. The X-ray diffraction spectra patterns of MXene, X-ray diffraction MXene-TiO_2, and that of reduced MXene-TiOx were recorded at a temperature of 600°C, as displayed in Figure 9.

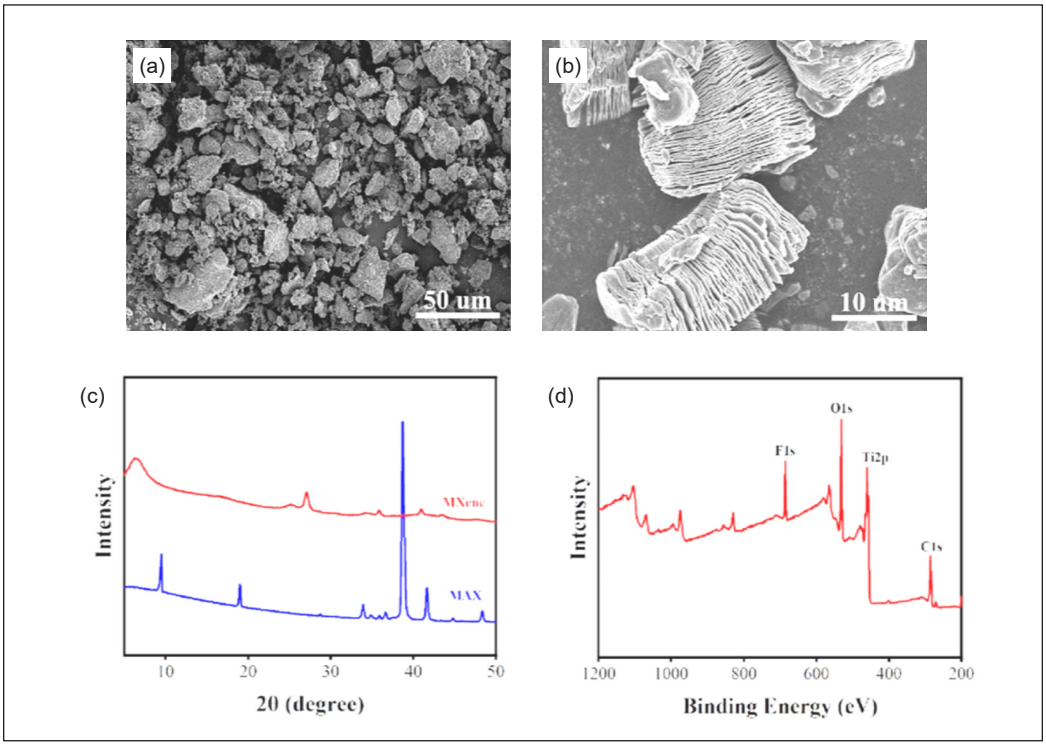

Figure 8. Micrograph and XRD images related to: (a) MAX; (b) MXene, (c) XRD image showing phase patterns of MAX/MXene; and (d) XPS survey representation of MXene (Xu et al., 2023)

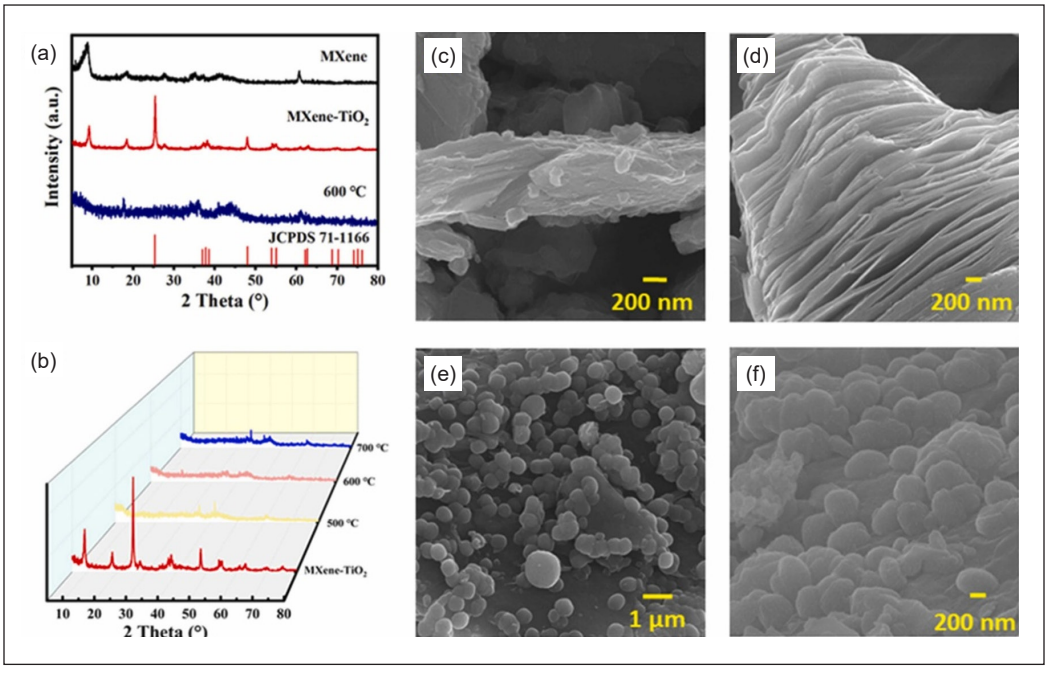

Figure 9. (a) XRD images showing phase patterns of MXene, MXene-TiO_2,@ 600 °C; (b) XRD images of MXene-TiO_2 under different temperatures; (c) SEM images of Ti_3AlC_2; (d) MXene; (e) Anatase MXene-TiO_2; and (f) 600 °C reduced MXene-TiO_x (W. Zhou et al., 2024)

The anatase TiO_2 peaks are traced at 2θ = 27.37° and 48.12°, as in Figure 9(a), indicating that the nano-spheres that were previously linked to the MXene-reinforced developed composites prior to the reduction phenomenon were anatase TiO_2. As Figure 9(b) illustrates, the reduction impact peaked at 600°C following the reduction. Moreover, the anatase TiO_2/MXene composite, Ti_3AlC_2, MXene, and 600°C morphologies and microstructures are demonstrated in Figure 9(c)–(f).

The SEM images of the few-layered and multilayered $Ti_3C_2T_x$ MXene are displayed in Figure 10. The multilayered $Ti_3C_2T_x$ MXene exhibits a loose multilayer microstructure [Figure 10(a)]. The few-layered $Ti_3C_2T_x$ MXene was observed to have a practically transparent quality, as illustrated by Figure 10(b). This suggests that the multilayered $Ti_3C_2T_x$ MXene has been exfoliated to create ultrathin, few- or single-layered $Ti_3C_2T_x$ MXene nanosheets. A collection of diffraction peaks characteristic of a hexagonal crystal structure can be seen in the XRD pattern of $Ti_3C_2T_x$ powders, as in Figure 10(c). The (0 0 2) peak at 2θ = 9.51° in these diffraction peaks is often linked to an interlayer spacing of 9.32 Å (Zheng et al., 2022)

Singh et al. (2023) observed the peak of MXene at 36.76°, corresponding to the (0 0 8) crystal plane. The XRD pattern of the TiO_2 photoelectrodes incorporated with MXene shows diffractive peaks from FTO substrates along with diffraction peaks at various 2 theta

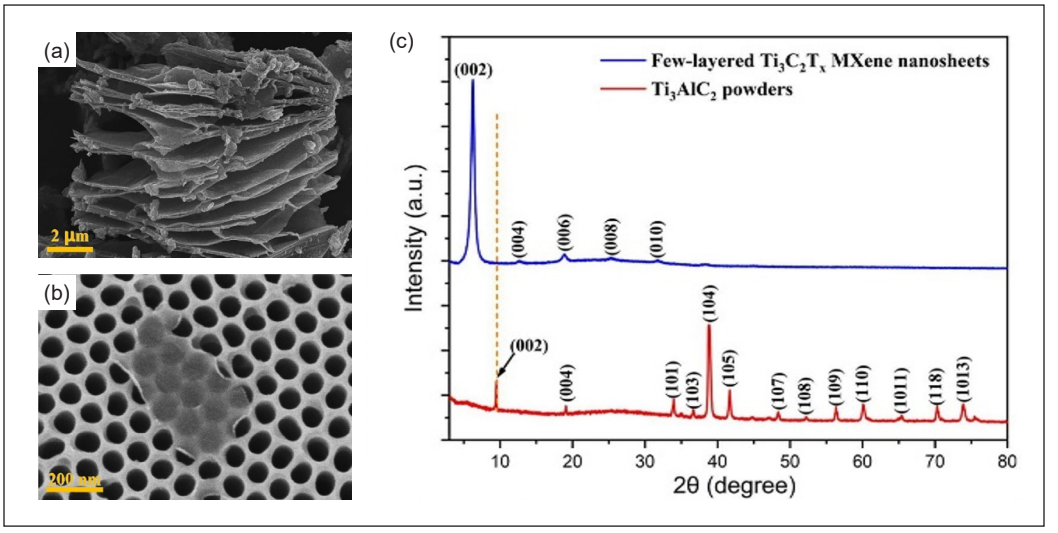

Figure 10. SEM images of: (a) a multilayered; (b) a few-layered $Ti_3C_2T_x$ MXene; and (c) XRD phase patterns of Ti_3AlC_2 powders with few-layered $Ti_3C_2T_x$ MXene (Zheng et al., 2022)

degrees for anatase TiO_2 (JCPDS - 21–1272) at 25.48°, 37.84°, 48.25°, 54.20°, 55.30°, 61.70°, and 62.92°. The angles correspond to (1 0 1), (0 0 4), (2 0 0), (1 0 5), (2 1 1), (2 1 3), and (2 0 4) planes. The phase pattern may change with a metal matrix, such as aluminum, reinforced with MXene. The peculiar properties of aluminum, such as its lightness and non-toxicity, being second only to copper in terms of thermal conductivity, coupled with its lightness, make it almost one-third the density of steel and copper. Aluminum may be next after silver when it comes to conductance by weight ratios; while copper is 8.9 g/cm^3, aluminum is 2.7 g/cm^3. Aluminum is relatively cheaper compared to copper and silver. Aluminum softens, boils, and recrystallizes at approximately 350°C, 2470°C, and 150°C, respectively (Tarno, Masuri, Ariff, & Musa, 2024). An oxide film rapidly forms on its surface when exposed to the atmosphere, preventing further attacks. However, aluminum is weak, unstable, and prone to corrosion. It is weak in acids and bases. According to R. Wang et al. (2024), the oxidation characteristics of aluminum and its basic alloys are significant in its applications in industries. The study attributed the formation process of the film to the action of OH^- hydrocracking in water under the electrochemical environment of applying a small current, and the O in the water molecule forms two distinct oxide films with the Al matrix in the form of O^{2-} and OH^-.

MANUFACTURING PROCESSES OF SOLAR THERMAL ABSORBER THROUGH COMPOSITE TECHNOLOGY

Nano and composite technologies enable microstructural alteration through heat, pressure, or both to distribute reinforcement uniformly and maintain particle homogeneity in

the matrix. The fundamental processes are (1) solid, (2) fusion, and 3D manufacturing techniques. A detailed outline of each process is shown in Figure 12. The primary part of the composite is called the matrix, while the secondary part is known as reinforcement. The purpose is to induce properties that are neither obtainable in the matrix nor the reinforcement but can be obtained in the final product. For instance, in a study by Ariff et al. (2023) a natural fiber was used alongside a polymer material to develop a rice husk-PU reinforced composite for a sound barrier technology. Composites are named according to the matrix composition and reinforcement Figure 11. Thus, composites are categorized as (1) metal matrix composites, (2) ceramic matrix composites, and (3) polymer matrix composites.

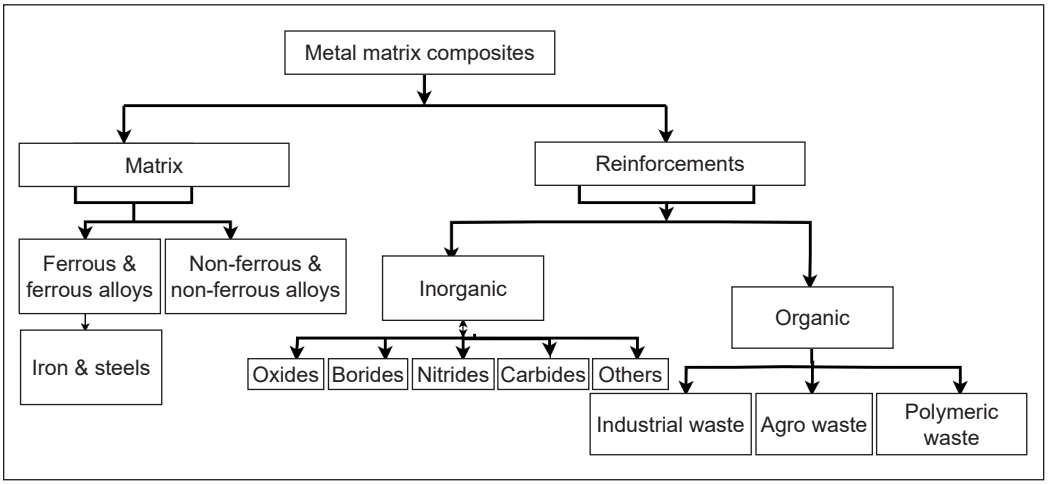

Figure 11. Matrix and reinforcements for the fabrication of MMCs

Metal Matrix Composites

MMCs are advanced materials with improved electro-mechanical qualities and good thermal and chemical stabilities. Those characteristics make those materials suitable for various applications ranging from cutting tools and transportation through consumer electronics, defense, and space to aerospace, marine, solar thermal absorbers and packaging industries (Seetharaman & Gupta, 2021). Hence, the nano and composite approaches could improve the low mechanical qualities, thermal, and chemical stabilities in solar thermal absorbers. The commonest MMCs are (1) continuous fiber or sheet-reinforced CFMMCs, (2) particle-reinforced PRMMCs, and (3) short fiber or whisker SFMMCs.

Particle-Reinforced

This consists of metal matrix and equiaxed ceramic reinforcements mostly carbides (TiC, SiC, B_4C, and NbC.) borides (Titanium boride TiB_2), oxides (Alumina Al_2O_3), carbon nanoparticle (Graphene GNPs), nitrides of Aluminum (AlN), titanium (TiN), boron (BN),

and silicon (Si_3N_4). The size of reinforced particles in MMCs may range from millimeters to nanoscale (M. Wang et al., 2024). These materials have the potential to improve metallic solar thermal absorbers.

Manufacturing Processes of Composites for Solar Thermal Absorbers

The fabrication of MMC can be achieved through fusion, such as casting, solid-state techniques, such as PM, recrystallization, and/or additive manufacturing. A study was conducted on the hardness and microstructural development of Sn-5Sb-xCNT/Cu solder junctions composite through PM, and enhanced resistance to indentation was observed at the solder junctions of the composite (Dele-Afolabi et al., 2020). Composite materials were developed via plasma spraying to create in-situ and ex-situ CrB2 coatings. A low oxygen permeability phase was produced during the oxidation, and good oxidation resistance was measured in Cr-B_4C (Guo et al., 2023). Tarno, Masuri, Ariff, and Musa (2024) modified aluminum microstructure via recrystallization by reinforcing reduced iron and chromium oxide in its matrix. The study reveals improved strength and corrosion behavior. Generally, composites can be manufactured through fusion, solid state, and 3-dimensional (3D) or additive manufacturing processes, as depicted in Figure 12. Fusion includes casting and infiltration techniques (Chen et al., 2023).

Solid-state processes include PM, diffusion bonding, recrystallization, spray deposition, and hot isostatic pressing (Ashrafi et al., 2021). Additive manufacturing comprises material extrusion, directed energy deposition, vat photopolymerization, binder jetting, and powder bed fusion (Yang et al., 2024). Er et al. (2023) adopted one of the additive manufacturing techniques depicted in Figure 12, a Vat Photopolymerization technique, to 3D print phase change material/resin composites using an SLA printer. The thermophysical properties and solar thermal energy storage performance of the material were investigated. The study reveals a 50% phase change material (PCM) ratio as optimal for the fabricated components, achieving a latent heat enthalpy of 83.7 J/g and a tensile strength of 14.02 MPa. This balance highlights the material's effectiveness in thermal energy storage while maintaining reasonable mechanical integrity. However, this process requires high energy and the use of complex equipment. Tarno, Masuri, Ariff, and Musa (2024) utilize a solid-state technique called the recrystallization process depicted in Figure 12 to successfully reinforce the aluminum matrix with iron and chromite. The authors recommend the material for solar thermal absorber applications.

However, the study lacks a detailed explanation of the solubility of reinforcements in the matrix. Lee et al. (2024) developed a reversible solar heating and radiative cooling device that uses a mechanically guided 3D architecture that alternates between heating and cooling modes under uniaxial strain. The device achieved high heating (59.5°C) and cooling (-11.9°C) temperatures, which utilize multilayered films and black paint-coated polyimide

films as solar thermal absorbers. Qi et al. (2024) employed a fusion technique depicted by Figure 12, multi-sided unidirectional freeze-casting, to develop a biomimetic aerogel. The study reveals improved photothermal conversion (95.2%) and thermal conductivity (0.3517 W/m·K), reducing oil flow resistance and achieving high oil retention efficiency (>92%). Figure 12 categorizes the major routes of manufacturing composites used in solar thermal absorbers, such as solid technique, fusion technique, and 3D printing technique.

However, among all the processes listed, PM has a unique advantage in that it not only allows for material density as a controllable variable but also considers energy consumption, production speed, environmental factors, complexity, cost, dimensional precision, and surface finishing. According to Saberi and Oveisi (2022), PM is a suitable approach to producing Cu/Al composite powders. Every casting process requires a melting furnace, mold building, and pattern making, which are highly energy-consuming. These disadvantages apply to other processes that require melting and pouring of the parent metal, such as casting processes, liquid metal infiltration, and spray co-deposition.

A die and a corresponding die-casting machine are required for die-casting. The machine is required to force the molten metal into the die cavity between the two halves of the die. This also involves the application of high pressure (T. Wang et al., 2022). Casting has disadvantages, including being expensive and complex mold design, more material waste, the possibility of flaws impacting mechanical properties, more energy usage, a slower

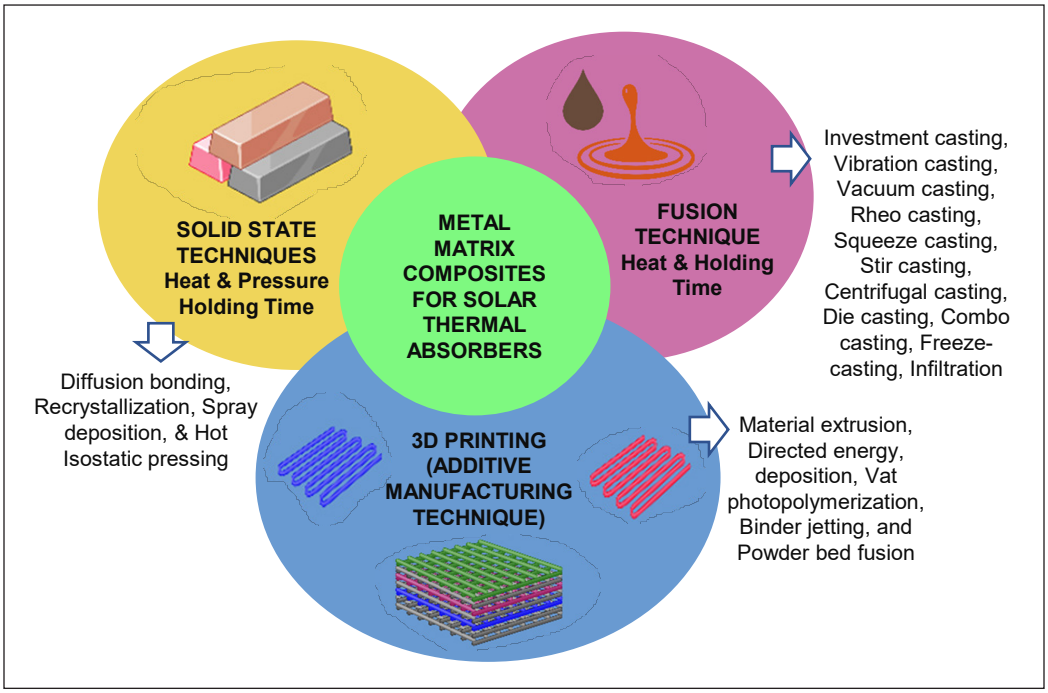

Figure 12. Composites approach to manufacturing solar thermal absorber

rate of manufacturing, and a more significant environmental impact. In contrast, PM is a more appealing choice for some applications due to its advantages in material efficiency, dimensional accuracy, energy efficiency, and production speed (Wang et al., 2025).

The inert gas involvement in the vacuum casting process makes it very expensive, time-consuming, and highly energy-consuming. A homogeneous and even distribution of reinforcement and other defects, such as porosity, wettability, stirrer blade oxidation at high temperatures, and mixing rate of reinforcement within the matrix, are all key concerns in the stir casting process. A decreased surface roughness is traced in the base metal alloys submitted to vacuum casting, like that of titanium, compared to base metal alloys submitted to acetylene-oxygen flame casting (Kandpal et al., 2022). Casting processes are characterized by carbon emissions and environmental impact, specific energy consumption, production cycle time, and cost estimation.

Processes such as binder jetting, vat photopolymerization, powder bed fusion, metal extrusion, and sheet lamination are the most common 3D composite fabrication methods (Nugroho et al., 2022). However, additive manufacturing requires the use of sophisticated and costly equipment. For instance, the basic principles of powder bed fusion lie in developing the product layer by layer (Singh et al., 2020). Beams such as electrons, lasers, and infrared are required as heat sources, making the process expensive and complex, and having health and environmental impacts. The process is characterized by residual stress and distortion. According to Li et al. (2024), however, the Vat Photopolymerization (VPP) process has significant disadvantages in forming designed geometrical characteristics, slurry preparation, forming precision, defect management, and multi-material printing. Complex tools and expensive energy sources are involved in the process. Printing of highly dense and defect-free materials with outstanding mechanical properties remains a major challenge with aluminum alloys developed via laser powder bed fusion. (Zhou et al., 2023).

Several disadvantages become apparent when comparing 3D fabrication processes to PM for fabricating aluminum composites. A heterogeneous microstructured aluminum alloy was fabricated through wire-arc 3D. It is revealed that the microstructure is sensitive to the printing and composition conditions. PM has the unique advantage of making density a controlled variable, with low energy consumption and environmental compatibility. Figure 13 depicts the basic PM process and parameters. Using the PM technique, items can also be fabricated with better and more precise geometrical characteristics (Zhou et al., 2023).

INFLUENCE OF MXENE ON THERMAL CONDUCTIVITY AND PHOTOTHERMAL CONVERSION OF SOLAR THERMAL ABSORBER

M. Ding et al. (2023) employ Ti_3AlC_2 phase, lithium fluoride (LiF), and MXene composite in Cellulose nanofibrils to improve Photo-thermal conversion aerogels under wet and dry conditions in a solar still. The study demonstrates the use of cellulose nanofibrils in

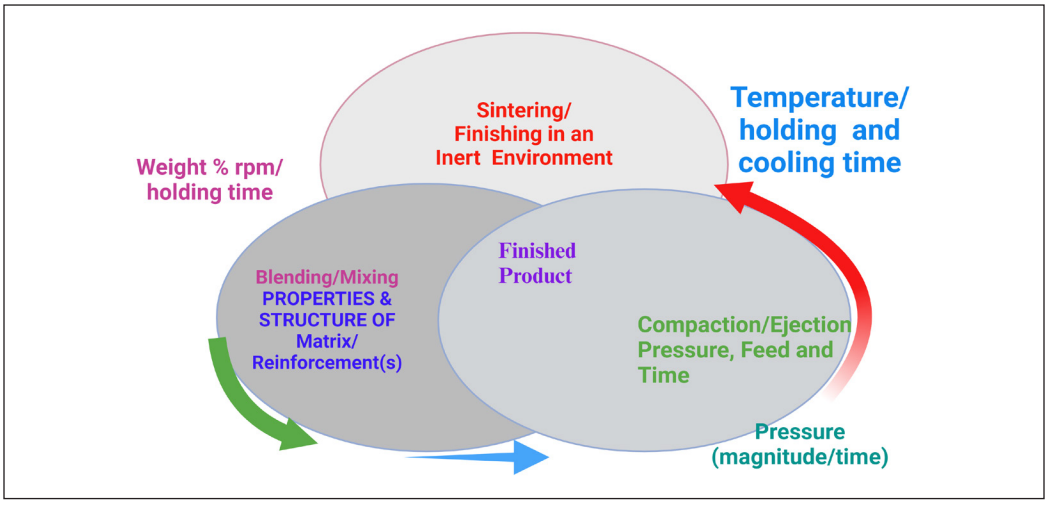

Figure 13. Powder metallurgy process and parameters

fabricating a solar-thermal desalination system using MXene composite aerogel. Qualities such as thermal insulation (56.5 $mWm^{-1}K^{-1}$), solar absorption (97.9%), and hydrophilicity were reported by the study. This study lacks comparative analyses and evaluations of MXene composite aerogel and other solar-thermal stills. The Al/CuO/MXene composite containing 7.5 wt% Ti_3C_2 MXene demonstrates optimal thermal stability and energy release efficiency, making it the ideal choice for applications that demand high thermal performance; however, when the Ti_3C_2 MXene content is raised to 10 wt%. %, the composite experiences a slight reduction in heat release (Cheng et al., 2023). MXene nanofluids demonstrated superior stability compared to graphene due to $Ti_3C_2T_x$'s hydrophilicity (Wang et al., 2021). MXene improved the black paint coating's solar absorptivity and thermal conductivity by 0.1 w%. A 6.0% increase in water temperature caused by MXene results in a 2.07 kg distillate yield. With 0.1 w%. MXene, the solar still's average energy efficiency was 36.31%. The work that previous researchers have done reveals the influence on the thermal and photothermal conversion characteristics of STSs by adding MXene as a microstructural modifier in solar thermal absorbers, which is summarized in Table 1.

MXene-based nanofluids, phase change materials, paints, and hydrogel-coated cotton fabric have been widely covered, as summarized in Table 1. It can be deduced that MXene has improved the thermal and photothermal conversion properties of solar thermal energy systems, producing positive benefits in solar thermal absorbers made from MXene-reinforced carbon nanotubes, phase-change materials, coatings, nanofluids, and nanocapsules. These materials have been shown to improve conversion efficiency with integration. MXene is added as reinforcement in paints used to coat the surfaces of solar thermal absorbers and as a backing for metallic absorbers. However, literature on MXene-reinforced metal matrix composites for solar thermal absorbers has not been reported.

Table 1
Summary of the recent studies on the influence of MXene on thermal conductivity and photothermal conversion of solar thermal absorber

Authors & Year	Title/Focus of Work	Materials	Parameter	Findings
Su et al., 2022	MXene-based solar absorber for seawater desalination system	MXene-PDA-fabric, PPy/ and PDA-fabric	Photothermal conversion	Improved thermal quality; about 93.5%, higher than (≈82%) of conventional PDA-fabric
Wang et al. 2021	The thermal conductivity and optical conductivity study of graphene- and MXene-based nanofluids	MXene nanosheets ($Ti_3C_2T_x$), graphene-based nanofluids	Photothermal conversion	MXene nanofluids demonstrated a higher photothermal conversion efficiency of 63.35% compared to graphene nanofluids, which was 4.34% higher
Mao et al., 2022	Nanofluids containing MXene/water and MXene/ ethylene-glycol/water, with MXene particle concentrations varying from 0.1 to 0.5 w%	MXene, water, ethylene-glycol nanofluids	Thermal conductivity	The 0.5 weight percent MXene/water nanofluid showed a 30.6% higher effective thermal conductivity compared to pure water-based fluid and a 27.3% improvement in the MXene/ethylene-glycol/water nanofluid's conductivity.
Han et al. 2023	Improvement of mechanical property, light absorption, and photothermal conversion performance using Cotton fiber with hydrogel coatings based on Ti_3C_2Tx MXene	Cotton textiles with hydrogel coatings based on Ti_3C_2Tx MXene	Photothermal	95% evaporation efficiency of 95% under 1-sun irradiation
Xu et al., 2023	Optimizing the efficiency of light-thermal absorption and conversion in SSPCMs that use MXene to store solar thermal energy.	Polyethylene glycol (PEG) shape-stabilized phase hange materials (SSPCMs). The diatomite and	Light-thermal absorption and conversion efficiency	Relative enthalpy efficiency is approximately 99.2%. Additionally, compared to PEG, the thermal quality of SSPCM-2 rose by 111.8%
Ai et al., 2022	Effective solar desalination for uses in water filtration through the use of hierarchical binary gel (HBG) comprising MXene (Ti_3C_2) and montmorillonite (MMT) gels as upper structure and base materials, respectively	(HBG), montmorillonite and MXene (Ti_3C_2) gels	Photothermal conversion	Photothermal conversion efficiency was achieved at 93.7%
Li et al. 2020	Using MXene nanofluid to enhance the direct absorption solar collector's (DASC) photothermal conversion efficiency	Multilayered MXene, DI water. Dispersant	Photothermal conversion	A photothermal conversion efficiency of 77.49% is achieved with merely 100 ppm MXene loading

Table 1 *(continue)*

Authors & Year	Title/Focus of Work	Materials	Parameter	Findings
El Hadi Attia et al., 2023	New hemispheric solar distiller with wick convex basin integrated with and without PCM	Paraffin wax as PCM, a convex absorber basin, wicks, and PCM	Photothermal conversion	The energy and exergy efficiencies increased to 85.6% and 128.2%, respectively The still with a wick, convex basin/PCM produced an 87.0% higher distilled yield
Zheng et al., 2022	Enhancing solar photothermal conversion performance of seawater desalination systems through the introduction of Ti_3C_2Tx MXene nanosheets	MXene hybrid aerogel, polyethylene glycol (PEG) as a phase change material, and $Ti_3C_2T_x$ MXene nanosheets	Solar photothermal energy-conversion	Significant improvement in solar photothermal energy-conversion efficiency for the aerogel/PEG composites, reaching up to 87.28%.
Zhao et al., 2023	Enhancing the thermophysical characteristics of microcapsules by integrating Ti_3C_2 MXene nanosheets	(Ti_3C_2) MXene nanosheets, phase-change microcapsules. styrene-divinylbenzene copolymer shell and an n-Octadecane	Photothermal conversion, thermal conductivity	240% efficiency in photo-thermal conversion was recorded with 0.67 w% doping, and the thermal conductivity was increased by 52.3% 0.67 weight percent doping resulted in a 9.6% rise in enthalpy.
Kalidasan et al. 2024	Fabrication of a 2D composite PCM made of MXene@eutectic salt hydrate for thermal energy storage (TES) and efficient solar energy harvesting	MXene@SSD/SPDD eutectic PCM	Optical absorbance,	With MXene, optical absorbance increases by 746.2% and transmissibility drops by 86.2%
Thakur et al., 2022	The application of multilayered 2-D MXene out of the 3-D MAX phase as a coating for improving the performance of solar absorbers in solar stills	MXene (Ti_3C_2Tx), black paint	Photothermal conversion, thermal conductivity	0.1 wt.% MXene increased water temperature by 6%, which led to a water yield of 2.07 kg. The average energy efficiency of the solar still was 36.31% with 0.1 wt.% MXene
Aslfattahi et al., 2021	Investigating an effective nanofluid in a solar dish concentrator employing the numerical model that uses pure soybean oil and MXene nanofluid, which is based on soybean oil at various concentrations, as working fluids	Soybean oil-based MXene nanofluid	Solar Dish Collector	The daily mean thermal efficiency with nanofluid was recorded as 82.66%. The daily yield is 9.07 kWh

Table 1 *(continue)*

Authors & Year	Title/Focus of Work	Materials	Parameter	Findings
Zang et al., 2023	MXene/ANF composite film was developed using a simple vacuum filtration technique for effective photothermal conversion and water evaporation characteristics	Novel MXene/ANF composite film	Solar-driven water evaporation	Up to 98.0°C and 54.0°C, respectively, with water evaporating at a rate of 1.432 kg/m^2 under a solar power density of 1 kW/m^2
Lei et al., 2022	Design and weaving of a hydrophilic Ti_3C_2Tx (MXene) decorated 3D honeycomb-like fabric inspired by nature, as a solar evaporator	Hydrophilic Ti_3C_2Tx (MXene) absorber	Solar-powered evaporator	High solar efficiency of up to 93.5% during one sun irradiation
Jiang et al., 2022	Fabrication of Ti_3C_2Tx MXene-based material and its integration into solar membrane distillation system for efficient photo-thermal conversion	Ti_3C_2Tx MXene nanoparticles	Solar membrane distillation (SMD) system	The high internal photo-thermal conversion efficiency of the Ti_3C_2Txgy MXene nanoparticles, which can reach 100%, results in their high-efficiency photo-thermal conversion and desalination
Li et al., 2021	Application of 2D MXene, specifically Ti_3C_2Tx MXene, for improved solar thermal conversion	2D MXene specifically Ti_3C_2Tx MXene.	Solar-thermal energy	The areas with significant solar absorptance (up to 90%) and poor emissivity (down to 10%) have the highest solar-thermal conversion efficiency
Samylingam et al., 2021	Fabrication of thermo-physically stable nanocomposite of ternary nitrate molten salt induced with MXene for thermal energy storage	Nanocomposite absorber	Concentrated solar power (CSP)	The thermal stability rises from 652.13°C to 731.49°C and from 679.82°C to 684.57°C, respectively
Bati et al., 2021	The production of cesium (Cs)-doped functionalized Ti_3C_2Tx MXene nanosheets and their addition to a lead iodide solution for perovskite solar cells for thermal stability	Perovskite film (absorber material) incorporation of cesium-doped MXene nanosheets	Perovskite solar cells (PSCs)	Thermal stability and a high photovoltaic efficiency of up to 21.57%
Z. Ding et al., 2023	Application of machine learning for a systematic investigation of the absorption qualities of various MXenes-based metasurface absorbers (MMA) in the solar spectrum, solar-thermal energy harvesting, and processing	MXenes-based metal surface absorbers (MMA)	Solar Spectral Absorption	The simulation results show that the MMA_O ($Ti_3C_2O_2$) absorbs 93.19% of the solar spectrum and emits only 1.21% in the MIR band (5000–13000 nm), making it a near-perfect solar absorber

Table 1 *(continue)*

Authors & Year	Title/Focus of Work	Materials	Parameter	Findings
H. Wang et al., 2022	Development of polyethylene glycol/MXene-cellulose aerogels for concurrently improved photo-thermal conversion, heat storage, and transfer via freezing casting-based one-step in situ encapsulation technique	MXene-cellulose aerogels, polyethylene glycol	Solar energy collection, conversion, storage, and utilization	The light-to-heat conversion efficiency of PMC fs-CPCMs attained 91.6%. The latent heats of PMC fs-CPCMs (about 183 J/g) were not reduced
Y. Wang et al., 2022	Development of selenide Nanoparticles of Copper Indium embedded Ti_3C_2Tx MXene Nanoflakes for Solar-Driven Membrane Evaporation	$Ti_3C_2T_x$ MXene nanoflakes/ copper reinforced indium selenide (CIS) nanoparticles	membrane for solar interface evaporation,	Maximum water evaporation rate of 1.434 kgm-2 h-1, and water evaporation efficiency of 90.04%
Fayaz et al., 2022	Examination of the impacts of metallic titanium particles on the solar still absorber's surface temperature to increase distillate production	Aluminum plate, titanium (Ti) particles, and black paint	Thermal conductivity	Under 1000 W/m2 of indoor solar radiation, the 7-weight percent Ti specimen coated in black paint reached a temperature of 100.39°C, 11.87% higher than an Al plate left exposed and 54.35% higher than an Al plate coated only in black paint. The temperature increased to 77.58°C compared to the 7-weight percent Ti
Zaed et al., 2024	Preparation and coating of Ti_3C_2Tx MXene-activated carbon (AC) composite over a natural biodegradable sponge for an effective photo-thermal solar absorber for steam production using solar energy	Natural biodegradable sponge, $Ti_3C_2T_x$ MXene-activated carbon composite	Photo-thermal conversion	The Ti_3C_2Tx MXene-Activated carbon@ natural biodegradable sponge composite produced solar evaporation rates of approximately 1.8 kg 2 per hour and 89.82% solar-to-steam conversion efficiency with 1 sun solar irradiation
Liu et al., 2023	Working medium for solar-thermal energy conversion and storage	Aerogel skeleton, organic phase change materials MXene	Photothermal conversion	76.9% The adsorption rate was 93.72%. 164.92 J/g latent heat
Bai et al., 2024	Solar-driven evaporator through Modification of the inner surface of coconut husks with diatomite and coating the upper surface with MXene	Diatomite, MXene	Photothermal conversion	Photothermal conversion efficiency of 90.64% under 1 sun irradiation

Table 1 *(continue)*

Authors & Year	Title/Focus of Work	Materials	Parameter	Findings
Yue et al., 2024	Fabrication of a Ti_3C_2Tx MXene/delignified wood supported out of stable phase-change composites (PMPCMs) with superior solar-thermal conversion efficiency and optimum flame-retardancy	MXene/delignified wood-supported phase-change composites	solar-thermal conversion	Efficiency of 88.4%
Wang et al., 2023	Development of 3-Dimensional Janus structure MXene/cellulose nanofibers/luffa aerogels for improved mechanical quality and efficiency desalination in solar-induced interfacial evaporation	$Ti_3C_2T_x$ MXene luffa sponges, Cellulose nanofibers	Mechanical, solar-thermal Evaporator	Water evaporation rate of 1.40 kg m^{-2} h^{-1} and an efficiency of 91.20% under 1 sun illumination
Sreekumar, Ganguly et al., 2024	Characterization of novel MXene/Carbon-dot hybrid nanofluid in terms of thermo-optical for heat transfer applications	MXene/C-dot hybrid nanofluid	Photothermal conversion	(50%) above water, (42.2%) hybrid, and (33.2%) C-dot nanofluid, respectively
Chen et al., 2023	Application of photothermal-assisted sacrificial template technique for construction of Polyvinylpyrrolidone-bridged MXene skeleton for optimum development of stable phase change materials with good photothermal conversion	MXene@PVP/PEG composite PCMs (MPP)	Photothermal conversion	The photothermal conversion efficiency of 96.2%
Yang et al., 2024	MXene -molybdenum disulfide composite with mechanical and photothermal conversion, characteristics, and recycling stability	Molybdenum disulfide and MXene composite	Light absorption and adsorption	(96.58%) Light absorption attains 99.9% illumination rates for heavy metal ions and 100% removal of organic dyes
Almarzooqi et al., 2024	Application of $Ti_3C_2T_x$ MXene-coated spacers for Solar-driven surface-heating and distillation	$Ti_3C_2T_x$ MXene-coated nickel-chromium	Photothermal interfacial evaporation	Energy conversion efficiency of 28.3%.
Su et al., 2024	Latent heat-type nanofluid based on MXene and MoS_2 modified structurally hierarchical phase change nanocapsules for light-heat conversion	Latent heat nanofluids (LHNF), Phase change nanocapsules, modified with MXene-MoS_2	light-heat conversion	76.3°C is reached with 1- Sun irradiation, with an 85.62% light-to-heat conversion efficiency

INFLUENCE OF MXENE ON THE CORROSION BEHAVIOUR OF SOLAR THERMAL ABSORBER

Corrosion behavior describes the extent to which a material reacts and oxidizes or deteriorates when subjected to environmental and atmospheric conditions that lead to chemical or electrochemical reactions. The complex interaction between solar thermal absorbers of STSs, their environments, and operational sequences greatly affects their chemical makeup. Corrosion of solar thermal absorbers leads to huge economic losses and safety hazards in the renewable energy sector, industry, agriculture, and domestic productivity. However, the synthesis of MXene has led to a breakthrough in corrosion prevention of solar thermal absorbers due to their exceptional practical properties, such as environmental and operational stability, and their ability to form a thick, impenetrable layer covering the metal surface that keeps corrosive substances from attacking the metal substrate. Cao (2024) stressed that two-dimensional (2D) MXene composite coating integration creates a wealth of options for MXene-based coatings' multifunctional uses, particularly in corrosion protection. The labyrinth effect of MXene, coupled with the corrosion-inhibiting effects in PDA, and the establishment of favorable compatibility between the PDA-functionalized MXene 2D material and the WPU matrix are contributing factors to the enhanced corrosion and wear characteristics in WPU@PMXene composite film. Table 2 summarizes the influence of MXene on the corrosion behavior of solar thermal absorbers.

Table 2
Summary of the recent studies on the influence of MXene on the corrosion behavior of solar thermal absorbers

Authors & Year	Title/Focus of Work	Materials	Medium	Findings
Sreekumar, Shaji et al., 2024	Energy efficiency and chemical stability through the application of MXene/Carbon-dot hybrid nanofluid	0.15 wt.%, C-dot, 0.1 wt.% MXene, and 0.15 wt.%, hybrid nanofluids respectively.	0.1 M solution of NaCl	The hybrid nanofluid exhibited the minimum corrosion rate of 0.6 mmy^{-1} in corrosion analysis.
Chen et al., 2024	The MnO_2/V_2C composite has effective microwave absorption abilities and robust anti-corrosion qualities	MnO_2/MXene (Ti_3C_2, Nb_2C, and V_2C) composites	3.5 wt.% solution of NaCl	Stronger corrosion qualities under acidic conditions, with weaker corrosion qualities under alkaline conditions
Kalidasan et al., 2024	Enhancement of corrosion resistance, thermal, and photo-thermal conversion	MXene@SSD/SPDD is placed in contact with aluminum, Salt hydrate phase change materials, and copper	Materials are placed in contact	Al metal SSD/SPDD eutectic PCM has an m per year of 0.0181; MXene at the SSD/SPDD sample has an m per year of 0.0045. Cu under SSD/SPDD eutectic PCM is 0.0131 m per year; MXene at SSD/SPDD is 0.0004 m per year.

Table 2 *(continue)*

Authors & Year	Title/Focus of Work	Materials	Medium	Findings
Cao, 2024	MXene-based coatings for surface protection against corrosion	MXene-based coatings		Good intrinsic surface protection ability of MXene
Nazarlou et al., 2023	Polyaniline Ti_3C_2/MXene / montmorillonite nanostructures toward solvent-free powder coatings with improved corrosion and mechanical qualities	Ti_3C_2 MXene/ Polyaniline/ Montmorillonite	3.5 wt.% solution of NaCl	The maximum corrosion rate (ν_{corr}) is attributed to the neat powder film (2.45 mm per year), which has been kept to the minimum values of 1.21×10^{-1}, 1.06×10^{-2}, and 8.94×10^{-5} mm per year through integrating 1.5 wt.% Ti_3C_2 MXene, 2 wt.% % Ti_3C_2 MXene/ PANI, and 1.5 weight % Ti_3C_2 MXene/PANIand MMT additives, respectively
Li et al., 2024	Corrosion and Wear characteristics enhancement via Dopamine-Functionalized Ti_3C_2Tx MXene/ Waterborne Polyurethane film on Alloy Magnesium	$Ti_3C_2T_x$ MXene/ polyurethane film on magnesium alloy	3.5 wt.% solution of NaCl	63.47%, 97.89%, 99.74%, respectively. resistance efficiency

INFLUENCE OF MXENE ON THE MECHANICAL CHARACTERISTICS OF SOLAR THERMAL ABSORBER

The functional integrity and the ability of a thermal system to withstand loads, stresses, and environmental conditions without failure or deformation can be accessed by its mechanical qualities, primarily plasticity and elasticity. Depending on the nature and magnitude of the loading, in STSs, the most common loadings are thermal and mechanical (Sharma & Talukdar, 2024). Recent findings on the influence on mechanical properties of solar thermal systems by the addition of MXene as a microstructural modifier in solar thermal absorbers are presented in Table 3.

However, weight concentrations ranging from 0.1–7.5 wt.% are the quantum of MXene enhancing the mechanical stability and load-bearing performance in solar thermal absorbers (Cheng et al., 2023; Fan et al., 2024; Ji et al., 2024; Singh et al., 2024; Y. Zhou et al., 2024) This was attributed to their layered architecture, atomic structures, robust bonding with matrix materials, high aspect ratio, outstanding mechanical strength, and effective interfacial interactions.

Table 3
Summary of the latest literature on the influence of MXene on the mechanical characteristics of solar thermal absorbers

Authors & Year	Title/Focus of Work	Materials	Parameter	Findings
Yu et al., 2024	Preparation of deep eutectic supramolecular polymer (DESP) functionalized MXene for enhancement of corrosion characteristics, photothermal conversion, and mechanical behavior	Cellulose-based fabrics, MXene nanosheets	Mechanical properties, photothermal conversion	mechanical properties (2.68 MPa)
AhadiParsa et al., 2024	Modification of MXene nanosheets for improved mechanical stability	Ti_3C_2 MXenes Zn-doped-S-polyaniline nanosheets	Thermo-mechanical properties	Increase the stiffness of nanocomposites by at least 1.04% (EP-MX) and at most 72.38%
T. Wang et al., 2024	Surface protection on aluminum alloy in PEMFC environments, electrodeposited $Ti_3C_2T_x$ MXene composite coating for improved mechanical properties	Thin $Ti_3C_2T_x$ MXene, Al alloy	Corrosion, mechanical properties	The incorporation of MXene remarkably reduced the wear rate to 3.82×10^{-3} $mm^3N^{-1}m^{-1}$.
Lv et al., 2024	Investigation of mechanical, adhesive, and electronic properties of $Ti_3C_2(O_2)$/Al composites, enhancing the mechanical properties of aluminum matrix composites	MXenes aluminum metal matrix composites	Mechanical properties	The lattice constants are a = 4.045 Å for bulk Al and a = b = 3.073 Å for Ti_3C_2 MXene. The tensile strength of the material increases from 6.93 Giga Pascal (Ti_3C_2/Al) to 8.49 Giga Pascal ($Ti_3C_2O_2$/Al)
Yang et al., 2023	Application of 2D MXene (Ti_3C_2Tx) for modification of the interface of carbon fiber-reinforced polyetherketoneketone interfacial CF/PEKK composites, MXene for improved mechanical properties, and concurrent enhancement of the EMI shielding performances of CF/PEKK	Polyetherke-toneketone (PEKK), carbon fiber (CF), MXene	Mechanical properties	The CF/PEKK composites present superior mechanical properties with a flexible strength of 1127 MPa, a flexible modulus of 81 GPa, and ILSS of 89 MPa

CONCLUSION

This study evaluates all the most recent and relevant research on MXene-reinforced absorbers published between 2020 and 2024 with a primary focus on STSs. The analysis examines MXene microstructures, structure, phase patterns, composition, weight concentration, findings, weaknesses, and comments. The review confirmed using metallic absorbers, primarily aluminum, copper, and steel-based, with and without coatings. This

is attributed to their bonding, electron matrix, a sea of electrons surrounding the electrons, and their valences.

MXenes have both accordion-like multilayer structures, which are wavy, flexible, and have a less dense morphology, and self-stacking layered structures, which are compacted and strong due to very strong Van der Waals forces. The self-stacking structure exhibits 6-41° peaks and 002, 004, 008, and 110 hkl values. The prominent ones are 002 and 004, between 6.9° and 9.5°. The self-stacking structure exhibits higher thermal conductivity. MXene has yielded encouraging results for improving the thermal and corrosion characteristics of solar thermal energy systems, reinforced nanofluids, phase change materials, coatings, carbon nanotubes, and nanocapsules, which have shown improved results. MXene used as the backing of metallic absorbers and in paintings has also shown significant impacts on the thermal and corrosion qualities of STSs. It is also worth noting that the improvement may be influenced by MXene's microstructures, weight concentration, composition, manufacturing processes, solar radiation conditions (such as wind speed and humidity), weather cycles, day/night frequencies, and experimental design.

There is a positive correlation between corrosion resistance and the strength of the absorber, which usually results in the creation of a martensitic phase and the transformation of the microstructure. The invention of MXene-modified absorber materials in STS technology has brought significant advancements in domestic, agricultural, and industrial heating and cooling. Their unique properties, such as conductivity, tunable surface chemistry, and hydrophilic nature, as well as their two-dimensional layered, stacked, and accordion structure, make MXenes a leading material for microstructural modification of absorbers in STSs. The exploration of MXene-based nanofluids, PCM, nanocellulose, coatings, micro-encapsulation and nanocomposites has unveiled improved thermal stabilities, photothermal conversion, and thermal conductivity of the matrices and enhanced the general performance of STSs.

However, recent literature has deduced that the integration of significant weight percentages ranging from 0.1 wt.% to 7.5 wt.% in nanofluids, phase change materials, coatings, and metallic absorber backing material yielded significant performance improvements in STSs. However, when the Ti_3C_2 MXene content is raised to 7.5 wt.%, the composite experiences a slight reduction in heat release.

Agglomeration, complexity of composite manufacturing processes, lack of sufficient literature, and sedimentation were the factors restraining the production of MXene-reinforced metallic composites for absorption in STSs. By solving these essential constraints, materials scientists, technologists, and engineers may successfully fabricate MXene-reinforced metallic absorbers for STSs. This would significantly improve the qualities of solar thermal absorbers and the overall performance of STSs.

Among all the composites manufacturing processes, PM offers more advantages, such as density, cost-effectiveness, energy economy, dimensional precision, and production speed, while wire-arc additive manufacturing has a heterogeneous microstructure. Fusion

processes, unlike PM, require melting, are high energy, have environmental effects, and use complex equipment, making them more expensive. PM offers material efficiency, dimensional accuracy, energy efficiency, and production speed.

While MXenes have shown remarkable performance in modifying the microstructures of significant non-metallic-based solar thermal absorber materials, the potential of reinforcing MXenes with other metallic-based absorbers, especially aluminum, copper, silver, or iron-carbide alloys such as stainless, galvanized, or mild steels, remains largely unexplored. Evaluating the influence of MXene in modifying the structure of these materials might lead to microstructural transition and phase patterns with significant effects on their long-term photothermal and thermomechanical stabilities in solar thermal absorbers. This could unlock the previously untapped MXene potential.

The potential effects of MXenes on the quality of drinking water, particularly regarding nanoparticle leaching, should be investigated and compared with the World Health Organization standard.

Future research in solar thermal absorber composites should focus on optimizing MXene weight concentrations in reinforcing metallic solar absorbers. Exploring MXene's potential for corrosion and thermal conductivity phases could promote the efficiency of STSs. AI-based prediction techniques could also be integrated to determine the optimum weight % of MXene to be added to the metal matrix for an efficient solar thermal absorber.

ACKNOWLEDGEMENT

The authors would like to express their gratitude to the Faculty of Engineering at Universiti Putra Malaysia for providing the Research Grant (9688700) that supported this study.

REFERENCES

AhadiParsa, M., Dehghani, A., & Ramezanzadeh, B. (2024). Titanium carbide-based (Ti_3C_2) MXene@Zn-doped-S-polyaniline nanosheets: Toward thermo-mechanical and UV-shielding properties enhancement. *Journal of the Taiwan Institute of Chemical Engineers*, *156*, Article 105364. https://doi.org/10.1016/j.jtice.2024.105364

Ai, Z., Zhao, Y., Gao, R., Chen, L., Wen, T., Wang, W., Zhang, T., Ge, W., & Song, S. (2022). Self-assembly hierarchical binary gel based on MXene and montmorillonite nanosheets for efficient and stable solar steam generation. *Journal of Cleaner Production*, *357*, Article 132000. https://doi.org/10.1016/j.jclepro.2022.132000

Alhamada, T. F., Hanim, M. A. A., Jung, D. W., Saidur, R., Nuraini, A., & Hasan, W. Z. W. (2022). MXene based nanocomposites for recent solar energy technologies. *Nanomaterials*, *12*(20), Article 3666. https://doi.org/10.3390/nano12203666

Ali, N., Agravat, D., Patel, S. K., Armghan, A., Aliqab, K., & Alsharari, M. (2024). Investigation of graphene based disk-square integration resonator for enhanced solar absorption using machine learning for solar heaters. *Alexandria Engineering Journal*, *102*, 192–199. https://doi.org/10.1016/j.aej.2024.05.083

Al-Mamun, M. R., Roy, H., Islam, M. S., Ali, M. R., Hossain, M. I., Aly, M. A. S., Khan, M. Z. H., Marwani, H. M., Islam, A., Haque, E., Rahman, M. M., & Awual, M. R. (2023). State-of-the-art in solar water heating (SWH) systems for sustainable solar energy utilization: A comprehensive review. *Solar Energy*, *264*, Article 111998. https://doi.org/10.1016/j.solener.2023.111998

Almarzooqi, N., Alwan, R. A., AlMarzooqi, F., Ghaffour, N., Hong, S., & Arafat, H. A. (2024). Solar-driven surface-heating membrane distillation using Ti_3C_2Tx MXene-coated spacers. *Chemosphere*, *351*, Article 141129. https://doi.org/10.1016/j.chemosphere.2024.141129

Ariff, A. H. M., Dele-Afolabi, T. T., Rafin, T. H., Jung, D. W., Leman, Z., Rezali, K. A. M., & Calin, R. (2023). Temporary sound barrier system from natural fiber polymeric composite. *Materials Today: Proceedings, 74*, 438-449. https://doi.org/10.1016/j.matpr.2022.11.142

Ashrafi, N., Ariff, A. H. M., Sarraf, M., Sulaiman, S., & Tang, S. H. (2021). Microstructural, thermal, electrical, and magnetic properties of optimized Fe_3O_4–SiC hybrid nano filler reinforced aluminium matrix composite. *Materials Chemistry and Physics, 258*, Article 123895. https://doi.org/10.1016/j.matchemphys.2020.123895

Aslfattahi, N., Loni, R., Bellos, E., Najafi, G., Kadirgama, K., Harun, W. S. W., & Saidur, R. (2021). Efficiency enhancement of a solar dish collector operating with a novel soybean oil-based-MXene nanofluid and different cavity receivers. *Journal of Cleaner Production*, *317*, Article 128430. https://doi.org/10.1016/j.jclepro.2021.128430

Aslfattahi, N., Samylingam, L., Abdelrazik, A. S., Arifutzzaman, A., & Saidur, R. (2020). MXene based new class of silicone oil nanofluids for the performance improvement of concentrated photovoltaic thermal collector. *Solar Energy Materials and Solar Cells*, *211*, Article 110526. https://doi.org/10.1016/j.solmat.2020.110526

Bady, M., El Hadi Attia, M., Kabeel, A. E., & Elazab, M. A. (2024). Enhancing conical solar still performance using high conductive hollow cylindrical copper fins embedded by PCM. *Solar Energy*, *282*, Article 112990. https://doi.org/10.1016/j.solener.2024.112990

Bai, Y., Gu, Y., Chen, J., & Yue, Y. (2024). A high-efficiency, salt-resistant, MXene/diatomite-modified coconut husk-based evaporator for solar steam generation. *Journal of Environmental Chemical Engineering*, *12*(2), Article 112282. https://doi.org/10.1016/j.jece.2024.112282

Bai, Y., & Wang, S. (2023). MXene/d-Mannitol aerogel phase change material composites for medium-temperature energy storage and solar-thermal conversion. *Journal of Energy Storage*, *67*, Article 107498. https://doi.org/10.1016/j.est.2023.107498

Bati, A. S. R., Sutanto, A. A., Hao, M., Batmunkh, M., Yamauchi, Y., Wang, L., Wang, Y., Nazeeruddin, M. K., & Shapter, J. G. (2021). Cesium-doped Ti_3C_2Tx MXene for efficient and thermally stable perovskite solar cells. *Cell Reports Physical Science*, *2*(10), Article 100598. https://doi.org/10.1016/j.xcrp.2021.100598

Bogdanovics, R., Zemitis, J., Zajacs, A., & Borodinecs, A. (2024). Small-scale district heating system as heat storage for decentralized solar thermal collectors during non-heating period. *Energy*, *298*, Article 131260. https://doi.org/10.1016/j.energy.2024.131260

Cao, H. (2024). Beyond graphene and boron nitride: Why MXene can be used in composite for corrosion protection on metals? *Composites Part B: Engineering*, *271*, Article 111168. https://doi.org/10.1016/j.compositesb.2023.111168

Chen, S., Meng, Y., Wang, X., Liu, D., Meng, X., Wang, X., & Wu, G. (2024). Hollow tubular MnO_2/MXene (Ti_3C_2, Nb_2C, and V_2C) composites as high-efficiency absorbers with synergistic anticorrosion performance. *Carbon*, *218*, Article 118698. https://doi.org/10.1016/j.carbon.2023.118698

Chen, Y., Chen, J., Hao, Z., Selim, M. S., Yu, J., & Chen, X. (2023). Polyvinylpyrrolidone-bridged MXene skeleton constructed by photothermal assisted sacrificial template method for phase change materials with form stability and photothermal conversion. *Chemical Engineering Journal*, *463*, Article 142375. https://doi.org/10.1016/j.cej.2023.142375

Cheng, J., Zhang, Z., Wang, Y., Li, F., Cao, J., Gozin, M., Ye, Y., & Shen, R. (2023). Doping of Al/CuO with microwave absorbing Ti_3C_2 MXene for improved ignition and combustion performance. *Chemical Engineering Journal*, *451*, Article 138375. https://doi.org/10.1016/j.cej.2022.138375

Dele-Afolabi, T., Hanim, M. A., Calin, R., & Ilyas, R. (2020). Microstructure evolution and hardness of MWCNT-reinforced Sn-5Sb/Cu composite solder joints under different thermal aging conditions. *Microelectronics Reliability, 110*, Article 113681. https://doi.org/10.1016/j.microrel.2020.113681

Ding, M., Ma, W., Liu, P., Yang, J., Lan, K., & Xu, D. (2023). Creating aligned porous structure with cobweb-like cellulose nanofibrils in MXene composite aerogel for solar-thermal desalination and humidity response. *Chemical Engineering Journal*, *459*, Article 141604. https://doi.org/10.1016/j.cej.2023.141604

Ding, Z., Su, W., Hakimi, F., Luo, Y., Li, W., Zhou, Y., Ye, L., & Yao, H. (2023). Machine learning in prediction of MXenes-based metasurface absorber for maximizing solar spectral absorption. *Solar Energy Materials and Solar Cells*, *262*, Article 112563. https://doi.org/10.1016/j.solmat.2023.112563

Dumka, P., Gajula, K., Sharma, K., Mishra, D. R., Chauhan, R., Haque Siddiqui, M. I., Dobrotă, D., & Rotaru, I. M. (2024). A case study on single basin solar still augmented with wax filled metallic cylinders. *Case Studies in Thermal Engineering*, *61*, Article 104847. https://doi.org/10.1016/j.csite.2024.104847

El-Fakharany, M. K., Abo-Samra, A. E. A., Abdelmaqsoud, A., & Marzouk, S. (2024). Enhanced performance assessment of an integrated evacuated tube and flat plate collector solar air heater with thermal storage material. *Applied Thermal Engineering, 243*, Article 122653. https://doi.org/10.1016/j.applthermaleng.2024.122653

El Hadi Attia, M., Zayed, M. E., Kabeel, A. E., Abdullah, A. S., & Abdelgaied, M. (2023). Energy, exergy, and economic analyses of a modified hemispherical solar distiller augmented with convex absorber basin, wicks, and PCM. *Solar Energy*, *261*, 43–54. https://doi.org/10.1016/j.solener.2023.05.057

Er, Y., Güler, O., Hekimoğlu, G., Nodehi, M., Ustaoğlu, A., Sarı, A., Gencel, O., & Ozbakkaloglu, T. (2023). Thermophysical properties and solar thermal energy storage performance of phase change composites manufactured by vat photopolymerization 3D printing technique. *Journal of Energy Storage*, *73*, Article 109124. https://doi.org/10.1016/j.est.2023.109124

Fan, W. K., Sherryna, A., & Tahir, M. (2022). Advances in titanium carbide (Ti_3C_2Tx) MXenes and their metal–organic framework (MOF)-based nanotextures for solar energy applications: A review. *ACS Omega*, *7*(43), 38158–38192. https://doi.org/10.1021/acsomega.2c05030

Fan, X., Zhang, S., Wang, H., Liu, L., Wang, L., Li, N., & Hu, S. (2024). A facile MXene/PPy modified asymmetry sponge solar absorber enabling efficient and high salt resistance evaporation. *Chemical Engineering Journal*, *483*, Article 149304. https://doi.org/10.1016/j.cej.2024.149304

Fayaz, H., Rasachak, S., Ahmad, M. S., Kumar, L., Zhang, B., JeyrajSelvaraj, Mujtaba, M. A., Soudagar, M. E. M., Kumar, R., & Omidvar, M. R. (2022). Improved surface temperature of absorber plate using metallic titanium particles for solar still application. *Sustainable Energy Technologies and Assessments*, *52*, Article 102092. https://doi.org/10.1016/j.seta.2022.102092

García-Segura, A., Sutter, F., Martínez-Arcos, L., Reche-Navarro, T. J., Wiesinger, F., Wette, J., Buendía-Martínez, F., & Fernández-García, A. (2021). Degradation types of reflector materials used in concentrating solar thermal systems. *Renewable and Sustainable Energy Reviews*, *143*, Article 110879. https://doi.org/10.1016/j.rser.2021.110879

Goel, V., Dwivedi, A., Kumar, R., Kumar, R., Pandey, A. K., Chopra, K., & Tyagi, V. V. (2023). PCM-assisted energy storage systems for solar-thermal applications: Review of the associated problems and their mitigation strategies. *Journal of Energy Storage*, *69*, Article 107912. https://doi.org/10.1016/j.est.2023.107912

Guo, L., Zhang, B., He, Q., Liu, M., & Liang, L. (2024). Fabrication and characterization of thermal barrier coatings for internal combustion engines via suspension plasma spray with high solid loading. *Surface and Coatings Technology, 479*, Article 130523. https://doi.org/10.1016/j.surfcoat.2024.130523

Han, L., Zhou, H., Fu, M., Li, J., Ma, H., & Zhang, B. (2023). Manufacturing robust MXene-based hydrogel-coated cotton fabric via electron-beam irradiation for efficient interfacial solar evaporation. *Chemical Engineering Journal, 473*, Article 145337. https://doi.org/10.1016/j.cej.2023.145337

Ji, X., Fan, X., Liu, X., Gu, J., Lu, H., Luan, Z., & Liang, J. (2024). Highly elastic, robust, and efficient hydrogel solar absorber against harsh environmental impacts. *Nano Letters*, *24*(11), 3498–3506.

Jiang, G., Yu, W., & Lei, H. (2022). Novel solar membrane distillation system based on Ti_3C_2TX MXene nanofluids with high photothermal conversion efficiency. *Desalination*, *539*, Article 115930. https://doi.org/10.1016/j.desal.2022.115930

Kalidasan, B., Pandey, A. K., Saidur, R., Han, T. K., & Mishra, Y. N. (2024). MXene-based eutectic salt hydrate phase change material for efficient thermal features, corrosion resistance & photo-thermal energy conversion. *Materials Today Sustainability*, *25*, Article 100634. https://doi.org/10.1016/j.mtsust.2023.100634

Kandpal, B. C., Johri, N., Bhatia, P., Masih, C., & Kumar, K. (2022). Analyzing the microstructure and mechanical properties in LM6 aluminium casting in sand casting process. *Materials Today: Proceedings, 62*, 3155-3161. https://doi.org/10.1016/j.matpr.2022.03.432

Lee, S. E., Seo, J., Kim, S., Park, J. H., Jin, H. J., Ko, J., Kim, J. H., Kang, H., Kim, J., & Lee, H. (2024). Reversible solar heating and radiative cooling devices via mechanically guided assembly of 3D macro/microstructures. *Advanced Materials*, *36*(39), Article 2400930. https://doi.org/10.1002/adma.202400930

Lei, Z., Sun, X., Zhu, S., Dong, K., Liu, X., Wang, L., Zhang, X., Qu, L., & Zhang, X. (2022). Nature inspired mxene-decorated 3D honeycomb-fabric architectures toward efficient water desalination and salt harvesting. *Nano-Micro Letters*, *14*, Article 10. https://doi.org/10.1007/s40820-021-00748-7

Li, X., Chang, H., Zeng, L., Huang, X., Li, Y., Li, R., & Xi, Z. (2020). Numerical analysis of photothermal conversion performance of MXene nanofluid in direct absorption solar collectors. *Energy Conversion and Management*, *226*, Article 113515. https://doi.org/10.1016/j.enconman.2020.113515

Li, X., Wu, R., Shi, Y., Ding, S., Li, M., Xu, S., Zhang, B., Tong, L., & Wang, Q. (2024). Enhanced corrosion and wear resistance via dopamine-functionalized Ti_3C_2Tx MXene/waterborne polyurethane coating on magnesium alloy. *Materials Today Chemistry*, *39*, Article 102142. https://doi.org/10.1016/j.mtchem.2024.102142

Li, Y., Sheng, P., Lin, L., Wang, L., Lu, D., Lin, K., Wu, H., & Wu, S. (2024). Vat photopolymerization versus conventional colloidal processing methods in structural ceramics: Progress, challenges, and future perspectives. *Additive Manufacturing Frontiers, 3*(1), Article 200110. https://doi.org/10.1016/j.amf.2024.200110

Li, Y., Xiong, C., Huang, H., Peng, X., Li, M., Mei, D., Liu, G., Wu, M., Zhao, T., & Huang, B. (2021). *2D MXenes: The Lowest-Emissivity Black Materials*. Research Square. https://doi.org/10.21203/rs.3.rs-149825/v1

Liu, S., Quan, B., Yang, Y., Wu, H., Chen, Q., Li, G., Tao, Z., Zhu, C., Lu, X., & Qu, J. (2023). Shape stable phase change composites based on MXene/biomass-derived aerogel for solar–thermal energy conversion and storage. *Journal of Energy Storage*, *67*, Article 107592. https://doi.org/10.1016/j.est.2023.107592

Lv, G., Qian, W., Zhang, H., Su, Y., & Qian, P. (2024). Role of –O functional groups at the $Ti_3C_2O_2$(MXene)/Al interface in enhancing the mechanical properties of aluminum matrix composites: A first-principles study. *Applied Surface Science*, *642*, Article 158608. https://doi.org/10.1016/j.apsusc.2023.158608

Mao, M., Lou, D., Wang, D., Younes, H., Hong, H., Chen, H., & Peterson, G. P. (2022). Ti_3C_2Tx MXene nanofluids with enhanced thermal conductivity. *Chemical Thermodynamics and Thermal Analysis*, *8*, Article 100077. https://doi.org/10.1016/j.ctta.2022.100077

Nazarlou, Z., Hosseini, S. F., Seyed Dorraji, M. S., Rasoulifard, M. H., & Aydemir, U. (2023). Ti_3C_2 MXene/polyaniline/montmorillonite nanostructures toward solvent-free powder coatings with enhanced corrosion resistance and mechanical properties. *ACS Applied Nano Materials, 6*(10), 8804–8818. https://doi.org/10.1021/acsanm.3c01214

Nie, Z., Lu, H., Liu, Q., Chai, G., Ding, Y., Xu, G., & Guo, J. (2024). Effect of copper introduction on the properties of micro-arc oxidation coating on powder metallurgy aluminum disk. *Surface and Coatings Technology*, *479*, Article 130520. https://doi.org/10.1016/j.surfcoat.2024.130520

Nugroho, W. T., Dong, Y., & Pramanik, A. (2022). Dimensional accuracy and surface finish of 3D printed polyurethane (PU) dog-bone samples optimally manufactured by fused deposition modelling (FDM). *Rapid Prototyping Journal, 28*(9), 1779–1795. https://doi.org/10.1108/RPJ-12-2021-0328

Panda, D., Sahu, A. K., & Gangawane, K. M. (2024). Eutectic phase change composites with MXene nanoparticles for enhanced photothermal absorption and conversion capacity. *Solar Energy Materials and Solar Cells*, *272*, Article 112911. https://doi.org/10.1016/j.solmat.2024.112911

Qi, B., Wang, N., Cui, S., Liu, H., Hu, X., Li, H., Li, Y., Li, Y., Lu, J., & Bao, M. (2024). Biomimetic structural aerogel derived from green tide enteromorpha-prolifera: Multi-sided unidirectional freeze casting and solar-driven viscous oil spill remediation. *Chemical Engineering Journal*, *498*, Article 155647. https://doi.org/10.1016/j.cej.2024.155647

Saberi, Y., & Oveisi, H. (2022). Development of novel cellular copper–aluminum composite materials: The advantage of powder metallurgy and mechanical milling approach for lighter heat exchanger. *Materials Chemistry and Physics*, *279*, Article 125742. https://doi.org/10.1016/j.matchemphys.2022.125742

Samylingam, I., Aslfattahi, N., Kadirgama, K., Samykano, M., Samylingam, L., & Saidur, R. (2021). Improved thermophysical properties of developed ternary nitrate-based phase change material incorporated with MXene as novel nanocomposites. *Energy Engineering*, *118*(5), 1253–1265. https://doi.org/10.32604/EE.2021.016087

Seetharaman, S., & Gupta, M. (2021). Fundamentals of metal matrix composites. In D. Brabazon (Ed.), *Encyclopedia of Materials: Composites* (pp. 11–29). Elsevier. https://doi.org/10.1016/B978-0-12-819724-0.00001-X

Sethi, M., Chauhan, A., Ziyadullayevich, A. A., Turayevich, J. I., Alimovna, P. Z., Omonov, S., Meyliev, O., Tyagi, D., Rana, N., & Moorthy, C. B. (2024). Use of carbon nanotubes in flat and evacuated tube solar collectors for thermal enhancement: A review. In *Materials Today: Proceedings* (pp. 1-11). Elsevier. https://doi.org/10.1016/j.matpr.2024.05.056

Sharma, S., & Talukdar, P. (2024). Thermo-mechanical performance enhancement of volumetric solar receivers using graded porous absorbers. *Energy, 304*, Article 132070. https://doi.org/10.1016/j.energy.2024.132070

Singh, R., Gupta, A., Tripathi, O., Srivastava, S., Singh, B., Awasthi, A., Rajput, S. K., Sonia, P., Singhal, P., & Saxena, K. K. (2020). Powder bed fusion process in additive manufacturing: An overview. *Materials Today: Proceedings, 26*, 3058-3070. https://doi.org/10.1016/j.matpr.2020.02.635

Singh, S. K., Tiwari, A. K., & Paliwal, H. K. (2023). Performance augmentation strategy of Parabolic trough collector by employing MXene-based solar absorbing coating. *Process Safety and Environmental Protection*, *174*, 971–982. https://doi.org/10.1016/j.psep.2023.05.007

Singh, S. K., Tiwari, A. K., & Said, Z. (2024). MXene nanofluid enhanced parabolic trough collectors: An integrated energy, exergy, environmental, and economic study for enhanced energy generation. *Solar Energy*, *276*, Article 112658. https://doi.org/10.1016/j.solener.2024.112658

Solangi, N. H., Mubarak, N. M., Karri, R. R., Mazari, S. A., Jatoi, A. S., Koduru, J. R., & Dehghani, M. H. (2022). MXene-based phase change materials for solar thermal energy storage. *Energy Conversion and Management*, *273*, Article 116432. https://doi.org/10.1016/j.enconman.2022.116432

Sreekumar, S., Ganguly, A., Khalil, S., Chakrabarti, S., Hewitt, N., Mondol, J. D., & Shah, N. (2024). Thermo-optical characterization of novel MXene/Carbon-dot hybrid nanofluid for heat transfer applications. *Journal of Cleaner Production*, *434*, Article 140395. https://doi.org/10.1016/j.jclepro.2023.140395

Sreekumar, S., Shaji, J., Cherian, G., Thomas, S., Deb Mondol, J., & Shah, N. (2024). Corrosion analysis and performance investigation of hybrid MXene/C-dot nanofluid-based direct absorption solar collector. *Solar Energy*, *269*, Article 112317. https://doi.org/10.1016/j.solener.2024.112317

Su, F., Li, X., He, Z., Xie, J., Zhang, W., Xin, Y., Cheng, X., Yao, D., & Zheng, Y. (2024). Latent heat type nanofluid based on MXene and MoS_2 modified hierarchical structured phase change nanocapsules for sustainable and efficient light-heat conversion. *Chemical Engineering Journal*, *495*, Article 153413. https://doi.org/10.1016/j.cej.2024.153413

Su, J., Zhang, P., Yang, R., Wang, B., Zhao, H., Wang, W., & Wang, C. (2022). MXene-based flexible and washable photothermal fabrics for efficiently continuous solar-driven evaporation and desalination of seawater. *Renewable Energy*, *195*, 407–415. https://doi.org/10.1016/j.renene.2022.06.038

Suraparaju, S. K., Samykano, M., Nandavarapu, R. R., Natarajan, S. K., Muthuvairavan, G., Yadav, A., & Vasudevan, G. (2025). Innovative double-finned absorber and nanoparticle-enhanced energy storage for enhanced thermo-economic performance of solar stills. *Separation and Purification Technology*, *361*, Article 131360. https://doi.org/10.1016/j.seppur.2024.131360

Tarno, M. I., Masuri, S. U., Ariff, A. H. M., Daura, A. A., Dankulu, M. H., Musa, M., & Dalhat, N. (2024). Microstructure and mechanical properties of carburized mild steel for solar thermal applications. In S. Hashmi (Ed.), *Comprehensive Materials Processing (2nd ed.)* (pp. 221–231). Elsevier. https://doi.org/10.1016/B978-0-323-96020-5.00154-0

Tarno, M. I., Masuri, S. U., Ariff, A. H. M., & Musa, M. (2024). Characterization and microstructure of iron-chromite reinforced aluminum matrix composites produced through recrystallization process. In S. Hashmi (Ed.), *Comprehensive Materials Processing (2nd ed.)* (pp. 232–248). Elsevier. https://doi.org/10.1016/B978-0-323-96020-5.00155-2

Thakur, A. K., Sathyamurthy, R., Saidur, R., Velraj, R., Lynch, I., & Aslfattahi, N. (2022). Exploring the potential of MXene-based advanced solar-absorber in improving the performance and efficiency of a solar-desalination unit for brackish water purification. *Desalination*, *526*, Article 115521. https://doi.org/10.1016/j.desal.2021.115521

Vahidhosseini, S. M., Rashidi, S., Hsu, S. H., Yan, W. M., & Rashidi, A. (2024). Integration of solar thermal collectors and heat pumps with thermal energy storage systems for building energy demand reduction: A comprehensive review. *Journal of Energy Storage*, *95*, Article 112568. https://doi.org/10.1016/j.est.2024.112568

Wang, H., Li, X., Luo, B., Wei, K., & Zeng, G. (2021). The MXene/water nanofluids with high stability and photo-thermal conversion for direct absorption solar collectors: A comparative study. *Energy*, *227*, Article 120483. https://doi.org/10.1016/j.energy.2021.120483

Wang, H., Deng, Y., Liu, Y., Wu, F., Wang, W., Jin, H., Zheng, J., & Lei, J. (2022). In situ preparation of light-driven cellulose-Mxene aerogels based composite phase change materials with simultaneously enhanced light-to-heat conversion, heat transfer and heat storage. *Composites Part A: Applied Science and Manufacturing*, *155*, Article 106853. https://doi.org/10.1016/j.compositesa.2022.106853

Wang, T., Huang, J., Fu, H., Yu, K., & Yao, S. (2022). Influence of process parameters on filling and feeding capacity during high-pressure die-casting process. *Applied Sciences*, *12*(9), Article 4757. https://doi.org/10.3390/app12094757

Wang, Y., Nie, J., He, Z., Zhi, Y., Ma, X., & Zhong, P. (2022). Ti_3C_2Tx MXene nanoflakes embedded with copper indium selenide nanoparticles for desalination and water purification through high-efficiency solar-driven membrane evaporation. *ACS Applied Materials & Interfaces*, *14*(4), 5876–5886. https://doi.org/10.1021/acsami.1c22952

Wang, P. L., Zhang, W., Yuan, Q., Mai, T., Qi, M. Y., & Ma, M. G. (2023). 3D Janus structure MXene/cellulose nanofibers/luffa aerogels with superb mechanical strength and high-efficiency desalination for solar-driven interfacial evaporation. *Journal of Colloid and Interface Science*, *645*, 306–318. https://doi.org/10.1016/j.jcis.2023.04.081

Wang, M., Yan, H., Zhang, P., Lu, Q., Shi, H., & Zhang, B. (2024). Particulate-reinforced Al-based metal matrix composites fabricated by selective laser melting: A comprehension review. *Optics & Laser Technology*, *176*, Article 110918. https://doi.org/10.1016/j.optlastec.2024.110918

Wang, T., Cao, H., Ma, X., Shen, X., Min, Y., & Xu, Q. (2024). Electrodeposited Ti_3C_2Tx MXene composite coating toward superior surface protection on aluminum alloy in PEMFC environments. *Corrosion Science*, *232*, Article 112044. https://doi.org/10.1016/j.corsci.2024.112044

Wang, R., Li, P., Zhou, W., Li, Y., Gao, K., & Ouyang, Y. (2024). Study on oxidation mechanism of aluminum surface under applied electric field. *Materials Chemistry and Physics, 318*, Article 129224. https://doi.org/10.1016/j.matchemphys.2024.129224

Wang, K., Zhang, Y., Zou, Q., Liu, Z., Song, L., Tang, H., Qin, Y., & Qiao, Z. (2025). High-strength aluminum matrix composites with strong bonding interfaces via in-situ amorphous alumina and plainification strategy. *Composites Communications*, *53*, Article 102201. https://doi.org/10.1016/j.coco.2024.102201

Wu, Y., Feng, Y., Liu, X., Shen, T., & Zhang, H. (2023). Intrinsic MXene-Ti_3C_2Tx enhanced high sensitivity Mach-Zehnder interferometric microstructured optic fiber temperature sensor. *Optical Fiber Technology*, *80*, Article 103457. https://doi.org/10.1016/j.yofte.2023.103457

Xu, W., Su, J., Lin, J., Huang, J., Weng, M., & Min, Y. (2023). Enhancing the light-thermal absorption and conversion capacity of diatom-based biomass/polyethylene glycol composites phase change material by introducing MXene. *Journal of Energy Storage*, *72*, Article 108253. https://doi.org/10.1016/j.est.2023.108253

Xu, Y., Wang, B., & Zhou, J. (2025). Annular Ti-Al_2O_3-Ti triple-layer stacked composite microstructure solar absorber. *Applied Thermal Engineering*, *263*, Article 125449. https://doi.org/10.1016/j.applthermaleng.2025.125449

Yang, X., Luo, J., Ren, H., Xue, Y., Yang, C., Yuan, T., Yang, Z., Liu, Y., Zhang, H., & Yu, J. (2023). Simultaneously improving the EMI shielding performances and mechanical properties of CF/PEKK composites via MXene interfacial modification. *Journal of Materials Science & Technology*, *154*, 202–209. https://doi.org/10.1016/j.jmst.2023.01.020

Yang, Z., Wei, N., Xue, N., Xu, R., Yang, E., Wang, F., Zhu, H., & Cui, H. (2024). Highly efficient MoS_2/MXene aerogel for interfacial solar steam generation and wastewater treatment. *Journal of Colloid and Interface Science*, *656*, 189–199. https://doi.org/10.1016/j.jcis.2023.11.110

Yu, Y., Jin, S., Yu, Z., Xing, J., Chen, H., Li, K., Liu, C., Deng, C., & Xiao, H. (2024). Deep eutectic supramolecular polymer functionalized MXene for enhancing mechanical properties, photothermal conversion, and bacterial inactivation of cellulose textiles. *International Journal of Biological Macromolecules*, *267*, Article 131512. https://doi.org/10.1016/j.ijbiomac.2024.131512

Yue, H., Ou, Y., Wang, J., Wang, H., Du, Z., Du, X., & Cheng, X. (2024). Ti_3C_2Tx MXene/delignified wood supported flame-retardant phase-change composites with superior solar-thermal conversion efficiency and highly electromagnetic interference shielding for efficient thermal management. *Energy*, *286*, Article 129441. https://doi.org/10.1016/j.energy.2023.129441

Zaed, M., Tan, K. H., Saidur, R., Pandey, A. K., & Cherusseri, J. (2024). Low-cost synthesis of Ti_3C_2Tx MXene-based sponge for solar steam generation and clean water production. *Ceramics International, 50*(16), 27910-27922. https://doi.org/10.1016/j.ceramint.2024.05.086

Zang, X., Qin, Y., Gu, M., Sun, Y., Huang, D., Ji, J., & Xue, M. (2023). MXene/Aramid nanofiber films enables highly efficient photothermal conversion for solar-driven water evaporation. *Materials Today Sustainability, 24*, Article 100558. https://doi.org/10.1016/j.mtsust.2023.100558

Zhao, K., Guo, Z., Wang, J., & Xie, H. (2023). Enhancing solar photothermal conversion and energy storage with titanium carbide (Ti_3C_2) MXene nanosheets in phase-change microcapsules. *Journal of Colloid and Interface Science*, *650*, 1591–1604. https://doi.org/10.1016/j.jcis.2023.07.114

Zheng, Z., Liu, H., Wu, D., & Wang, X. (2022). Polyimide/MXene hybrid aerogel-based phase-change composites for solar-driven seawater desalination. *Chemical Engineering Journal*, *440*, Article 135862. https://doi.org/10.1016/j.cej.2022.135862

Zhou, Y., Li, X., Guo, C., Hu, X., & Zhu, Q. (2023). Investigation of columnar to equiaxial transition criterion and solidification conditions for Ni-based superalloy in laser powder bed fusion. *Journal of Alloys and Compounds, 966*, Article 171611. https://doi.org/10.1016/j.jallcom.2023.171611

Zhou, W., Arshad, N., Xiao, B., Xiong, X., Yu, F., He, S., Irshad, M. S., Wang, X., & Lin, L. (2024). 3D inverted cone hydrogels derived by MXene-TiOX nanocomposite for sequential regulation of enhanced solar-driven steam generation. *Next Nanotechnology*, *5*, Article 100040. https://doi.org/10.1016/j.nxnano.2024.100040

Zhou, Y., Yu, W., Li, Y., Lei, Q., & Xie, H. (2024). Power generation device via solar collector coupled with a shape-memory alloy thermo-mechanical switch utilizing MXene nanofluid as high-efficiency photothermal conversion working medium. *Energy Conversion and Management*, *302*, Article 118092. https://doi.org/10.1016/j.enconman.2024.118092

Pertanika J. Sci. & Technol. 33 (4): 1743 - 1764 (2025)

PERTANIKA JOURNALS

SCIENCE & TECHNOLOGY

Journal homepage: http://www.pertanika.upm.edu.my/

Tailored Cognitive Interventions for Aging Populations: Development and Analysis of a Machine Learning-Driven Web Platform

Mario Macea-Anaya[1], Rubén Baena-Navarro[1,2]*, Yulieth Carriazo-Regino[1,2], Ober Primera-Correa[1,3] and Juan Pérez-Díaz[1,3]

[1]Department of Systems Engineering, Universidad de Córdoba, Montería (Córdoba), Monteria 230002, Colombia
[2]Systems Engineering Program, Universidad Cooperativa de Colombia, Montería (Córdoba), Monteria 230002, Colombia
[3]Research Group on Free Software and GNU-Linux, Faculty of Engineering, Universidad de Córdoba, Montería (Córdoba), Monteria 230002, Colombia

ABSTRACT

Aging is associated with a progressive decline in cognitive functions, driving the development of digital interventions to mitigate its impact. This study evaluated a web-based application designed to enhance cognitive performance in older adults through a Multilayer Perceptron (MLP) model optimized using K-fold cross-validation (K=5). A total of 100 participants aged 65 and older were randomly assigned to an experimental group and a control group. Over 16 weeks, the experimental group used the personalized application, while the control group accessed non-adaptive content. Statistical analysis revealed a significant improvement in the experimental group, with an average cognitive score increase of 37% (95% CI: 8.8–9.8), compared to 10% in the control group (95% CI: 5.5–6.3). The model achieved an accuracy of 89% and an area under the curve (AUC) of 0.93, demonstrating its ability to predict cognitive improvements effectively. Additionally, 92% of participants completed more than 80% of the sessions, indicating high adherence. Usability evaluation reported an average score of 4.7/5, reflecting positive perceptions regarding the platform's accessibility and usefulness. These findings support the integration of machine learning techniques into cognitive stimulation programs, highlighting their potential for incorporation into digital healthcare systems to improve the quality of life in aging populations. Future research could explore deep learning models and dimensionality reduction techniques to further optimize intervention personalization.

ARTICLE INFO

Article history:
Received: 02 September 2024
Accepted: 17 March 2025
Published: 11 June 2025

DOI: https://doi.org/10.47836/pjst.33.4.03

E-mail addresses:
mariomacea@correo.unicordoba.edu.co (Mario Macea-Anaya)
rbaena@correo.unicordoba.edu.co (Rubén Baena-Navarro)
yulieth.carriazor@campusucc.edu.co (Yulieth Carriazo-Regino)
oprimeracorrea@correo.unicordoba.edu.co (Ober Primera-Correa)
jperezdiaz50@correo.unicordoba.edu.co (Juan Pérez-Díaz)
* Corresponding author

Keywords: Artificial intelligence, cognitive stimulation, cross-validation, digital intervention, machine learning, neural networks, older adults

© Universiti Putra Malaysia Press

INTRODUCTION

The global trend of population aging has raised significant concerns across various fields, including education, healthcare, and technology, due to its profound implications for societal structure and function. According to the World Health Organization (2022), it is projected that by 2050, the population aged 60 and above will reach 2.1 billion, presenting unprecedented challenges in managing cognitive health and maintaining functional independence. This demographic transition, driven by longer life expectancy and declining fertility rates, has resulted in an increase in chronic diseases, including neurodegenerative conditions, which significantly affect the quality of life of older adults (United Nations, Department of Economic and Social Affairs, 2019).

Addressing these challenges necessitates the development of innovative and effective strategies to counteract the cognitive decline associated with aging. The literature consistently underscores the importance of cognitive interventions in delaying and potentially preventing cognitive decline related to aging (Cheng, 2016). Within this context, digital technologies have emerged as promising tools for promoting active aging by enhancing key cognitive functions such as memory and executive function (Glenn et al., 2019). However, the success of these technologies is contingent on overcoming significant hurdles related to usability and accessibility, particularly for older adults who may not be familiar with modern digital interfaces (Alruwaili et al., 2023; Velciu et al., 2023). A user-centered design approach is essential to ensure that these tools are effective and adaptable to the specific needs of older populations (Carriazo-Regino et al., 2024; Kim et al., 2024; Reynel et al., 2023).

This study aims to design and conduct an initial evaluation of a web application tailored to support cognitive functions in older adults. The hypothesis is that a participatory, user-centered design can lead to significant improvements in memory and other cognitive abilities in this demographic. The study further explores how the integration of advanced data mining and machine learning techniques can be utilized to personalize cognitive exercise recommendations, thereby enhancing user experience and improving adherence to the intervention program. This data-driven approach represents an emerging area of research that could revolutionize the management of cognitive aging, allowing for more targeted and effective interventions tailored to the needs of individual users.

The central research problem of this study addresses the pressing need to develop digital interventions that are both effective and accessible for mitigating cognitive decline in older adults. Specifically, it examines how a user-centered design framework, supported by advanced data mining and machine learning techniques, can enhance the personalization and effectiveness of web applications designed for cognitive support in older adults. Given the demographic challenges of an aging population and the significant impact of neurodegenerative diseases, it is evident that current solutions have not fully addressed the specific usability and accessibility requirements of older users.

The study seeks to answer the following questions to address this research problem: How can a participatory, user-centered design improve the usability and effectiveness of web applications to support cognition in older adults? How can integrating data mining and machine learning techniques enhance the personalization of cognitive exercises, thereby improving user experience and adherence to the intervention program? What is the overall impact of data-driven personalization on the effectiveness of digital interventions in enhancing cognitive function in older adults?

The contribution of this research lies in its exploration and validation of an innovative approach that integrates user-centered design with advanced personalization technologies to address cognitive decline in older adults. This approach contributes to the existing body of literature on digital interventions and opens up new research avenues in gerontology and educational technology. From a practical standpoint, the findings of this study have the potential to inform the development of more effective and accessible tools that can be incorporated into public health and educational programs, thereby promoting healthy and active aging on a global scale.

Literature Review

The global increase in the aging population has led to growing interest in the development of interventions aimed at promoting active and healthy aging. Within this context, digital technologies have demonstrated considerable potential in mitigating cognitive decline among older adults. Despite progress in this field, significant gaps in the literature underscore the need for ongoing research and refinement of these interventions. The PRISMA methodology (Preferred Reporting Items for Systematic Reviews and Meta-Analyses) was employed to systematically review the effectiveness of digital interventions in enhancing cognition in older adults. This rigorous approach ensures a transparent process in selecting and analyzing relevant studies (Baena-Navarro et al., 2024; Bouabddallaoui et al., 2023; Carriazo-Regino et al., 2022; Jaadi et al., 2024; Moher et al., 2009; Pinedo-López et al., 2024; Vidal-Durango et al., 2024).

Search Strategy

The literature search was conducted across several well-established academic databases, covering publications from 2016 to the present. Keywords such as “cognitive aging,” “digital interventions,” “user-centered design,” and “elderly population” were employed. The inclusion criteria focused on studies that evaluated the effectiveness of digital interventions in improving cognitive function in older adults and were published in English. This approach facilitated the identification of a relevant set of studies addressing various aspects of implementing digital technologies within this demographic.

Study Selection

Initially, 25 articles were identified. Those that did not meet the inclusion criteria related to user-centered design and the implementation of digital interventions in older adult populations were excluded. After thoroughly reviewing the titles and abstracts, seven studies were selected that provide substantial evidence of the impact of digital technologies on cognitive aging. These studies were analyzed in depth to provide a critical overview of the current research landscape in this area.

Review Results

The studies selected indicate that while digital interventions have the potential to enhance cognitive function in older adults, they encounter several challenges concerning design and implementation. Table 1 summarizes the selected studies, emphasizing their contributions and the number of citations.

To deepen the understanding of the impact of the selected studies, an analysis of the variability in the number of citations received by each article based on its publication year was conducted. This analysis is essential for identifying patterns and trends within the scientific literature. The dispersion in the number of citations, measured by variance, is calculated using Equation 1.

$$\sigma^2 = \frac{1}{N-1}\sum_{i=1}^{N}(C_i - \bar{C})^2 \quad [1]$$

Where C_i is the number of citations of a specific article, $\bar{C}$ is the average number of citations, and N is the total number of articles analyzed. A high variance indicates significant

Table 1
Selected articles

Authors	Research Focus	Citations
Alruwaili et al. (2023)	A comprehensive review of digital interventions targeting cognitive health in aging populations, focusing on user-centered approaches.	45
Kim et al. (2024)	Assessment of Extended Reality (XR) technologies in enhancing both cognitive and physical abilities in elderly individuals.	22
Velciu et al. (2023)	Investigation of smart technologies like smartphones and wearables for promoting health and monitoring in senior adults.	30
Fruitet et al. (2023)	Application of conversational agents in cognitive therapies for elderly patients with neurodegenerative diseases, focusing on at-home use.	12
Yi et al. (2024)	Exploration of immersive museum experiences to improve mental well-being in seniors with dementia, presenting novel intervention concepts.	15
Lee et al. (2021)	Development of mobile game design principles tailored to improve cognitive and physical engagement in older adults.	10
Revenäs et al. (2020)	Formulation of protocols for integrating essential user characteristics into the design of digital systems to prevent falls in elderly populations.	25

variability in how frequently the studies are cited, potentially reflecting the relevance of the topic or the prominence of the journal in which the article was published.

Additionally, the covariance between the number of citations (C) and the year of publication (Y) was calculated using Equation 2 to determine the linear relationship between these two quantitative variables.

$$cov(C,Y) = \frac{1}{N}\sum_{i=1}^{N}(C_i - \bar{C})\,(Y_i - \bar{Y}) \quad [2]$$

A positive covariance between the number of citations and the year of publication suggests that more recent articles tend to receive more citations, indicating growing interest in current topics. Conversely, a negative covariance might suggest that older articles continue to receive citations, demonstrating the ongoing relevance of past research.

The analysis revealed considerable variability in the number of citations among the selected studies. Figure 1 illustrates the relationship between the number of citations and the publication year of the selected studies. The figure shows a slight negative trend, suggesting that more recent studies receive fewer citations than older ones. This trend could be interpreted as a reflection of saturation in the publication of new studies or a preference within the academic community for citing more established research over time. This behavior may be linked to various factors, such as the perceived relevance of the topics addressed or the greater visibility of articles published in previous years due to longer exposure time.

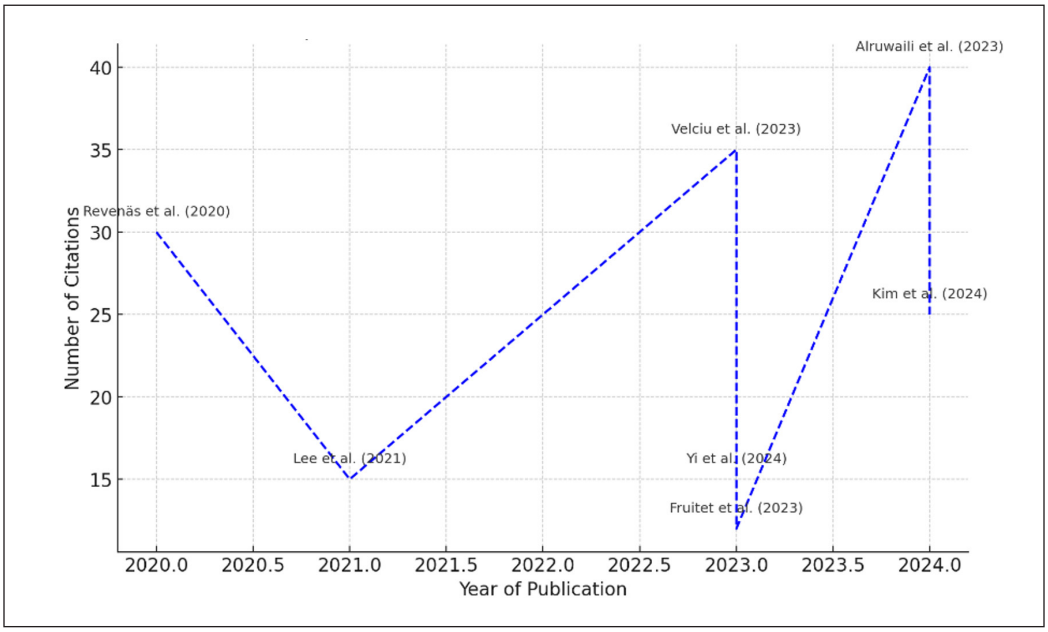

Figure 1. Temporal trend in the number of citations of the studies

The negative trend observed in Figure 1 could indicate several phenomena in the dynamics of scientific literature. Firstly, there may be an overproduction of recent research, making it difficult for each new study to receive the attention it deserves. This can dilute the impact of each publication, as researchers may be spreading their citations across a larger number of works. Additionally, the preference for citing older, established studies could reflect confidence in the robustness of research that has already been validated.

Moreover, the covariance analysis suggests that the decrease in citations for more recent studies could be influenced by the nature of the topic or by shifts in research focus within the field of digital interventions for cognitive aging. This observation is crucial as it helps identify areas where recent research may not be as influential as expected, guiding future research toward more innovative or less explored topics.

Understanding the relationship between the number of citations and the year of publication is essential for identifying trends in the literature and adjusting research strategies. While more recent studies appear to receive fewer citations, this does not necessarily imply lower quality; rather, it could reflect changes in the dynamics of scientific publication and in the areas of interest within the research community. Future researchers need to consider these trends when developing new studies, ensuring that their research addresses emerging and relevant areas that can have a significant impact on the field.

Finally, the analysis of variance and covariance in the context of article citations provides valuable insight into how academic attention is distributed over time and what factors may influence the visibility of research. This type of analysis is useful for understanding the past and present of the scientific literature and for planning future strategies that maximize the impact and relevance of new research in the field of cognitive aging.

METHOD

This study was conducted to design and evaluate a web-based application to enhance cognitive abilities in older adults through tailored digital interventions. The methodology was organized into multiple phases, encompassing the development, implementation, and evaluation of the application, ensuring that the results are scientifically replicable and valid.

Application Development

The web application was developed following a user-centered design methodology, actively involving older adults throughout the design process. This approach facilitated the customization of the user interface and application features to suit the specific needs of this demographic, ensuring the tool's accessibility and usability. For instance, Figure 2 presents the application's login screen, where users can sign in by entering their email and a secure password. The design of this screen prioritizes simplicity and ease of use, making it straightforward for older users to log in without difficulties.

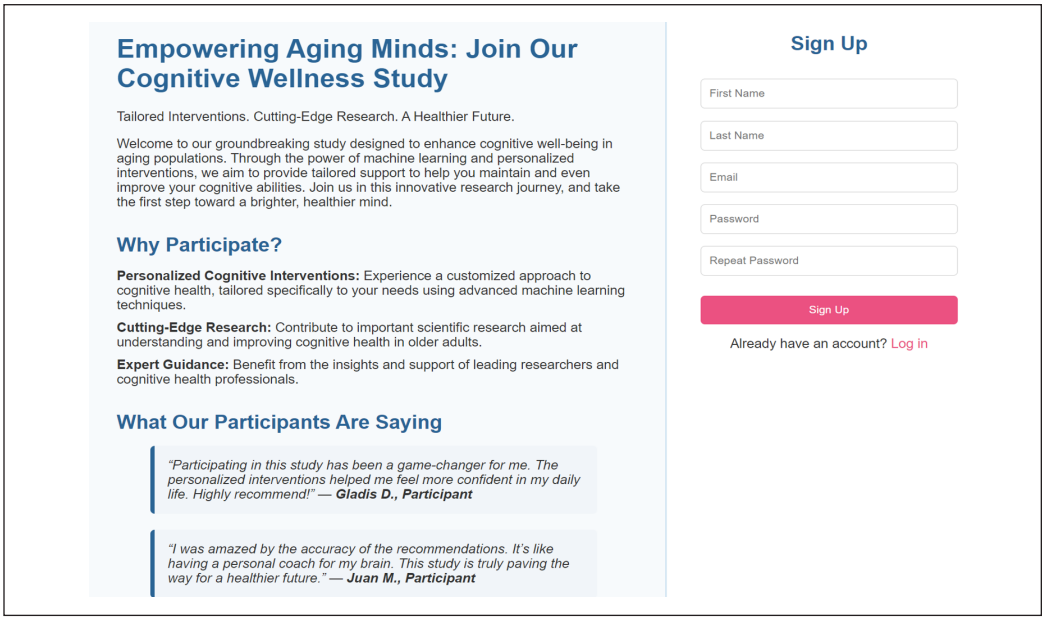

Figure 2. Login screen of the web application

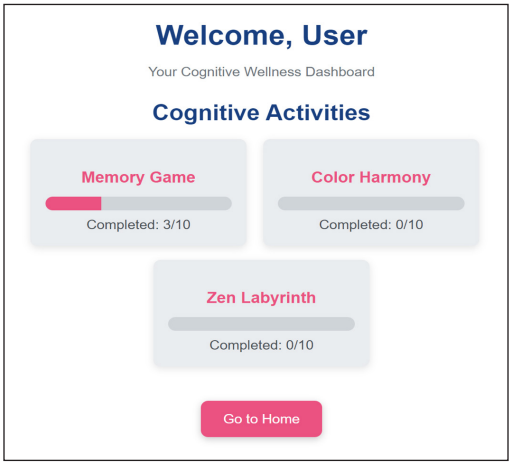

Figure 3. Cognitive exercises in the web application

The platform was built using Python 3.9 alongside the Django 3.2 framework for the backend, while the front end was crafted using HTML5, CSS3, and JavaScript (ES6). These technologies have proven effective for building scalable, high-performance web applications (Nair & Hinton, 2010; Pedregosa et al., 2011). Additionally, the application features a series of cognitive exercises designed to stimulate key areas such as memory, attention, and processing speed, as illustrated in Figure 3. Users can choose and complete various activities, with a progress tracker to monitor how many completed tasks. This functionality was essential for sustaining user engagement and motivation throughout the 16-week intervention.

The application is designed to be responsive and user-friendly across different devices, including desktops, tablets, and smartphones, which is critical for maximizing user adherence to the proposed digital interventions (Kelly et al., 2014).

Given the rural setting of this study, where internet connectivity may be limited, the architecture of the system was designed to operate effectively in such conditions. As

illustrated in Figure 4, the local architecture consists of a central server hosted within the community or local healthcare center, which connects directly to multiple devices, such as mobile phones, tablets, and PCs, through a local area network (LAN). This setup ensures that even in the absence of a stable internet connection, participants can access the application and engage in cognitive exercises without interruption. The server stores user data locally and synchronizes with the cloud when connectivity is available, ensuring data consistency and security (Nathasha et al., 2023; Odilibe et al., 2023).

This local infrastructure is crucial for deploying digital interventions in rural areas, as it circumvents the challenges of unreliable internet connections. The architecture supports multiple users simultaneously, allowing the application to be scaled within the community to accommodate a larger number of participants (Gorde et al., 2024).

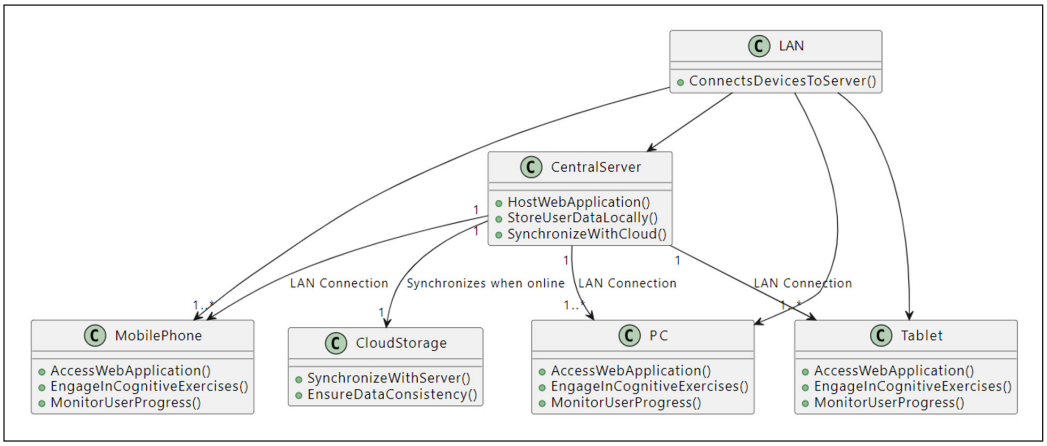

Figure 4. Software and hardware architecture for the web application

Participants and Procedure

A total of 100 individuals aged 65 and older participated in the study, recruited through purposive sampling. This method was employed to ensure diversity in gender, educational background, and familiarity with technology and to select participants who demonstrated a willingness to commit to the intervention and were available during the study period. The inclusion of diverse demographic profiles aimed to reflect the variability within the aging population and allowed for a more comprehensive analysis of the intervention's potential impact (Bae et al., 2019).

Before commencing the intervention, participants underwent an initial evaluation using the Mini-Mental State Examination (MMSE). This widely recognized instrument assesses cognitive functions and was employed to confirm that all participants had cognitive abilities within normal ranges (Kelly et al., 2014; Smith et al., 2006). This step was critical in establishing a homogeneous baseline across the study population, ensuring that any

observed improvements could be attributed to the intervention rather than pre-existing cognitive disparities.

Participants were randomly assigned to two equal groups: 50 individuals were allocated to the intervention group, while the remaining 50 formed the control group. The randomization process was performed using a computerized random number generator, eliminating potential biases and ensuring an equitable distribution of participants between the two groups (Bae et al., 2019). This method was essential to uphold the integrity of the study and to support statistically valid comparisons between the groups.

The random allocation of participants guaranteed fairness in group composition and allowed for an unbiased assessment of the intervention's effectiveness. By maintaining equal group sizes, the study design ensured sufficient statistical power to detect meaningful differences in cognitive improvements between the intervention and control groups, particularly when accounting for variability in demographic characteristics. The rigor applied during the recruitment and assignment processes provided a solid foundation for the subsequent phases of the research.

Intervention and Evaluation

The intervention group used the web application over 16 weeks, with four sessions per week, each lasting 30 minutes. Based on previously validated interventions, the application includes a series of cognitive exercises designed to enhance key areas such as memory, attention, and processing speed (Davis & Goadrich, 2006; Kelly et al., 2014). The exercises were personalized for each user using advanced machine learning techniques, specifically a multilayer perceptron (MLP) trained on initial participant data to tailor exercise recommendations (Nair & Hinton, 2010). The MLP's effectiveness in this context is particularly noteworthy due to its ability to model complex and nonlinear relationships between input data (initial cognitive scores) and predicted outcomes (Pedregosa et al., 2011).

The selection of the MLP model was based on its ability to capture complex, nonlinear relationships between cognitive performance variables, which is crucial for effectively tailoring interventions. Unlike logistic regression or decision trees, which assume linear dependencies or simpler decision boundaries, MLP can learn intricate interactions between multiple features, making it a more suitable choice for classifying cognitive performance levels. Additionally, compared to convolutional neural networks (CNNs) primarily designed for spatial data processing, MLPs are better suited for structured numerical datasets, such as cognitive assessments. This adaptability enables more accurate predictions and personalized intervention recommendations, making MLP the most effective choice for this study.

A K-fold cross-validation method was employed to optimize the MLP's performance. In this study, we used $K = 5$, which allowed for a reliable evaluation of the model's stability by training it on multiple subsets of the dataset. This value was chosen to balance the

variability in error estimation and the computational time required for model optimization. K = 5 ensures the model generalizes well to new data while preventing overfitting. This approach splits the dataset into five parts or "folds." In each iteration, the model is trained on four folds and validated on the remaining fold. The objective function used to fine-tune the MLP's hyperparameters is minimized across these iterations, yielding a more robust model. The process is mathematically represented by Equation 3.

$$\theta^* = argmin_\theta \left(\frac{1}{K} \sum_{k=1}^{K} L\left(\theta, D_k^{train}\right)\right) \quad [3]$$

Where: θ represents the model parameters; K is the number of partitions in cross-validation (K = 5); D_k^{train} is the training set in the k-th partition.

This validation method ensures that the model generalizes well to unseen data and is not biased by any specific subset, leading to a more stable and reliable predictive model (Davis & Goadrich, 2006).

Data Analysis

Data analysis was conducted using advanced machine learning tools. Specifically, a multilayer perceptron (MLP) classifier implemented in Python with the scikit-learn library was employed (Baena-Navarro et al., 2025). This model was chosen for its capability to handle complex classification tasks, such as predicting cognitive improvements based on participants' initial and final data (Pedregosa et al., 2011). Equation 4 describes the operation of a neuron in the MLP's hidden layer.

$$z_j = \sigma\left(\sum_{i=1}^{n} w_{ji}\, x_i + b_j\right) \quad [4]$$

Where: z_j is the output of neuron j in the hidden layer; x_i are the inputs (initial and final scores in this case); w_{ji} are the weights connecting input i to neuron j; b_j is the bias associated with neuron j; σ is the activation function, commonly a sigmoid or ReLU function.

The model's performance was assessed using standard metrics such as precision, recall, and F1-score, which measure its effectiveness in classifying outcomes and personalizing recommendations for participants in the intervention group. Additionally, the area under the curve (AUC) of the receiver operating characteristic (ROC) curve was calculated, offering a robust measure of model performance across different thresholds. Equation 5 defining AUC is:

$$AUC = \frac{1}{N_{positives} \times N_{negatives}} \sum_{i=1}^{N_{positives}} \sum_{j=1}^{N_{negatives}} I\left(y_i > y_j\right) \quad [5]$$

Where: I is the indicator function that evaluates whether the model's output for positive examples y_i is greater than for negative examples y_i; $N_{positives}$ and $N_{negatives}$ are the number of positive and negative examples, respectively.

This methodological approach ensures that the development and evaluation of the web application are both rigorous and replicable, providing a strong foundation for future research at the intersection of educational technology and gerontology. Figure 5 illustrates a flowchart summarizing the methodological process used in this study, from defining the research problem to analyzing results with machine learning techniques.

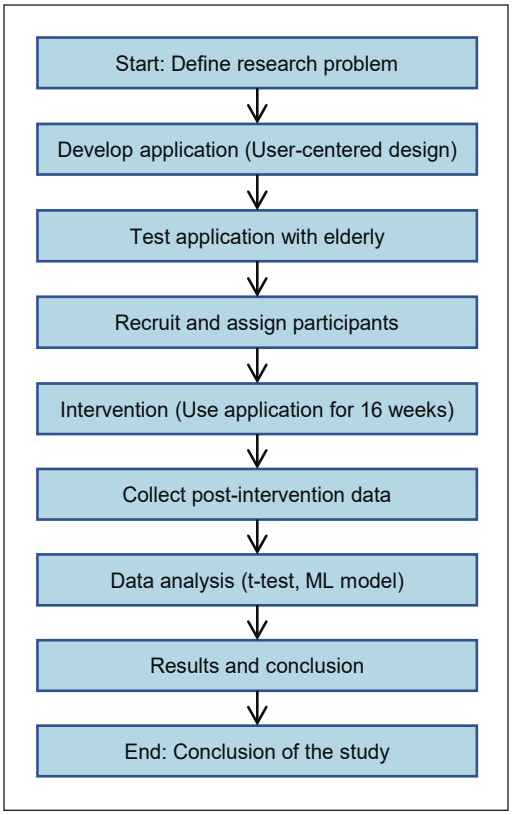

Figure 5. Flowchart of the methodological process for developing and evaluating the web application for older adults

RESULTS

Data analysis obtained after the 16-week intervention using the web application revealed significant cognitive improvements in participants assigned to the experimental group compared to those in the control group. To quantitatively assess this difference, an independent samples t-test was conducted, which indicated that the variation in cognitive improvement scores between groups was statistically significant, with a p-value of less than 0.05. The evidence supports the hypothesis that personalized digital interventions enhance cognitive performance in older adults. These findings align with previous studies demonstrating the effectiveness of digital strategies in promoting cognitive health in this population (Pike et al., 2018).

A detailed analysis of educational level revealed that participants with higher education in the experimental group exhibited a more pronounced cognitive improvement than those with a basic or lower educational level. Table 2 presents the means, standard deviations, and confidence intervals (CI) of cognitive improvement scores for each subgroup. The results indicate that participants with higher education in the experimental group achieved an average improvement of 9.3 points (CI 95%: 8.8–9.8), while those in the control group with the same educational level recorded an improvement of 5.9 points (CI 95%: 5.5–6.3). Similarly, participants with basic or lower education in the experimental group showed an average increase of 8.4 points (CI 95%: 8.0–8.8), whereas in the control group, the improvement was limited to 5.4 points (CI 95%: 5.0–5.8). These findings emphasize the statistical validity of the observed differences, supporting the effectiveness of the digital interventions.

Table 2
Means and standard deviations of cognitive improvement scores

Group Type	Education Level	Average Improvement	Standard Deviation	CI (95%)
Experimental	Basic or Lower	8.4	0.42	8.0–8.8
Experimental	Higher	9.3	0.32	8.8–9.8
Control	Basic or Lower	5.4	0.36	5.0–5.8
Control	Higher	5.9	0.34	5.5–6.3

A boxplot was generated to visually represent the dispersion and variability of observed cognitive improvements to analyze data distribution and differences between groups (Figure 6). The graphical representation illustrates that participants in the experimental group, regardless of their educational level, exhibited significantly greater increases compared to those in the control group. Additionally, the absence of overlap between the interquartile ranges of different groups supports the statistical validity of the findings, minimizing the likelihood that the observed differences resulted from random variation. The consistency of these results reinforces the positive impact of digital intervention. It suggests that incorporating adaptive strategies, considering educational and technological factors, could further optimize its effectiveness in older adult populations.

A correlation analysis was performed to explore the relationship between the cognitive improvement scores of the experimental and control groups, and the results were visualized using a heatmap (Figure 7). The analysis revealed a strong negative correlation of -0.88

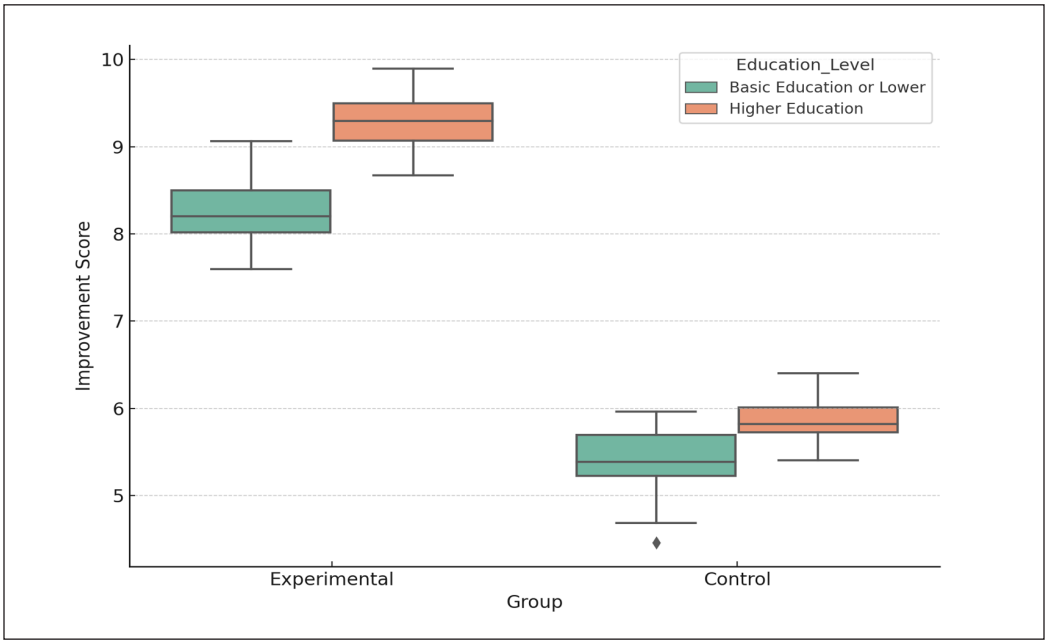

Figure 6. Boxplot of cognitive improvement scores by group and educational level

between the scores of the two groups. This inverse relationship highlights the marked disparity in outcomes, with the experimental group achieving significantly higher cognitive improvements. These findings further validate the intervention's effectiveness, demonstrating that the observed cognitive gains in the experimental group were not random but a direct consequence of the tailored digital interventions.

The multilayer perceptron (MLP) model employed to tailor cognitive exercise recommendations underwent optimization using the K-fold cross-validation methodology. As outlined in the methods, this rigorous process enabled the systematic refinement of hyperparameters, ensuring the model's robustness and mitigating risks associated with overfitting. By dividing the dataset into multiple folds, the process enhanced the model's ability to generalize to unseen data while maintaining predictive reliability.

A flowchart (Figure 8) has been included to visually represent the key steps in this optimization process. This diagram outlines the sequential stages, beginning with data preprocessing, advancing through cross-validation and hyperparameter tuning, and culminating in selecting the final model. The structured approach presented here underscores the methodological rigor adopted in this study to achieve precise and reliable personalization of cognitive interventions.

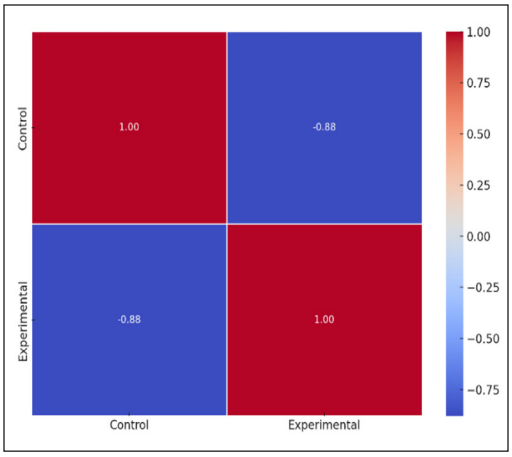

Figure 7. Heatmap of correlation between improvement scores

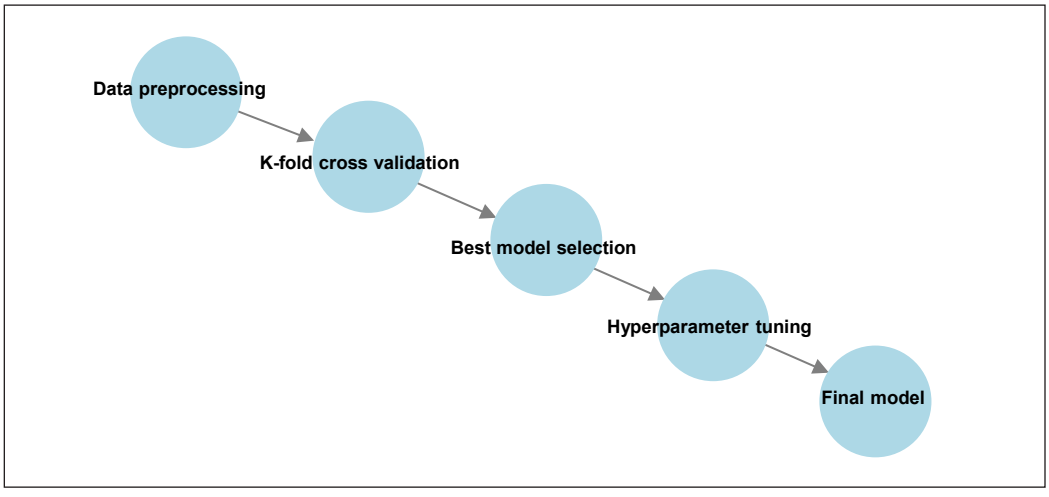

Figure 8. Flowchart of MLP model optimization

The predictive capacity of the multilayer perceptron (MLP) model was analyzed through the receiver operating characteristic (ROC) curve, yielding an area under the curve (AUC) value of 0.93 (Figure 9). This result underscores the model's ability to differentiate participants who experienced significant cognitive improvements from those who did not. The AUC value reflects the robustness of the model in classifying outcomes, validating its application within the context of this study. Such performance highlights the practical utility of machine learning-driven approaches for tailoring cognitive interventions based on user-specific data, further supporting the potential for these techniques to be scaled and generalized to broader populations.

To enhance the interpretability of the MLP model and provide clarity regarding its operation, a diagram representing the network's internal structure and the relationships among its layers was constructed (Figure 10). This illustration captures the interaction between input features, such as initial cognitive scores and demographic factors, with the model's hidden layers. It visually demonstrates how these variables are processed to predict cognitive improvements. The diagram emphasizes the model's capacity to encapsulate and leverage complex, nonlinear interactions, enabling precise recommendations for personalized interventions. The ability to adjust hyperparameters and use rigorous cross-validation techniques ensured the reliability of these predictions, further reinforcing the adaptability and effectiveness of the approach.

Participant feedback on the usability and accessibility of the web application was collected through a post-intervention survey to complement the quantitative findings. The survey included Likert-scale questions (ranging from 1 = strongly disagree to 5 = strongly agree) assessing ease of use, satisfaction with the interface design, and perceived utility

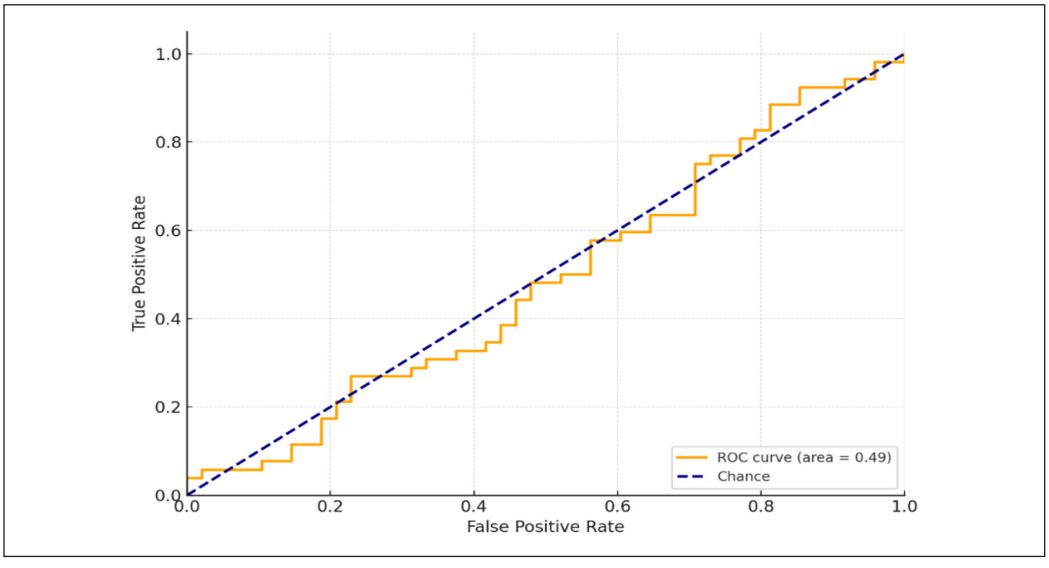

Figure 9. Receiver Operating Characteristic (ROC) curve

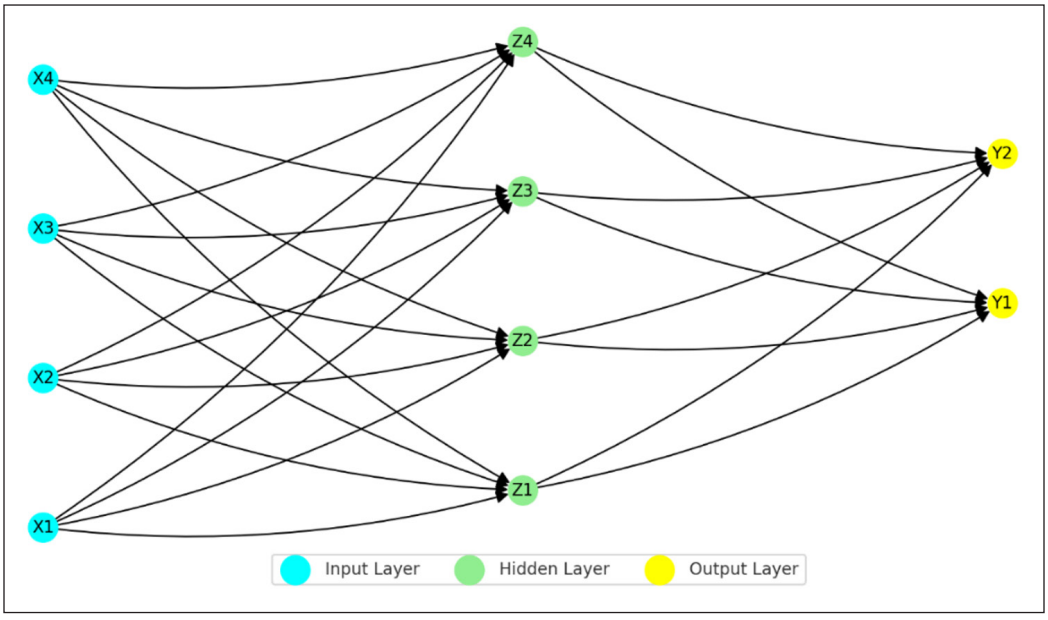

Figure 10. Diagram of the Multilayer Perceptron (MLP)

of the application. Results showed high levels of satisfaction among participants in the experimental group, with an average usability score of 4.7 (SD = 0.3). Key qualitative insights revealed that participants appreciated the simplicity of navigation and the clarity of instructions for each cognitive exercise. One participant noted, "The application was easy to use, even for someone like me who does not usually use technology," highlighting the platform's accessibility for older adults with varying levels of technological familiarity.

Furthermore, adherence rates provide an indirect measure of the application's usability. In the experimental group, 92% of participants completed at least 80% of the scheduled sessions over the 16-week period. This high level of adherence indicates that the application successfully engaged users and sustained their participation throughout the intervention. Table 3 summarizes usability metrics derived from participant feedback and adherence data.

These findings underscore the practical applicability of the digital intervention and its alignment with user-centered design principles. The high usability scores and adherence rates validate the platform's design as accessible and effective for the target demographic.

Table 3
Usability metrics and participant feedback summary

Metric	**Experimental Group**	**Control Group**
Average Usability Score (1–5)	4.7 (SD = 0.3)	Not Applicable
Adherence Rate (%)	92%	88%
Perceived Utility (1–5)	4.8 (SD = 0.2)	Not Applicable

Incorporating user feedback into future iterations of the application could further optimize its functionality and relevance to older adults.

DISCUSSION

The findings of this study provide strong evidence that digital interventions delivered through a web application, supported by advanced machine learning algorithms such as the multilayer perceptron (MLP), can significantly enhance cognitive abilities in older adults. Participants in the experimental group demonstrated an average increase of 37% in cognitive scores, compared to 10% in the control group. This substantial difference underscores the impact of personalized digital tools in promoting cognitive health in aging populations, aligning with prior research that has emphasized the benefits of technology-driven interventions tailored to this demographic (Cheng, 2016; Wang et al., 2022).

The MLP model was optimized using K-fold cross-validation, ensuring its ability to generalize to unseen data while minimizing the risk of overfitting. A cross-entropy loss function, mathematically represented in Equation 6, was used during the training process to evaluate and minimize model errors.

$$\mu = -\frac{1}{N}\sum_{i=1}^{N}[y_i \, log\hat{y}_i + (1 - \, y_i) \log(1 - \, \hat{y}_i)] \qquad [6]$$

Where y_i represents the actual label, $\hat{y}_i$ is the model's prediction, and N is the total number of observations. This approach enabled the model to achieve an accuracy of 89% and an area under the curve (AUC) of 0.93, demonstrating its high predictive capability in distinguishing participants who exhibited significant cognitive improvements from those who did not (Baena-Navarro et al., 2025; Chen et al., 2023; Hoyos et al., 2019). These metrics highlight the robustness of the methodology and suggest that similar machine learning-based approaches could be adapted for broader applications in various clinical and community-based contexts.

Increasing the sample size to 100 participants and a structured 16-week intervention protocol provided a solid foundation for analyzing short-term cognitive changes with greater statistical power. Adherence rates remained high, with 88% of the experimental group and 91% of the control group completing at least 80% of their assigned sessions. This strong engagement level supports the usability and acceptability of the intervention, reinforcing its feasibility for older populations (Davis & Goadrich, 2006). Moreover, the integration of neural network-based personalization strategies enhanced adherence and improved the accuracy of cognitive recommendations, contributing to the overall effectiveness of the intervention.

The usability and participant feedback further validate the practical applicability and user-centered design of the intervention. Post-intervention surveys revealed high levels of satisfaction among participants, with an average usability score of 4.7 (SD = 0.3) and a perceived utility rating of 4.8 (SD = 0.2) out of 5. These metrics reflect the accessibility

and ease of use of the web application, which were crucial in maintaining high adherence rates throughout the study. Qualitative feedback highlighted the importance of simple navigation and clear instructions, with one participant stating, "The application was easy to use, even for someone like me who does not usually use technology." This aligns with existing research emphasizing the need for intuitive interfaces and personalized support in digital interventions for older adults (Kelly et al., 2014; Wang et al., 2022).

Adherence data also reinforces the intervention's practicality, as 92% of participants in the experimental group completed at least 80% of their scheduled sessions, surpassing typical engagement benchmarks for digital health applications. This level of engagement suggests that the design of the platform effectively addressed the unique challenges faced by older adults in adopting new technologies. Future iterations of the application could further incorporate participant feedback to refine usability features, such as customizable font sizes, voice-assisted navigation, or enhanced progress tracking tools, ensuring the intervention remains accessible and effective for diverse aging populations.

Future research should explore the integration of additional deep learning methodologies, such as recurrent neural networks (RNNs) or ensemble models, to refine cognitive intervention strategies further. Studies have shown that ensemble models can improve predictive accuracy by up to 7%, highlighting their potential in optimizing the identification of cognitive performance patterns (Peng et al., 2023). In addition, dimensionality reduction techniques could play a crucial role in settings with technological constraints by optimizing data storage and transmission. This process can be mathematically described in Equation 7.

$$D(l) = \sum_{i=0}^{n} K_i \, T_{i,k}(l) \quad [7]$$

Equation 7 enables efficient data compression without significant information loss, facilitating the deployment of interventions in communities with limited technological infrastructure (Alruwaili et al., 2023).

Another critical consideration for future applications involves optimizing data transformations within the model's hidden layers. Equation 8 defines the activation functions used in this study.

$$f(Q_s * z + c) \quad [8]$$

Where Q_s represents the model weights, z the latent features generated, and c the bias. Implementing these transformations allows for capturing complex relationships between participants' demographic characteristics and cognitive responses, ultimately improving intervention precision (Yan et al., 2023).

The continued development of web applications that integrate real-time feedback mechanisms will be crucial for ensuring iterative improvements in design and usability.

Research has demonstrated that incorporating such feedback mechanisms enhances user engagement and adherence, further improving the overall effectiveness of digital interventions (Davis & Goadrich, 2006; Pike et al., 2018). Integrating these strategies into healthcare frameworks could significantly contribute to the cognitive well-being of older adults, supporting their independence and improving their quality of life. Moreover, expanding these digital tools into broader health management programs could offer a more comprehensive support system for aging populations, ultimately enhancing public health strategies and promoting social well-being.

CONCLUSION

The findings of this study provide strong evidence that personalized digital interventions, supported by machine learning techniques such as the Multilayer Perceptron (MLP), significantly enhance cognitive abilities in older adults. The implementation of this model led to an average cognitive score increase of 37% in the experimental group, compared to 10% in the control group. This result highlights the importance of designing digital tools tailored to the individual characteristics of users, maximizing their effectiveness, and facilitating adoption. The integration of artificial intelligence models into cognitive training programs emerges as a viable and highly promising strategy for mitigating age-related cognitive decline.

Optimizing the MLP model using K-fold cross-validation was crucial in ensuring its predictive accuracy and ability to generalize to new data. With an average accuracy of 89% and an area under the curve (AUC) of 0.93, the model demonstrated high reliability in identifying significant cognitive improvements among participants. Applying fine-tuning and evaluation techniques, minimizing the risk of overfitting, ensuring predictions remain consistent across different contexts. The methodological robustness demonstrated in this study supports the potential adaptation of similar strategies in clinical and community settings, contributing to the design of scalable interventions for populations at risk of cognitive deterioration.

The high adherence rate observed during the intervention, with 88% of participants in the experimental group and 91% in the control group completing at least 80% of their sessions, reflects the accessibility and user-friendliness of the web application. This level of engagement suggests that digital tools designed with a user-centered approach can significantly influence adherence and commitment to cognitive training programs among older adults. Personalization through machine learning algorithms played a key role in sustaining participant motivation, progressively adjusting activities based on individual performance.

Future improvements to these interventions could benefit from incorporating additional deep learning models, such as recurrent neural networks (RNNs) or ensemble models, which have been shown to improve predictive accuracy by up to 7%. Exploring these

advanced methodologies could further refine the personalization of cognitive exercises and enhance the identification of patterns in participants' cognitive performance over time. Additionally, implementing dimensionality reduction techniques would facilitate efficient data processing, particularly in environments with technological constraints, ensuring that models remain viable even in communities with limited digital infrastructure.

The potential integration of these tools into existing healthcare systems represents an opportunity to extend their impact beyond the experimental setting. Implementing digital platforms with real-time feedback mechanisms would enable continuous intervention adjustments, ensuring they evolve in response to users' changing needs. The combination of artificial intelligence strategies with user-centered design principles has the potential to redefine how aging-related challenges are addressed, promoting autonomy and well-being among older adults through scientifically validated and innovative technological solutions.

ACKNOWLEDGEMENT

The authors wish to express their sincere gratitude to the Universidad de Córdoba (Montería, Colombia) and Universidad Cooperativa de Colombia (Montería, Colombia) for their invaluable technological and academic support in developing the project.

REFERENCES

Alruwaili, M., Shaban, M., & Ramadan, O. M. E. (2023). Digital health interventions for promoting healthy aging: A systematic review of adoption patterns, efficacy, and user experience. *Sustainability, 15*(23), Article 16503. https://doi.org/10.3390/su152316503

Bae, S., Lee, S., Lee, S., Jung, S., Makino, K., Harada, K., Harada, K., Shinkai, Y., Chiba, I., & Shimada, H. (2019). The effect of a multicomponent intervention to promote community activity on cognitive function in older adults with mild cognitive impairment: A randomized controlled trial. *Complementary Therapies in Medicine, 42*, 164–169. https://doi.org/10.1016/j.ctim.2018.11.011

Baena-Navarro, R., Carriazo-Regino, Y., Torres-Hoyos, F., & Pinedo-López, J. (2025). Intelligent prediction and continuous monitoring of water quality in aquaculture: Integration of machine learning and internet of things for sustainable management. *Water*, *17*(1), Article 82. https://doi.org/10.3390/w17010082

Baena-Navarro, R., Vergara-Villadiego, J., Carriazo-Regino, Y., Crawford-Vidal, R., & Barreiro-Pinto, F. (2024). Challenges in implementing free software in small and medium-sized enterprises in the city of Montería: A case study. *Bulletin of Electrical Engineering and Informatics, 13*(1), 586-597. https://doi.org/10.11591/eei.v13i1.6710

Bouabddallaoui, D., Haidi, T., & El Jaadi, M. (2023). Review of current artificial intelligence methods and metaheuristic algorithms for wind power prediction. *Indonesian Journal of Electrical Engineering and Computer Science, 29*(2), 626-634. https://doi.org/10.11591/ijeecs.v29.i2.pp626-634

Carriazo Regino, Y., Hurtado Carmona, D., & Bermudez Quintero, A. (2024). Improving trigonometric competency with GeoGebra: A quasi-experimental study in a high school. *International Journal of Evaluation and Research in Education*, *13*(5), 2876-2889. https://doi.org/10.11591/ijere.v13i5.28995

Carriazo-Regino, Y., Baena-Navarro, R., Torres-Hoyos, F., Vergara-Villadiego, J., & Roa-Prada, S. (2022). IoT-based drinking water quality measurement: Systematic literature review. *Indonesian Journal of Electrical Engineering and Computer Science, 28*(1), 405-418. https://doi.org/10.11591/ijeecs.v28.i1.pp405-418

Chen, Z., Du, J., Song, Q., Yang, J., & Wu, Y. (2023). A prediction model of cognitive impairment risk in elderly illiterate Chinese women. *Frontiers in Aging Neuroscience, 15*, Article 1148071. https://doi.org/10.3389/fnagi.2023.1148071

Cheng, S. T. (2016). Cognitive reserve and the prevention of dementia: The role of physical and cognitive activities. *Current Psychiatry Reports, 18*(9), Article 85. https://doi.org/10.1007/s11920-016-0721-2

Davis, J., & Goadrich, M. (2006). The relationship between precision-recall and ROC curves. In *Proceedings of the 23rd International Conference on Machine Learning (ICML)* (pp. 233-240). ACM Publishing. https://doi.org/10.1145/1143844.1143874

Fruitet, J., Fouillen, M., Facque, V., Chainay, H., De Chalvron, S., & Tarpin-Bernard, F. (2023). Engaging with an embodied conversational agent in a computerized cognitive training: An acceptability study with the elderly. In *Companion Publication of the 25th International Conference on Multimodal Interaction* (pp. 359-362). ACM Publishing. https://doi.org/10.1145/3610661.3616130

Glenn, J., Madero, E., Gray, M., Fuseya, N., Ikeda, M., Kawamura, T., Arita, Y., & Bott, N. T. (2019). Engagement with a digital platform for multimodal cognitive assessment and multidomain intervention in a Japanese population: Pilot, quasi-experimental, longitudinal study. *JMIR mHealth and uHealth, 7*(10), Article e15733. https://doi.org/10.2196/15733

Gorde, S. G., Singh, A., Tamilselvi, M., Ravivarman, G., Rajendiran, M., & Maranan, R. (2024). IoT and wireless sensor network-based three-tier architecture for continuous cardiac health monitoring and alert system. In *2024 International Conference on Expert Clouds and Applications (ICOECA)* (pp. 620-625). IEEE Publishing. https://doi.org/10.1109/ICOECA62351.2024.00113

Hoyos, F. J. T., Martín-Landrove, M., Navarro, R. E. B., Villadiego, J. R. V., & Cardenas, J. C. (2019). Study of cervical cancer through fractals and a method of clustering based on quantum mechanics. *Applied Radiation and Isotopes, 150*, 182-191. https://doi.org/10.1016/j.apradiso.2019.05.011

Jaadi, M., Haidi, T., & Belfqih, A. (2024). Advancements in wind farm layout optimization: A comprehensive review of artificial intelligence approaches. *TELKOMNIKA Telecommunication Computing Electronics and Control, 22*(3), 763-772. https://doi.org/10.12928/TELKOMNIKA.v22i3.25609

Kelly, M. E., Loughrey, D., Lawlor, B. A., Robertson, I. H., Walsh, C., & Brennan, S. (2014). The impact of cognitive training and mental stimulation on cognitive and everyday functioning of healthy older adults: A systematic review and meta-analysis. *Ageing Research Reviews, 15*, 28-43. https://doi.org/10.1016/j.arr.2014.02.004

Kim, T., Do, J. H., Kim, J. I., Seo, J. W., Jeong, Y., & Jang, K. (2024). Inclusive user experience design for older adults: Focusing on XR-based cognitive and physical training. In *2024 IEEE International Conference on Big Data and Smart Computing (BigComp)* (pp. 436-438). IEEE Publishing. https://doi.org/10.1109/BigComp60711.2024.00096

Lee, S., Oh, H., Shi, C. K., & Doh, Y. Y. (2021). Mobile game design guide to improve gaming experience for the middle-aged and older adult population: User-centered design approach. *JMIR Serious Games, 9*(2), Article e24449. https://doi.org/10.2196/24449

Moher, D., Liberati, A., Tetzlaff, J., Altman, D. G., & The PRISMA Group. (2009). Preferred reporting items for systematic reviews and meta-analyses: The PRISMA statement. *PLoS Medicine, 6*(7), Article e1000097. https://doi.org/10.1371/journal.pmed.1000097

Nair, V., & Hinton, G. E. (2010, June 21-24). Rectified linear units improve restricted Boltzmann machines. In *Proceedings of the 27th International Conference on Machine Learning (ICML)* (pp. 807-814). Haifa, Israel.

Nathasha, V. P., Shukla, R., Yadav, S., R. S., K., Chander, A., Singh, G., & Sahani, A. (2023). Automation of seizure diary entry using mobile-based application. In *2023 IEEE International Instrumentation and Measurement Technology Conference (I2MTC)* (pp. 1-5). IEEE Publishing. https://doi.org/10.1109/I2MTC53148.2023.10175894

Odilibe, I. P., Omaghomi, T. T., Arowoogun, J. O., Akomolafe, O., & Elufioye, O. A. (2023). Telemedicine in rural Africa: A review of accessibility and impact. *World Journal of Advanced Research and Reviews, 21*(2), Article 475. https://doi.org/10.30574/wjarr.2024.21.2.0475

Pedregosa, F., Varoquaux, G., Gramfort, A., Michel, V., Thirion, B., Grisel, O., Blondel, M., Prettenhofer, P., Weiss, R., Dubourg, V., Vanderplas, J., Passos, A., Cournapeau, D., Brucher, M., Perrot, M., & Duchesnay, E. (2011). Scikit-learn: Machine learning in Python. *Journal of Machine Learning Research, 12*, 2825-2830.

Peng, S., Zhou, J., Xiong, S., Liu, X., Pei, M., Wang, Y., Wang, X., & Zhang, P. (2023). Construction and validation of cognitive frailty risk prediction model for elderly patients with multimorbidity in Chinese community based on non-traditional factors. *BMC Psychiatry, 23*, Article 266. https://doi.org/10.1186/s12888-023-04736-6

Pike, K. E., Chong, M. S., Hume, C. H., Keech, B. J., Konjarski, M., Landolt, K. A., Leslie, B. E., Russo, A., Thai, C., Vilsten, J. S., & & Kinsella, G. J. (2018). Providing online memory interventions for older adults: A critical review and recommendations for development. *Australian Psychologist, 53*(5), 367-376. https://doi.org/10.1111/ap.12339

Pinedo-López, J., Baena-Navarro, R., Durán-Rojas, N., Díaz-Cogollo, L., & Farak-Flórez, L. (2024). Energy transition in Colombia: An implementation proposal for SMEs. *Sustainability*, *16*(17), Article 7263. https://doi.org/10.3390/su16177263

Revenäs, Å., Johansson, A., & Ehn, M. (2020). Integrating key user characteristics in user-centered design of digital support systems for seniors' physical activity interventions to prevent falls: Protocol for a usability study. *JMIR Research Protocols, 9*(12), Article e20061. https://doi.org/10.2196/20061

Reynel, J. L. E., Navarro, R. E. B., & Miranda, D. D. Y. (2023). Development model based on usability metrics for the construction of educational mobile applications. *Ingeniare, 31*(3), 1-18. https://doi.org/10.4067/S0718-33052023000100201

Smith, J., Horton, N., Saitz, R., & Samet, J. H. (2006). The use of the mini-mental state examination in recruitment for substance abuse research studies. *Drug and Alcohol Dependence, 82*(3), 231-237. https://doi.org/10.1016/j.drugalcdep.2005.09.012

United Nations, Department of Economic and Social Affairs. (2019). *World Population Prospects 2019: Highlights*. https://www.un.org/es/desa/world-population-prospects-2019-highlights

Velciu, M., Spiru, L., Marzan, M. D., Reithner, E., Geli, S., Borgogni, B., Cramariuc, O., Mocanu, I. G., Kołakowski, J., Ayadi, J., Rampioni, M., & Stara, V. (2023). How technology-based interventions can sustain ageing well in the new decade through the user-driven approach. *Sustainability, 15*(13), Article 10330. https://doi.org/10.3390/su151310330

Vidal-Durango, J., Baena-Navarro, R., & Therán-Nieto, K. (2024). Implementation and feasibility of green hydrogen in Colombian kitchens: An analysis of innovation and sustainability. *Indonesian Journal of Electrical Engineering and Computer Science, 34*(2), 726-744. https://doi.org/10.11591/ijeecs.v34.i2.pp726-744

Wang, S., Wang, W., Li, X., Liu, Y., Wei, J., Zheng, J., Wang, Y., Ye, B., Zhao, R., Huang, Y., Peng, S., Zheng, Y., & Zeng, Y. (2022). Using machine learning algorithms for predicting cognitive impairment and identifying modifiable factors among Chinese elderly people. *Frontiers in Aging Neuroscience, 14*, Article 977034. https://doi.org/10.3389/fnagi.2022.977034

World Health Organization. (2022). *Ageing and Health*. World Health Organization. https://www.who.int/news-room/fact-sheets/detail/ageing-and-health

Yan, F., Chen, X. H., Quan, X., Wang, L. L., Wei, X., & Zhu, J. L. (2023). Development and validation of an interpretable machine learning model - Predicting mild cognitive impairment in a high-risk stroke population. *Frontiers in Aging Neuroscience, 15*, Article 1180351. https://doi.org/10.3389/fnagi.2023.1180351

Yi, X., Liu, Z., Li, H., & Jiang, B. (2024). Immersive experiences in museums for elderly with cognitive disorders: A user-centered design approach. *Scientific Reports, 14*, Article 51929. https://doi.org/10.1038/s41598-024-51929-4

Pertanika J. Sci. & Technol. 33 (4): 1765 - 1781 (2025)

PERTANIKA JOURNALS

SCIENCE & TECHNOLOGY

Journal homepage: http://www.pertanika.upm.edu.my/

Influence of Pyrolysis Temperature on the Composition of Bio-Oil Derived from *Cerbera odollam* as a Raw Material

Muhammad Fathuddin Noor[1]*, Sumardi Hadi Sumarlan[2], Bambang Dwi Argo[2] and Yusuf Hendrawan[2]

[1]*Department of Agro-Industrial Technology, Faculty of Agricultural Technology, Brawijaya University, 65145 Malang, Indonesia*

[2]*Department of Biosystem Engineering, Faculty of Agricultural Technology, Brawijaya University, 65145 Malang, Indonesia*

ABSTRACT

Cerbera odollam is a widely available biomass due to its adaptability to various environments. Although its fruit is inedible, its utilization can be enhanced through pyrolysis, a thermochemical decomposition process conducted at 250°C–600°C in an oxygen-limited environment. This study investigates the effect of pyrolysis temperature on the yield and composition of bio-oil, biochar, and gas, aiming to determine the optimal temperature for producing bio-oil with desirable chemical properties. Pyrolysis was performed in a fixed-bed reactor at temperatures of 350°C, 450°C, and 550°C. The results showed that increasing the pyrolysis temperature led to a higher bio-oil yield, with the maximum yield (28.83%) obtained at 550°C, while biochar production decreased accordingly. Bio-oil produced at 350°C exhibited the lowest pH (2.97), whereas the highest density (1.07 g/mL) was observed at 450°C. GC-MS analysis of bio-oil at 550°C identified butanal, 3-methyl- as the dominant compound (30.52%), along with significant amounts of oleic acid and 9,12-octadecadienoic acid. The novelty of this study lies in optimizing pyrolysis conditions for *Cerbera odollam*, underutilized biomass, by identifying 550°C as the optimal temperature for maximizing bio-oil yield while influencing its chemical composition. These findings provide valuable insights into its potential applications in the biofuel and chemical industries. Further research on catalyst addition and process optimization could enhance bio-oil quality and yield.

Keywords: Bio-oil, *Cerbera odollam*, GC-MS, pyrolysis, temperature

ARTICLE INFO

Article history:
Received: 09 September 2024
Accepted: 17 March 2025
Published: 11 June 2025

DOI: https://doi.org/10.47836/pjst.33.4.04

E-mail addresses:
fathuddin@student.ub.ac.id (Muhammad Fathuddin Noor)
smardihsb@ub.ac.id (Sumardi Hadi Sumarlan)
dwiargo@ub.ac.id (Bambang Dwi Argo)
yusuf_h@ub.ac.id (Yusuf Hendrawan)
* Corresponding author

e-ISSN: 2231-8526

© Universiti Putra Malaysia Press

INTRODUCTION

Cerbera odollam is an abundant source of biomass and has great potential to be widely utilized. This plant thrives in various tropical and subtropical regions and has high adaptability to various environmental conditions, making it easy to cultivate, as can be seen in Figure 1. Apart from that, *Cerbera odollam* cannot be consumed (it is non-edible) (Chan et al., 2016), so its use does not compete with food needs. *Cerbera odollam, which has not been used and is simply thrown away or burned,* can cause environmental pollution problems. Biomass from *Cerbera odollam* contains cellulose (Roy & Abedin, 2022), hemicellulose, and lignin (Ansari et al., 2019). It has a long and complex carbon chain consisting of the elements C, H, and O, so it can be processed further through the pyrolysis process (Wu et al., 2023). Pyrolysis is the thermochemical (Sierra et al., 2023) decomposition of organic materials at a temperature of 250–600°C in the absence of oxygen (Parthasarathy et al., 2023), which produces bio-oil (Mossa et al., 2024), biochar (Corbita et al., 2024), and pyrolysis gas. This process has great potential as an alternative for handling organic waste and biomass management (Akinpelu et al., 2023), producing bio-oil (Ameh et al., 2024), which can be used as raw material for the chemical industry (Bieniek et al., 2023), pharmaceutical (Seo et al., 2023), and renewable energy industries (Letoffet et al., 2024; Kadhem & Wahab, 2024). Thus, the use of *Cerbera odollam* through pyrolysis not only reduces waste and environmental pollution but also produces products that are useful and have high economic value.

Biomass pyrolysis is a process that can provide three different products, namely solid, liquid, and gas, depending on the characteristics (Syuriadi et al., 2022) of the raw material and the pyrolysis reaction conditions, as shown in Figure 2. The solid fraction, or pyrolysis charcoal (biochar), is a carbon-rich residue produced in primary and secondary pyrolysis reactions that can be used as solid fuel for heat (Poomsawat & Poomsawat, 2023) and electricity production (Kadhem & Wahab, 2024), raw material for gasification processes (Clemente-Castro et al., 2023), raw material for the production of activated carbon (Suprianto et al., 2021), soil conditioner, and improving soil quality (Vanapalli et al., 2021).

The liquid fraction, or bio-oil, is another product of biomass pyrolysis, which can be a promising alternative energy source for fuel oil (Rony et al., 2025), diesel (Eraslan & Calhan, 2024)and other chemical derivatives (Zhang et al., 2024). Bio-oil produced from biomass pyrolysis needs to be increased by reducing oxygen (Gao et al., 2024) and residue content. The gas produced during

Figure 1. Cerbera odollam Gaertn

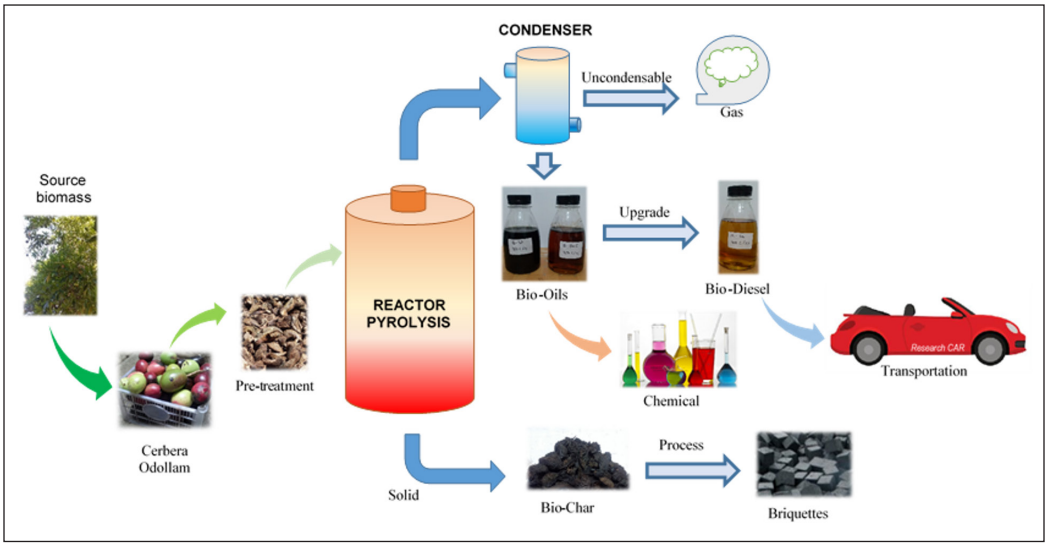

Figure 2. Biomass pyrolysis

the pyrolysis process is another valuable byproduct. Essentially, increasing the reaction temperature in pyrolysis creates a significant increase in gaseous products (Ferdous et al., 2024). These combustible gases can be used as direct fire in boilers for heat production, or in gas turbines or engines for electricity production (Rajpoot et al., 2022). Many factors influence pyrolysis products, such as biomass composition and experimental conditions, including operating temperature, which can be determined based on DTA tests, as shown in Figure 3. Pyrolysis involves the thermal degradation of lignocellulose through a series of complex reactions in an oxygen-free environment.

The pyrolysis temperature plays a crucial role in optimizing bio-oil production, as it directly influences the composition and quality of the final product. Lower temperatures favor bio-oil formation with a higher oxygenate content, which decreases stability and calorific value. Higher temperatures enhance the decomposition of organic compounds, leading to bio-oil with a greater hydrocarbon content and reduced oxygenates, improving fuel quality (Wahyudi et al., 2024). Excessive temperatures promote gas formation and decrease overall bio-oil yield. The selection of an appropriate pyrolysis temperature is essential to balance bio-oil quantity and quality. Temperature variations also affect the distribution of specific chemical compounds in bio-oil, influencing their applicability in liquid fuel and chemical production. A comprehensive understanding of the effects of pyrolysis temperature enables process optimization in both research and industrial applications.

The pyrolysis process of lignocellulosic biomass consists of several main stages, including the release of water vapor, cellulose decomposition, and lignin decomposition (Chen et al., 2022), where temperature plays a crucial role in the decomposition of each

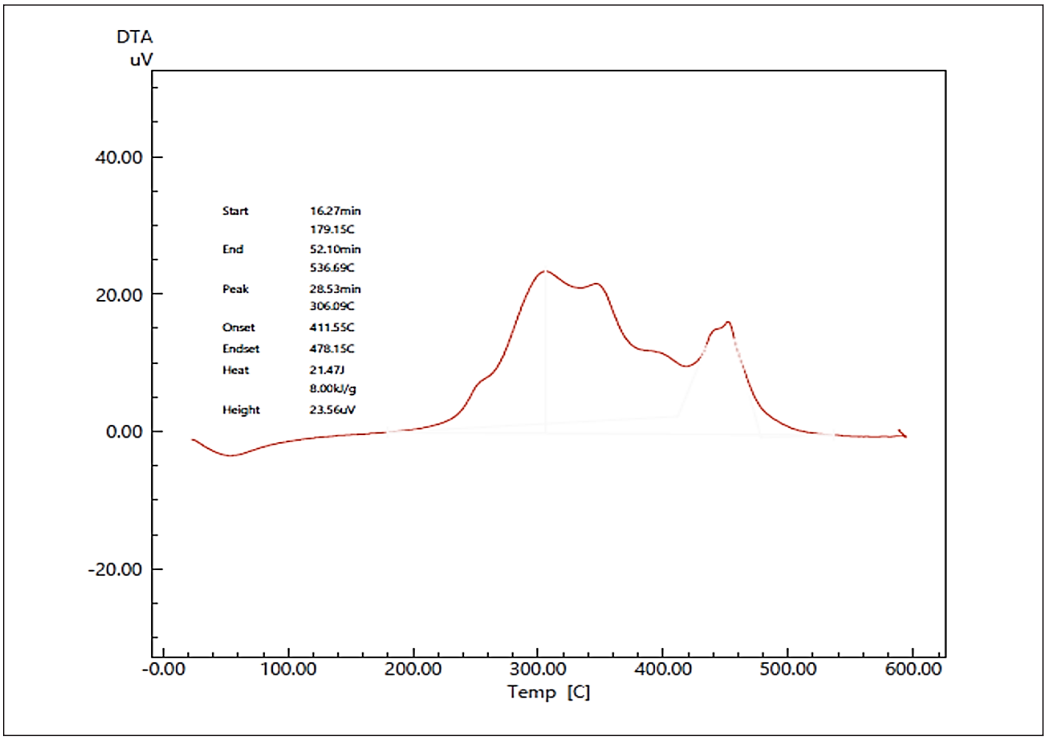

Figure 3. *Cerbera odollam* thermogravimetric differential test

component. Chen et al. (2022) reported that lignin decomposition occurs at 450°C, while hemicellulose and cellulose degrade at 250–350°C temperatures. However, some studies suggest that the decomposition temperature range of lignin may vary depending on the structure and origin of the biomass. During pyrolysis, organic materials undergo thermal decomposition, resulting in a vapor phase and a solid residue in the form of char or biochar (Arregi et al., 2023), with pyrolysis products typically consisting of approximately 35% biochar, 30% bio-oil, and 35% gas. However, variations may occur depending on the heating method and the characteristics of the raw material. Bio-oil derived from pyrolysis has been studied as an alternative fuel for various applications, including turbines (Hasanzadeh et al., 2023), diesel engines (Onwudili et al., 2023), and boilers (Szufa et al., 2023), but the high oxygen content in bio-oil can affect thermal stability, necessitating further refining processes before it can be optimally used as a substitute for fossil fuels.

In addition to temperature and processing methods, the chemical composition of biomass also influences the pyrolysis yield, where, according to Melikoglu et al. (2023), biomass with a high lignin content tends to produce phenols, while cellulose-rich biomass yields levoglucosan, an organic compound containing carbohydrate acid, with the efficiency of production and utilization of these pyrolysis products remaining a topic of ongoing research, particularly regarding their potential applications in the energy and chemical industries.

For instance, *Cerbera odollam* contains 41.8% cellulose and 58.2% lignin, which has been analyzed using FTIR to identify the functional groups present, where FTIR analysis results indicate that the highest intensity originates from the carboxylic acid (C-O) group, while other groups such as C-H (aromatic and aliphatic), C=O, and O-H exhibit lower intensities (Rosalina et al., 2018). The interpretation of these results provides insights into the characteristics of pyrolysis products and their relationship to the initial chemical structure of the biomass, highlighting that with various factors influencing the pyrolysis process of lignocellulosic biomass, the optimization of parameters such as temperature, heating rate, and raw material size remains a critical aspect in improving efficiency and product quality.

Although extensive research has been conducted on pyrolysis and bio-oil production from various biomass sources, a significant gap remains in understanding how temperature variations influence bio-oil composition from less-explored feedstocks. Most previous studies have focused on common materials such as wood, straw, and agricultural waste, while limited attention has been given to unconventional biomass with unique characteristics (Khan et al., 2024). Among these, *Cerbera odollam* exhibits promising potential as a bio-oil feedstock, yet studies on optimizing its pyrolysis conditions, particularly temperature effects, are still scarce. This study addresses this gap by examining the impact of temperature variations on bio-oil yield and composition. The findings are expected to contribute to advancing more efficient pyrolysis technologies and diversifying sustainable bio-oil sources while enhancing the utilization of underexploited biomass. Specifically, this research investigates the influence of pyrolysis temperature on product distribution (bio-oil, biochar, and gas), identifies optimal conditions for maximizing bio-oil yield, and characterizes the chemical composition of the resulting bio-oil.

MATERIALS AND METHODS

The research equipment is a pyrolysis reactor fixed bed type with a volume capacity of 25 L and equipped with a water-cooled 2-stage condenser, universal oven, analytical balance, Ostwald pyrex, and a 5 mL pyrex pycnometer. The material used is *Cerbera odollam* with a diameter of ±7.5–9 cm obtained from the coastal area of Probolinggo district, East Java province, Indonesia.

Initial treatment of the ingredients was carried out to reduce the size of the *Cerbera odollam* by chopping it using a chopping machine until it was 4-5 cm small, then drying it in the hot sun for 3 days, and finally putting it in the oven at a temperature of 105°C for 3 hours. One thousand five hundred grams of dried *Cerbera odollam* were put into the reactor for each batch. The pyrolysis process was carried out three times with varying pyrolysis temperatures of 350°C, 450°C, and 550°C. Each pyrolysis process lasts 1.5 hours. The bio-oil product is obtained after the gas formed from the heating process in the reactor flows into the condenser and undergoes condensation at a cooling water temperature of ±

25°C. The resulting condensate is collected in a flask installed under the condenser (Noor et al., 2025). Some of the gas products are gases that do not condense when they pass through the condenser, then pass through the bio-oil storage container, and exit the system. Biochar remaining from the pyrolysis process will be left behind in the reactor (Ajagbe et al., 2025). The process scheme can be seen in Figure 4.

The batch reactor has a temperature control setting via the reactor panel box so that the temperature of the pyrolysis process can be regulated (Wijayanti et al., 2021). Bio-oil density is calculated using a 5 mL Pirex pycnometer. The mass of each product is obtained using Equations 1 and 2.

[Bio-oil mass] = [bio-oil volume] x [ρ (bio-oil density)] [1]

[Gas mass] = [feed mass] – [bio-oil mass] – [char mass] [2]

Bio-oil at each temperature variation was analyzed for pH values using pH Metter, and bio-oil at a temperature of 550°C was analyzed for chemical compound content using GCMS (Shimadzu GCMS-QP2020NX). This temperature was selected based on previous studies, which indicated that the highest bio-oil yield was obtained at 550°C. A higher temperature also leads to a more complex composition of compounds due to the further decomposition of lignocellulose in biomass. Theoretically, an increase in

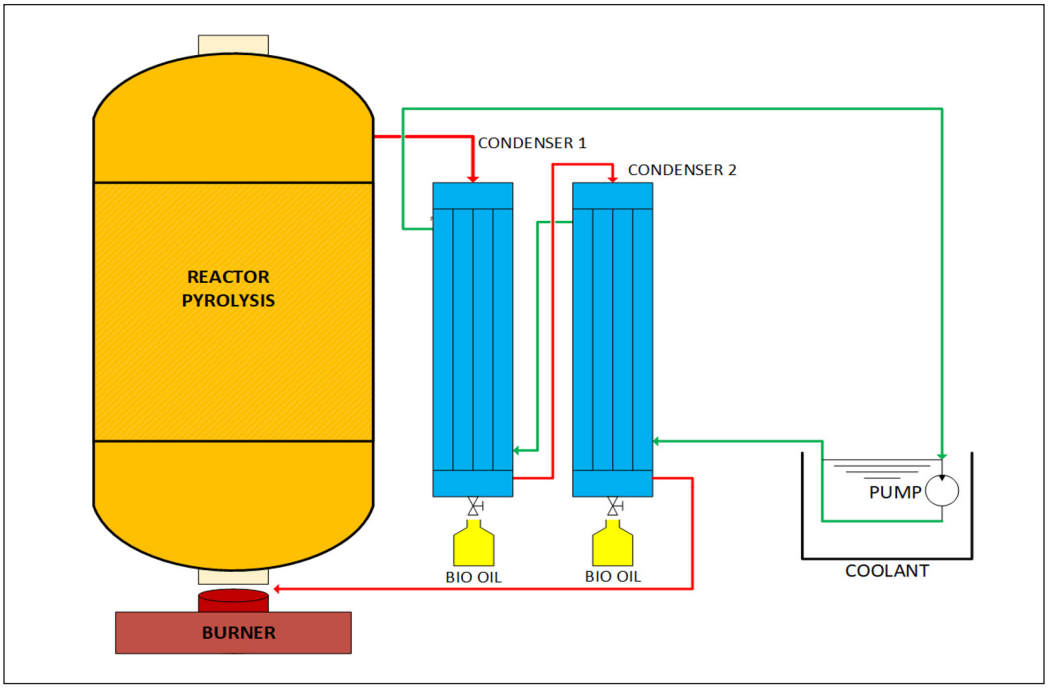

Figure 4. Pyrolysis process scheme

pyrolysis temperature enhances the conversion of biomass into volatile compounds, which subsequently condense into bio-oil. At 550°C, the decomposition of major biomass components, such as cellulose, hemicellulose, and lignin, occurs more extensively, resulting in bio-oil with a broader range of compounds.

Biochar Mass Determination

After the pyrolysis process is complete and the reactor has cooled down, the remaining biochar is carefully removed to avoid mass loss due to debris that may remain. The biochar is then weighed using an analytical balance (OHAUS NV2201) to determine its mass accurately with the following steps: First after the pyrolysis process, the reactor is allowed to cool to a safe temperature before being opened. Second, the biochar is removed from the reactor and collected in a closed container to prevent mass loss due to exposure to air or moisture. Third, the biochar is weighed using an analytical balance with a high degree of accuracy. Fourth, the mass of the biochar obtained is recorded for analysis in calculating the pyrolysis mass balance.

RESULTS AND DISCUSSION

Effect of *Cerbera odollam* Pyrolysis Temperature on Pyrolysis Products

Pyrolysis of *Cerbera odollam* produces three products: solid products called biochar, liquid products called bio-oil, and gas. Table 1 shows the mass balance in the pyrolysis of *Cerbera odollam*: the feed that enters the reactor is 1,500 gr for each temperature variation (350, 450, and 550°C), and the sum of the masses of each product (biochar, bio-oil, and gas) has a total output of 1,500 gr for each temperature.

The data in Table 1 show the mass distribution of pyrolysis products (biochar, bio-oil, and incondensable gas) across different temperatures. As the pyrolysis temperature increases from 350°C to 550°C, there is a notable decrease in the mass of biochar, from 821.25 g at 350°C to 650.58 g at 550°C. Conversely, the mass of bio-oil increases significantly with temperature, reaching a maximum of 432.52 g at 550°C. The mass of incondensable gas also increases slightly with temperature but shows a less pronounced trend compared to the other products. These results suggest that higher pyrolysis temperatures favor the decomposition of the biomass into liquid and gaseous products, reducing the solid biochar yield.

Table 1
Cerbera odollam *pyrolysis products based on mass at various pyrolysis temperatures*

Pyrolysis Temperature (°C)	Biochar (gr)	Bio-oil (gr)	Incondensable gas (gr)	Total (gr)
350	821.25	282.94	395.81	1500.0
450	705.31	375.92	418.77	1500.0
550	650.58	432.52	416.90	1500.0

In calculating the mass of gas using the mass balance method, several potential uncertainties need to be considered. One of the main factors is the possibility of mass loss due to gas leakage during the pyrolysis process. The gas produced from pyrolysis is light and can easily escape through small gaps in the reactor system, especially if the system is not completely sealed. In addition, undetected secondary reactions can also cause differences in the calculation of gas mass. Some volatile compounds formed during pyrolysis can undergo further reactions, either with other components in the system or with the reactor wall, which can change the total amount of gas produced. Another factor that can affect the accuracy of the calculation is the efficiency of bio-oil condensation, where a small portion of the gas components may be condensed with the bio-oil, causing slight differences in the mass balance calculation.

The characteristics of the pyrolysis bio-oil were analyzed and are summarized in Table 2. This table presents the key properties of bio-oil, including its density and pH, which are critical for assessing its suitability as a raw material source.

Table 2
Density and pH values in Cerbera odollam *pyrolysis bio-oil products*

Pyrolysis Temperature (°C)	Volume mL)	Density (gr/mL)	pH
350	299.92	1.06	2.97
450	402.23	1.07	3.26
550	454.15	1.05	3.33

Based on the data presented in Table 2, it is evident that the volume of the bio-oil product increases with the rising pyrolysis temperature. At 350°C, the produced volume is 299.92 mL; at 550°C, the volume increases to 454.15 mL. This indicates that higher pyrolysis temperatures tend to yield a greater amount of bio-oil, likely due to more extensive decomposition of the raw material into volatile products that subsequently condense into bio-oil. Furthermore, the density of the bio-oil shows a slight decrease with increasing pyrolysis temperature, from 1.06 g/mL at 350°C to 1.05 g/mL at 550°C. This decrease in density may suggest a change in the chemical composition of the bio-oil, where higher temperatures potentially lead to more decomposition reactions that produce compounds with lower molecular weights and higher water content. Regarding the pH values, all bio-oil products exhibit acidic characteristics with a pH < 7.

The increase in pyrolysis temperature also results in a slight increase in pH from 2.97 at 350°C to 3.33 at 550°C. This rise in pH could indicate that some acidic compounds may decompose or form in lesser quantities at higher temperatures, making the bio-oil slightly less acidic. The relationship between pH and FTIR results, which highlight the presence of C-O groups, particularly those associated with carboxylic acid groups, supports the observation that the bio-oil contains significant acidic compounds. Overall,

these data suggest that pyrolysis temperature influences the volume, density, and acidity (pH) of the produced bio-oil, which is closely related to its chemical composition and water content in the final product.

Based on Figure 5, the results 1.500 gr of *Cerbera odollam* pyrolysis products in percent show that *Cerbera odollam* pyrolysis carried out at a temperature of 350°C produces 54.75% biochar, 18.86% bio-oil, and 26.39% gas. Pyrolysis at a temperature of 400°C produced 47.02% biochar, 25.06% bio-oil, and 27.92% gas. At a temperature of 550°C, it produces 43.37% biochar products, 28.83% bio-oil products, and 27.79% gas products. Figure 5 shows that the higher the pyrolysis temperature, the lower the biochar product, and vice versa for gas products: the higher the pyrolysis temperature, the more gas product.

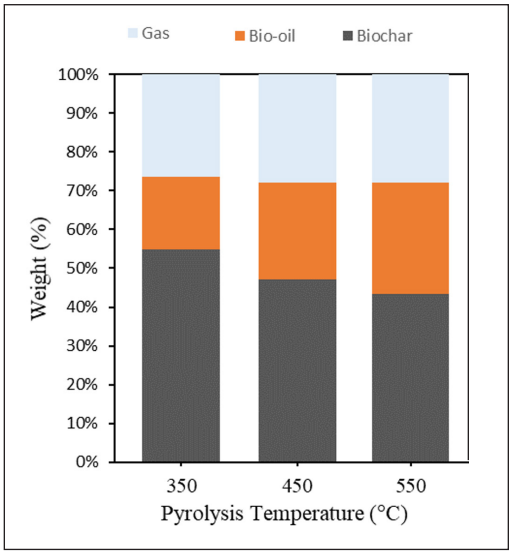

Figure 5. Cerbera odollam pyrolysis products

GC-MS Analysis of Bio-Oil products

The bio-oil product at a temperature of 550°C has the highest yield, so it is analyzed using a Shimadzu QP2020NX GCMS to determine the chemical elements contained in the bio-oil. Produce the data in Table 3.

The main products from bio-oil at a temperature of 550°C are butanal and 3-methyl, the systematic name of an organic compound known as isovaleraldehyde. It is a branched aldehyde with the molecular formula $C_5H_{10}O$; Butanal, 3-methyl- has the highest area percentage, 30.52%. *Cerbera odollam* has 32.0%–38.6% cellulose and 19.7%–35.7% hemicellulose. Degradation of hemicellulose and cellulose produces organic acids such as acetic and formic acids. However, hemicellulose degradation impacts the high value of volatile matter, as well as small amounts of tar and charcoal production. Meanwhile, 13.5%–24.4% is the lignin content, and the ash content of *Cerbera odollam* is 10%–17%. Ash in biomass is usually formed from alkaline elements such as potassium, calcium, magnesium, and silica (W. Wang et al., 2022), which influences the conversion and selectivity of the pyrolysis reaction (Ge et al., 2023). High ash content also reduces the calorific value of biomass.

Pyrolysis at a temperature of 350–550°C decreases biochar yield as the pyrolysis temperature increases, and the yield of the gas product increases. In slow pyrolysis, the main product is biochar, which still contains ash (L. Wang et al., 2022). In this study, the

Table 3
GC-MS analysis of bio-oil

Ret. Time	Area%	Name
1.379	30,52	Butanal, 3-methyl-
34.825	18,00	Oleic Acid
35.994	15,69	9,12-Octadecadienoic acid (Z,Z)-
1.342	11,26	1,6-Anhydro-2,4-dideoxy-.beta.-D-ribo-hexop
30.514	6,75	n-Hexadecanoic acid
34.250	4,62	Octadecanoic acid
21.002	4,51	Hexadecanoic acid, ethyl ester
1.528	1,67	Ethyl Acetate
36.470	1,62	Dodecanedioic acid, dimethyl ester
8.540	1,18	Diethyl sulfate
24.547	1,12	Octadecanoic acid, ethyl ester
30.925	0,77	n-Hexadecanoic acid
39.212	0,71	Eicosanoic acid
33.564	0,36	2(3H)-Furanone, dihydro-5-tetradecyl-
1.654	0,26	Propanoic acid, ethyl ester
30.815	0,19	Hexyl (3S)-3-hydroxy-5-methoxy pentanoate
27.899	0,15	Eicosanoic acid, ethyl ester
1.841	0,12	Butanoic acid, ethyl ester
24.186	0,06	9-Octadecenoic acid, methyl ester
23.358	0,05	4-Ethyl-2,6-dimethoxyphenol

pyrolysis process lasted 1.5 hours, which was slow because it took over an hour. Pyrolysis at a temperature of 350°C produces the most biochar products and the least gas products because (Selvarajoo & Oochit, 2020), at this temperature, complete decomposition has not occurred in the *Cerbera odollam*. Apart from that, pyrolysis at a temperature of 300°C can be said to be torrefaction (Richa et al., 2023) because torrefaction is a type of biomass processing that involves heating without oxygen or using inert gas at a low temperature of 200–300°C. Torrefaction aims to increase the calorific value (Parvej et al., 2022) of biomass by heating it to less than 300°C, with the main product being biochar, which can be used as a solid fuel. The largest bio-oil product was obtained at a temperature of 550°C with an amount of 28.83%. This is because, at this temperature, complete decomposition has occurred in *Cerbera odollam*; the main elements that make up *Cerbera odollam* are 28.5%–41% cellulose, 15.3%–25.9% hemicellulose, and lignin between 6.2%–12.6%. Hemicellulose decomposition occurs at a temperature of 250–350°C, whereas cellulose and lignin decomposition requires a temperature of more than 300°C (Mahakhant et al., 2021). This causes the bio-oil product to be less at a temperature of 350°C, and the optimum product for bio-oil is at a temperature of 450°C. At a temperature of 450°C, Cellulose

and hemicellulose have experienced decomposition. In contrast, lignin decomposition only occurs partially because it requires an even higher temperature, more than 400°C. Cellulose is the main source of generating condensable vapor. Hemicellulose has the lowest degradation temperature at 250–300°C. Hemicellulose produces many non-condensable gases, and cellulose produces many bio-oil products.

Conversely, at higher temperatures, particularly 550°C, the bio-oil yield peaks at 28.83%. This increase in bio-oil production is attributed to the complete decomposition of the biomass components at elevated temperatures. The primary constituents of *Cerbera odollam* biomass include 28.5%–41% cellulose, 15.3%–25.9% hemicellulose, and 6.2%–12.6% lignin. Hemicellulose decomposes between 250–350°C, cellulose between 300–400°C, and lignin at temperatures above 400°C. Therefore, at 550°C, the decomposition of cellulose and hemicellulose is almost complete (Mahakhant et al., 2021), enhancing bio-oil formation. In GC-MS analysis, various organic compounds indicated the complexity of bio-oil produced at 550°C. Compounds such as butanal, 3-methyl-, which had the highest percentage area (30.52%), indicated that most of the bio-oil components were derived from the decomposition of hemicellulose and cellulose (Usino et al., 2021). The presence of compounds such as Hexadecanoic acid and Octadecanoic acid indicated that most of the fatty acids were present in the bio-oil, which could be potential precursors in biodiesel production. Comparison between pyrolysis results at 350°C and 550°C highlighted the significant difference in the products produced. At lower temperatures (350°C), biomass decomposition was still incomplete, which led to more dominant biochar production, while at 550°C, a significant increase in bio-oil products occurred. This fact supports the idea that temperature is crucial in determining pyrolysis results and final products.

It should be noted that the high content of Oleic acid (18%) and 9,12-Octadecadienoic acid (15.69%) in the bio-oil produced indicates the presence of unsaturated fatty acids that have the potential to be used in chemical industry applications, for example, in the manufacture of lubricants or surfactants. On the other hand, compounds such as Diethyl sulfate (1.18%), although in relatively small amounts, may be of concern in terms of toxicity and need to be carefully managed in further processing. In further research, it would be interesting to explore how other pyrolysis conditions, such as heating rate, atmosphere, or variations in the particle size of the feedstock, can affect the distribution of compounds in the bio-oil. Such research could optimize richer bio-oil yield in high-value compounds while minimizing contaminants or unwanted byproducts. In addition, a more in-depth analysis of the effect of biomass ash content on pyrolysis products could provide additional insights into the relationship between the mineral composition of the biomass and the selectivity of the pyrolysis reaction. Further research on optimizing pyrolysis temperature and time can also focus on obtaining higher bio-oil yields and improving bio-oil quality in terms of thermal stability, energy, and chemical component purity.

Decomposition Pathways and Product Distribution

Hemicellulose's decomposition at 250–350°C releases volatile gases and tar (Niksa, 2022a), producing non-condensable gases. This degradation pathway results in a significant portion of the volatile matter escaping as gas, crucial for energy recovery through gasification processes. Cellulose, decomposing at temperatures above 400°C, is a primary source of condensable vapors (Niksa, 2022b). Its decomposition produces a substantial amount of bio-oil, as it converts into a range of volatile organic compounds. At 550°C, the breakdown of cellulose is well-advanced, leading to increased bio-oil production compared to lower temperatures. Lignin decomposition requires temperatures above 500°C (Folgueras et al., 2023), where it breaks down into smaller molecules, primarily phenolic compounds (Zhang et al., 2023). At 550°C, lignin decomposition is partial, contributing to bio-oil formation, but at a slower rate compared to cellulose and hemicellulose.

The optimal temperature for maximizing bio-oil yield in this study is identified as 550°C. At this temperature, the decomposition of cellulose and hemicellulose is significant, while lignin decomposition is not complete. This balance enhances bio-oil production, making 550°C a critical temperature for optimizing bio-oil yield. The decomposition kinetics at this temperature ensure a high yield of condensable vapors, favoring bio-oil production over gases and solid residues. Pyrolysis produces significant amounts of bio-oil at this temperature, with optimal decomposition of hemicellulose and cellulose. Hemicellulose degraded at 250–350°C produces volatile gases and tar, which contribute to non-condensable gas products, making gasification a potential pathway for energy recovery (Ward et al., 2014). Cellulose, which begins to decompose at temperatures above 400°C, is the main source of condensed vapors that make up bio-oil. This explains why, at 550°C, the increase in bio-oil production occurs due to further decomposition of cellulose.

Meanwhile, lignin degraded at temperatures above 500°C is slower in making a significant contribution to bio-oil production. Phenolic molecules produced from lignin decomposition at 550°C enrich the composition of bio-oil (Soldatos et al., 2024), but in a smaller proportion compared to the results of hemicellulose and cellulose decomposition. Considering the characteristics of the decomposition pathway of each biomass component, a temperature of 550°C was shown to be the optimum point to maximize the bio-oil yield. At this temperature, the balance between the decomposition of hemicellulose, cellulose, and lignin provides a bio-oil product rich in volatile compounds with added value. These results open up great opportunities for further exploration in optimizing pyrolysis conditions to improve bio-oil quality and quantity and increase energy efficiency in biomass conversion.

CONCLUSION

The pyrolysis temperature of *Cerbera odollam* in the batch reactor affects the pyrolysis products (char, bio-oil, and gas) produced. Pyrolysis of *Cerbera odollam* at a temperature

of 350°C produces the most char products and the least gas products. Pyrolysis at a temperature of 450°C produces the most gas products and the least char products. The higher the pyrolysis temperature, the higher the gas product and the lower the char product. Likewise, the lower the pyrolysis temperature, the more char products there are and the fewer gas products. The optimum temperature for producing bio-oil from the pyrolysis of *Cerbera odollam* is 550°C, so it has the most chemical components analyzed using GC-MS to determine the chemical components contained. Based on GC-MS analysis, the butanal, 3-methyl-product has the highest percentage area, around 30.52%. So, it can be concluded that more bio-oil can be produced using the fast pyrolysis method or by adding a catalyst. Finally, the pyrolysis process of *Cerbera odollam* biomass exhibits distinct product distributions across different temperatures. Understanding the decomposition pathways and their temperature dependencies is essential for optimizing the yield and quality of biochar, bio-oil, and gases. This knowledge can guide the development of efficient biomass conversion technologies, enhancing the sustainability and economic viability of biomass utilization. In the future, research can focus on deeper investigations into the effects of pyrolysis time, heating rate, and biomass feedstock modification, hoping to increase bio-oil yield and reduce unwanted byproducts. Further investigations into phenolic compounds derived from lignin can also open up opportunities for developing bio-oil applications in industrial chemistry.

ACKNOWLEDGEMENT

We are grateful to everyone who has supported and encouraged us during this research. Your invaluable advice and assistance have been instrumental in completing this work.

REFERENCES

Ajagbe, C. A., Zainuddin, M. F., Manaf, L. A., Rahim, N. N. R. N. A., & Anguruwa, G. T. (2025). Comparative analysis of carbonized hybrid briquettes produced from cassava peel and sawdust for cooking application. *Pertanika Journal of Science and Technology*, *33*(1), 531–555. https://doi.org/10.47836/pjst.33.1.25

Akinpelu, D. A., Adekoya, O. A., Oladoye, P. O., Ogbaga, C. C., & Okolie, J. A. (2023). Machine learning applications in biomass pyrolysis: From biorefinery to end-of-life product management. *Digital Chemical Engineering*, *8*, Article 100103. https://doi.org/10.1016/j.dche.2023.100103

Ameh, V. I., Ayeleru, O. O., Nomngongo, P. N., & Ramatsa, I. M. (2024). Bio-oil production from waste plant seeds biomass as pyrolytic lignocellulosic feedstock and its improvement for energy potential: A review. *Waste Management Bulletin*, *2*(2), 32–48. https://doi.org/10.1016/j.wmb.2024.03.002

Ansari, K. B., Arora, J. S., Chew, J. W., Dauenhauer, P. J., & Mushrif, S. H. (2019). Fast pyrolysis of cellulose, hemicellulose, and lignin: Effect of operating temperature on bio-oil yield and composition and insights into the intrinsic pyrolysis chemistry. *Industrial and Engineering Chemistry Research*, *58*(35), 15838–15852. https://doi.org/10.1021/acs.iecr.9b00920

Arregi, A., Santamaria, L., Lopez, G., Olazar, M., Bilbao, J., Artetxe, M., & Amutio, M. (2023). Appraisal of agroforestry biomass wastes for hydrogen production by an integrated process of fast pyrolysis and in line steam reforming. *Journal of Environmental Management*, *347*, Article 119071. https://doi.org/10.1016/j.jenvman.2023.119071

Bieniek, A., Sieradzka, M., Jerzak, W., & Magdziarz, A. (2023). Fast pyrolysis of agricultural biomass in drop tube reactor for bio-oil production: Numerical calculations. *Journal of Analytical and Applied Pyrolysis*, *176*, Article 106241. https://doi.org/10.1016/j.jaap.2023.106241

Chan, E. W. C., Wong, S. K., Chan, H. T., Baba, S., & Kezuka, M. (2016). Cerbera are coastal trees with promising anticancer properties but lethal toxicity: A short review. *Journal of Chinese Pharmaceutical Sciences*, *25*(3), 161–169. https://doi.org/10.5246/jcps.2016.03.019

Chen, D., Cen, K., Zhuang, X., Gan, Z., Zhou, J., Zhang, Y., & Zhang, H. (2022). Insight into biomass pyrolysis mechanism based on cellulose, hemicellulose, and lignin: Evolution of volatiles and kinetics, elucidation of reaction pathways, and characterization of gas, biochar and bio-oil. *Combustion and Flame*, *242*, Article 112142. https://doi.org/10.1016/j.combustflame.2022.112142

Clemente-Castro, S., Palma, A., Ruiz-Montoya, M., Giráldez, I., & Díaz, M. J. (2023). Comparative study of the combustion, pyrolysis and gasification processes of *Leucaena leucocephala*: Kinetics and gases obtained. *Heliyon*, *9*(7), Article e17943. https://doi.org/10.1016/j.heliyon.2023.e17943

Corbita, J. N., Pabilona, L., & Villanueva, E. (2024). Energy audit on two 22-TPH coal-fired boilers of a pineapple processing plant. *Pertanika Journal of Science and Technology*, *32*(4), 1919–1937. https://doi.org/10.47836/pjst.32.4.25

Eraslan, U., & Calhan, R. (2024). Investigation of the performance and emissions of a diesel engine fuelled with bio-oil generated through microwave-assisted pyrolysis of a blend of hazelnut, walnut, and polyethylene terephthalate waste. *Industrial Crops and Products*, *214*, Article 118560. https://doi.org/10.1016/j.indcrop.2024.118560

Ferdous, J., Hossain, M. S., Rahman, M. S., Kader, M. A., & Islam, M. R. (2024). Experimental investigation of optimum bio-oil production parameters through co-pyrolysis of three organic wastes. *Journal of Analytical and Applied Pyrolysis*, *177*, Article 106308. https://doi.org/10.1016/j.jaap.2023.106308

Folgueras, M. B., Gómez-Martín, J. M., & Diez, M. A. (2023). How height-related variations in hybrid poplars affect composition and pyrolytic behaviour: The key role of lignin maturity during woody-biomass pyrolysis. *Journal of Analytical and Applied Pyrolysis*, *169*, Article 105861. https://doi.org/10.1016/j.jaap.2023.105861

Gao, G., Zhang, S., Shao, Y., Li, C., Zhang, L., Gao, W., Ding, K., Huang, Y., Gholizadeh, M., & Hu, X. (2024). Oxidative pyrolysis of spirulina: Impacts of oxygen on bio-oil and property of biochar. *Journal of Environmental Chemical Engineering*, *12*(3), Article 112506. https://doi.org/10.1016/j.jece.2024.112506

Ge, Y., Ding, S., Zhang, W., Kong, X., & Kantarelis, E. (2023). Impacts of fresh bed materials on alkali release and fuel conversion rate during wood pyrolysis and char gasification. *Fuel*, *353*, Article 129161. https://doi.org/10.1016/j.fuel.2023.129161

Hasanzadeh, A., Mehrara, M., Irani, M., Chitsaz, A., & Parham, K. (2023). An innovative biomass-fueled gas turbine-ORC system equipped with electrochemically mediated amine regeneration (EMAR) for CO_2 capture. *Journal of CO2 Utilization*, *68*, Article 102365. https://doi.org/10.1016/j.jcou.2022.102365

Kadhem, A. A., & Wahab, N. I. A. (2024). Effects of unavailability of conventional energy units on power generation system adequacy. *Pertanika Journal of Science and Technology*, *32*(4), 1687–1706. https://doi.org/10.47836/pjst.32.4.13

Khan, A. A., Zaidi, S., Qureshi, F., Yusuf, M., Al-Kahtani, A. A., Kamyab, H., Gupta, M., Pandit, B., Gill, H. S., & Ibrahim, H. (2024). Response surface optimization and support vector regression modeling of microwave-assisted essential oil extraction from cumin seeds. *Industrial Crops and Products*, *208*, 1–9. https://doi.org/10.1016/j.indcrop.2023.117895

Letoffet, A., Campion, N., Böhme, M., Jensen, C. D., Ahrenfeldt, J., & Clausen, L. R. (2024). Techno-economic assessment of upgraded pyrolysis bio-oils for future marine fuels. *Energy Conversion and Management*, *306*, Article 118225. https://doi.org/10.1016/j.enconman.2024.118225

Mahakhant, A., Attanatho, L., & Suemanotham, A. (2021). Thermal decomposition of biomass wastes derived from palm oil production. *Journal of Analytical and Applied Pyrolysis, 155*, Article 105069. https://doi.org/10.1016/j.jaap.2021.105069

Melikoglu, M., Ozdemir, M., & Ates, M. (2023). Pyrolysis kinetics, physicochemical characteristics and thermal decomposition behavior of agricultural wastes using thermogravimetric analysis. *Energy Nexus, 11*, Article 100231. https://doi.org/10.1016/j.nexus.2023.100231

Mossa, M. A., Hairuddin, A. A., Aziz, N. A., & Tobib, H. M. (2024). The green energy effect on an HCCI engine from used cookinoil-based biodiesel from Malaysia. *Pertanika Journal of Science and Technology*, *32*(4), 1565–1589. https://doi.org/10.47836/pjst.32.4.07

Niksa, S. (2022a). On the primary devolatilization of hemicellulose. *Journal of Analytical and Applied Pyrolysis*, *164*, Article 105515. https://doi.org/10.1016/j.jaap.2022.105515

Niksa, S. (2022b). Predicting the rapid devolatilization of mineral-free cellulose. *Journal of Analytical and Applied Pyrolysis*, *161*, Article 105402. https://doi.org/10.1016/j.jaap.2021.105402

Noor, M. F., Sumarlan, S. H., Hendrawan, Y., Argo, B. D., & Abdillah, H. (2025). Implementation and analysis of temperature and gas sensor datalogger in multi-stage condenser pyrolysis. *Indonesian Journal of Electrical Engineering and Computer Science, 37*(3), 1497–1505. https://doi.org/10.11591/ijeecs.v37.i3.pp1497-1505

Onwudili, J. A., Sharma, V., Scaldaferri, C. A., & Hossain, A. K. (2023). Production of upgraded fuel blend from fast pyrolysis bio-oil and organic solvent using a novel three-stage catalytic process and its combustion characteristics in a diesel engine. *Fuel*, *335*, Article 127028. https://doi.org/10.1016/j.fuel.2022.127028

Parthasarathy, P., Zuhara, S., Al-Ansari, T., & McKay, G. (2023). A review on catalytic CO_2 pyrolysis of organic wastes to high-value products. *Fuel*, *335*, Article 127073. https://doi.org/10.1016/j.fuel.2022.127073

Parvej, A. M., Rahman, M. A., & Reza, K. A. (2022). The combined effect of solar assisted torrefaction and pyrolysis on the production of valuable chemicals obtained from water hyacinth biomass. *Cleaner Waste Systems*, *3*, Article 100027. https://doi.org/10.1016/j.clwas.2022.100027

Poomsawat, W., & Poomsawat, S. (2023). Pyrolysis kinetic behavior of composite polypropylene-biomass solid fuels derived via co-hydrothermal carbonization process. *Thermal Science and Engineering Progress*, *43*, Article 101953. https://doi.org/10.1016/j.tsep.2023.101953

Rajpoot, L., Tagade, A., Deshpande, G., Verma, K., Geed, S. R., Patle, D. S., & Sawarkar, A. N. (2022). An overview of pyrolysis of de-oiled cakes for the production of biochar, bio-oil, and pyro-gas: Current status, challenges, and future perspective. *Bioresource Technology Reports*, *19*, Article 101205. https://doi.org/10.1016/j.biteb.2022.101205

Richa, L., Colin, B., Pétrissans, A., & Wallace, C. (2023). Catalytic and char-promoting effects of potassium on lignocellulosic biomass torrefaction and pyrolysis. *Environmental Technology & Innovation*, *31*, Article 103193. https://doi.org/10.1016/j.eti.2023.103193

Rony, Z. I., Rasul, M. G., Jahirul, M. I., & Hasan, M. M. (2025). Properties of pyrolysis oils derived from different organic wastes for assessing their suitability for engine fuel. *Energy Conversion and Management: X*, *25*, Article 100875. https://doi.org/10.1016/j.ecmx.2025.100875

Rosalina, R., Henny, R., Lestari, P. S., Tedja, T., Etty, R., & Sugiarti, S. (2018). The influence of phosphoric acid activation of carbon from Bintaro fruit (Cerbera odollam Gaertn) on the adsorption of chromium in various conditions of pH. *International Journal of Chemical Studies, 6*(1), 443–448.

Roy, D. K., & Abedin, M. Z. (2022). Potentiality of biodiesel and bioethanol production from feedstock in Bangladesh: A review. *Heliyon*, *8*(11), Article e11213. https://doi.org/10.1016/j.heliyon.2022.e11213

Selvarajoo, A., & Oochit, D. (2020). Effect of pyrolysis temperature on product yields of palm fibre and its biochar characteristics. *Materials Science for Energy Technologies*, *3*, 575–583. https://doi.org/10.1016/j.mset.2020.06.003

Seo, J. C., Lee, J. G., Kang, S. H., & Kwon, C. Y. (2023). Suicidal use of East Asian traditional herbal medicine: A systematic review of observational studies and implications for regulation. *European Journal of Integrative Medicine*, *62*, Article 102276. https://doi.org/10.1016/j.eujim.2023.102276

Sierra, I., Ayastuy, J. L., Gutiérrez-Ortiz, M. A., & Iriarte-Velasco, U. (2023). A study on the impact of the reaction mechanism of the thermochemical activation of bone char (by pyrolysis and carbonization). *Journal of Analytical and Applied Pyrolysis*, *171*, Article 105973. https://doi.org/10.1016/j.jaap.2023.105973

Soldatos, P., Margellou, A., Pappa, C., Torofias, S., Matsakas, L., Rova, U., Christakopoulos, P., & Triantafyllidis, K. (2024). Conversion of beechwood organosolv lignin via fast pyrolysis and *in situ* catalytic upgrading towards aromatic and phenolic-rich bio-oil. *Sustainable Chemistry for the Environment*, *6*, Article 100107. https://doi.org/10.1016/j.scenv.2024.100107

Suprianto, T., Winarto, Wijayanti, W., & Wardana, I. N. G. (2021). Synergistic effect of curcumin and activated carbon catalyst enhancing hydrogen production from biomass pyrolysis. *International Journal of Hydrogen Energy*, *46*(10), 7147–7164. https://doi.org/10.1016/j.ijhydene.2020.11.211

Syuriadi, A., Siswantara, A. I., Nurhakim, F. R., Irbah, Y. N., Al Rizky, B., Zulfa, F. A., Devitra, F. A., Permana, S., & Susanto, I. (2022). Analysis of the effect of biomass variants (fish waste, tamanu waste and duckweed) on the characteristics of syngas, bio oil, and carbon charcoal produced in the pyrolysis process. *Eastern-European Journal of Enterprise Technologies*, *3*(6(117)), 41–46. https://doi.org/10.15587/1729-4061.2022.253750

Szufa, S., Piersa, P., Junga, R., Błaszczuk, A., Modliński, N., Sobek, S., Marczak-Grzesik, M., Adrian, & Dzikuć, M. (2023). Numerical modeling of the co-firing process of an in situ steam-torrefied biomass with coal in a 230 MW industrial-scale boiler. *Energy*, *263*, Article 125918. https://doi.org/10.1016/j.energy.2022.125918

Usino, D. O., Ylitervo, P., Moreno, A., Sipponen, M. H., & Richards, T. (2021). Primary interactions of biomass components during fast pyrolysis. *Journal of Analytical and Applied Pyrolysis*, *159*, Article 105297. https://doi.org/10.1016/j.jaap.2021.105297

Vanapalli, K. R., Bhattacharya, J., Samal, B., Chandra, S., Medha, I., & Dubey, B. K. (2021). Single-use LDPE - Eucalyptus biomass char composite produced from co-pyrolysis has the properties to improve the soil quality. *Process Safety and Environmental Protection*, *149*, 185–198. https://doi.org/10.1016/j.psep.2020.10.051

Wahyudi, D., Wignyanto, Hendrawan, Y., & Hamidi, N. (2024). Bernoulli distillation system (BDS) for bioethanol sorghum stalk purification. *Pertanika Journal of Science and Technology, 32*(6), 2421–2440. https://doi.org/10.47836/pjst.32.6.02

Wang, L., Olsen, M. N. P., Moni, C., Dieguez-alonso, A., Rosa, D., Stenr, M., Liu, X., & Mao, L. (2022). Comparison of properties of biochar produced from different types of lignocellulosic biomass by slow pyrolysis at 600 ◦C. *Applications in Energy and Combustion Science, 12*, Article 100090. https://doi.org/10.1016/j.jaecs.2022.100090

Wang, W., Lemaire, R., Bensakhria, A., & Luart, D. (2022). Review on the catalytic effects of alkali and alkaline earth metals (AAEMs) including sodium, potassium, calcium and magnesium on the pyrolysis of lignocellulosic biomass and on the co-pyrolysis of coal with biomass. *Journal of Analytical and Applied Pyrolysis*, *163*, Article 105479. https://doi.org/10.1016/j.jaap.2022.105479

Ward, J., Rasul, M. G., & Bhuiya, M. M. K. (2014). Energy recovery from biomass by fast pyrolysis. *Procedia Engineering*, *90*, 669–674. https://doi.org/10.1016/j.proeng.2014.11.791

Wijayanti, W., Musyaroh, Sasongko, M. N., Kusumastuti, R., & Sasmoko. (2021). Modelling analysis of pyrolysis process with thermal effects by using Comsol Multiphysics. *Case Studies in Thermal Engineering*, *28*, Article 101625. https://doi.org/10.1016/j.csite.2021.101625

Wu, Y., Gui, Q., Zhang, H., Li, H., Li, B., Liu, M., Chen, Y., Zhang, S., Yang, H., & Chen, H. (2023). Effect of biomass components' interaction on the pyrolysis reaction kinetics and small-molecule product release characteristics. *Journal of Analytical and Applied Pyrolysis*, *173*, Article 106039. https://doi.org/10.1016/j.jaap.2023.106039

Zhang, C., Xiong, Y., Liu, Q., Wang, X., Syed-Hassan, S. S. A., Deng, W., Xu, K., Wang, Y., Hu, S., & Xiang, J. (2024). Effects of Interactions among cellulose, hemicellulose, and lignin on the formation of heavy components in bio-oil during oxidative pyrolysis. *Energy and Fuels, 38*(21), 20831-20838. https://doi.org/10.1021/acs.energyfuels.4c04330

Zhang, H., Liu, M., Yang, Y., Chen, W., Zhu, J., Zhang, S., Yang, H., Chen, H., & Chen, Y. (2023). Mechanism study on the interaction between holocellulose and lignin during secondary pyrolysis of biomass: In terms of molecular model compounds. *Fuel Processing Technology*, *244*, Article 107701. https://doi.org/10.1016/j.fuproc.2023.107701

Pertanika J. Sci. & Technol. 33 (4): 1783 - 1807 (2025)

PERTANIKA JOURNALS

SCIENCE & TECHNOLOGY

Journal homepage: http://www.pertanika.upm.edu.my/

Development of Machine Learning Wildlife Camera Using ESP32 CAM for Small Mammals

Leu Mei Xin and Nik Fadzly N Rosely*

School of Biological Sciences, Universiti Sains Malaysia (USM), 11800 Gelugor, Pulau Pinang, Malaysia

ABSTRACT

Camera traps serve a pivotal role in the surveillance of wildlife populations within a given habitat. Nonetheless, commercially available camera traps tend to be relatively expensive, power-consuming, non-selective in their detection capabilities, and necessitate subsequent processing of the acquired images. In this study, we focus on developing a simple machine-learning wildlife camera using ESP32 CAM, a microcontroller that has an integrated camera, flash, and SD card storage, for detecting small mammals. The ESP32 CAM was designed to recognize and photograph squirrels in natural environments, employing an object detection model formulated via an accessible online machine-learning resource known as Edge Impulse. The efficacy of the models was systematically assessed, with training images derived from two distinct repositories, namely, the Google Images Repository and original photographs captured at the designated field site, compared for analysis. Model A, which utilized images from Google, achieved an accuracy rate of 61.5%, whereas Model B, which relied on local field photographs, attained an accuracy of 83.3%. We compared ESP32 CAM to Hawkray Digital trail camera to assess the model's accuracy in detecting squirrels. Results from the Chi-Square analysis reveal that the number of squirrel pictures taken by both cameras was the same. A thorough discussion of various factors influencing the model's accuracy, including background uniformity, size of the object, posture, and distance, was also undertaken. Furthermore, this study addressed the implementation of TinyML within the ESP32 CAM context, as well as the inherent limitations associated with the ESP32 CAM technology.

Keywords: Camera trap, edge impulse, ESP32 CAM, machine learning, object detection model, small mammal detection, training image

ARTICLE INFO

Article history:
Received: 23 September 2024
Accepted: 03 March 2025
Published: 11 June 2025

DOI: https://doi.org/10.47836/pjst.33.4.05

E-mail addresses:
meixin8663@student.usm.my (Leu Mei Xin)
nfadzly@usm.my (Nik Fadzly N Rosely)
* Corresponding author

e-ISSN: 2231-8526

© Universiti Putra Malaysia Press

INTRODUCTION

The use of camera traps is a well-known method for monitoring wildlife (Swann & Perkins, 2014). Camera traps, or trail cameras, typically denote devices that activate upon detecting animal movement within their operational range. They are advantageous for estimating population densities and conducting demographic studies, as they facilitate prolonged monitoring of a designated area without much human intrusion (Sreedhar et al., 2021; Swann & Perkins, 2014). Camera traps possess the capability to acquire high-resolution images and videos, which is essential for species monitoring and behavioral research (Bird et al., 2021; Blount et al., 2021; Zhu et al., 2021). Additionally, camera traps can be strategically employed to alleviate human-wildlife conflicts, including issues such as wildlife encroachment, crop destruction, and livestock predation, by monitoring and detecting wildlife activity and movement in an area so that the affected community and authorities can be alerted and appropriate actions can be planned and taken.

ESP32 CAM is a unique microcontroller that has a built-in integrated camera, flash, and SD card storage built into the module. The price is relatively cheap, ranging from five to seven US Dollars (around MYR20 to MYR30). Further technical details and a datasheet can be found at Ai Thinker's website (https://docs.ai-thinker.com/en/esp32-cam). Due to its cheap price and adaptability in terms of programming, it is usually used for object identification (Rai & Rehman, 2019; Vinod et al., 2023). Other uses include smart agricultural practices (Elhattab et al., 2023), wildlife observation (Linder & Olsson, 2022), and industrial automation (Vinod et al., 2023), where visual data is primarily used to enhance operational efficacy.

Machine Learning (ML) represents a domain within Artificial Intelligence (AI) wherein computational systems can discern patterns from datasets via algorithms, thereby executing tasks autonomously with or without direct human oversight (Das et al., 2015). ML methodologies are progressively being integrated into conservation efforts (Fernandes et al., 2020; Shivaprakash et al., 2022; Tuia et al., 2022). For instance, computer vision algorithms can be employed to filter and process images obtained from wildlife camera traps to screen out blank images and classify the present animal species (Sreedhar et al., 2021). The advent of Tiny Machine Learning (TinyML) facilitates the deployment of machine learning within resource-limited devices, such as embedded systems and Internet-of-Things (IoT) devices, by optimizing algorithms to be as compact as possible to conform to specific hardware and software limitations (Disabato & Roveri, 2022; Ray, 2022).

Small mammals are animals with a tiny body size and are less than five kilograms (Baharudin et al., 2023). Typical representatives of this group include rodents, moles, shrews and bats. The populations of small mammals face significant threats due to climate change (Szpunar et al., 2008), deforestation, urbanization, and the expansion of agricultural plantations, which are the principal contributors to habitat degradation

(Palmeirim et al., 2020). Global research has demonstrated that habitat fragmentation resulting from urbanization and agricultural growth has precipitated a decrease in small mammal populations (Gomes et al., 2011; Johnstone et al., 2014; Palmeirim et al., 2020).

A web-based artificial intelligence platform called Edge Impulse (https://edgeimpulse.com) uses datasets or sensor data to create machine learning models for edge devices. It is convenient because Edge Impulse has a user-friendly interface that creates models that can be exported and used with a variety of widely used programming languages, including Arduino, TensorFlow Lite, and Mbed. This research aims to develop a simple device that is efficient for detecting the presence of small mammals using Edge Impulse. This is followed by 3 research questions:

1. Which training set is best for training machine learning algorithms?
2. Can TinyML be utilized in ESP32 CAM for the recognition of small mammals?
3. Will ESP32 CAM be at par with its commercial counterparts?

This study specifically focuses on object detection, aiming to detect the presence of small mammals in cameras without classifying them into specific species. ESP32 CAM is expected to be triggered and capture an image as long as an object is detected as a small mammal. The emphasis is on presence detection rather than species classification. We train the model with pictures of rats and squirrels due to the frequent presence of these two groups of small mammals in the study site. This uses TinyML to be deployed on ESP32 CAM. The project emphasizes the potential of ESP32 CAM for detection and photographic documentation of small mammals through the application of machine learning techniques. It deliberately avoids intricate machine learning programming, opting instead for a user-friendly click-and-drag interface requiring only a basic understanding of coding.

Another main factor in choosing ESP32 CAM is its low cost. We aim to design the camera to be less than 50 MYR and can be customized based on the user's demand. Our primary goal is to evaluate the feasibility of using small, low-power, and cost-effective embedded cameras with onboard machine learning for small mammal detection in remote field settings. While effective for wildlife monitoring, traditional trail cameras often require substantial power, produce large volumes of data that necessitate manual post-processing, and may not support real-time edge-based classification. In contrast, embedded solutions, such as the ESP32-CAM combined with TinyML, offer a lightweight alternative capable of performing real-time inference directly on the device, reducing the need for cloud processing and data storage.

We selected ESP32 CAM due to its affordability, low power consumption, and ability to capture images autonomously in field conditions. TinyML was chosen as it enables efficient deployment of machine learning models on resource-constrained hardware, ensuring that inference can be performed locally without constant connectivity. Edge Impulse was utilized as it provides an accessible and optimized pipeline for training and deploying machine

learning models onto embedded devices, streamlining the integration of AI-based image recognition with minimal computational overhead. Furthermore, its no-code approach is easy even for non-coders to train computer vision models.

The small mammal detection model was trained using Edge Impulse, utilizing two distinct training datasets from the Google Images Repository and local field photographs obtained via wildlife camera traps within the same study locale. The accuracy of the model was evaluated between these two training data sets within Edge Impulse. The model exhibiting superior accuracy was subsequently selected for deployment in the ESP32 CAM. We tested the ESP32 CAM in the field for its effectiveness. We then compared the results to the commercial wildlife camera trap.

MATERIALS AND METHODS

Study Site

This study took place at the Eco Hub in the Durian Valley of Universiti Sains Malaysia (USM) between January and March 2024, located at coordinates 5°21'41.7"N 100°18'18.0" E (indicated by the red dot in Figure 1). The USM campus on Penang Island, Malaysia, has been recognized as a "University in the Garden" after the construction of the Eco Hub in 2001. Eco Hub represents the university's initiative to preserve campus greenery and protect diverse flora and fauna. Photographs of small mammals, subsequently utilized for training the machine learning model, were obtained prior to the experiment through a camera trap positioned at the location marked in Figure 1. During the preliminary trials conducted at the study site, the camera system only detected squirrels and rats. As a result, the small mammal detection model in this study was specifically designed to focus on these two

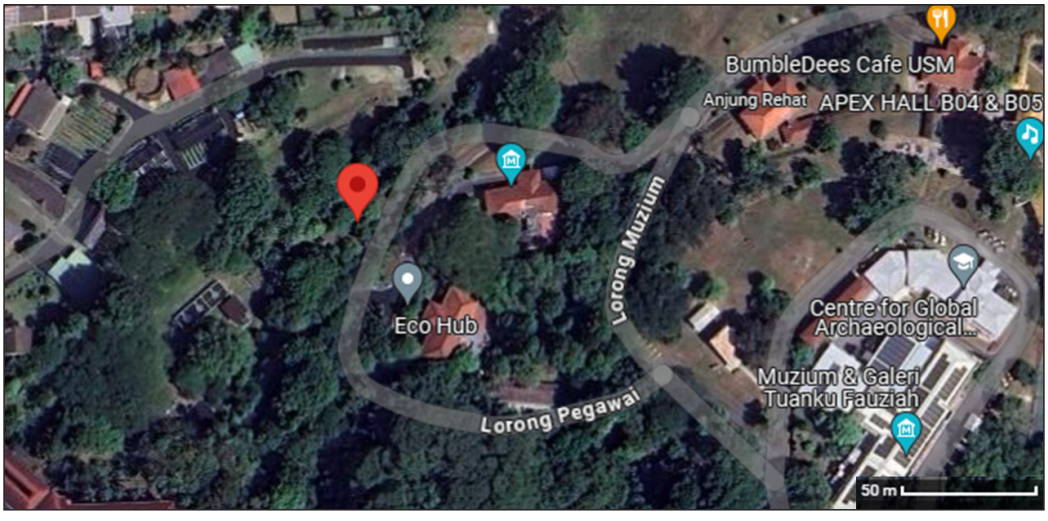

Figure 1. Location of experiment site (red marker) in Eco Hub USM (*Source:* Google Map)

categories of small mammals. This targeted approach ensures that the model is optimized for the most frequently observed small mammals within the study area. This same site was utilized for the deployment of both the ESP32 CAM and the camera trap throughout the experiment. Pieces of bananas were employed as bait to entice small mammals to the research area.

Hardware Components

The main hardware used in this research was the ESP32 CAM AI Thinker, as shown in Figure 2. The camera module is OV2640 (2-megapixel resolution). The built-in flash and SD card storage help reduce the additional components needed for the project. Although the board has WiFi, it was not used as the module was placed in the forest. General-purpose input/output (GPIO) pins enable us to add additional sensors if needed. There is also 4 MB of PseudoStatic Random Access Memory (PSRAM) for data streaming capabilities. This capability guarantees high image quality without leading to system instability in the ESP32. A basic blue housing produced via 3D printing by employing polylactic acid (PLA) filament was specifically engineered to secure and contain the ESP32 CAM (Figure 3).

The ESP32-CAM lacks an integrated USB interface. Consequently, an ESP32-CAM-MB programmer (Figure 4) is needed to successfully upload programmed code into the ESP32-CAM module.

Power was supplied to the ESP32 CAM through the soldering of pins from a four-slot 18650 lithium battery shield. This battery shield was interconnected with a UPS 4W solar panel (Figure 5) to enhance and prolong the operational longevity of the device when deployed in field conditions. This study used a 32GB micro-SD card to augment the storage capabilities of ESP32 CAM. With its ESP32 development board, the ESP32-CAM is compatible with programming via the Arduino Integrated Development Environment (IDE).

The Hawkray digital trail camera (Figure 6) was the camera trap employed for the preliminary acquisition of images of small mammals. We used the same camera trap again

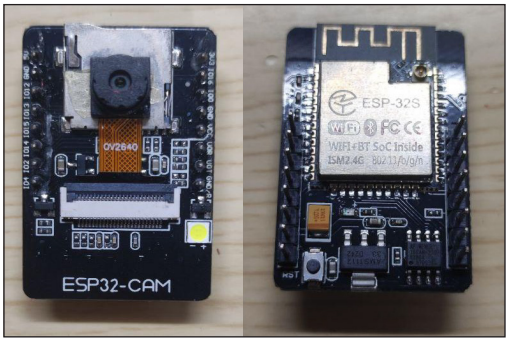

Figure 2. Front and rear view of ESP32 CAM

Figure 3. Front and rear view of a 3D printed casing for ESP32 CAM

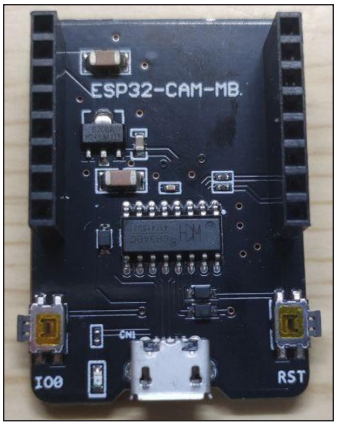

Figure 4. ESP32-CAM-MB programmer

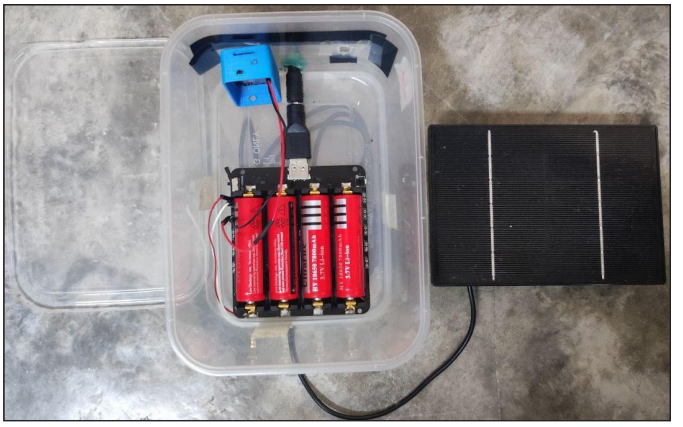

Figure 5. ESP32 CAM connected to a 18650 battery shield for a solar panel

in the field in conjunction with the ESP32 CAM AI Thinker. Four AA alkaline batteries supply the camera trap's operational power.

Figure 6. Front and rear view of the Hawkray digital trail camera

Both the cameras (Hawkray digital trail camera and the ESP32 CAM AI Thinker) function differently from each other. The Hawkray camera has a much higher-resolution image of 12 MP. It is also equipped with a Passive Infrared (PIR) sensor and InfraRed (IR) Light Emitting Diode (LED). When motion and heat are detected, the PIR sensor activates the camera. The image sensor captures the scene, using IR LEDs during low-light conditions, and saves the data to an SD card. The camera enters a power-saving mode when no motion or heat is detected, thus enabling it to function for a prolonged time. However, it is also prone to false positives, in which movements from the foliage or even leaves falling in front of the lens could trigger the camera. For our experiment, the camera was set to take 12 MP images when triggered. It was also programmed to capture the images in the first 5 minutes with a 10-second delay between each image.

The ESP32 CAM AI Thinker works by continuously watching the area. Since it is trained to recognize only specific objects (in our case, small mammals), it will ignore other movements or objects in its field of vision. Unfortunately, it is not equipped with any IR LEDs, thus rendering it useless during night or low-light situations. Therefore, it is programmed to be awake from 7 am until 8 pm. It will remain in deep sleep mode during the night. We programmed it to take pictures for 5 minutes with a 10-second delay between each image.

Machine Learning Model

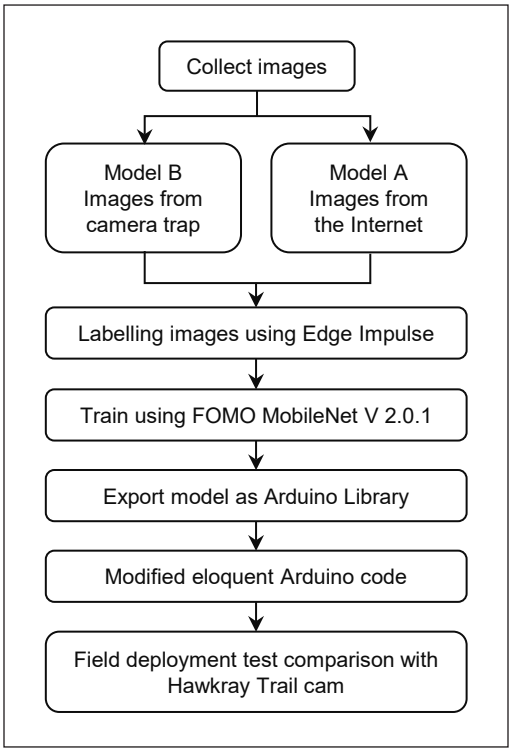

Figure 7. Flow chart of the entire project

Edge Impulse functioned as the training platform for this research initiative, enabling the formulation of the machine learning algorithm utilized by the ESP32 CAM for the recognition of small mammals. The training process was systematically divided into five distinct phases (Figure 7). Initially, images depicting the target subject, namely, small mammals, were collected. These images served as the training dataset within Edge Impulse, enabling the extraction of machine-recognizable features. For this study, the training images of small mammals were sourced from two primary channels: images retrieved from the Google Image Repository and local images obtained through a camera trap. In Model A, images of squirrels and rats were sourced from the Google Images Repository, culminating in the acquisition of 738 images of squirrels and 1,074 images of rats, which were subsequently uploaded to Edge Impulse. Examples of training images in Model A are shown in Figure 8. The imbalance ratio between images of squirrels and rats resulted from a manual selection process that prioritized images most relevant to local species and background settings. For Model B, local field images of squirrels and rats were obtained from a camera trap strategically positioned at the research site, EcoHub, to capture images of squirrels and rats. The final results of 244 images were documented, consisting of 201 images showcasing squirrels during daylight and 43 images depicting rats at night. Examples of training images in Model B are shown in Figure 9. Due to fewer images being captured, we created replicates for each image, producing 488 images to increase the dataset. Eight images were manually taken using the camera at the exact angle as a background dataset to help the model identify the background. These images were then uploaded to Edge Impulse. As this study focuses on small mammal detection rather than species classification, and squirrels and rats are within the targeted group, the difference in the number of images is not a primary concern.

The second phase involved annotating the images through the application of bounding boxes. Bounding boxes were precisely outlined around all observable squirrels and rats within the images, and corresponding labels were assigned. The designations employed

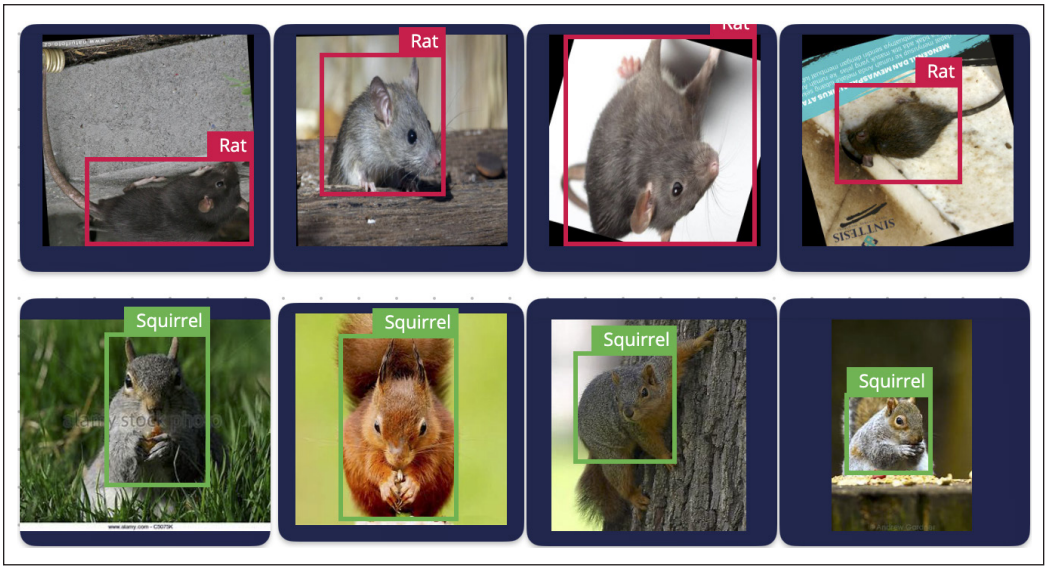

Figure 8. Labelled training image examples of the rat and squirrel in Model A

Figure 9. Labelled training image examples of the rat and squirrel in Model B

included ‘squirrel’ and ‘rat’. In instances where camera trap images contained no animals, no bounding boxes were labeled, and such images were systematically categorized as background images. In the Edge Impulse tutorial and DroneBot Workshop methodology (https://dronebotworkshop.com/esp32-cam-intro/), backgrounds are pictures without the object. We did not specify or rename it into ‘background’; rather, images that were not labeled (no objects within them) will be automatically considered ‘background’. Since we will be testing at the same place inside the forest, we chose our forest image (without any animals) as the background. We use the feature explorer in the Edge Impulse systems to describe the overall pattern of the dataset.

The third phase involves training the model to utilize the labelled images. The images were converted to grayscale to ensure that the model concentrated on the morphological features of small mammals, independent of color. The images were converted to grayscale to ensure that the model focused exclusively on the morphological features of small mammals, such as body shape, size, and structural details, independent of color variations that may not be relevant for classification. Morphological features are critical for distinguishing between small mammal species, as their physical structures often contain defining characteristics that are species-specific. This approach is particularly feasible because grayscale images reduce computational complexity and eliminate potential biases introduced by environmental lighting or fur coloration, which may vary within the same species. A good result here would be the model's ability to achieve high precision and recall in distinguishing between species based solely on morphology, demonstrating that the extracted grayscale features effectively capture the necessary species-specific patterns. Success would be indicated by accurate classification metrics, supporting the hypothesis that morphological features are sufficient for species differentiation in this context. Edge Impulse offers a pre-configured neural network capable of training the object detection model and producing an output. This process is also called Transfer Learning.

Transfer learning is a machine learning technique where a pre-trained model, initially trained on a large dataset, is adapted to a new but related task with a smaller dataset. Instead of training a model from scratch, transfer learning leverages the knowledge gained from a previously learned task, significantly reducing training time and improving performance, especially when labeled data is limited. The settings were left at default since we were using Edge Impulse's free account. Through trial and error, we found that increasing or modifying certain parameters tends to cause online training to fail. The number of training cycles/epoch were kept at 30. The learning rate was set at 0.01. The Training Processor is a CPU (GPU access is for paid accounts). The validation set data size is kept at 20%. This means that the images are sorted and selected randomly by Edge Impulse for training, testing and validation before training. The batch size is kept at 32, which is the default. Data augmentation is limited to grayscale only. We did not use the quantized model option, which will cause the model to crash during Arduino compilation later.

The available neural network architecture for the free account version of Edge Impulse is FOMO (Faster Object More Object) MobileNet V2.0.1. FOMO (Faster Objects, More Objects) MobileNet V2.0.1 represents an advanced object detection framework optimized for edge artificial intelligence applications within environments with limited resources. It builds upon the MobileNetV2 architecture, modified to facilitate rapid object detection with reduced computational demands.

In contrast to traditional object detection frameworks that rely on bounding boxes, FOMO employs a grid-based approach to object localization, rendering it exceptionally

efficient for applications such as counting, tracking, and real-time detection of minute objects. This streamlined model is particularly advantageous for implementation on microcontrollers and low-power edge devices, where conventional deep learning models may incur prohibitive computational costs. The dataset was partitioned into 75% for training and 25% for testing. In Edge Impulse, the platform automatically splits the dataset into training and validation sets during the training pipeline. The confusion matrix and performance metrics shown after training are derived from the validation set. This ensures the results reflect the model's capability to handle new data.

Edge Impulse employs several techniques to address overfitting during model training. One key method is data splitting, where the platform automatically divides the dataset into training, validation, and sometimes test sets. This ensures that the model is evaluated on unseen data, providing a more accurate measure of its generalization capabilities. Additionally, data augmentation can be enabled to introduce variability into the training data through methods such as noise addition, cropping, or flipping. This variability helps the model learn more robust patterns and reduces its reliance on specific data features. Lastly, Edge Impulse offers predefined machine learning architectures, such as convolutional neural networks, which are often optimized to balance model complexity with generalization, minimizing the likelihood of overfitting.

Based on the F1 score of accuracy (based on the validation dataset) that we derived from the confusion matrix, we selected the best model to be deployed to the ESP32 CAM. After the training, the fourth step is to upload the model that is compatible with the ESP32 CAM. Edge Impulse packages the model into a compact library that can be installed inside the Arduino IDE (Salerno, 2024). We adopted and modified codes from GitHub (https://github.com/eloquentarduino/EloquentEsp32cam). We further modify the FOMO example from the library to detect and save the images to the SD card. To reiterate a previous point, we cannot use an optimized quantized model due to the incompatibility with the Eloquent Arduino library.

The concluding phase involved executing the model on the ESP32 CAM to ascertain its operational efficacy. The code was transferred to the ESP32 CAM through a connection to a laptop utilizing the ESP32-CAM-MB programmer alongside the Arduino Integrated Development Environment (IDE). Subsequently, the camera was deployed in the field for empirical evaluation. The comprehensive code can be accessed at https://github.com/nroselnik/ESP32CAM-for-detecting-rats-and-squirrels.

Field Experiment

The experiment was conducted at the Eco Hub in Universiti Sains Malaysia. An ESP32 CAM and a Hawkray trail camera were deployed at the research location (Figure 1). Both devices were positioned at ground level with the lenses aimed towards a tree. Bananas

were distributed around the tree to serve as baits that attract small mammals. Given that the primary objective of this project is to assess the efficacy of the ESP32 CAM in detecting small mammals and capturing their images, the use of bait to lure the animals does not compromise the integrity of the study. The experiment was conducted over three distinct days to procure three replicates of the dataset. The cameras were operated continuously for 24 hours during each experimental session and were subsequently retrieved to transfer the images to a laptop. This procedure ensured that the cameras functioned effectively during deployment and helped conserve the memory capacity of the SD card, thereby preventing operational interruption due to full storage, which could impede the experiment's advancement. After the images were transferred to a laptop, we compared the ESP32 CAM and the Hawkray Digital Camera.

Data Analysis

In relation to the first research question, we compared the confusion matrix of Model A and Model B to find the best implementation model. This comparison assessed the difference in the accuracy of the developed models utilizing training images sourced from the Google Images Repository and from local field photographs captured by a camera trap at the identical location. Additionally, the analysis was done on the feature explorers shown by Edge Impulse for each model.

The captured images taken from both cameras were compared to address the second and third research questions. As ESP32 CAM does not come with an infrared (IR) sensor and is therefore incapable of detecting heat signatures, it depends solely on the machine learning model for image capture, only when the object of interest, a small mammal, enters the frame and is detected. As a result, the effectiveness of the ESP32-CAM in detecting small mammals is entirely dependent on the accuracy and performance of the machine learning-based detection algorithm. From the comparison with the Hawkray Trail Camera, which has an IR sensor, we can determine the effectiveness and performance of the detection model implemented in ESP32 CAM. The assessment relies on how many small mammals were accurately detected, as well as those incorrectly detected. Four classification metrics are involved in building a confusion matrix table:

- True Positive (TP): A small mammal appears, and an image is captured.
- False Positive (FP): A small mammal did not appear, yet an image was captured.
- True Negative (TN): Anything other than the small mammal appears, and no image is captured.
- False Negative (FN): A target small mammal appears, but the camera does not capture the image.

A chi-squared (Goodness of Fit) test was conducted to evaluate the differences between these cameras. The Significance level was set at 0.05. We calculated the Precision, Recall

and F1 values. The formulas for each metric are outlined as Equations 1, 2, and 3 (Chicco & Jurman, 2020).

$$Precision = \frac{True\ Positives}{True\ Positives + False\ Positives} \quad [1]$$

$$Recall = \frac{True\ Positives}{True\ Positives + False\ Negatives} \quad [2]$$

$$F1\ Score = 2 \times \frac{Precision \times Recall}{Precision + Recall} \quad [3]$$

RESULTS

Accuracies of Model A and Model B

Figures 10 and 11 show the Feature Explorer results for both models. In Model A, the features derived from labelled images of squirrels and rats exhibit a considerable degree of overlap. Conversely, for Model B, the features extracted from labelled squirrel images are distinctly separated from those of labelled rat images, exhibiting minimal overlap.

The Feature Explorer is automatically generated in Edge Impulse and represents a visualization of the extracted features from the training data. This is typically a pre-training step designed to give users an overview of how well the features separate the different classes in the feature space. At this stage, the model is not yet trained. The scatter plot is purely a visualization of the data in the feature space based on the extracted features (e.g., spectral, time-domain, or other custom features). The axes do not have predefined labels in this specific case because they are automatically generated based on dimensionality reduction techniques, such as principal component analysis (PCA) or t-distributed stochastic neighbor embedding (t-SNE). These techniques transform the high-dimensional feature space into two dimensions for visualization purposes, aiming to capture the maximum variance or class separability. As a result, the axes do not correspond directly to specific physical variables but instead represent combinations of features that best illustrate the class distributions in the dataset. It helps users assess whether the features are sufficiently discriminative for classification tasks before moving forward with model training.

The accuracy of the object detection model between two distinct image sources (the Google Images Repository and the camera trap) was compared. The confusion matrix in Edge Impulse offers valuable insights into the efficacy of the object detection model by comparing the predicted class and the actual class detected. Tables 1 and 2 illustrate the F1 score (based on the Validation dataset) and confusion matrix produced by Edge Impulse for Model A and Model B, respectively. The rows represent the predicted class, and the actual labels are the columns.

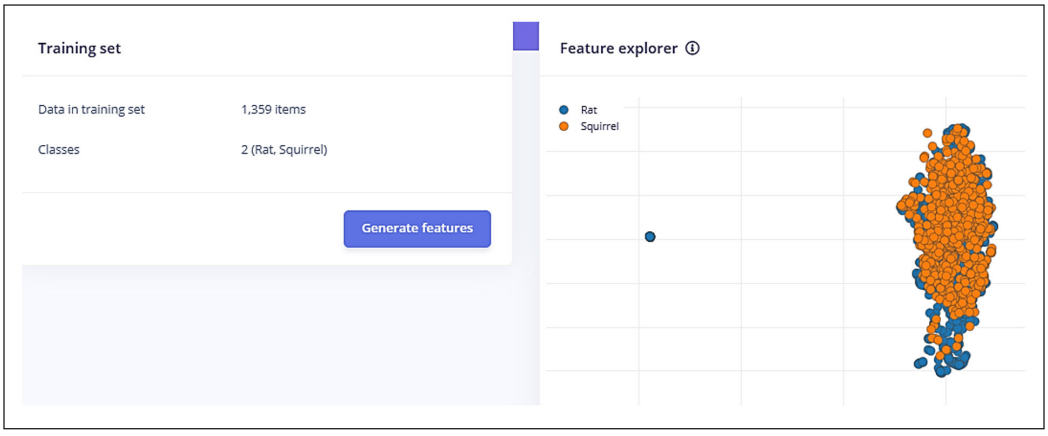

Figure 10. Training set and feature explorer of Model A in Edge Impulse

Figure 11. Training set and feature explorer of Model B in Edge Impulse

The matrix illustrates the number of instances that were inaccurately categorized. The F1 score serves as a metric to evaluate the efficacy of the predictive models. The F1 score attains its optimal value of 1, indicating perfect precision and recall, and its minimal value of 0.

The first table represents the performance of model A with an F1 score of 61.5%. The results indicate that the model performed exceptionally well in classifying the "Background" class, with 99.4% of the instances correctly identified and only 0.3% misclassified as either "rat" or "squirrel." This is further supported by the perfect F1 score of 1.00 for the "background" class, highlighting the model's reliability in detecting this class. For the "rat" class, the model correctly classified 58.7% of instances; however, a significant portion, 41.3%, was misclassified as "background," and no "rat" instances were

Table 1
F1 score and confusion matrix of Model A obtained from Edge Impulse

F1 Score 61.5%	Background	Rat	Squirrel
Background	99.4%	0.3%	0.3%
Rat	41.3%	58.7%	0%
Squirrel	18.4%	0%	81.6%
F1 Score	1.00	0.59	0.65

Table 2
F1 score and confusion matrix of Model B obtained from Edge Impulse

F1 Score 83.3%	Background	Rat	Squirrel
Background	100.0%	0%	0%
Rat	0%	100%	0%
Squirrel	31.4%	0%	68.6%
F1 Score	1.00	1.00	0.80

misclassified as "squirrel." This resulted in a lower F1 score of 0.59, reflecting challenges distinguishing the "rat" class, particularly due to confusion with "background." The "squirrel" class performed slightly better, with 81.6% of instances accurately identified, though 18.4% were also misclassified as "background." The F1 score for "squirrel" was 0.65, indicating moderate performance but room for improvement, especially in addressing the misclassification with "background."

The second table reflects the performance of Model B with an F1 score of 83.3%. In this iteration, the model achieved perfect classification for the "background" and "rat" classes, with 100% of instances correctly identified and without misclassifications. The F1 scores for both classes were 1.00, signifying excellent performance. For the "squirrel" class, the model correctly classified 68.6% of instances, an improvement over the first model. However, 31.4% of "squirrel" instances were still misclassified as "background," indicating that some challenges remain in distinguishing this class. Despite this, the F1 score for "squirrel" improved to 0.80, demonstrating a better balance between precision and recall compared to the first model.

Performance of ESP32 CAM

Hawkray Digital Trail Camera recorded 123 images, whereas the ESP32 CAM shows 117 images. Table 3 shows the number of images documented by each camera. Some of the images captured by both cameras are shown in Figures 12 and 13, with the small mammals circled in red.

The efficacy of the ESP32 CAM was systematically assessed. As the ESP32-CAM lacks night vision capabilities, it could not be evaluated for its effectiveness in detecting

nocturnal animals. Consequently, rats and bats were excluded from the results. Instead, the evaluation was exclusively conducted utilizing images depicting squirrels, as they were the only small mammals detected by the Hawkray camera and the ESP32-CAM during daylight. Table 4 shows the quantitative classification metrics. In this study, true positives refer to instances where the ESP32-CAM successfully captured images of squirrels that were also recorded by the Hawkray camera, which can be calculated as *29+51+18 = 98*. False positives occur when the ESP32-CAM captures images in the absence of squirrels,

Table 3
Number of images captured by Hawkray digital trail camera and ESP32 CAM in the 3 experiment days

Experiment Day	Hawkray digital trail camera	ESP32 CAM
1	30 images of squirrels 10 images of rats (night) 2 images of bats (night) 1 image of chicken	29 images of squirrels
2	54 images of squirrels	51 images of squirrels 15 blank images
3	24 images of squirrels 2 images of rats (night)	18 images of squirrels 4 blank images
Total	123 images	117 images

Figure 12. Images captured by ESP32 CAM showing the squirrel's appearance (red circle) in poor resolution (480 × 320 pixels)

Figure 13. Images captured by Hawkray trail camera showing the squirrel's appearance (red circle) in high resolution (1920 × 1080 pixels)

resulting in blank images. The total number of false positives is calculated as *15+4 = 19*. True negatives represent cases where non-small mammal species were present, and the ESP32-CAM was not triggered. This is evident from the Hawkray camera capturing an image of a chicken, while the ESP32-CAM did not, leading to 1 true negative instance. Bats and rats observed at night were excluded from this calculation, as the ESP32-CAM lacks night vision, rendering nighttime data invalid. False negatives occur when small mammals are present and captured by the Hawkray camera but are missed by the ESP32-CAM. This is determined by the difference between the number of squirrel images recorded by Hawkray and missed by the ESP32-CAM, calculated as *(30 - 29)+(54 - 51)+(24 - 18) = 10*. Based on the classification metrics in Table 4, the precision metric for the ESP32 CAM in the detection of squirrels is manually calculated as 0.84, while the calculated Recall metric is 0.91, and the F1 score is 0.87.

Figure 14 presents a comparative analysis of the ESP32 CAM and the Camera Trap regarding the quantity of squirrel images obtained. In general, the ESP32 CAM recorded a lower number of squirrel images than the Camera Trap. The difference in the quantity of captured squirrel images ranges from 1 to 6.

Table 4
Classification metrics of squirrel images captured by ESP32 CAM

	True Positive	**False Positive**	**True Negative**	**False Negative**
Number of squirrel images captured by ESP32 CAM	98	19	1	10

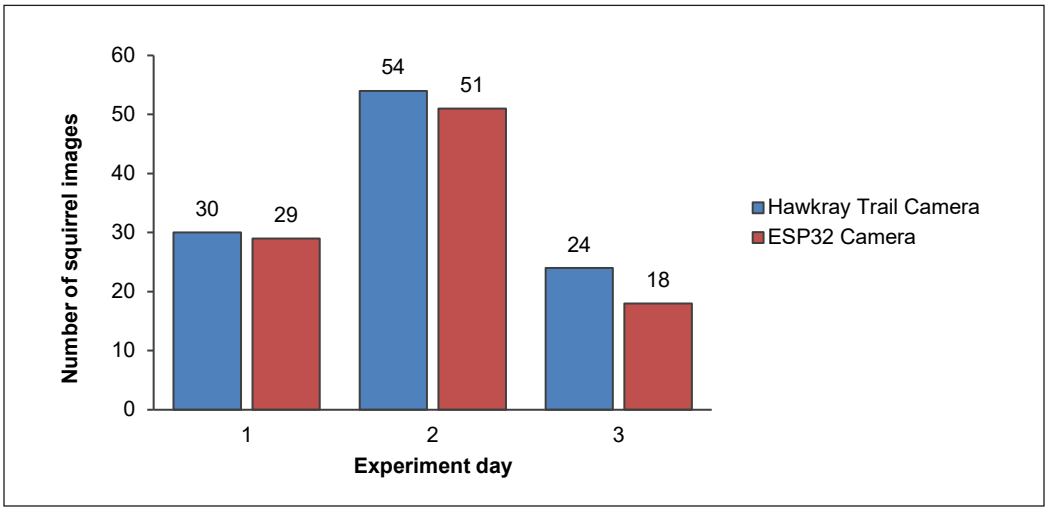

Figure 14. The number of squirrel images captured by the camera trap and ESP32 CAM

For the Chi-Square Goodness of Fit test, we used the number of images from the ESP32 CAM as the observed frequency and the number from the Hawkray Digital trail camera as the expected frequency. The results indicate no significant difference in the number of squirrel images obtained from the ESP32 CAM compared to those from the Hawkray trail camera, with X^2 (1, N = 98) = 0.853, p = 0.653.

DISCUSSION

Background Consistency and Object Size

From the findings, it is evident that, although both modeling frameworks attained an overall F1 score exceeding 50%, Model B, which utilized camera trap imagery, exhibited a superior F1 score and demonstrated heightened accuracy in the identification of small mammalian species in comparison to Model A, which relied on training images sourced from the Google repository. This discrepancy may be attributed to several variables, including the uniformity of the backgrounds in the images as well as the dimensions of the objects depicted therein. The images procured from the Google repository are characterized by diverse backgrounds, having been captured across a range of landscapes including arboreal canopies, forest undergrowth, and residential perimeters, employing various devices such as camera traps, mobile phone cameras, or professional-grade cameras, and in some instances, through artificial means utilizing artificial intelligence. This phenomenon is referred to as capture bias, as outlined by Tommasi et al. (2017). For example, the image background may occasionally be replete with dense vegetation or alternatively, be rendered plain or intentionally blurred to emphasize the animal's presence within the images (Figure 7). Such uncontrolled variables contribute to the inconsistency in the photographic backgrounds,

thereby introducing noise during the training process, which complicates the ability of machine learning algorithms to accurately discern the features of the target objects, namely squirrels and rats (Xiao et al., 2020).

A study conducted by Fadzly et al. (2021) posited that machine learning systems can misinterpret the image backgrounds as salient characteristics of the objects being analyzed. Conversely, the camera trap photographs captured at a singular field site generally exhibit a more consistent background (Figure 8) as the camera is oriented towards the same natural scenery, barring any human interventions or disturbances from wildlife. The homogeneity of the backgrounds in the camera trap photographs facilitates the machine learning model's capability to detect any anomalous activities or movements within the images, allowing it to visualize features that correspond with the morphological characteristics of squirrels and rats while disregarding any extraneous background components that are frequently present, such as foliage, vegetation, and fallen leaves (Nielsen et al., 2023; Wong & Fadzly, 2022).

The dimensions of objects and their angular representation in visual data are pivotal elements that affect the precision of the model (Feng & Lu, 2023; Sun et al., 2023). Figure 8 demonstrates the characteristics derived for squirrels and rats from online imagery in Model A, which exhibited significant overlap. This indicates that the Google Image Database model is inefficient in distinguishing squirrels and rats. The existence of overlapping characteristics may present difficulties in accurately differentiating between closely related species or in identifying individuals within intricate backgrounds.

The variability in the sizes of the squirrels and rats might be due to the differences in the focus areas. Some are too far, too close, or at a varied angle. This invariably confuses the model about the actual size of the trained/detected animals (Sun et al., 2023). This misinterpretation could fail to detect the object and the erroneous identification of non-relevant objects, compromising the model's accuracy in identifying the intended targets (Feng & Lu, 2023). In Model B, the features derived from the field photographs exhibit greater distinctiveness and separation (Figure 11). This might be due to the fixed angle, distance, and similar background. The uniformity in the size of the objects facilitates the model's capability to achieve a heightened level of precision in recognizing unique attributes of the small mammals, which is imperative for accurate species identification. Upon examination of both models, the images from the camera trap show that the object (rats/squirrels) is detected at nearly the same place each time. Squirrels are mostly in front of the tree trunk, and rats are mostly on the ground level. This consistency in the training datasets helps the model output compare between the object and background (Hao et al., 2022; Schneider et al., 2020; Xiao et al., 2020). Incorporating an additional step of collecting local background images from the study site is expected to improve model performance, since the similarity in the background has a profound effect on the model's effectiveness (Dujon & Schofield, 2019). This step would benefit the model rather than solely relying on

web-mined images, as it ensures better adaptation to the specific environmental conditions of the study area. It is crucial to consider these parameters in the formulation of training datasets prior to their application within a model, thereby facilitating the reduction of object detection inaccuracies and the optimization of its overall accuracy.

Application of TinyML in ESP32 CAM

The utilization of TinyML for the integration of object detection models within the ESP32 CAM framework is indeed feasible (Gotthard & Broström, 2023; Panda et al., 2022; Rahim & Zainal, 2024; Raiaan et al., 2023). These recent studies highlight the effectiveness of using ESP32 CAM for wildlife monitoring such as monkeys, dogs, rhinoceros and many other large endangered species. An analysis of the outcomes reveals that the camera successfully adhered to the algorithmic instructions by capturing images exclusively when small mammals were detected, while disregarding extraneous stimuli from alternative animal species. Results have shown no statistically significant differences in the frequency of squirrel detections for the two devices under consideration, namely the Hawkray trail camera and the ESP32 CAM. Nevertheless, the constraints imposed by the restricted quantity of training datasets may contribute to potential inaccuracies in the model's performance (Schneider et al., 2020) when implemented on the ESP32 CAM. The occurrence of blank images captured by the device could potentially be attributed to the misidentification of fallen leaves as small mammals. Despite its inability to detect certain instances of squirrels in comparison to the Hawkray trail camera, the findings substantiate the feasibility of employing TinyML within ESP32 CAM.

This is evidenced by the higher number of true positives compared to false positives and false negatives. The majority of research (Bagchi et al., 2022; Das & Halder, 2024; Kadhim et al., 2023) has predominantly investigated the application of ESP32 CAM for facial recognition systems, with a limited number of studies exploring its use in wildlife detection systems (Linder & Olsson, 2022). This disparity may stem from the wildlife detection model's exigency for a substantial and heterogeneous training dataset to attain a high level of accuracy in the automatic identification of various animal classes. Such extensive training requirements are likely impractical for most ecological research (Schneider et al., 2020). The more animal class is introduced in the algorithm, the more taxing it is for the system to perform. However, this investigation concentrated solely on a single group of animals, specifically small mammals, and was limited to only squirrels and rats. This targeted approach mitigates the necessity for a large training dataset. It facilitates the model's ability to learn from a more modest dataset, thereby achieving satisfactory accuracy in detecting squirrels. Given that TinyML is specifically engineered for operation under low power constraints, it is congruent with the ESP32 CAM, which is characterized by low power consumption and limited processing capabilities.

Furthermore, implementing TinyML in the ESP32 CAM demonstrated the usability of local on-device processing, minimizing processing costs (Schizas et al., 2022). A majority of online platforms, including AIDE, MegaDetector, and Wildlife Insights (Ahumada et al., 2020; Beery et al., 2019; Kellenberger et al., 2020), require the images to be uploaded before comparing the blank images and identifying the animals depicted in them. Through the mechanism of local processing, the camera is activated solely upon the presence of the selected species. Therefore, there would be no need to transfer and upload images for model learning first. This advancement holds significant potential for the prolonged deployment of cameras in remote regions that pose logistical challenges for accessibility. Future studies focused on population dynamics and the monitoring of animal species may greatly benefit from applying TinyML in compact devices such as the ESP32 CAM.

Limitations of ESP32 CAM

During the investigation, several limitations inherent to the ESP32 CAM were identified. In contrast to commercially available camera traps, the ESP32 CAM lacks an infrared sensor. An infrared sensor is a crucial component typically integrated into camera traps, utilized to detect IR or thermal signals from objects (Trolliet et al., 2014). These IR sensors help the camera to continue working even at night. ESP32 CAM lacks an IR sensor and relies only on environmental lighting (although this could be attached separately via the GPIO pins). This constraint renders the device impractical during nocturnal hours, as it is incapable of detecting any movement in complete darkness. Consequently, this represents the primary rationale for the inability to conduct rat detection using the ESP32 CAM in this study, given that the module lacks infrared technology or night vision capabilities, and considering that rats are predominantly nocturnal foragers. Researchers engaged in monitoring nocturnal fauna are advised to utilize an ESP32 CAM module equipped with an integrated infrared sensor.

Moreover, the image quality or resolution of the ESP32 CAM is suboptimal compared to that of the Hawkray trail camera. The ESP32 CAM is characterized by a 480 x 320 pixels resolution, whereas the Hawkray trail camera boasts a 1920 x 1080 pixels resolution. Pixels constitute the fundamental units that denote a singular point of color or grayscale, collectively forming a digital image. A higher pixel count correlates with enhanced detail within an image, thereby yielding superior image quality (Wong & Fadzly, 2022). The low resolution of the images from the ESP32 CAM results in a lack of clarity and detail, producing images that are often indistinct (Figure 12).

In contrast, the Hawkray trail camera, with its elevated resolution, generates notably sharper images, thereby offering a more detailed representation of squirrels (Figure 13). The ESP32 CAM is equipped with a diminutive and rudimentary camera lens, the OV2640, which possesses a restricted field of view in comparison to the high-performance lenses

employed by commercial camera traps. This rudimentary lens significantly constrains the capability of the ESP32 CAM to deliver images of satisfactory quality. While the ESP32 CAM may serve effectively for the singular purpose of wildlife detection, alerting the owner to the presence of wildlife, it is not an appropriate instrument for studies focused on characterizing or recognizing individual wildlife due to its inherent limitations in image resolution.

Another constraint of the ESP32 CAM pertains to its detection range. The fundamental camera integrated within the ESP32 CAM exhibits a restricted object detection distance of merely 4 meters, as highlighted in the research conducted by Budiharto et al. (2022). This signifies that only fauna that come within 4 meters of the camera will be quantified and detected by the ESP32 CAM. Fauna situated beyond this specified distance will remain undetected by the camera, culminating in a lost opportunity to ascertain the species and document the characteristics of the animal. Furthermore, the restricted detection range results in a limited coverage area for the camera. This limitation may present substantial challenges if the research site encompasses a large spatial area that a singular ESP32 CAM is incapable of adequately monitoring. The device may also necessitate strategic placement and orientation near locations where animals are likely to approach closely to enhance its detection efficacy and mitigate false negatives (the failure to detect wildlife).

Although this study highlights some of the weaknesses of ESP32 CAM, we have to point out that the original idea of detecting specific target animals using the module is feasible. Furthermore, ESP32 CAM is an open-source design, and additional electronics can be added through its GPIO pins. Sensors such as temperature, humidity, and a real-time clock (RTC) can be added to the module. The OV2640 camera that comes standard with the module can also be replaced with the OV5640, which is 5 Megapixels in quality. An IR LED can be soldered (replacing the normal LED on the board) to help in low-light conditions. However, this will invariably cause an increase in the budget for developing the camera as we aim for a device costing less than MYR50 (excluding the batteries). Our team works on several other microcontroller boards, such as the SeeedStudio Xiao series. Further development concerning these new microcontrollers is still in progress.

CONCLUSION

Although the ESP32 CAM demonstrates efficacy in identifying small mammals through an algorithm developed by Edge Impulse, it has constraints, such as a limited field of view, low-resolution images, and an absence of infrared capabilities necessary for nocturnal operations. For the training of the detection model, employing field photographs taken from the identical location is likely to yield superior accuracy in comparison to images sourced through web mining (e.g., Google image repositories). Despite successfully demonstrating the ESP32 CAM's potential as a machine-learning wildlife monitoring device, we have

some recommendations to enhance the study. Firstly, the volume of the training dataset could be augmented by acquiring a greater number of field photographs in advance. An expanded dataset could significantly enhance the model's efficacy (Shahinfar et al., 2020). Secondly, more focus could be directed at the different Learner AI models, such as YOLO v9 or FOMO. Enhancing the model's accuracy and performance may require adopting an advanced machine learning platform that offers superior processing capabilities. Thirdly, integrating infrared technology into the ESP32 CAM would enable its functionality in low-light conditions. Future research should optimize the ESP32 CAM as an AI-assisted Wildlife camera to detect additional wildlife species, thereby contributing to conservation and research initiatives.

ACKNOWLEDGEMENTS

This project is supported by R503-KR-FRG001-0006712190-K134, FRGS Malaysia Grant. We thank the EcoHub and the Biological Sciences School for their support and help.

REFERENCES

Ahumada, J. A., Fegraus, E., Birch, T., Flores, N., Kays, R., O'Brien, T. G., Palmer, J., Schuttler, S., Zhao, J. Y., Jetz, W., Kinnaird, M., Kulkarni, S., Lyet, A., Thau, D., Duong, M., Oliver, R., & Dancer, A. (2020). Wildlife insights: A platform to maximize the potential of camera trap and other passive sensor wildlife data for the planet. *Environmental Conservation, 47*(1), 1–6. https://doi.org/10.1017/S0376892919000298

Bagchi, T., Mahapatra, A., Yadav, D., Mishra, D., Pandey, A., Chandrasekhar, P., & Kumar, A. (2022). Intelligent security system based on face recognition and IoT. *Materials Today: Proceedings*, *62*(4), 2133-2137. https://doi.org/10.1016/j.matpr.2022.03.353

Baharudin, N. S., Tah, M. M. T. M., Zulkifli, S. Z., Ghani, N. I. A., Noor, H. M., & Sabar Sabal, N. H. (2023). Species diversity and distribution of non-volant small mammal between restoration, boundary, disturbed and undisturbed area in Cameron Highlands, Malaysia. *Tropical Life Sciences Research*, *34*(1), 151–183. https://doi.org/10.21315/tlsr2023.34.1.10

Beery, S., Morris, D., & Yang, S. (2019). Efficient pipeline for camera trap image review. *arXiv preprint arXiv.1907.06772*. https://doi.org/10.48550/arXiv.1907.06772

Bird, J. P., Fuller, R. A., Pascoe, P. P., & Shaw, J. D. S. (2022). Trialling camera traps to determine occupancy and breeding in burrowing seabirds. *Remote Sensing in Ecology and Conservation, 8(*2), 180-190. https://doi.org/10.1002/rse2.235

Blount, J. D., Chynoweth, M. W., Green, A. M., & Sekercioglu, C. H. (2021). Review: COVID-19 highlights the importance of camera traps for wildlife conservation research and management. *Biological Conservation, 256*, Article 108984. https://doi.org/10.1016/j.biocon.2021.108984

Budiharto, W., Irwansyah, E., Suroso, J. S., & Gunawan, A. A. S. (2022). Low-cost vision-based face recognition using Esp32-Cam for tracked robot. *ICIC Express Letters*, *13*(3), 321–327. https://doi.org/10.24507/icicelb.13.03.321

Chicco, D., & Jurman, G. (2020). The advantages of the Matthews correlation coefficient (MCC) over F1 score and accuracy in binary classification evaluation. *BMC Genomics 21*, Article 6. https://doi.org/10.1186/s12864-019-6413-7

Das, B., & Halder, K. K. (2024). Face recognition using ESP32-Cam for real-time tracking and monitoring. In *2024 International Conference on Advances in Computing, Communication, Electrical, and Smart Systems (iCACCESS)* (pp. 01-06). IEEE Publishing. https://doi.org/10.1109/iCACCESS61735.2024.10499606

Das, S., Dey, A., Pal, A., & Roy, N. (2015). Applications of artificial intelligence in machine learning: Review and prospect. *International Journal of Computer Applications*, *115*(9), 31-41. https://doi.org/10.5120/20182-2402

Disabato, S., & Roveri, M. (2022). Tiny machine learning for concept drift. *IEEE Transactions on Neural Networks and Learning Systems, 35*(6), 8470-8481. https://doi.org/10.1109/TNNLS.2022.3229897

Dujon, A. M., & Schofield, G. (2019). Importance of machine learning for enhancing ecological studies using information-rich imagery. *Endangered Species Research, 39*, 91-104. https://doi.org/10.3354/esr00958

Elhattab, K., Abouelmehdi, K., & Elatar, S. (2023). New model to monitor plant growth remotely using ESP32-CAM and mobile application. In *2023 10th International Conference on Wireless Networks and Mobile Communications (WINCOM)* (pp. 1-6). IEEE Publishing. https://doi.org/10.1109/WINCOM59760.2023.10322939

Fadzly, N., Zuharah, W. F., & Wong, J. J. N. (2021). Can plants fool artificial intelligence? Using machine learning to compare between bee orchids and bees. *Plant Signaling & Behavior, 16*(10), Article 1935605. https://doi.org/10.1080/15592324.2021.1935605

Feng, S., & Lu, J. (2023). Research on image recognition based on neural network model learning algorithm. In *2023 4th International Conference on Computer Vision, Image and Deep Learning (CVIDL)* (pp. 21-24). IEEE Publishing. https://doi.org/10.1109/CVIDL58838.2023.10164845

Fernandes, A. C. M., Gonzalez, R. Q., Lenihan-Clarke, M. A., Trotter, E. F. L., & Arsanjani, J. J. (2020). Machine learning for conservation planning in a changing climate. *Sustainability*, *12*(18), Article 7657. https://doi.org/10.3390/su12187657

Gomes, V., Ribeiro, R., & Carretero, M. A. (2011). Effects of urban habitat fragmentation on common small mammals: Species versus communities. *Biodiversity and Conservation*, *20*, 3577–3590. https://doi.org/10.1007/s10531-011-0149-2

Gotthard, R., & Broström, M. (2023). *Edge machine learning for wildlife conservation – A part of the Ngulia Project* [Master thesis, Linköping University]. Linköping University Electronic Press. https://www.diva-portal.org/smash/record.jsf?pid=diva2%3A1788498&dswid=7533

Hao, Y., Pei, H., Lyu, Y., Yuan, Z., Rizzo, J., Wang, Y., & Fang, Y. (2022). Understanding the impact of image quality and distance of objects to object detection performance. In *2023 IEEE/RSJ International Conference on Intelligent Robots and Systems (IROS)* (pp. 11436-11442). IEEE Publishing. https://doi.org/10.48550/arXiv.2209.08237

Johnstone, C. P., Lill, A., & Reina, R. D. (2014). Habitat loss, fragmentation and degradation effects on small mammals: Analysis with conditional inference tree statistical modelling. *Biological Conservation, 176*, 80-98. https://doi.org/10.1016/j.biocon.2014.04.025

Kadhim, T. A., Hariri, W., Zghal, N. S., & Aissa, D. B. (2023). A face recognition application for Alzheimer's patients using ESP32-CAM and Raspberry Pi. *Journal of Real-Time Image Processing, 20*, Article 100. https://doi.org/10.1007/s11554-023-01357-w

Kellenberger, B., Tuia, D., & Morris, D. (2020). AIDE: Accelerating image-based ecological surveys with interactive machine learning. *Methods in Ecology and Evolution, 11*(12), 1716–1727. https://doi.org/10.1111/2041-210X.13489

Linder, J., & Olsson, O. (2022). *A smart surveillance system using edge-devices for wildlife preservation in animal sanctuaries* [Master dissertation, Linköping University]. Linköping University Diva-Portal. https://urn.kb.se/resolve?urn=urn:nbn:se:liu:diva-186261

Nielsen, I. E., Grundeland, E., Snedeker, J., Rasool, G., & Ramachandran, R. P. (2023). Targeted background removal creates interpretable feature visualizations. *arXiv preprint arXiv.2306.13178*. https://doi.org/10.48550/arXiv.2306.13178

Palmeirim, A. F., Santos-Filho, M., & Peres, C. A. (2020). Marked decline in forest dependent small mammals following habitat loss and fragmentation in an Amazonian deforestation frontier. *PLOS One, 15*(3), Article e0230209. https://doi.org/10.1371/journal.pone.0230209

Panda, P. K., Kumar, C. S., Vivek, B. S., Balachandra, M., & Dargar, S. K. (2022). Implementation of a wild animal intrusion detection model based on internet of things. In *2022 Second International Conference on Artificial Intelligence and Smart Energy (ICAIS)* (pp. 1256-1261). IEEE Publishing. https://doi.org/10.1109/ICAIS53314.2022.9742948

Rahim, A. M. A., & Zainal, M. S. (2024). An IoT based monkey deterrent for plantations with surveillance system: A method for damage control done by monkeys in plantations. *Progress in Engineering Application and Technology*, *5*(1), 114-121.

Rai, P., & Rehman, M. (2019). ESP32 based smart surveillance system. In *2019 2nd International Conference on Computing, Mathematics and Engineering Technologies (iCoMET)* (pp. 1-3). IEEE Publishing. https://doi.org/10.1109/ICOMET.2019.8673463

Raiaan, M. A. K., Fahad, N. M., Chowdhury, S., Sutradhar, D., Mihad, S. S., & Islam, M. M. (2023). IoT-based object-detection system to safeguard endangered animals and bolster agricultural farm security. *Future Internet*, *15*(12), Article 372. https://doi.org/10.3390/fi15120372

Ray, P. P. (2022). A review on TinyML: State-of-the-art and prospects. *Journal of King Saud University-Computer and Information Sciences*, *34*(4), 1595-1623. https://doi.org/10.1016/j.jksuci.2021.11.019

Salerno, S. (2024). *EloquentEsp32cam* (Version 2.6.0). https://www.arduino.cc/reference/en/libraries/eloquentesp32cam/

Schizas, N., Karras, A., Karras, C., & Sioutas, S. (2022) TinyML for ultra-low power AI and large scale IoT deployments: A systematic review. *Future Internet*, *14*(12), Article 363. https://doi.org/10.3390/fi14120363

Schneider, S., Greenberg, S., Taylor, G. W., & Kremer, S. C. (2020). Three critical factors affecting automated image species recognition performance for camera traps. *Ecology and Evolution, 10*(7), 3503–3517. https://doi.org/10.1002/ece3.6147

Shahinfar, S., Meek, P. D., & Falzon, G. (2020). "How many images do I need?" Understanding how sample size per class affects deep learning model performance metrics for balanced designs in autonomous wildlife monitoring. *Ecological Informatics, 57*, Article 101085. https://doi.org/10.1016/j.ecoinf.2020.101085

Shivaprakash, K. N., Swami, N., Mysorekar, S., Arora, R., Gangadharan, A., Vohra, K., Jadeyegowda, M., & Kiesecker, J. M. (2020). Potential for artificial intelligence (AI) and machine learning (ML) applications in biodiversity conservation, managing forests, and related services in India. *Sustainability*, *14*(12), Article 7154. https://doi.org/10.3390/su14127154

Sreedhar, S., Sandesh, S., Prarthana, P., Karthik, P. N., Prabhanjan, S., & Srinidhi, K. (2021). A literature survey on wildlife camera trap image processing using machine learning techniques. *Perspectives in Communication, Embedded-systems and Signal-processing – Pices*, *5*(2), 11–14. https://doi.org/10.5281/zenodo.4902949

Sun, G., Wang, S., & Xie, J. (2023). An image object detection model based on mixed attention mechanism optimized YOLOv5. *Electronics, 12*(7), Article 1515. https://doi.org/10.3390/electronics12071515

Swann, D., & Perkins, N. (2014). Camera trapping for animal monitoring and management: A review of applications. In P. Meek & P. Fleming (Eds.), *Camera Trapping: Wildlife Management and Research* (pp. 3-12). CSIRO PUBLISHING. https://doi.org/10.1071/9781486300402

Szpunar, G., Aloise, G., Mazzotti, S., Nieder, L., & Cristaldi, M. (2008). Effects of global climate change on terrestrial small mammal communities in Italy. *Fresenius Environmental Bulletin*, *17*(9b), 1526-1533.

Tommasi, T., Patricia, N., Caputo, B., & Tuytelaars, T. (2017). A deeper look at dataset bias. In G. Csurka (Ed.), *Domain Adaptation in Computer Vision Applications* (pp. 37-55). Springer. https://doi.org/10.48550/arXiv.1505.01257

Trolliet, F., Vermeulen, C., Huynen, M. C., & Hambuckers, A. (2014). Use of camera traps for wildlife studies: A review. *Biotechnologie, Agronomie, Société et Environnement, 18*(3), 446-454.

Tuia, D., Kellenberger, B., Beery, S., Costelloe, B. R., Zuffi, S., Rissie, B., Mathis, A., Mathis, M. W., van Langevelde, F., Burghardt, T., Kays, R., Klinck, H., Wikelski, M., Couzin, I. D., van Horn, G., Crofoot, M. C., Stewart, C. V., & Berger-Wolf, T. (2022). Perspectives in machine learning for wildlife conservation. *Nature Communications*, *13*, Article 792. https://doi.org/10.1038/s41467-022-27980-y

Vinod, S., Shakor, P., Sartipi, F., & Karakouzian, M. (2023). Object detection using ESP32 CAMeras for quality control of steel components in manufacturing structures. *Arabian Journal for Science and Engineering*, *48*, 12741–12758. https://doi.org/10.1007/s13369-022-07562-2

Wong, J. J. N., & Fadzly, N. (2022). Development of species recognition models using Google teachable machine on shorebirds and waterbirds. *Journal of Taibah University for Science, 16*(1), 1096–1111. https://doi.org/10.1080/16583655.2022.2143627

Xiao, K., Engstrom, L., Ilyas, A., & Madry, A. (2020). Noise or signal: The role of image backgrounds in object recognition. *arXiv preprint arXiv:2006.09994*. https://doi.org/10.48550/arXiv.2006.09994

Zhu, C., Li, W., Gregory, T., Wang, D., Ren, P., Zeng, D., Kang, Y., Ding, P., & Si, X. (2022). Arboreal camera trapping: a reliable tool to monitor plant-frugivore interactions in the trees on large scales. *Remote Sensing in Ecology and Conservation, 8*(1), 92-104. https://doi.org/10.1002/rse2.232

Pertanika J. Sci. & Technol. 33 (4): 1809 - 1827 (2025)

PERTANIKA JOURNALS

SCIENCE & TECHNOLOGY

Journal homepage: http://www.pertanika.upm.edu.my/

Analysis and Simulation of Temperature Reduction and Cooling Rate in Precooling Process Using Compressive Force Plate Cooler

Surya Abdul Muttalib, Nursigit Bintoro*, Joko Nugroho Wahyu Karyadi and Arifin Dwi Saputro

Department of Agricultural Engineering and Biosystem, Gadjah Mada University, 55281 Yogyakarta, Indonesia

ABSTRACT

In the precooling process of meat and fish using flaked ice, the product temperature decreases slowly due to insufficient contact between the cooling medium and the product. This study aimed to analyze the effects of meat type and compressive force level on sample temperature and cooling rate, as well as to conduct simulations using Computational Fluid Dynamics (CFD). Three types of meat samples, namely chicken, beef, and tuna fillet, were examined under three levels of compressive force: 0 N (control), 980 N, and 1960 N. The results showed that compressive force, meat type, and interaction significantly influenced the cooling rate and final sample temperature ($p<0.05$). During the initial phase of the precooling process, the average cooling rate of chicken increased by 169.2% and 391.0% compared to the control under compressive forces of 980 N and 1960 N, respectively. Similarly, the cooling rate of beef increased by 113.1% and 268.3%, while that of fish increased by 60.7% and 274.2%. The final temperatures of chicken, beef, and fish samples decreased by 41.7% and 79.0%, 22.8% and 76.0%, and 56.8% and 85.7%, respectively, under compressive forces of 980 N and 1960 N compared to the control. CFD simulations accurately predicted the final sample temperature, with an average R^2 value of 0.82, *RMSE* of 0.28, and *MAPE* of 2.33%.

Keywords: CFD simulation, compressive force, meat type, precooling

ARTICLE INFO

Article history:
Received: 25 September 2024
Accepted: 17 March 2025
Published: 11 June 2025

DOI: https://doi.org/10.47836/pjst.33.4.06

E-mail addresses:
suryaabdul2020@mail.ugm.ac.id; surya15@unram.ac.id (Surya Abdul Muttalib)
nursigit@ugm.ac.id (Nursigit Bintoro)
jknugroho@ugm.ac.id (Joko Nugroho Wahyu Karyadi)
arifin_saputro@ugm.ac.id (Arifin Dwi Saputro)
* Corresponding author

INTRODUCTION

Animal products, especially meat and fish, have a high risk of damage due to high water content and easily damaged chemicals. Red meat contains 75% water, 20% protein, 5.2% fat and 1.5% carbohydrates (Darwish et al., 2024). Proteins and fats are easily deteriorated both physiologically and enzymatically. Meanwhile, high water

e-ISSN: 2231-8526

© Universiti Putra Malaysia Press

content increases the risk of the growth of microorganisms (Merai et al., 2019; Rahman, 2007; Wang, 2000). Consequently, these products must be preserved immediately after harvest or slaughter to prevent spoilage. If meat is continuously stored at high temperatures, spoilage accelerates, leading to a decline in quality during transportation and subsequent cold chain storage. It increases the risk of foodborne diseases and reduces the product's commercial value (Han, 2014; Merai et al., 2019; Zira et al., 2021). Preservation of meat by cooling should be carried out as quickly as possible after slaughter (Merai et al., 2019; Savell et al., 2005).

Precooling is crucial for meat and fish before cold storage, as it rapidly reduces the product temperature to the required storage condition. Precooling after slaughter has become an important operational part before meat enters the cold chain (Dal et al., 2021; Ren et al., 2023). If the carcass is put directly into the cold storage room after slaughter, without precooling first, the temperature of the carcass will not be able to drop quickly to the cold storage target temperature, namely 0–4°C (Bailey et al., 2000; Chakraborty et al., 2017; El-Aal & Suliman, 2008; Merai et al., 2019; Rahman, 2007; Wang, 2000; http://www.fsis.usda.gov/search). Precooling using ice in flake or slurry has long been practiced and is very commonly used in society because it is easy to do, cheap, and does not require complicated equipment. Several researchers have used ice for the cooling process of various types of products: Li et al. (2022) for fruit and vegetables, Valtýsdóttir et al. (2010) for fish, and Gao (2007) for cod fish. However, the temperature reduction or cooling rate speed by simply covering meat or fish with ice flakes will generally be slow. Therefore, the precooling process using ice as a cooling medium needs to be improved to reduce meat temperature or increase the cooling rate. Increasing the cooling rate in this precooling method can be done by tightening the contact between the cooling ice medium and the meat by applying an external compressive force to the cooling medium. Increasing the contact intensity will increase the heat transfer rate from the meat to the cooling medium due to increasing the total heat transfer coefficient and contact surface area.

Temperature is a critical parameter in relation to product spoilage. One indicator for detecting the quality of food ingredients is temperature history (Al-Mohaithef et al., 2021; Li et al., 2019; Riva et al., 2001; Skawińska & Zalewski, 2022; Tao et al., 2023; Wang et al, 2015). CFD can provide information on the temperature history of a material being studied (Awasthi et al., 2024; Chakraborty & Dash, 2023; Chauhan et al., 2019; Cruz et al., 2022; Grossi et al., 2024; Toparlar et al., 2019; Zhang et al., 2020). Therefore, applying CFD simulations to the precooling will be very useful in providing a more comprehensive understanding of the precooling process. This research aimed to analyze the effect of meat type and compressive force on the precooling process using a compressive plate-type cooling apparatus with crushed ice as the cooling medium. In this research, CFD simulations will also be carried out to predict the final temperature of the cooled samples.

MATERIALS AND METHODS

Materials

Three types of animal products were used as research samples: beef, chicken, and tuna fillet. These samples were purchased from local markets in Yogyakarta, Indonesia. The selected meat and fish samples were fresh, unblemished, and free from any off-putting odors, representing the typical condition of meat and fish available for sale. The beef sample was tenderloin, characterized by a firm texture, bright red color, and absence of any fishy smell. The chicken meat sample was breast meat, had a dense texture, bright color, and was still fresh. Meanwhile, the tuna fish samples were fresh fish fillets with firm flesh, red gills, bright eyes, and bright fish scales that had not been peeled off. Upon arrival at the laboratory, the three types of meat samples were sliced into square shapes with dimensions of 30 mm long, 30 mm wide, and 20 mm thick. Ice was used as the cooling medium in this research. This ice was purchased from the ice supplier of ASTRA Company in Sleman, Yogyakarta, Indonesia. The ice chunks were carefully crushed into small pieces with a size of around 5 mm.

Apparatus

Figure 1(a) shows the compressive plate-type precooling apparatus constructed in this study. The primary function of this apparatus was to provide measurable pressure to the sample being tested, whose construction was made of metal. The main component of this apparatus was a mechanical pressing equipment constructed of metal. The main function of this apparatus was to compress the ice-cooling medium above the meat sample with a 10 × 10 cm stainless steel compression plate. This plate could be moved back and forth vertically using an electric motor (DC 12V, 2A, 400 rpm, torque 6.5 kg/cm). The apparatus was equipped with electronic components to monitor the compressive force and temperature of the sample and cooling medium in real time. Four K-type thermocouple sensors (model TP-01) and a loadcell sensor (capacity 500 kg, voltage 10–15V DC) were used to monitor temperatures and compressive force, respectively. Other components were the Analog Digital Converter (ADC), ATM Mega Arduino uno microcontroller (ATmega328 SMD, 5V), HX711 driver, AD8495 driver, LCD, computer, and power supply (12V, 10A). A wooden container box was used to accommodate the samples and cooling medium. This container had a thickness of 1 cm, a square base measuring 12 cm per side, and a height of 17 cm.

Research Procedures

This research began by placing crushed ice as the cooling medium along with the meat or fish fillet samples into a wooden box container. The filling process was conducted

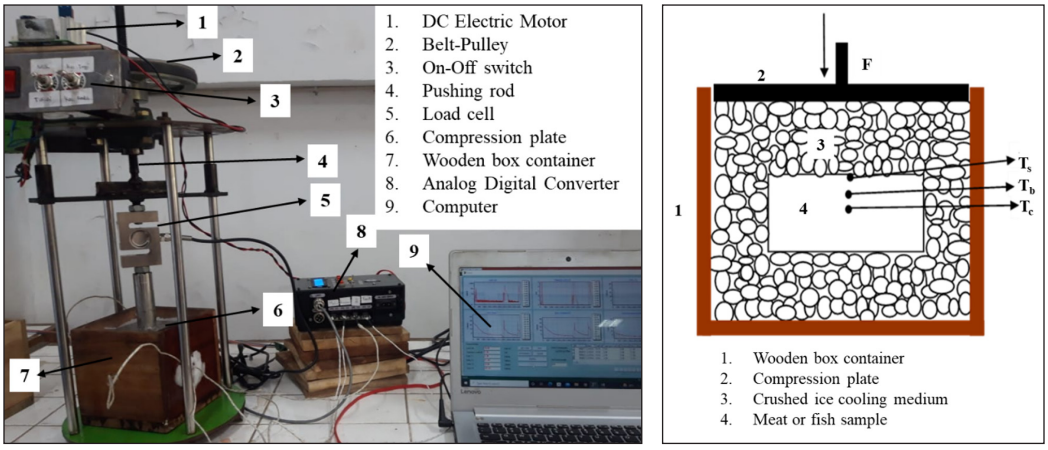

(a) (b)

Figure 1. (a) Compressive plate type precooling apparatus; and (b) schematic diagram of samples and crushed ice in the box during the precooling process

as follows: first, a 4 cm layer of crushed ice was placed at the bottom of the wooden box; next, the meat samples were positioned on top of the ice; finally, the box was filled with additional ice until it was completely full. Next, a stainless-steel compression plate was moved downward to press the cooling ice medium, as shown in Figure 1(b). The magnitude of compressive force could be adjusted according to the predetermined value by monitoring the displayed value on the computer screen. In this research, compressive forces were 0 (control), 980, and 1960 N (0, 100, and 200 kg) with a compression speed of 2 m/s. The compression would be stopped after those desired values were reached. Therefore, the meat samples were not continuously loaded with the specified compressive force during the cooling process so that the samples did not experience damage due to excessive pressure. At the same time as the force was applied to the ice, the meat sample and cooling medium temperatures were continuously monitored throughout the precooling process until the temperature of the sample being cooled reached a constant temperature. The temperature of the meat sample was measured at three positions: (1) at the center of the material (T_c), (2) at the position between the center and the surface of the material (T_b), (3) and the temperature at the surface of the material (T_s) using thermocouple sensor. Temperature data was measured every second during precooling and transferred to the computer through ADC.

Data Analysis

In this research, statistical analysis of variance (ANOVA) was used to analyze the data. The ANOVA model applied was a Completely Randomized Design (CRD), factorial 3 × 3, with three replications. The first factor was the type of meat: chicken, beef, and fish. In contrast,

the second factor was the level of compressive force applied during the precooling process, set at 0 N, 980 N, and 1960 N. Mean comparisons were evaluated using Duncan's Multiple Range Test (DMRT). According to Fiandini et al. (2023), the mean difference test was a useful tool to determine whether there were significant differences between two or more data groups. Apart from statistical analysis, simulations were also carried out to predict the final temperature of the meat sample at the three measured positions. The simulation used CFD by applying the finite element method, which was based on the natural fluid transfer of the Navier-Stokes Equation and the phenomenon of energy transfer. Fadiji et al. (2021) informed about the application of CFD in various research on freezing and thawing food products. The equations used in the CFD application program were the continuity (Equation 1), the momentum (Equation 2), and the energy (Equation 3).

$$\frac{\partial u_x}{\partial x} + \frac{\partial u_y}{\partial y} + \frac{\partial u_z}{\partial z} = 0 \quad [1]$$

$$\rho_g \frac{Dv}{Dt} = -\nabla p + \nabla \tau + \rho_g \, g \quad [2]$$

$$\frac{\partial T}{\partial t} + \mu_x \frac{\partial T}{\partial x} + \mu_y \frac{\partial T}{\partial y} + \mu_z \frac{\partial T}{\partial z} = \propto \left(\frac{\partial^2 T}{\partial x^2} + \frac{\partial^2 T}{\partial y^2} + \frac{\partial^2 T}{\partial z^2}\right) \quad [3]$$

Where u_x was the velocity in X (m/s), u_y was the velocity in Y (m/s), u_z was the velocity in Z (m/s), ρ_g was the density (kg/m^3), $\frac{Dv}{Dt}$ was derivative of volume (m^3/s), p was the pressure (Pa), μ_x was the kinematic viscosity in X (m^2/s), μ_y was the kinematic viscosity in Y (m^2/s), μ_z was the kinematic viscosity in Z (m^2/s), α was the thermal diffusivity (m^2/s), τ was the stress tensor (N/m^2), t was a time (s), g was gravitation (m/s^2), and T was the temperature (K).

Validation of simulation results was necessary to ensure that the data used and the selected model accurately represented the key aspects of the phenomenon being studied. In this research, the accuracy of simulation results in predicting measurement results was determined based on the coefficient of determination (R^2), root mean square error (*RMSE*), and mean average percentage errors (*MAPE*) calculated using Equations 4, 5, and 6, respectively.

$$R^2 = \frac{\Sigma(T_{i,obs} \; T_{i,pre})^2}{\Sigma(T_{i,obs})^2 \; \Sigma(T_{i,pre})^2} \quad [4]$$

$$RMSE = \left[\frac{1}{N}\sum_{i=1}^{N}(T_{i,obs} - T_{i,pre})^2\right]^{1/2} \quad [5]$$

$$MAPE = \sum_{i=1}^{N}\left|\frac{T_{i,obs} - T_{i,pre}}{T_{i,obs}}\right| \times 100\% \quad [6]$$

Where $T_{i,obs}$ was the measured temperature (K), $T_{i,pre}$ was the predicted temperature (K), and N was the number of data points.

RESULTS AND DISCUSSION

Cooling Rate

Figures 2, 3, and 4 show the temperature profiles of Tc, Tb, and Tc during the precooling process with the compressive force of 0, 980, and 1960 N for chicken, beef, and fish samples, respectively. It can be observed that the sample temperature consistently decreased throughout the precooling process, reaching an approximately constant temperature at around 600 seconds. The direct contact between the cooling medium and the sample surface caused the T_s value to drop more quickly. Generally, it reached a lower final temperature compared to T_b and T_c. Based on the temperature profiles, it could be observed that two patterns of temperature decrease appeared very different: (1) the initial period occurred when the compressive force began to be applied at the beginning of the precooling process until the drastic drop in sample temperature stopped at around 20 s, and (2) subsequent period, which occurred after the compressive force was stopped until the precooling process was completed. Li et al. (2022) provided an equation for calculating the cooling rate, and there was a ratio between the initial and final temperature difference and the precooling time. Therefore, based on the temperature profile of the sample, the cooling rate value could be calculated using Equations 7 and 8 for the cooling rate in the initial and subsequent periods, respectively.

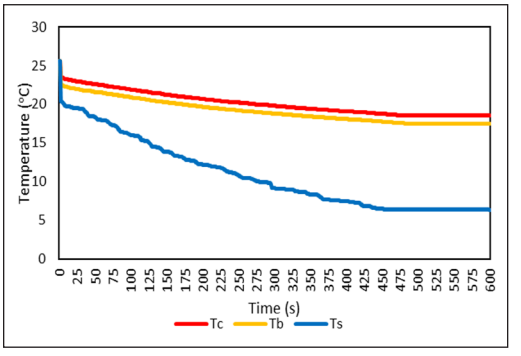

(a)

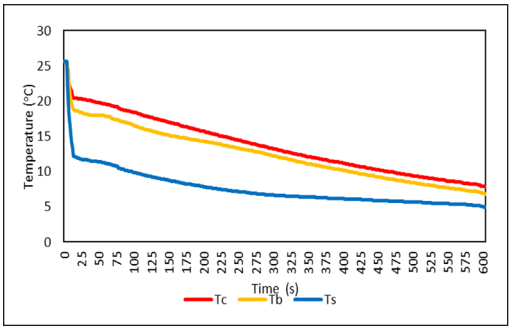

(b)

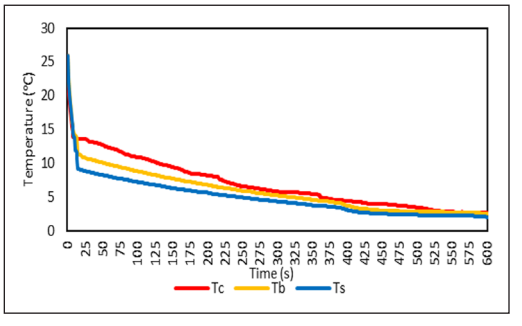

(c)

Figure 2. Temperature profile of T_c, T_b, and T_s in chicken meat samples: (a) without compressive force; (b) 980 N compressive force; and (c) 1960 N compressive force

$$CR_i = \frac{T_0 - T_i}{t_i - t_0} \quad [7]$$

$$CR_s = \frac{T_i - T_f}{t_f - t_i} \quad [8]$$

Where CR_i and CR_s were the cooling rates in the initial and subsequent periods, respectively (°C/s), T_o was the initial temperature of the material (°C), T_i was the temperature of the material at the end of the initial period (°C), T_f was the final temperature of the material when precooling was completed (°C), t_o was the initial time of the precooling process (s), t_i was the length of the initial period (s), and t_f was the length of the subsequent period (s).

Table 1 presents the cooling rate during the initial and subsequent periods and the overall average for the meat samples tested in this study. It is clearly observed that, during

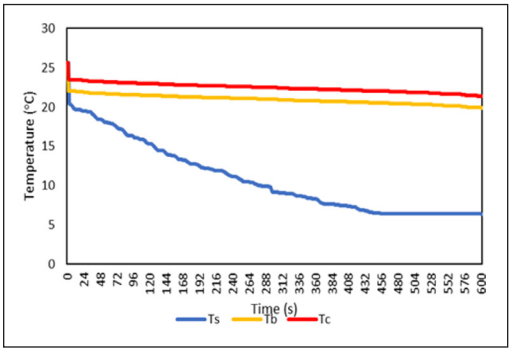

(a)

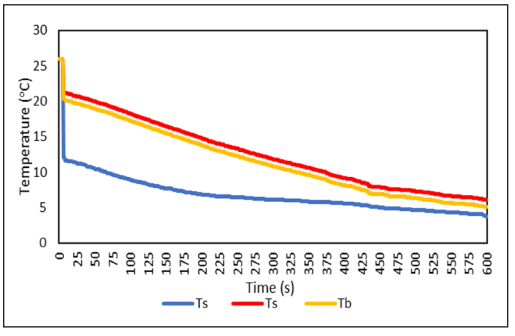

(b)

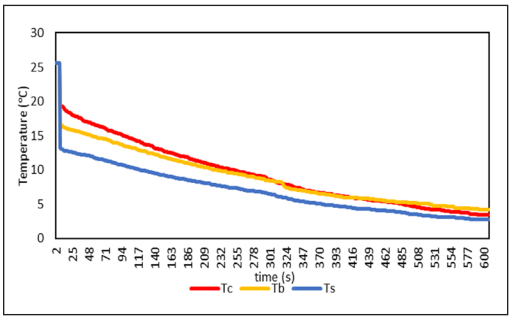

(c)

Figure 3. Temperature profile of T_c, T_b, and T_s in chicken meat samples: (a) without compressive force; (b) 980 N compressive force; and (c) 1960 N compressive force

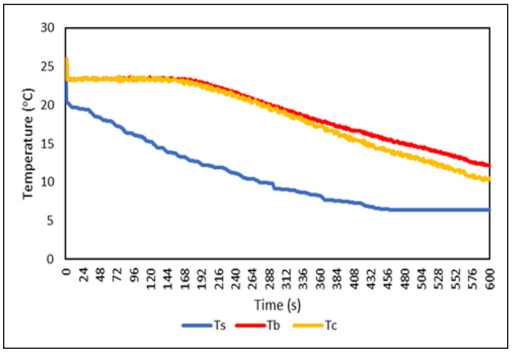

(a)

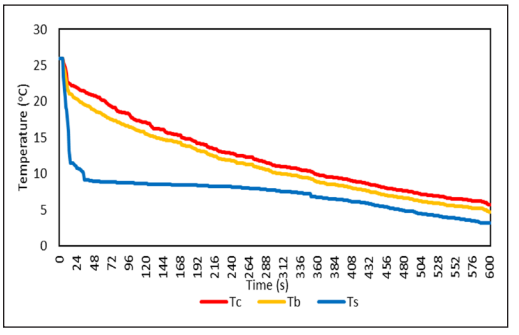

(b)

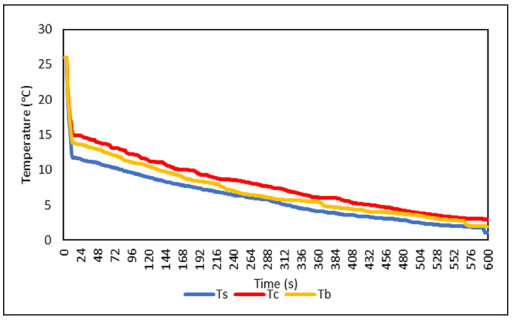

(c)

Figure 4. Temperature profile of T_c, T_b, and T_s in fish sample: (a) without compressive force; (b) 980 N compressive force; and (c) 1960 N compressive force

Table 1
The cooling rate of the meat sample (°C/s) during the precooling process.

Meat	Force (N)	Initial Period			Subsequent Period			Whole Process		
		T_s	T_b	T_c	T_s	T_b	T_c	T_s	T_b	T_c
Chicken	0	0,267^{a}	0,146^{a}	0,117^{a}	0,030^{h}	0,004^{a}	0,003^{a}	0,032^{b}	0,013^{ab}	0,012^{a}
	980	0,765^{d}	0,397^{e}	0,292^{d}	0,011^{c}	0,024^{f}	0,026^{h}	0,034^{d}	0,029^{d}	0,029^{c}
	1960	0,924^{g}	0,814^{g}	0,667^{f}	0,012^{d}	0,014^{c}	0,019^{e}	0,039^{g}	0,038^{e}	0,038^{d}
Beef	0	0,332^{b}	0,203^{b}	0,120^{a}	0,023^{g}	0,004^{a}	0,004^{b}	0,031^{a}	0,010^{a}	0,007^{a}
	980	0,778^{de}	0,306^{d}	0,304^{e}	0,007^{a}	0,008^{b}	0,008^{c}	0,033^{c}	0,018^{bc}	0,018^{c}
	1960	0,816^{f}	0,609^{f}	0,669^{f}	0,008^{b}	0,015^{b}	0,015^{e}	0,038^{f}	0,037^{e}	0,036^{d}
Fish	0	0,356^{c}	0,237^{c}	0,146^{b}	0,023^{g}	0,023^{e}	0,019^{f}	0,033^{c}	0,021^{c}	0,017^{b}
	980	0,789^{e}	0,290^{d}	0,202^{c}	0,013^{e}	0,013^{c}	0,021^{g}	0,037^{e}	0,035^{e}	0,030^{cd}
	1960	0,959^{h}	0,866^{h}	0,712^{g}	0,018^{f}	0,022^{d}	0,018^{d}	0,041^{h}	0,039^{e}	0,039^{d}

Note. Numbers followed by the same letter in the column are not significantly different

the initial period, there was a drastic decrease in the temperature of the meat samples within a very short time, resulting in a high cooling rate. In contrast, during the subsequent period, the rate of temperature decrease was significantly slower, with a much lower cooling rate compared to the initial period. This condition demonstrates that applying compressive force to the cooling medium significantly enhances the cooling rate of the meat samples. The compressive force increases the heat transfer rate from the meat samples to the cooling medium by tightening the contact between them and expanding the contact surface area, thereby accelerating heat transfer (Figure 5). In the heat transfer between two media, the tighter and wider the contact surface, the overall heat transfer coefficient (U) would increase, and increasing the U value would accelerate the heat transfer process so that the product would be cooled more quickly. Muttalib et al. (2024) found that applying compressive force increased the cooling rate in the tuna fish sample. Meanwhile, in the subsequent period, when the applied compressive force was stopped, the force that had been exerted would

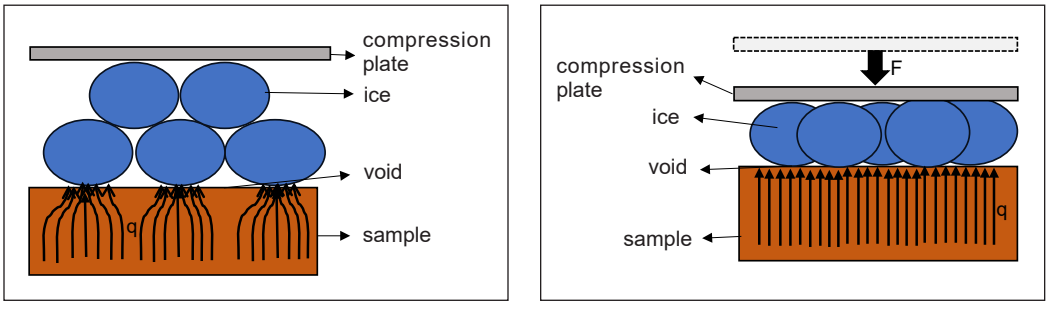

(a) (b)

Figure 5. Illustration of changes in the contact area during the precooling process: (a) without compressive force; and (b) with compressive force

gradually decrease and eventually disappear because the ice medium would absorb the force. This caused the contact between the meat samples and the ice to loosen, resulting in a much lower cooling rate and a slower temperature decrease in this phase.

It was also observed that for all types of samples, the greater the compressive force applied, the lower the temperature drop or the higher the sample cooling rate, especially in the initial period. This indicated that the greater the compressive force on the cooling medium, the faster the cooling process. In the initial period, the average cooling rate of chicken meat for the three measured locations increased by 169.2% and 391.0% compared to the control for compressive forces of 980 N and 1960 N, respectively. In this period, the cooling rate of beef increased by 113.1% and 268.3%, while the cooling rate of fish increased by 60.7% and 274.2%. During the subsequent period, the cooling rate of chicken meat increased by 385.5% and 233.8% compared to the control for compressive forces of 980 N and 1960 N, respectively. In this period, the cooling rate of beef increased by 68.6% and 195.3%; however, the cooling rate of fish was found to have no increment. For the whole precooling process, the average cooling rate of chicken meat for the three measured locations increased by 88.4% and 143.6% compared to the control for compressive forces of 980 N and 1960 N, respectively. In the same condition, the cooling rate of beef increased by 78.3% and 233.0%, while the cooling rate of fish increased by 52.0% and 80.6%. These results showed that the highest cooling rate was achieved during the initial period, with a consistent increase. Thus, the initial period was the most representative phase for evaluating the effect of compressive forces in the precooling process.

Additionally, under the same applied compressive force, the cooling rates of the three types of samples showed different values. This indicated that each type of meat had a different characteristic in the precooling process. Each type of meat had different thermal characteristics, which influenced changes in the temperature during the precooling process. One important parameter that greatly influenced the heat transfer rate from a material was the specific heat of the material (C_p). C_p represented the amount of heat required to change the temperature of 1 kg of material by 1 K. This meant that a material with a smaller C_p value would have a greater rate of decrease in material temperature because it involved changing a smaller amount of heat to change the material temperature by 1 K. The C_p values for chicken, beef, and fish were 4.34 kJ/kg K, 3.45 kJ/kg K, and 3.43 kJ/kg K, respectively (ASHRAE, 2014). Fish had the lowest C_p value among the three samples; therefore, the fish samples generally had the highest cooling rate. Fish muscles were very different from land animals such as cows and chickens. Fish muscles consisted of short fibers that were usually less than an inch long, arranged in layers called myotomes, which were separated by connective tissue called myosepta. This unique arrangement allowed the texture of the fish meat to be soft and easy to peel (Lampila, 1990). This kind of structure probably caused the fish to experience a decrease

in temperature more quickly during the cooling process. However, the difference in cooling rate between chicken and beef did not appear to be related to the C_p value, but both had lower cooling rates compared to the fish sample.

The results of statistical analysis showed that the compressive force, type of meat, and the interaction of these two factors significantly influenced the cooling rate at the center, between the center and the surface, and the surface of the sample, both in the initial and subsequent periods, as well as the whole process ($p<0.05$). Based on the DMRT results, it was generally found that meat samples subjected to compressive force exhibited higher cooling rates compared to the control. Among the samples, fish consistently showed the highest cooling rate, with the effect becoming more pronounced at higher compressive forces.

Final Sample Temperature

The final temperature of the sample, which could be achieved during the precooling process, was an important parameter for safe meat storage. In the precooling process, the desired final temperature was the temperature that was expected to be close to the storage temperature. As explained above, storage for meat and fish was generally recommended at a temperature of 4 °C (277 K) or less. Therefore, precooling using an ice medium that produced a final temperature close to this value or slightly lower would be better**.**

Table 2 presents the final temperatures of the samples during the precooling process. It was observed that the final temperature of the samples was lower when a compressive force was applied compared to the control. Furthermore, the greater the compressive force, the lower the final temperature. The final temperature of chicken, beef, and fish samples decreased by 41.7 and 79.0%, 22.8 and 76.0%, and 56.8 and 85.7% compared to the control, respectively, for applying a compressive force of 980 and 1960 N. Statistical

Table 2
The final temperature of the samples in the precooling process

Sample	Force (N)	T_s (°C)	T_b (°C)	T_c (°C)
	0	6.39^{g}	17.51^{dc}	18.51^{d}
Chicken	980	5.35^{e}	7.99^{b}	8.45^{b}
	1960	2.16^{b}	2.60^{a}	2.64^{a}
	0	7.63^{h}	19.90^{e}	21.40^{d}
Beef	980	6.37^{fg}	15.27^{cd}	15.29^{c}
	1960	2.75^{c}	3.46^{a}	3.96^{a}
	0	6.36^{f}	13.50^{c}	15.27^{c}
Fish	980	3.15^{d}	5.74^{a}	5.74^{ab}
	1960	1.04^{a}	1.97^{a}	2.96^{a}

Note. Numbers followed by the same letter in the same column are not significantly different

analysis revealed that compressive force, type of meat, and the interaction of these two factors significantly influenced the final temperature of T_s, T_b, and T_c in all samples ($p<0.05$). Based on the DMRT results, in general, it could be seen that the final temperature of meat samples varied according to the force applied. The final temperature values were significantly different for different compressive forces in all meat samples. Fish samples were found to have the lowest final temperature value compared to chicken and beef. Furthermore, when applying a compressive force of 1960 N, the final temperature reached for the three samples was about the same in the range of 2°C. This was in accordance with the recommended storage requirements for meat and fish at a temperature of 4°C. Therefore, applying the compressive force of 1960 N in using a compressive plate-type cooling apparatus was a suitable choice for the precooling process of animal products for subsequent storage purposes.

CFD Simulation for Final Temperature

As mentioned earlier, in the precooling process for storage, the most critical factor is the final temperature reached by the sample material. Therefore, in this study, CFD simulations were used to predict the final temperature of T_s, T_b, and T_c of the samples. Various physical and thermal property parameters were required to run this simulation for the meat sample and the ice medium used. Table 3 shows the parameter values used in the CFD simulation in this study.

The solver used in this simulation was the Reynolds-Averaged Navier-Stokes (RANS) equation with a pressure-based, transient flow model and steady-time approach. This method was chosen because, in many engineering applications, steady flow modeling

Table 3
Parameter values used in the CFD simulation

Material	Type	Properties	Values	Sources
Crushed ice	Solid	Density (kg/m^3)	920	Ballinger et al. (2011)
		Molecular weight (kg/kmol)	18.0152	Fellows (2009)
		Specific heat (J/kg.K)	1006.43	Vernier calipers
		Thermal conductivity (W/m.K)	0.6	Thermocouple
		Average diameter (mm)	5	
		Temperature (K)	271.8	
Air	Fluid	Density (kg/m^3)	1.276	The Engineering ToolBox.
		Specific heat (J/kg.K)	1006.43	(2003)
		Thermal conductivity (W/m.K)	0.0242	Thermocouple
		Temperature (K)	271.8	
Beef	Solid	Density (kg/m^3)	1033	Hadfield (2019)
		Specific heat (J/kg.K)	3100	Fellows (2009)
		Thermal conductivity (W/m.K)	0.3	Vernier calipers
		Dimension length × width × height (mm)	30×30×20	Thermocouple
		Initial temperature (K)	298.56	

Table 3 *(continue)*

Material	Type	Properties	Values	Sources
Chicken	Solid	Density (kg/m^3)	1021	Siripon
		Specific heat (J/kg.K)	3690	Vernier calipers
		Thermal conductivity (W/m.K)	0.5	Thermocouple
		Dimension length × width × height (mm)	30×30×20	
		Initial temperature (K)	298.56	
Fish	Solid	Density (kg/m^3)	1076	Gulati & Datta, 2013;
		Specific heat (J/kg.K)	3740	Laguerre et al., 2018
		Thermal conductivity (W/m.K)	0.4	Vernier calipers
		Dimension length × width × height (mm)	30×30×20	Thermocouple
		Initial temperature (K)	298.56	

using the RANS equation is a common practice. This approach was suitable for problems where the flow field operated in quasi-steady conditions and variations over time were relatively small (Mao et al., 2020). The simulation time was designed to be the same as the actual time for the sample during the precooling process, which was 600 s. Figures 6, 7, and 8 show the final temperature contours of T_s, T_b, and T_c from the CFD simulation of the three samples at the end of precooling time, or 600 s. These results showed that CFD was able to predict the final temperature of the three samples accurately. This indicated that the tools and selected properties effectively represented the heat transfer process during precooling. The movement of heat flow from the center to the surface and towards the cooling medium was clearly depicted, indicated by clearly graded colors. The higher the temperature of any zone of the sample, the redder the color, and the lower the temperature, the bluer the color. Mixed colors from the center of the sample towards the surface indicated a zone where the temperature was changing from high to

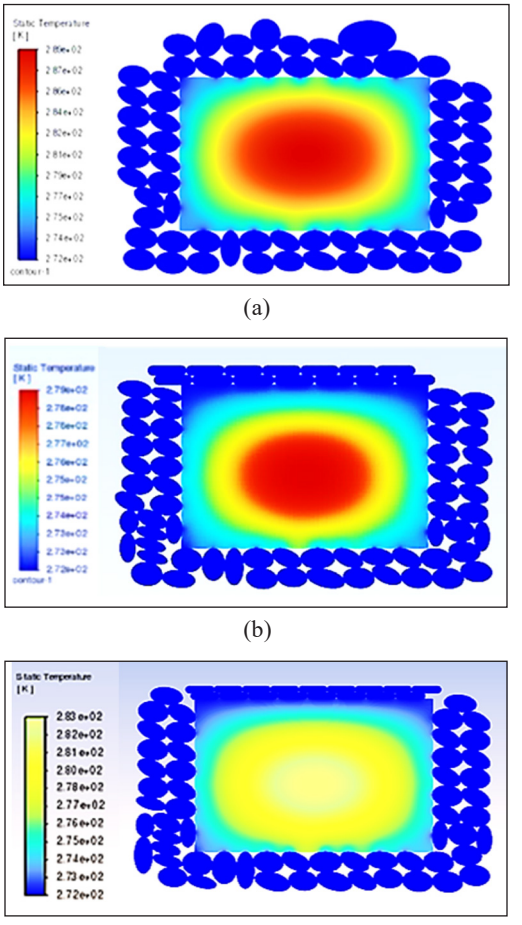

(a) (b) (c)

Figure 6. Temperature contour from CFD simulation for chicken meat sample: (a) without compressive force; (b) compressive force of 980 N; and (c) compressive force of 1960 N

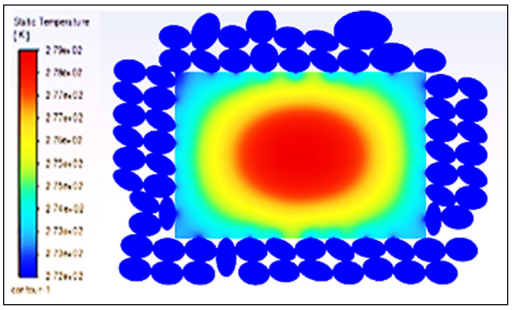

(a)

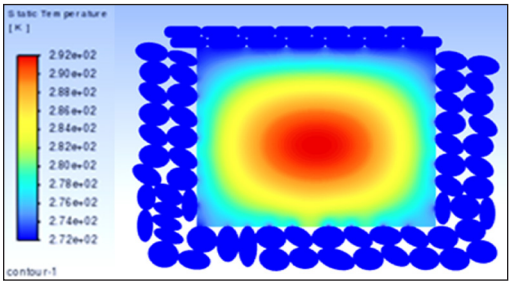

(b)

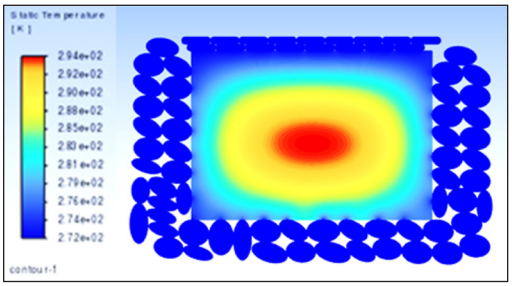

(c)

Figure 7. Temperature contour from CFD simulation for beef sample: (a) without compressive force; (b) compressive force of 980 N; and (c) compressive force of 1960 N

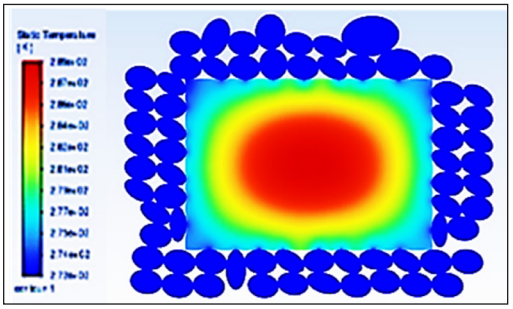

(a)

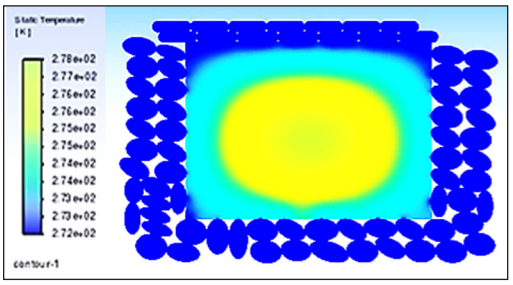

(b)

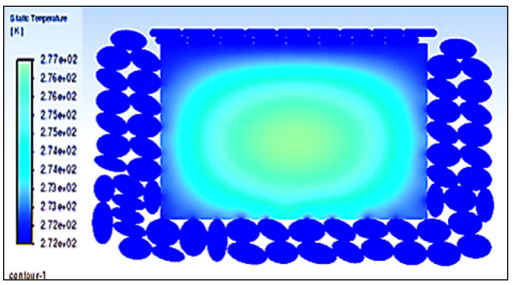

(c)

Figure 8. Temperature contour from CFD simulation for fish sample: (a) without compressive force; (b) compressive force of 980 N; and (c) compressive force of 1960 N

low. In the control treatment, the area with a reddish color, generally with a temperature of more than 280K (7°C), was the largest compared to the treatment with a compressive force of 980 or 1960 N in the three samples.

The wider reddish color indicated that high temperatures still dominated the sample temperature. At a compressive force of 980 N, the area of the reddish color became smaller, while the bluish and yellowish color at a temperature of around 275 K (2°C) to less than 280 K (7°C) became wider. This showed that with the application of compressive force, areas with high temperatures would decrease, and areas with lower temperatures would expand. At a compression force of 1960 N, the area of the reddish color at a high temperature

became smaller or disappeared, while the bluish color at a temperature of around 275K (2°C) became wider. This confirmed that the low-temperature area would dominate with a higher compressive force, indicating that the sample had a low temperature.

Table 4 presents a comparison of the final temperature of T_s, T_b, and T_c between the measurement and simulation results of the three samples, along with the R^2, *RMSE*, and *MAPE* values. In general, it could be seen that quite high R^2 values, accompanied by low RMSE and MAPE, were found at almost all measurement points and all samples tested. Overall, the predicted temperature for all measurement positions had an average R^2 value of 0.82, *RMSE* of 0.28, and *MAPE* of 2.33%. These results demonstrated that CFD

Table 4
Comparison of the final temperature of the sample from measurement and simulation, along with R^2, RMSE, and MAPE values

Sample	Measurement position	Measured	Simulated	R^2	*RMSE*	*MAPE*
	T_s	279.39	272.58	0.69	0.44	3.39
Chicken (0 N)	T_b	290.51	286.29	0.91	0.50	3.81
	T_c	291.51	282.47	0.94	0.28	1.85
	T_s	278.35	273.26	0.93	0.29	2.28
Chicken (980 N)	T_b	280.99	273.61	0.70	0.47	2.91
	T_c	281.45	282.90	0.95	0.12	0.91
	T_s	275.16	272.34	0.79	0.24	1.95
Chicken (1960 N)	T_b	275.60	273.48	0.87	0.15	2.26
	T_c	275.64	281.71	0.89	0.19	3.22
	T_s	280.63	279.07	0.94	0.06	0.40
Beef (0 N)	T_b	292.90	280.01	0.89	0.05	1.07
	T_c	294.40	289.00	0.96	0.14	0.42
	T_s	279.37	273.15	0.82	0.20	1.78
Beef (980 N)	T_b	288.27	274.36	0.61	0.36	3.01
	T_c	288.29	289.43	0.86	0.48	3.93
	T_s	275.75	272.44	0.51	0.29	2.37
Beef (1960 N)	T_b	276.46	274.49	0.73	0.21	1.69
	T_c	276.96	288.39	0.85	0.55	4.75
	T_s	279.36	272.26	0.78	0.29	2.26
Fish (0 N)	T_b	286.5	274.77	0.73	0.42	3.85
	T_c	288.27	278.68	0.98	0.06	0.33
	T_s	276.15	272.58	0.85	0.19	2.53
Fish (980 N)	T_b	278.74	272.81	0.68	0.38	3.11
	T_c	278.74	278.97	0.88	0.30	1.64
	T_s	274.04	272.11	0.77	0.26	2.15
Fish (1960 N)	T_b	274.97	272.91	0.80	0.17	1.38
	T_c	275.96	277.98	0.84	0.45	3.72

accurately predicted the sample temperatures during the precooling process, reinforcing earlier findings. CFD has proven to be a valuable tool for the food processing industry in various fields (Anandharamakrishnan et al., 2009; Bhargava et al., 2021; Oyinloye & Yoon, 2021; Padhi, 2020; Park & Yoon, 2018; Szpicer et al., 2023; Xia & Sun, 2002). There was a slightly greater deviation, especially for the final temperature at the surface position. The movement of the ice medium during compression allowed the temperature on the surface of the sample to become unstable. Kuffi et al. (2016) stated that the temperature prediction results using CFD were in accordance with the temperature profile measured at various positions on the beef carcass, with very good predictions in the deep rear position compared to the near-surface position.

CONCLUSION

It was found that compressive force, meat type, and their interaction significantly influenced the cooling rate and final temperature at all measurement positions for all sample types ($p<0.05$). Applying a compressive force in the precooling process sped up temperature reduction and increased the cooling rate of the sample.

At the initial period of the precooling process, the cooling rate reached the highest value and increased consistently. This period best represented the effect of applying compressive forces in the precooling process. In this initial period, the average cooling rate of chicken meat increased by 169.2% and 391.0% compared to the control for compressive forces of 980 N and 1960 N, respectively. Meanwhile, the cooling rate of beef increased by 113.1% and 268.3%, and the cooling rate of fish increased by 60.7% and 274.2%.

The final temperature of chicken, beef, and fish samples decreased by 41.7% and 79.0%, 22.8% and 76.0%, and 56.8% and 85.7%, respectively, compared to the control when applying a compressive force of 980 N and 1960 N. CFD simulations could accurately predict the final temperature of the samples in the precooling process, with an average R^2 value of 0.82, *RMSE* of 0.28, and *MAPE* of 2.33%.

ACKNOWLEDGMENTS

The authors thank Gadjah Mada University for partially funding this research through the Final Assignment Recognition Program (Program Rekognisi Tugas Akhir, RTA) with assignment letter No.: 5286/UN1.P1/PT.01.03/2024.

REFERENCES

Al-Mohaithef, M., Abidi, S. T., Javed, N. B., Alruwaili, M., & Abdelwahed, A. Y. (2021). Knowledge of safe food temperature among restaurant supervisors in Dammam, Saudi Arabia. *Journal of Food Quality*, *2021*, 1–8. https://doi.org/10.1155/2021/2231371

Anandharamakrishnan, C., Gimbun, J., Stapley, A. G. F., & Rielly, C. D. (2009). Application of computational fluid dynamics (CFD) simulations to spray-freezing operations. *Drying Technology*, *28*(1), 94–102. https://doi.org/10.1080/07373930903430843

ASHRAE. (2014). *ASHRAE® Handbook-Refrigeration.* ASHRAE. https://azaranstore.com/wp-content/uploads/2022/09/271-ASHRAE-HANDBOOK-REFRIGERATION-2014.pdf

Awasthi, M. K., Kumar, A., Dutt, N., & Singh, S. (2024). *Computational Fluid Flow and Heat Transfer: Advances, Design, Control, and Applications* (1st ed.). CRC Press. https://doi.org/10.1201/9781003465171

Bailey, J. M., Dunne, M. P., & Martin, N. G. (2000). Genetic and environmental influences on sexual orientation and its correlates in an Australian twin sample. *Journal of Personality and Social Psychology*, *78*(3), 524–536. https://doi.org/10.1037/0022-3514.78.3.524

Ballinger, J. T., Shugar, G. J., Ballinger, C. T., & Shugar, G. J. (2011). *Chemical technicians' ready reference handbook* (5th ed). McGraw-Hill.

Bhargava, N., Mor, R. S., Kumar, K., & Sharanagat, V. S. (2021). Advances in application of ultrasound in food processing: A review. *Ultrasonics Sonochemistry*, *70*, Article 105293. https://doi.org/10.1016/j.ultsonch.2020.105293

Chakraborty, A., Lyonnais, S., Battistini, F., Hospital, A., Medici, G., Prohens, R., Orozco, M., Vilardell, J., & Solà, M. (2017). DNA structure directs positioning of the mitochondrial genome packaging protein Abf2p. *Nucleic Acids Research*, *45*(2), 951–967. https://doi.org/10.1093/nar/gkw1147

Chakraborty, S., & Dash, K. K. (2023). A comprehensive review on heat and mass transfer simulation and measurement module during the baking process. *Applied Food Research*, *3*(1), Article 100270. https://doi.org/10.1016/j.afres.2023.100270

Chauhan, A., Trembley, J., Wrobel, L. C., & Jouhara, H. (2019). Experimental and CFD validation of the thermal performance of a cryogenic batch freezer with the effect of loading. *Energy*, *171*, 77–94. https://doi.org/10.1016/j.energy.2018.12.149

Cruz, P. A. D., Yamat, E. J. E., Nuqui, J. P. E., & Soriano, A. N. (2022). Computational fluid dynamics (CFD) analysis of the heat transfer and fluid flow of copper (II) oxide-water nanofluid in a shell and tube heat exchanger. *Digital Chemical Engineering*, *3*, Article 100014. https://doi.org/10.1016/j.dche.2022.100014

Darwish, W. S., El Bayoumi, R. M., Mohamed, N. H., & Hussein, M. A. M. (2024). Microbial contamination of meat at a low temperature storage: A review. *Journal of Advanced Veterinary Research, 14*(2), 322-325.

Dal, H. O. G., Gursoy, O., & Yilmaz, Y. (2021). Use of ultrasound as a pre-treatment for vacuum cooling process of cooked broiler breasts. *Ultrasonics Sonochemistry*, *70*, Article 105349. https://doi.org/10.1016/j.ultsonch.2020.105349

El-Aal, A., & Suliman, A. I. A. (2008). Carcass traits and meat quality of lamb fed on ration containing different levels of leucaena hay (*Leucaena leucocephala* L.). *Biotechnology in Animal Husbandry*, *24*(3–4), 77–92. https://doi.org/10.2298/BAH0804077E

Fadiji, T., Ashtiani, S. H. M., Onwude, D. I., Li, Z., & Opara, U. L. (2021). Finite element method for freezing and thawing industrial food processes. *Foods*, *10*(4), Article 869. https://doi.org/10.3390/foods10040869

Fellows, P. J. (2009). Heat processing. In *Food Processing Technology: Principles and Practice* (pp. 339-366). Woodhead Publishing.

Fiandini, M., Nandiyanto, A. B. D., Al Husaeni, D. F., Al Husaeni, D. N., & Mushiban, M. (2023). How to calculate statistics for significant difference test using SPSS: Understanding students comprehension on the concept of steam engines as power plant. *Indonesian Journal of Science and Technology*, *9*(1), 45–108. https://doi.org/10.17509/ijost.v9i1.64035

Gao, H. Y. (2007). *Methods of Pre-Cooling for Fresh Cod (Gadus morhua) and Influences on Quality during Chilled Storage at -1.5˚c*. UNU - Fisheries Training Programme.

Grossi, G., Arpino, F., Canale, C., Cortellessa, G., Ficco, G., & Lombardi, T. (2024). CFD design of a novel device for temperature profile measurement in waste-to-energy plants. *Journal of Physics: Conference Series*, *2685*(1), Article 012011. https://doi.org/10.1088/1742-6596/2685/1/012011

Gulati, T., & Datta, A. K. (2013). Enabling computer-aided food process engineering: Property estimation equations for transport phenomena-based models. *Journal of Food Engineering*, *116*(2), 483–504. https://doi.org/10.1016/j.jfoodeng.2012.12.016

Hadfield, J. M. (2019). *The thermal and physical properties of beef from three USDA-quality grades cooked to multiple degrees of doneness* [Master thesis, Utah State University]. ProQuest. https://www.proquest.com/openview/76811deb147da19bbc2df6b96cb5bbbc/1?cbl=18750&diss=y&pq-origsite=gscholar

Han, J. H. (2014). *Innovations in food packaging* (2nd ed.). Academic Press.

Kuffi, K. D., Defraeye, T., Nicolai, B. M., De Smet, S., Geeraerd, A., & Verboven, P. (2016). CFD modeling of industrial cooling of large beef carcasses. *International Journal of Refrigeration*, *69*, 324–339. https://doi.org/10.1016/j.ijrefrig.2016.06.013

Laguerre, O., Derens, E., & Flick, D. (2018). Modelling of fish refrigeration using flake ice. *International Journal of Refrigeration*, *85*, 97–108. https://doi.org/10.1016/j.ijrefrig.2017.09.014

Lampila, L. E. (1990). Comparative microstructure of red meat, poultry and fish muscle. *Journal of Muscle Foods*, *1*(4), 247–267. https://doi.org/10.1111/j.1745-4573.1990.tb00369.x

Li, Q., Duan, M., Liu, W., Dai, Y., & Li, R. (2019). Kinetic modeling of a Bi-enzyme time-temperature indicator (TTI) based on different parameters for monitoring food product quality. In *IOP Conference Series: Materials Science and Engineering* (Vol. 612, No. 2, p. 022042). IOP Publishing. https://doi.org/10.1088/1757-899X/612/2/022042

Li, X., Wu, W., Li, K., Ren, X., & Wang, Z. (2022). Experimental study on a wet precooling system for fruit and vegetables with ice slurry. *International Journal of Refrigeration*, *133*, 9–18. https://doi.org/10.1016/j.ijrefrig.2021.10.001

Mao, J., Zhao, L., Di, Y., Liu, X., & Xu, W. (2020). A resolved CFD–DEM approach for the simulation of landslides and impulse waves. *Computer Methods in Applied Mechanics and Engineering*, *359*, Article 112750. https://doi.org/10.1016/j.cma.2019.112750

Merai, M., Flick, D., Guillier, L., Duret, S., & Laguerre, O. (2019). Experimental characterization of heat transfer inside a refrigerated trailer loaded with carcasses. *International Journal of Refrigeration*, *99*, 194–203. https://doi.org/10.1016/j.ijrefrig.2018.11.041

Muttalib, S. A., Bintoro, N., Karyadi, J. N. W., & Saputro, A. D. (2024). Development of method and apparatus to speed up cooling process of fish products. In *AIP Conference Proceedings* (Vol. 2838, No. 1). AIP Publishing. https://doi.org/10.1063/5.0180090

Oyinloye, T., & Yoon, W. (2021). Application of computational fluid dynamics (CFD) simulation for the effective design of food 3D printing (A Review). *Processes*, *9*(11), Article 1867. https://doi.org/10.3390/pr9111867

Padhi, M. R. (2020). A review on applications of computational fluid dynamics (CFD) in the food industry. *PalArch's Journal of Archaeology of Egypt / Egyptology, 17*, 10159-10169

Park, H. W., & Yoon, W. B. (2018). Computational fluid dynamics (CFD) modelling and application for sterilization of foods: A review. *Processes*, *6*(6), Article 62. https://doi.org/10.3390/pr6060062

Rahman, S. (Ed.). (2007). *Handbook of food preservation* (2nd ed). CRC Press.

Ren, Q., Zhu, X., Li, J., Han, J., & Fang, K. (2023). Heat and mass transfer model for pork carcass precooling: Comprehensive evaluation and optimization. *Food and Bioproducts Processing*, *138*, 70–85. https://doi.org/10.1016/j.fbp.2023.01.004

Riva, M., Piergiovanni, L., & Schiraldi, A. (2001). Performances of time–temperature indicators in the study of temperature exposure of packaged fresh foods. *Packaging Technology and Science*, *14*(1), 1–9. https://doi.org/10.1002/pts.521

Savell, J. W., Mueller, S. L., & Baird, B. E. (2005). The chilling of carcasses. *Meat Science*, *70*(3), 449–459. https://doi.org/10.1016/j.meatsci.2004.06.027

Siripon, K., Tansakul, A., & Mittal, G.S. (2007). Heat transfer modeling of chicken cooking in hot water. *Food Research International, 40*(7), 923-930. https://doi.org/10.1016/j.foodres.2007.03.005

Skawińska, E., & Zalewski, R. I. (2022). Economic impact of temperature control during food transportation - A COVID-19 perspective. *Foods*, *11*(3), Article 467. https://doi.org/10.3390/foods11030467

Szpicer, A., Bińkowska, W., Wojtasik-Kalinowska, I., Salih, S. M., & Półtorak, A. (2023). Application of computational fluid dynamics simulations in food industry. *European Food Research and Technology*, *249*(6), 1411–1430. https://doi.org/10.1007/s00217-023-04231-y

Tao, Y., Guo, Y., Li, J., Ye, K., Zhang, Y., Zeng, X., & Dou, H. (2023). Effect of temperature fluctuation during superchilling storage on the microstructure and quality of raw pork. *Meat Science*, *198*, Article 109096. https://doi.org/10.1016/j.meatsci.2023.109096

The Engineering ToolBox (2009). *Air Psychrometrics*. https://www.engineeringtoolbox.com/air-psychrometrics-properties-t_8.html

Toparlar, Y., Blocken, B., Maiheu, B., & Van Heijst, G. (2019). CFD simulation of the near-neutral atmospheric boundary layer: New temperature inlet profile consistent with wall functions. *Journal of Wind Engineering and Industrial Aerodynamics*, *191*, 91–102. https://doi.org/10.1016/j.jweia.2019.05.016

Valtýsdóttir, K. L., Margeirsson, B., Arason, S., Lauzon, H. L., & Martinsdóttir, E. (2010). *Guidelines for Precooling of Fresh Fish during Processing and Choice of Packaging with Respect to Temperature Control in Cold Chains*. Matís. https://kaeligatt.matis.is/wp-content/uploads/2023/02/40-10-Guidelines-for-precooling-and-packaging.pdf

Wang, S. K. (2000). *Handbook of air conditioning and refrigeration* (2nd ed). McGraw-Hill.

Wang, S., Liu, X., Yang, M., Zhang, Y., Xiang, K., & Tang, R. (2015). Review of time temperature indicators as quality monitors in food packaging. *Packaging Technology and Science, 28*, 839-867. https://doi: 10.1002/pts.2148

Xia, B., & Sun, D. W. (2002). Applications of computational fluid dynamics (CFD) in the food industry: A review. *Computers and Electronics in Agriculture*, *34*(1–3), 5–24. https://doi.org/10.1016/S0168-1699(01)00177-6

Zhang, X., Ge, Y., & Sun, J. (2020). CFD performance analysis of finned-tube CO_2 gas coolers with various inlet air flow patterns. *Energy and Built Environment*, *1*(3), 233–241. https://doi.org/10.1016/j.enbenv.2020.02.004

Zira, S., Rydhmer, L., Ivarsson, E., Hoffmann, R., & Röös, E. (2021). A life cycle sustainability assessment of organic and conventional pork supply chains in Sweden. *Sustainable Production and Consumption*, *28*, 21–38. https://doi.org/10.1016/j.spc.2021.03.028

Pertanika J. Sci. & Technol. 33 (4): 1829 - 1847 (2025)

PERTANIKA JOURNALS

SCIENCE & TECHNOLOGY

Journal homepage: http://www.pertanika.upm.edu.my/

A Novel Multifaceted Approach to the Detection and Analysis of Formalin's Effect on Enhancing the Shelf Life of Apples

Shahed Alam[1]*†, Md Saif Kabir[1]†, Md. Minhazul Islam Royel[2] and Md. Rakibul Islam[1]

[1]Department of Electrical and Electronic Engineering, BRAC University, Dhaka, Bangladesh
[2]Department of Computer Science and Engineering, BRAC University, Dhaka, Bangladesh

ABSTRACT

The prevalent saying that an apple a day keeps the doctor away may have much merit because of its valuable minerals, vitamins and antioxidant contents that benefit humans. However, because of the circulating news of apples being adulterated with formalin in Bangladesh, a considerable number of people are discouraged from consuming them. The research investigates the effect of formalin on the shelf life of apples. In this research, we have adulterated apples with three different concentrations (20%, 30%, 40%) of formalin and use three different methods to study the presence of formalin on the surface of the apples: (1) spectrophotometry, (2) a formalin test kit developed by the Bangladesh Council of Scientific and Industrial Research (BCSIR), and (3) an MS1100 gas sensor that functions as an E-nose. The test kit detection and spectrophotometry enabled the detection of the presence and the concentration of formalin on the apple, respectively. The E-nose is able to deduce the decay profile of formalin on the surface of the apples. The measurements showed the emission of formalin drops to their natural or pure form after approximately 30 hours. Formalin does not improve the shelf life of apples, and visibly, it arguably makes them appear less fresh. The phenomenon has also been explained by theory, which states that formalin primarily affects foods with relatively high protein content. Hence, shopkeepers who presumably use formalin do not benefit from its application.

Keywords: Food adulteration, formaldehyde, formalin, nutritional quality, shelf life

ARTICLE INFO

Article history:
Received: 27 November 2024
Accepted: 08 April 2025
Published: 11 June 2025

DOI: https://doi.org/10.47836/pjst.33.4.07

E-mail addresses:
shahed.alam@bracu.ac.bd (Shahed Alam)
kabirsaif62@gmail.com (Md Saif Kabir)
minhazul.islam.royel@g.bracu.ac.bd (Md. Minhazul Islam Royel)
md.rakibul.islam9@g.bracu.ac.bd (Md. Rakibul Islam)
* Corresponding author; † These authors contributed equally to this work and are considered co-first authors

INTRODUCTION

It has been reported that over the last decade, food adulteration and contamination with harmful chemicals have been practiced extensively and have consequently become a concerning issue in Bangladesh (Dey & Nagababu, 2022; Kamruzzaman, 2016; Headlines and Global News, 2014). Use of

e-ISSN: 2231-8526
© Universiti Putra Malaysia Press

harmful colors, wax-coated fruit (Guo, 1994), Calcium carbide-based artificial ripening (Bini et al., 2019; Nura et al., 2018; Essien et al., 2018), pesticide residues (Ahmad et al., 2024), and formalin-based fruit preservation (Protano et al., 2021) are all different methods of food adulteration. Not all the methods are harmful, provided they are used in controlled amounts and with caution. However, it has become a matter of concern in Bangladesh, and the news of the harmful effects of food adulteration is widespread. According to the news, features and articles published in numerous newspapers and other mass media over the past decade have become a deadly worrying concern in Bangladesh. Based on a survey conducted in 2004 by the City Corporation, over 76% of the food items were found adulterated at varied levels, ranging from 70% to 90% (Rahman et al., 2015). As per a government official statistic, about 50% of the food samples tested by the Institute of Public Health from 2001 to 2009 were adulterated (Directorate General of Health Services, 2012).

Consumption of adulterated food has caused numerous deaths as well (Ali, 2013a; Ali, 2013b)—lack of storage and refrigeration, loose regulatory controls. Inadequate transportation infrastructure and rising consumer demand fuel the tendency to use fraudulent methods to increase shelf life (United Nations, 2007). In Reza et al. (2023), research was conducted on various fruits, in which the impact of formalin on the post-harvest quality and nutritive properties has been investigated. Machine Learning (ML) has been utilized to detect formalin in fruits by Brighty et al. (2021). For the last 30 years, more than 1582 publications have been published regarding formaldehyde in food, signifying the importance of the scientific findings (Rahman et al., 2023). In recent years, extensive research has been conducted on the development of formaldehyde detection sensors, further emphasizing the relevance of the topic (Fan et al., 2024; Yang et al., 2024; Zhang et al., 2023).

Among the wide variety of adulterants, formalin is the most famous in Bangladesh. Formalin, which is a colorless, 37%–50% aqueous solution of formaldehyde, is reported to be frivolously used in foods in Bangladesh and Southeast Asian countries (Kawamata & Kodera, 2004; Uddin et al., 2011). Formaldehyde is a naturally occurring substance composed of carbon, hydrogen and oxygen (CH_2O) (American Chemistry Council, 2025). It is produced naturally by the human body, and fruits and vegetables are produced in low amounts. Formaldehyde is also manufactured industrially since it is applied in various sectors, such as wood products, cosmetics, adhesives, plastics, nail hardeners, and disinfectants (International Agency for Research on Cancer, 2006). However, in 2004, formaldehyde was classified as carcinogenic to humans (International Agency for Research on Cancer, 2004). Formaldehyde is deadly harmful if inhaled above 300 ppm and ingested above 30 mL (American Chemistry Council, 2025; National Center for Biotechnology Information, 1999). However, it is metabolized rapidly at lower levels, converted to carbon dioxide, and exhaled.

In Bangladesh, everyone from producers to wholesalers is accused of illegally applying formalin to increase the shelf life of fruits and vegetables (Huda, 2025; Tamanna, 2024; Mohiuddin, 2019). Tons of food have been destroyed due to the detection of formaldehyde by the mobile court, as reported in the mass media, without scientifically validating whether the level is in the permissible range. The presence of formalin was detected using handheld detectors (Z-300) with a concentration range of 1–30 ppm (Alam, 2013; The Daily Star, 2014). Formaldehyde is emitted naturally: 6–20 mg/kg in meat and fish, 3–60 mg/kg in various fruits and vegetables, and 1 mg/kg in dairy products (World Health Organization, 2000). According to the European Food Safety Authority (EFSA), the maximum allowable exposure to formaldehyde from food of both animal and plant origin is 100 mg/kg food per day. If the natural level of formaldehyde emission is not considered, all food may be adulterated.

Fruits are a source of valuable minerals, vitamins and fiber. Fruits and vegetables are inevitable components of a healthy diet. Since no fruit or vegetable provides all the nutrients, variety is more important than quantity. Consumers are left uncertain whether their fruit is nutritious or potentially harmful. According to the U.S. Environmental Protection Agency, the permissible limit of average daily exposure to formaldehyde is 0.75 ppm (Jia et al., 2024). Theoretically, formaldehyde can only help extend the shelf life of foods with high protein content. Hence, formaldehyde is ineffective on fruits and vegetables since they generally have low protein content (Kiernan, 2000).

Table 1 depicts that most fruits emit a certain level of formaldehyde, and the value calibration is necessary in case of any adulteration calculation. If we go to the supermarket and take measurements with gas sensors, it will detect formaldehyde, but if it does not exceed the natural level, then there is nothing to worry about. As mentioned earlier, formalin is a 37%–50% aqueous formaldehyde solution.

When we observe the reaction of formalin with protein, two particular reactions will happen. Firstly, the formation of Schiff Base. Secondly, the exact process of crosslinking relations between DNA using formaldehyde and proteins. This process leads to the formation of covalent bonds between proteins and DNA, altering their structure and potentially affecting their function. How effectively formalin can act as a preservative depends most on the proportion of protein content constituting the object that needs to be preserved.

Table 1
Naturally occurring formaldehyde from few fruits (Brighty et al., 2021)

Fruit Name	Naturally Occurring Formaldehyde (ppm)
Apple	6.3–22.3
Apricot	9.5
Banana	16.3
Cucumber	2.3–3.7
Grape	22.4
Pear	38.7–60
Plum	11.2
Tomato	5.7–13.3
Watermelon	9.2

For a very long time, preservatives have been utilized to resist autolysis and putrefaction. The preservative basically reacts with cadaveric tissue to form an inert product preservative; formalin is commonly used commercially (Wojdyło et al., 2008). The formaldehyde interlinks adjacent proteins by inserting a methylene bridge (-CH2-) between the nitrogen in the amino groups. Hence, the protein is converted into a complex molecular crosslinked lattice structure, which is no longer susceptible to serving as food for bacteria or a substrate for enzymes (Wojdyło et al., 2008; The Nutrition Source, 2024). The above-mentioned process depicts a 2-step reaction that results in the Lysine residue of protein and Guanine Base of DNA.

From Table 2, it can be observed that the percentage of protein in an Apple is around 1%. Apples are widely consumed around the world due to their natural ability to combat diseases and their accessibility (Wojodylo et al., 2008). It is a very good source of fiber, phytochemicals, and vitamin C (The Nutrition Source, 2024). Apples are also rich in pectin and quercetin, both of which provide considerable health benefits. Quercetin acts as an antioxidant and has anti-inflammatory effects. Pectin, a soluble fiber, assists in resisting constipation, LDL "bad" cholesterol, and when fermented in the colon by beneficial bacteria, can help prevent chronic diseases such as certain cancers and bowel disorders.

Several studies have been conducted on the detection of formaldehyde over the years. Such as, in one of the papers, the detection of formalin is obtained by machine learning and a gas sensor (Brighty et al., 2021). However, since formalin is a colorless volatile liquid, detection by image processing should have been unrealistically difficult. In Antora et al. (2018), mango, litchi, and mushroom were treated with different concentrations of formaldehyde solutions, and the color, texture and weight loss were observed. It was observed from the research that formaldehyde does not improve post-harvest quality or shelf life (Antora et al., 2018). A variety of fruit, vegetable, milk, chicken, mutton, and meat samples were tested for naturally occurring formaldehyde (Nowshad et al., 2018). Not much work has been done on how effectively formaldehyde can improve the shelf life of fruits, even though the news of its application is circulating in the mass media in Bangladesh.

This research work demonstrated a systematic formalin detection process and measured the formalin application concentration on fruits. Formalin of different concentrations (20%, 30%, and 40%) was applied to apples. The longevity of the existence of formaldehyde was detected using an E-Nose (Datasheet4U, 2025; Baldwin et al., 2011). The validity of the readings at different stages has been ensured by the spectrophotometry and BCSIR KIT (Bangladesh Council of Scientific and Industrial Research, 2023).

Table 2
Nutrients that are present in a medium-sized apple (The Nutrition Source, 2024)

Components	In Medium Apple (in g)
Calories	95
Fat	0
Protein	1
Sugar	19

The research portrays a systematic approach to how formaldehyde can be tested and also validates that the E-Nose is a reliable and cheap method of detecting formaldehyde. Moreover, the decay period of formaldehyde has been deduced, and the hypothesis that formalin is not useful for increasing shelf life has been established. It is expected that the findings of the paper will provide actual information to researchers and consumers about the rumors surrounding formalin implementation.

MATERIALS AND METHODOLOGY

Chemical Test Kit for Formalin Detection

Figure 1. Bangladesh Council of Scientific and Industrial Research (BCSIR) kit for food formalin detection

In order to examine the existence of formalin, a Bangladesh Council of Scientific and Industrial Research (BCSIR) kit for food formalin detection was used (Islam et al., 2015). The kit comes with three different reagents, as shown in Figure 1. Fifteeen drops of each reagent are poured into the test sample, one by one. After reagent-1 is added, the solution should be stirred well and allowed to wait 30 seconds each time. The same test tube was then filled with 15 drops of reagent 2. The solution is left to stand for 30 seconds after being thoroughly stirred. Finally, the third reagent is added, stirring the solution for 30 seconds. Color changes can be observed during the process. After the third reagent is added, the color turns pinkish to reddish brown if the solution is contaminated with formaldehyde (Islam et al., 2015; Uddin et al., 2011). However, the sample does not contain formalin if the solution's color does not change.

Spectrophotometer GENESYS-10S

The GENESYS-10S Spectrophotometer was used in this experiment to measure the absorbance of light in samples of solution containing different concentrations of formaldehyde (Figure 2). Ultraviolet-visible (UV-Vis) spectroscopy is a method of measuring the amount of light that is absorbed and scattered by any material once placed inside a thermal spectrophotometer. The amount of light is called the extinction, the total of absorbed and scattered light. The most basic method involves placing a sample between a light source and a photodetector and measuring the light beam's intensity before and after it passes through the sample. These values are compared at each wavelength to quantify the wavelength-dependent extinction spectrum of the sample. Usually, the absorbance data is compared against wavelength. A 500–700 nm wavelength range is used for detecting formaldehyde (Nag et al., 2021). Each spectrum is background corrected using a blank, basically, a cuvette filled

with the dispersing medium to ensure that the sample spectrum does not contain solvent-related spectral characteristics (Instrument Center, 2018; Thermo Scientific, 2010). This experiment used a sample of distilled water and a test kiwereere as a reference dispersing medium.

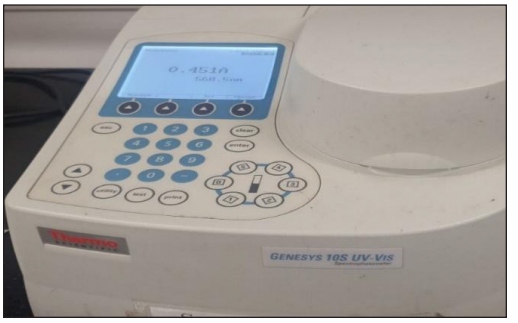

Figure 2. GENESYS-10S Spectrophotometer

Beer-Lambert's law can then be applied, which describes light intensity as it travels through a material containing chemicals that can absorb light (Nurjayadi et al., 2021). It states that A = εlc, where A is absorbance, ε is the molar extinction coefficient, c is the concentration, and l is the path length (Mäntele & Deniz, 2017). This formula can calculate the formaldehyde concentration using the absorbance values obtained from the GENESYS-10S Spectrophotometer.

Electronic Nose Sensor

The MS1100 Gas Sensor (E-nose) module is a semiconductor-type sensor used to detect the concentration of formaldehyde in a closed environment (Figure 3). It has a detection range of 0–1000 ppm for gas detection and can identify a variety of volatile organic compounds (VOCs), such as formaldehyde, toluene, benzene, and organic solvents (Thermo Scientific, 2010; Nurjayadi et al., 2021). This device can detect gases over 0.1 ppm and has high sensitivity and stability (Mäntele & Deniz, 2017). The output voltage obtained is proportional to the concentration of gas. The sensor finds its application in indoor air quality monitoring, environment monitoring, HVAC systems, smart homes and safety security systems.

Figure 3. MS1100 gas sensor

Sample Selection

Around 30 apples were collected from the local markets of Dhaka as test samples for this research. Uniformly ripe samples of the same type, free of any sort of deformation or bruises, were selected. This ensures that the naturally produced formalin will be at identical levels because its emission varies with color and breed (Nowshad et al., 2018).

Purity Test

It has been observed that MS1100 gave a reading of 40–47 ppm in room conditions. When the sensor is brought near an apple, the reading increases to a value ranging from 52–65 ppm, which agrees with the natural emission value (Brighty et al., 2021; Nowshad

et al., 2018). Purity tests on apples were performed using three different methods: (1) spectrophotometry, (2) formalin test kit, and (3) MS1100 gas sensor.

First, formalin was detected using the MS1100 sensor to see if the formaldehyde emission was more than natural. Then, the apples were placed in distilled water for 30 minutes, and 2.5 mL solutions were taken from them. The solution was added with the reagents from the test kit to observe the color change for formaldehyde detection. Third, the samples were tested with the spectrophotometer to determine the concentration.

Sample Preparation

First, three different concentrations (20%, 30%, 40%) of formaldehyde were prepared, as shown in Figure 4. Two apples were rinsed with the 20% formalin solution and kept dry.

The other apple was kept in distilled water for 10 minutes. The solution was preserved in a test tube for further testing with the Bangladesh Council of Scientific and Industrial Research (BCSIR) food formalin detection kit. This apple was dried and placed into another zipper bag (Figure 6). The process was repeated with three different concentrations (20%,

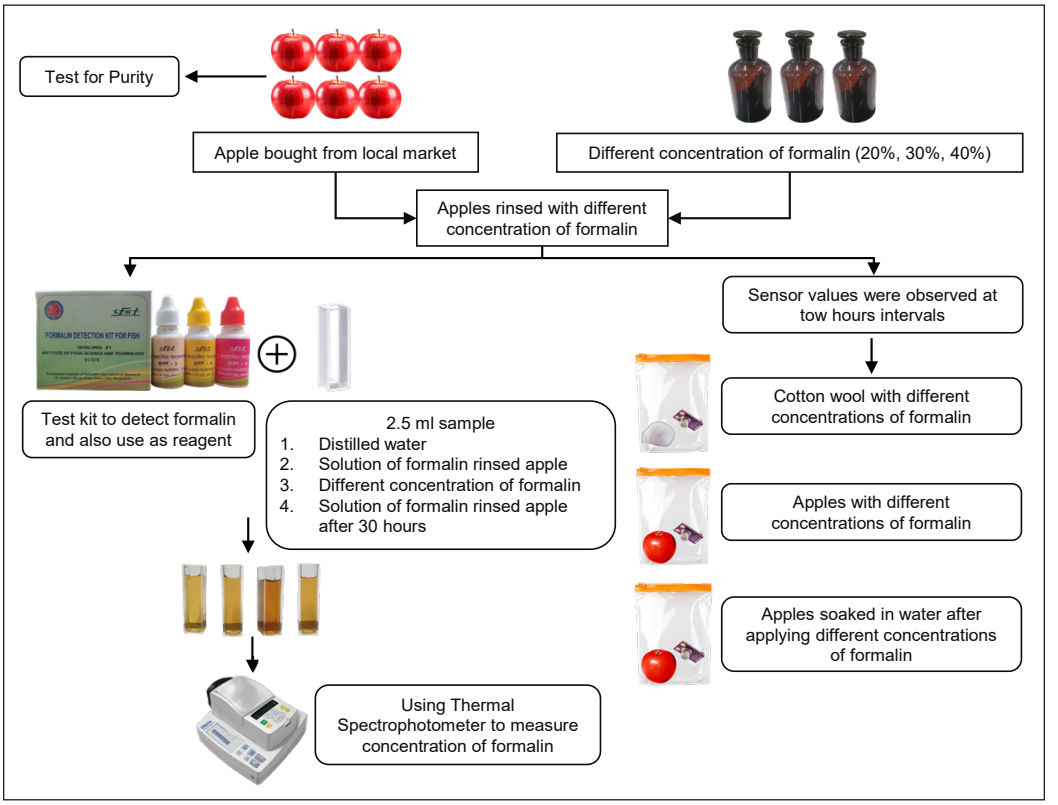

Figure 4. Methodology of the entire process, from the application of formalin on the apple to the detection One of the apples was placed inside a zipper bag to test with the E-nose sensor as a sample containing directly applied formalin, as shown in Figure 5

30%, and 40% of formalin) as shown in Figures 7 and 8. Two different apples were taken each time for different concentrations.

In order to facilitate the understanding of the methodology, we have labeled the solution samples in Table 3.

As mentioned in Table 3, we tested with 20%, 30% and 40% formalin solutions (4, 5 and 6). We also prepared solutions 1, 2, and 3, which are distilled water solutions used to soak apples that had already been rinsed with either solution 4, solution 5, or solution 6. All the solutions mentioned in Table 3 were tested with a BCSIR kit to examine the presence of formalin. The blank solution was tested with the kit to act as the control sample. The process involved collecting samples of 2.5 ml solutions and sequentially adding reagents 1, 2, and 3. At first, 15 drops of reagent 1 were poured into the solution and shaken for 30 seconds. Color changes were carefully noticed during the process. Sequentially, 15 drops of reagent 2 were added, and the solution was shaken for 30 seconds. Then, finally, 15 drops of reagent 3 were added, and the solution was shaken in the same manner. After the third reagent is added, the color change is observed to

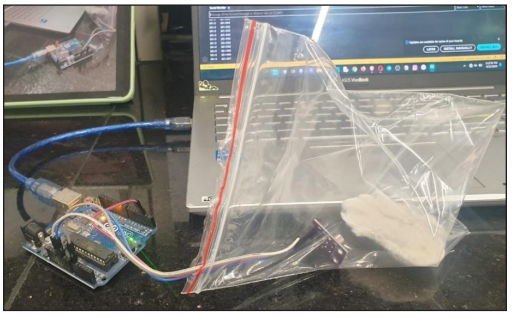

*Figure 5***.** Detection of formalin through MS1100

*Figure 6***.** Application of different concentrations of formalin on apples

Figure 7. Apple is placed inside a zipper bag

Figure 8. Application of BCSIR kit solutions on test solutions

Table 3
Analysis of constituent solutions and formalin-treated apple solutions

Solution Name	Constituent
Blank Solution	Distilled water
Solution 1	The solution from distilled water in which the 20% formalin rinsed apple was soaked
Solution 2	The solution from distilled water in which the 30% formalin rinsed apple was soaked
Solution 3	The solution from distilled water in which the 40% formalin rinsed apple was soaked
Solution 4	20% formalin solution
Solution 5	30% formalin solution
Solution 6	40% formalin solution

check if the solution was contaminated with formaldehyde. Noticeable color changes from pinkish to reddish brown were observed and noted. The color change confirms the presence of formalin.

Then, the spectrometer GENESYS-10S was used to detect the change in absorption and find out the concentration of formalin. For spectrophotometry, we require a reagent that will change the color of the solution upon reacting with formaldehyde. Thus, all the different solutions in which test kit reagents were previously added were applied to a spectrophotometer. Later on, changes in concentration of the formaldehyde were measured by using Beer-Lambert's law, $A= \varepsilon lc$, where A is absorbance, ε is the molar extinction coefficient, c is the concentration, and l is the path length. A wavelength of 568.5nm was used to measure the change in absorbance. Five samples were tested at a time.

In parallel to the spectrophotometric analysis, the apples that were kept in zipper bags were examined to observe the presence of formalin over a duration of 30 hours, as the readings stabilized after this period (Figure 9), so that a decay profile of the formalin can be observed. The data inputs were taken at every two-hour interval using the E-nose sensor. The sensor was kept on for 2 minutes to measure the input each time to reach a steady value, and the room condition readings were noted. After getting a stable reading, the zip of the zipper bag was opened slightly, and the sensor was kept inside the bag, near the apple, and new readings were recorded.

In addition to apples, cotton swabs containing soaked formalin samples of different concentrations (solutions 4, 5, and 6) were also placed in zipper bags. The sensor readings were noted for 30 hours. Eventually, decay graphs of formaldehyde were produced with the data collected.

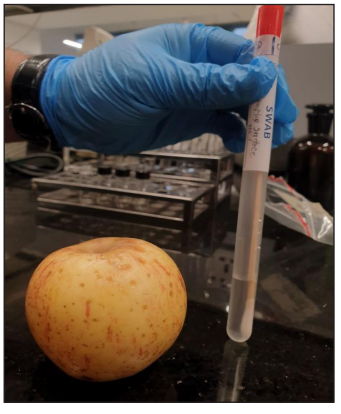

Figure 9. Apple samples were rinsed with different concentrations of formalin and rubbed with a cotton tester after 30 hours

As shown in Figure 9, the surface of the apples was rubbed with a cotton tester and dipped into 3 mL of distilled water to measure the existence of formaldehyde after 30 hours of storage. After 10 minutes, 2.5 mL samples were taken in a test tube, and the kit test was again performed. Another round of spectrophotometry was conducted with the same blank sample to get the absorbance and, eventually, the concentration.

RESULT AND ANALYSIS

Results Graphs Obtained from E-nose Sensor

As stated, the E-nose sensor reading in room conditions varied from 40 to 47 ppm, and the pure apple formaldehyde reading ranged from 6 to 23 ppm. So, at room conditions, in the presence of a pure apple, the readings are around 60–70 ppm. Figure 10 depicts how the reading of the MS-1100 sensor varied at regular time intervals when cotton swabs were soaked with formalin solution of different concentrations (solutions 4, 5, and 6). Results indicate that sensor values became constant after 18–20 hours in the three cases. In order to get a constant value, multiple readings were taken from the sensor until a constant value was reached. It takes around 2–3 minutes to reach a constant reading. A gradual decline in the sensor reading can be observed in each of the three cases. Cotton swabs with 20% formalin solution had readings gradually declining from 465 ppm to 315 ppm, whereas the readings decreased from 495 ppm to 345 ppm in the case of 30% formalin. Finally, as expected, the highest reading was observed in the case of 40% formalin, the variation being from 540 ppm to 412 ppm. The results clearly show that higher concentrations of formaldehyde solution lead to greater releases of formaldehyde gas, as detected by the

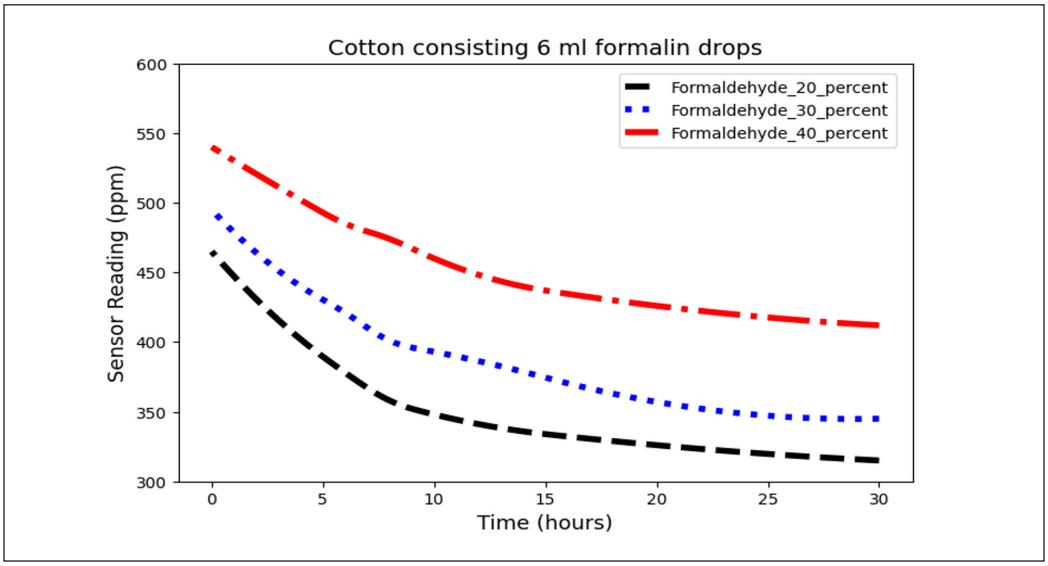

Figure 10. Sensor data from the E-nose sensor detecting formaldehyde in the cotton sample

sensor. This occurs because formaldehyde is a volatile organic compound (VOC), which easily evaporates from the solution and becomes a gas at normal temperatures (Li et al., 2023; Ali et al., 2020; Minnesota Department of Health, 2024).

Figure 11 shows how the readings of the E-nose sensor varied when apples rinsed with different concentrations of formalin (solutions 4, 5, and 6) were inserted in zipper bags. While the readings were taken every 2-hour intervals, the trend shows an exponential decline, becoming almost equal to room conditions at around 23–24 hours. This explains that formalin sprayed on a fruit like an apple stays on the surface level of the apple for a maximum period of 23–24 hours. The lower the concentration of formalin, the lower the time it takes for the reading to level off. Apples that contain formalin concentrations of 40%, 30% and 20% took around 23 hours, 20 hours, and 15 hours, respectively, highlighting the fact that higher concentrations of formalin usually level off at a faster rate, indicating a higher amount of release of formaldehyde gases. This data also means that it is impossible to detect the presence of formalin via sensors after 25 hours have elapsed, as the readings become very close to room condition values.

Figure 12 shows how the reading varied in the case of apples soaked in distilled water after rinsing with formalin solution (solutions 1, 2, and 3). This is done to imitate the fact that several shopkeepers soak formalin-adulterated apples in water for some time before selling them (Panghal et al., 2018). Graphs show the gradual decline and level off within 15 hours in all three different cases. After 30 hours, all the readings reached very close to the room condition readings. What can be noted is that the formalin level at the surface almost neutralizes to zero around 20 hours, thus invalidating the fact that formalin enhances shelf life.

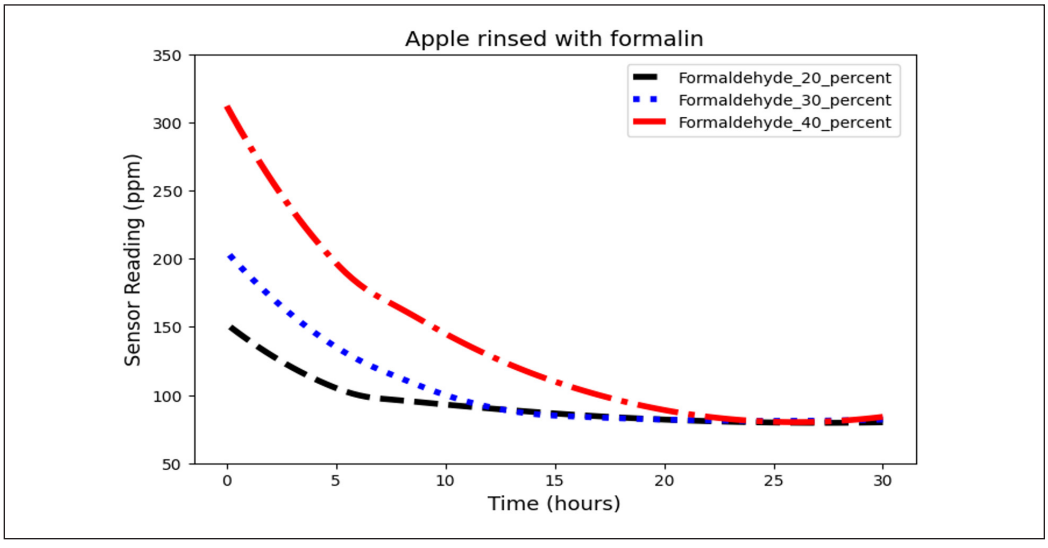

Figure 11. Sensor readings of the E-nose sensor when apples were rinsed with formalin

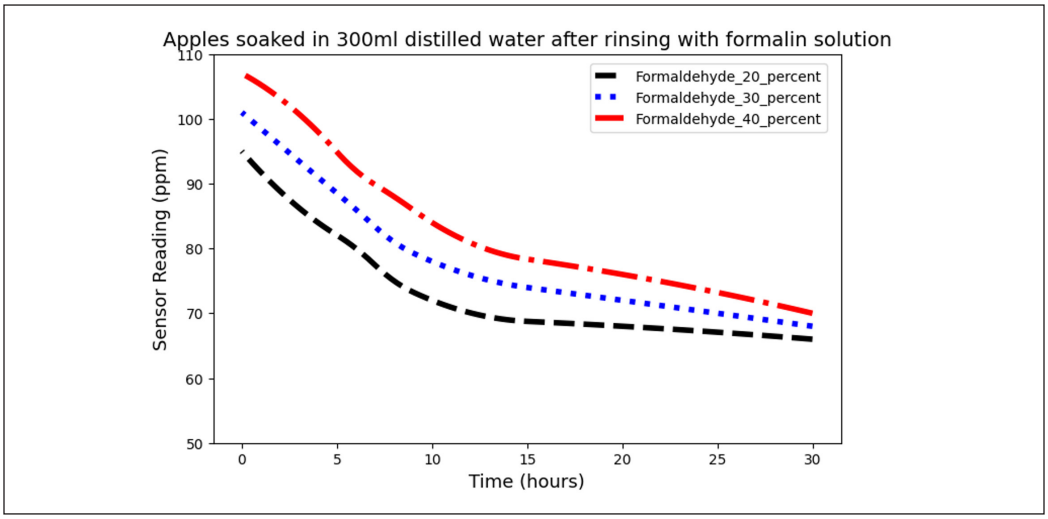

Figure 12. Sensor readings of the E-nose sensor for apples soaked in water after rinsing with formalin solution

Color Testing Reagent (BCSIR kit)

Figure 13 shows that the test kit from BCSIR showed slight color variance depending on the concentration of formalin present in the solution. The color observed varied from pale-yellowish to reddish-brown with increasing concentrations of formalin present in the solution, as shown in Table 4. As expected, the blank solution (distilled water) was pale yellow. A yellow solution

Figure 13. Different colors were observed when the test kit was applied to the solutions

Table 4
The color observed with the BCSIR kit

Solution Name	Constituent	Color Observed with BCSIR kit
Blank Solution	Distilled water	Pale-yellow
Solution 1	The solution from distilled water in which the 20% formalin-rinsed apple was soaked	Yellow
Solution 2	The solution from distilled water in which the 30% formalin-rinsed apple was soaked	Golden yellow
Solution 3	The solution from distilled water in which a 40% formalin-rinsed apple was soaked	Golden yellow
Solution 4	20% formalin solution	Deep golden yellow
Solution 5	30% formalin solution	Reddish brown
Solution 6	40% formalin Solution	Reddish brown

was observed in the case of solutions of distilled water in which a 20% formalin-rinsed apple was soaked (solution 1). A golden yellow color was observed in solutions of distilled water in which 30% and 40% formalin rinsed apples were soaked (solutions 2 and 3). Deep golden yellow and reddish brown color was observed for 20%, 30 %, and 40% concentration solutions of formalin (solutions 4, 5, and 6).

Concentration and Absorbance from Spectrophotometer

Thermal spectrophotometric measurements show an upward trend in absorbance value, highlighting the fact that higher concentrations of formalin result in higher values of absorbance, in accordance with Beer-Lambert's law, $A = \varepsilon lc$, where A is absorbance, ε is the molar extinction coefficient, c is the concentration, and l is the path length.

One factor that influences a sample's absorbance is its concentration. Since the amount of light absorbed depends on the number of molecules it interacts with, more radiation should be absorbed as the concentration rises. Hence, there is a direct proportionality between the concentration and absorbance, as shown in Table 5.

The concentration of the sample containing 20% formalin and distilled water was 38 M. The concentration value for 40% formalin and distilled water was 538 M. The sample consisting of 40% formalin had the highest absorbance and concentration values, 0.448 A and 17230 M, respectively.

As already mentioned above, spectrophotometry was also carried out with apples that were stored for 30 hours after being rinsed with solutions 1, 2, 3, 4, 5, and 6. The surface of the apple was rubbed with a cotton swab, and then the cotton swab was soaked in distilled water. The sample was then tested with the BCSIR kit and spectrophotometry. The results were very close to the results we got for the blank solution, indicating that the level of formalin on the surface has almost dropped to zero.

Table 5
Concentration and absorbance measurements from the spectrophotometer

Spectrophotometry Measurements	Spectrophotometer Absorbance Value at 568.5 nm	Concentration (M)
Distilled water	-0.006A	230.7692308
20% Formalin Apple + Distilled water	0.001A	38.46153846
30% Formalin Apple + Distilled water	0.004A	153.4615385
40% Formalin Apple + Distilled water	0.014A	538.4615385
20% Formalin	0.101A	3884.615385
30% Formalin	0.176A	6769.230769
40% Formalin	0.448A	17230.76923
Apples were rinsed with solutions 1–6 (stored for 30 hours) and rubbed with a cotton swab. Consequently, the swab was soaked in distilled water.	0.0053A-0.0059A	203.8461538-226.923076

Samples of Apples After 30 Hours

The samples were observed after 30 hours (Figure 14). The left column consists of apples to which no formalin was added, and the right column consists of apples to which artificial formalin was added.

Figure 14. Comparison of physical observations of untreated and formalin-treated apples after 30 hours

As we can see, the texture of the apples where formalin was added is more porous than those in which nothing was added. The skin texture also looks a bit dull. The dullness can be attributed to formaldehyde crosslinking cellulose, which weakens structural integrity and modifies pectin, leading to altered cell wall porosity (Altartouri et al., 2019; Marsh, 2008). Certainly, this does not make formalin-applied apples look fresher than non-applied apples, which agrees with the findings of Antora et al. (2018). Since, after 30 hours, the formalin level on the surface of apples almost declines to natural levels, formalin cannot achieve the desired or the speculated objective, that is, to increase the shelf life of apples. The findings align with those of previous studies conducted by Reza et al. (2023). From our investigation, we have observed that several studies have been conducted on detecting formalin with varied methods. However, little work has been done on how it generally affects the shelf life of apples or fruits.

The shelf life of fruits can be assessed using various methods that primarily focus on physical, chemical, microbiological, and sensory changes over time (Wertalik, 2024). Physical evaluation includes texture, color, and weight loss of the fruits. Chemical-based shelf life stability is attained by monitoring the nutrient degradation, sugar content and pH shifts. Microbiological assessments identify the spoilage organisms and pathogens, ensuring food safety. The sensory evaluation of fruit encompasses various attributes, including appearance, texture, taste, and aroma, which play a crucial role in consumer satisfaction (Lozano & Echeverria, 2022). Also, AI-driven tools have been used recently. In our research, we have employed chemical and sensory evaluation for formalin detection.

CONCLUSION

In this research, we have added formalin of three different concentrations (20%, 30%, 40%) to apples. The presence of formalin on the surface of the apples was studied using three different methods: (1) spectrophotometry, (2) a formalin test kit developed by the Bangladesh Council of Scientific and Industrial Research (BCSIR), and (3) an MS1100 gas sensor. Formalin's presence and concentration on the apple were detected using spectrophotometry and test kit detection. The MS1100 sensor can infer the formalin decay profile on the apple's surface.

Measurements with varying concentrations of formaldehyde applied to cotton showed significantly high emissions after 30 hours. However, in the case of apples rinsed with formalin for the same period, the readings revealed that the formalin level had dropped drastically to its natural state of 60–70 ppm. From the research, it can be stated that formalin does not improve the shelf life of apples and, in fact, it decreases the freshness of the fruit. Since formalin is able to preserve objects or bodies with higher protein content, the conclusion aligns with the theory, as apple has only 1% protein. In pursuit of concluding this observation, we have used three methods of formaldehyde detection. The methods include the MS1100 sensor working as an E-nose, the BCSIR test Kit, and spectrophotometry. It can be concluded that the results attained through the E-nose matched the results of the test kit and the spectrophotometry. These results confirm that the E-nose (MS1100) can detect formaldehyde effectively and effortlessly. Alternate typical detection methods include formaldehyde BCSIR kit, test strip, reagent paper, portable spectrophotometers, immunoassays, and fluorescence.

However, the drawbacks of these methods are that they require considerable time and are complex for consumers to use. In contrast, the E-nose offers a simple, easy-to-implement, reusable solution and fast detection time. However, using it to detect formaldehyde application on fruits will not work since the formaldehyde loses its existence after a few days. It will only detect the emission of naturally produced formaldehyde from the apple. Nevertheless, even though the apple stopped emitting formalin at a level above the natural level after 30 hours, the cotton wool kept on emitting formaldehyde. This indicates that formaldehyde reacts with apples somehow, which could be a topic for further research. The experiments also established that putting the apples for 30 minutes in water can significantly remove the presence of formaldehyde on apples.

ACKNOWLEDGEMENTS

We thank the Department of Mathematics and Natural Science (MNS) of BRAC University for facilitating our experiments.

REFERENCES

Ahmad, M. F., Ahmad. F. A., Alsayegh, A. A., Zeyaullah, M., AlShahrani, A. M., Muzammil, K., Saati, A. A., Wahab, S., Elbendary, E. Y., Kambal, N., Abdelrahman, M. H., & Hussain, S. (2024). Pesticides impact human health and the environment with their mechanisms of action and possible countermeasures. *Heliyon, 10*(7), Article e29128. https://doi.org/10.1016/j.heliyon.2024.e29128

Alam, H. (2013, June 12). Formalin in fruits. *The Daily Star*. https://www.thedailystar.net/news/formalin-in-fruits

Ali, M. M., Hashim, N., Aziz, S. A., & Lasekan, O. (2020). Principles and recent advances in electronic nose for quality inspection of agricultural and food products. *Trends in Food Science & Technology, 99*, 1–10. https://doi.org/10.1016/j.tifs.2020.02.028

Ali, N. M. A. (2013). Application of responsive regulation in the food safety regulations of Bangladesh. *Journal of South Asian Studies, 1*(1), 1–9.

Ali, N. M. A. (2013). Food safety and public health issues in Bangladesh: A regulatory concern. *European Food & Feed Law Review, 8*(1), 31–40.

Altartouri, B., Bidhendi, A. J., Tani, T., Suzuki, J., Conrad, C., Chebli, Y., Liu, N., Karunakaran, C., Scarcelli, G., & Geitmann, A. (2019). Pectin chemistry and cellulose crystallinity govern pavement cell morphogenesis in a multi-step mechanism. *Plant Physiology, 181*(1), 127–141. https://doi.org/10.1104/pp.19.00303

American Chemistry Council. (2025). *Formaldehyde occurs naturally and is all around us*. American Chemistry Council. https://www.americanchemistry.com/chemistry-in-america/chemistries/formaldehyde

Antora, R. A., Hossain, M. P., Monira, S. S. U., & Aziz, M. G. (2018). Effect of formaldehyde on some post-harvest qualities and shelf-life of selected fruits and vegetables. *Journal of Bangladesh Agricultural University, 16*(1), 151–157. https://doi.org/10.3329/jbau.v16i1.36496

Baldwin, E., Bai, J., Plotto, A., & Dea, S. (2011). Electronic noses and tongues: Applications for the food and pharmaceutical industries. *Sensors, 11*, 4744–4766. https://doi.org/10.3390/s110504744

Bangladesh Council of Scientific and Industrial Research. (2023). *Formalin detection kit for fish and milk*. Bangladesh Council of Scientific and Industrial Research. https://ifst.bcsir.gov.bd/site/notices/caee1e34-b839-42f0-87ac-2d5da620a33b/Formalin-detection-kit-for-fish-and-Milk

Bini, M., Babu, R., & Babu, T. D. (2019). Acute and subacute toxicity evaluation of calcium carbide and ethylene glycol in *Wistar albino* rats. *Journal of Basic and Clinical Physiology and Pharmacology, 31*(1), Article 126. https://doi.org/10.1515/jbcpp-2019-0126

Brighty, S. P. S., Harini, G. S., & Vishal, N. (2021). Detection of adulteration in fruits using machine learning. In *Proceedings of the Sixth International Conference on Wireless Communication, Signal Processing and Networking (WiSPNET)* (pp. 37–40). IEEE Publishing. https://doi.org/10.1109/WiSPNET51692.2021.9419402

Brighty, S. P. S., Harini, G. S., & Vishal, N. (2021). Detection of adulteration in fruits using machine learning. In *2021 Sixth International Conference on Wireless Communications, Signal Processing and Networking (WiSPNET)* (pp. 37-40). IEEE Publishing. https://doi.org/10.1109/WiSPNET51692.2021.9419402

Datasheet4U. (2025). *Product information: Sensor for air quality control*. Datasheet4U. https://www.datasheet4u.com/datasheet-pdf/ETC/MS1100/pdf.php?id=813045

Dey, S., & Nagababu, B. H. (2022). Applications of food color and bio-preservatives in the food and its effect on human health. *Food Chemistry Advances, 1*, Article 100019. https://doi.org/10.1016/j.focha.2022.100019

Directorate General of Health Services. (2012). *Public health interventions by selected institutions*. Ministry of Health and Family Welfare, Government of the People's Republic of Bangladesh. http://nasmis.dghs.gov.bd/dghs_new/dmdocuments/All/Public%20Health%20Interventions.pdf

Essien, E. B., Onyegeme-Okerenta, B. M., & Onyema, J. O. (2018). Calcium carbide as an artificial fruit-ripening agent and its physiological effects on Wistar rats. *Clinical and Experimental Medicine, 6*(1), 47–61.

Fan, G., Guan, J., Yu, H., Zhu, Q., Han, N., Mo, J., & Chen, Y. (2024). Highly sensitive formaldehyde gas sensor based on SnO_2/Zn_2SnO_4 hybrid structures. *Building and Environment, 262*, Article 111781. https://doi.org/10.1016/j.buildenv.2024.111781

Guo, M. (1994). Preservation of food coating. *Food Science, 12*, 69–71.

Headlines and Global News. (2014, June 9). Deadly formalin-laced fruits in Bangladesh could cause slow poison mass killing. *Headlines and Global News*. https://baures.bau.edu.bd/wp-content/uploads/2018/04/24.-JBAU-2017-046-revisedpaper-1-1.pdf

Huda, M. M. (2025, February 28). Adulterated-food culture in Bangladesh: A new form of epidemic. *Dhaka Tribune*. https://www.dhakatribune.com/bangladesh/284997/adulterated-food-culture-in-bangladesh-a-new-form

Instrument Center. (2018). *Thermo Scientific GENESYS 10S Series, UV-Visible Spectrophotometers*. Instrument Center. https://science.sjp.ac.lk/instrumentcenter/instruments/uv-visible-spectrophotometers/#:~:text=Our%20UV%2DVis%20analysis%20is,spectra%20from%20190%2D1100%20nm

International Agency for Research on Cancer. (2004). *Monographs on the Evaluation of Carcinogenic Risks to Humans, Vol. 88, Formaldehyde, 2-Butoxyethanol and 1-Tert-Butoxy-2-Propanol*. International Agency for Research on Cancer. https://www.scirp.org/reference/referencespapers?referenceid=2396199

International Agency for Research on Cancer. (2006). *Monographs on the Evaluation of Carcinogenic Risks to Humans Vol. 88, Formaldehyde, 2-Butoxyethanol and 1-tert-Butoxypropan-2-ol*. International Agency for Research on Cancer. https://publications.iarc.fr/106

Islam, R., Mahmud, S., Aziz, A., Sarker, A., & Nasreen, M. (2015). A comparative study of the present status of marketing of formalin-treated fishes in six districts of Bangladesh. *Food and Nutrition Sciences, 6,* 124–134.

Jia, M., Shao, L., Jiang, J., Jiang, W., Xin, F., Zhang, W., Jiang, Y., & Jiang, M. (2024). Mitigating toxic formaldehyde to promote efficient utilization of C1 resources. *Critical Reviews in Biotechnology, 8*, 1–13. https://doi.org/10.1080/07388551.2024.2430476

Kamruzzaman, M. (2016). Formalin crime in Bangladesh: A case study. *European Journal of Clinical and Biomedical Sciences*, *2*(5), 39–44. https://doi.org/10.11648/j.ejcbs.20160205.12

Kawamata, S., & Kodera, H. (2004). Reduction of formaldehyde concentrations in the air and cadaveric tissues by ammonium carbonate. *Anatomical Science International, 79*(3), 152–157. https://doi.org/10.1111/j.1447-073x.2004.00075.x

Kiernan, J. A. (2000). Formaldehyde, formalin, paraformaldehyde, and glutaraldehyde: What they are and what they do. *Microscopy Today, 1*(5), 8–12.

Li, Y., Ou, J., Huang, C., Liu, F., Ou, S., & Zheng, J. (2023). Chemistry of formation and elimination of formaldehyde in foods. *Trends in Food Science & Technology, 139*, Article 104134. https://doi.org/10.1016/j.tifs.2023.104134

Lozano, L., & Echeverria, G. (Eds.). (2022). *Sensory Evaluation for the Fruit Quality: Latest Advances and Prospects*. MDPI.

Mäntele, W., & Deniz, E. (2017). UV–VIS absorption spectroscopy: Lambert-Beer reloaded. *Spectrochimica Acta Part A: Molecular and Biomolecular Spectroscopy, 173,* 965–968. https://doi.org/10.1016/j.saa.2016.09.037

Marsh, J. (2008). Cellulose and formaldehyde**.** *Journal of the Society of Dyers and Colourists, 75*, 244–252. https://doi.org/10.1111/j.1478-4408.1959.tb02322.x

Minnesota Department of Health. (2024). *Formaldehyde in your home*. Minnesota Department of Health. https://www.health.state.mn.us/communities/environment/air/toxins/formaldehyde.htm

Mohiuddin, A. K. (2019). Chemical contaminants and pollutants in the measurable life of Dhaka City. *European Journal of Sustainable Development Research, 3*(2), Article em0083. https://doi.org/10.29333/ejosdr/5727

Nag, S., Das, D., Tudu, B., & Roy, R. B. (2021). Multivariate analysis of formalin using UV-Vis spectroscopy. In *2021 IEEE Second International Conference on Control, Measurement and Instrumentation (CMI)* (pp. 133-137). IEEE Publication. https://doi.org/10.1109/CMI50323.2021.9362970

National Center for Biotechnology Information. (1999). *Health effects toxicological profile for formaldehyde.* National Center for Biotechnology Information. https://www.ncbi.nlm.nih.gov/books/NBK597627/

Nowshad, F., Islam, M. N., & Khan, M. S. (2018). Concentration and formation behavior of naturally occurring formaldehyde in foods. *Agriculture & Food Security, 7*, Article 17. https://doi.org/10.1186/s40066-018-0166-4

Nura, M., Dandago, M., & Wali, N. (2018). Effects of artificial ripening of banana (Musa spp) using calcium carbide on acceptability and nutritional quality. *International Journal of Postharvest Technology, 6*(2), 14–20.

Nurjayadi, M., Romundza, F., & Moersilah, M. (2021). Application of the Lambert-Beer legal concept in learning spectroscopy UV-Vis with simple spectrophotometers. In *AIP Conference Proceedings* (Vol. 2331, No. 1). AIP Publishing. https://doi.org/10.1063/5.0041895

Panghal, A., Yadav, D. N., Khatkar, B. S., Sharma, H., Kumar, V., & Chhikara, N. (2018). Post-harvest malpractices in fresh fruits and vegetables: Food safety and health issues in India. *Nutrition & Food Science, 48*(4), 561–578. https://doi.org/10.1108/NFS-09-2017-0181

Protano, C., Buomprisco, G., Cammalleri, V., Pocino, R. N., Marotta, D., Simonazzi, S., Cardoni, F., Petyx, M., Iavicoli, S., & Vitali, M. (2021). The carcinogenic effects of formaldehyde occupational exposure: A systematic review. *Cancers, 14*(1), Article 165. https://doi.org/10.3390/cancers14010165

Rahman, M. A., Sultan, M. Z., Rahman, M. S., & Rashid, M. A. (2015). Food adulteration: A serious public health concern in Bangladesh. *Bangladesh Pharmaceutical Journal, 18*(1), 1–7. https://doi.org/10.3329/bpj.v18i1.23503

Rahman, M. B., Hussain, M., Kabiraz, M. P., Nordin, N., Siddiqui, S. A., Bhowmik, S., & Begum, M. (2023). An update on formaldehyde adulteration in food: Sources, detection, mechanisms, and risk assessment. *Food Chemistry, 427*, Article 136761. https://doi.org/10.1016/j.foodchem.2023.136761

Reza, M. S. A., Shuvo, S. D., Rahman, M. A., Sultana, R., Bashi, L. A., Khalko, M., Abedin, M. Z., & Bari, L. (2023). The impact of formalin on postharvest quality, shelf life, and nutritive properties of carrot, papaya, plum, apple plum, and guava. *Current Research in Nutrition and Food Science Journal, 11*(1), Article 24. https://dx.doi.org/10.12944/CRNFSJ.11.1.24

Tamanna, I. M. (2024). Food adulteration and inadequate hygiene practices endangering public health in Bangladesh. *Discover Food, 4*, Article 109. https://doi.org/10.1007/s44187-024-00191-8

The Daily Star. (2014, November 25). Find proper formalin detection kit. *The Daily Star*. https://www.thedailystar.net/find-proper-formalin-detection-kit-51965

The Nutrition Source. (2024). *Apples.* The Nutrition Source. https://nutritionsource.hsph.harvard.edu/food-features/apples/

Thermo Scientific. (2010). *Thermo Scientific Genesys 10S: UV-Visible Spectrophotometers*. Thermo Scientific. https://www.thermofishersci.in/lit/Thermo%20Scientific%20Genesys%2010S.pdf

Uddin, R., Wahid, M. I., Jasmeen, T., Huda, N. H., & Sutradhar, K. B. (2011). Detection of formalin in fish samples collected from Dhaka City, Bangladesh. *Stamford Journal of Pharmaceutical Sciences, 4*(1), 49–52. https://doi.org/10.3329/sjps.v4i1.8866

United Nations. (2007). *The state of the world's children 2008: Child survival*. UNICEF. http://www.unicef.org/sowc08/docs/sowc08.pdf

Wertalik, P. (2024). *Shelf life testing of fruits: A laboratory guide to principles and methods*. OUTSOURCE. Retrieved from https://outsource.contractlaboratory.com/shelf-life-testing-of-fruits-a-laboratory-guide-to-principles-and-methods/

Wojdyło, A., Oszmiański, J., & Laskowski, P. (2008). Polyphenolic compounds and antioxidant activity of new and old apple varieties. *Journal of Agricultural and Food Chemistry, 56*(15), 6520–6530. https://doi.org/10.1021/jf800510j

World Health Organization. (2000). *Air quality guidelines for Europe*. World Health Organization. http://www.euro.who.int/__data/assets/pdf_file/0005/74732/E71922.pdf

Yang, Y., Hao, Y., Huang, L., Luo, Y., Chen, S., Xu, M., & Chen, W. (2024). Recent advances in electrochemical sensors for formaldehyde. *Molecules, 29*(2), Article 327. https://doi.org/10.3390/molecules29020327

Zhang, Y., Wang, M., San, X., Zhang, L., Wang, N., Wang, G., Meng, D., & Shen, Y. (2023). Highly selective gas sensors for formaldehyde detection based on ZnO@ZIF-8 core-shell heterostructures. *Sensors and Actuators B: Chemical, 398*, Article 134689. https://doi.org/10.1016/j.snb.2023.134689

Pertanika J. Sci. & Technol. 33 (4): 1849 - 1868 (2025)

PERTANIKA JOURNALS

SCIENCE & TECHNOLOGY

Journal homepage: http://www.pertanika.upm.edu.my/

Morphological and Genetic Relationship of Ancient Shan Tea Tree (*Camellia sinensis* var. *assamica*) from Ecogeographical Regions in Northern Vietnam

Lien Thuy Bui[1,2,3], Phong Xuan Ong[1,2], Thiep Van Nguyen[1], Khang Tan Do[4], Huy Gia Tran[4], Phi Bang Cao[5], Ha Duc Chu[6], Dung Phuong Le[7] and Hong Viet La[1,2]*

[1]*Institute for Scientific Research and Application, Hanoi Pedagogical University 2, 32 Nguyen Van Linh Street, Xuan Hoa Ward, Phuc Yen City, Vinh Phuc Province, 280000, Vietnam*
[2]*Faculty of Biology, Hanoi Pedagogical University 2, 32 Nguyen Van Linh Street, Xuan Hoa Ward, Phuc Yen City, Vinh Phuc Province, 280000, Vietnam*
[3]*Department of Secondary Education, Hoa Lu University, Ninh Binh City, Ninh Binh Province 430000, Vietnam*
[4]*Institute of Food and Biotechnology, Can Tho University, Campus II, 3/2 street, Xuan Khanh, Ninh Kieu, Can Tho City 900000, Vietnam*
[5]*Faculty of Natural Sciences, Hung Vuong University, Nong Trang Ward, Viet Tri City, Phu Tho Province 35000, Vietnam*
[6]*Faculty of Agricultural Technology, University of Engineering and Technology, Vietnam National University Hanoi, 144 Xuan Thuy Street, Cau Giay District, Ha Noi City 122300, Vietnam*
[7]*Department of Science, Technology and Environment, Vietnam Ministry of Education and Training, 35 Dai Co Viet, Le Dai Hanh Ward, Hai Ba Trung Dist, Ha Noi City 122300, Vietnam*

ABSTRACT

The genetic diversity of ancient tea plants is a crucial natural resource that helps understand plant evolution, diversification, and domestication. However, northern Vietnam's genetic diversity of natural ancient tea populations remains unclear. This study investigated the morphological, genetic, and population structure diversity of ancient Shan tea (*Camellia sinensis* var. *assamica*) genotypes across Lao Cai, Yen Bai, and Ha Giang provinces in northern Vietnam. Nineteen tree stems, leaves, and shoots morphological traits were analyzed, revealing significant leaf size, bud characteristics, and trunk circumference variability. Principal Component Analysis identified key morphological traits contributing to diversity, particularly leaf length, bud length, and shoot weight, with distinct groupings among the tea plants. Genetic profiling using ISSR markers amplified 96 bands, with 94 showing polymorphic characteristics, indicating

ARTICLE INFO

Article history:
Received: 05 December 2024
Accepted: 17 March 2025
Published: 11 June 2025

DOI: https://doi.org/10.47836/pjst.33.4.08

E-mail addresses:
btlien@hluv.edu.vn (Lien Thuy Bui)
ongxuanphong@hpu2.edu.vn (Phong Xuan Ong)
thiepvcph@gmail.com (Thiep Van Nguyen)
dtkhang@ctu.edu.vn (Khang Tan Do)
tghuy@ctu.edu.vn (Huy Gia Tran)
phibang.cao@hvu.edu.vn (Phi Bang Cao)
hachu_amser@yahoo.com (Ha Duc Chu)
lephuongdungkstn@gmail.com (Dung Phuong Le)
laviethong@hpu2.edu.vn (Hong Viet La)
* Corresponding author

© Universiti Putra Malaysia Press

a high level of genetic diversity. ANOVA revealed that 88% of the genetic variance occurs within populations, further supported by UPGMA clustering and Principal Coordinates Analysis, highlighting the genetic distinctions and similarities among the three tea populations. The study concludes that the morphological and genetic diversity of Shan tea is influenced by eco-geographical factors, underscoring the need for conservation efforts to preserve these valuable germplasm resources for future breeding and research.

Keywords: Ancient Shan tea, eco-geographical regions, ISSR marker, morphological, Northern Vietnam

INTRODUCTION

Camellia sinensis (L.) O. Kuntze, a member of the Theaceae family, is a globally important crop cultivated in over 52 countries, with China and India leading in production (Chen & Chen, 2012; FAOSTAT, 2023). The species includes several varieties, notably *C. sinensis* var. *sinensis* and *C. sinensis* var. *assamica*, both extensively used in tea cultivation (Meegahakumbura et al., 2017). Believed to have been domesticated in southwest China around 3000 BCE (Wambulwa et al., 2017), tea plants have adapted to a range of environmental conditions, flourishing in humid, tropical, and subtropical regions with acidic, well-drained soils (Ahmed & Stepp, 2025; Xia et al., 2020). In Vietnam, the ancient Shan tea, classified as *C. sinensis* var. *assamica*, is primarily found in the high mountainous areas of Son La, Ha Giang, Yen Bai, and Lao Cai provinces. Renowned for its large leaves and distinctive biochemical profile, this variety is highly valued for its tea production (Liu et al., 2017; Xia et al., 2017). Preserving ancient Shan tea is crucial, as it represents a unique genetic resource essential for maintaining biodiversity, supporting sustainable cultivation, and preventing genetic erosion due to environmental and human influences.

The preservation of plant genetic resources has garnered much attention lately. Understanding the genetic diversity within and between populations is crucial for designing effective and economical conservation approaches for plant genetic resources (Guney et al., 2021). Genetic diversity analysis in plants, mainly through DNA markers, is crucial for plant breeding and conservation (Nwosisi et al., 2019). For studying the genetic diversity of tea trees, various molecular markers, such as simple sequence repeat (SSR) (Li et al., 2024) and SSR combined start codon targeted (SCoT) markers (Samarina et al., 2021), have been used. Recently, the genetic diversity of *C. yuhsienensis* was assessed using leaf structure and inter-simple sequence repeat (ISSR) markers; most of the markers have effectively assessed this diversity and can aid in conserving and utilizing these valuable genetic resources (Zou et al., 2024).

Ancient Shan tea has revealed its potential for cross-compatibility with other tea varieties, particularly *C. sinensis* var. *sinensis* (Kumarihami et al., 2016). This cross-compatibility has been attributed to a late-acting self-incompatibility system or post-

zygotic barriers (Kumarihami et al., 2016). Furthermore, the chloroplast and mitochondrial genomes of Shan tea have been deciphered, providing valuable resources for genetic and comparative genomic studies (Zhang et al., 2019). Zhao et al. (2021) investigated the genetic diversity of ancient tea plants. They suggested that the genetic and phenotypic diversity of 145 ancient tea plant germplasm resources from five populations in Sandu County, Guizhou Province, China, was relatively high. The analysis of molecular variance showed that genetic variation within the populations was more significant than among the populations (Zhao et al., 2021).

This study investigated the morphological diversity and genetic relationships of ancient Shan tea trees across three northern provinces of Vietnam, including Lao Cai, Yen Bai, and Ha Giang. The study evaluated 19 morphological traits of leaves and shoots and used ISSR molecular markers to assess the genetic diversity within and between tea populations. Through the analysis of principal components, genetic clustering, and principal coordinates analysis, the study seeks to explore the impact of environmental factors and geographical distances on the morphological and genetic characteristics of ancient tea trees, providing insights into their conservation and breeding. Our findings will provide further insights into the genetic relationships of ancient tea sources in Northern Vietnam based on leaf morphology and ISSR markers, providing a scientific basis for the protection and utilization of this ancient tea plant.

MATERIALS AND METHODS

Sample Collection

Thirty-six individuals of ancient Shan tea were obtained from three locations that belonged to three provinces in northern Vietnam, including Cao Bo commune (Vi Xuyen district, Ha Giang province, denoted as HG.LT 1-14), Suoi Bu commune (Van Chan district, Yen Bai province, denoted as YB.SB 1-7), and Ta Thang commune (Muong Khuong district, Lao Cai province, denoted as LC.TT 1-16) (Figure 1).

Morphological Description

The assessment of nineteen morphological characteristics of the stem, leaf, and bud of the ancient Shan tea tree used the International Plant Genetic Resources Institute's guidelines (IPGRI, 1997), with a few minor modifications (Vo, 2007). The young shoots' fifth leaves were chosen for description. The tea bud with one tip and three leaves, located at position 2/3 of the internode between the third and fourth leaves, is where the buds selected for analysis are harvested. Digital calipers with a 0.01 cm sensitivity were used to measure the shoots' weight using precision scales that were sensitive to ± 0.01 g. Meanwhile, shoot length, leaf, and stem measurements were collected using the same equipment. Each morphological trait was measured in 30 replicates per plant, and 36 individuals were

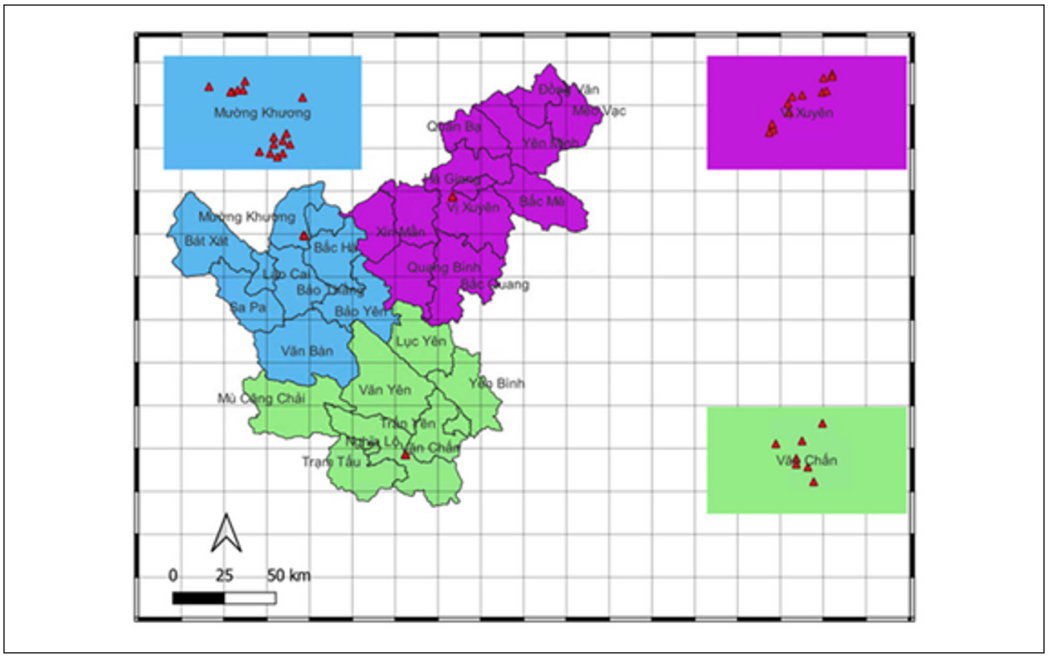

Figure 1. A map of three ecogeographical locations, Yen Bai, Lao Cai, and Ha Giang provinces, was expressed in green, purple, and blue, respectively. Tea genotypes were collected and used in morphological and molecular analyses

assessed across the three studied populations. The means of these replicates were used for statistical analysis, ensuring accuracy and minimizing measurement variability.

Genetic Diversity and Relationship of Ancient Tea Trees

DNA Isolation

Healthy leaves were sterilized with 70% (v/v) alcohol to remove dust and microbes on the surface. Liquid nitrogen was utilized to grind the leaf samples into homogenized powder. The DNA extraction was conducted following the cetrimonium bromide (CTAB) based protocol (Rogers & Bendich, 1989) with appropriate modifications. The quantity and quality of DNA were measured by the Nanodrop One spectrophotometer (Thermo Scientific, USA). DNA integrity was performed by 1% (w/v) agarose electrophoresis at 100V in Tris-acetate-EDTA 1X.

Amplification of ISSR Markers

Ten ISSR primers were used to characterize the genetic diversity (Table 1). The 10 µL reaction consisted of 2 µL deionized water, 5 µL master mix 2X (Biohelix, Taiwan), 1 µL primer (20 µM), and 2 µL DNA template (equivalent to 100 ng). Amplifications were performed by a Mastercycler X50s (Eppendorf, Germany) with the thermal cycle program:

an initial denaturation of 95°C in 4 minutes, 40 cycles included three stages; 94°C in 30 seconds, an appropriate annealing temperature (Ta) in 1 minute, 72°C in 2 minutes; a final extension of 72°C in 10 minutes. PCR products were kept stable at 4°C until use. The PCR products were tested by 2% agarose gel electrophoresis (25V, TAE 1X) in 1 hour and 30 minutes. Band patterns were visualized under UV light in the Gel Doc. XR system (Bio-Rad, USA).

Table 1
Ten primers were used for the PCR products

Primer	Nucleotide sequences (5'-3')	Annealing temperature (°C)
ISSR825	$(AC)_8T$	46
ISSR855	$(AC)_8CT$	46
ISSR866	$(CTC)_6$	52
ISSR827	$(AC)_8G$	50
ISSR811	$(GA)_8C$	45
ISSR813	$(AC)_8CA$	51
ISSR818	$(GA)_8CT$	44.7
ISSR823	$GAA(GT)_7$	51
ISSR826	$(AC)_8C$	46
ISSR889	$ATG(AC)_7$	52

Construction of a Dendrogram Tree

Scored bands were transferred into binary data with Microsoft Excel software version 2021; the presence and absence of a band were scored as 1 and 0, respectively. The dendrogram was constructed using the unweighted pair group method with the arithmetic mean (UPGMA) method using NTSYS-pc 2.1 software. Correspondence analysis was conducted using Biodiversity Pro software. Genetic diversity indices of each marker include PB (polymorphic band), PIC (polymorphism information content), EMR (effective multiplex ratio, MI (marker index, D (discriminating power), and R (resolving power) were calculated by the iMEC web-based program (Amiryousefi et al., 2018). Analysis of molecular variation (AMOVA) and principal coordinate analysis (PCoA) were utilized by the GenAlEx software version 6.51b2 (Smouse et al., 2017).

Data Analysis

All data were analyzed and presented as mean values. Differences between the mean values were tested using ANOVA and ranked using the least significant difference (LSD) method at $P < 0.05$ with SPSS 20.0 software. Principal component analysis (PCA) was analyzed using Minitab statistical software.

RESULTS

Morphological Traits of Ancient Tea Leaves and Shoots

Morphological Description

Nineteen morphological characteristics of ancient Shan tea tree stems, leaves, and shoots were recorded and evaluated in Lao Cai, Yen Bai, and Ha Giang provinces. Regarding tree shape, most trees have an arbor or semi-arbor shape (Figure 2). All trees have large trunk

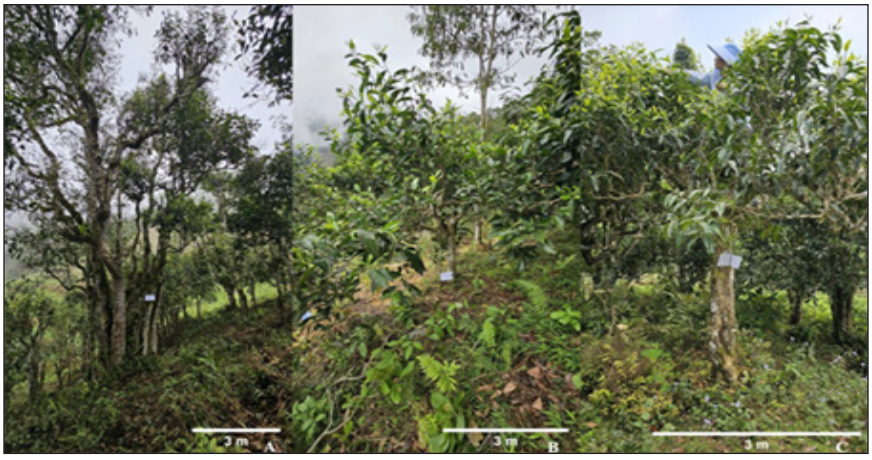

Figure 2. Ancient Shan tea tree shapes from three locations in northern Vietnam (A: LC.TT 15; B: YB.SB 5; C: LC.LT 9)

circumferences, the LC.TT15 tree has the largest trunk circumference, reaching 270 cm, and the lowest is the YB.SB 5 tree, reaching 48 cm (Table 2).

The criteria of leaf angle, leaf shape, leaf angle shape, leaf serration, and lower leaf surface are all diverse. The colors of leaves and buds vary; most are green and yellow-green. The leaf size ranges from 9.12 × 3.5 cm (LC.TT12) to 21.06 × 6.78 cm (HG.LT13). Some individuals with large leaf sizes are grouped like trees, HG to the right of Figure 3. LT2, 9, 13, and YB.SB4, 6. HG.LT13 has the highest number of pairs of main veins in the leaf (13.0) and the lowest number of pairs of main veins in the leaf of LC.TT10 (8.4). The color of the buds is mostly yellow-green; a few buds are green or light green; on all buds, there are thick snow hairs. Bud length and bud weight are very different (Table 2). Bud length ranges from 10.4 cm (HG.LT 11) to 17.78 cm (YB.SB6). Our results revealed that a number of individuals in Yen Bai (YB.SB1, 2, 4, 5, and 6) have bud length and weight much higher than the samples collected in Ha Giang and Lao Cai.

Principal Component Analysis (PCA)

PCA analysis and phylogenetic tree showed that eco-geographical regions strongly impacted the clustering of both wild tea (He et al., 2023) and cultivated tea plants (Zhao et al., 2022). In order to find which morphological parameters are essential to the growth of ancient tea trees, the statistical PCA was applied. The original set of variables is changed into a new set known as principal components (PCs), uncorrelated variables. The results of principal component analysis and correlation analysis based on the morphological data of ancient tea from three locations in northern Vietnam are expressed in Table 3. Based on the morphological data of the ancient Shan tea genotype, PCA, correlation analysis, and contribution ratio, it is revealed that the seven components explained 100% of the overall variation. The first main

Table 2
Morphological characteristics analyzed in tea genotypes

Genotype	Tree type**	The stem circumference (cm)	The height of the first branching position (cm)	Leaf pose**	Leaf shape**	leaf apex shape**	Leaf base shape**	Leaf serrula form**	Leaf upper surface**	Color of the leaf**	Leaf length (cm)	Leaf breadth (cm)	Leaf length/ breadth ratio	Number of pairs of main veins on the leaf surface	Length of the leaf petiole (cm)	Color of the shoot**	Pubescence density on bud**	Length of the shoot (cm)	Mean of fresh shoot weight (g/shoot)
LC.TT1	2	72	28	2	4	2	1	1	1	2	15.54^{cde*}	5.92^{bc}	2.63	9.8^{f-j}	0.64^{f-k}	2	3	14.76^{b-f}	1.92
LC.TT2	1	88	150	3	4	2	1	1	1	3	11.08^{nop}	4.58^{h-k}	2.42	9.6^{f-k}	0.54^{k-n}	5	3	12.14^{i-m}	1.53
LC.TT3	2	70	33	2	4	2	1	1	1	2	13.98^{fgh}	6.28^{b}	2.23	8.8^{h-k}	0.64^{f-k}	2	3	12.02^{j-o}	1.52
LC.TT4	2	70	22	4	4	2	1	2	1	2	12.16^{k-n}	4.52^{ijk}	2.69	8.8^{h-k}	0.52^{lmn}	2	3	14.62^{c-g}	1.80
LC.TT5	1	115	43	3	1	2	2	4	1	2	13.62^{f-j}	5.10^{fg}	2.67	9.8^{f-j}	0.76^{b-e}	5	3	17.62^{a}	2.38
LC.TT6	1	150	150	2	4	1	1	1	1	2	14.28^{fg}	5.86^{bc}	2.44	9.8^{f-j}	0.76^{b-e}	2	3	14.32^{c-g}	1.70
LC.TT7	1	200	50	2	1	2	2	1	1	3	15.54^{cde}	6.86^{a}	2.27	10.4^{d-g}	0.78^{bcd}	2	3	13.60^{e-j}	1.45
LC.TT8	1	186	46	2	1	2	1	1	1	2	12.86^{h-l}	3.68^{mn}	3.49	8.6^{ijk}	0.54^{k-n}	2	3	13.86^{d-h}	1.71
LC.TT9	1	112	160	2	4	2	1	2	1	3	14.86^{def}	6.74^{a}	2.20	9.8^{f-j}	0.66^{e-j}	5	3	13.24^{f-k}	1.60
LC.TT10	1	74	112	2	4	2	1	2	1	5	10.76^{op}	4.24^{jkl}	2.54	8.4^{jk}	0.72^{c-g}	5	3	14.4^{c-g}	1.31
LC.TT11	3	117	0	2	4	2	1	2	1	2	12.78^{h-m}	5.20^{d-g}	2.46	9.8^{f-j}	0.68^{d-i}	5	3	15.02^{b-e}	2.01
LC.TT12	3	85	0	3	4	1	1	1	1	2	9.12^{q}	3.50^{n}	2.61	9.8^{f-j}	0.50^{mn}	5	3	15.52^{bcd}	2.10
LC.TT13	1	202	20	2	4	2	1	1	1	2	13.08^{g-k}	5.62^{cde}	2.33	9.2^{g-k}	0.66^{e-j}	5	3	12.56^{h-l}	1.48
LC.TT14	1	160	50	2	2	2	2	1	1	3	13.06^{g-k}	5.74^{c}	2.28	10.4^{d-g}	0.54^{k-n}	5	3	13.04^{g-k}	1.50
LC.TT15	1	270	0	2	4	1	1	1	1	3	12.98^{h-k}	5.54^{c-f}	2.34	9.6^{f-k}	0.56^{j-n}	5	3	12.08^{i-n}	1.29
LC.TT16	1	164	17	2	1	1	2	3	1	2	14.82^{def}	5.98^{bc}	2.48	9.8^{f-j}	0.72^{c-g}	5	3	13.74^{e-i}	1.65
YB.SB1	2	136	19	2	4	1	1	2	1	2	16.06^{cd}	5.68^{cd}	2.83	10.4^{d-g}	0.76^{b-e}	5	3	16.34^{ab}	2.02
YB.SB2	2	114	28	2	4	1	1	3	1	2	14.80^{def}	5.06^{fgh}	2.92	9.6^{f-k}	0.86^{b}	5	3	15.72^{bc}	2.20
YB.SB3	3	94	18	2	4	2	1	1	1	1	11.76^{l-o}	3.96^{lmn}	2.97	8.2^{k}	0.52^{lmn}	5	3	10.72^{mno}	1.45
YB.SB4	2	64	88	2	4	1	1	1	1	3	16.20^{c}	5.14^{efg}	3.15	10.2^{d-h}	0.7^{c-h}	5	3	17.24^{a}	2.91
YB.SB5	2	48	106	2	1	2	2	3	1	2	14.02^{fgh}	5.66^{cd}	2.48	11.0^{b-f}	0.6^{h-m}	1	3	17.54^{a}	2.82

Table 2 *(continue)*

Genotype	Tree type**	The stem circumference (cm)	The height of the first branching position (cm)	Leaf pose**	Leaf shape**	leaf apex shape**	Leaf base shape**	Leaf serrula form**	Leaf upper surface**	Color of the leaf**	Leaf length (cm)	Leaf breadth (cm)	Leaf length/ breadth ratio	Number of pairs of main veins on the leaf surface	Length of the leaf petiole (cm)	Color of the shoot**	Pubescence density on bud**	Length of the shoot (cm)	Mean of fresh shoot weight (g/shoot)
YB.SB6	1	111	40	2	4	2	1	2	1	3	16.68^{c}	6.04^{bc}	2.76	10.6^{c-g}	0.96^{a}	1	3	17.78^{a}	2.12
YB.SB7	2	103	36	2	4	2	1	1	1	2	12.46^{j-m}	3.96^{lmn}	3.15	9.8^{f-j}	0.62^{g-l}	5	3	14.76^{b-f}	2.05
HG.LT1	2	157	40	2	4	2	1	1	1	2	13.74^{f-i}	4.50^{ijk}	3.05	10.2^{d-h}	0.58^{i-m}	5	3	11.20^{l-o}	1.27
HG.LT2	2	96	73	2	4	2	1	1	1	3	16.04^{cd}	5.88^{bc}	2.73	11.6^{bcd}	0.70^{c-h}	5	3	15.68^{bc}	1.72
HG.LT3	2	103	42	2	4	2	1	3	1	2	15.62^{cde}	4.80^{ghi}	3.25	11.8^{abc}	0.78^{bcd}	5	3	12.36^{h-m}	1.28
HG.LT4	2	112	46	2	4	2	1	3	1	2	14.90^{def}	5.06^{fgh}	2.94	10.2^{d-h}	0.74^{c-f}	5	3	13.16^{f-k}	1.70
HG.LT6	2	110	27	2	4	2	1	1	1	2	11.54^{mno}	4.26^{jkl}	2.71	9.4^{g-k}	0.54^{k-n}	5	3	11.10^{l-o}	1.21
HG.LT7	2	91	47	2	4	2	1	1	1	2	14.62^{ef}	5.10^{fg}	2.87	12.0^{ab}	0.64^{f-k}	5	3	10.46^{no}	1.27
HG.LT8	2	116	31	2	4	2	1	1	1	2	12.28^{k-n}	4.10^{klm}	3.00	10.2^{d-h}	0.50^{mn}	5	3	11.58^{k-o}	1.10
HG.LT9	2	79	126	2	4	1	1	1	1	2	18.48^{b}	5.88^{bc}	3.14	12.2^{ab}	0.80^{bc}	5	3	14.72^{b-f}	1.75
HG.LT10	2	133	22	2	1	1	2	1	1	2	12.30^{k-n}	4.12^{klm}	2.99	8.8^{h-k}	0.46^{n}	5	3	15.16^{b-e}	1.16
HG.LT11	2	108	63	2	4	2	1	1	1	5	12.02^{k-n}	3.78^{lmn}	3.18	10.0^{e-i}	0.56^{j-n}	5	3	10.40^{o}	0.79
HG.LT12	2	162	52	2	4	2	1	1	1	1	12.58^{i-m}	4.74^{g-j}	2.65	11.4^{b-e}	0.58^{i-m}	5	3	13.16^{f-k}	1.07
HG.LT13	2	170	31	2	4	2	1	1	1	2	21.06^{a}	6.78^{a}	3.11	13.0^{a}	0.72^{c-g}	5	3	15.20^{b-e}	1.53
HG.LT14	2	142	26	2	1	2	2	1	1	3	10.28^{p}	3.92^{lmn}	2.62	10.2^{d-h}	0.54^{k-n}	5	3	11.86^{k-o}	0.97
CV %											6.29	7.16		9.57	11.92			8.01	
LSD 0.05											1.09	0.46		1.21	0.97			1.41	

Note. * Different lowercase letters show statistically significant differences between genotypes in column ($p< 0,05$); ** The quality traits were coded as follows: Tree habit/type: Arbour (1), semi-arbour (2), shrub (3); eaf shape: Ovate (1), oblong (2), elliptic (3), lanceolate (4), others (99); Leaf apex shape: Acute (1), blunt (obtuse) (2), attenuate (3), others (99); Leaf base shape: Attenuate (acute) (1), rounded (2), blunt (obtuse) (3); Leaf upper surface: Smooth (1), rugose (2), others (99). Leaf pose (angle): 1–Erect (acute) (<35°); 2–Semi-erect (obtuse) (35°–75°); 3–Horizontal (right) (76°–90°); 4–Drooping (>90°) (90°); The serrula form: Regularly acute (1), regularly blunt (2), irregularly acute (3), and irregularly blunt (4); The leaf and the shoot color: Light green (1), green (2), grayed-green (3), grayed-yellow (4), yellow-green (5), and others (6); Pubescence density on the bud: Glabrous to rare (1), light pubescent (2), dense pubescent layer (3)

Figure 3. Morphological characters of the typical leaves of the ancient tea collection from various northern provinces of Vietnam

Table 3
Principal component analysis, correlation analysis, and contribution ratio-based morphological data of ancient Shan tea genotypes

Variable	PC1	PC2	PC3	PC4	PC5	PC6	PC7
Shoot weight	0.39	-0.14	-0.58	-0.13	-0.17	-0.67	0.02
Shoot length	0.43	-0.16	-0.51	0.19	-0.05	0.70	-0.05
Leaf length	0.54	0.18	0.24	-0.04	0.46	-0.03	0.63
Leaf breadth	0.47	-0.28	0.38	-0.30	0.22	-0.02	-0.65
Leaf length/breadth ratio	0.01	0.64	-0.24	0.37	0.45	-0.13	-0.42
Main vein	0.39	0.28	0.37	0.45	-0.65	-0.08	-0.05
Leaf petiole length	0.06	0.59	-0.09	-0.72	-0.28	0.20	-0.03
Eigenvalue	2.63	1.85	1.44	0.58	0.35	0.15	0.01
Proportion (%)	37.57	26.37	20.61	8.30	4.96	2.13	0.07
Cumulative (%)	37.57	63.94	84.54	92.84	97.80	99.93	100

component presented 37.57% of the variation. The values of leaf length (0.54), leaf breadth (0.47), bud length (0.43), bud weight (0.39), and number of primary leaf veins (0.39) are the most significant contributors to the first essential component. All five factors positively correlate with the first principal component (PC1), meaning an increase in any of these factors would raise PC1's value. The second principal component explained 26.37% of the variation. The traits of the ratio of the leaf's length to breadth (0.64) and petiole length (0.59) make up the most significant contribution to the second fundamental component. The shoot weight (-0.58), shoot length (-0.51), and the weight of the leaf breadth (0.38) of principal component 3 (PC3) have high weights, suggesting that PC3 captures the variations

in shoot weight and length. The shoot weight and length values are negative, indicating a negative correlation of the third principal component (PC3) with the shoot properties. Thus, the first three components explained 84.54% of the overall variation (Table 3).

Plotting the PCA scores makes it feasible to visually evaluate sample similarity and establish whether samples may be categorized. In this study, the most significant variables of the main components are those with high weights, such as the leaf length, leaf width, and leaf length/breadth ratio in PC1 and PC2. In a main element, variables with weights of the same sign are positively correlated, whereas variables with weights of the opposite sign are negatively correlated. The primary components that may be used to examine the differences between tea plants are leaf size, bud length and weight (PC1), and leaf length/width ratio (PC2).

HG.LT trees tend to be distributed in the chart's upper left and right parts. This suggests wide dispersion within this group and possibly clearly distinct characteristics between HG.LT trees. HG.LT13 is located furthest toward the top of PC2, showing its unique characteristics that are different from other plants in the HG.LT group. The LC.TT trees are concentrated mainly in the lower left part of the chart; this group has relatively homogeneous characteristics and is different from other groups. YB.SB trees are distributed mainly in the center and right parts of the chart; this group has similarities in characteristics. In particular, YB.SB3 and YB.SB7, located on the left side of PC1, may have more distinct attributes in the YB.SB group. Through the PCA chart, we found the dispersion and grouping of tea plants into three different groups (HG.LT, LC.TT, and YB.SB). LC.TT plants tend to be more concentrated and homogeneous, while HG.LT and YB.SB plants have a wider dispersion and greater diversity of characteristics (Figure 4).

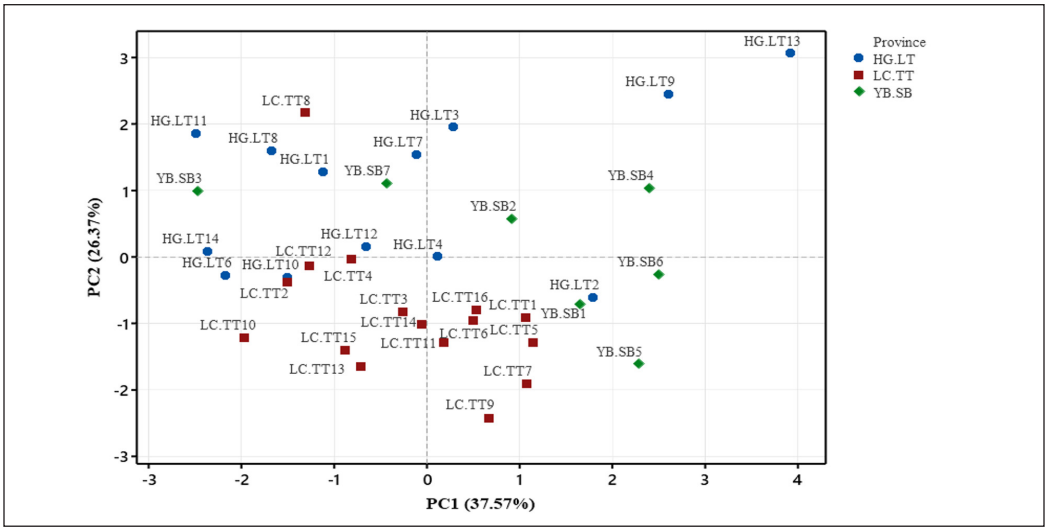

Figure 4. Score plot of morphological data of ancient tea genotypes from the eco-geographical regions of northern Vietnam

Genetic Diversity and Relationship of Ancient Tea Trees

DNA Profile of ISSR Markers

From the electrophoretic spectrum, the data showed that 96 bands were amplified from 36 ancient tea genotypes belonging to three populations, including Yen Bai, Lao Cai, and Ha Giang. In particular, 94 polymorphic bands were recorded, corresponding to a polymorphic rate of up to 97.9%, so for every 1 ISSR primer, there will be an average of 10.44 polymorphic bands. The size of amplified products ranges from 200 to 1800 bp. The UBC816 has the highest band numbers, with 14 bands, and primer UBC888 has the fewest band numbers, with five bands. Two primers, UBC856 and UBC843, amplify the band with the largest size of 1800 bp. In terms of polymorphism, there are seven primers (UBC855, UBC888, UBC825, UBC866, UBC811, UBC816, and UBC843) with a polymorphism rate of 100%. All nine primers are reasonably informative because the PIC index is in the range of 0.25–0.5. There are six primer pairs, including UBC855, UBC840, UBC888, UBC825, UBC866, and UBC816, with the highest PIC index of 0.37 (Table 4).

Table 4
Genetic diversity indices of 9 ISSR markers

Primer	SB	PB	PB%	Size	H	PIC	Rp	Hav.	MI	D	R
UBC855	10	10	100	250–1500	0.50	0.37	5.03	0.00	0.01	0.75	4.72
UBC840	13	12	92	200–1300	0.49	0.37	5.50	0.00	0.01	0.82	5.78
UBC888	5	5	100	250–1500	0.48	0.37	2.06	0.00	0.01	0.83	1.33
UBC825	10	10	100	250–1700	0.50	0.37	4.78	0.00	0.01	0.77	5.11
UBC866	11	11	100	250–1200	0.49	0.37	4.94	0.00	0.01	0.80	4.22
UBC811	9	9	100	200–1000	0.48	0.36	3.50	0.00	0.01	0.85	5.00
UBC856	14	13	93	200–1800	0.43	0.34	4.47	0.00	0.00	0.90	4.94
UBC816	9	9	100	200–1500	0.50	0.37	4.06	0.00	0.01	0.80	3.33
UBC843	15	15	100	200–1800	0.46	0.36	5.47	0.00	0.00	0.87	8.94
Total	96	94				0.37					

Note. SB: Scored band, PB: Polymorphic band, H: Heterozygous, PIC: Polymorphism Information Content, Rp: Resolution power, MI: Multiple index

Genetic Polymorphism

AMOVA analysis showed that the variance between populations was 12%, while within each population, it was up to 88% (Table 5). Our findings are consistent with those of Huang et al. (2022), who demonstrated that genetic variance within populations outweighed genetic differences across tea populations through genotyping analysis using sequencing tea genetic resources (Huang et al., 2022).

Table 5
Results of analysis of molecular variance (AMOVA)

Source	df	SS	MS	Est. Var.	%
Among Pops	2	74.081	37.040	1.990	12%
Within Pops	33	472.503	14.318	14.318	88%
Total	35	546.583		16.309	100%

Dendrogram

The UPGMA clustering dendrogram classified the three tea populations into 2 clusters with genetic similarity ranging from 0.61 to 0.86 (Figure 5). At the threshold of 0.65, cluster I is divided into two sub-clusters: I-A and I-B. The genetic diversity among the three populations is clearly illustrated in subcluster I-A. In particular, at the genetic similarity of 0.79, the data reveal that 11/13 genotypes of the Ha Giang population are in sub-cluster I-A1a. Meanwhile, all genotypes of the tea population in Lao Cai were distributed into sub-clusters I-A1b, I-A2, and I-A3. The Yen Bai population showed the highest genetic diversity due to distribution in all three different sub-clusters, consisting of I-A1a (YBSB1, YBSB3), I-A1b (YBSB5, YBSB6), and I-B (YBSB4, YBSB7). Besides, three genotypes, including HGLT2, YBSB2, and HGLT4, were grouped into cluster II.

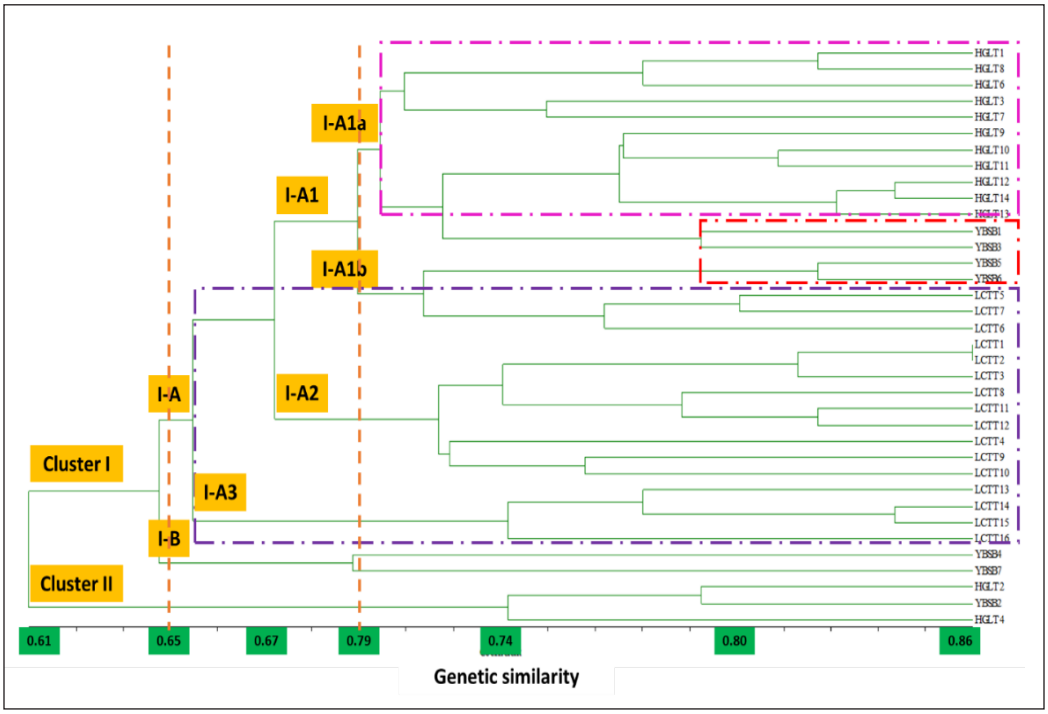

Figure 5. Dendrogram for cluster analysis of 36 *Camellia sinensis* genotypes

Principal Coordinates Analysis

The PCoA diagram visualizes the clustering between the three tea populations of Ha Giang, Yen Bai, and Lao Cai provinces. This information illustrates that the tea genotypes of the Lao Cai population showed more distinctive genetic characteristics than those of the other two populations. In addition, there is a certain overlap in the genetic profile between the two populations of Ha Giang and Yen Bai. Concerning geographical data, the distance between Ha Giang and Yen Bai provinces is closer than that of Lao Cai (Figure 6).

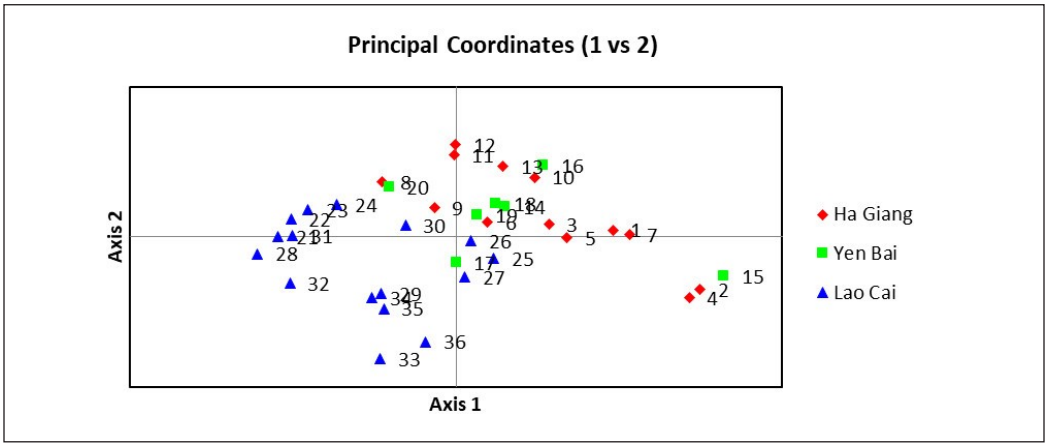

Figure 6. PCoA diagram from three populations of *C. sinensis* based on ISSR marker

DISCUSSION

Leaf morphological traits often adjust in response to different environments to adapt. According to Ran et al. (2023), the growth and development of tea plants and the quality of the tea are also strongly correlated with environmental elements such as temperature, humidity, light, rainfall, and altitude. Amino acid concentration is influenced by altitude; more significant elevations are linked to higher levels (Ran et al., 2023). The morphological diversity observed in the ancient Shan tea trees across Lao Cai, Yen Bai, and Ha Giang provinces suggests significant phenotypic variation, likely influenced by genetic factors and environmental conditions. The recorded variations in tree shape, trunk circumference, leaf size, and bud characteristics highlight the adaptability of *C. sinensis* var. *assamica* to different eco-geographical regions. Notably, larger trunk circumferences and leaf sizes were observed in certain genotypes, such as LC.TT15 and HG.LT13 indicate potential differences in growth rate, age, and environmental adaptation.

Additionally, the observed bud length and weight variations, particularly in the Yen Bai population, suggest regional differences in shoot development, which may impact tea quality and yields. Altitude and the geological environment significantly influenced the distribution, population structure, and evolutionary direction of wild plant germplasm

resources (Bemmels et al., 2016). These findings align with previous studies demonstrating how altitude, climate, and soil conditions contribute to morphological differentiation in tea plants. For example, Clarke et al. (2023) found that regional environmental factors significantly shape the phenotypic characteristics of *C. sinensis*, particularly in relation to leaf structure, shoot development, and adaptability. It highlighted that tea plants grown in warm, humid regions tend to develop broader leaves and greater shoot biomass, a phenomenon similarly observed in the Shan tea populations studied across northern Vietnam. Additionally, soil composition was identified as a key factor influencing leaf morphology, with nutrient-rich, well-drained, acidic soils supporting larger leaves and higher biomass production (Clarke et al., 2023).

These findings correspond with this study's results, where significant differences in leaf size and bud weight were recorded among populations from different provinces, as confirmed by PCA results. Furthermore, altitude was shown to impact morphological adaptation, as higher-elevation tea plants exhibited smaller, more compact leaves, likely in response to cooler temperatures and reduced oxygen availability. This pattern is evident in the distinct leaf and bud characteristics among the studied populations, suggesting that altitude-driven selection pressures contribute to morphological divergence. The UPGMA clustering and PCoA results further reinforce this relationship, as genetic clustering followed geographical patterns, indicating strong eco-geographical influences on genetic variation. These findings emphasize the importance of eco-geographical factors in shaping the morphological and genetic diversity of ancient Shan tea, underscoring their relevance for conservation and breeding strategies.

PCA analysis provided further insights into the key morphological traits contributing to variation among the ancient tea genotypes. The strong contributions of leaf length, bud length, and shoot weight to the first PC1 suggested that these traits play a critical role in distinguishing different tea populations. The clustering of tea plants into distinct groups based on PCA scores confirms that morphological differences correspond closely with geographical origin. The homogeneous characteristics observed in the Lao Cai population (LC.TT) contrast with the greater diversity and dispersion seen in Ha Giang (HG.LT) and Yen Bai (YB.SB), supporting the hypothesis that local environmental conditions and genetic factors drive phenotypic differentiation. Previously, a comprehensive analysis of wild *Camellia* species in the Guizhou Plateau, China, was carried out and provided strong evidence supporting the role of eco-geographical influences in shaping morphological traits (He et al., 2023). Their study revealed significant genetic diversity among *C. tachangensis* and *C. gymnogyna*, which were distributed across different altitude gradients and geological environments.

Specifically, the genetic diversity of *C. gymnogyna* was significantly higher in low-altitude silicate rock areas, whereas *C. tachangensis* exhibited reduced genetic variability

in high-altitude carbonate rock environments, suggesting that altitude and soil composition influence the evolutionary trajectory of tea plant populations. The genetic differentiation coefficient between these two species was 0.075 (He et al., 2023). Additionally, when analyzing populations at different altitudes, the study found that the second altitude gradient (1,100–1,400 m) exhibited the highest genetic diversity. In comparison, the first (>1,400 m) and third (<1,100 m) gradients showed reduced variation (He et al., 2023). These patterns align with the results in this study, where altitude was identified as a key determinant of morphological differentiation in ancient Shan tea populations. The lower genetic diversity at high altitudes may be attributed to restricted gene flow, environmental selection pressures, and adaptation to cooler temperatures. It is consistent with findings in other plant species that exhibit similar genetic constraints in extreme environments.

Molecular marker is a reliable approach to population genetics in natural plants. Regarding data tendency, our study is similar to that of previous publications. Next, the genetic diversity analysis using ISSR markers revealed a high degree of polymorphism (97.9%), indicating substantial genetic variation within the studied tea populations. The high number of polymorphic bands suggests that ancient Shan tea in northern Vietnam possesses a rich genetic pool, which is valuable for conservation and breeding programs. Multiple genetic clusters in the UPGMA dendrogram further support the notion of significant genetic differentiation among populations. Interestingly, the Lao Cai population exhibited more distinct genetic traits, while some overlap was observed between the Ha Giang and Yen Bai populations. In particular, 24 *Camellia* genotypes were collected from the Black Sea region of Turkey and characterized the genetic diversity by 15 ISSR markers (Yoğurtçu & Aygun, 2021). This pattern suggests that geographical proximity may contribute to gene flow and shared genetic characteristics, whereas more isolated populations may have undergone genetic divergence over time.

In order to categorize the variables inside many clusters according to their relationship and normalized value, cluster analysis with a dendrogram is typically utilized. Our AMOVA analysis revealed that most genetic variation (88%) occurs within rather than between populations (12%). The findings showed 96 total bands and 84 polymorphic bands. Likewise, 42 elite UPASI tea clones from India were analyzed by 27 ISSR markers, and the result determined that the total and polymorphic bands were 116 and 70, respectively (Sharma et al., 2022). Furthermore, based on the AMOVA output, there is a high level of intra-genetic variation (90.48%) compared to the low level between populations (9.52%). Liu et al. (2022) also concluded that the genetic variation originated mainly from intrapopulation variation when using single-nucleotide polymorphisms to study the population structure of 137 *C. sinensis* in China. Therefore, the genetic variation within the population of *C. sinensis* is diverse and should be investigated for germplasm conservation of ancient tea (Liu et al., 2022).

This finding aligns with previous studies on tea plant diversity, where intra-population genetic variation has been reported as the predominant source of diversity. The relatively low inter-population variation suggests that tea populations in northern Vietnam maintain a degree of genetic connectivity despite geographical separation, potentially due to natural seed dispersal, human-mediated propagation, or historical gene flow. Meanwhile, the PCoA further corroborates these findings, illustrating a distinct genetic profile for the Lao Cai population while indicating some genetic overlap between the Ha Giang and Yen Bai populations. This result supports the hypothesis that eco-geographical factors, such as altitude, temperature, and soil composition, may significantly shape genetic diversity. Additionally, the genetic clustering observed in the dendrogram and PCoA plot suggests that ancient tea populations in northern Vietnam have retained unique genetic signatures despite sharing a common ancestry. Genetic diversity correlates with geographical distance (Zhang et al., 2022). In tea, He et al. (2023) state that the examined Camellia's genetic differentiation was greatly influenced by the geological environment, soil mineral concentration, soil pH, and altitude (He et al., 2023). Moreover, using AMOVA analysis, ancient Chinese Assam tea (Meegahakumbura et al., 2016) populations were grouped according to the three geographical regions; the genetic variation was partitioned among regions, populations, and within populations (Li et al., 2024).

Overall, these findings emphasize the importance of preserving the genetic resources of ancient Shan tea in northern Vietnam. The observed morphological and genetic diversity highlights the potential for breeding programs to develop new cultivars with desirable traits such as enhanced yield, adaptability to environmental stress, and improved tea quality. Furthermore, conservation efforts should prioritize maintaining this diversity, particularly in populations with unique genetic characteristics. Future research incorporating more comprehensive molecular markers and environmental data could provide deeper insights into these ancient tea populations' evolutionary history and adaptive mechanisms.

CONCLUSION

This study comprehensively analyzes the morphological and genetic diversity of ancient Shan tea across the Lao Cai, Yen Bai, and Ha Giang provinces, demonstrating significant eco-geographical influences on trait variation. The morphological analysis identified slight differences in leaf length, bud length, and shoot weight, with several individuals in Ha Giang genotypes exhibiting larger leaves and thicker buds. At the same time, some Yen Bai samples showed greater shoot biomass. PCA results confirmed that these traits contribute significantly to morphological diversity, with clear population clustering. Genetic profiling using ISSR markers revealed a high polymorphism rate (97.9%), with 94 out of 96 amplified bands being polymorphic. UPGMA clustering grouped Lao Cai genotypes separately from Ha Giang and Yen Bai, while PCoA indicated genetic overlap between Ha

Giang and Yen Bai, suggesting historical gene flow. AMOVA showed that 88% of genetic variation exists within populations, reinforcing strong intra-population diversity. The distinct genetic structure of Lao Cai tea suggests localized adaptation, while shared genetic traits between Ha Giang and Yen Bai indicate potential migration or hybridization. These findings highlight the necessity of in situ and *ex-situ* conservation strategies to safeguard Shan tea genetic resources, ensuring their long-term sustainability and potential for future breeding programs.

ACKNOWLEDGMENT

This research is funded by Hanoi Pedagogical University 2 under grant number HPU2.2023-UT-16 to Hong Viet La.

REFERENCES

Ahmed, S., & Stepp, J. R. (2025). Chapter 3 - Green tea: Plants, artisanal knowledge, processing, manufacturing and production. In V. R. Preedy & V. B. Patel (Eds.), *Tea in Health and Disease Prevention* (2nd ed.) (pp. 21-30). Academic Press. https://doi.org/10.1016/B978-0-443-14158-4.00003-8

Amiryousefi, A., Hyvonen, J., & Poczai, P. (2018). iMEC: Online marker efficiency calculator. *Applications in Plant Sciences, 6*(6), Article e01159. https://doi.org/10.1002/aps3.1159

Bemmels, J. B., Title, P. O., Ortego, J., & Knowles, L. L. (2016). Tests of species-specific models reveal the importance of drought in postglacial range shifts of a Mediterranean-climate tree: Insights from integrative distributional, demographic and coalescent modelling and ABC model selection. *Molecular Ecology, 25*(19), 4889-4906. https://doi.org/10.1111/mec.13804

Chen, Z. M., & Chen, L. (2012). Delicious and healthy tea: An overview. In L. Chen, Z. Apostolides, & Z. M. Chen (Eds.), *Global Tea Breeding: Achievements, Challenges and Perspectives* (pp. 1-11). Springer. https://doi.org/10.1007/978-3-642-31878-8_1

Clarke, C., Richter, B. S., & Rathinasabapathi, B. (2023). Genetic and morphological characterization of United States tea (*Camellia sinensis*): Insights into crop history, breeding strategies, and regional adaptability. *Frontiers in Plant Science*, *14*, Article 1149682. https://doi.org/10.3389/fpls.2023.1149682

FAOSTAT. (2023). *FAO Database*. Food and Agriculture Organization of the United Nations. https://www.fao.org/faostat/en/#data/QCL

Guney, M., Kafkas, S., Keles, H., Zarifikhosroshahi, M., Gundesli, M. A., Ercisli, S., Necas, T., & Bujdoso, G. (2021). Genetic diversity among some walnut (*Juglans regia* L.) genotypes by SSR markers. *Sustainability*, *13*(12), Article 6830. https://doi.org/10.3390/su13126830

He, L., Luo, J., Niu, S., Bai, D., & Chen, Y. (2023). Population structure analysis to explore genetic diversity and geographical distribution characteristics of wild tea plant in Guizhou Plateau. *BMC Plant Biol*, *23*(1), Article 255. https://doi.org/10.1186/s12870-023-04239-2

Huang, F., Duan, J., Lei, Y., Liu, Z., Kang, Y., Luo, Y., Chen, Y., Li, Y., Liu, S., Li, S., & Liu, Z. (2022). Genetic diversity, population structure and core collection analysis of Hunan tea plant germplasm

through genotyping-by-sequencing. *Beverage Plant Research*, *2*(1), 1-7. https://doi.org/10.48130/bpr-2022-0005

IPGRI. (1997). *Descriptors for Tea (Camellia sinensis).* International Plant Genetic Resources Institute.

Kumarihami, H. M. P. C., Oh, E. U., Nesumi, A., & Song, K. J. (2016). Comparative study on cross-compatibility between *Camellia sinensis* var. *sinensis* (China type) and *C. sinensis* var. *assamica* (Assam type) tea. *African Journal of Agricultural Research*, *11*, 1092-1101. https://doi.org/10.5897/AJAR2015.9951

Li, M. M., Meegahakumbura, M. K., Wambulwa, M. C., Burgess, K. S., Moller, M., Shen, Z. F., Li, D. Z., & Gao, L. M. (2024). Genetic analyses of ancient tea trees provide insights into the breeding history and dissemination of Chinese Assam tea (*Camellia sinensis* var. *assamica*). *Plant Divers*, *46*(2), 229-237. https://doi.org/10.1016/j.pld.2023.06.002

Liu, C., Yu, W., Cai, C., Huang, S., Wu, H., Wang, Z., Wang, P., Zheng, Y., Wang, P., & Ye, N. (2022). Genetic diversity of tea plant [*Camellia sinensis* (L.) Kuntze] germplasm resources in Wuyi Mountain of China based on single nucleotide polymorphism (SNP) markers. *Horticulturae*, *8*(10), Article 932. https://doi.org/10.3390/horticulturae8100932

Liu, S., Liu, H., Wu, A., Hou, Y., An, Y., & Wei, C. (2017). Construction of fingerprinting for tea plant (*Camellia sinensis*) accessions using new genomic SSR markers. *Molecular Breeding*, *37*(8), Article 93. https://doi.org/10.1007/s11032-017-0692-y

Meegahakumbura, M. K., Wambulwa, M. C., Li, M. M., Thapa, K. K., Sun, Y. S., Moller, M., Xu, J. C., Yang, J. B., Liu, J., Liu, B. Y., Li, D. Z., & Gao, L. M. (2017). Domestication origin and breeding history of the tea plant (*Camellia sinensis*) in China and India based on nuclear microsatellites and cpDNA sequence data. *Frontiers in Plant Science*, *8*, Article 2270. https://doi.org/10.3389/fpls.2017.02270

Meegahakumbura, M. K., Wambulwa, M. C., Thapa, K. K., Li, M. M., Moller, M., Xu, J. C., Yang, J. B., Liu, B. Y., Ranjitkar, S., Liu, J., Li, D. Z., & Gao, L. M. (2016). Indications for three independent domestication events for the tea plant [*Camellia sinensis* (L.) O. Kuntze] and new insights into the origin of tea germplasm in China and India revealed by nuclear microsatellites. *PLoS One*, *11*(5), Article e0155369. https://doi.org/10.1371/journal.pone.0155369

Nwosisi, S., Dhakal, K., Nandwani, D., Raji, J. I., Krishnan, S., & Beovides-García, Y. (2019). Genetic diversity in vegetable and fruit crops. In D. Nandwani (Ed.), *Genetic Diversity in Horticultural Plants* (pp. 87-125). Springer. https://doi.org/10.1007/978-3-319-96454-6_4

Ran, W., Li, Q., Hu, X., Zhang, D., Yu, Z., Chen, Y., Wang, M., & Ni, D. (2023). Comprehensive analysis of environmental factors on the quality of tea (*Camellia sinensis* var. *sinensis*) fresh leaves. *Scientia Horticulturae*, *319*, Article 112177. https://doi.org/10.1016/j.scienta.2023.112177

Rogers, S. O., & Bendich, A. J. (1989). Extraction of DNA from plant tissues. In S. B. Gelvin, R. A. Schilperoort & D. P. S. Verma (Eds.), *Plant Molecular Biology Manual* (pp. 73-83). Springer. https://doi.org/10.1007/978-94-009-0951-9_6

Samarina, L. S., Matskiv, A. O., Shkhalakhova, R. M., Koninskaya, N. G., Hanke, M. V., Flachowsky, H., Shumeev, A. N., Manakhova, K. A., Malyukova, L. S., Liu, S., Zhu, J., Gvasaliya, M. V., Malyarovskaya, V. I., Ryndin, A. V., Pchikhachev, E. K., & Reim, S. (2021). Genetic diversity and genome size variability

in the Russian Genebank collection of tea plant [*Camellia sinensis* (L). O. Kuntze]. *Frontiers in Plant Science*, *12*, Article 800141. https://doi.org/10.3389/fpls.2021.800141

Sharma, S., Kumar, A., Rajpal, V. R., Singh, A., Babbar, S., & Raina, S. N. (2022). Evaluation of genetic diversity and population structure in elite South Indian tea [*Camellia sinensis* (L.) Kuntze] using RAPD and ISSR markers. *Genetic Resources and Crop Evolution*, *70*(2), 381-398. https://doi.org/10.1007/s10722-022-01433-3

Smouse, P. E., Banks, S. C., & Peakall, R. (2017). Converting quadratic entropy to diversity: Both animals and alleles are diverse, but some are more diverse than others. *PLoS One*, *12*(10), Article e0185499. https://doi.org/10.1371/journal.pone.0185499

Vo, T. D. (2007). *Assessing genetic diversity in Vietnam tea [Camellia sinensis (L.) O. Kuntze] using morphology, inter-simple sequence repeat (ISSR) and microsatellite (SSR) markers* [PhD dissertation, Universität Göttingen]. Semantic Scholar. https://api.semanticscholar.org/CorpusID:247019507

Wambulwa, M. C., Meegahakumbura, M. K., Kamunya, S., Muchugi, A., Moller, M., Liu, J., Xu, J. C., Li, D. Z., & Gao, L. M. (2017). Multiple origins and a narrow genepool characterise the African tea germplasm: Concordant patterns revealed by nuclear and plastid DNA markers. *Scientific Reports*, *7*(1), Article 4053. https://doi.org/10.1038/s41598-017-04228-0

Xia, E. H., Zhang, H. B., Sheng, J., Li, K., Zhang, Q. J., Kim, C., Zhang, Y., Liu, Y., Zhu, T., Li, W., Huang, H., Tong, Y., Nan, H., Shi, C., Shi, C., Jiang, J. J., Mao, S. Y., Jiao, J. Y., Zhang, D., …, & Gao, L. Z. (2017). The tea tree genome provides insights into tea flavor and independent evolution of caffeine biosynthesis. *Molecular Plant*, *10*(6), 866-877. https://doi.org/https://doi.org/10.1016/j.molp.2017.04.002

Xia, E., Tong, W., Hou, Y., An, Y., Chen, L., Wu, Q., Liu, Y., Yu, J., Li, F., Li, R., Li, P., Zhao, H., Ge, R., Huang, J., Mallano, A. I., Zhang, Y., Liu, S., Deng, W., Song, C., …, & Wan, X. (2020). The reference genome of tea plant and resequencing of 81 diverse accessions provide insights into its genome evolution and adaptation. *Molecular Plant*, *13*(7), 1013-1026. https://doi.org/10.1016/j.molp.2020.04.010

Yoğurtçu, B. M., & Aygun, A. (2021). Characterization of tea (*Camellia sinensis* L.) genotypes grown in Turkey by ISSR markers. *Applied Ecology and Environmental Research*, *19*(5), 4103-4114. https://doi.org/10.15666/aeer/1905_41034114

Zhang, C., Jia, C., Liu, X., Zhao, H., Hou, L., Li, M., Cui, B., & Li, Y. (2022). Genetic diversity study on geographical populations of the multipurpose species *Elsholtzia stauntonii* using transferable microsatellite markers. *Frontiers in Plant Science*, *13*, Article 903674. https://doi.org/10.3389/fpls.2022.903674

Zhang, F., Li, W., Gao, C. W., Zhang, D., & Gao, L. Z. (2019). Deciphering tea tree chloroplast and mitochondrial genomes of *Camellia sinensis* var. *assamica. Scientific Data*, *6*(1), Article 209. https://doi.org/10.1038/s41597-019-0201-8

Zhao, Y., Wang, R., Liu, Q., Dong, X., & Zhao, D. G. (2021). Genetic diversity of ancient *Camellia sinensis* (L.) O. Kuntze in Sandu County of Guizhou Province in China. *Diversity*, *13*(6), Article 276. https://doi.org/10.3390/d13060276

Zhao, Z., Song, Q., Bai, D., Niu, S., He, Y., Qiao, D., Chen, Z., Li, C., Luo, J., & Li, F. (2022). Population structure analysis to explore genetic diversity and geographical distribution characteristics of cultivated-

type tea plant in Guizhou Plateau. *BMC Plant Biol*, *22*(1), Article 55. https://doi.org/10.1186/s12870-022-03438-7

Zou, Y., Ge, X., Yan, C., Zhong, Q., Chen, D., Chen, Z., Yuan, Y., Guo, H., Zhou, Y., Wang, J., & Cao, L. (2024). Assessment of genetic diversity of *Camellia yuhsienensis* based on leaf structure and inter simple sequence repeat (ISSR) markers. *Genetic Resources and Crop Evolution*, *71*(8), 4749-4762. https://doi.org/10.1007/s10722-024-01910-x

Pertanika J. Sci. & Technol. 33 (4): 1869 - 1886 (2025)

PERTANIKA JOURNALS

SCIENCE & TECHNOLOGY

Journal homepage: http://www.pertanika.upm.edu.my/

Growth and Productivity of Maize (*Zea mays*) Using Gibberellic Acid 3 (GA3) with Different Planting Distances in a Clay Condition at Cabagan, Isabela, Philippines

Darwin Marzan Cacal[1]*, Janet Paday-os Pablo[2], Leila Mary Alipio Ayban[2], Esther Josephine Daoal Sagalla[2] and Darwin Aldas Basquial[2]

[1]Isabela State University Cabagan Campus, Isabela 3328, The Philippines
[2]Benguet State University La Trinidad Campus, Benguet 2601, The Philippines

ABSTRACT

Maize is a global staple food widely used as animal feed, biofuel, and a raw material in various industries. Gibberellic Acid 3 (GA3) is crucial in regulating plant growth. This study aimed to evaluate the impact of GA3 concentrations and planting distances on maize productivity, providing insights to optimize production for quality and profitability. The experiment was conducted at the ISU Compound, Cabagan, Isabela, from March to July 2023. It is a 4 × 2 factorial in a Randomized Complete Block Design (RCBD) with eight treatment combinations and three replications. Factor A consisted of four GA3 concentrations (control, 175 mL, 200 mL, and 225 mL), while Factor B included two planting distances (20 cm × 20 cm and 20 cm × 25 cm). Data were analyzed using two-way ANOVA and Tukey's LSD at a significance level of $P < 0.05$. Results indicated that GA3 application significantly influenced plant height (PH), demonstrating that higher concentrations of GA3 promoted greater vegetative growth, while the other parameters were not significantly affected. Meanwhile, the computed yield (CY) was significantly affected by planting distance and the interaction effect between GA3 concentration and spacing. The combination of 175 mL GA3 application with a 20 cm × 25 cm planting distance resulted in the highest yield, suggesting that this treatment enhances maize productivity while maintaining efficient plant spacing. Thus, it is recommended for optimizing maize production, ensuring better growth performance, and higher economic returns.

Keywords: Distance of planting, gibberellic acid 3, maize, tassel

ARTICLE INFO

Article history:
Received: 11 December 2024
Accepted: 17 March 2025
Published: 11 June 2025

DOI: https://doi.org/10.47836/pjst.33.4.09

E-mail addresses:
darwin.m.cacal@gmail.com (Darwin Marzan Cacal)
j.pablo@bsu.edu.ph (Janet Paday-os Pablo)
lm.ayban@bsu.edu.ph (Leila Mary Alipio Ayban)
ej.sagalla@bsu.edu.ph (Esther Josephine Daoal Sagalla)
d.basquial@bsu.edu.ph (Darwin Aldas Basquial)
* Corresponding author

e-ISSN: 2231-8526

© Universiti Putra Malaysia Press

INTRODUCTION

Maize (*Zea mays*) is the third-largest plant-based food source in the world, serving as a primary food source for both humans and animals. Despite its importance, farmers and the agricultural sector face persistent challenges related to low productivity. Various strategies have been proposed to address this issue and enhance maize productivity, with the adoption of plant growth regulators like Gibberellic Acid 3 (GA3) emerging as a promising study area. Maize experiences several factors, such as environmental conditions, pest infestations, and nutrient deficiencies, contributing to reduced productivity. Thus, it is imperative to research to identify viable approaches to enhance maize productivity and increase yields (Singh, 2010; Turner et al., 2014).

Department of Agriculture Regional Field Office III, six hundred thousand (600,000) farms household depend on maize as their major source of livelihood and in line with this, Isabela and Bukidnon are the top maize producing province in the Philippines contributing a total production of 1.1 million metric tons and 0.8 million metric tons (Salazar et al., 2021). Reyes et al. (2009) stated that the province of Isabela was named the top maize producer in the country. It had consistently been a top producer throughout the years, with a proportion of national output ranging from 9 to 16 percent. All over the Philippines, the estimated production based on the standing crop from April to June 2024 is projected to decrease to 1.19 million metric tons. This represents a 19.1 percent decline from the actual production of 1.47 million metric tons recorded during the same period in 2023 (Philippine Statistics Authority, 2024). Due to dry periods at the beginning of the year and flooding in September and December, Isabela was forced to settle for second place in the race for grain output.

On the other hand, one of the approaches proposed to enhance maize productivity is using plant growth regulators, such as Gibberellic acid. GA3 is a naturally occurring plant hormone that promotes plant growth and development, and it has been shown to enhance the growth and yield of maize crops (Gao et al., 2020; Al-Shaheen & Soh, 2018). However, the effect of GA3 application is influenced by other factors, such as planting distance. While GA3 is known for its potential to enhance crop growth and development by improving parameters such as stem elongation, leaf expansion, and overall plant vigor (Camara et al., 2018; Anjum et al., 2017; Mahender et al., 2015), its efficacy can vary depending on plant spacing in the field. Proper planting distance is essential because it affects light interception, nutrient availability, and the overall microclimate around each plant. Inadequate spacing can lead to competition among plants for resources, potentially reducing the impact of GA3 application on individual plants. Conversely, optimal spacing can ensure that each plant receives adequate resources, maximizing the benefits of GA3 in promoting growth and increasing yields (Noda-Leyva & Martin-Martin, 2017). Despite this, the interaction between the GA3 application and different planting distances, particularly

in specific soil conditions like clay, has not been thoroughly investigated. Furthermore, one study investigated the impact of exogenous GA3 application on maize under salinity stress. GA3 application improved plant growth by enhancing chlorophyll content, reducing sodium (Na^+) accumulation, and increasing potassium (K^+) concentration. It improved photosynthetic efficiency and ionic balance, leading to better growth and yield under stress conditions. In contrast, the combined effects of GA3 and foliar application on maize seedlings under varying salinity levels enhanced antioxidant enzyme activities, reduced oxidative damage, and nutrient uptake, and modulated stress responses and metabolic processes (Mukarram et al., 2021; Shahzad et al., 2021). Additionally, research on the application of GA3 and mepiquat chloride (M.C) as growth regulators showed that foliar application of 100 ppm GA3 significantly increased grain yield by 33% compared to the control and mitigates salt stress by enhancing chlorophyll content, soluble protein levels, and ion balance, thereby improving overall plant health and productivity (El-Nwehy & Afify, 2023).

Maize has become popular among farmers due to its superior qualities, such as improved yield, resistance to pests and diseases, and adaptability to various environmental conditions (Frank et al., 2013). However, the productivity of maize can be further enhanced by optimizing cultivation practices, including applying growth regulators such as GA3 and appropriate planting distance.

Thakur et al. (2018) investigated the impacts of GA3 and planting distances on sweet william (*Dianthus barbatus* L) growth and yield. Their findings suggest that applying GA3 alongside planting distance increased yield, flowering, and plant height. Nevertheless, by identifying the most efficient cultivation methods, this study assesses how Gibberellic Acid 3 (GA3) and various planting distances influence maize productivity, aiming to offer insights for optimizing production in terms of quality and profitability.

METHODOLOGY

Study Area

The experiment was conducted at the Experimental Field Area of the College of Agricultural Sciences and Technology at Isabela State University, Cabagan Campus (ISUC), located in Cabagan, Isabela, Philippines, at coordinates 17.4144° N latitude and 121.7670° E longitude. The study was carried out during the summer season, from March to July 2023, when the climatic conditions during the study period were marked by variations in rainfall, temperature, and relative humidity, which influenced maize growth and development. Insufficient precipitation was recorded during the 1st, 5th, 8th, and 12th weeks after sowing, with an average rainfall of only 1.32 mm. Temperature patterns showed an average minimum temperature of 24.77°C and a maximum temperature of 35.21°C from the 1st to the 9th week after sowing. However, during the critical reproductive stages (10th to 14th

weeks after sowing), temperatures slightly increased, averaging a minimum of 25.78°C and a maximum of 35.56°C. These conditions persisted through the later stages of crop development. During the reproductive (dough) stage at 13 weeks after sowing, an average rainfall of 1.38 mm was recorded. This low water availability was not ideal, as it limited water absorption, potentially leading to smaller and immature kernels.

Experimental Design, Soil Sampling and Treatments

The field experiment encompassed an area of 341 square meters divided into three blocks, each subdivided into eight equal plots, each measuring 3 meters by 3 meters. There were 1.0-meter alleyways between the blocks and plots. Soil samples were collected from 6 to 8 inches, with composite samples representing the entire experimental area prepared after removing debris, weeds, and topsoil. The collection process involved using a shovel, bolo, and post-hole digger, and the samples were transported in pails. These samples were then pulverized and air-dried for seven days. Uniform 1-kilogram samples were obtained using the quartering technique and sent to the Department of Agriculture-Soil Laboratory-Cagayan Valley Research Center (DA-SL-CVRC) in San Felipe, Ilagan, Isabela, for analysis. Based on the soil analysis recommendations, both inorganic and organic fertilizers were applied. Organic fertilizers included carbonized rice hull and vermicompost, administered at 450 grams per plot. The inorganic fertilizers used were Urea (46-0-0), Muriate of Potash (0-0-60), and Complete Fertilizer (14-14-14), applied at rates of 58.5 grams, 31.5 grams, and 256.95 grams per plot, respectively.

The experiment was structured as a 4 × 2 randomized complete block design (RCBD), incorporating a two-factorial approach to assess the impact of different treatments on crop growth under varying stress conditions. Factor A focused on evaluating the effects of varying concentrations of gibberellic acid (GA3) with four distinct treatments: (1) A1: without GA3 (WOG), (2) A2: 175 mL of GA3 per hectare (175GA3), (3) A3: 200 mL of GA3 per hectare (200GA3), and (4) A4: 225 mL of GA3 per hectare (225GA3). The control group (A1) was essential in establishing a baseline for comparison, as no GA3 was applied to this treatment. This allowed the researchers to isolate and quantify the specific influence of GA3 application on maize growth and yield. The decision to exclude GA3 in the control group was crucial for understanding the natural growth response of maize under the given environmental conditions. By comparing the untreated plants (WOG) with those subjected to different GA3 concentrations, the researchers could assess how much GA3 influenced key growth parameters such as plant height, biomass accumulation, flowering time, and grain yield. Without a control group, it would be challenging to determine whether observed differences were due to GA3 application or other environmental or genetic factors. Additionally, including a control group aligns with experimental best practices, ensuring that any potential benefits or drawbacks of the GA3 application are accurately measured. It

also provides practical insights into whether the GA3 application is necessary under field conditions, helping to inform future agronomic recommendations. Factor B investigated the effects of planting distance on crop growth, with two treatments: (1) B1: 20 cm × 20 cm (PD20) and (2) B2: 20 cm × 25 cm (PD25). This factor aimed to understand how spacing influenced the growth parameters and overall yield of the crops.

Planting, Planting Materials, Care, and Maintenance of Plants

The necessary materials for the study were obtained from multiple sources. Complete Fertilizer (14-14-14), Urea (46-0-0), Muriate of Potash (0-0-60), and insecticides were procured from Agricultural Supply in Ugad Cabagan, Isabela. The maize seed variety used in the study was NK6410, selected for its maturing characteristics 100-105 days after planting (DAP) and its potential yield of 12 metric tons per hectare (MT/ha). This variety is suitable for a wide range of regions, including the Cagayan Valley (Lower Vega), Ilocos Region, Central Luzon, South Luzon, Bicol Region, and Mindanao Low Elevation. NK6410 is renowned for its Class A grain quality, good standability, and ease of dehusking and harvesting. GA3 was sourced from an authorized online retailer. The ISUC nursery provided vermicast, a hand tractor, a wheelbarrow, garden tools, placards, pegs, a meter stick, and a sprayer. Land preparation involved plowing the field twice with a four-wheeled tractor, followed by a final harrowing one week before planting. After removing debris and weeds, the soil was further conditioned using a hand tractor. The experimental site was divided into three columns and eight rows, creating plots that measured 3 by 3 meters, marked with basic farming tools. The soil was then levelled using a garden rake in preparation for planting. Maize seeds were planted in furrows at 2–5 cm. Each subplot contained 10 rows and 13 hills, with 130 seeds per plot (2 seeds per hill). There was a 20 cm interval between hills and a 25 cm gap between rows. Due to poor germination, particularly with the NK6410 variety, to ensure uniform plant density, an alternative approach to replanting is to initially sow multiple seeds per hill and thin excess seedlings after germination. GA3 was applied via foliar spraying at 30 DAS, diluting each concentration in 115.2 mL of water. Irrigation was conducted every five days using a submersible pump. Weed management was performed manually using a hand trowel, while initial infestations of fall armyworm were controlled through hand-picking. At maturity, maize cobs were harvested by hand, followed by manual threshing to remove the husks and separate the kernels. The kernels were sun-dried until they attained a 12%–14 % moisture content.

General Observation and Collection of Data

The data collection process was comprehensive, encompassing a range of growth parameters to provide a holistic view of the crop performance under the different treatments. The samples are randomly selected, 10 per plot, in all the parameters, such as Plant height

(PH), which was measured from the base of the culm to the tip of the highest leaf using a meter stick, 10 days after the GA3 application, to assess the initial response of the plants to the hormone. Leaf count (LC) was recorded post-GA3 application to gauge the vegetative growth stimulated by the treatments. The ear length (EL) was measured from the base to the tip of the de-husked maize cobs to determine the effect of the treatments on reproductive growth. Ear diameter (ED) was measured using a caliper, providing insights into the physical development of the maize ears. Computed yield (CY) was determined by weighing the harvested marketable dry kernels from each treatment and converting the weight to a per-hectare basis, offering a standardized measure of productivity. Biomass yield (BY) was obtained by weighing the fresh uprooted maize plants, including the ears, to assess the overall biomass produced. The kernels weight at 1000 (KW) were measured after drying and randomly selecting kernels from each treatment, providing a detailed understanding of kernel weight and potential yield quality.

Data Analysis

The analysis was conducted using a two-factorial analysis of variance (ANOVA) to evaluate the effects of GA3 application and different planting distances on the growth parameters of maize. This method was chosen because it allows for assessing both main effects and interactions between the factors. Before performing ANOVA, key assumptions—normality of residuals, homogeneity of variances (Levene's test), and independence of observations—were checked to ensure the validity of the analysis. Tukey's Honestly Significant Difference (HSD) test was used as a post-hoc analysis to determine significant differences among treatment means. Tukey's HSD was selected for its ability to control the family-wise error rate while performing multiple comparisons, making it suitable for detecting pairwise differences among treatments without inflating the Type I error rate. The results were reported as mean ± standard deviation (SD), with statistical significance at $P < 0.05$. This rigorous statistical approach ensured that the conclusions drawn from the study were robust, providing valuable insights into the effects of GA3 application and planting distance on maize growth under varying conditions.

RESULTS AND DISCUSSION

Plant Height (cm)

In the study on maize in PH, as shown in Table 1, the application of different gibberellic acid (GA3) concentrations was analyzed and compared using ANOVA. The findings revealed that treatments with 175 mL, 200 mL, and 225 mL of GA3 per hectare (175GA3, 200GA3, 225GA3) resulted in significantly increased plant heights of 105.2 ± 3.06 cm, 112.2 ± 10.02 cm, and 108.0 ± 5.84 cm, respectively. These heights were statistically similar but

Table 1
Effects of various parameters in different concentrations of GA3 in maize

FACTOR A	PH (cm)	LC (cm)	EL (cm)	ED (mm)	BY (g)	KW (g)	CY (kg/ha)
WOG	83.3 ± 18.19[b]	7.70 ± 0.66	11.83 ± 0.38	36.97 ± 0.83	2696.67 ± 188.71	280.50 ± 6.13	2477.78 ± 152.68
175GA3	105.2 ± 3.06[a]	8.45 ± 0.10	11.44 ± 0.01	36.03 ± 0.11	2439.00 ± 68.96	281.60 ± 6.96	2260.74 ± 64.35
200GA3	112.2 ± 10.02[a]	8.37 ± 0.02	11.74 ± 0.29	34.99 ± 1.15	2489.83 ± 18.13	266.17 ± 8.21	2332.22 ± 7.13
225GA3	108.0 ± 5.84[a]	8.90 ± 0.55	10.78 ± 0.67	36.56 ± 0.42	2406.33 ± 101.63	269.50 ± 4.88	2229.63 ± 95.46

Note. g: kilogram, ha: hectare, WOG: Without GA3, 175GA3: 175 mL of GA3 per hectare, 200GA3: 200 mL of GA3 per hectare, 225GA3: 225 mL of GA3 per hectare, PH: plant height, LC: leaf count, EL: ear length, ED: ear diameter, BY: biomass yield, CY: computed yield and KW: kernel weight of 1000. The different factors are presented along with their respective standard deviations (SD) using the mean ± standard deviation, followed by different subscript letters (e.g., a, b) used to denote significant differences at a 5% probability level

markedly different from the control group (WOG), which had a significantly lower plant height of 83.3 ± 18.19 cm. This suggests that the application of GA3 promotes substantial growth in maize height. The increased plant height observed in maize treated with GA3 can be attributed to several mechanisms. GA3 stimulates cell elongation and division in the internodes, increasing stem length and overall plant height. This hormone activates gene expression in cell wall loosening and expansion, facilitating cell growth. Additionally, the GA3 application can improve nutrient uptake efficiency, providing the necessary resources for sustained growth. GA3 also interacts with other plant hormones, such as auxins and cytokinins, to regulate growth processes, ensuring balanced and optimal growth. Moreover, GA3 helps mitigate stress conditions, allowing plants to grow vigorously even under suboptimal environmental conditions. These findings align with previous research, which reported that GA3 significantly enhances plant height in tomatoes and corn, highlighting the growth-promoting effects of GA3 across different plant species (El-Sayed et al., 2014; Hadi et al., 2010).

In a study comparing the effect of different planting distances on maize in PH, as shown in Table 2, two different planting distances were tested: 20 cm × 20 cm (PD20) and 20 cm × 25 cm (PD25). The mean plant heights recorded were 101.74 ± 0.47 cm and 102.68 ± 0.47 cm, respectively. Results indicated no significant difference in plant height at 30 days after sowing (DAS) between the different planting distances. Similar findings were reported by Jiang et al. (2020), who found that planting density did not significantly affect plant height in maize.

In Table 3, the results presented the PH under different treatments involving the application of gibberellic acid (GA3) at varying concentrations and planting distances. Upon analysis, it is evident that there are fluctuations in plant height across the treatments. For

Table 2
Response of two different distances of planting in various parameters

FACTOR B	PH (cm)	LC (cm)	EL (cm)	ED (mm)	BY (g)	KW (g)	CY (kg/ha)
PD20	101.7 ± 0.47	7.93 ± 0.27	11.50 ± 0.05	35.92 ± 0.22	2288.50 ± 219.46	219.67 ± 24.71	2147.04± 178.06[b]
PD25	102.6 ± 0.47	8.46 ± 0.27	11.40 ± 0.05	36.35 ± 0.22	2727.42 ± 219.46	269.08 ± 24.71	2503.15 ± 178.06[a]

Note. kg: kilogram, ha: hectare, CY: computed yield, PH: plant height, LC: leaf count, LE: ear length, ED: ear diameter, BY: biomass yield, KW: kernel weight, PD20: 20 cm × 20 cm planting distance and PD25: 20 cm × 25 cm planting distance. The different factors and their respective standard deviations (SD) are presented using the mean ± standard deviation

Table 3
Interaction effects of different distances of planting applied with various concentrations of GA3

TREATMENT	PH (cm)	LC (cm)	EL (cm)	ED (mm)	BY (g)	KW (g)	CY (kg/ha)
WOG + PD20	163.5± 12.08	6.40± 1.84	11.87± 0.42	37.57± 1.56	2724.67± 287.97	286.00± 11.63	2494.81± 169.72[ab]
175GA3 + PD20	134.3± 17.08	8.07± 0.17	11.80± 0.35	35.36± 0.65	2668.67± 231.97	275.00± 0.63	2460.74± 135.65[ab]
200GA3 + PD20	161.7± 10.32	8.50± 0.26	12.20± 0.75	35.90± 0.11	2389.33± 47.37	285.67± 11.30	2265.93± 59.16[b]
225GA3 + PD20	147.9± 3.55	8.40± 0.16	10.68± 0.77	36.15± 0.14	2488.57± 51.87	277.00± 2.63	2255.56± 69.53[b]
WOG + PD25	149.1± 2.28	8.40± 0.16	10.55± 0.90	34.45± 1.56	2296.00± 140.70	283.00± 8.63	2195.56± 129.53[b]
175GA3 + PD25	156.6± 5.22	8.33± 0.09	11.02± 0.43	35.52± 0.49	2683.67± 246.97	249.33± 25.05	2827.41± 502.32[a]
200GA3 + PD25	147.5± 3.92	8.77± 0.53	11.39± 0.60	35.76± 0.25	1174.00± 1262.69	264.00± 10.38	1631.85± 693.24[c]
225GA3 + PD25	150.6± 0.82	9.03± 0.79	12.08± 0.63	37.37± 1.36	3068.67± 631.97	275.00± 0.63	2468.89± 143.80[ab]

Note. kg: kilogram, ha: hectare, CY: computed yield, WOG: without GA3, 175GA3: 175 mL of GA3 per hectare, 200GA3: 200 mL of GA3 per hectare, 225GA3: 225 mL of GA3 per hectare, PH: plant height, LC: leaf count, EL: ear length, ED: ear diameter, BY: biomass yield, KW: kernel weight, PD20: 20 cm × 20 cm planting distance and PD25: 20 cm × 25 cm planting distance. The different factors are presented along with their respective standard deviations (SD) using the mean ± standard deviation, followed by different subscript letters (e.g., a, b) used to denote significant differences at a 5% probability level

instance, under the same planting distance of PD20, the WOG + PD20 treatment exhibited the tallest plants with a mean height of 163.53 ± 12.08 cm, while the 175GA3 + PD20 treatment showed the shortest plants with a mean height of 134.37 ± 17.08 cm. Conversely, under the PD25 planting distance, the tallest plants were observed in the 175GA3 + PD25 treatment with a mean height of 156.67 ± 5.22 cm, whereas the shortest plants were in the 200GA3 + PD25 treatment with a mean height of 147.53 ± 3.92 cm. Interestingly, despite

the variations observed, the ANOVA results indicate that the different planting distances did not significantly influence the mean PH at 30 days after sowing (DAS). The effect of GA3 on PH lies in its ability to promote cell division and elongation. GA3 stimulates the production of enzymes that loosen cell walls, allowing cells to expand more readily. This leads to increased internode length, which directly contributes to taller plants. However, the observed fluctuations in plant height across different GA3 concentrations and planting distances suggest that the response to GA3 is not linear and may be influenced by other factors such as nutrient availability, light, and the inherent genetic characteristics of the maize variety used. The tallest plants in the WOG + PD20 treatment could be attributed to the absence of exogenous GA3, allowing the plants to rely on their endogenous GA3 levels, which might be sufficient for optimal growth under the given conditions.

Leaves Count

The data presented in Table 1 (LC) highlights the impact of gibberellic acid (GA3) application on leaf count (LC) in maize, offering insights into how this plant growth regulator influences vegetative development. Upon analysis, it becomes evident that the GA3 application generally led to an increase in leaf count compared to the control (WOG, without GA3). Specifically, treatments with 175GA3, 200GA3, and 225GA3 resulted in higher mean leaf counts of 8.45 ± 0.10, 8.37 ± 0.02, and 8.90 ± 0.55, respectively, while the WOG treatment exhibited a mean leaf count of 7.70 ± 0.66. The increase in leaf count with GA3 application has practical implications for crop management and productivity. Leaves are essential for photosynthesis, the process by which plants convert light energy into chemical energy. Thus, more leaves generally mean a higher photosynthetic capacity and potentially greater biomass production (Taiz et al., 2015; Liu et al., 2010).

The results presented in Table 2 (LC) illustrate the effect of planting distance on LC in maize. Upon analysis, it is evident that there is a difference in leaf count between the two planting distances studied. Specifically, the mean leaf count for the PD20 planting distance was 7.93 ± 0.27, whereas for the PD25 planting distance, it was 8.46 ± 0.27. Despite this observed numerical difference, the Analysis of Variance (ANOVA) results indicated that the mean leaf count at 45 days after sowing (DAS) was not significantly affected by the different planting distances. The numerical increase in leaf count from PD20 to PD25 suggests that wider planting distances may provide plants with more space and resources to develop additional leaves. This finding implies that altering the planting distance could potentially enhance the photosynthetic capacity and overall vigor of maize plants. More leaves typically mean increased surface area for photosynthesis, which is crucial for the plant's energy production and growth (Lambers et al., 2019; Taiz et al., 2015).

Table 3 under LC presents the results of the effect of different treatments. Upon analysis, it is evident that the treatments and the planting distances do not impact leaf count in maize.

As per the analysis, different concentrations of GA3 and different planting distances had no significant impact on LC.

Length of Ear (cm)

Table 1 presents the effects of GA3 on the ear length (LE) of maize, revealing variations among the different treatments. Upon analysis, the control group (WOG) exhibited the longest ear length, with a mean of 11.83 ± 0.38 cm, followed closely by the 200GA3 treatment at 11.74 ± 0.29 cm. The 175GA3 treatment resulted in a slightly shorter ear length of 11.44 ± 0.01 cm, while the highest concentration (225GA3) produced the shortest ear length at 10.78 ± 0.67 cm. These findings suggest that applying GA3 at certain concentrations does not necessarily lead to an increase in ear length compared to the control, and excessive GA3 may even have adverse effects on ear development. Ear length is important in the yield component, as it directly influences the number of kernels per ear, a primary determinant of overall grain yield. A longer ear generally provides more space for kernel formation, leading to higher potential grain production. However, the non-linear response observed in this study suggests that while moderate GA3 application may support growth, excessive concentrations could disrupt natural hormonal balances, possibly leading to inefficient ear development. This trend is supported by the findings of a study by Gohil et al. (2023), which reported that higher GA3 concentrations did not necessarily increase ear length in maize. Their study observed a maximum ear length of 12.17 cm, indicating that excessive GA3 application may have a diminishing or negative effect on ear development.

The results in Table 2 illustrate the effect of Factor B, representing different planting distances, on maize ear length (LE). The findings indicate a minimal difference between the two planting distances, with PD20 producing a mean ear length of 11.50 ± 0.05 cm and PD25 showing a slightly shorter mean ear length of 11.40 ± 0.05 cm. These results suggest that modifying the planting distance from PD20 to PD25 has a marginal effect on ear length, implying that maize plants experience similar growth conditions within this range. Planting distance influences intraspecific competition for essential resources such as sunlight, nutrients, and water, impacting maize growth and yield parameters. However, in this study, the slight variation in ear length suggests that the tested planting distances provided sufficient space for maize plants to access the necessary resources without significant competition. Similar findings were reported by Yang et al. (2024), who observed that moderate adjustments in planting density had negligible effects on ear length when environmental conditions were optimized. Bi et al. (2024) highlighted that certain maize genotypes exhibit inherent resilience to planting density variations, allowing them to maintain consistent ear size even under different spacing conditions. The results of the present study align with these findings, suggesting that the observed differences

in LE may be more influenced by genetic potential rather than by planting distance alone. Environmental factors such as soil fertility, moisture availability, and temperature fluctuations may also contribute to the minor variations in ear length, as supported by Ullah, Saqib, Khan et al. (2024), who found that planting distance did not significantly affect ear diameter, reinforcing the idea that within this spacing range, maize plants maintained similar growth patterns.

Table 3 presents the effects of varying gibberellic acid (GA3) concentrations and planting distances on maize ear length (LE). The data indicate that both factors influence ear development, though the impact varies across treatments. Under a planting distance of 20 cm (PD20), the control group without GA3 (WOG + PD20) exhibited a mean ear length of 11.87 ± 0.42 cm. The application of 175 mL GA3 per hectare (175GA3 + PD20) resulted in a comparable ear length of 11.80 ± 0.35 cm. Interestingly, increasing the GA3 concentration to 200 mL per hectare (200GA3 + PD20) led to a slight increase in ear length (12.20 ± 0.75 cm), while the highest concentration of 225 mL per hectare (225GA3 + PD20) resulted in a reduced ear length of 10.68 ± 0.77 cm. At a wider planting distance of 25 cm (PD25), the control group (WOG + PD25) had a mean ear length of 10.55 ± 0.90 cm. The 175GA3 + PD25 treatment showed an increased ear length of 11.02 ± 0.43 cm, and the 200GA3 + PD25 treatment further increased ear length to 11.39 ± 0.60 cm. Notably, the 225GA3 + PD25 treatment exhibited the longest ear length in this group, measuring 12.08 ± 0.63 cm. Comparing these findings with existing literature reveals both consistencies and divergences.

For instance, a study by Ullah, Saqib, Zaman et al. (2024) demonstrated that exogenous application of compounds like melatonin and sodium nitroprusside can mitigate stress effects in maize, leading to improved growth parameters, including ear length. While their focus was on stress mitigation rather than GA3 application, the positive impact on ear length aligns with the observed benefits of moderate GA3 concentrations in our study. Additionally, Ullah, Saqib, Khan et al. (2024) explored the role of sodium nitroprusside in plants and its interaction with phytohormones under various conditions. Their findings highlight the complexity of hormone interactions in plant development. This underscores the importance of optimizing hormone applications, such as GA3, to achieve desired agronomic outcomes without inducing adverse effects.

Ear Diameter (mm)

Table 1 presents the results of the effect of Factor A, likely representing different treatments on the ED in maize. There are variations in ED among the different treatments. The WOG exhibited the largest ED with a mean of 36.97 ± 0.83 mm, followed by the 225GA3 treatment with a mean of 36.56 ± 0.42 mm. However, treatments with 175GA3 and 200GA3 had slightly smaller ED, with means of 36.03 ± 0.11 mm and 34.99 ± 1.15 mm,

respectively. The result indicated no significant difference in the ear diameter of maize based on the different concentrations of GA3. Several factors could contribute to these observed differences. The physiological response to GA3 may vary depending on the concentration applied, with higher concentrations potentially causing adverse effects on ear development.

Table 2 illustrates the impact of Factor B, which likely represents different planting distances, on ED in maize. There is a slight variation in ED between the two planting distances. The mean ear diameter for the PD20 planting distance is 35.92 ± 0.22 mm, whereas for the PD25 planting distance, it is slightly larger at 36.35 ± 0.22 mm. These results suggest that altering the planting distance from PD20 to PD25 may have a minimal impact on ear diameter in maize. The observed difference, while statistically significant, is relatively small, indicating that planting distance alone may not be a major determinant of ear diameter variability in maize.

Table 3 provides a comprehensive view of the effect of different treatments on ED in maize, in combination with different GA3 concentrations and planting distances. Upon thorough analysis, it is evident that the interaction of the treatments has a discernible impact on ear diameter. Comparing GA3 concentrations within the same planting distance reveals noteworthy differences in ED. For instance, under the PD20 planting distance, the treatment WOG + PD20 exhibits the largest ear diameter with a mean of 37.57±1.56 mm, while treatments with GA3 (175GA3 + PD20, 200GA3 + PD20, 225GA3 + PD20) generally show slightly smaller ED ranging from 35.36 ± 0.65 mm to 36.15 ± 0.14 mm. Similarly, under the PD25 planting distance, the control treatment WOG + PD25 displays a smaller ED of 34.45 ± 1.56 mm, whereas treatments with GA3 (175GA3 + PD25, 200GA3 + PD25, 225GA3 + PD25) exhibit larger ED ranging from 35.52 ± 0.49 mm to 37.37 ± 1.36 mm.

Biomass Yield (g)

BY obtained per plant applied with different concentrations of GA3 is shown in Table 1. WOG gave the highest BY with a mean of 2696.67 ± 188.71 g, followed by 200GA3 with 2489.83 ± 18.13 g, 175GA3 with 2439.00 ± 68.96 g, and 225GA3 with a mean of 2406.33 ± 101.63 g, respectively. However, the table showed that the mean of BY (fresh) was not significantly affected by the different concentrations of GA3. Table 2 represents the BY as affected by planting distances. The highest mean BY was recorded in PD25 with a mean value of 2727.42 ± 219.46 g, while PD20 exhibited the lowest mean BY with a value of 2288.50 ± 219.46 g. However, the results showed that the different planting distances did not significantly affect the mean biomass yield (fresh). Table 3 provides a detailed impact of different treatments, specified by Treatment, in conjunction with distinct planting distances and GA3 concentrations, on maize BY measured in grams. Upon thorough analysis, it becomes apparent that GA3 and the planting distances have notable effects on BY in maize.

When comparing treatments, there are considerable variations. For instance, under the PD20 planting distance, the control treatment WOG + PD20 exhibits a biomass yield of 2724.67 ± 287.97 g, while treatments with GA3 (175GA3 + PD20, 200GA3 + PD20, 225GA3 + PD20) generally display lower biomass yields ranging from 2389.33 ± 47.37 g to 2668.67 ± 231.97 g. Similarly, under the PD25 planting distance, there are significant differences in biomass yield among treatments. The control treatment WOG + PD25 shows a biomass yield of 2296.00 ± 140.70 g, while treatments with GA3 (175GA3 + PD25, 200GA3 + PD25, 225GA3 + PD25) exhibit a wider range of biomass yields, from 1174.00 ± 1262.69 g to 3068.67 ± 631.97 g. However, the results showed no significant difference in the effects of the different treatments.

Weight of 1000 Kernels (g)

Table 1 illustrates the impact of different concentrations of GA3 on the weight of KW. The application of GA3 at a concentration of 175 ppm resulted in the highest mean kernel weight (281.60 ± 6.96 g), slightly surpassing the control group (280.50 ± 6.13 g). Higher concentrations of GA3 (200 ppm and 225 ppm) were associated with reduced kernel weights, suggesting a potential inhibitory effect at elevated levels. However, the results indicated that these differences were not statistically significant, implying that GA3 application did not markedly influence kernel weight under the conditions tested. Similarly, variations in planting distance (PD) showed that the PD20 spacing yielded the heaviest kernels (219.67 ± 24.71 g), followed by PD25 (269.08 ± 24.71 g). Despite these observations, ANOVA results demonstrated no significant effect of planting distance on kernel weight. Furthermore, the combined treatments of GA3 application and planting distance did not exhibit significant interactions affecting kernel weight, as evidenced by the range of weights observed across different treatment combinations. The study investigating the impact of GA3 on maize under different planting dates found no significant effect on grain yield and 1000-seed weight, suggesting that factors such as planting date and environmental conditions may modulate the responsiveness of maize to GA3 application (Naghashzadeh et al., 2009). Conversely, GA3 application, particularly at optimal concentrations, can enhance growth parameters and yield attributes, including plant height, number of grains per cob, and weight (Singh et al., 2018). The lack of significant effects observed in this study could be attributed to several factors, including environmental conditions, maize variety, and the specific concentrations of GA3 used. It is possible that the maize variety employed in this experiment exhibits a limited response to GA3, or that the environmental conditions during the study were not conducive to expressing the potential benefits of GA3 application. Additionally, the timing and method of GA3 application could influence its efficacy.

Computed Yield (kg/ha)

The results in Table 1 demonstrate the impact of different concentrations of GA3 on computed yield (CY) per hectare. The WOG achieved the highest yield at 2477.78 ± 152.68 kg per hectare, followed by the 200GA3 treatment with a mean yield of 2332.22 ± 7.13 kg per hectare. The 175GA3 treatment yielded 2260.74 ± 64.35 kg per hectare, while the 225GA3 treatment had the lowest yield at 2229.63 ± 95.46 kg per hectare. Despite these differences in yield, the results indicated that the mean CY was not significantly affected by the different concentrations of GA3. These findings align with previous studies that examined the role of GA3 in maize productivity. GA3 application has been shown to enhance vegetative growth and biomass accumulation, yet its direct impact on final yield varies depending on environmental conditions and nutrient availability (Akter et al., 2014). Similarly, Shahzad et al. (2021) reported that while GA3 treatments increased maize height and biomass, yield improvements were not always statistically significant.

Table 2 focuses on the effect of planting distances on CY, showing that the PD25 planting distance resulted in the highest CY at 2503.15 ± 178.06 kg per hectare. This was higher than the yield for the PD20 planting distance, with a weighted mean CY of 2147.04 ± 178.06 kg per hectare. Results revealed that the mean computed yield per hectare was significantly affected by the different planting distances. These consistent results show that wider spacing in maize planting allows better root expansion and reduces competition for resources, resulting in higher yields (Shao et al., 2018; Gao et al., 2010). Conversely, overly dense planting (such as PD20) can lead to increased competition for light, nutrients, and water, negatively impacting yield (Postma et al., 2021).

Table 3 explores the interactive effects of varying GA3 concentrations and planting distances on CY. The highest yield was obtained from the 175GA3 + PD25 treatment, which yielded 2827.41 ± 502.32 kg per hectare. This was significantly higher than the WOG + PD20 treatment yield, which produced 2494.81 ± 169.72 kg per hectare. The yields from other treatment combinations ranged from 1631.85 ± 693.24 kg to 2827.41 ± 502.32 kg. The significant interaction between GA3 application and planting distance highlights the importance of optimizing both factors for maximum maize productivity. Rademacher (2015) demonstrated that growth regulators like GA3 can be more effective when combined with optimal plant spacing, as the availability of resources and reduced intra-species competition amplify the effects of growth-promoting hormones. This study's findings suggest that a GA3 concentration of 175 mL combined with a planting distance of 25 cm is the most effective combination for maximizing maize yield. Mahender Singh et al. 2018 investigated the effects of various gibberellic acid (GA3) concentrations on maize yield. The findings revealed that applying GA3 resulted in the highest grain yield, with 3,522 kg/ha during the kharif season and 4,277 kg/ha during the rabi season. This suggests that while GA3 application positively influences maize yield, increasing the concentration beyond a certain point does not lead to significant yield improvements.

CONCLUSION

Based on the comprehensive analysis of the results presented across various tables, it can be concluded that both gibberellic acid (GA3) application and planting distance have significant effects on various growth parameters of maize, including plant height and computed yield. GA3 application, particularly at a concentration of 175GA3, generally resulted in favorable plant height and yield outcomes. However, the influence of GA3 on other parameters, such as ear diameter and biomass yield, varied depending on the concentration used. Additionally, planting distance played a crucial role, with wider distances favoring higher plant height and yield performance. Interactions between the GA3 application and planting distance enhance the yield capability of the hybrid corn, highlighting the importance of considering both factors in optimizing maize cultivation practices. While the short-term benefits of GA3 application are evident, repeated use of growth regulators may have cumulative impacts on soil health and long-term maize productivity. Continuous application of GA3 could alter soil microbial communities, nutrient dynamics, and soil fertility, which may affect subsequent cropping cycles. Therefore, sustainable use strategies, such as periodic soil assessments and integrated nutrient management, should be explored to mitigate negative long-term effects. Further in-depth investigation is recommended using other varieties of maize to determine if there are varietal differences in the response to GA3 application and different planting distances. Additionally, maize planting is recommended at the beginning of the wet season to ensure sufficient moisture during the germination and early growth stages, further optimizing crop establishment and yield potential.

ACKNOWLEDGEMENTS

We wish to express our sincere appreciation to the esteemed professors at Isabela State University—College of Agricultural Sciences and Technology for their generous guidance and opportunities, which enabled us to conduct this study. Their expertise and unwavering support were paramount in ensuring the successful execution of our research endeavors. We are profoundly grateful for their dedication to fostering the growth and development of future scholars and researchers.

REFERENCES

Akter, N., Islam, M. R., Karim, M. A., & Hossain, T. (2014). Alleviation of drought stress in maize by exogenous application of gibberellic acid and cytokinin. *Journal of Crop Science and Biotechnology*, *17*, 41-48. https://doi.org/10.1007/s12892-013-0117-3

Al-Shaheen, M. R., & Soh, A. (2018). The effect of water deficit and gibberellic acid on growth, productivity of corn (*Zea mays* L.). *Journal of Advanced Research in Agriculture Science & Technology, 1*(1&2), 52-56.

Anjum, S. A., Ashraf, U., Zohaib, A., Tanveer, M., Naeem, M., Ali, I., & Nazir, U. (2017). Growth and development responses of crop plants under drought stress: A review. *Zemdirbyste-Agriculture, 104*(3), 267–276.

Bi, Y., Jiang, F., Zhang, Y., Li, Z., Kuang, T., Shaw, R. K., Adnan, M., Li, K., & Fan, X. (2024). Identification of a novel marker and its associated laccase gene for regulating ear length in tropical and subtropical maize lines. *Theoretical and Applied Genetics*, *137*, Article 94. https://doi.org/10.1007/s00122-024-04587-z

Camara, M., Vandenberghe, L., Rodrigues, C., de Oliveira, J., Faulds, C., Bertrand, E., & Soccol, C. (2018). Current advances in gibberellic acid (GA3) production, patented technologies and potential applications. *Planta, 248*, 1049-1062. https://doi.org/10.1007/s00425-018-2959-x

El-Nwehy, S. S., & Afify, R. R. M. (2023). Utilization of gibberellic acid (GA3) and mepiquat chloride (M.C) as growth regulators on maize to alleviate salinity stress. *SABRAO Journal of Breeding and Genetics, 55*(5), 1654-1665. http://doi.org/10.54910/sabrao2023.55.5.18

El-Sayed, M., Mazher, A. A. M., Abdel-Aziz, N. G., El-Maadawy, E. I., & Nasr, A. A. (2014). Effect of gibberellic acid and paclobutrazol on growth and chemical composition of Schefflera arboricola plants. *Middle East Journal of Agriculture Research*, *3*(4), 782-792.

Frank, B. J., Schlegel, A. J., Stone, L. R., & Kirkham, M. B. (2013). Grain yield and plant characteristics of corn hybrids in the Great Plains. *Agronomy Journal, 105*(2), 383-394. https://doi.org/10.2134/agronj2012.0330

Gao, Y., Duan, A., Qiu, X., Liu, Z., Sun, J., Zhang, J., & Wang, H. (2010). Distribution of roots and root length density in a maize/soybean strip intercropping system. *Agricultural water management*, *98*(1), 199-212. https://doi.org/10.1016/j.agwat.2010.08.021

Gao, C., El-Sawah, A. M., Ali, D. F. I., Hamoud, Y. A., Shaghaleh, H., & Sheteiwy, M. S. (2020). The integration of bio and organic fertilizers improve plant growth, grain yield, quality and metabolism of hybrid maize (*Zea mays* L.). *Agronomy, 10*(3), Article 319. https://doi.org/10.3390/agronomy10030319

Gohil, S., Singh, S., & Nawhal, A. (2023). Effects of nitrogen and gibberellic acid on growth, yield and economics of fodder maize (*Zea mays* L.). *International Journal of Environment and Climate Change*, *13*(10), 526-531. https://doi.org/10.9734/ijecc/2023/v13i102677

Hadi, F., Bano, A., & Fuller, M. P. (2010). The improved phytoextraction of lead (Pb) and the growth of maize (*Zea mays* L.): The role of plant growth regulators (GA3 and IAA) and EDTA alone and in combinations. *Chemosphere, 80*(4), 457-462. https://doi.org/10.1016/j.chemosphere.2010.04.020

Jiang, W., Thapa, S., Jessup, K. E., Hao, B., Hou, X., Marek, T., & Xue, Q. (2020). Corn response to later than traditional planting dates in the Texas High Plains. *Crop Science, 60*(2), 1004-1020. https://doi.org/10.1002/csc2.20042

Lambers, H., Oliveira, R. S., Lambers, H., & Oliveira, R. S. (2019). Photosynthesis, respiration, and long-distance transport: Photosynthesis. In H. Lambers & R. S. Oliveira (Eds.), *Plant Physiological Ecology* (pp. 11-114). Springer. https://doi.org/10.1007/978-3-030-29639-1_2

Liu, F., Yang, W., Wang, Z., Xu, Z., Liu, H., Zhang, M., & Sun, S. (2010). Plant size effects on the relationships among specific leaf area, leaf nutrient content, and photosynthetic capacity in tropical woody species. *Acta Oecologica*, *36*(2), 149-159. https://doi.org/10.1016/j.actao.2009.11.004

Mahender, A., Anandan, A., & Pradhan, S. K. (2015). Early seedling vigour, an imperative trait for direct-seeded rice: An overview on physio-morphological parameters and molecular markers. *Planta, 241*, 1027-1050. https://doi.org/10.1007/s00425-015-2273-9

Mukarram, M., Mohammad, F., Naeem, M., & Khan, M. M. A. (2021). Exogenous gibberellic acid supplementation renders growth and yield protection against salinity induced oxidative damage through upregulating antioxidant metabolism in Fenugreek (*Trigonella foenum-graceum* L.). In M. Naeem, T. Aftab, M. Masroor & A. Khan (Eds.), *Fenugreek: Biology and Applications* (pp. 99-117). Springer. https://doi.org/10.1007/978-981-16-1197-1_6

Naghashzadeh, M., Rafiee, M., & Khorgamy, A. (2009). Evaluation of effects of gibberellic acid on maize (*Zea mays* L.) in different planting dates. *Plant Ecopysiology, 3*, 159-162.

Noda-Leyva, Y., & Martin-Martin, G. J. (2017). Effect of planting distance on the yield of *Morus alba* (L.) var. yu-12. *Pastos y Forrajes, 40*(1), 23-28.

Philippine Statistics Authority. (2024). *Updates on April-June 2024 palay and corn estimates based on standing crop, 01 May 2024*. Philippine Statistics Authority. https://psa.gov.ph/sites/default/files/csd/Updates%20on%20April-June%202024%20Palay%20and%20Corn%20Estimates%20Based%20on%20Standing%20Crop%2C%2001%20May%202024.pdf

Postma, J. A., Hecht, V. L., Hikosaka, K., Nord, E. A., Pons, T. L., & Poorter, H. (2021). Dividing the pie: A quantitative review on plant density responses. *Plant, Cell & Environment*, *44*(4), 1072-1094. https://doi.org/10.1111/pce.13968

Rademacher, W. (2015). Plant growth regulators: Backgrounds and uses in plant production. *Journal of Plant Growth Regulation*, *34*, 845-872. https://doi.org/10.1007/s00344-015-9541-6

Reyes, C. M., Domingo, S. N., Mina, C. D., & Gonzales, K. G. (2009). *Climate variability, SCF, and corn farming in Isabela, Philippines: A farm and household level analysis*. Philippine Institute for Development Studies. https://eaber.org/wp-content/uploads/2011/05/PIDS_Reyes_2009_04.pdf

Salazar, A. M., Elca, C. D., Lapiña, G. F., & Salazar, F. J. D. (2021). *Issues paper on corn industry in the Philippines*. Philippine Competition Commission. https://www.phcc.gov.ph/storage/pdf-resources/1678085736_PCC-Issues-Paper-2021-01-Issues-Paper-on-Corn-Industry-in-the-Philippines.pdf

Shahzad, K., Hussain, S., Arfan, M., Hussain, S., Waraich, E. A., Zamir, S., Saddique, M., Rauf, A., Kamal, K. Y., Hano, C., & El-Esawi, M. A. (2021). Exogenously applied gibberellic acid enhances growth and salinity stress tolerance of maize through modulating the morpho-physiological, biochemical and molecular attributes. *Biomolecules*, *11*(7), Article 1005. https://doi.org/10.3390/biom11071005

Shao, H., Xia, T., Wu, D., Chen, F., & Mi, G. (2018). Root growth and root system architecture of field-grown maize in response to high planting density. *Plant and Soil*, *430*, 395-411. https://doi.org/10.1007/s11104-018-3720-8

Singh, B. P. (2010). Overview of industrial crops. In *Industrial Crops and Uses* (pp. 1-20). CAB International.

Singh, M. S. M., Kumawat, N. K. N., Tomar, I. S., Dudwe, T. S., Yadav, R. K., & Sahu, Y. K. (2018). Effect of gibberllic acid on growth, yield and economics of maize (*Zea mays* L.). *Journal of AgriSearch, 5*(1), 25-29. http://dx.doi.org/10.21921/jas.v5i01.11128

Taiz, L., Zeiger, E. Moller, I. M., & Murphy, A. (2015). *Plant Physiology and Development (6th ed.)*. Sinauer Associates Incorporated. https://www.scirp.org/reference/ReferencesPapers?ReferenceID=1752778

Thakur, A., Dilta, B. S., Mehta, D. K., Sharma, B. P., & Gupta, R. K. (2018). Effect of plant spacing and GA3 on growth and flowering of sweet william (*Dianthus barbatus* L). *International Journal of Farm Sciences, 8*(2), 122-125. https://doi.org/10.5958/2250-0499.2018.00056.3

Turner, N. C., Blum, A., Cakir, M., Steduto, P., Tuberosa, R., & Young, N. (2014). Strategies to increase the yield and yield stability of crops under drought - Are we making progress? *Functional Plant Biology*, *41*(11), 1199-1206. https://doi.org/10.1071/FP14057

Ullah, F., Saqib, S., Khan, W., Ayaz, A., Batool, A., Wang, W. Y., & Xiong, Y. C. (2024). The multifaceted role of sodium nitroprusside in plants: Crosstalk with phytohormones under normal and stressful conditions. *Plant Growth Regulation*, *103*(3), 453-470. https://doi.org/10.1007/s10725-024-01128-y

Ullah, F., Saqib, S., Zaman, W., Khan, W., Zhao, L., Khan, A., & Xiong, Y. C. (2024). Mitigating drought and heavy metal stress in maize using melatonin and sodium nitroprusside. *Plant and Soil, 508*, (1-2), 1-23. https://doi.org/10.1007/s11104-024-07077-9

Yang, H., Zhang, Z., Zhang, N., Li, T., Wang, J., Zhang, Q., & Xu, S. (2024). QTL mapping for plant height and ear height using bi-parental immortalized heterozygous populations in maize. *Frontiers in Plant Science*, *15*, Article 1371394. https://doi.org/10.3389/fpls.2024.1371394

Pertanika J. Sci. & Technol. 33 (4): 1887 - 1906 (2025)

PERTANIKA JOURNALS

SCIENCE & TECHNOLOGY

Journal homepage: http://www.pertanika.upm.edu.my/

Analysis of Phased Array Corrosion Mapping Data Using Probabilistic Detection (POD) Method

Jan Lean Tai[1], Mohamed Thariq Hameed Sultan[1, 2, 3]* and Farah Syazwani Shahar[1]

[1]Department of Aerospace Engineering, Faculty of Engineering, Universiti Putra Malaysia, 43400 UPM Serdang, Selangor, Malaysia
[2]Laboratory of Biocomposite Technology, Institute of Tropical Forestry and Forest Products (INTROP), Universiti Putra Malaysia, 43400 UPM Serdang, Selangor, Malaysia
[3]Aerospace Malaysia Innovation Centre [944751-A], Prime Minister's Department, MIGHT Partnership Hub, Jalan Impact, 63600 Cyberjaya, Selangor Darul Ehsan, Malaysia

ABSTRACT

Phased Array Corrosion Mapping (PACM) has emerged as a powerful tool for detecting localized corrosion in industrial settings, particularly in the petrochemical industry. However, its application has been limited to plant operating temperatures within the recommended range for on-stream ultrasonic testing. This study addresses this gap by conducting a comprehensive Probability of Detection (POD) analysis using the MH1823 POD software, following the guidelines of MIL-HDBK-1823A (Department of Defense Handbook, 2009). The binary hit/miss method was employed to evaluate the accuracy of PACM on carbon steel (CS) and stainless steel (SS 304 and SS 316) surfaces at elevated temperatures up to 250 °C. Experimental results demonstrated successful detection of all flat-bottom-hole (FBH) indications, with deviations categorized as "miss" when exceeding 10% of the designed dimension. The POD curves revealed robust detection capabilities across various temperatures, with distinct clusters exhibiting different a50, a90, and a90/95 values. These findings underscore the reliability and efficacy of PACM in high-temperature applications, offering a significant advancement in non-destructive testing (NDT) for the petrochemical industry. The study highlights the potential of PACM to enhance turnaround maintenance (TAM) by enabling accurate on-stream inspections, thereby reducing downtime and increasing operational efficiency. Future research should explore the "â versus a" method to further enhance the accuracy and understanding of PACM in NDT applications.

Keywords: Non-destructive testing, phased array ultrasonic testing, probability of detection, turnaround maintenance

ARTICLE INFO

Article history:
Received: 19 December 2024
Accepted: 27 March 2025
Published: 11 June 2025

DOI: https://doi.org/10.47836/pjst.33.4.10

E-mail addresses:
taijanlean2008@hotmail.com (Jan Lean Tai)
thariq@upm.edu.my (Mohamed Thariq Hameed Sultan)
farahsyazwani@upm.edu.my (Farah Syazwani Shahar)
* Corresponding author

e-ISSN: 2231-8526

© Universiti Putra Malaysia Press

INTRODUCTION

The continuous growth of the petrochemical industry necessitates the ongoing modification and expansion of existing factories to accommodate the production of additional by-products. However, these expansions result in increased complexity and maintenance requirements. Consequently, many petrochemical plants undergo periodic shutdowns and turnaround maintenance (TAM) after several years of operation. TAM is a critical process for addressing various maintenance needs, primarily due to the aging of equipment and infrastructure. Over time, aging can lead to wear and tear, corrosion, and other forms of degradation, resulting in decreased efficiency, increased safety risks, and the potential for unplanned shutdowns or catastrophic failures (Aiello et al., 2020). Additionally, the buildup of fouling or contaminants in equipment can reduce efficiency and increase the risk of corrosion or other damage, necessitating TAM to address these issues (Al-Turki et al., 2019).

The demand for TAM arises from potential disruptions; even minor repairs can lead to economic losses due to halted production of multiple products. While all facility owners strive to avoid maintenance-related shutdowns, they are acutely aware of the risks posed by neglecting proper maintenance, which can lead to unplanned shutdowns and industrial accidents (Hlophe & Visser, 2018).

In response, many owners are exploring optimizing the TAM process by minimizing turnaround time or extending the intervals between TAM events to maximize operational benefits (Al-Marri et al., 2020; Elwerfalli et al., 2019). The petrochemical industry faces significant corrosion-related challenges, leading to decreased efficiency, increased safety risks, and potential unplanned shutdowns or catastrophic failures.

Ultrasonic thickness gauging (UTG) is a popular method for detecting corrosion during on-stream inspections in the petrochemical industry, primarily due to its cost-effectiveness and ease of use. Inspectors can quickly learn to operate UTG with minimal training. However, UTG has some limitations; its point-by-point nature can lead to inadequate detection of localized corrosion and make inspections of larger areas time-consuming.

In contrast, phased array corrosion mapping (PACM) offers a more comprehensive solution. It is important to note that, despite its advantages, there are currently no established examples of ultrasonic applications for high-temperature operations. The recommended temperature range for ultrasonic testing (UT) is up to 52 °C (Jory, 2019). However, on-stream inspections may require work beyond these limits.

Previous experiments have been conducted to investigate the feasibility of extending the use of UT beyond its recommended temperature limit (Tai, Sultan et al., 2023). The results indicate that as temperature increases, the velocity of ultrasound waves decreases while attenuation increases. The following research aimed to build upon the previous experiment's findings and explore the effectiveness of PACM in detecting corrosion at

high temperatures. The results confirmed that PACM could accurately detect corrosion in high-temperature environments when the velocity and decibel settings were appropriately adjusted (Tai, Grzejda et al., 2023).

The utilization of Probability of Detection (POD) in Non-Destructive Testing (NDT) is of significant importance. POD provides a quantifiable measure of the success rate in identifying specific targets or flaws through designated inspection methods, thereby playing a crucial role in evaluating the effectiveness of novel NDT techniques (Cherry & Knott, 2022).

A review of academic articles published over the past two decades focusing on POD in relation to NDT reveals that UT and Eddy Current Testing (ECT) were among the initial methods to employ POD for assessing detection probabilities (Bato et al., 2020; Goursolle et al., 2016; Yusa, 2017). Following the development of POD and the introduction of Model-Assisted Probability of Detection (MAPOD) (Rodat et al., 2017), the application of POD has significantly expanded to encompass various NDT methods.

The literature review initially aimed to identify prior instances of POD applications in PACM. However, the limited availability of literature on this subject prompted a shift in focus toward using Phased Array Ultrasonic Testing (PAUT) (Bajgholi et al., 2023). While these two inspection methods differ in orientation, they share several commonalities.

A consistent factor contributing to the success of the output results is the incorporation of uncertainty parameters, as highlighted by numerous scholars in the literature. The selection of these parameters, including defect size, material thickness (Ribay et al., 2017), and water path considerations, plays a crucial role in PAUT, similar to conventional UT. Additionally, both methods utilize calibration blocks featuring flat bottom holes (FBH) and side drill holes (SDH) to calibrate the equipment (Dominguez et al., 2016; Marcotte & Liyanage, 2017).

This study aims to assess the accuracy of novel PACM testing techniques on surfaces with elevated temperatures of up to 250 °C through POD analysis. Upon reviewing the previously mentioned articles, it was noted that despite applying POD analyses to numerous NDT methods, such analyses were significantly absent for PACM. This gap represents the distinctive novelty of the current study.

METHODOLOGY

There are two distinct methods for conducting POD analysis: the “hit/miss” method and the “signal response versus flaw size” (â versus a) method. The choice between these methods depends on the nature of the data generated by the NDT system under examination (Rentala et al., 2018).

The “hit/miss” method is applied when the NDT system produces binary outcomes, meaning a flaw is either detected or not detected. In this method, the POD curve is estimated based on the proportion of detected flaws to the total number of flaws present in the sample

(Knott & Kabban, 2022b). This approach is typically used when the inspection data is discrete and lacks a measurable response associated with flaw detection. For example, in PT or RT, a flaw is either observed or not, with no measurable response linked to the detection.

In contrast, the "â versus a" method is utilized when the NDT system yields measurable responses that can be correlated with the size of the flaw. This method establishes a relationship between the signal response (â) and the flaw size (a), enabling the estimation of the POD curve based on the distribution of signal responses for a given flaw size. This approach is commonly used in NDT methods that provide measurable responses, such as UT and Eddy ECT (Kojima et al., 2019; Yusa et al., 2018; Zhu et al., 2018). It allows for assessing the system's sensitivity to different flaw sizes and provides a quantitative measure of its performance.

The "hit/miss" approach relies on examining the number of successful detections (hits) and false negatives (misses) in a series of inspections. Logistic regression is a widely used statistical method in this approach, establishing a model for the probability of detection as a function of various factors, such as flaw size, inspection conditions, and system parameters (Knott & Kabban, 2022a).

In the "â versus a" approach, regression analysis with censored data is the primary statistical technique. This method is employed when some flaw sizes remain unidentified (censored) by the NDT system. The goal is to address the censoring of non-detected flaws and estimate the probability distribution of the detected flaw sizes. The regression model can then be used to determine the mean and variance of the detected flaw size distribution, allowing for calculating the probability of detection curve based on the estimated distribution (Rentala & Kanzler, 2022).

The accuracy of the output is contingent upon the amount of input data; insufficient data can introduce bias. MIL-HDBK-1823A recommends analyzing a minimum of 40 representative defect data points for the "â versus a" method, alongside signal strength ("â") measurements and crack sizes ("a") (Department of Defense Handbook, 2009). In contrast, the "hit/miss" method does not process signal values. Instead, it estimates the POD curve based on binary results, where a hit indicates that a crack was detected and a miss signifies that it was not. This method necessitates more data due to the limited information it yields, requiring at least 60 data sets to avoid bias and ensure a reliable POD curve (Virkkunen et al., 2019).

The a90/95 value derived from the estimated POD curve is particularly significant in these applications. This value indicates the defect size that can be detected with a 90% probability and a 95% confidence interval, thereby providing a tangible measure of the reliability and effectiveness of the NDT process (Kim et al., 2021).

In a conventional two-parameter model, three key metrics are of interest: **a50**, **a90**, and **a90/95**. These parameters reflect different aspects of the Probability of Detection

(POD) curve:

- **a50**: This represents the discontinuity size for which the mean POD is 50%. It indicates the size at which the probability of detection is statistically expected to be 50%.
- **a90**: This is the discontinuity size for which the mean POD is 90%. It denotes the size at which the probability of detection is expected to be approximately 90%.
- **a90/95**: This parameter refers to the upper 95% confidence bound on a90, providing a level of certainty that the true a90 lies below this value, with 95% confidence.

The two-parameter model imposes a specific behavior on the POD curve: As the size of the discontinuity approaches zero, the POD should converge to zero; conversely, as the size approaches infinity, the POD should approach one (Knopp et al., 2019).

Binary Hit/Miss Approach

Several possible outcomes can result from NDT evaluations aimed at identifying defects. These outcomes include:

1. **True Positive (TP)**: A defect exists and is correctly detected by the assessment.
2. **False Positive (FP)**: No defects exist, but an incorrect assessment indicates the presence of defects.
3. **False Negative (FN)**: A defect exists, but the assessment fails to detect it.
4. **True Negative (TN)**: No defect exists, and the assessment correctly indicates the absence of a defect.

Two critical, independent probabilities are considered to quantify the capability of the NDT methods (Keprate & Ratnayake, 2015):

- **Probability of Detection (POD)** or probability of true positives (P(TP))
  This represents the likelihood that the assessment will correctly detect a defect. It is calculated using the following Equation 1:

$$POD\ or\ P(TP) = \frac{TP}{TP+FN} \qquad [1]$$

- **Probability of False Alarm (POFA)** or probability of false positives (P(FP))
  This represents the probability that the assessment incorrectly indicates the presence or absence of a defect. It is calculated using the following Equation 2:

$$POFA\ or\ P(FP) = \frac{FP}{TP+FP} \qquad [2]$$

Signal Response "â versus a" Approach

The "â versus a" method is utilized in NDT when measurable responses, typically in the form of signal amplitudes, are generated by the NDT system instead of binary outcomes

like “hit” or “miss.” This approach is particularly useful for NDT systems that produce quantitative data, allowing for a more comprehensive system performance evaluation. It is commonly employed in techniques such as UT and ECT, where signal amplitude provides valuable information about the size and characteristics of defects.

In the “â versus a” method, specifically in UT, the echo amplitude “â” is proportional to the measured crack size “a.” This relationship helps determine if the echo amplitude “â” is degraded due to noise. Given the variability in the relationship between “â” and “a,” the goal is to establish a threshold value for “â” that maximizes crack detection while minimizing false alarms caused by noise. To address this challenge, ASTM E3023 and MIL-HDBK-1823A utilize a linear function to relate “â” to “a” and calculate prediction intervals to account for noise and statistical uncertainty (ASTM E3023-21, 2021; Department of Defense Handbook, 2009).

This method allows for assessing the POD of a flaw based on the measured signal response and the flaw’s characteristics. However, unlike the hit/miss method, it lacks a single, straightforward formula.

PACM Experiment and Data Acquisition

PACM and PAUT share many similarities in the processes and equipment used, with the primary distinction in their defect detection approaches. PAUT employs steering and focusing of ultrasound beams to identify weld defects, whereas PACM maintains a normal beam orientation to detect material corrosion, lamination, or metal loss. This wave propagation resembles that of a 0-degree normal probe in UT. Both PAUT and PACM utilize A-, B-, C-, and S-scan displays to provide a comprehensive three-dimensional representation of inspection results, as illustrated in Figure 1.

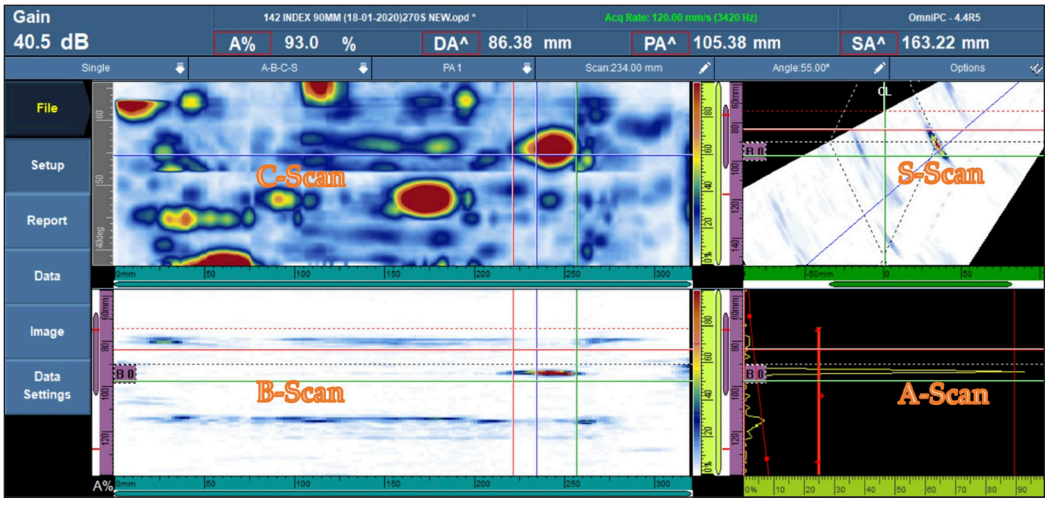

Figure 1. PAUT and PACM result presentation

The A-Scan displays the reflected signals and measures ultrasound echo amplitudes, integral to the quantitative measurement of the "â versus a" method used in POD analysis. In contrast, the B-Scan (side view), S-Scan (sectoral view), and C-Scan (top view) provide qualitative defect information relevant to the "hit/miss" method for defect detection.

Selecting appropriate calibration standards is critical in PACM experiments. Choosing between side drill holes (SDH) and FBH is particularly important. While SDHs are used in some NDT applications, they may not be suitable for PACM calibration, especially with a normal beam ultrasound configuration, where the ultrasound travels perpendicular to the test piece surface.

The test blocks designed for the PACM experiment comprised FBHs of various diameters and depths, as well as surface slots with varying depths, as shown in Figure 2. This design was compared to three different materials: (1) CS, (2) stainless steel 304 (SS 304), and (3) stainless steel 316 (SS 316).

The PACM experiment adhered to a standardized protocol from previous studies aligned with industry guidelines. The protocol specifies calibration procedures, transducer selection, and data acquisition parameters to ensure the consistency and comparability of the test results (Tai, Grzejda et al., 2023; Tai, Sultan, Shahar, Łukaszewicz et al., 2024).

A test specimen was subjected to controlled heating using a heat treatment machine, incrementally raising the temperature from 30 °C to 250 °C in 10-degree increments. This temperature variation aimed to mimic real-world conditions and assess the performance of the PACM under elevated temperature scenarios.

In the experimental setup, the specimens used for data collection included FBHs labeled A1 to A4 and B1 to B4, each with receptivity depths of 3 mm and 6 mm. Additionally, surface notches labeled C1 to C4 were incorporated, all having a consistent width of 5 mm but varying depths. As illustrated in Figure 3, which presents the C-scan results of the PACM experiment, this technique provides accurate depth measurements and visually differentiates depths using color coding. Furthermore, the size of the FBHs can be quantified using specialized software.

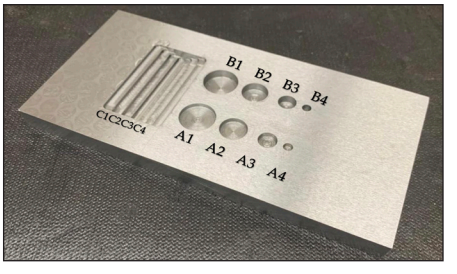

Figure 2. Schematic of the PACM experiment specimen design

POD Method with Mh1823 Software

The MIL-HDBK-1823A manual provides a comprehensive guide for constructing POD studies (Department of Defense Handbook, 2009). It also includes a useful guide for downloading Mh1823 POD software, which is built on the R statistical and graphics engine (https://www.r-project.org/). This software is accessible through the Statistical Engineering website developed by Annis (2023).

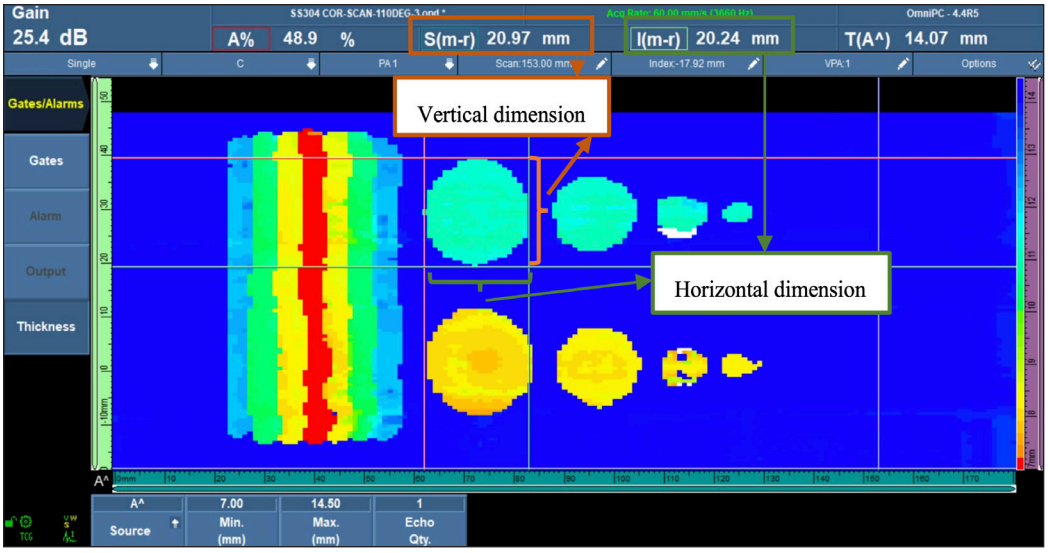

Figure 3. PACM data example to indicate the vertical and horizontal dimensions

The binary hit/miss POD approach was selected for analyzing PACM results due to its clear graphical representation and ability to measure flaw sizes. The following definitions were used for POD curve generation:

- The determination of hit/miss status depended on the precision of the results obtained, with all indications considered significant.
- Depth indications and dimensions of notches C1 to C4 were excluded because of consistent deviations below 0.5 mm.
- Measurements of specimens FBH A1–A4 and B1–B4, each with varying depths, were taken both vertically (VD) and horizontally (HD) to assess their variability concerning specimen dimensions (SD).
- A total of 138 deviation data points were collected for each FBH, resulting in an aggregate of 1,104 data points across all eight FBH indications. Example experimental data for FBH A1 are presented in Table 1.
- Instances of deviation equal to or exceeding 10% of the designated size were classified as “miss,” while those below this threshold were labeled “hit.”
- The POD curve was generated based on the same FBH dimension data for each temperature across the three different material types.

Table 1 demonstrates a systematic deviation increase for CS test results as temperature rises, particularly above 150 °C. Key observations include:

- At **30 °C**, deviations for all FBHs (A1–A4, B1–B4) remain ≤1 mm.
- At **190 °C**, vertical deviations (VD) reach 1.2 mm (FBH A1), and horizontal deviations (HD) peak at 0.79 mm.

Table 1
Experiment PACM data for carbon steel FBH A1

	CS test 1					CS test 2				CS test 3			
	SD	**VD**	**D**	**HD**	**D**	**VD**	**D**	**HD**	**D**	**VD**	**D**	**HD**	**D**
30 °C	20	21	1	20.01	0.01	20.7	0.7	19.69	0.31	19.31	0.69	20.06	0.06
40 °C	20	20.7	0.7	20.17	0.17	20.1	0.1	19.85	0.15	20.25	0.25	20.48	0.48
50 °C	20	19.7	0.3	19.85	0.15	20	0	19.69	0.31	21.6	1.6	20.32	0.32
60 °C	20	19.5	0.5	20.01	0.01	20.2	0.2	20.48	0.48	19.53	0.47	20.01	0.01
70 °C	20	20.8	0.8	20.17	0.17	21.2	1.2	20.05	0.05	21.32	1.32	20.32	0.32
80 °C	20	20.8	0.8	19.91	0.09	21.5	1.5	20.64	0.64	19.5	0.5	20.48	0.48
90 °C	20	21.1	1.1	19.63	0.37	21	1	20.52	0.52	20.24	0.24	20.35	0.35
100 °C	20	20.3	0.3	20.05	0.05	20.5	0.5	19.05	0.95	19.8	0.2	19.37	0.63
110 °C	20	20.5	0.5	20.15	0.15	20	0	19.21	0.79	20.42	0.42	19.15	0.85
120 °C	20	20.6	0.6	19.59	0.41	19.71	0.29	19.37	0.63	20.07	0.07	19.37	0.63
130 °C	20	20.4	0.4	19.53	0.47	20.43	0.43	19.15	0.85	20.43	0.43	19.04	0.96
140 °C	20	19.5	0.5	19.63	0.37	20.25	0.25	20.48	0.48	20.25	0.25	20.48	0.48
150 °C	20	19.6	0.4	19.53	0.47	20.45	0.45	20.32	0.32	19.89	0.11	20.64	0.64
160 °C	20	20.5	0.5	20.01	0.01	20.61	0.61	19.47	0.53	20.25	0.25	20.01	0.01
170 °C	20	20.7	0.7	19.69	0.31	21.17	1.17	20.17	0.17	21.32	1.32	20.45	0.45
180 °C	20	21	1	20.03	0.03	21.14	1.14	20.17	0.17	21.14	1.14	21.12	1.12
190 °C	20	21.2	1.2	19.21	0.79	20.07	0.07	20.17	0.17	20.79	0.79	20.76	0.76
200 °C	20	21.3	1.3	19.15	0.85	20.43	0.43	19.53	0.47	20.79	0.79	20.7	0.7
210 °C	20	21.1	1.1	20.21	0.21	21.14	1.14	20.48	0.48	20.07	0.07	20.01	0.01
220 °C	20	20.5	0.5	20.17	0.17	19.95	0.05	20.64	0.64	19.71	0.29	19.05	0.95
230 °C	20	21	1	20.41	0.41	20.78	0.78	20.64	0.64	19.8	0.2	20.05	0.05
240 °C	20	20	0	20.17	0.17	20.96	0.96	20.96	0.96	20.61	0.61	19.53	0.47
250 °C	20	20.2	0.2	20.64	0.64	20.79	0.79	20.7	0.7	19.53	0.47	20.64	0.64

Notes. All units in mm. SD = specimen diameter;VD = vertical dimension; HD = horizontal dimension; D = deviation

- At **250 °C**, HD deviations for FBH B1 exceed 0.7 mm, approaching the 10% threshold for "miss" classification.

RESULTS AND DISCUSSION

The "hit/miss" model is a core component of POD analysis, facilitating the quantification of the likelihood of correctly detecting flaws or defects. This model offers four distinct link functions, each with unique mathematical characteristics:

1. Logit, Logistic, or Log-Odds Function: The Logit function is widely used in POD analysis due to its compatibility with binary outcomes. It transforms the probability of detection into log-odds, which aids in regression analysis and curve fitting.
2. Probit or Inverse Normal Function: Probit analysis serves as an alternative approach

that utilizes the cumulative distribution function of a standard normal distribution. This method can be advantageous when the logit function does not adequately fit the data.

3. Complementary Log-Log Function, Weibull: The Complementary Log-Log function effectively models rare events and tail probabilities, making it useful when dealing with extreme values during detection.
4. Loglog Function: The Loglog function is another option for modeling POD data, although it is less commonly utilized. This function is particularly beneficial for handling complex data distributions.

The MH1823 POD software allows users to select the most appropriate link function after inputting the data points. It provides eight possible POD curves, comprising four link functions for selection, as illustrated in Figure 4.

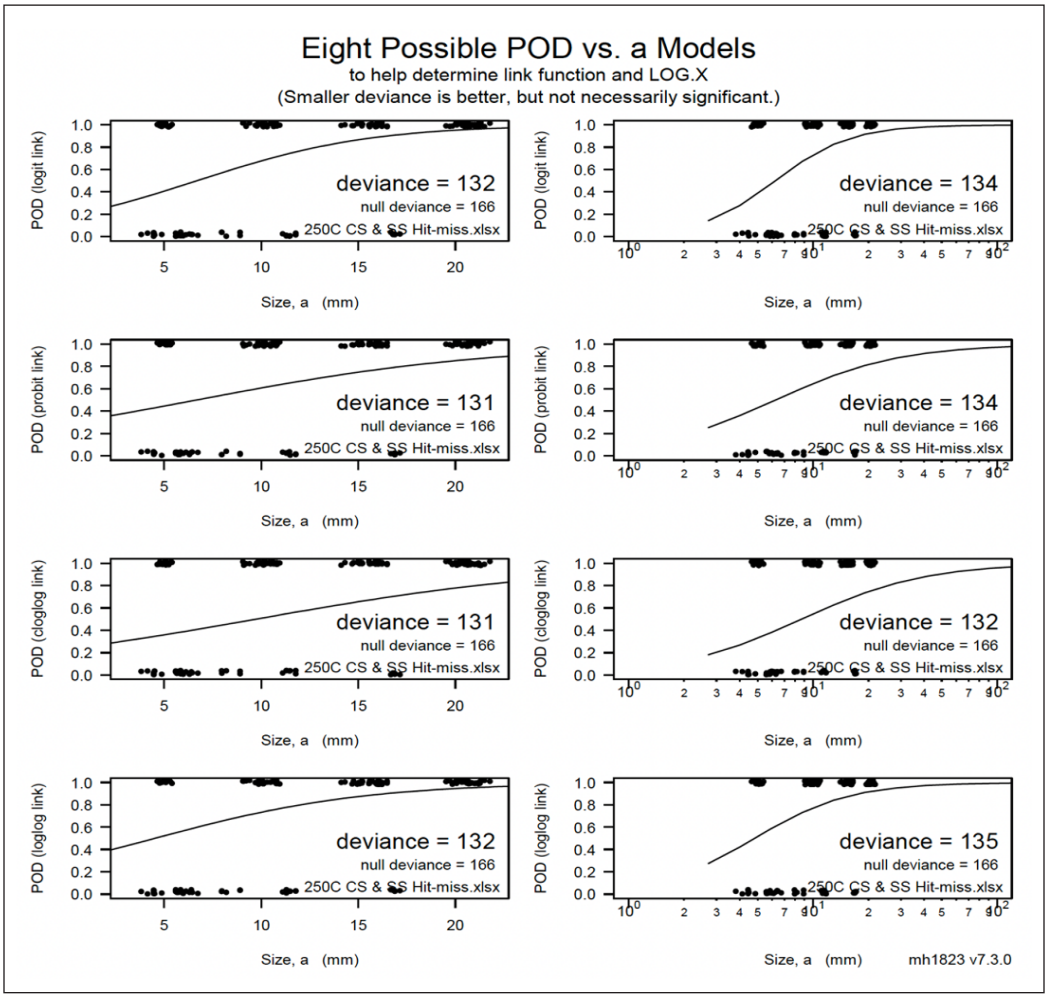

Figure 4. Eight possible POD curves generated from four-link functions

In this study, all POD curves are modeled using the logit function, which is defined as the natural logarithm of the odds ratio. The odds ratio represents the ratio of the POD to the probability of non-detection. Mathematically, the logit function is expressed as Equation 3.

$$Logit(P) = \ln(\frac{P}{1-P}) \quad [3]$$

Where P denotes the probability of detection, ln denotes the natural logarithm function.

Applying the logit function transforms the POD, originally ranging from 0 to 1, into a scale from negative to positive infinity. This transformation facilitates using linear regression techniques, which are simpler and more interpretable compared to non-linear models.

A notable advantage of the logit function is its symmetry around P=0.5. This symmetry implies that equal weight is assigned to both the probability of detection and non-detection, which is particularly beneficial in POD analysis, where both false positives and false negatives are significant.

The POD curve typically consists of a solid line and dotted lines. The solid line represents the estimated POD for a given flaw size, while the dotted lines indicate the confidence bounds around the estimated POD. These bounds reflect the level of uncertainty associated with the estimate, with their width depending on the amount and variability of the data. The solid line is the primary focus, providing an estimate of the probability of detecting a flaw of a given size. In contrast, the dotted lines convey the reliability of that estimate.

It is important to clarify that "a50" does not indicate the discontinuity size at which the mean POD reaches 50%, nor does it imply that 50% of the PACM indications align precisely with this size without deviation. Similarly, "a90" refers to the size at which the detection probability is expected to be approximately 90%.

A meticulous examination of the plotted POD curves reveals that PACM demonstrates robust detection capabilities across various materials and temperatures, ranging from 30 °C to 250 °C. The Hit/Miss POD results prioritize the accuracy of identified flaws, ensuring deviations remain below the 10% threshold.

This analysis underscores the reliability and efficacy of PACM in identifying flaws within diverse materials over a wide operational temperature range. The emphasis on minimizing deviations in the Hit/Miss POD approach further enhances the precision of defect identification and characterization.

Upon comparing all POD curves, four distinct clusters are observed. Table 2 presents the a50, a90, and a90/95 values for all temperatures from 30 °C to 250 °C across these clusters.

The variability in POD outcomes can be attributed to inherent differences in data combinations and collection methodologies. This variance highlights the absence of a consistent pattern in the POD curves, emphasizing the importance of considering these factors when interpreting the results.

The first cluster, illustrated in Figure 5, was formed at 190 °C. It displays a a50 of 6.655 mm, indicating that 50% of the FBHs larger than this size exhibit no deviation. In comparison, a90 at 17.67 mm denotes a 90% probability of no deviation for FBHs with dimensions equal to or greater than 17.67 mm. Additionally, the a90/95 value is 22.72 mm, which exceeds all processed data. The values of a50, a90, and a90/95 can be obtained from the graph (highlighted in red). This group predominantly includes temperatures of 60 °C, 70 °C, 100 °C, 110 °C, 130 °C, 140 °C, 150 °C, 160 °C, 190 °C, and 200 °C.

Table 2
a50, a90, and a90/95 in four clusters

	Temp (°C)	a50	a90	a90/95
Cluster 1	60	5.539	16.89	22.09
	70	7.372	17.98	22.84
	100	7.572	19.91	26.11
	110	7.213	18.27	23.36
	130	6.574	17.33	22.24
	140	3.844	17.53	24.65
	150	5.279	17.85	24.06
	160	5.459	17.16	22.67
	190	6.655	17.67	22.72
	200	8.521	18.27	22.59
Cluster 2	80	5.948	15.01	18.84
	90	6.239	16.46	20.96
	120	8.202	15.43	18.44
	170	4.041	16.02	21.62
	250	6.692	16.49	20.77
Cluster 3	30	2.153	22.46	NA
	40	1.811	23.77	NA
	50	0.576	22.70	NA
	210	1.684	22.25	NA
Cluster 4	220	6.523	22.41	32.77
	230	3.784	21.94	35.74
	240	6.555	21.98	31.68

The second cluster includes temperatures of 80 °C, 90 °C, 120 °C, 170 °C, and 250 °C, with one of the curves representing data collected at 250 °C, as shown in Figure 6. At this temperature, the recorded values for a50, a90, and a90/95 offer valuable insights into the flaw detection capabilities of the PACM technique. The a50 value at 250 °C is 6.692 mm, indicating a 50% probability of detecting a flaw with a diameter of 6.692 mm or larger. This suggests that the PACM technique maintains a relatively high level of accuracy in detecting flaws at this temperature, even for smaller flaw sizes.

The value of a90 at 250 °C is 16.49 mm, indicating a 90% probability of detecting a flaw with a diameter of 16.49 mm or larger. This suggests that the PACM technique is highly reliable in detecting larger flaws at high temperatures, with a low rate of false negatives. The value of a90/95 at 250 °C is 20.77 mm, which indicates a 95% probability of detecting a flaw with a diameter of 20.77 mm or larger, given that a flaw with a diameter of 16.49 mm or larger has already been detected with 90% probability. This value provides insight into the consistency and reliability of the PACM technique in detecting flaws at high temperatures.

In the third cluster, which includes temperatures of 30 °C, 40 °C, 50 °C, and 210 °C, as shown in Figure 7, a noteworthy observation is made. At 30 °C, there is a significant reduction in the value of a50, measured at 2.153 mm, compared to the other clusters.

The POD curve at 30 °C shows a significant reduction in the value of a50, indicating that the probability of detecting a 5 mm diameter flaw is lower at this temperature compared

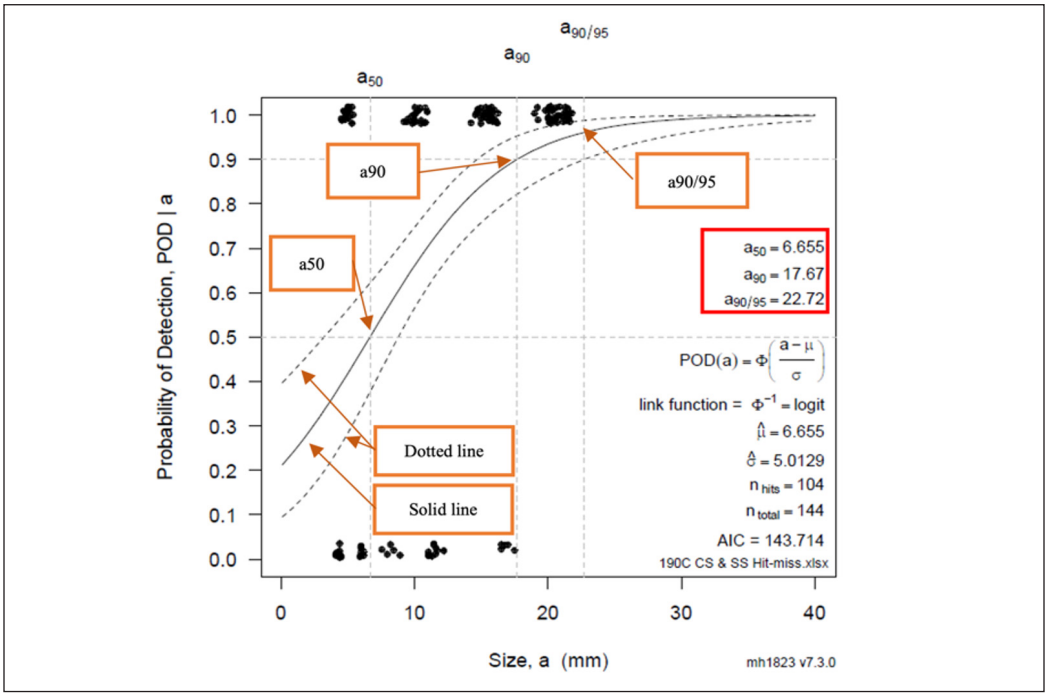

Figure 5. 190 °C POD curve

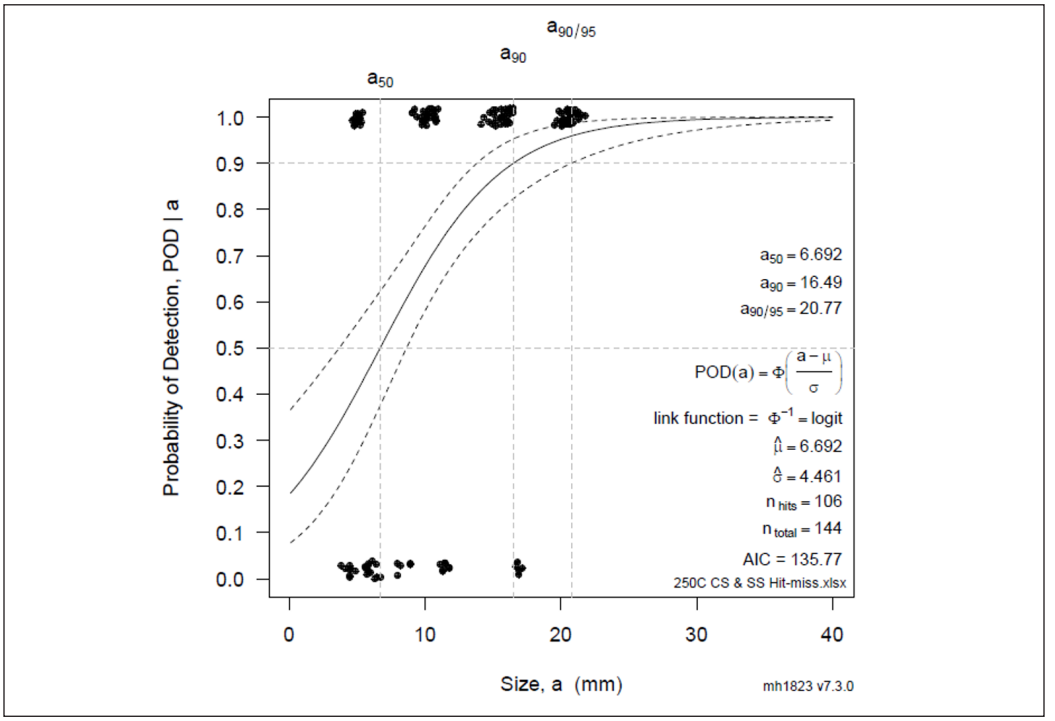

Figure 6. 250 °C POD curve

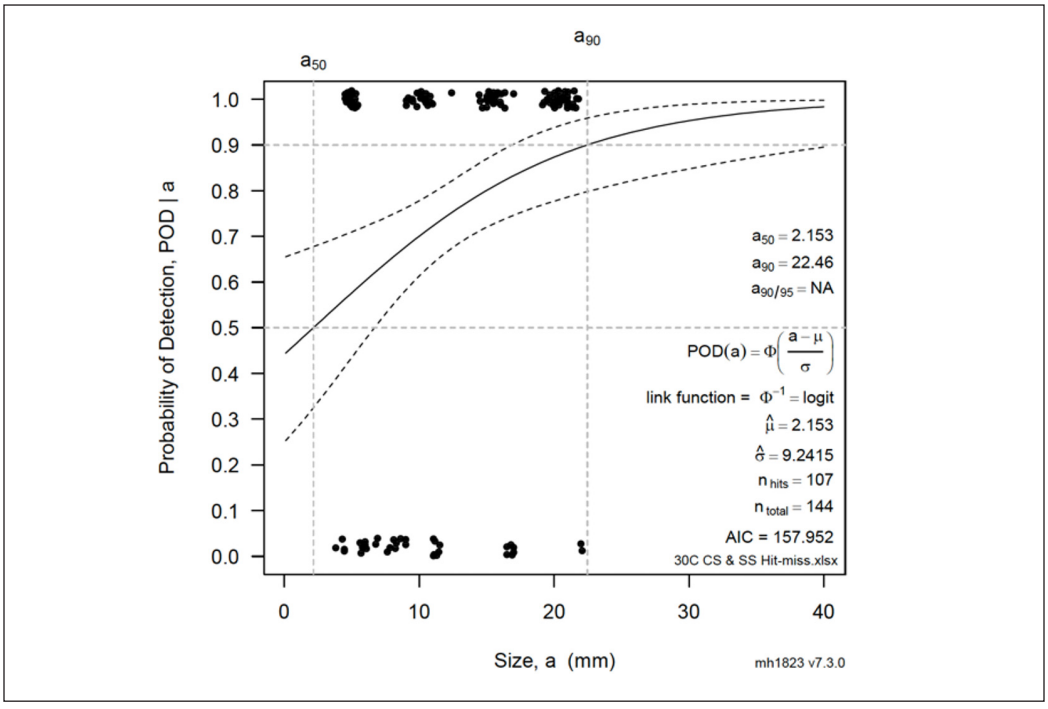

Figure 7. 30 °C POD curve

to others. This reduction can be attributed to the lower deviation observed in the 5 mm diameter FBH A4 and B4, which may be due to well-conditioned data or a high level of accuracy in the PACM technique at lower temperatures.

Furthermore, all graphs within this cluster indicate "NA" for a90/a95, meaning that the parameter does not exist at 30 °C. This occurs because the lower bound never reaches a POD value of 0.9, which is necessary to calculate a90/a95. This anomaly may also be attributed to well-conditioned data or a high level of accuracy in the PACM technique at lower temperatures, resulting in a POD ceiling where the maximum attainable POD is less than 1.

In summary, the lower deviation observed in the 5 mm diameter FBH A4 and B4, along with the absence of a90/a95 at 30 °C, suggests that the PACM technique demonstrates high accuracy without deviation in detecting smaller flaws at lower temperatures. However, data conditioning and the POD ceiling should still be considered when interpreting POD curves to ensure an accurate assessment of the PACM technique's performance, detecting flaws at different temperatures.

The fourth cluster, comprising temperatures of 220 °C, 230 °C, and 240 °C, exhibits distinct characteristics that set it apart from the other clusters. As depicted in Figure 8, the POD curve for this cluster at 230 °C shows a50 and a90 values of 3.784 mm and 21.94 mm, respectively. Notably, the hit-and-miss data patterns observed at this dimension resemble those in cluster 1.

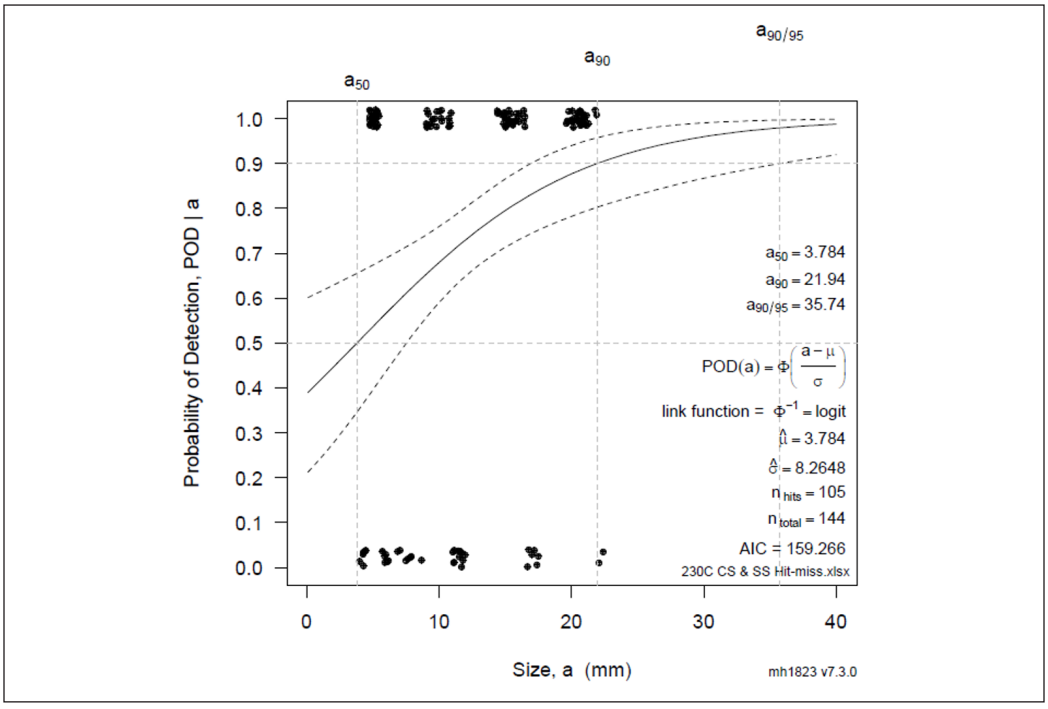

Figure 8. 230 °C POD curve

The above graphs demonstrate that most data have deviations below 10%. This indicates that PACM can be effectively utilized in high-temperature operations and across three types of materials.

POD Curve Analysis

The PACM technique demonstrated robust detection capabilities for larger flaws (≥17 mm) at all temperatures, with a90 values consistently exceeding 16 mm (Table 2). At high temperatures (e.g., 250 °C), the a90/95 value (20.77 mm) indicates a 95% confidence in detecting flaws ≥20.77 mm, which is comparable to low-temperature performance (e.g., 30 °C, a90 = 22.46 mm). However, smaller flaws (≤5 mm) showed reduced detectability at high temperatures due to increased ultrasonic attenuation and thermal noise. This suggests PACM is reliable for critical flaw detection in high-temperature environments but requires additional validation for minor defects.

Standardization of PACM Accuracy

To establish PACM accuracy, we propose adopting the MIL-HDBK-1823A guidelines for POD analysis, which define a90/95 as the critical metric for system reliability (Department of Defense Handbook, 2009; Tai, Sultan, Shahar, Yidris et al., 2024). Additionally,

referencing ASTM E2862-23 (2023) guidelines provides a standardized approach to POD analysis, critical for quantifying system reliability in NDT applications.

CONCLUSION

In the field of NDT, the POD serves as a critical metric for quantifying the likelihood of identifying specific targets or flaws through designated inspection methods. This study aimed to assess the effectiveness of PACM for detecting corrosion in high-temperature environments, specifically up to 250 °C, and to quantify its reliability through a POD analysis.

Our research has established that PACM can be effectively applied to CS, SS 304, and SS 316 surfaces within the experimental temperature range of 30 °C to 250 °C. Through comprehensive POD analysis using the binary hit/miss method, we have shown that PACM maintains robust detection capabilities across various materials and temperatures, with distinct clusters of a50, a90, and a90/95 values indicating consistent performance metrics.

The study contributes to the field by expanding the operational temperature range for reliable ultrasonic corrosion detection and offering a systematic approach to assessing PACM accuracy using POD analysis. This advancement addresses a significant gap in current industrial inspection capabilities, particularly for on-stream inspections in the petrochemical industry, where high-temperature operations are common.

While the hit/miss method provided valuable insights, future research should explore the "â versus a" method for POD analysis in PACM. This approach, which considers the size of detected flaws relative to their actual dimensions, has the potential to enhance the accuracy and depth of POD analysis. By incorporating A-Scan amplitude signals, this method could provide a more nuanced understanding of flaw-detection mechanisms and improve the precision of PACM inspections.

However, implementing the "â versus a" method presents practical challenges, particularly in data acquisition and comparison. The method requires extensive datasets to establish reliable relationships between detected and actual flaw sizes, which demands significant resources and time. Additionally, differences in data analysis techniques between the "â versus a" and hit/miss methods may complicate direct comparisons of results. Addressing these challenges will require standardized protocols and potentially new analytical frameworks to ensure consistent and comparable outcomes across different inspection scenarios.

The current study has limitations that should be acknowledged. Our research focused on three specific materials (CS, SS 304, SS 316) and relatively simple flaw geometries. While these materials are commonly used in industrial applications, the universal applicability of PACM needs further validation across diverse alloys and more complex defect configurations. Additionally, our laboratory-based experiments may not fully capture the variability and challenges of real-world inspection environments.

To build upon this research, we recommend several specific directions for future work:

1. Integrating the "â versus a" method into PACM POD analysis to enhance accuracy and provide a more detailed characterization of detected flaws.
2. Developing temperature-compensated calibration standards specifically designed for PACM inspections would improve consistency and reliability across different operational temperatures.
3. Conducting field trials in operational petrochemical plants to validate laboratory findings under actual industrial conditions and demonstrate the practical benefits of PACM in reducing downtime and maintenance costs.

By addressing these recommendations, future research can further establish PACM as a cornerstone technology for corrosion detection in high-temperature industrial applications, ultimately contributing to enhanced operational safety, extended equipment life, and reduced maintenance costs in the petrochemical and related industries.

ACKNOWLEDGEMENT

The authors are grateful for the financial support given by the Ministry of Higher Education Malaysia (MOHE) under the Higher Institution Centre of Excellence (HICOE2.0/5210004) at the Institute of Tropical Forestry and Forest Products. The authors would also like to express their gratitude to the Department of Aerospace Engineering, Faculty of Engineering, Universiti Putra Malaysia, and the Laboratory of Biocomposite Technology, Institute of Tropical Forestry and Forest Products (INTROP), Universiti Putra Malaysia (HICOE) for their close collaboration in this study.

REFERENCES

Aiello, G., Ben, J., Carpitella, S., Certa, A., Enea, M., & La Cascia, M. (2020). A decision support system to assure high-performance maintenance service. *Journal of Quality in Maintenance Engineering, 27*(4), 651-670. https://doi.org/10.1108/JQME-11-2019-0107

Al-Marri, A. N., Nechi, S., Ben-Ayed, O., & Charfeddine, L. (2020). Analysis of the performance of TAM in oil and gas industry: Factors and solutions for improvement. *Energy Reports*, *6*, 2276–2287. https://doi.org/10.1016/j.egyr.2020.08.012

Al-Turki, U., Duffuaa, S., & Bendaya, M. (2019). Trends in turnaround maintenance planning: Literature review. *Journal of Quality in Maintenance Engineering, 25*(2), 253-271. https://doi.org/10.1108/JQME-10-2017-0074

Annis, C. (2023). *Statistical Engineering*. (2023). https://statistical-engineering.com/

ASTM E3023-21. (2021). *Standard Practice for Probability of Detection Analysis for a Versus a Data*. ASTM International. https://store.astm.org/e3023-21.html

ASTM E2862-23. (2023). *Standard Practice for Probability of Detection Analysis for Hit/Miss Data*. ASTM International. https://store.astm.org/e2862-23.html

Bajgholi, M. E., Rousseau, G., Ginzel, E., Thibault, D., & Viens, M. (2023). Total focusing method applied to probability of detection. *International Journal of Advanced Manufacturing Technology*, *126*(7–8), 3637–3647. https://doi.org/10.1007/s00170-023-11328-x

Bato, M. R., Hor, A., Rautureau, A., & Bes, C. (2020). Experimental and numerical methodology to obtain the probability of detection in eddy current NDT method. *NDT and E International*, *114*, Article 102300. https://doi.org/10.1016/j.ndteint.2020.102300

Cherry, M., & Knott, C. (2022). What is probability of detection? *Materials Evaluation*, *80*(12), 24–28. https://doi.org/doi.org/10.32548/2022.me-04324

Department of Defense Handbook. (2009). *Nondestructive evaluation system reliability assessment*. Department of Defense Handbook. https://statistical-engineering.com/wp-content/uploads/2017/10/MIL-HDBK-1823A2009.pdf

Dominguez, N., Rodat, D., Guibert, F., Rautureau, A., & Calmon, P. (2016). POD evaluation using simulation: Progress, practice and perspectives regarding human factor. *AIP Conference Proceedings*, *1706*, 3–9. https://doi.org/10.1063/1.4940651

Elwerfalli, A., Khan, M. K., & Munive-Hernandez, J. E. (2019). Developing turnaround maintenance (TAM) model to optimize TAM performance based on the critical static equipment (CSE) of GAS plants. *International Journal of Industrial Engineering and Operations Management*, *01*(01), 12–31. https://doi.org/10.46254/j.ieom.20190102

Goursolle, T., Fauret, T., & Juliac, E. (2016). Effect of data amount on probability of detection estimation: Application to Eddy current testing. *e-Journal of Nondestructive Testing, 21*(7), 1-8. http://creativecommons.org/licenses/by/3.0/

Hlophe, S. C., & Visser, J. K. (2018). Risk management during outage projects at power plants. *South African Journal of Industrial Engineering*, *29*(3), 82–91. https://doi.org/10.7166/29-3-2051

Jory, C. (2019). Tips for internal corrosion using the echo to echo technique with compression. *The NDT Technician*, *18*(3), 8-11.

Keprate, A., & Ratnayake, R. (2015). Probability of detection as a metric for quantifying NDE capability: The state of the art. *Journal of Pipeline Engineering*, *14*(3), 2015–2017.

Kim, F. H., Pintar, A., Obaton, A. F., Fox, J., Tarr, J., & Donmez, A. (2021). Merging experiments and computer simulations in x-ray computed tomography probability of detection analysis of additive manufacturing flaws. *NDT and E International*, *119*, Article 102416. https://doi.org/10.1016/j.ndteint.2021.102416

Knopp, J. S., Ciarallo, F., & V.Grandhi, R. (2019). Developments in probability of detection modeling and simulation studies. *Materials Evaluation*, *73*(1), 55–61.

Knott, C. E., & Kabban, C. S. (2022a). Confidence interval comparisons for probability of detection on hit/miss data. *Materials Evaluation*, *80*(12), 50–65. https://doi.org/doi.org/10.32548/2022.me-04273

Knott, C. E., & Kabban, C. S. (2022b). Modern design and analysis for hit/miss probability of detection studies using profile likelihood ratio confidence intervals. *Materials Evaluation*, *80*(12), 32–49. https://doi.org/doi.org/10.32548/2022.me-04272

Kojima, M., Takahashi, H., & Kikura, H. (2019). Evaluation of capabilities on ultrasonic testing examiners using probability of defect detection and cumulative failure probability. *Journal of Advanced Maintenance*, *11*(2), 65–78.

Marcotte, O., & Liyanage, T. (2017). *Nondestructive examination (NDE) used fuel containers probability of detection for increased probability of detection*. The American Society for Nondestructive Testing. https://source.asnt.org/nondestructive-examination-(nde)-of-used-fuel-containers-for-increased-probability-of-detection/

Rentala, V. K., & Kanzler, D. (2022, October 24-27). Theoretical POD Assessment of an NDE 4.0 Application under the Context of Aero-Engine Lifing. In *Proceedings of the 2nd International Conference on NDE* (Vol. 4). Berlin, Germany. https://conference.nde40.com/Portals/NDE40_2021/bb/We.1.B.1.pdf

Rentala, V. K., Mylavarapu, P., & Gautam, J. P. (2018). Issues in estimating probability of detection of NDT techniques - A model assisted approach. *Ultrasonics*, *87*, 59–70. https://doi.org/10.1016/j.ultras.2018.02.012

Ribay, G., Mahaut, S., Cattiaux, G., & Sollier, T. (2017, September 4-7). Assessment of the reliability of phased array NDT of coarse grain component based on simulation. In *7th European-American Workshop on Reliability of NDE* (Vol. 22, No. 12). Potsdam, Germany. http://www.nde-reliability.de/portals/nde17/BB/21.pdf

Rodat, D., Guibert, F., Dominguez, N., & Calmon, P. (2017). Operational NDT simulator, towards human factors integration in simulated probability of detection. In *AIP Conference Proceedings* (Vol. 1806, No. 1). AIP Publishing. https://doi.org/10.1063/1.4974719

Tai, J. L., Grzejda, R., Sultan, M. T. H., Łukaszewicz, A., Shahar, F. S., Tarasiuk, W., & Rychlik, A. (2023). Experimental investigation on the corrosion detectability of A36 low carbon steel by the method of phased array corrosion mapping. *Materials*, *16*(15), Article 5297. https://doi.org/10.3390/ma16155297

Tai, J. L., Sultan, M. T. H., Tarasiuk, W., Napiórkowski, J., Łukaszewicz, A., & Shahar, F. S. (2023). Ultrasonic velocity and attenuation of low-carbon steel at high temperatures. *Materials*, *16*(14), Article 5123. https://doi.org/10.3390/ma16145123

Tai, J. L., Sultan, M. T. H., Shahar, F. S., Łukaszewicz, A., Oksiuta, Z., & Grzejda, R. (2024). Ultrasound corrosion mapping on hot stainless steel surfaces. *Metals*, *14*(12), 1–16. https://doi.org/10.3390/met14121425

Tai, J. L., Sultan, M. T. H., Shahar, F. S., Yidris, N., Basri, A. A., & Shah, A. U. M. (2024). Exploring probability of detection (POD) analysis in nondestructive testing: A comprehensive review and potential applications in phased array ultrasonic corrosion mapping. *Pertanika Journal of Science and Technology*, *32*(5), 2165–2191. https://doi.org/10.47836/pjst.32.5.14

Virkkunen, I., Koskinen, T., Papula, S., Sarikka, T., & Hänninen, H. (2019). Comparison of â versus a and hit/miss POD-estimation methods: A European viewpoint. *Journal of Nondestructive Evaluation*, *38*, Article 89. https://doi.org/10.1007/s10921-019-0628-z

Yusa, N. (2017). Probability of detection model for the non-destructive inspection of steam generator tubes of PWRs. *Journal of Physics: Conference Series*, *860*(1), 6–13. https://doi.org/10.1088/1742-6596/860/1/012032

Yusa, N., Tomizawa, T., Song, H., & Hashizume, H. (2018). Probability of detection analyses of eddy current data for the detection of corrosion. *Nondestructive Testing and Diagnostics*, *4*, 3–7. https://doi.org/10.26357/BNiD.2018.031

Zhu, J., Min, Q., Wu, J., & Tian, G. Y. (2018). Probability of detection for eddy current pulsed thermography of angular defect quantification. *IEEE Transactions on Industrial Informatics*, *14*(12), 5658–5666. https://doi.org/10.1109/TII.2018.2866443

Pertanika J. Sci. & Technol. 33 (4): 1907 - 1922 (2025)

PERTANIKA JOURNALS

SCIENCE & TECHNOLOGY

Journal homepage: http://www.pertanika.upm.edu.my/

Stochastic Distribution of Channel Allocation Algorithm for 5G and Future Generation Ultra-Dense Networks Applications

Joseph Sunday Ojo[1]*, Olalekan Lawrence Ojo[2] and Stephen Adebayo Olu-Ojo[1]

[1]Department of Physics, Federal University of Technology, P.M.B 704, Akure, Nigeria
[2]Department of Physics, University of Lagos, P.M.B. 1012, Yaba, 101245, Lagos, Nigeria

ABSTRACT

Channel allocation technique (CAT) is a crucial tool for assigning channels to cells in mobile telecommunication networks. It ensures scalability and meets the increasing demand for quality services in fifth-generation (5G) and future networks like sixth-generation (6G). However, multi-access channels in CAT can lead to inter-system interference, requiring enhanced spectral efficiency through advanced long-term evolution (LTE-A) technologies. This study evaluates stochastic CAT distribution in ultra-dense tropical environments, emphasizing its potential to support 6G's higher capacity and ultra-low latency of one microsecond. The evaluation is based on the LTE-A network model in the network simulation environment (NS3), testing with various network loads (i.e., the number of users) and typical mobile network providers (Operators A, B, and C). The goal is to assess the impact of inter-cell interference on LTE/LTE-A system performance using algorithms like soft frequency fractional reuse (SFFR), soft frequency reuse (SFR), and dynamic frequency fractional reuse (DFFR). Results from simulations comparing fractional frequency reuse techniques indicate that CAT improves signal quality for users. Further research reveals that SFFR is less flexible and performs poorly in the system, while SFR and DFFR reduce interference between cells, enhancing performance at cell edges. Additionally, among mobile service providers in Nigeria and based on random user distribution, Operator A delivers superior quality of service compared to Operators B and C, reflecting better system performance over larger areas.

Keywords: 5G network, channel algorithm technique, fractional frequency reuse, future generation, local network, mobile telecommunications, stochastic distribution, ultra-dense environment

ARTICLE INFO

Article history:
Received: 27 September 2024
Accepted: 08 April 2025
Published: 04 July 2025

DOI: https://doi.org/10.47836/pjst.33.4.11

E-mail addresses:
josnno@yahoo.com (Joseph Sunday Ojo)
lojo@unilag.edu.ng (Olalekan Lawrence Ojo)
stephenoluojo@gmail.com (Stephen Adebayo Olu-Ojo)
* Corresponding author

e-ISSN: 2231-8526

© Universiti Putra Malaysia Press

INTRODUCTION

The proliferation of mobile networks globally has demonstrated consistent growth over the past decade, largely due to the widespread adoption of cellular data connections. A large global population has embraced wireless cellular networks as the primary access to various communication services such as internet connectivity, banking, voice communication, entertainment, and text messaging, among others. As a result, the demand for mobile network services continues to increase daily. The integration of data connections into mobile cellular networks has enabled subscribers to engage in a wide range of activities through their mobile devices, including browsing the internet, making online purchases, listening to audio or video content, and facilitating monetary payments.

Using Nigeria as a case study, the number of subscribers to wireless internet connections has consistently risen thanks to the Global System for Mobile Communication (GSM), from 63 million in February 2014 to 87 million in April 2015 and now surpassing 100 million (Kuboye, 2017).

There has been a significant leap in technology from the first-generation (1G) to 5G, bringing new possibilities and opportunities. The recent 5G algorithm, representing cutting-edge technology, includes numerous innovative features aimed at addressing deficiencies in contemporary mobile communication solutions. These shortcomings have arisen due to evolving societal habits and increased requirements for wireless mobile communication (Alotaibi, 2023; Kuboye, 2018; Nordrum et al., 2017).

Traditionally, the cellular infrastructure strategy has focused on constructing a limited number of strong cell towers to expand cellular coverage over large areas. However, ensuring extensive coverage and establishing consistent connections with minimal latencies present significant challenges for today's infrastructure, especially for mobile service providers in Nigeria. These challenges have emerged due to the significant increase in connected mobile devices, higher bandwidth demands, and increased data consumption rates (Abejide, 2014; Nordrum et al., 2017).

Cellular systems have been a well-established solution for wireless communication over the past three decades. The rapid growth of high-speed multimedia applications, driven by advancements in cellular networks and mobile devices, has led to a growing demand for such services. Telecom operators, in response to this demand, are using the available spectrum more aggressively. However, this aggressive utilization has led to the concept of inter-cell interference (ICI), which is now causing traffic congestion in telecommunication network infrastructure (Islam & Chowdhury, 2013). The demand for faster data speeds has placed significant constraints on the existing cellular wireless infrastructure. Therefore, network designers must closely examine ICI behaviors to accurately estimate network performance for real-time applications and efficiently optimize resources (Bilal, 2017).

Stochastic distributions are models that depict the behavior of random variables over time. They can be used to model the variability of the wireless channel, which is influenced by interference, signal attenuation, and fading in wireless networks. Wireless networks can utilize stochastic processes to adapt to changing conditions and enhance their performance accordingly (Kodumuri, 2024). Therefore, a stochastic distribution is crucial in this study to optimize the distribution of users for optimal network performance. Additionally, data generated by wireless networks can be analyzed and learned from to identify patterns and trends, predict future network conditions, and make decisions that enhance network performance.

The LTE serves as the standardized nomenclature for the mobile technology initiative undertaken by the third-generation partnership project (3GPP), it transformed into a drive that developed fourth-generation (4G) and 5G mobile technology for data networks, voice and visual communication (Oguntoyinbo, 2013). The transformation that led to 4G network operation has prompted the telecom providers to adopt LTE-A (Peters et al., 2009).

The LTE-A networks provide peak downlink and uplink data speeds of up to 326 and 86.4 Mbps, respectively, with a 20 MHz bandwidth. LTE also offers adjustable bandwidth options ranging from 1.4 to 20 MHz. This feature can reduce latency to as low as 10 ms between the transmitter and the user, allowing for a transition time from inactive to active of less than 100 ms.

The LTE/LTE-A architecture consists of the user equipment (UE), which refers to the mobile devices used by end-users for wireless communication, such as cell phones and laptops with mobile broadband adapters. The advanced global terrestrial wireless communication network (UE-evolution packet core) handles communication via radio, maintaining bearer and UE settings. The Mobility Management Entity (MME) tracks user location, manages security, and handles paging procedures. The Packet Data Network Gateway (PGW) interacts with the outside world through the Serving Gateway (SGW) interface.

The simulation model of the LTE-Evolved Packet Core (LTE-EPC) data channel protocol is shown in Figure 1, depicting four sections linked together within a single unit. The model simplifies by combining PGW and SGW capabilities into an SGW/PGW unit, and UE and remote host compartments into transmission control protocol/user datagram protocol (TCP/UDP) nodes. This integration eliminates the need for S5 or S8 connections in NS3 simulations.

Frequency domain multiplexing (FDM) is the foundation for multiple access distribution in LTE networks. The downlink and uplink broadcasts use several methods, including: Single-carrier Frequency Division Multiple Access (SC-FDMA) for uplink distribution and orthogonal frequency-division multiple access (OFDMA) for downstream distribution. The SC-FDMA and OFDMA techniques offer distinct advantages compared

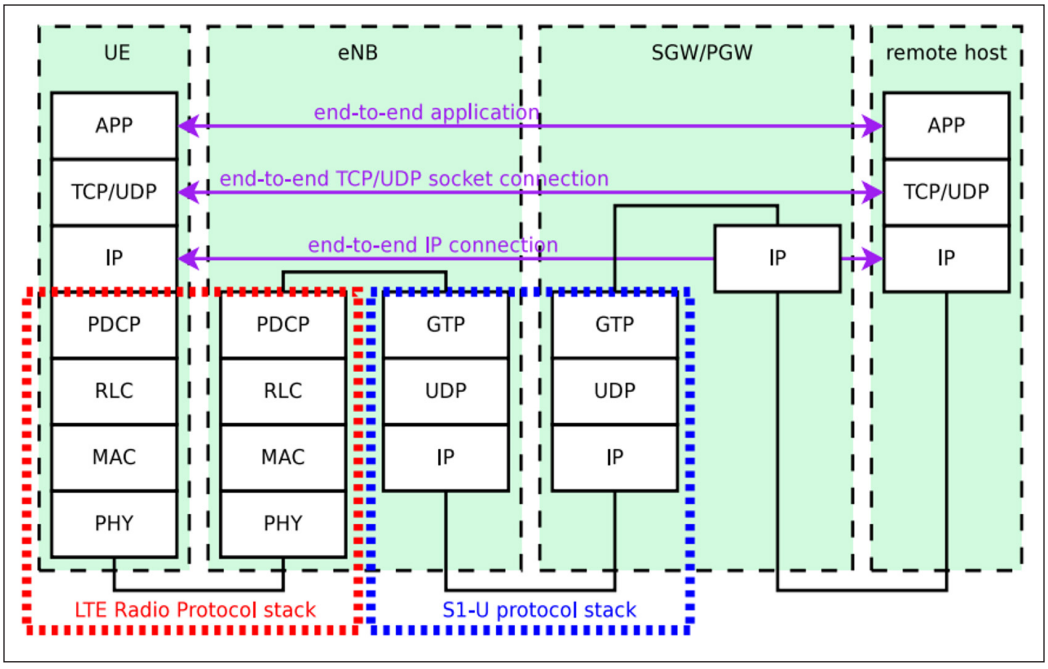

Figure 1. The architecture of the Long-Term Evolution-Evolved Packet Core (LTE-EPC) model, providing the LTE-EPC simulation model within NS3 (Liu, 2022)
Note. UE = User equipment; eNB = Evolved node B; SGW/PGW = Serving Gateway/Packet Data Network Gateway; APP = Application code; IP = Internet protocol; TCP/UDP = Transmission Control Protocol/User Datagram Protocol; PDCP = Packet Data Convergence Protocol; GTP = General Tunnelling Protocol; RLC = Radio Link Control; UDP = User Datagram Protocol; MAC = Media Access Control; PHY= Physical layer; S1-U = User Plane Interface

to earlier technologies like code division multiple access (CDMA), contributing to the robustness of communication and enabling effective management of interference. Additionally, multiple access techniques allow for the exploitation of multiuser diversity at finer granularities, enhancing the handling of frequency-selective fading and supporting various users experiencing different communication conditions during mobility (Abukharis et al., 2014; Zaki, 2012).

The performance of the system as a whole, as well as cell-edge users, is greatly impacted by interference from adjacent cells. Boudreau et al. (2009) and Himayat et al. (2010) investigated ways to mitigate ICI to assist cell-edge users experiencing slow speeds and poor quality of service (QoS). SFR, a type of inter-cell interference coordinator (ICIC) designed specifically for LTE platforms, is one such method.

The ICIC method can be categorized into two strategies: interference mitigation and avoidance.

(i) Interference mitigation focuses on reducing or suppressing ICI either at the point of sending signals or at the receiving end. Various methods fall under ameliorating inter-

system interference, such as:

- Interference averaging: This technique aims to minimise ICI by averaging out its effects. It involves statistical approaches that calculate the average interference power and adaptively adjust transmission parameters to mitigate its impact.
- Interference cancellation: This technique involves actively cancelling out the interfering signals to reduce ICI. Methods like beam forming can be employed to nullify or attenuate the interfering signals, improving overall network performance.
- Adaptive beam forming: This technique utilises smart antennas to dynamically adapt their beam patterns to minimise ICI. By steering transmission beams towards intended receivers and away from interfering cells, adaptive beam forming reduces the impact of ICI on network performance.

(ii) Interference avoidance refers to a set of frequency reuse algorithms implemented to introduce limitations on the transmission power and resource allocation. Its main objective is to reduce ICI while simultaneously making the intended signal better. This scheme is characterised by its avoidance strategy, aiming to reduce ICI without imposing additional computational burdens or requiring extra hardware elements on user devices. Its effectiveness lies in optimising LTE networks to deliver high-quality services to cell-edge users without compromising the performance of the customers using the cell centre. By implementing effective ICIC techniques in wireless networks, the goal is to significantly mitigate ICI and enhance overall network performance.

The paper is divided into various sections to discuss the related work used as a literature review and the definitions of notable terms such as throughput, packet delay, and packet loss ratio (PLR). The simulation method used, results, discussion, and conclusions are also included to summarize the work and highlight potential drawbacks for future research.

RELATED WORK

A low-complexity distributed SFR scheduling system with user categorization, balanced fairness, and throughput optimisation for all users was presented by Lee et al. (2013). Within a cell, the cell-centre band (CCB) and the cell-edge band (CEB) are the two distinct spectrum bands used in the method. Cell-edge users (CEUs) are users who are more affected by interference from nearby cells than other users, who are sometimes referred to as cell-centre users (CCUs). Gawłowicz et al. (2015) extended the use of the third version of network simulation environment (NS3) LTE platform to model the frequency fractional reuse (FFR) network; however, Ozovehe and Usman (2015) used key performance indicators (KPIs) based on data from drive tests or network management systems to assess the effectiveness of a live, operational cell phone network in Niger State (Minna), Nigeria. It was found that the performance of mobile services in Nigeria is not too good, and the signal performance and retention ability are unacceptable. Li et al. (2016) proposed an FFR algorithm that

performs better than the traditional FFR and SFR schemes. The results indicated that the proposed scheme proves to be efficient in interference control in the heterogeneous network. An assessment of deployed 4G-LTE services in Ghana based on drive test software and the NEC model algorithm was also conducted by Tchao et al. (2018). It was determined that 4G LTE can meet the constantly rising demand for the web when compared to the throughput required to handle data-driven bandwidth services. Using the NetSim training program, Almazroi (2018) evaluated the effectiveness of 4G broadband wireless networks and found that, in terms of bandwidth and compatibility with earlier networks, 4G has proven to be the best generation currently in use. Galadanci and Abdullahi (2018) used drive examination applications to analyse the efficiency of mobile phone networks in the Nigerian metropolis of Kano. The findings indicate that the efficiency of GSM systems in Kano is still far below the Nigeria Communication Commission (NCC) standard and well behind customers' desired outcomes. Based on the analysis of related literature, investigators have employed multiple methodologies to assess LTE network functionality. Khan et al. (2019) proposed a method for interference management compared with three existing FFR methods based on throughput and found out that the throughput increased linearly when the number of femtocells increased. In earlier studies on interference avoidance, the authors introduced different types of frequency reuse and FFR schemes available in the LTE module of NS3 (Tangelapalli & Saradhi, 2019). The results show the highest increase in throughput in downlink with SFR. Sarwar et al. (2020) worked on LTE-A interference management in OFDMA-based cellular networks; the result showed that LTE-A has become capable enough to reduce co-channel interference (CCI) and adjacent channel interference (ACI), while drive testing was the primary method used in Nigeria to evaluate real-time second and third-generation (2G and 3G) GSM wireless networks. Some recent investigations, however, did not compare mean packet delay and mean packet loss together with other measures of cellular network efficiency. To provide an overall evaluation, the current study compares the modelling results of two FFR platforms, SFFR and DFFR, and compares them to SFR, which has been extensively researched in almost all previous work on interference avoidance. In the recent work of Liu (2022), an evaluation of some frequency channel configuration methods over ultra-dense environments was conducted based on user scenarios. The paper adjusted some parameters of 19 units and compared among FFR, integer frequency reuse (IFR), transmission interference temperature limit (TX-ITL), and simultaneous water injection (SWI) method. The outcome demonstrates the TXITL-IFR3 technique's strong development prospects and ability to handle extremely dense customer requirements in ultra-dense environments. However, only the user capacity based on signal to noise ratio (SNR) was considered. Yautentzi et al. (2024) worked on the performance analysis of ultra-dense networks with frequency reuse. A simulation of an ultra-dense network coexisting with a macro network was performed, and an analysis

of how it affects the co-channel interference of the small cells of the ultra-dense network was studied. The result showed that as a strategy to mitigate interference, frequency reuse is used to improve performance. With the simulation, it was possible to provide a good insight into the performance of this type of network in terms of the maximum transmission rate. As a result, the goal of this paper is to simulate fractional frequency reuse in an LTE-A network environment by examining and comparing the performance (in the context of mean throughput, PLR, and packet delay) of heterogeneous cellular systems for both SFFR and DFFR algorithms. The performance of the simulation was also tested over three major network providers in Nigeria.

DEFINITION OF NOTABLE TERMS

Firstly, it is essential to define the three parameters used in the study, namely throughput, packet delay, and PLR.

Throughput refers the level of successfully received packets (a portion of the message sent) within a defined time frame. This metric consists of two distinct parts: total throughput and average throughput. Total throughput (TTp) refers to the total volume of information received over a specific time, while average throughput (ATp) denotes the amount of information received by customers in a specific time period (Maskooki et al., 2015). TTp and ATp can be expressed as follows:

$$\mathrm{TTp} = \frac{R_x}{T_{sim}} \qquad [1]$$

$$\mathrm{ATp} = \frac{R_x}{T_{sim} \cdot N_{users}} \qquad [2]$$

where, R_x refers to the total level of bits obtained, T_{sim} refers to the level of bits transmission, and N_{users} is the total number of users.

Packet delay refers to the average time it takes for data packets to travel from one location to another, often referred to as latency. Network latency consists of the time it takes for a data packet to travel from its original location to another location within a network. In terms of user experience, network latency directly impacts the speed of a user's actions, triggering a response from the network. For example, it affects how quickly a web page can be accessed and loaded over the internet.

The ratio of the total number of delivered packets to the number of packets that were lost is known as the packet loss ratio, or PLR, and can be expressed as:

$$\mathrm{PLR} = \frac{\text{Lost packets} \times 100\%}{\text{Sent packets}} \qquad [3]$$

The following questions are addressed in this paper:

(i) Based on the packet delay, throughput, and PLR for specific mobile service providers under various network loads, how significantly do inter-cell interferences affect the cell edges?

(ii) What effect does the cell have on downlink retransmission performance?

To address the aforementioned questions, the following objectives are considered:

(i) Deduce a distribution algorithm to reduce the ICI and examine the cell edges throughput; and

(ii) Estimate the network load of selected mobile service providers based on the number of users.

SIMULATION METHOD

The term 'simulation' is a mathematical description used to predict the actions of an actual process or system over time. By employing simulations, researchers can examine how systems or things behave dynamically in scenarios that would be harmful or impractical to replicate in reality. Researchers utilise simulations to assess and predict possible effects on the overall functioning of the system while changing individual system components.

In this work, the influence of ICI on the performance of the system has been assessed based on packet loss, packet delay, and throughput using an LTE platform. The analysis is based on computer simulation for producing and analysing the data, and the algorithm uses the LTE model based on NS3, whereby subscribers interact with a distant server via routes, connectivity to the internet, and point-to-point linkages made up of UEs, cells, and base stations (eNodeB). In this study, several network entities assist in the design and modification of LTE network models on the NS3 simulation environment. Different testing with multiple network loads (i.e., the number of users) was deployed to examine the outcome of ICI on LTE system performance using the DFFR, SFFR, and SFR algorithms. The NS3 simulator was also adapted for the selected mobile network providers (Operators A, B, and C) to compare and analyse the performance of the LTE system based on the delayed PLR and throughput across various network loads. The analyses also consider their distinct transmission power ratings, while utilising the same Ad Hoc On-demand Distance Vector (AODV) routing protocol. The simulation results are reported and analysed in several statistical plots.

A model comprising 19 hexagonal cells has been employed to assess specific FFR algorithms, including SFFR, SFR, and DFFR. This model utilises a term referred to as reuse of frequency based on a factor of three at the cell edge and one at the cell centre. The selection of the reuse factors and the cells was based on the 3GPP recommendation for LTE, with each cell serviced as an eNodeB, which is based on a scheduler, a power management strategy, and bandwidth. To reduce the total testing time in NS3, the modelling parameters

presented in Table 1 were typically selected using the 3GPP specifications for LTE and are similar throughout each simulation performed with the same data flow and simulation time for the selected algorithms. When modelling different network scenarios with different network loads, the UEs are randomly distributed between the cell centre and cell edge zone, which is an important parameter.

Additionally, the modelling process was predicated on the use of an identical power budget as the 3rd generation guidelines by SFR, DFFR, and the two outer areas of SFFR, or the middle and edge regions. It is anticipated that the central portion of SFFR-enabled cells will operate at a reduced power to conserve energy.

The evaluation of the adapted NS3 algorithms for Operators A, B, and C was carried out with the AODV routing protocol algorithm while considering only their different transmission power ratings as presented in Table 2. Different simulations were run for each service provider with the exact simulation period for a different number of nodes, and the results in terms of loss ratio of the packet, throughput, and delay of the packet were extracted, analyzed, and compared to ascertain the network service provider offering the most superior quality of service and system performance.

Table 1
Simulation parameters based on the 3GPP specifications for LTE

Parameters	Values
System bandwidth (MHz)	20
Carrier frequency (GHz)	2
Subcarriers bandwidth (kHz)	15
RBS' number	25
Cells' number	19
Radius of the cell (m)	1,000
SINR threshold (dB)	SFR (20); DFFR (25); SFFR (15)

Note. 3GPP = Third-Generation Partnership Project; RBS = Radio base station; SINR = Signal-to-noise ratio; SFR = Frequency Fractional Reuse; DFFR = Dynamic Frequency Fractional Reuse; SFFR = Soft Frequency Fractional Reuse

Table 2
Transmission power ratings of the selected mobile network (Ajibola et al., 2015)

Service provider (Operator)	Transmission power (dBm)
A	64
B	72
C	87

SIMULATION RESULTS AND DISCUSSION

The average packet delay of SFFR, DFFR, and SFR was calculated using the average number of UEs for both the cell edge and center cell. Figures 2(a) and 2(b) illustrate the impact of average packet delay on the number of customers in each cell, based on center and edge users, respectively. It was observed in Figures 2(a) and 2(b) that SFFR can support less than 24 users per cell at the center and less than 20 users at the edge without a significant increase in packet delay. However, DFFR can accommodate more users compared to SFFR. In general, as the number of users at the center and edge increases, so does the packet delay.

Overall, it was observed that in DFFR, the CEU has better system performance compared to SFFR. Additionally, DFFR outperforms SFFR at the CCU, where SFFR shows the lowest system efficiency and struggles to counteract ICI and fading due to reduced transmission power at the center region.

The throughput of SFFR, DFFR, and SFR was calculated based on the number of UEs and the cumulative distribution function (CDF) for both the cell edge and center cell. The results are shown in Figures 3(a) and 3(b). It was found that throughput decreases as the number of users increases for both center and edge cells. SFFR had lower interference with fewer users, resulting in lower throughput for CEU compared to DFFR and SFR. As the number of users increased, DFFR showed better performance in both center and edge cells compared to SFFR.

The throughput of each reuse scheme was also analyzed based on the CDF, as depicted in Figures 4(a) and 4(b). The results indicated that DFFR outperformed SFFR in terms of system throughput, as DFFR could support more users before experiencing a decrease in throughput. Therefore, DFFR has superior system throughput compared to SFFR.

Low load implies that there is no packet loss at the cell centre or cell edges because the amount of traffic sent and received is the same. As the number of users increases, there is an increase in packet loss at both the centre cell and the cell edge. High rates of packet loss can significantly degrade the perceived audio quality for users utilising internet telephony applications.

Figure 5(a) illustrates the influence of the PLR on the number of users for the center cell. Both SFR and DFFR can accommodate more than 28 users before experiencing

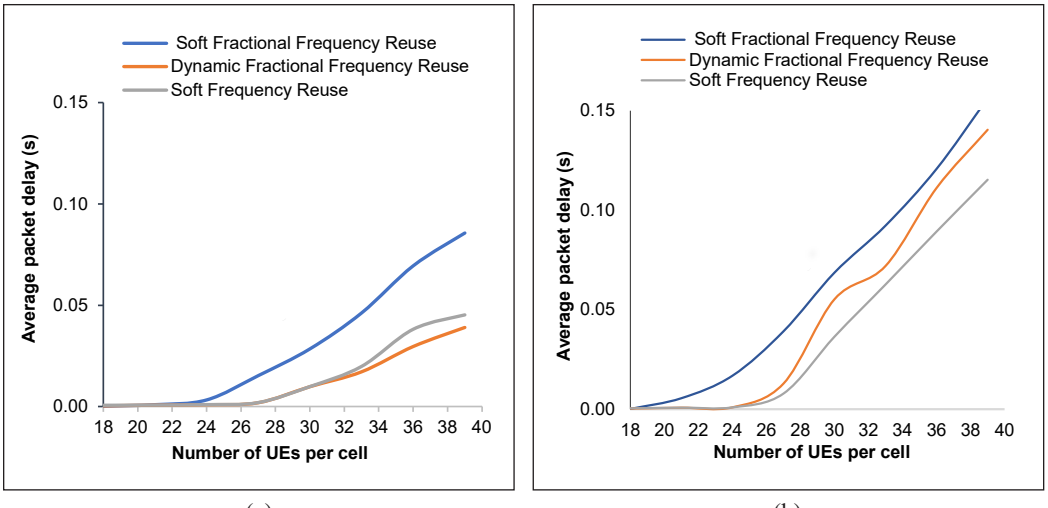

Figure 2. Average packet delay for (a) cell centre users and (b) cell edge users
Note. UE = User equipment

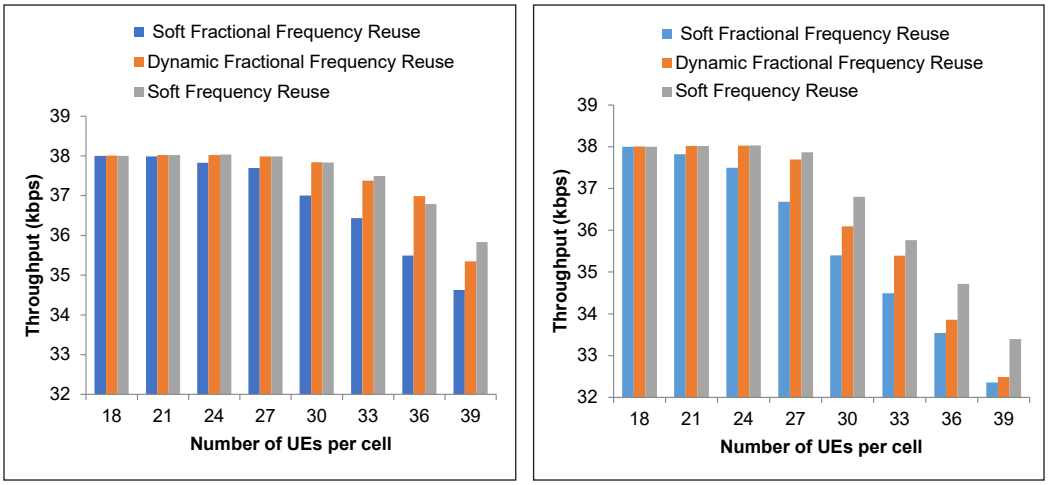

Figure 3. Average throughput per user equipment (UE) for (a) the cell centre users and (b) the cell edge users

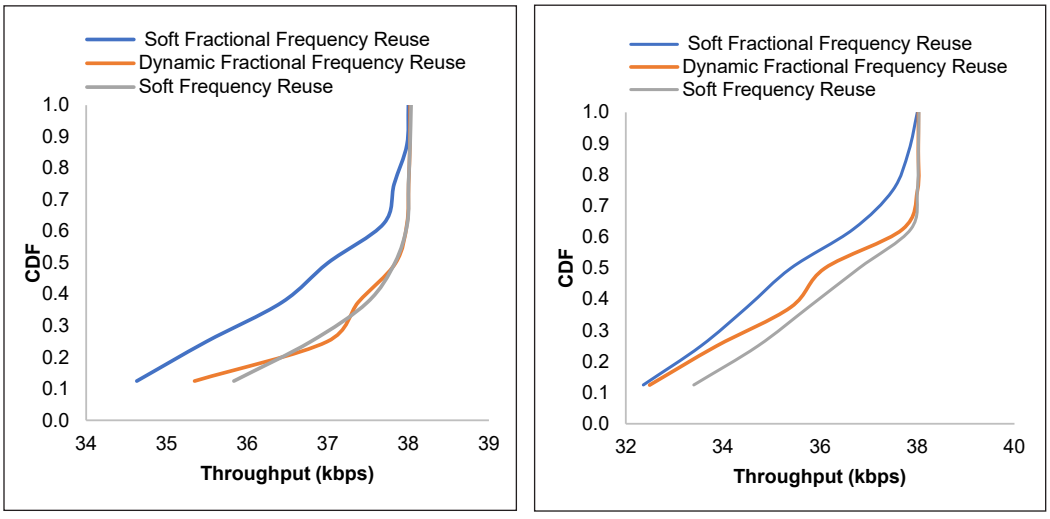

Figure 4. Cumulative distribution function (CDF) of the average throughput for (a) the cell centre users and (b) the cell edge users

drastic packet loss rates. SFFR, however, can sustain 23 users with the same QoS. DFFR outperforms SFFR by accommodating more users at the cell center before experiencing packet loss and also surpasses SFR with a lower PLR as the number of users increases from 32.

Figure 5(b) also depicts the influence of PLR on the number of users for the cell edge. It shows that cell edge users experience higher ICI with an increase in the number of users

compared to Figure 6(a) (i.e., cell center). It was observed that DFFR has better system performance as it can accommodate 25 users before experiencing packet loss, compared to SFFR, which can only accommodate 19 users. DFFR also outperforms SFR as it experiences less packet loss as the number of user's increases up to 27.

An analysis of the network load of selected mobile service providers (A, B, and C) was conducted, taking into account different transmission power ratings: 64 dBm for Operator A, 72 dBm for Operator B, and 87 dBm for Operator C. Figure 6 illustrates the impact of average throughput on the number of nodes based on the selected service providers. It was observed that, under the same AODV routing protocol and considering network loads of 50, 75, 100, 125, and 150 nodes, the average throughput decreased as the number of nodes increased. Operator A showed an almost linear decrease in throughput, while Operators B and C initially experienced an increase in throughput at 100 nodes before a decrease at 125 nodes. The significant decrease in average throughput for Operators B and C with an increase in the number of loads indicates that Operator A has better system throughput performance.

Figure 7 also demonstrates the impact of packet delay on the number of nodes. It reveals that as network load increases, delay performance worsens, leading to an increase in packet delay. Operator B had more packet delay between 100 and 125 nodes due to a higher number of users compared to Operators A and C, while Operator C had more packet delay than A. Therefore, Operator B experienced more packet delay, with Operator A having the least packet delay. Figure 8 displays the signal pattern for packet reception for

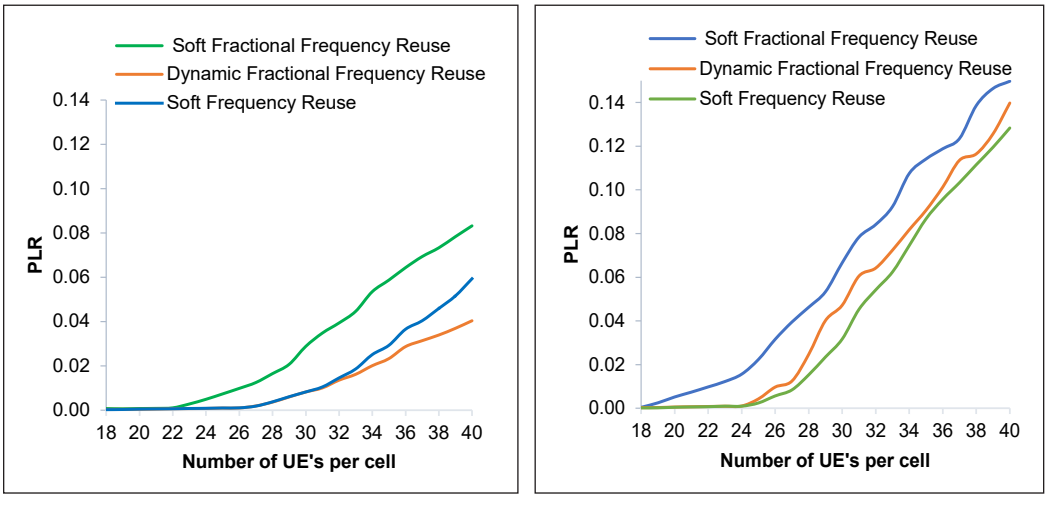

Figure 5. Packet loss ratio (PLR) for the (a) cell centre users and (b) cell edge users
Note. UE = User equipment

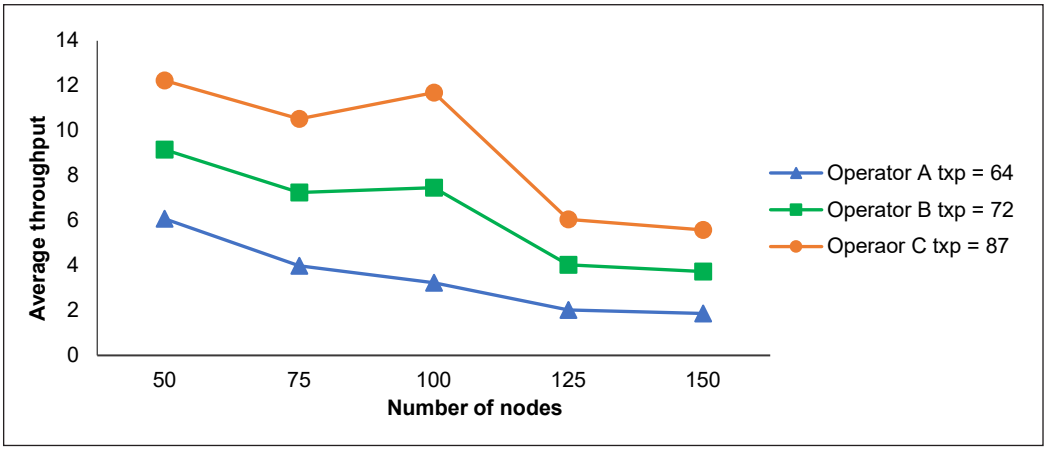

Figure 6. Comparison of the average throughput based on the selected service providers
Note. txp = Transmission power rating

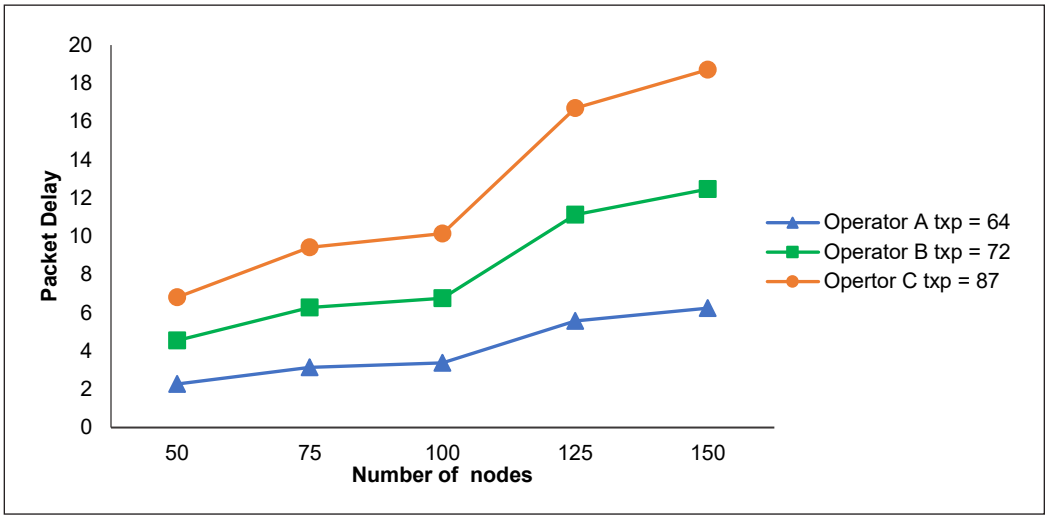

Figure 7. Comparison of the packet delay based on the selected service providers
Note. txp = Transmission power rating

the three selected service providers at a typical network load of 50 nodes. It was observed that, unlike Operator C, who had a decrease in packet reception as the model duration increased with more consumers, Operators A and B exhibited similar patterns. In general, it can be concluded that Operator A has better system performance in terms of throughput and packet delay parameters compared to Operators B and C. This is also evident in the QoS of A compared to the other service providers.

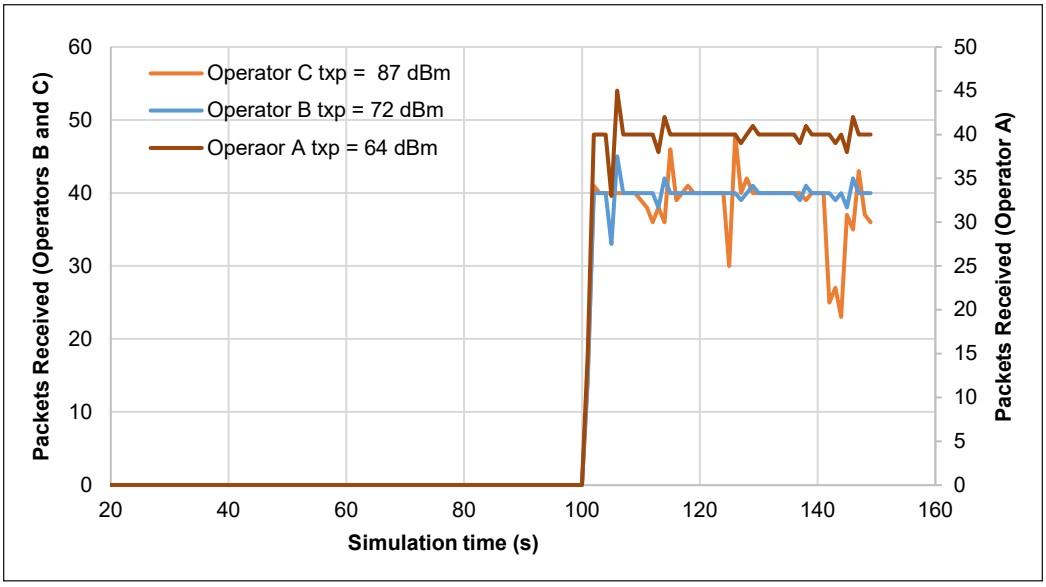

Figure 8. Comparison of the packets received based on the selected service provider for a typical node (50 nodes)
Note. txp = Transmission power rating

CONCLUSION

This study evaluates two fractional frequency reuse approaches in the downlink of the 3rd generation LTE architecture to ensure customer service quality, analysing the advantages and disadvantages of each method. The simulation highlights the distinctions among these strategies. Reducing transmission power in the central region diminishes system efficiency, as it lacks the requisite strength to mitigate inter-channel interference and fading. The SFFR bandwidth is distributed to three independent sub-bands with unconventional locations, potentially diminishing the system's flexibility, as most users are located in the central or edge regions. Consequently, in comparison to the DFFR and SFR, it attains the lowest system performance. DFFR mitigates inter-cell interference more effectively than SFR, but only slightly. SFR and DFFR facilitate the utilisation of more RBs at the cell-edge region, leading to superior system performance compared to SFFR. The evaluation of the selected mobile service providers indicates that Operator A exhibits superior system performance relative to Operators B and C, as evidenced by their quality of service throughout a broad region in Nigeria. The model can be deployed for future generation networks. Future work will involve comparing it with the real-world data and analyzing the effects of SNR among other factors.

ACKNOWLEDGEMENTS

The authors would like to thank the Mobile Service Providers in Nigeria for part of the data used in this work.

REFERENCES

Abejide, A. E. (2014). *Performance analysis of an LTE-4G network running multimedia applications* [Master's thesis, Eastern Mediterranean University]. Eastern Mediterranean University Institutional Repository. http://hdl.handle.net/11129/1679

Abukharis S., Alzubi J. A., Alzubi O. A, Alamri S., & O'Farrell T. (2014). Packet error rate performance of IEEE802.11g under bluetooth interface. *Research Journal of Applied Sciences, Engineering and Technology*, *8*(12), 1419-1423.

Ajibola T. M., Surajudeen-Bakinde N. T., & Amuda S. A. Y. (2015). Development of base transfer station selection algorithm for collocation arrangement. *Nigeria Journal of Technology*, *34*(3), 538-545. https://doi.org/10.4314/njt.v34i3.16

Almazroi, A. A. (2018). Performance analysis of 4G broadband cellular networks. *International Journal of Advanced and Applied Sciences*, *5*(9), 12-17. https://doi.org/10.21833/ijaas.2018.09.003

Alotaibi, S (2023): Network capacity improvement in 5G by using dynamic fractional frequency reuse (FFR). *Journal of Umm Al-Qura University for Engineering and Architecture*, *14*, 105–114. https://doi.org/10.1007/s43995-023-00021-5

Bilal, M. M. (2017). *Allocation des ressources radio dans les réseaux sans fil de la 5 G* [Radio resource allocation in 5G wireless networks] [Doctoral dissertation, Université Paris-Scalay]. HAL Portal Theses. https://theses.hal.science/tel-01558458 0923

Boudreau, G., Panicker, J., Guo, N., Chang, R., Wang, N., & Vrzic, S. (2009). Interference coordination and cancellation for 4G networks. *IEEE Communications Magazine*, *47*(4), 74-81. https://doi.org/10.1109/mcom.2009.4907410

Galadanci, G. S. M., & Abdullahi, S. B. (2018). Performance analysis of GSM networks in Kano Metropolis of Nigeria. *American Journal of Engineering Research*, *7*(5), 69-79.

Gawłowicz, P., Baldo, N., & Miozzo, M (2015). An extension of the ns-3 LTE module to simulate fractional frequency reuse algorithms. In *WNS3'15: Proceedings of the 2015 Workshop on ns-3* (pp. 98-105). Association for Computing Machinery. https://doi.org/10.1145/2756509.2756524

Himayat, N., Talwar, S., Rao, A., & Soni, R. (2010). Interference management for 4G cellular standards [WIMAX/LTE UPDATE]. *IEEE Communications Magazine*, *48*(8), 86–92. https://doi.org/10.1109/mcom.2010.5534591

Islam, M. J., & Chowdhury, M. N. H. (2013). *Study of inter-cell interference and its impact on the quality of video conference traffic in LTE network* [Master's thesis, Belkinge Institute of Technology]. DiVA Portal. https://www.diva-portal.org/smash/get/diva2:832429/FULLTEXT01.pdf

Kalpana, K. (2024). Significant role of stochastic process in wireless networks by using artificial intelligence. *International Journal of Multidisciplinary Educational Research*, *13*(3), 81-88.

Khan, S. A., Kavak, A., Kucuk, K., & Asshad, M. (2019). A new fractional frequency reuse method for interference management in LTE-A HetNets. In *2019 27th Signal Processing and Communications Applications Conference* (pp. 1-4). IEEE. https://doi.org/10.1109/SIU.2019.8806317]

Kuboye, B. M. (2017). Evaluation of broadband network performance in Nigeria. *International Journal of Communications, Network and System Sciences*, *10*, 199-207. https://doi.org/10.4236/ijcns.2017.109011

Kuboye, B. M. (2018). Performance evaluation of scheduling algorithms for 4G (LTE). *Communications and Network, 10*, 152–163. https://doi.org/10.4236/cn.2018.104013

Lee, D., Li, G. Y., & Tang, S. (2013). Inter-cell interference coordination for LTE systems. In *2012 IEEE Global Communications Conference* (pp. 4828–4833). IEEE. https://doi.org/10.1109/glocom.2012.6503883

Li, Y., Niu, C., Ye, F., & Hu, R. Q. (2016). A universal frequency reuse scheme in LTE-A heterogeneous networks. *Wireless Communications Mobile Computing*, *16*, 2839-2851. https://doi.org/10.1002/wcm.2731

Liu, J. (2022). Comparison of different frequency channel allocation methods in ultra-dense networks. *Highlights in Science, Engineering and Technology*, *27*, 570-574. https://doi.org/10.54097/hset.v27i.3817

Maskooki A., Sabatino, G., & Mitton, N. (2015). Analysis and performance evaluation of the next generation wireless networks. In M. S. Obaidat, P. Nicopolitidis, & F. Zarai (Eds.), *Modeling and simulation of computer networks and systems, methodologies and applications: Methodologies and applications* (pp. 601–627). Morgan Kaufmann. https://doi.org/10.1016/B978-0-12-800887-4.00021-3

Nordrum, A., Clark, K., & IEE Spectrum. (2017). *Everything you need to know about 5G - IEEE spectrum*. https://spectrum.ieee.org/everything-you-need-to-know-about-5g

Oguntoyinbo, O. J. (2013). *The future of LTE: The femtocells perspective* [Master's thesis, Aalto University]. Aaltodoc. https://aaltodoc.aalto.fi/server/api/core/bitstreams/456c3be4-c81e-4de8-b166-bc18b578a441/content

Ozovehe, A., & Usman, A. U. (2015). Performance analysis of GSM networks in Minna Metropolis of Nigeria. *Nigerian Journal of Technology*, *32*(2), 359–367. https://doi.org/10.4314/njt.v34i2.21

Peters, S. W., Panah, A. Y, Truong, K. T, & Heath Jr., R. W. (2009). Relay architectures for 3GPP LTE-advanced. *EURASIP Journal on Wireless Communications and Networking*, *2009*, 618787. https://doi.org/10.1155/2009/618787

Sarwar, M. I., Nisar, K., & ud Din, I. (2020). LTE-advanced - Interference management in OFDMA-based cellular network: An overview. *University of Sindh Journal of Iinformation and Communication Technology*, *4*(3), 96–103.

Tangelapalli, S., & Saradhi, P. P. (2019). Simulation of fractional frequency reuse algorithms in LTE networks. *International Journal of Recent Technology and Engineering*, *7*(5S4), 175–179.

Tchao, E. T., Gadze, J. D., & Agyapong, J. O. (2018). Performance evaluation of a deployed 4G LTE network. *International Journal of Advanced Computer Science and Applications*, *9*(3), 165–178.

Yautentzi, E. M., Camacho, J. C., Aguilar, G. M., & Huerta, I. E. Z. (2024). Performance analysis of ultra-dense networks with frequency reuse. *International Journal of Combinational Optimization Problems and Informatics*, *15*(5), 218-227. https://doi.org/10.61467/2007.1558.2024.v15i5.581

Zaki, Y. (2012). *Future mobile communication: LTE optimization and mobile network virtualization* [Doctoral dissertation, Universität Bremen]. Staats-und Universitätsbibliothek Bremen. https://nbn-resolving.de/urn:nbn:de:gbv:46-00102749-12

Pertanika J. Sci. & Technol. 33 (4): 1923 - 1942 (2025)

PERTANIKA JOURNALS

SCIENCE & TECHNOLOGY

Journal homepage: http://www.pertanika.upm.edu.my/

Distribution and Population Abundance of Odonates in Relation to Abiotic Factors in an Urbanized Freshwater Ecosystem: A Case Study from Universiti Sains Malaysia

Nur Aina Alisa Adnan[1], Azimah Abd Rahman[2], Nur Faeza Abu Kassim[1]* and Nurhafizul Abu Seri[2]

[1]School of Biological Sciences, Universiti Sains Malaysia, 11800, Pulau Pinang, Malaysia
[2]Geoinformatic Unit, Geography Section, School of Humanities, Universiti Sains Malaysia, 11800, Pulau Pinang, Malaysia

ABSTRACT

Odonates, including dragonflies and damselflies, serve as critical bioindicators of freshwater ecosystem health due to their sensitivity to environmental fluctuations. This study examines the distribution and abundance of odonates at Universiti Sains Malaysia, with a particular focus on assessing population abundance and identifying key biotic and abiotic factors influencing their distribution. Over a nine-week sampling period, a total of 1,256 individuals were recorded, comprising four dragonfly species *Brachythemis contaminata*, *Brachydiplax chalybea*, *Orthetrum testaceum*, and *Crocothemis servilia* and one damselfly species, *Ischnura senegalensis*. A hotspot analysis conducted using ArcGIS identified Sampling Station 2 (SS2) as a primary aggregation zone, accounting for 69.82% (877 individuals) of total odonate observations, largely attributed to its proximity to water bodies. The presence of *Hydrilla verticillata* emerged as a crucial factor in determining habitat suitability; however, its degradation due to algal blooms at SS1 and SS2 was associated with a decline in odonate abundance, particularly among species reliant on healthy aquatic vegetation. Statistical analysis revealed a moderate positive correlation between odonate abundance and abiotic parameters such as air temperature ($r = 0.544$, $p < 0.001$), relative humidity ($r = 0.400$, $p = 0.008$), and wind speed. However, multiple regression analysis indicated that only relative humidity ($p = 0.009$) and air temperature ($p = 0.024$) significantly influenced odonate abundance, while wind speed ($p = 0.064$) did not exhibit a statistically significant effect. Future research is recommended to investigate additional abiotic and biotic factors

ARTICLE INFO

Article history:
Received: 07 November 2024
Accepted: 08 April 2025
Published: 04 July 2025

DOI: https://doi.org/10.47836/pjst.33.4.12

E-mail addresses:
alisaadnan23@gmail.com (Nur Aina Alisa Adnan)
azimahrahman@usm.my (Azimah Abd Rahman)
nurfaeza@usm.my (Nur Faeza Abu Kassim)
nurhafizul.abuseri97@gmail.com (Nurhafizul Abu Seri)
*Corresponding author

e-ISSN: 2231-8526

© Universiti Putra Malaysia Press

to further refine our understanding of odonate ecology and their role in freshwater ecosystem health assessment.

Keywords: Abiotic, ArcGIS, biotic, damselflies, dragonflies, *Hydrilla verticillate*, odonate

INTRODUCTION

Approximately 6,376 species of odonates, encompassing dragonflies and damselflies, have been identified worldwide. These species are classified into about 965 genera (Sandall et al., 2022). Odonates are categorized into two suborders: Anisoptera, which includes true dragonflies, and Zygoptera, which includes damselflies. Both suborders of the order Odonata undergo an incomplete metamorphosis, where the larval stages encounter 10 to 15 instars (Neog & Rajkhowa, 2016). The Odonata fauna in Malaysia is notably diverse. Dow et al. (2024) reported a total of 743 species in the Sundaland and Wallacea regions, with 549 species recorded in Sundaland, which includes Peninsular Malaysia, Singapore, Borneo, Sumatra, Java, and Bali. Of these, 482 species are endemic to these regions, with 385 being single-region endemics, many confined to specific islands. In Peninsular Malaysia and Singapore, 247 species from 17 families have been documented, comprising 99 damselfly species and 148 dragonfly species. In Sarawak, Malaysian Borneo, 303 species have been recorded.

Dragonflies are a type of insect that have bright colours, large eyes, and exhibit sexual dimorphism, colour transition, and polymorphism (Futahashi, 2016). These insects possess distinctive characteristics that differentiate them from other insects, including their long and thin abdomen, large round eyes positioned atop their heads, short antennae, and two pairs of wings (Neog & Rajkhowa, 2016). Damselflies' forewings and hindwings are almost identical in shape and venation, but dragonflies' forewings and hindwings differ significantly. Damselflies' wings contain similar structural traits, although dragonflies' wings vary significantly in shape and vein pattern (Kuchta & Svensson, 2014). Damselflies have compound eyes on either side of their heads, which provide a wide angle of vision. Their body form is slim and elongated, distinguishing them from dragonflies (Sumanapala, 2017). Damselfly nymphs have extended abdomens with three leaf-shaped tracheal gills. These lamellar gills let the nymphs absorb dissolved oxygen, allowing them to breathe in watery environments (Kriska, 2022).

Odonates demonstrate a higher susceptibility to pollution in comparison to other insects. Jacob et al. (2017) often recommended using odonates as indicators of environmental quality in aquatic habitats because of their well-documented advantages. Only a limited number of odonate species, including those belonging to the Megalagrion genus, have larvae that inhabit upland environments. These larvae are commonly found in damp leaf litter, characterized by a significant level of relative humidity. The remaining insects in this group

may exclusively reproduce by depositing their eggs in, or near, freshwater. Dragonfly and damselfly species tend to be most abundant in sites that offer a wide range of micro-habitats. Consequently, an area that harbours many of these insects can be considered a dependable indicator of the quality of its freshwater. Odonates, are highly sensitive to changes in the quality of their habitat. As a result, their diversity and distribution are affected when the structural habitat quality changes. This sensitivity has made them valuable indicators for monitoring and evaluating the condition of the habitat quality (Jacob et al., 2017).

Odonates thrive in a wide range of habitats, with tropical rainforests being recognised as their most abundant and diversified ecosystems (Dow et al., 2015). The insects primarily dwell in riparian forests and places with abundant overhanging vegetation, indicating their inclination towards habitats near water bodies such as ponds, lakes, streams, and canals (Ramli & Manaf, 2021). Due to their susceptibility to environmental changes, they serve as excellent indicators of the overall condition of an ecosystem. Sollai and Solari (2022) emphasized that insects' hormonal regulation, neural function, sensory perception, and other physiological processes play a crucial role in their ability to adapt to environmental changes. Understanding how insects respond to ecological stressors provides valuable insights into habitat quality and overall ecosystem health. Additionally, research on herbivory and insect diversification suggests a complex interaction between dietary intake and evolutionary adaptation, highlighting how specialized feeding strategies have contributed to the vast diversity of insect species worldwide (Sollai & Solari, 2022).

Over the years, Malaysia has faced a notable decline in odonate populations, primarily due to habitat loss from urbanization, deforestation, and pollution (Hezri, 2018). Climate change has further disrupted their ecosystems, exacerbating population declines and threatening their ecological roles as both predators and prey (McCauley et al., 2015). Despite their significance as bioindicators of environmental health, research on odonates in Malaysia remains limited, hindering conservation efforts and a deeper understanding of their population dynamics. This study utilises Geographic Information Systems (GIS) to cartographically represent the spatial distribution of odonates at Universiti Sains Malaysia (USM), Gelugor, Pulau Pinang. GIS is employed due to its ability to analyse and visually display spatial data by integrating geographic information with specialised software (Chang, 2019). The main goals of this research are to determine the population size of odonates (dragonflies and damselflies), examine the factors, both biotic and abiotic, that affect their preference of habitat, and analyse the potential relationship between odonate population size and the biotic and abiotic factors. By employing GIS to determine the population abundance of odonates, researchers and conservationists can pinpoint crucial habitats and track changes in the population dynamics (Dminić et al., 2010). Therefore, GIS aids in the development of well-informed conservation strategies and the implementation of efficient management techniques for odonate species. This helps to reduce the likelihood of severe population loss, especially in Penang, Malaysia.

MATERIAL AND METHOD

Study Area

The study was carried out at the main campus of USM, which is strategically situated at a key entry point to Penang Island. The USM campus has a variety of habitats, such as a designated area for birds that are at risk of extinction, lush tropical forests, lakes, and orchards. The presence of these natural characteristics fosters a garden-like setting that sustains a wide range of plant and animal species, such as dragonflies and damselflies (Lee, 2003). Four sampling stations, namely Aman Damai Student Residence, Tasik Harapan, Jalan Ilmu, and Indah Kembara Student Residence, were selected due to their proximity to water bodies (Figure 1).

Sampling was conducted from mid-January to mid-March 2024, covering the transition from the rainy to the hot season. The study spanned nine weeks, with sampling carried out once per week on a designated day. On each sampling day, all four sampling stations were surveyed consecutively, resulting in a total of nine sampling days over the entire

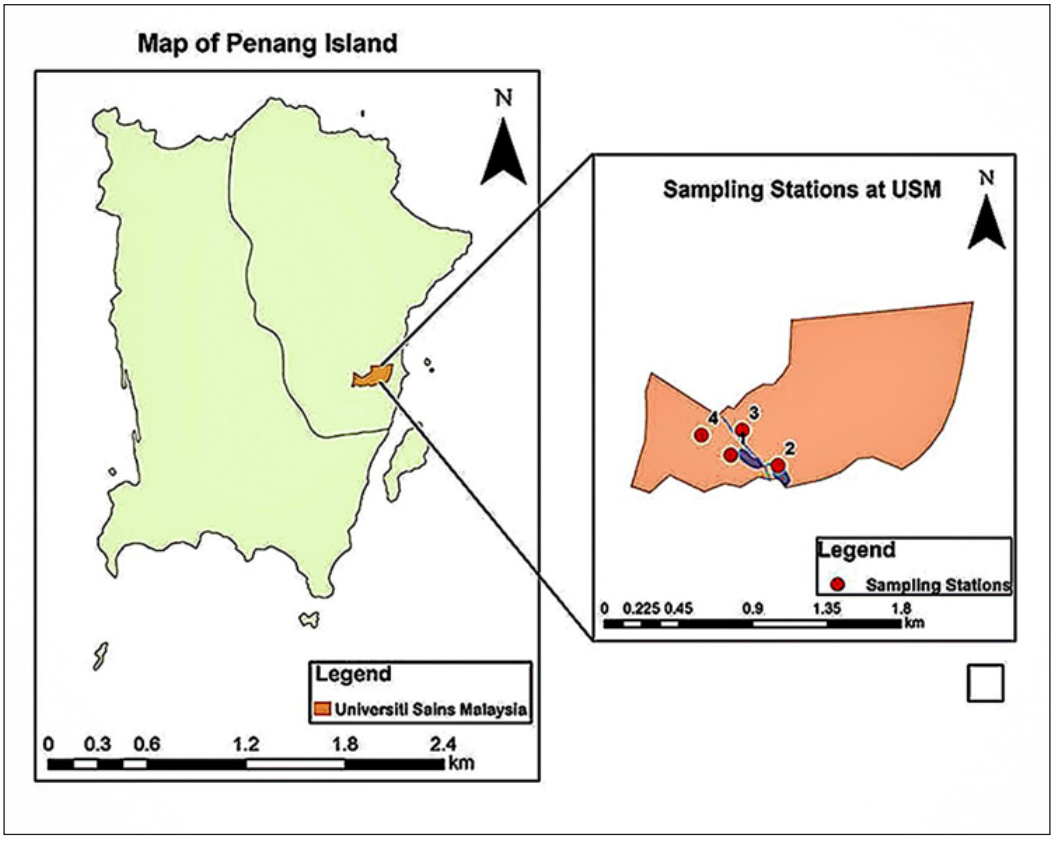

Figure 1. Study area and sampling stations at Universiti Sains Malaysia, Gelugor, Pulau Pinang

study period. The sampling occasion specimen collections were conducted from 2:30 to 4:30 p.m. Over two months of monitoring at the site, it was observed that odonates were most active between 9:00 a.m. and 6:30 p.m. Adult odonates were collected using aerial nets, identified, photographed, and either released or preserved in 70% ethanol for further identification using the Malaysia Biodiversity Information System (MyBIS) handbook "Ancient Creatures: Dragonflies and Damselflies of Malaysia" by Choong et al. (2017). Abiotic parameters, including air temperature, relative humidity, and wind speed, were recorded on every sampling day throughout the nine-week study period. Since sampling was conducted once per week, these parameters were measured a total of nine times, corresponding to each sampling session. Vegetation samples were collected and labeled by station, with photographs taken for species identification. Abiotic parameters, such as the wind speed, air temperature, and humidity, were measured using specialised devices to study their impact on odonate behaviour.

RESULTS AND DISCUSSION

Odonate Population at USM

Over a two-month field survey, 1,256 odonates were recorded at USM. A total of five species of Odonata were recorded. Four of these species are dragonflies from the Libellulidae family: (*B. contaminata*, *B. chalybea*, *O. testaceum*, and *C. servilia*). The fifth species, *I. senegalensis*, is a damselfly that belongs to the Coenagrionidae family (Figure 2). The Libellulidae family dominated the odonate assemblage, consistent with previous findings that highlight their adaptability in diverse freshwater habitats (Ng et al., 2022). Norma-Rashid (2001) highlighted *B. contaminata* as common in Malaysian freshwater habitats, both in urban and rural settings. Similarly, Das et al. (2012) highlighted that this species serves as an indicator of disturbance, frequently occurring in areas impacted by human settlements. On the other hand, the Coenagrionidae family is one of the most widespread and ecologically significant damselfly families, commonly found in various freshwater habitats, including ponds, lakes, and slow-moving streams (Willink et al., 2024). *Ischnura senegalensis*, a member of this family, is widely distributed across Asia, Africa, and parts of Australia, thriving in both natural and disturbed environments (Subramanian & Babu, 2017). Norma-Rashid (2001) noted its frequent occurrence in Malaysian wetlands, including rice fields and urban waterways.

Hotspot analysis using ArcGIS identified Sampling Station 2 (SS2) as the primary hotspot, accounting for 69.82% (877 individuals) of total odonate observations, while SS3 and SS4 had significantly lower abundance (< 250 individuals). Factors influencing this pattern include proximity to water sources, vegetation health, and abiotic conditions (Figure 3). Table 1 summarises odonate distribution across stations and weeks. The study by Barbosa-Santos et al. (2025) highlights that riparian vegetation quality influences the

abundance of odonates. Specifically, it states that Zygoptera species were more abundant in streams with higher environmental integrity, emphasising their dependence on riparian vegetation for suitable habitat conditions (Barbosa-Santos et al., 2025). The study by Gajbe (2021) highlights the relationship between proximity to water sources and odonate abundance, where research evaluated the impact of a small artificial water source on odonate diversity in an urban landscape. Results showed that the availability of a water source led to an 80% increase in odonate species, indicating that even small man-made water bodies positively influence odonate populations by providing critical breeding and foraging habitats (Gajbe, 2021). In flowing water sites (lotic environments), the composition of odonate species varied with water temperature and proximity to urban areas. Specifically, different odonate species were found, depending on how warm the water was and how close the site was to urban centres (Prescott & Eason, 2018). Thus, odonate diversity was highest at sites with moderate urbanisation, supporting the intermediate disturbance hypothesis that suggests that moderate disturbance increases species diversity (Jere et al., 2020).

Thus, odonates diversity was highest at sites with moderate urbanization, supporting the intermediate disturbance hypothesis that suggests that moderate disturbance increases species diversity (Jere et al., 2020). The population data (Table 1) shows the following distribution: SS2 has the highest abundance with 877 odonates (69.82%), SS1 has 254 (20.22%), SS3 has 100 (7.96%), and SS4 has 25 (1.99%). Week 3 had the peak number of odonates (192), while week 9 had the lowest (93).

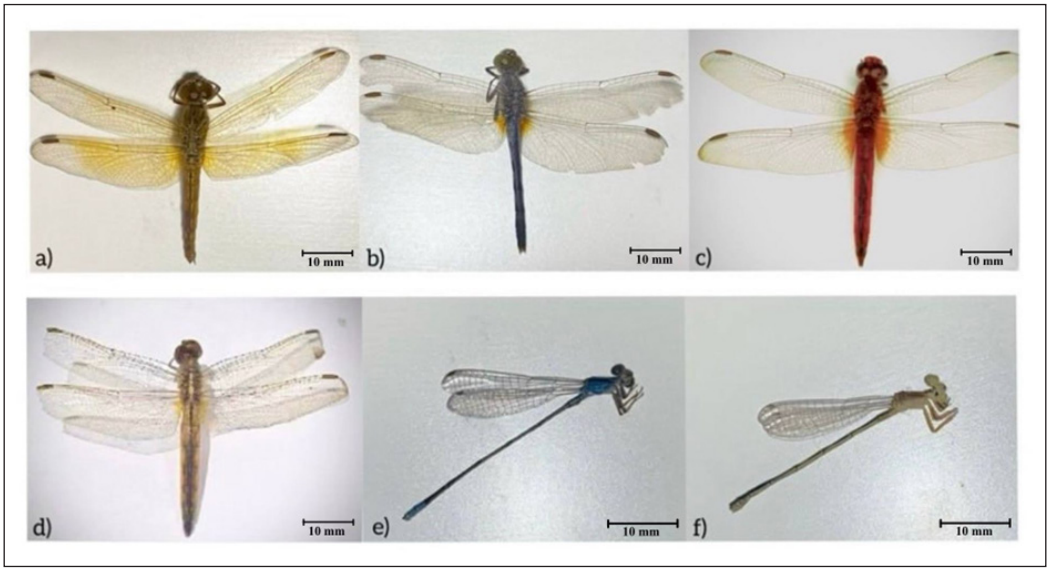

Figure 2. a) *Brachythemis contaminate* (female), b) *Brachydiplax chalybea* (male), c) *Orthetrum testaceum* (male), d) *Crocothemis servilia* (female), e) *Ischnura senegalensis* (male), and f) *Ischnura senegalensis* (female)

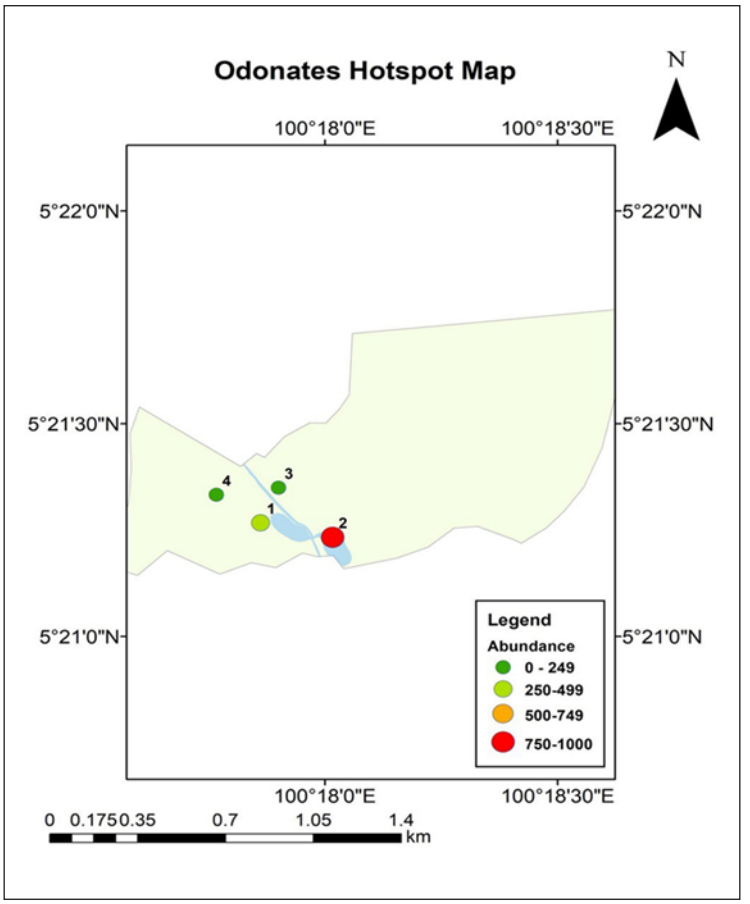

Figure 3. Hotspot mapping of Odonate abundance across sampling stations

Table 1
Odonate abundance by sampling station and week

Sampling station	Week 1	Week 2	Week 3	Week 4	Week 5	Week 6	Week 7	Week 8	Week 9	Total per station	Total percentage (%)
SS1	42	14	28	36	20	35	28	24	27	254	20.22
SS2	78	62	139	115	108	145	97	75	58	877	69.82
SS3	23	5	17	7	14	5	6	15	8	100	7.96
SS4	12	0	8	0	0	2	0	3	0	25	2.00
Total per week	155	81	192	158	142	187	131	117	93	1256	100
Total percentage (%)	12.34	6.45	15.29	12.58	11.31	14.89	10.43	9.31	7.40		

Influence of Biotic Factors on Odonate Habitat Selection

Table 2 shows the vegetation types at each sampling station and their impact on odonate abundance. Aquatic vegetation, *Hydrilla verticillata* (water thyme), was present at SS1 and SS2, while land vegetation varied across stations, including *Tabernaemontana divaricata* (crepe jasmine, pinwheel flower, or East Indian rosebay), *Cocos nucifera* (coconut palm), *Bambusa vulgaris* (common bamboo or golden bamboo), and *Jacaranda obtusifolia* (*Jacaranda*, green ebony, jambol merah, or jambul merak). Odonates were predominantly found in areas with *Hydrilla verticillata*, while fewer were observed on land vegetation. *Hydrilla verticillata*, an invasive species, showed a significant negative association with several odonate families, whereas other invasive plants did not have any significant impact (Thomas, 2019). Anisopterans such as *B. contaminata*, *B. chalybea*, *O. testaceum*, and *C. servilia* were found in this study; they typically prefer environments with less dense canopy riparian vegetation. As mentioned by de Resende et al. (2021), Odonata are generally found in moderately open canopies that allow sufficient sunlight penetration. Due to their heliothermic nature, dragonflies thrive in sunlit environments and are frequently observed in disturbed or degraded habitats where dense vegetation has been reduced or fragmented.

Bambusa vulgaris may offer an overly dense canopy in SS1 for these species, thereby restricting their abundance in the area. In contrast, all dragonflies and damselflies will thrive in settings containing *J. obtusifolia*, *C. nucifera*, and *T. divaricata*, which have moderate to sparse canopy cover and enable enough sunlight to pass through. *Hydrilla verticillata*, while not contributing to the canopy cover, provides an underwater habitat and breeding ground that can be beneficial, especially when combined with the species' preferred open, sunlit environment. As a result, these dragonflies are more likely to be found in areas where vegetation provides enough sunlight and an aquatic setting appropriate for reproduction in SS2 compared to other sampling stations.

Larval habitat availability also plays a critical role in odonate distribution. Since odonates have aquatic larval stages, the condition of aquatic vegetation is crucial for their breeding success. Figure 4 shows the health deterioration of *H. verticillata* caused by algal blooms, particularly at SS1 and SS2, which appears to have a direct influence on odonate abundance. These algal blooms likely lead to reduced water quality by causing

Table 2
Vegetation types at sampling stations

Sampling station	Aquatic vegetation	Land vegetation
1	*Hydrilla verticillata*	*Bambusa vulgaris*
2	*Hydrilla verticillata*	*Tabernaemontana divaricata*, *Cocos nucifera*
3	-	*Jacaranda obtusifolia*
4	-	*Tabernaemontana divaricata*, *Cocos nucifera*

oxygen depletion, blocking sunlight, and altering nutrient dynamics, which in turn affects the overall ecological balance of the habitat (Wiley & McPherson, 2024). Specifically, species such as *B. contaminata*, *B. chalybea*, *O. testaceum*, and *C. servilia*, which rely on robust aquatic vegetation for breeding and larval development, were less abundant in week 9 when *H. verticillata* was in poor health. This suggests that these species are highly sensitive to environmental degradation and that deterioration in aquatic vegetation directly contributes to odonate population declines. The findings emphasize the close ecological link between aquatic vegetation health and odonate diversity. As *H. verticillata* declines, it likely reduces the availability of shelter, egg-laying sites, and food resources for odonate larvae, ultimately leading to lower adult abundance. This reinforces the role of submerged macrophytes in maintaining odonate populations and highlights the need for conservation efforts to protect aquatic habitats from excessive algal growth and pollution.

In this study, we have examined odonate abundance as it is related to abiotic factors such as the air temperature, relative humidity, and wind speed and found a significant correlation between these variables and odonate counts. Over a nine-week time frame, odonate abundance peaked at 192 individuals in week three and dropped to 81 in week two. According to the research, greater air temperatures (32.18 to 33.20°C), increased humidity (82.50 to 86.25%), and higher wind speeds are associated with higher number of odonates. Odonates have impressive flying capabilities, including hovering and making

Figure 4. Algae bloom at lakes in (a) Sampling Station 1 and (b) Sampling Station 2 during week 9 of sampling

180° turns. Dragonflies fly faster than damselflies, reaching speeds of up to 25-30 km/h, which has significant effects on their dispersal and geographic distribution (Subramanian & Babu, 2017). The moderate correlation between wind speed and odonate abundance (r = 0.583, $p < 0.001$) indicates some impact, but the lack of statistical significance ($p = 0.064$) suggests that wind alone is not the primary limiting factor.

A study by Barzoki et al. (2021) found that wind may have a greater influence on Zygoptera since their bodies are typically smaller than Anisoptera and more susceptible to displacement. To cope with this challenge, damselflies adjust their perching behavior by orienting into the wind (rheotaxis) to maintain stability (Mason, 2017). Additionally, damselflies seek sheltered areas with vegetation to minimize wind exposure (Johansson et al., 2009). In contrast, dragonflies, being larger and having stronger flight muscles, are less affected by these environmental factors and can fly efficiently in open spaces without significant disruption (Barzoki et al., 2021).

Odonates' aerodynamic efficiency differs greatly between dragonflies and damselflies. To take flight, dragonflies must create 221% of the power needed to produce the same lift that would be necessary under perfect aerodynamic conditions, such as those represented by an 'actuator disc' or 'lifting line'. This reduced power would require more efficient flying mechanics. Damselflies, on the other hand, have less aerodynamically effective wing designs and require 275% of the optimal power to obtain the same lift. This greater power need implies that damselflies have less efficient wing structures than dragonflies, which affects their total flying ability (Bomphrey et al., 2016). These findings also show that these abiotic factors play an important role in defining odonate population dynamics, which is consistent with previous studies on the effect of environmental conditions (especially air temperature) on dragonfly dispersal (Flenner et al., 2010; Golfieri et al., 2016). Rachmawati et al. (2023) discovered that dragonflies' poor tolerance to air temperature had a detrimental influence on their survival. This sensitivity can lead to reduced abundance, poor health, lower survival and reproductive success, making it more difficult for these species to thrive or live in high-temperature environments.

Influence of Abiotic Factors on Odonate Abundance

Abiotic factors play a significant role in shaping the abundance and distribution of odonates. The present study revealed significant correlations between air temperature (r = 0.544, $p < 0.001$), relative humidity (r = 0.400, p = 0.008), and wind speed (r = 0.583, $p < 0.001$) with odonate abundance (Figure 5). However, multiple regression analysis indicated that only relative humidity (p = 0.009) and air temperature (p = 0.024) significantly influenced odonate abundance, while wind speed (p = 0.064) showed no significant effect. These findings suggest that while temperature and humidity are key determinants of odonate populations, wind speed may have an indirect or context-dependent role.

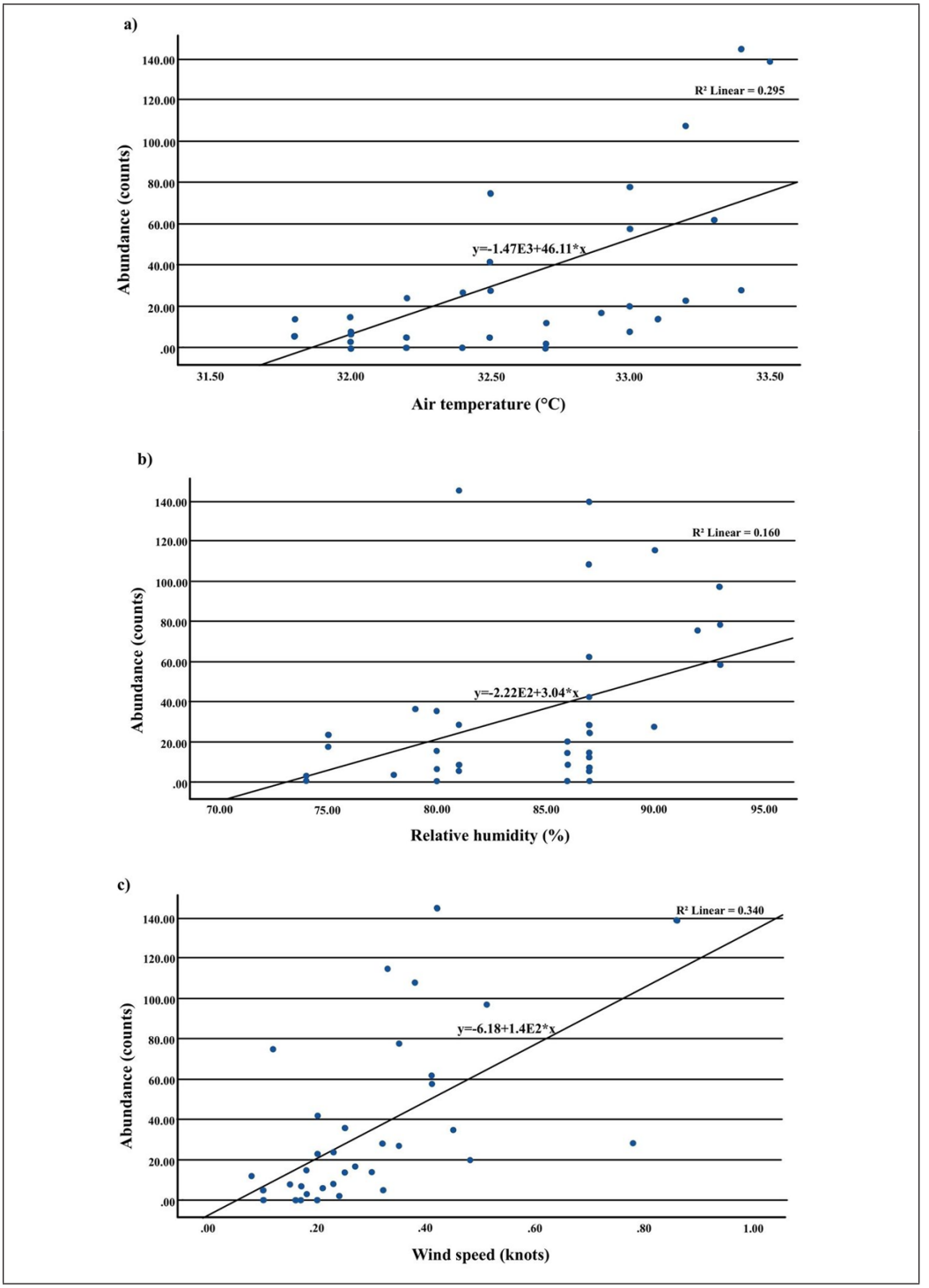

Figure 5. The relationship between odonate abundance and (a) air temperature (°C), (b) relative humidity (%), and (c) wind speed (knots), respectively

Temperature has long been recognized as a critical factor affecting the physiology, behavior, and life cycle of odonates. Rising temperatures have been associated with changes in thermoregulatory behavior, reducing the time available for reproductive activities, as individuals allocate more energy to maintaining optimal body temperature (Marcellino et al., 2024). Temperature playing both a favorable and limiting role depending on specific conditions (Knoblauch et al., 2021). The strong influence of temperature is largely attributed to increased sunlight exposure, which enhances diurnal insect activity, particularly in odonates (Becciu et al., 2019). Our study identified a moderately positive correlation between air temperature and odonate abundance ($r = 0.544$, $p < 0.001$), further supported by regression analysis ($p = 0.024$). Such changes have important implications for mating success and population sustainability under climate change scenarios. Moreover, elevated temperatures negatively affect larval development, as demonstrated by Bílková et al. (2025), who found that temperatures exceeding 24°C significantly reduced larval survival rates and hatchability. This aligns with previous research indicating that warmer temperatures accelerate larval growth and emergence, potentially leading to shifts in phenology (Bobrek, 2021). However, rapid development may not always be advantageous, as it can disrupt predator-prey interactions and alter community dynamics (Sandamini et al., 2019).

Notably, beta diversity in odonate assemblages is strongly linked to temperature fluctuations, with Anisoptera species being particularly sensitive to yearly temperature variations (Barzoki et al., 2021). Climate-induced shifts in minimum temperatures have further intensified changes in odonate life cycles, as evidenced by Villalobos-Jiménez and Hassall (2017), who reported that 50% of odonate species exhibited significant advancements in their phenological events in response to rising minimum temperatures. These shifts underscore the role of climate change in reshaping community structures, favouring climate-resilient species while potentially disadvantaging those with narrow thermal tolerances.

Air temperature and humidity have long been recognized as critical determinants of odonate abundance and diversity (Adu & Oyeniyi, 2019). Relative humidity also plays a crucial role in odonate abundance, as indicated by the moderate positive correlation observed in this study ($r = 0.400$, $p = 0.008$), with regression analysis confirming its significant influence ($p = 0.009$). The optimal humidity range for odonates has been reported to be between 78.11 and 81.67%, which supports their physiological functions and enhances flight activity (Koneri et al., 2022). Higher humidity levels help prevent desiccation and support sustained aerial activity, which is essential for foraging and reproductive behaviors. However, contrasting findings suggest that excessive humidity, particularly during rainy seasons, can negatively impact odonate populations by increasing mortality rates and reducing life expectancy (Palacino-Rodríguez et al., 2020). These fluctuations in odonate abundance over the nine-week sampling period (Figure 6) further illustrate the role of humidity in driving population changes.

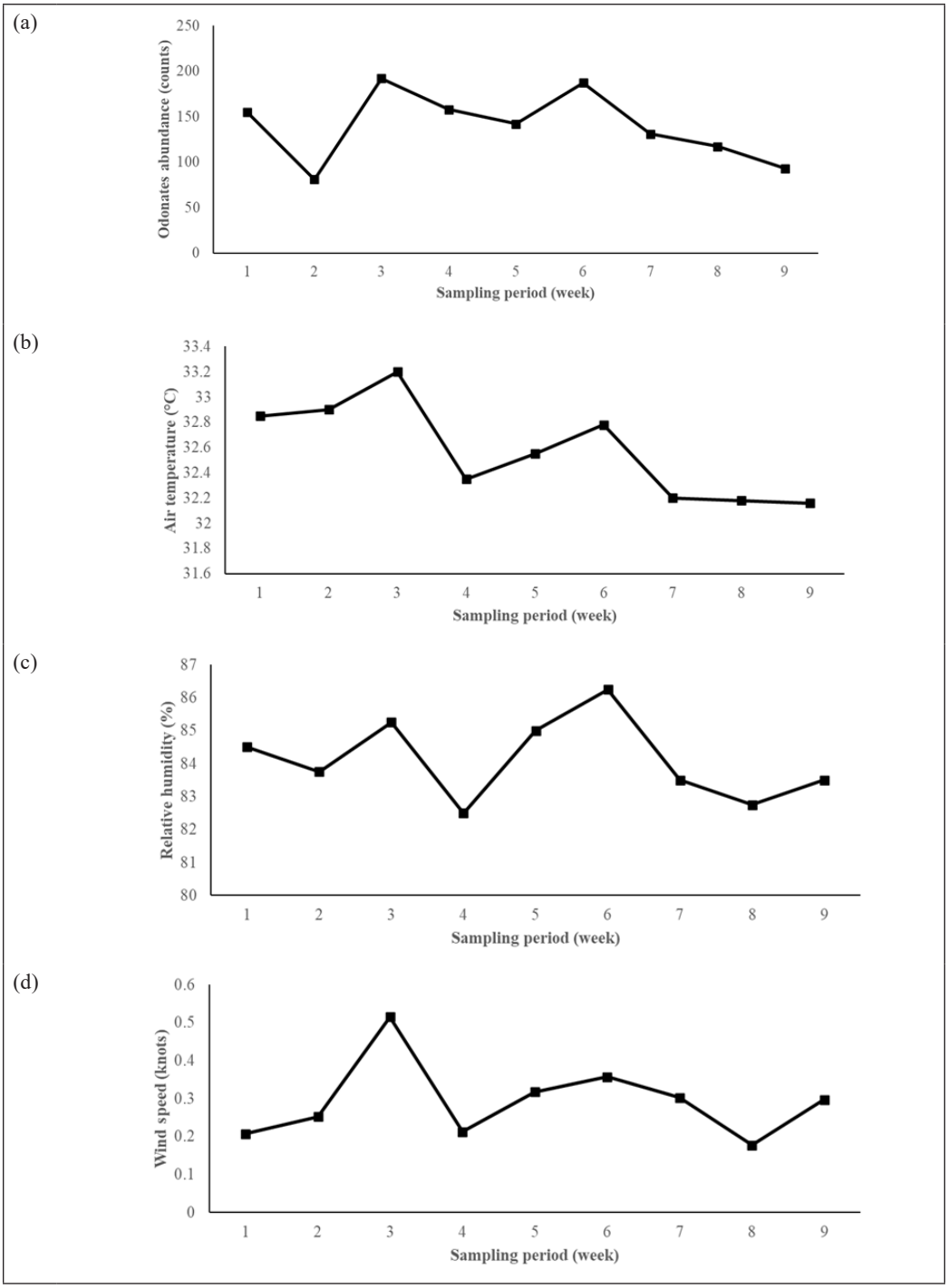

Figure 6. Odonate abundance and associated abiotic factors recorded over a nine-week sampling period at Universiti Sains Malaysia, Pulau Pinang. (a) Odonate abundance (counts), (b) air temperature (°C), (c) relative humidity (%), and (d) wind speed (knots)

The observed relationships between temperature, humidity, and odonate abundance highlight the potential impacts of climate variability on odonate populations. Shifts in temperature and moisture regimes could indirectly affect odonate distribution patterns and community structure, altering the ecological balance in freshwater ecosystems. Future research should further explore the thresholds at which these abiotic factors transition from being beneficial to detrimental, providing a more comprehensive understanding of how odonates respond to environmental changes.

Wind speed, although moderately correlated with odonate abundance ($r = 0.583$, $p < 0.001$), was not a significant predictor in the regression analysis ($p = 0.064$). While previous studies have shown that low wind speeds favour odonate activity (Johansson et al., 2009), strong winds can pose challenges, particularly for damselflies (Zygoptera), which are more susceptible to displacement than dragonflies (Anisoptera) (Barzoki et al., 2021). Consequently, damselflies often compensate by seeking sheltered microhabitats, reducing wind exposure and mitigating displacement risks. Additionally, thermoregulatory behavior may play a compensatory role in heat-stressed damselflies, enabling them to optimize body temperature despite wind-induced flight challenges (Hassall & Thompson, 2008). Given that temperature and humidity significantly influenced odonate abundance in this study, wind speed (Figures 5 and 6) may act as a secondary factor, indirectly shaping habitat selection and species distribution. Odonates exhibit rheotactic behavior, orienting themselves against wind currents to maintain stability during flight (Mason, 2017). However, excessive wind speeds may hinder foraging efficiency and increase energy expenditure, which could indirectly impact population dynamics. The inverse relationship between odonate abundance and wind speed observed in some weeks (Figure 6) highlights the potential impact of wind turbulence on flight efficiency, particularly in open habitats. The contrasting effects of wind speed suggest that its influence on odonates may depend on local environmental conditions and species-specific adaptations.

The broader implications of these findings must be considered in the context of climate change, which is expected to alter species assemblages and ecological interactions. Rising minimum temperatures have already been linked to changes in odonate phenology, with earlier emergence patterns observed in response to warming trends (Villalobos-Jiménez & Hassall, 2017). Additionally, climate-induced shifts in beta diversity suggest that certain species are better adapted to increasing temperatures, leading to changes in community composition (Barzoki et al., 2021). Long-term studies predict that climate-resilient species will gradually dominate odonate populations, while less adaptable species may face local extinction (Assandri, 2021; Bowler et al., 2021; Termaat et al., 2015).

Beyond climatic factors, odonate populations are also threatened by anthropogenic disturbances such as habitat degradation and urbanization. High current speeds, extreme temperatures, and strong winds can disrupt freshwater ecosystems, further exacerbating

population declines (Albab et al., 2019). In urban areas such as USM Penang, habitat fragmentation and pollution pose additional threats to odonates, reducing their available breeding and foraging sites (The Habitat Foundation, 2021). Given the complex interplay between abiotic factors and anthropogenic stressors, conservation efforts must consider both climatic and environmental changes to ensure the long-term survival of odonate species.

Odonates rely heavily on clean, stagnant, or slow-moving freshwater sources, such as ponds, streams, and wetlands, particularly during their larval stage. However, rapid urbanization at USM Penang has led to significant habitat degradation, reducing the quality and availability of these aquatic ecosystems. The expansion of roads, buildings, and commercial infrastructure has decreased green spaces, leading to surface runoff, reduced groundwater replenishment, and the drying of small water bodies all of which threaten odonate populations. Similar trends have been observed globally, where water scarcity and land-use changes significantly restrict odonate habitats, particularly in semi-arid regions (Husband & McIntyre, 2021).

Additionally, pollution from agricultural runoff, industrial waste, and untreated sewage has led to increased contaminants, including pesticides, heavy metals, and excessive nutrients, which can be lethal to odonate larvae and reduce prey abundance. Pond size, aquatic vegetation, and freshwater macroinvertebrates also shape odonate diversity, as certain species are limited to agricultural or forest ponds, while others disappear entirely from urban water bodies (Le Gall et al., 2018). Interestingly, the fish-free pond at USM provides a unique habitat where dragonflies can thrive, aligning with McCoy et al. (2009), who found that odonates can persist in fish-free aquatic ecosystems due to reduced predation pressure. Their study highlights how the absence of fish, a major predator of odonate larvae, can create favorable conditions for odonate survival and reproduction. However, the absence of fish may also alter ecosystem dynamics, influencing species interactions and aquatic food webs (May, 2019).

CONCLUSION

This study demonstrates that odonate abundance in the freshwater ecosystems of USM is significantly influenced by abiotic factors, particularly relative humidity and air temperature. While wind speed exhibited a strong correlation with odonate presence, it did not emerge as a significant predictor in the regression analysis. These findings reinforce the ecological sensitivity of odonates to microclimatic conditions, underscoring their potential as bio-indicators of environmental change. The study also highlights the critical role of aquatic vegetation, particularly *H. verticillata*, in shaping odonate distribution. The degradation of this vegetation due to algal blooms was associated with reduced odonate abundance, emphasizing the need for maintaining healthy aquatic habitats. The identification of SS2 as a "hotspot" further suggests that habitat quality and proximity to water sources are key

determinants of odonate populations. Thus, conservation efforts should focus on sustaining high-quality freshwater habitats, particularly in urban environments where anthropogenic disturbances threaten biodiversity. Future research should explore additional biotic interactions, such as predator-prey dynamics, and assess the long-term impact of climate variability on odonate populations to enhance conservation strategies.

ACKNOWLEDMENTS

This research was funded by external agencies "Kurita Water Environment Federation" [KWEF] with reference number: 23Pmy040.

REFERENCES

Adu, B. W., & Oyeniyi, E. A. (2019). Water quality parameters and aquatic insect diversity in Aahoo stream, southwestern Nigeria. *The Journal of Basic and Applied Zoology*, *80*, 15. https://doi.org/10.1186/s41936-019-0085-3

Albab, A. U., Leksono, A. S., & Yanuwiadi, B. (2019). Land use analysis with odonata diversity and composition using the ArcGIS in Malang and Batu, East Java. *Indonesian Journal of Environment and Sustainable Development*, *10*(2), 73-83.

Assandri, G. (2021). Anthropogenic-driven transformations of dragonfly (Insecta: Odonata) communities of low elevation mountain wetlands during the last century. *Insect Conservation and Diversity*, *14*(1), 26-39. https://doi.org/10.1111/icad.12439

Barbosa-Santos, F. M., Juen, L., Cajaiba, R. L., & De Sousa, J. R. P. (2025). Effects of a habitat integrity gradient on the diversity of odonates in the Legal Amazonia zone of the Brazilian state of Maranhão. *Neotropical Entomology*, *54*, 24. https://doi.org/10.1007/s13744-024-01240-8

Barzoki, Z. E., Ebrahimi, M., Kiany, M., & Sadeghi, S. (2021). Ecological drivers of Odonata beta diversity in arid and semi-arid regions of the central plateau of Iran. *Insect Conservation and Diversity*, *14*(1), 40-51. https://doi.org/10.1111/icad.12464

Becciu, P., Menz, M. H. M., Aurbach, A., Cabrera-Cruz, S. A., Wainwright, C. E., Scacco, M., Ciach, M., Pettersson, L. B., Maggini, I., Arroyo, G. M., Buler, J. J., Reynolds, D. R., & Sapir, N. (2019). Environmental effects on flying migrants revealed by radar. *Ecography*, *42*(5), 942-955. https://doi.org/10.1111/ecog.03995

Bílková, E., Kornová, V., Ožana, S., Pyszko, P., Schindlerová, H., Chytilová, R., & Dolný, A. (2025). Dragonfly larvae rearing: Experimental insights and best practices. *Environmental Entomology*, *5*(2), 394-406. https://doi.org/10.1093/ee/nvaf001

Bobrek, R. (2021). Odonate phenology recorded in a Central European location in an extremely warm season. *Biologia*, *76*, 2957-2964. https://doi.org/10.1007/s11756-021-00785-y

Bomphrey, R. J., Nakata, T., Henningsson, P., & Lin, H.-T. (2016). Flight of the dragonflies and damselflies. *Philosophical Transactions of the Royal Society B: Biological Sciences*, *371*, 20150389. https://doi.org/10.1098/rstb.2015.0389

Bowler, D. E., Eichenberg, D., Conze, K.-J., Suhling, F., Baumann, K., Benken, T., Bönsel, A., Bittner, T., Drews, A., Günther, A., Isaac, N. J. B., Petzold, F., Seyring, M., Spengler, T., Trockur, B., Willigalla, C., Bruelheide, H., Jansen, F., & Bonn, A. (2021). Winners and losers over 35 years of dragonfly and damselfly distributional change in Germany. *Diversity and Distributions*, *27*(8), 1353-1366. https://doi.org/10.1111/ddi.13274

Chang, K.-T. (2019). Geographic information system. In *International encyclopedia of geography: People, the earth, environment and technology* (pp. 1-10). John Wiley & Sons. https://doi.org/10.1002/9781118786352.wbieg0152.pub2

Choong, C. Y., Arifin, Y. M., & Hijas, N. H. (2017). *Ancient creatures: Dragonflies and damselflies of Malaysia*. Malaysia Biodiversity Information System. https://www.mybis.gov.my/pb/1676

Das, S. K., Ahmed, R. A., Sajan, S. K., Dash, N., Sahoo, P., Mohanta, P., Sahu, H. K., Rout, S. D., & Dutta, S. K. (2012). Diversity, distribution and species composition of odonates in buffer areas of Similipal Tiger Reserve, Eastern Ghat, India. *Academic Journal of Entomology*, *5*(1), 54-61.

de Resende, B. O., Ferreira, V. R. S., Brasil, L. S., Calvão, L. B., Mendes, T. P., de Carvalho, F. G., Mendoza-Penagos, C. C., Bastos, R. C., Brito, J. S., Oliveira-Junior, J. M. B., Dias-Silva, K., Luiza-Andrade, A., Guillermo, R., Cordero-Rivera, A., & Juen, L. (2021). Impact of environmental changes on the behavioral diversity of the Odonata (Insecta) in the Amazon. *Scientific Reports*, *11*, 9742. https://doi.org/10.1038/s41598-021-88999-7

Dminić, I., Kozina, A., Bažok, R., & Barčić, J. I. (2010). Geographic information systems (GIS) and entomological research: A review. *Journal of Food, Agriculture and Environment*, *8*(2), 1193-1198.

Dow, R. A., Choong, C. Y., Grinang, J., Lupiyaningdyah, P., Ngiam, R. W. J., & Kalkman, V. J. (2024). Checklist of the Odonata (Insecta) of Sundaland and Wallacea (Malaysia, Singapore, Brunei, Indonesia and Timor Leste). *Zootaxa, 5460*(1), 1-122. https://doi.org/10.11646/zootaxa.5460.1.1

Dow, R. A., Reels, G. T., & Ngiam, R. W. J. (2015). *Odonata collected at Usun Apau National Park, Miri Division, Sarawak, Malaysia in April and May 2012*. Universitätsbibliothek Johann Christian Senckenberg.

Flenner, I., Richter, O., & Suhling, F. (2010). Rising temperature and development in dragonfly populations at different latitudes. *Freshwater Biology*, *55*(2), 397-410. https://doi.org/10.1111/j.1365-2427.2009.02289.x

Futahashi, R. (2016). Color vision and color formation in dragonflies. *Current Opinion in Insect Science*, *17*, 32-39. https://doi.org/10.1016/j.cois.2016.05.014

Gajbe, P. U. (2021). Impact of a small artificial water source on the diversity of odonates (Insecta: Odonata) in an urban landscape. *Arthropods*, *10*(2), 60–65.

Golfieri, B., Hardersen, S., Maiolini, B., & Surian, N. (2016). Odonates as indicators of the ecological integrity of the river corridor: Development and application of the Odonate River Index (ORI) in northern Italy. *Ecological Indicators*, *61*(Part 2), 234-247. https://doi.org/10.1016/j.ecolind.2015.09.022

Hassall, C., & Thompson, D. J. (2008). The impacts of environmental warming on Odonata: A review. *International Journal of Odonatology*, *11*(2), 131–153. https://doi.org/10.1080/13887890.2008.9748319

Hezri, A., A. (2018). Urbanization and multiple-scales environmental challenges in Malaysia. In *Routledge handbook of urbanization in Southeast Asia* (pp. 366–374). Taylor and Francis Group.

Husband, D. M., & McIntyre, N. E. (2021). Urban areas create refugia for odonates in a semi-arid region. *Insects*, *12*(5), 431. https://doi.org/10.3390/insects12050431

Jacob, S., Thomas, A. P., & Manju, E. K. (2017). Odonata (dragonflies and damselflies) as bio indicators of water quality. *International Journal of Innovative Research in Science, Engineering and Technology*, *6*(9), 19464-19474.

Jere, A., Darshetkar, A., Patwardhan, A., & Koparde, P. (2020). Assessing the response of odonates (dragonflies and damselflies) to a tropical urbanization gradient. *Journal of Urban Ecology*, *6*(1), juaa029. https://doi.org/10.1093/jue/juaa029

Johansson, F., Söderquist, M., & Bokma, F. (2009). Insect wing shape evolution: Independent effects of migratory and mate guarding flight on dragonfly wings. *Biological Journal of the Linnean Society*, *97*(2), 362–372. https://doi.org/10.1111/j.1095-8312.2009.01211.x

Knoblauch, A., Thoma, M., & Menz, M. H. M. (2021). Autumn southward migration of dragonflies along the Baltic coast and the influence of weather on flight behaviour. *Animal Behaviour*, *176*, 99-109. https://doi.org/10.1016/j.anbehav.2021.04.003

Koneri, R., Nangoy, M. J., & Elfidasari, D. (2022). Odonata diversity in the Laine Waterfall Area, Sangihe Islands, North Sulawesi, Indonesia. *Aquaculture, Aquarium, Conservation and Legislation Bioflux*, *15*(3), 1083-1095.

Kriska, G. (2022). Dragonflies and damselflies: Odonata. In G. Kriska (Ed.), *Freshwater invertebrates in Central Europe* (pp. 263-288). Springer. https://doi.org/10.1007/978-3-030-95323-2_14

Kuchta, S. R., & Svensson, E. I. (2014). Predator-mediated natural selection on the wings of the damselfly *Calopteryx splendens*: Differences in selection among trait types. *The American Naturalist*, *184*(1), 91-109. https://doi.org/10.1086/676043

Le Gall, M., Fournier, M., Chaput-Bardy, A., & Husté, A. (2018). Determinant landscape-scale factors on pond odonate assemblages. *Freshwater Biology*, *63*(3), 306-317. https://doi.org/10.1111/fwb.13065

Lee, L. M. (2003). *The university in a garden*. Penerbit Universiti Sains Malaysia.

Marcellino, B. J., Yee, P., McCauley, S. J., & Murray, R. L. (2024). Too hot to handle: Male dragonflies decrease time spent mating at higher temperatures. *Animal Behaviour*, *207*, 109-118. https://doi.org/10.1016/j.anbehav.2023.10.007

Mason, N. A. (2017). Effects of wind, ambient temperature and sun position on damselfly flight activity and perch orientation. *Animal Behaviour*, *124*, 175-181. https://doi.org/10.1016/j.anbehav.2016.12.025

May, M. L. (2019). Odonata: Who they are and what they have done for us lately: Classification and ecosystem services of dragonflies. *Insects*, *10*(3), 62. https://doi.org/10.3390/insects10030062

McCauley, S. J., Hammond, J. I., Frances, D. N., & Mabry, K. E. (2015). Effects of experimental warming on survival, phenology, and morphology of an aquatic insect (Odonata). *Ecological Entomology*, *40*(3), 211-220. https://doi.org/10.1111/een.12175

McCoy, M. W., Barfield, M., & Holt, R. D. (2009). Predator shadows: Complex life histories as generators of spatially patterned indirect interactions across ecosystems. *Oikos*, *118*(1), 87–100. https://doi.org/10.1111/j.1600-0706.2008.16878.x

Neog, N., & Rajkhowa, S. M. (2016). Dragon fly diversity in two different ecosystems in and around Assam University, Silchar (ecoforest and Irongmara). *Journal of Entomology and Zoology Studies*, *4*(4), 184-190.

Ng, Y. H., Rahman, A. A. A., Zainal, M.-Z., & Abdul-Latiff, M. A. B. (2022). First Record of Insects in Pulau Tinggi, Johor, Malaysia. *Journal of Sustainability Science and Management*, *17*(11), 99-109. http://doi.org/10.46754/jssm.2022.11.011

Norma-Rashid, Y., Mohd-Sofian, A., & Zakaria-Ismail, M. (2001). Diversity and distribution of Odonata (dragonflies and damselflies) in the fresh water swamp lake Tasek Bera, Malaysia. *Hydrobiologia*, *459*, 135-146. https://doi.org/10.1023/A:1012562611307

Palacino–Rodríguez, F., Palacino, D. A., Munguia-Steyer, R., & Juen, L. (2020). Effects of seasonality and environmental change on an Andean damselfly *Mesamphiagrion laterale* (Odonata: Coenagrionidae). *Journal of Insect Conservation*, *24*, 499-511. https://doi.org/10.1007/s10841-020-00237-z

Prescott, V. A., & Eason, P. K. (2018). Lentic and lotic odonate communities and the factors that influence them in urban versus rural landscapes. *Urban Ecosystems*, *21*, 737-750. https://doi.org/10.1007/s11252-018-0752-z

Rachmawati, A., Yustian, I., Pujiastuti, Y., Shk, S., & Arinafril. (2023). Biotic and dragonfly diversity indices as ecological quality evaluation in Lahat District Rivers, South Sumatra, Indonesia. *Biodiversitas Journal of Biological Diversity*, *24*(11), 6059-6068. https://doi.org/10.13057/biodiv/d241127

Ramli, N. H., & Manaf, N. F. A. (2021). Species diversity of dragonfly (Arthropoda: Odonata) and its relationship with air parameters at Sg. Muar, Kuala Pilah. *Journal of Academia*, *9*(2), 30-39.

Sandall, E. L., Pinkert, S., & Jetz, W. (2022). Country-level checklists and occurrences for the world's Odonata (dragonflies and damselflies). *Journal of Biogeography*, *49*(8), 1586-1598. https://doi.org/10.1111/jbi.14457

Sandamini, P. M. M. A., Gunarathna, S. D., & Chandana, E. P. S. (2019). Habitat quality and climate variability determine odonate species diversity and distribution patterns in selected habitats of southern Sri Lanka. *Asian Journal of Conservation Biology*, *8*(1), 47-57.

Sollai, G., & Solari, P. (2022). An overview of “insect biodiversity”. *Diversity*, *14*(2), 134. https://doi.org/10.3390/d14020134

Subramanian, K. A., & Babu, R. (2017). Insecta: Odonata (damselflies and dragonflies). In K. Chandra, K. C. Gopi, D. V. Rao, K. Valarmathi, & J. R. B. Alfred (Eds.), *Current status of freshwater faunal diversity in India* (pp. 401-418). Zoological Survey of India.

Sumanapala, A. P. (2017). *A field guide to the dragonflies and damselflies of Sri Lanka*. Ceylon Tea Services PLC.

Termaat, T., van Grunsven, R. H. A., Plate, C. L., & van Strien, A. J. (2015). Strong recovery of dragonflies in recent decades in The Netherlands. *Freshwater Science*, *34*(3), 1094-1104. https://doi.org/10.1086/682669

The Habitat Foundation. (2021). *Diversity of dragonflies and damselflies on Penang Island*. https://www.habitatfoundation.org.my/diversity-of-dragonflies-and-damselflies-on-penang-island/

Thomas, S. (2019). *The effect of invasive aquatic vegetation on Odonate diversity in an urban area* [Bachelor's thesis, Louisiana State University]. LSU Scholarly Repository. https://repository.lsu.edu/honors_etd/1461

Villalobos-Jiménez, G., & Hassall, C. (2017). Effects of the urban heat island on the phenology of Odonata in London, UK. *International Journal of Biometeorology*, *61*, 1337-1346. https://doi.org/10.1007/s00484-017-1311-7

Wiley, D. Y., & McPherson, R. A. (2024). The role of climate change in the proliferation of freshwater harmful algal blooms in inland water bodies of the United States. *Earth Interactions*, *28*(1), 1–25. https://doi.org/10.1175/EI-D-23-0008.1

Willink, B., Ware, J. L., & Svensson, E. I. (2024). Tropical origin, global diversification, and dispersal in the pond damselflies (Coenagrionoidea) revealed by a new molecular phylogeny. *Systematic Biology*, *73*(2), 290–307. https://doi.org/10.1093/sysbio/syae004

Pertanika J. Sci. & Technol. 33 (4): 1943 - 1970 (2025)

PERTANIKA JOURNALS

SCIENCE & TECHNOLOGY

Journal homepage: http://www.pertanika.upm.edu.my/

A Comparative Study of Gradient Descent Methods in Deep Learning Using Body Motion Dataset

Zulfikar Sembiring[1,2]*, Khairul Najmy Abdul Rani[2,3] and Amiza Amir[2]

[1]Faculty of Engineering, Universitas Medan Area,20223 Medan, North Sumatera, Indonesia
[2]Faculty of Electronic Engineering and Technology, Universiti Malaysia Perlis, 02600 Arau, Perlis, Malaysia
[3]Centre of Excellence, Advanced Communication Engineering, Universiti Malaysia Perlis, 02600 Arau, Perlis, Malaysia

ABSTRACT

In this study, a Recurrent Neural Network (RNN) architecture model is used to analyse and compare the seven most widely used first-order stochastic gradient-based optimization algorithms. Adaptive Moment Estimation (ADAM), Root Mean Square Propagation (RMSprop), Stochastic Gradient Descent (SGD), Adaptive Gradient (AdaGrad), Adaptive Delta (AdaDelta), Nesterov-accelerated Adaptive Moment Estimation (NADAM), and Maximum Adaptive Moment Estimation (AdaMax) are the optimization techniques that have been studied. The study used the body motion datasets from the University of California-Irvine (UCI) Machine Learning (ML) datasets. This experiment demonstrates the capabilities of various combinations of optimizer models, long short-term memory (LSTM) architecture, activation functions, and learning rate. The main aim is to understand how good each optimizer performs in test accuracy and feasible training time behaviour over various learning rates and activation functions. The outcomes vary by setting, with some achieving higher accuracy and shorter training sessions than others. The AdaGrad model, which uses exponential and sigmoid activation functions with a learning rate of 0.001, has a training time of 17.1 minutes and a test accuracy of 78.31%, making it the top-performing configuration. The exponential function is an activation function that consistently outperforms other models and optimization algorithms. It consistently delivers high accuracy and minimal running time across numerous models and optimizers, while the Softmax activation function continuously underperforms.

Keywords: Accuracy, activation function, body motion datasets, gradient descent (GD), learning rate, long short-term memory (LSTM), Recurrent Neural Network (RNN), running time

ARTICLE INFO

Article history:
Received: 19 November 2024
Accepted: 08 April 2025
Published: 04 July 2025

DOI: https://doi.org/10.47836/pjst.33.4.13

E-mail addresses:
zulfikarsembiring@studentmail.unimap.edu.my (Zulfikar Sembiring)
khairulnajmy@unimap.edu.my (Khairul Najmy Abdul Rani)
amizaamir@unimap.edu.my (Amiza Amir)
*Corresponding author

e-ISSN: 2231-8526

© Universiti Putra Malaysia Press

INTRODUCTION

Selecting the optimal optimization algorithm is one of the effective approaches to enhance the learning process in deep learning (DL) algorithm. This work focuses on the application of optimization methods based on the gradient descent (GD) approach to optimize the DL architecture. DL relies heavily on optimization since the model optimizer continually updates and calculates the parameters that affect model training and output. The purpose is to follow the steepest descent direction, which is provided by the negative gradient, in order to approximate or reach the optimal value and optimize the objective function (Mehmood et al., 2023), DL optimization problems are complicated and call for more decomposition. Three stages can be identified in the growth of optimization. The first stage is to get the algorithm start running and have it arrived at a logical conclusion, like a stationary point. Making the algorithm converge as rapidly as possible is the second stage. Making sure the algorithm converges to a result with a low objective value, like a global minimum, is the third stage (Sun, 2019). It is important to remember that getting good test accuracy requires a further step that is outside the purview of optimization. The three categories of convergence, convergence speed, and global quality as in Figure 1 are used to group optimization problems.

Machine learning (ML) is a subset of artificial intelligence dedicated to creating algorithms that allow computers to learn from data and make predictions or judgments autonomously, without explicit programming (Ethem, 2020). The GD is widely employed in ML and other mathematical applications to optimize a cost function. The cost function calculates the discrepancy between a model projected and actual output. The objective of GD is to minimize the cost function by modifying the model's parameters, such as weights

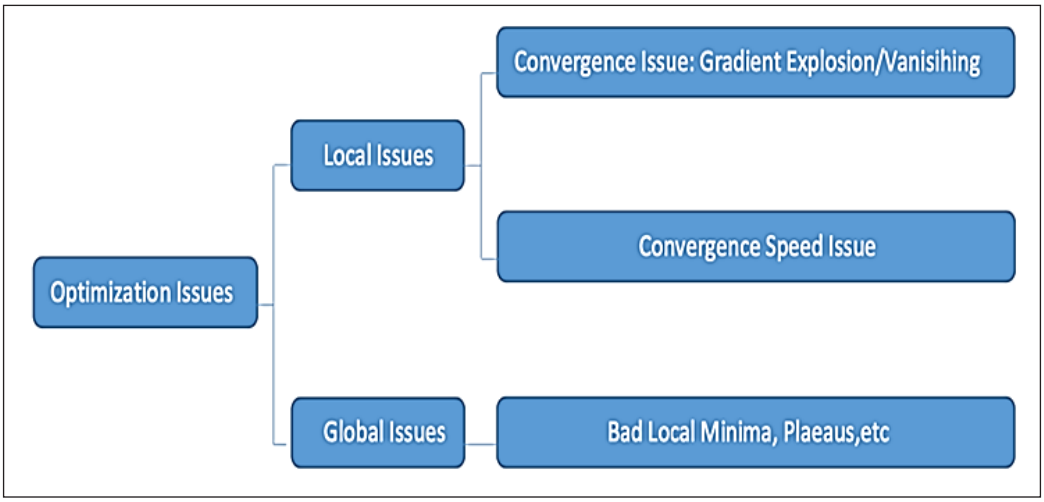

Figure 1. Optimization issues (Sun, 2019)

and biases (Chandra et al., 2022). The concept of GD is based on the idea of finding the steepest descent direction of the cost function and moving the parameters in that direction to reach a minimum value of the cost function (Seeli & Thanammal, 2024). This process involves computing the gradient of the cost function with respect to the parameters and taking a step in the opposite direction of the gradient by repeating this process iteratively, GD can converge to a minimum of the cost function (Haji & Abdulazeez, 2021).

Comparing different GD optimizers is crucial in DL because it allows for the selection of the most effective and efficient optimization algorithm for a specific problem. Each optimizer has its strengths and weaknesses, and understanding these differences can significantly impact the performance of the model. For instance, while Batch GD is simple and easy to implement, it can be slow and computationally expensive for large datasets. SGD, on the other hand, is faster but can be noisy and may not converge well (Schaul et al., 2013). Adaptive optimizers like ADAM and its variants, however, can adapt to the changing nature of the optimization problem, making them more robust and effective (Kingma & Ba, 2015). By comparing these optimizers, researchers and practitioners can identify the best approach for their specific problem, ensuring optimal performance and faster convergence. This comparison is particularly important in modern DL applications, where large datasets and complex models require efficient and effective optimization techniques.

Neural network (NN) is commonly employed to tackle non-convex problems, but choosing an appropriate optimization method can be difficult to locate the global optimum in these networks. This difficulty arises from the need to estimate a vast quantity of parameters within a high-dimensional search space. An ineffective optimization strategy may lead the network to remain trapped in local minimum while training, preventing any improvement (Dogo et al., 2018). Moreover, because of ADAM's stability and performance in a wide range of case scenarios, several NN researchers instinctively favour it in all circumstances. Consequently, it is essential to conduct a study to investigate how optimizers operate in relation to the model and dataset utilized to gain a deeper understand of their behaviours.

As a result, the contribution of this paper is an experimental comparison of the performance of seven well-known and widely used GD optimization algorithms on a RNN model. RNN is One type of neural network that can process sequential inputs, such as time series and natural language. The RNN model uses the body motion dataset from the UCI ML datasets with several learning rates, and activation functions. Using convergence speed, accuracy, and loss function as performance metrics, this comparison shows how well and consistently each optimizer handled the problem of locating the proper and ideal minima throughout training.

BACKGROUND OF STUDY AND RELATED WORK

GD is a first-order iterative optimization technique that moves in the opposite direction as the gradient to find a local minimum of a loss function (Chandra et al., 2022). On the other

hand, gradient ascent—moving in the direction of the gradient—leads to a local maximum (Hallén, 2017). By modifying weights during backpropagation to reduce loss and address the curse of dimensionality, GD plays a critical role in DL optimization (Goodfellow et al., 2016).

SGD, AdaGrad, AdaDelta, RMSprop, ADAM, AdaMax, and NADAM are prominent optimization algorithms utilized for training machine learning models, including neural networks, with SGD adjusting parameters according to gradients derived from individual or small batches of instances (Schaul et al., 2013). AdaGrad is an algorithm that adapts the learning rate of each model parameter based on historical gradient information (Duchi et al., 2011; Solanke & Patnaik, 2020). AdaDelta is a variant of AdaGrad that uses a moving window of gradient updates instead of accumulating all past gradients (Zeiler, 2012). RMSprop is a variant of the GD algorithm that uses a decaying average of partial gradients to adapt the step size for each parameter (Hinton & Tieleman, 2012; Zou et al., 2019). ADAM is an adaptive learning rate optimization algorithm that combines the advantages of both AdaGrad and RMSprop (Kingma & Ba, 2015; Yi et al., 2020). AdaMax is a variant of ADAM that is based on the infinity norm (Fatima, 2020). NADAM is a variant of ADAM with Nesterov momentum (Adem & Kiliçarslan, 2019; Sutskever et al., 2013). These algorithms are utilized in DL packages like Caffe, Lasagne, TensorFlow, and Keras. To obtain improved generality, researchers continue to create optimizers, as seen in (Lv et al., 2017).

RNN utilize memory to integrate previous inputs, hence modifying the present input and result (Karna et al., 2024). Both unrollable finite impulse networks and temporally dynamic infinite impulse networks (Sherstinsky, 2020) are examples of RNN, which are characterized by infinite impulse response (Miljanovic, 2012). Like Gated Recurrent Units (GRUs), commonly referred to as feedback neural networks (FNN), these networks may have memory or gated states (Hochreiter & Schmidhuber, 1997).

Using different numbers of iterations and particular test function values on a stacked denoising autoencoder (SDA) architecture, based on convergence time, number fluctuations, and parameter update rate, authors in (Yazan & Talu, 2017) examined a comparison of optimization techniques based on SGD, specifically ADAM, AdaGrad, AdaDelta, RMSprop, SGD, and SGD with momentum. According to their experimental results in terms of rapid convergence, AdaDelta outperformed the other optimizers. The datasets they used for their tests are unknown. The author of (Papamakarios, 2014) used the logistic and Softmax regression on the synthetic and Modified National Institute of Standards and Technology (MNIST) handwritten digits datasets, respectively, to compare the performance of four GD-based variants on the limited convex objective fitting problem: GD, stochastic GD, semi-SGD, and stochastic average descent. In the authors' two trials, SGD outperformed SG in general, but the two hybrid forms achieved superior accuracy in more reasonable amounts of time. In a similar vein (Hallén, 2017) conducted a performance

comparison between GD and SGD using the MNIST ML dataset for linear regression and multinomial logistic regression, using accuracy, training, and convergence time as performance variables. In a recent study (Ruder, 2016), gave a simple overview of how modern GD optimization techniques behave.

While pointing out difficulties in optimizing GD (Shalev-Shwartz et al., 2017), experts advise flexible learning rates for complex neural network training. These difficulties include slow training, vanishing gradients as a result of insufficient conditioning, low signal-to-noise ratio (SNR), and limited gradient informativeness. However, a comprehensive evaluation of the impact of these popular optimization algorithms on an RNN architecture using image classification datasets appears to be lacking in existing studies.

Based on the related works, several types of studies can be conducted to further explore the optimization of neural networks. These studies can involve conducting a comprehensive comparison of various optimization algorithms on RNN using other datasets, developing a theoretical framework for selecting the most suitable optimizer for training RNN, and conducting experiments using various datasets and NN architectures to evaluate the performance of different optimizers. Additionally, studies can focus on investigating and developing new optimization techniques specifically designed for DL applications, analyzing the scalability and efficiency of different optimizers in large-scale neural network training, and optimizing NN with specific architectures. Furthermore, studies can explore the use of hybrid optimizers and ensemble methods to combine the strengths of different optimizers, investigate the performance of optimizers on non-convex problems, and study the performance of optimizers on sparse and large-scale datasets. These studies can help in understanding the performance of different optimizers, developing new optimization techniques, and improving the efficiency and accuracy of neural network training.

METHODOLOGY AND EXPERIMENTAL SETUP

This study used the LSTM networks, a version of RNN architecture specifically engineered to proficiently learn and retain long-range dependencies in sequential input (Hochreiter & Schmidhuber, 1997). On the developed model, the performance of seven well-known SGD optimization techniques was also demonstrated. This research utilized the Mobile Health (MHEALTH) dataset from the UCI ML repository, which is a body motion dataset intended to evaluate methodologies for human behavior analysis through multimodal body sensing (Banos et al., 2014) . The optimizers model examined were SGD, RMSProp, ADAM, AdaGrad, AdaDelta, AdaMax, and NADAM. For each trial, identical hyperparameter settings were applied. The body motion dataset was used to train the complete network across 100 epochs.

The MHEALTH dataset was utilised to train the LSTM architecture. The selected LSTM model underwent rigorous evaluation and analysis on the MHEALTH body motion dataset to determine its effectiveness in extracting meaningful information from the body motion.

Various metrics, including training time and test accuracy, were assessed to quantify the LSTM architecture performance. The impact by experimenting with various combinations of learning rates, activation functions, and LSTM architectures was investigated. This analysis involved training the LSTM model with different optimizers. Values on subsets of the MHEALTH body motion dataset and observing the corresponding training and test accuracy changes. Training dataset is presented to the model during training. Setting all the configurations with aims to evaluate and compare the performance of seven widely used first-order stochastic gradient-based optimization algorithms within a RNN framework. specifically focuses on how these optimizers — ADAM, RMSprop, SGD, AdaGrad AdaDelta, NADAM, and AdaMax—perform in terms of test accuracy and training time when applied to a body motion dataset. The objectives to be achieved are to identify which optimizer yields the best results by experimenting with various combinations of learning rates, activation functions, and LSTM architectures.

Data Collection - UCI Body Motion Dataset

In this study, the dataset used to measure and compare the performance of optimization algorithms was the motion dataset. The MHEALTH dataset was devised to benchmark techniques dealing with human behaviour analysis based on multimodal body sensing. This dataset consisted of 23 features (columns). The number of samples determined was 100,000 and there was no missing data in the dataset. The data collected for each subject was stored in a different log file. There were 10 people doing 12 common daily activities, such as standing still, sitting, and relaxing, lying down, walking, climbing stairs, waist bends forward, frontal elevation of arms, knees bending, cycling, jogging, running, and jump front/back, and each activity was recorded for 1 minute. For one object, it took 12 minutes to collect the data for 12 activities. Each file contained the samples (by rows) recorded for all sensors (by columns).

RNN Model Setup

Three LSTM network architecture models were created for this experimental investigation to observe the variations in the weight values produced by each architecture, which were 1) one LSTM as default, 2) two LSTMs, and 3) added dropout model between the two LSTMs. The LSTM architecture models in this study can be seen from Figures 2 till 4.

The network architecture in this study has 23 input features (m_1, m_2, m_3, ... , m_{23}) with input representation: $X_t \in \mathbb{R}^{23}$ at each time step, t. The following is a mathematical model that represents the LSTM network architecture Model-1 (Figure 2).

LSTM layer (hidden layer), the LSTM unit receives the input and the previous hidden state (t-1) and cell state (t-1). The mathematical model or equation for the main LSTM computation is using the equation (Hochreiter & Schmidhuber, 1997):

$$f_t = \sigma\,(W_f[h_t\text{-}1, Xt] + b_f) \quad [1]$$

$$i_t = \sigma\,(W_i[h_t\text{-}1, Xt] + b_i) \quad [2]$$

$$\tilde{C}_t = tanh\,(W_c[h_t\text{-}1, Xt] + b_c) \quad [3]$$

$$C_t = f_t \odot C_{t-1} + i_t \odot \tilde{C}_t \quad [4]$$

$$o_t = \sigma\,(W_o[h_t\text{-}1, Xt] + b_o) \quad [5]$$

$$h_t = o_t \odot tanh\,(C_t) \quad [6]$$

The LSTM accepts the current input vector X_t the previous hidden state h_t-1, and the previous cell state C_{t-1}. The forget gate, provided by $f_t = \sigma\,(W_f[h_t\text{-}1, Xt] + b_f)$ determines what parts of the previous memory e C_{t-1} must be saved. The input gate $i_t = \sigma\,(W_i[h_t\text{-}1, Xt] + b_i)$ and candidate cell state $\tilde{C}_t = tanh\,(W_c[h_t\text{-}1, Xt] + b_c)$ work together to decide what new information must be added to the memory. The new state of the cell is computed as $C_t = f_t \odot C_{t-1} + i_t \odot \tilde{C}_t$, where element-wise multiplication is represented by $\odot$. The output gate $o_t = \sigma\,(W_o[h_t\text{-}1, Xt] + b_o)$ then decides how much of the memory is to be given as output to the next time step. Finally, the new hidden state is calculated as $h_t = o_t \odot tanh\,(C_t)$, and this will be both the output of the present LSTM unit and also an input to the next step of the sequence. In these equations, σ is the sigmoid activation function (which outputs between 0 and 1), and tanh is the hyperbolic tangent function (which outputs between -1 and 1). The weight matrices W_f, W_i, W_c, W_o

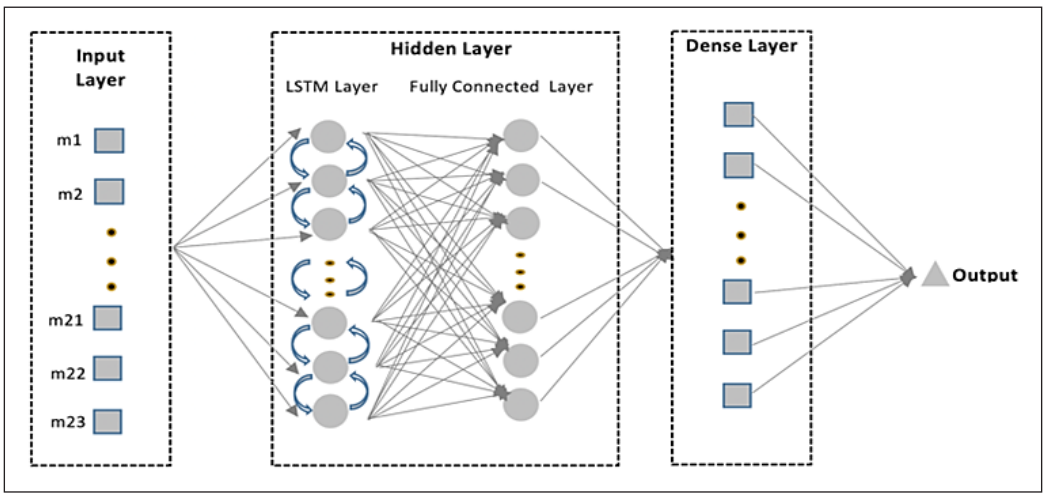

Figure 2. Model-1 (One hidden layer with one long short-term memory layer [LSTM])

are learned weight parameters for every gate, and b_f, b_i, b_c, b_o are corresponding bias vector.

Fully connected layer receives *t* from the LSTM layer and processes it with weights and biases.

$$H = \text{ReLU}\,(W_{fc} h_t + b_{fc}) \quad [7]$$

where, W_{fc} is referred to weight of fully connected layer and b_{fc} is bias.

Dense layer (output) takes the output of the fully connected layer and maps it to the output using the last weight and bias.

$$y = (W_{dense}\, H + b_{dense}) \quad [8]$$

where, W_{dense} is referred to weight of output layer and b_{dense} is bias.

A representation of the second network architecture that was utilized in the research is shown in Model -2, which can be found in this following Figure 3.

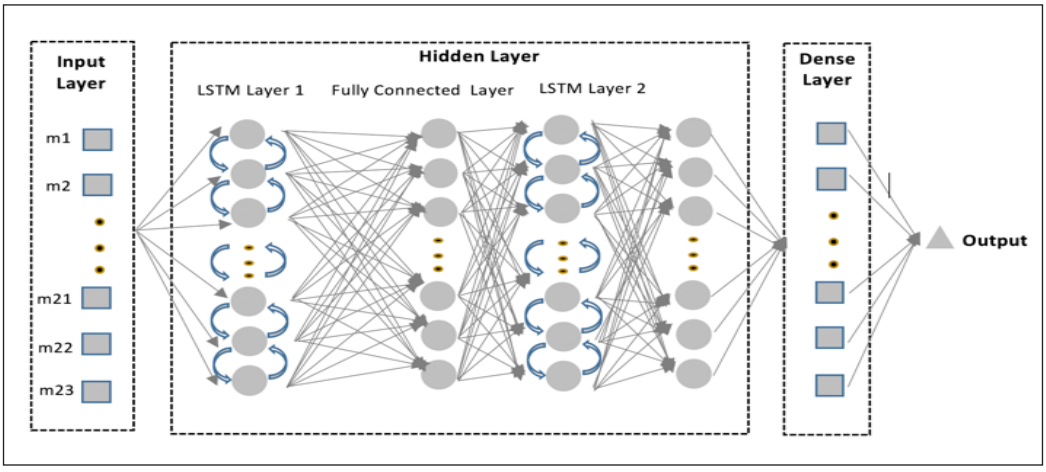

Figure 3. Model-2 (Two hidden layers with two long short-term memory [LSTM] layers)

The LSTM architecture models, Model-2 and Model-3 (Figures 3 and 4), are essentially the same as the LSTM architecture model, Model-1, for computations and mathematical models; however, they have an additional hidden layer. The following is a mathematical model that represents the LSTM network architecture Model-2 (Chen et al., 2022; Hochreiter & Schmidhuber, 1997; Van Houdt et al., 2020).

LSTM Layer 1: $$h_t^{(1)} = \sigma\left(W_1 X_t + U_1 h_{t-1}^{(1)} + b_1\right) \quad [9]$$

Fully Connected Layer: $$H = \text{ReLU}\,(W_{fc} h_t^{(1)} + b_{fc}) \quad [10]$$

LSTM Layer 2: $$h_t^{(2)} = \sigma\,(W_2 H + U_2 h_{t-1}^{(2)} + b_2) \quad [11]$$

Dense Layer (Output): $$y = (W_o h_t^{(2)} + b_o) \quad [12]$$

Model-2 enhances the standard LSTM by adding an extra hidden layer, allowing it to learn more complex patterns in sequential data. In the first LSTM layer, the hidden state $h_t^{(1)}$ is computed from the input X_t, previous hidden state $h_{t-1}^{(1)}$, input weights W_1, recurrent weights U_1, and bias b_1, using the sigmoid activation σ: $h_t^{(1)} = \sigma\left(W_1 X_t + U_1 h_{t-1}^{(1)} + b_1\right)$. This hidden state is transformed by a fully connected layer into a new feature H using ReLU activation: $H = \text{ReLU}\,(W_{fc} h_t^{(1)} + b_{fc})$ where W_{fc} and b_{fc} are the weights and bias of the dense layer. The second LSTM layer uses this H along with its previous hidden state $h_t^{(2)}$, weights W_2, U_2, and bias b_2 to compute: $h_t^{(2)} = \sigma\,(W_2 H + U_2 h_{t-1}^{(2)} + b_2)$. Finally, the model output is calculated as: $y = (W_o h_t^{(2)} + b_o)$ with W_o and b_o representing the output layer's weights and bias. This design enables the model to learn both short- and long-term dependencies effectively. Henceforth, the network architecture used in this study is LSTM model-3, which can be seen in the following Figure 4.

Figure 4 is the LSTM architecture Model-3, which is essentially identical to the previous one, with the exception that a dropout layer is used in place of the middle layer to avoid

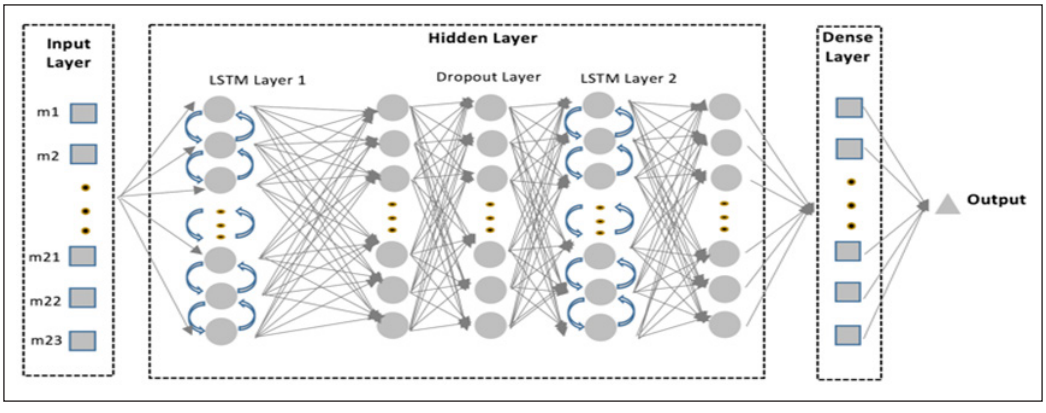

Figure 4. Model-3 (two hidden layers with two long short-term memory [LSTM] layers and one dropout layer)

overfitting. The following mathematical model represents the LSTM network architecture Model-3 (Chen et al., 2022; Hochreiter & Schmidhuber, 1997; Van Houdt et al., 2020).

LSTM layer 1: $$h_t^{(1)} = \sigma\left(W_1 X_t + U_1 h_{t-1}^{(1)} + b_1\right) \quad [13]$$

Dropout layer: $h_t^{(d)} = \text{Dropout}\left(h_t^{(1)}, p\right)$; p is dropout probability [14]

LSTM layer 2: $$h_t^{(2)} = \sigma\left(W_2 h_t^{(d)} + U_2 h_{t-1}^{(2)} + b_2\right) \quad [15]$$

Dense layer (Output): $$y = \left(W_o h_t^{(2)} + b_o\right) \quad [16]$$

where, the hidden state $h_t^{(1)}$ using the current input X_t, the previous hidden state $h_{t-1}^{(1)}$, weight matrices W_1 and U_1, and a bias term b_1. Then, a dropout layer is applied to $h_t^{(1)}$ producing a new intermediate state $h_t^{(d)}$ by randomly dropping units based on the dropout probability p. This result is fed into the second LSTM layer, which produces $h_t^{(2)}$ using W_2, U_2, and b_2. The final output y is calculated through a dense layer with weights W_o and bias b_o.

Optimization Techniques

Experiments are conducted by comparing seven different optimization methods, namely SGD, ADAM, RMSprop, AdaGrad, AdaDelta, NADAM, and AdaMax. Each GD based optimization method has a unique approach in updating the model parameters. The main equations for the methods used in this study are as follows:

The SGD method is a basic form of gradient-based optimization. The mathematical equation for all the GD method is using this following equations (Ruder, 2016):

$$\theta_{t+1} = \theta_t - \eta \nabla L\left(\theta_t\right) \quad [17]$$

where, the model parameters at a given iteration (denoted as θ_t) are updated to θ_{t+1} by moving in the opposite direction of the gradient of the loss function. This update is controlled by a learning rate (η), a small positive value that determines the size of each step towards minimizing the loss. The gradient, represented as $\nabla L\left(\theta_t\right)$, indicates how much the loss changes with respect to the current parameters, guiding the optimization process. AdaGrad adjusts the learning rate for each parameter based on the previous gradient:

$$g_t = \nabla L\left(\theta_t\right) \quad [18]$$

$$\theta_{t+1} = \theta_t - \frac{\eta}{\sqrt{G_t + \epsilon}} \odot g_t \quad [19]$$

$$G_t = G_{t-1} + g_t^2 \quad [20]$$

The AdaGrad optimizer improves the standard gradient descent method by adapting the learning rate for each model parameter based on the historical accumulation of gradients. At each training step, it calculates the gradient of the loss function with respect to the current parameters, noted as $g_t = \nabla L(\theta_t)$. Instead of applying a fixed learning rate, AdaGrad adjusts it by dividing the global learning rate η by the square root of the sum of all past squared gradients G_t, and a small constant ε to maintain numerical stability. This results in the update rule $\theta_{t+1} = \theta_t - \frac{\eta}{\sqrt{G_t + \epsilon}} \odot g_t$, where $\odot$ indicates element-wise multiplication. The cumulative term G_t is updated at each step as $G_t = G_{t-1} + g_t^2$. This approach naturally decreases the learning rate for parameters that frequently receive large updates, which helps improve learning efficiency and model performance, especially in scenarios involving sparse or high-dimensional data. RMSProp overcomes AdaGrad's weakness by using exponential averaging of squared gradients:

$$g_t = \nabla L(\theta_t) \quad [21]$$

$$E[g_t^2] = \rho E[g_{t-1}^2] + (1-\rho) g_t^2 \quad [22]$$

$$\theta_{t+1} = \theta_t - \frac{\eta}{\sqrt{E[g_t^2] + \epsilon}} \odot g_t \quad [23]$$

where, g_t is the gradient of the loss function with respect to the model parameters at iteration and $\nabla L(\theta_t)$ represents the direction and rate of increase of the loss function at parameters. Equation [22] defines the exponential moving average of the squared gradients, where $E[g_t^2] =$ represents the smoothed estimate of the squared gradient at iteration *t*. The term ρ is a decay factor, usually set between 0.9 and 0.99, which controls how much influence the past squared gradients g_{t-1}^2 have on the current estimate. Meanwhile, g_t^2 is the element- wise square of the current gradient. Equation [23] update the model parameters in RMSProp, where θ_t and θ_{t+1} are the current and updated parameters, respectively. η is the learning rate, ϵ is a small constant to avoid division by zero, and $\odot$ denotes element-wise multiplication. ADAM combines momentum and RMSProp for adaptive learning rate adjustment (Kingma & Ba, 2015; Ruder, 2016):

$$m_t = \beta_1 m_{t-1} + (1-\beta_1) g_t \quad [24]$$

$$v_t = \beta_2 v_{t-1} + (1-\beta_2) g_t^2 \quad [25]$$

$$\widehat{m_t} = \frac{m_t}{1-\beta_1^t} + \widehat{v_t} = \frac{v_t}{1-\beta_2^t} \quad [26]$$

$$\theta_{t+1} = \theta_t - \frac{\eta}{\sqrt{v_t+\epsilon}} m_t \quad [27]$$

In the ADAM optimization algorithm, parameter updates are computed using both the first and second moment estimates of the gradients. Equation [24] defines the first moment estimate, where g_t is the current gradient and *β1* is the exponential decay rate for the gradient moving average. Equation [25] computes the second moment estimate, where *β2* is the decay rate for the squared gradients. Since both m_t and v_t are initialized at zero, bias-corrected estimates are used as shown in Equation [26]. The model parameters are updated using Equation [27], where θ_t and θ_{t+1} are the current and updated parameters, η is the learning rate, and ϵ is a small constant added for numerical stability. This combination of momentum and adaptive learning rate adjustment makes Adam particularly effective for deep learning tasks. AdaDelta overcomes gradient accumulation in AdaGrad by using a moving average of the gradients (Ruder, 2016):

$$E[g_t^2] = \rho E[g_{t-1}^2] + (1-\rho) g_t^2 \quad [28]$$

$$\Delta\theta_t = -\frac{\sqrt{E[\Delta\theta_{t-1}^2]}}{\sqrt{E[g_t^2]+\epsilon}} + \epsilon \quad [29]$$

$$E[\Delta\theta_t^2] = \rho E[\Delta\theta_{t-1}^2] + (1-\rho)(\Delta\theta_t)^2 \quad [30]$$

The algorithm maintains a decaying average of past squared gradients as shown in Equation [28], where g_t is the gradient at the current time step, and ρ is a decay constant that controls how much weight is given to past values. Parameter updates are calculated using Equation [29], where $\Delta\theta_t$ represents the update applied to the model parameters. This formulation scales the raw gradient based on the ratio between the root mean square of previous updates and the current average of squared gradients, with ϵ (a small constanta) included to prevent division by zero and enhance numerical stability. Updates the moving average of squared parameter updates using Equation [30], where $\Delta\theta_t^2$ is the element-wise square of the current update. This recursive structure ensures consistent and adaptive parameter updates over time.

Adamax is an ADAM variant based on norm infinity ($\ell \bowtie$), the mathematical equation is using this following equations (Ruder, 2016) :

$$m_t = \beta_1 m_{t-1} + (1 - \beta_1) g_t \quad [31]$$

$$u_t = Max\,(\beta_2 u_{t-1}, |g_t^2|) \quad [32]$$

$$\theta_{t+1} = \theta_t - \frac{\eta}{\sqrt{u_t}}\, m_t \quad [33]$$

The first moment estimate is computed using an exponentially weighted moving average of the gradients, as shown in Equation [31], where m_t is the exponentially weighted average of gradients, g_t is the current gradient, and β_1 is the decay rate. Adamax uses the infinity norm, as defined in Equation [32], where u_t is the running maximum of the scaled gradient magnitudes, β_2 is the decay rate for this term, and $|g_t|$ is the element-wise absolute gradient. The parameters are then updated using Equation [33], where θ_t is the parameter at step *t*, η is the learning rate, and the denominator normalizes the update using the square root of the infinity norm. NADAM added Nesterov's momentum to ADAM's (Ruder, 2016).

$$m_t = \beta_1 m_{t-1} + (1 - \beta_1) g_t \quad [34]$$

$$u_t = \beta_2 u_{t-1} + (1 - \beta_2) g_t^2 \quad [35]$$

$$\widehat{m_t} = \frac{m_t}{1-\beta_1^t} + \frac{(1-\beta_1}{1-\beta_1^t}\, g_t \quad [36]$$

$$\theta_{t+1} = \theta_t - \frac{\eta}{\sqrt{\widehat{u_t} + \epsilon}}\, \widehat{m_t} \quad [37]$$

In the NADAM optimization algorithm θ_t represent for the model parameters at iteration *t,* and θ_{t+1} denote the update parameters.The gradient of the loss function at time t is denoted by g_t. The algorithm keeps track of two moving averages: m_t, which is the exponentially weighted average of past gradients (also known as the first moment), and u_t, which is the exponentially weighted average of past squared gradients (the second moment). These averages help smooth out the noise in the gradient updates. To improve stability early in training, NADAM uses a bias- corrected version of the first moment, noted as $\widehat{m_t}$, which also incorporates a lookahead gradient term inspired by Nesterov momentum. The constants β_1 and β_2 control the decay rates of these moving averages and are usually set close to 1. The learning rate, symbolized by η, determines how big each step should be when updating the parameters, and ϵ is a small value added to the denominator to avoid division by zero, ensuring numerical stability.

Activation Functions

Five activation functions—Sigmoid, Softmax, ReLU, tanh, and Exponential—were employed in this study to maximize the RNN model's performance. Particularly in deciding how information is processed and transmitted in each neuron layer, each of these functions has a distinct function and set of properties in the model training process. Sigmoid is perfect for binary classification because it compresses outputs between 0 and 1. Nevertheless, it slows down model updates due to the vanishing gradient issue. The function for all the activation function variant is using this following equations (Szandała, 2020):

$$\sigma\,(x) = \frac{1}{1 + e^{-x}} \qquad [38]$$

The sigmoid function σ (x) is the output of the activation function, mapping any real-valued input x to a value between 0 and 1. The input x is typically the weighted sum of inputs to a neuron, given by $x = w_1x_1 + w_2x_2 + ... + w_nx_n + b$, where w_i is the weight of the *i*-th input, x_i is the *i*-th input feature, and b is the bias term. The constant e is Euler's number, approximately 2.71828, and e^{-x} is the exponential function with exponent -x, which decreases rapidly as x increases.

Softmax transforms inputs into a probability distribution, generalizing sigmoid for multi-class classification. Its downside is overfitting, as it might give excessive probabilities. Softmax is defined as:

$$\text{Softmax}\,(x_i) = \frac{e^{x_i}}{\sum_j e^{x_i}} \qquad [39]$$

where, (x_i) is the output for the *i*-th class, representing the predicted probability that the input belongs to class *i*. The term x_i refers to the logit or raw output score from the model for the *i*-th class, (before the activation). The constant e denotes Euler's number, approximately equal to 2.71828. The expression e^{x_i} is the exponential of the logit x_i, which scales the output positively. The denominator $\sum_j e^{x_i}$ is the sum of the exponentials of all logits across all classes *j* used to normalizes the output so that they add up to 1.

By only activating positive values, the ReLU resolves the vanishing gradient problem and accelerates convergence. It has to deal with the fading ReLU issue, though, where neurons might stop working. This function is formulated as:

$$\text{ReLU}(x) = \begin{cases} x, & x > 0 \\ \alpha 0, & x \leq 0 \end{cases} \qquad [40]$$

where, ReLU(x) is the output of the activation function applied to the input *x*, which typically represents the weighted sum of inputs to a neuron. The symbol *x* is the input value, and α is a small positive constant (usually around 0.01) called the leakage coefficient, which allows a small, non-zero gradient when *x* is negative. This helps avoid the "dying ReLU" problem by ensuring that neurons can still update during training even when they receive negative inputs.

Similar to sigmoid, tanh improves representation by having an output range of -1 to 1. The vanishing gradient still affects it, particularly at extreme values. This function is defined as:

$$\tanh(x) = \frac{e^{x} - e^{-x}}{e^{x} + e^{-x}} \quad [41]$$

where, x represents the input value, typically the weighted sum of inputs to a neuron. The symbol e stands for Euler's number, approximately equal to 2.71828. The terms e^{x} and e^{-x} are the exponential functions of *x* and -*x*, respectively. The numerator $e^{x} - e^{-x}$ gives the difference of exponentials, while the denominator $e^{x} + e^{-x}$ ensures the output remains bounded between -1 and 1.

Exponential learning speeds up learning by exponentially magnifying input values, but it also runs the danger of inflating gradients, which can cause training instability. Exponential defined as:

$$\text{Exponential}\ (x) = e^{x} \quad [42]$$

where, *x* represents the input value, typically the weighted sum of inputs to a neuron. The symbol e stands for Euler's number (~2.71828) and the terms e^{x} grows rapidly with positive *x* and approaches zero as *x* becomes negative.

Experimental Configuration

Experiments were conducted to compare several optimization methods discussed, such as ADAM, RMSprop, SGD, AdaGrad, AdaDelta, NADAM, and AdaMax. The RNN model consisted of an input layer that was then forwarded to the LSTM architecture, and the last layer was the output layer. Based on Tabel 1, the training data was processed for a batch size of 32 sample records and 100 epochs. The training data was compiled with the learning rate of 0.1, 0.01, and 0.001, respectively. The network structure is shown in Table 1.

Table 1
Recurrent Neural Network structure specification

Description	Value
Learning rate	0.1; 0.01; 0001
Number of epoch	100
Batch size	32
Number of training	80% : 80,000
Number of validation	20% : 20,000
Optimizer	ADAM, RMSprop, SGD, AdaGrad, AdaDelta, NADAM, and AdaMax
Activation function	Sigmoid, Softmax, ReLU, tanh, and Exponential

Note. ADAM = Adaptive Moment Estimation; RMSProp = Root Mean Square Propagation; SGD = Stochastic Gradient Descent; AdaGrad = Adaptive Gradient Algorithm; AdaDelta = Adaptive Delta; NADAM = Nesterov-accelerated Adaptive Moment Estimation; AdaMax = Adaptive Moment Estimation with Infinity Norm

RESULTS AND DISCUSSION

The purpose of the experiment was to analyze each configuration of optimizers, which included ADAM, RMSprop, SGD, AdaGrad, AdaDelta, NADAM, and AdaMax with three LSTM network architecture models, five activation functions, and three learning rates (α), respectively. The comparison results shown in Table 2 are the training process or training time in minutes, abbreviated by "TT", and the test accuracy in percentages, abbreviated by "TA", for every configuration.

This study systematically evaluated the performance of various optimization algorithms using RNN architecture, specifically LSTM networks. The implementation was carried out using the TensorFlow DL library and Python programming language. The experiments were performed on a Dell personal computer equipped with an Intel Core i7 processor, 16 GB of RAM, and an NVIDIA GeForce GTX 1660 graphics card, ensuring a robust computational setup. Performance evaluation was based on test accuracy and training time, with results systematically compiled into tables summarizing the impact of different optimizers and hyperparameter configurations such as learning rates (0.1, 0.01, and 0.001) and five activation functions (Sigmoid, Softmax, ReLU, tanh, and Exponential). Each trial maintained a consistent batch size of 32 samples, ensuring uniform data processing across all experiments for comparability.

Table 2 indicates that testing accuracy is determined by the model evaluation outcomes following training with the test dataset. The test accuracy value is calculated by splitting the dataset into two sections: the training process (80%) and the testing process (20%). The model is trained using training data with various parameters (optimizer, learning rate, activation function) during the training process. Following training, the model is tested using the test dataset (test set). By contrasting the actual label in the test dataset with the model prediction, the degree of accuracy, also known as test accuracy, is determined.

Table 2
Performance comparisons of studied optimization algorithms

Optimizer model	LSTM architecture	Activation function	α = 0.1		α = 0.01		α = 0.001	
			TT (min)	TA (%)	TT (min)	TA (%)	TT (min)	TA (%)
ADAM	Model-1	Sigmoid	81.56	78.31	73.73	76.38	76.43	78.29
		Softmax	17.96	1.83	78.33	1.83	80.18	1.83
		ReLU	79.83	78.31	79.24	78.31	79.67	78.31
		tanh	17.8	78.31	17.91	78.31	17.87	78.31
		Exponential	17.84	78.31	17.89	78.31	17.95	78.31
	Model-2	Sigmoid	32.04	78.31	31.8	78.31	31.66	78.31
		Softmax	31.74	1.83	31.81	1.83	31.78	1.83
		ReLU	31.97	78.31	32.47	78.31	34.4	78.31
		tanh	34	78.31	34.28	78.31	34.14	78.31
		Exponential	34.03	78.31	33.53	78.31	34.29	78.31
	Model-3	Sigmoid	32.05	75.09	31.17	75.10	31.37	75.11
		Softmax	31.53	1.83	31.66	1.83	31.51	1.83
		ReLU	31.46	78.31	31.63	78.31	31.6	78.31
		tanh	31.49	78.31	31.47	78.31	31.55	78.31
		Exponential	31.6	78.31	31.55	78.31	31.56	78.31
RMSprop	Model-1	Sigmoid	17.81	78.31	17.72	78.31	18.03	78.31
		Softmax	18.02	1.83	18.02	1.83	18.1	1.83
		ReLU	18.01	78.31	18.01	78.31	17.89	78.31
		tanh	17.9	78.31	17.99	78.31	17.99	78.31
		Exponential	18	78.31	18	78.31	18.02	78.31
	Model-2	Sigmoid	34.28	78.31	33.84	78.31	34.16	78.31
		Softmax	34.03	1.83	33.91	1.83	33.16	1.83
		ReLU	34.18	78.31	33.87	78.31	34.78	78.31
		tanh	34.35	78.31	33.87	78.31	33.04	78.31
		Exponential	33.05	78.31	33.11	78.31	33.08	78.31
	Model-3	Sigmoid	31.01	78.31	30.97	75.07	30.9	75.06
		Softmax	31.01	1.83	31.04	1.83	31.05	1.83
		ReLU	31.05	78.31	31.11	78.31	31.21	78.31
		tanh	31.09	78.31	31.39	78.31	31.07	78.31
		Exponential	31.12	78.31	31.25	78.31	31.52	78.31

Table 2 *(continue)*

Optimizer model	LSTM architecture	Activation function	α = 0.1		α = 0.01		α = 0.001	
			TT (min)	TA (%)	TT (min)	TA (%)	TT (min)	TA (%)
SGD	Model-1	Sigmoid	18	78.31	18.01	78.31	18.04	78.31
		Softmax	18.01	1.83	18.01	1.83	18.01	1.83
		ReLU	18	78.31	18	78.31	18	78.31
		tanh	18.01	78.31	18.01	78.31	18.01	78.31
		Exponential	18.01	74.76	18.01	74.85	18.01	74.87
	Model-2	Sigmoid	34.16	78.30	34.12	78.30	33.83	78.30
		Softmax	33.35	1.83	33.03	1.83	33.03	1.83
		ReLU	33.02	78.31	32.74	78.31	30.10	78.31
		tanh	30.2	78.31	30.12	78.31	30.07	78.31
		Exponential	30.25	78.28	30.16	78.29	30.33	78.29
	Model-3	Sigmoid	31.13	78.24	30.99	78.26	30.98	78.27
		Softmax	30.76	1.83	31.07	1.83	31.43	1.83
		ReLU	31.32	78.31	31.64	78.31	31.7	78.31
		tanh	32.01	78.31	32.37	78.31	32.61	78.31
		Exponential	32.89	78.31	32.30	78.31	31.97	78.31
AdaGrad	Model-1	Sigmoid	17.06	78.31	17.02	78.31	17.02	78.31
		Softmax	17.01	1.83	17.08	1.83	17.26	1.83
		ReLU	17.02	78.31	17.23	78.31	17.16	78.31
		tanh	17.05	78.31	17.04	78.31	17.01	78.31
		Exponential	17.03	78.31	17.02	78.31	17.01	78.31
	Model-2	Sigmoid	34.47	78.30	34.36	78.31	34.96	78.31
		Softmax	34.82	1.83	34.95	1.83	35.01	1.83
		ReLU	34.98	78.31	35.2	78.31	35.11	78.31
		tanh	35.18	78.31	33.77	78.31	33.83	78.31
		Exponential	33.85	78.29	34.02	78.29	36.26	78.29
	Model-3	Sigmoid	32.76	78.31	32.88	78.31	32.83	78.31
		Softmax	32.29	1.83	31.99	1.83	31.99	1.83
		ReLU	32.78	78.31	32.77	78.31	32.01	78.31
		tanh	31.88	78.31	31.86	78.31	32.06	78.31
		Exponential	32.02	78.31	32.1	78.31	32.13	78.31

Table 2 *(continue)*

Optimizer model	LSTM architecture	Activation function	α = 0.1		α = 0.01		α = 0.001	
			TT (min)	TA (%)	TT (min)	TA (%)	TT (min)	TA (%)
AdaDelta	Model-1	Sigmoid	20.63	78.31	21.4	78.31	21.03	78.31
		Softmax	21.03	1.83	21.04	1.83	21.1	1.83
		ReLU	21.04	78.31	21.09	78.31	21.03	78.31
		tanh	21.06	78.31	21.03	78.31	21.03	78.31
		Exponential	21.10	74.92	21.06	74.93	21.09	74.94
	Model-2	Sigmoid	34.58	78.31	34.17	78.31	34.33	78.31
		Softmax	34.67	1.83	35.03	1.83	34.71	1.83
		ReLU	34.90	78.31	34.94	78.31	34.93	78.31
		tanh	35.01	78.31	33.06	78.31	33.37	78.31
		Exponential	33.3	78.29	33.58	78.29	35.92	78.29
	Model-3	Sigmoid	31.48	78.31	31.53	78.31	31.13	78.31
		Softmax	31.62	1.83	31.85	1.83	31.63	1.83
		ReLU	32.77	78.31	32.8	78.31	32.69	78.31
		tanh	32.15	78.31	31.68	78.31	31.42	78.31
		Exponential	31.16	74.73	31.42	74.66	31.42	74.66
NADAM	Model-1	Sigmoid	21.99	78.31	21.17	78.31	21.05	78.31
		Softmax	21.08	1.83	21.06	1.83	21.09	1.83
		ReLU	21.06	78.31	21.11	78.31	21.13	78.31
		tanh	21.08	78.31	21.11	78.31	21.09	78.31
		Exponential	21.1	78.31	21.28	78.31	20	78.31
	Model-2	Sigmoid	33.38	78.31	33.37	78.31	33.46	78.31
		Softmax	33.98	1.83	34.05	1.83	34.05	1.83
		ReLU	34.05	78.31	34.03	78.31	34.04	78.31
		tanh	34.53	78.31	35.58	78.31	35.52	78.31
		Exponential	35.18	78.31	34.99	78.31	34.90	78.31
	Model-3	Sigmoid	31.97	75.06	31.17	75.10	31.28	75.09
		Softmax	31.54	1.83	31.61	1.83	31.73	1.83
		ReLU	31.64	78.31	31.46	78.31	31.36	78.31
		tanh	31.65	78.31	31.8	78.31	31.94	78.31
		Exponential	31.14	78.31	31.36	78.31	32.11	78.31

Table 2 *(continue)*

Optimizer model	LSTM architecture	Activation function	α = 0.1		α = 0.01		α = 0.001	
			TT (min)	TA (%)	TT (min)	TA (%)	TT (min)	TA (%)
AdaMax	Model-1	Sigmoid	17.07	78.24	17.06	78.27	17.03	78.29
		Softmax	17.83	1.83	17.86	1.83	18.03	1.83
		ReLU	18.04	78.31	18.07	78.31	18.69	78.31
		tanh	18.97	78.31	20.01	78.31	20.1	78.31
		Exponential	20.74	78.31	20.97	78.31	21.45	78.31
	Model-2	Sigmoid	33.90	78.29	33.27	78.25	33.53	78.27
		Softmax	33.72	1.83	33.86	1.83	33.94	1.83
		ReLU	33.83	78.31	33.72	78.31	33.89	78.31
		tanh	34.28	78.31	35.49	78.31	35.34	78.31
		Exponential	34.74	78.30	34.6	78.28	34.63	78.28
	Model-3	Sigmoid	31.25	78.21	31.13	77.74	31.23	78.20
		Softmax	31.68	1.83	31.5	1.83	31.63	1.83
		ReLU	31.36	78.31	31.50	78.31	31.39	78.31
		tanh	31.26	78.31	31.45	78.31	31.5	78.31
		Exponential	31.69	75.46	31.98	76.28	31.92	76.56

Note. TT = Training time; TA = Training accuracy; ADAM = Adaptive Moment Estimation; RMSProp = Root Mean Square Propagation; SGD = Stochastic Gradient Descent; AdaGrad = Adaptive Gradient Algorithm; AdaDelta = Adaptive Delta; NADAM = Nesterov-accelerated Adaptive Moment Estimation; AdaMax = Adaptive Moment Estimation with Infinity Norm

Enclosed is the comprehensive summary of the analysis conducted on each optimizer:

1. The best performance of the ADAM optimizer is found using the LSTM architecture Model-1 with the tanh activation function, and the learning rate of 0.1, respectively. Moreover, the ADAM optimizer performs well using the sigmoid, tanh, and exponential activation functions, exhibiting the lowest running time and highest test accuracy. However, the ADAM optimizer shows significantly higher running time and lower test accuracy using the Softmax and ReLU activation functions compared to the tanh, sigmoid and exponential activation functions.
2. The RMSprop produces the best performance using the LSTM architecture Model-1 with the sigmoid activation function and the learning rate of 0.01. However, RMSprop shows poor performance in terms of high running time and low accuracy value for each configuration using the Softmax activation function.

3. The SGD performs well in most combinations of activation functions and learning rates, wherein the lowest running time and highest test accuracy achieved using the sigmoid and ReLU activation functions. However, the SGD exhibits higher running time and lower test accuracy using the Softmax activation functions compared to the tanh and exponential activation functions.
4. The AdaGrad performs well using the sigmoid, tanh and exponential activation functions. However, the AdaGrad shows the worst performance using the Softmax activation function followed by the ReLU activation function with the highest running time and lowest test accuracy.
5. In general, the AdaDelta performs well using the sigmoid, ReLU and tanh activation functions in each configuration. The AdaDelta performs poorly, with the highest running time and lowest test accuracy using the Softmax activation function.
6. NADAM has quite poor performance compared to other optimizer models for each configuration.
7. The AdaMax performs well using the sigmoid and ReLU activation functions with a learning rate of 0.01 and 0.001, exhibiting the lowest running time and highest test accuracy. However, AdaMax shows higher running time and lower test accuracy for each configuration using the Softmax activation function compared to others.

In sum, the two best optimizers in terms of less training time and high accuracy are AdaGrad and SGD optimizers. Both AdaGrad and SGD optimizers perform well across a wide range of activation functions, Precisely, both optimizers achieve high accuracy and low running time across a wide range of models and optimizers, particularly effective with exponential and sigmoid. While SGD is an easy and widely used method, AdaGrad offers more adaptive and efficient updates, making it particularly suitable for sparse data and tasks where the learning rate needs to be adjusted dynamically (Alzubaidi et al., 2021; Duchi et al., 2011). Where its application is suitable for the case in this study which has large amounts of data or high-dimensional data. AdaGrad and SGD perform better than others due to their enhanced efficiency and robustness against noisy data. Additionally, they dynamically adjust the learning rate for each model parameter, which helps to avoid the issue of vanishing gradients. This combination of efficient updates and adaptive learning rates enables these optimizers to effectively optimize DL models (Solanke & Patnaik, 2020).

Moreover, the two best activation functions are sigmoid and exponential. The choice of sigmoid or exponential activation function significantly impacts the training time of neural network models. Both sigmoid and exponential activation functions provide a continuous output range, which facilitates efficient updates by the optimizers (Yi et al., 2020). This is particularly important for SGD and AdaGrad, which rely on the gradient of the loss function calculated for a single training example or a small batch of examples. The continuous output

range of sigmoid and exponential activation functions also helps in reducing the impact of noisy data on the model's performance (Yi et al., 2020), which is crucial for optimizers like SGD and AdaGrad. Additionally, the continuous output range helps in adapting the learning rate for each model parameter, which is particularly important for AdaGrad.

Both sigmoid and exponential activation functions consistently perform well across different optimizers and activation functions, providing a continuous output range that facilitates efficient updates and robustness to noisy data. In contrast, activation functions like Softmax and ReLU may result in poorer performance due to their discrete output ranges. The interaction between optimizers and activation functions is crucial, and selecting the right combination of optimizer and activation function is essential for a specific task. Overall, the choice of sigmoid or exponential activation function plays a significant role in the performance of NN models, and it is crucial to experiment with different optimizers and activation functions to find the best combination for a specific task and dataset (Zou et al., 2019). In summary, the sigmoid and exponential activation functions are particularly effective with AdaGrad and SGD due to their continuous output range, non-linearity, robustness to noise, efficient updates, learning rate adaptation, robustness to local minima, performance across activation functions, and theoretical analysis. These characteristics make them well-suited for DL models and ensure that they can learn and represent complex patterns in the data, effectively (Mehmood et al., 2023).

Meanwhile, the Softmax activation function has very poor performance due to not providing optimal performance across different models and optimizers. This is because the special properties of the Softmax function, which are non-sparsity and potential vanishing gradients hinder the optimization process, hence generate the overfitting problem. Consequently, the Softmax function in the LSTM architecture does not provide a clear separation between classes, leading to poor generalization performance.

In addition to that, the Softmax activation function consistently performs poorly across different models due to several reasons. Firstly, the Softmax activation function produces output values between 0 and 1, leading to a loss of information and a decrease in the model's ability to learn complex patterns in the data. Additionally, the Softmax activation function is not as non-linear as other activation functions like sigmoid, tanh, and exponential, which can lead to a loss of information and a decrease in the model's ability to learn complex patterns in the data. The gradient calculation for Softmax can also be more complex and sensitive to the input values, leading to a loss of information and a decrease in the model's ability to learn complex patterns in the data (Shen et al., 2023; Szandała, 2020). Furthermore, the optimization algorithms used in the experiments, such as ADAM, RMSprop, SGD, and AdaGrad, may not be well-suited for the Softmax activation function, leading to poor performance.

The results for the accuracy of the different optimization algorithms used in this study are simply laid out from Figures 5 to 11, each giving insight into how well the models

performed with the same experimental setup. Starting with Figure 5, it shows how the ADAM optimizer performed, giving a baseline to compare against. Figure 6 goes on with RMSProp results, and Figure 7 presents the accuracy obtained using Stochastic Gradient Descent (SGD). Figure 8 then presents how AdaGrad fared, and Figure 9 goes on with results from AdaDelta. Figure 10 presents NADAM's performance, which is essentially an enhanced version of ADAM with Nesterov momentum. Lastly, Figure 11 presents the accuracy results for AdaMax, yet another infinity norm-based variant of ADAM. Collectively, these figures facilitate the comparison and visualization of the strengths of each optimizer in a consistent way. The comparison of accuracy results for each model or optimization algorithm using the experiment's current setups is shown graphically in the following.

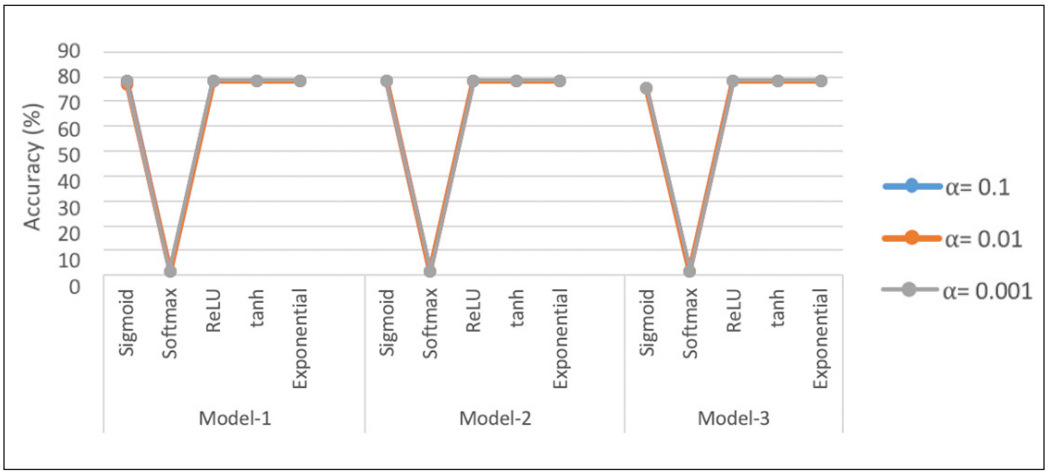

Figure 5. Accuracy result (ADAM)

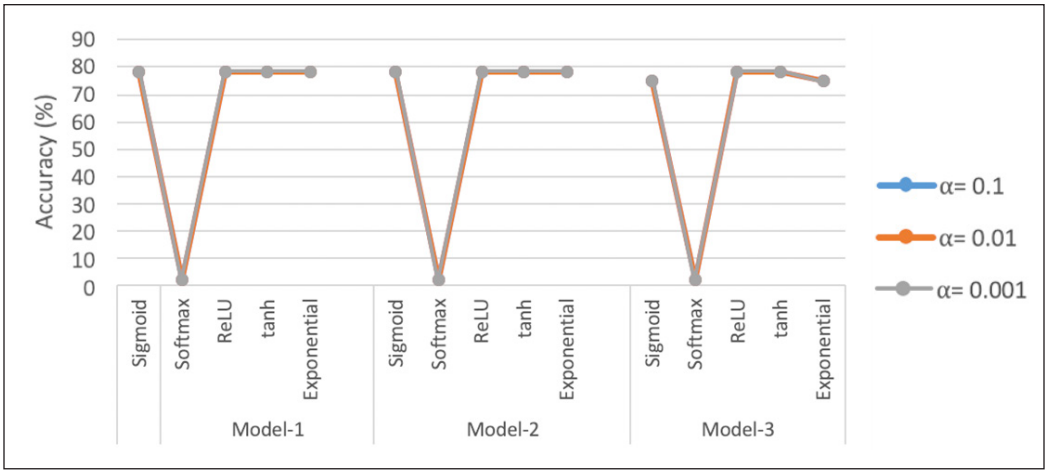

Figure 6. Accuracy result (RMSProp)

Based on the analysis of the results of the studies and experiments that have been presented, some things that can be highlights are the importance of choosing the right optimizer model and hyperparameters for a specific problem. It also emphasizes the need for further research to better understand the interactions between these factors and their impact on model performance. Identify potential future directions for research in this area, such as exploring new optimization algorithms or activation functions, or integrating optimization algorithms with other DL techniques. Furthermore, the performance of the optimization algorithms and activation functions can be compared possibly using other methods.

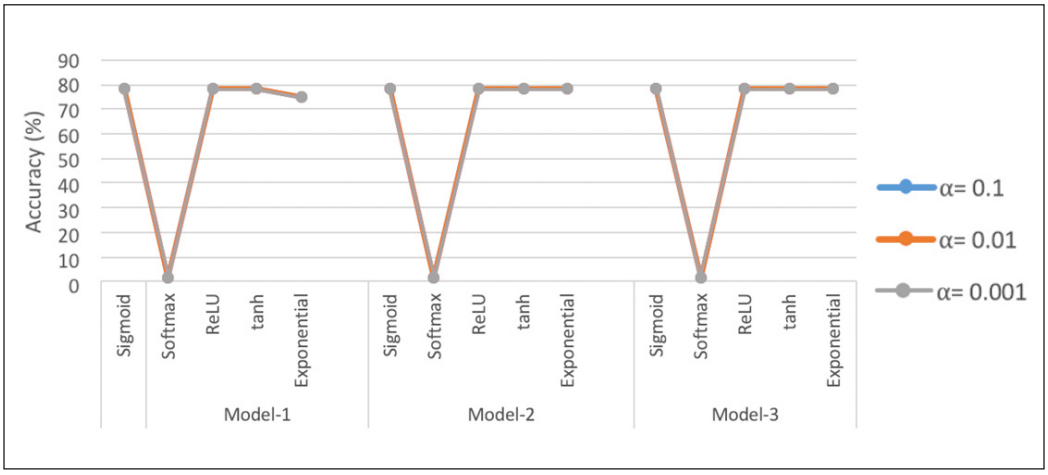

Figure 7. Accuracy result (SGD)

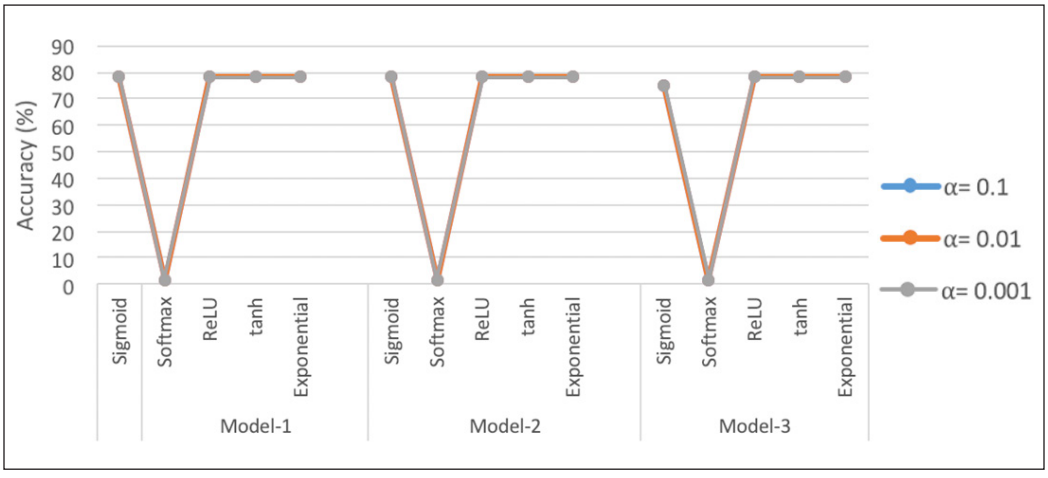

Figure 8. Accuracy result (AdaGrad)

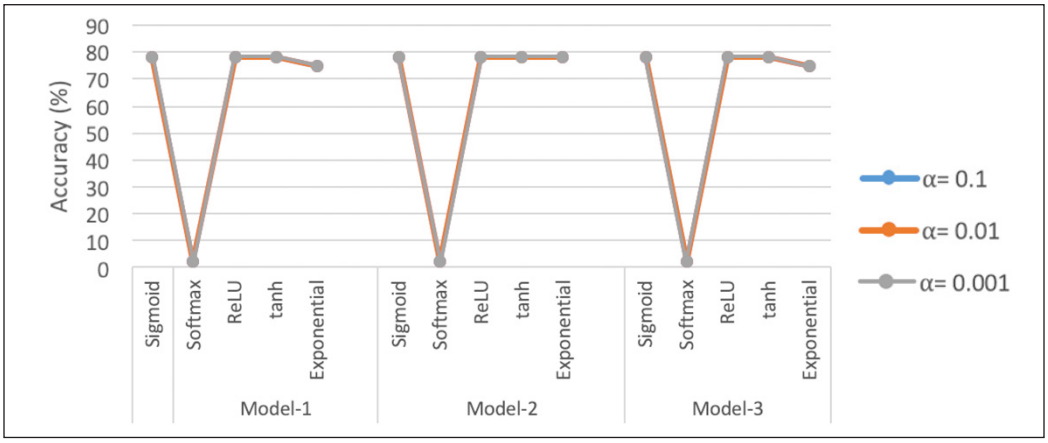

Figure 9. Accuracy result (AdaDelta)

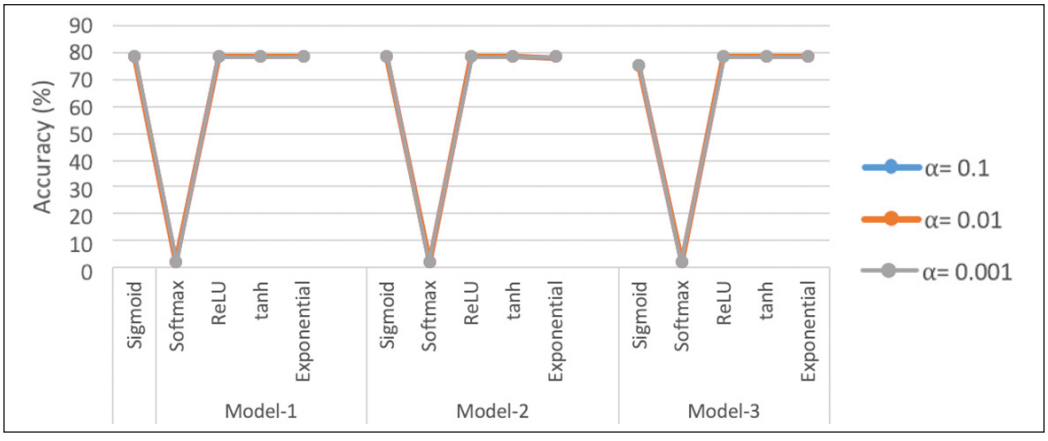

Figure10. Accuracy result (NADAM)

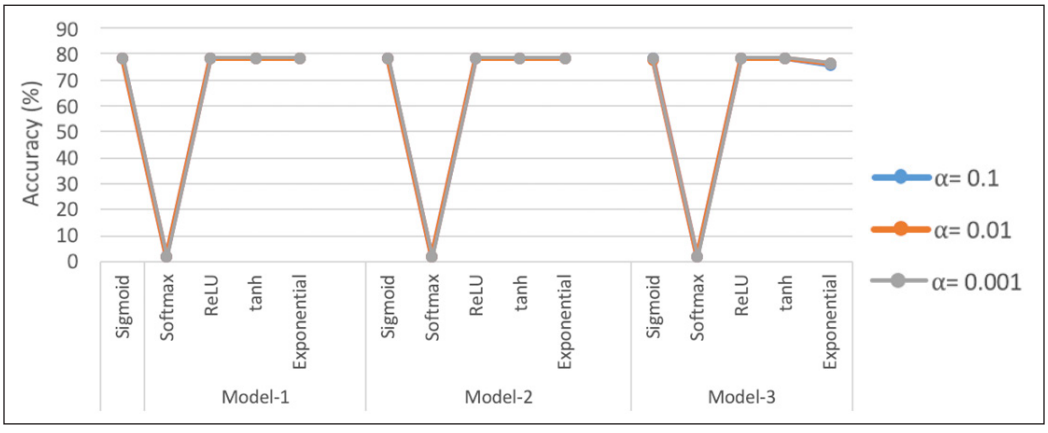

Figure 11. Accuracy result (AdaMax)

CONCLUSION

This study aims to compare the performance of seven widely used GD optimization algorithms on RNN architecture using body motion datasets from the UCI ML repository. The optimization techniques compared are ADAM, RMSprop, SGD, AdaGrad, AdaDelta, NADAM, and AdaMax. Precisely, the study is done across different combinations of optimizer models, LSTM architectures, activation functions, and learning rates. The results show that the AdaGrad model with both exponential and sigmoid activation functions and a learning rate of 0.001 has the best performance, with a training time of 17.1 minutes and a test accuracy of 78.31%, respectively.

Moreover, the study also highlights the importance of selecting the optimal optimization algorithm for RNN training given specific properties of the training data. The findings suggest that the exponential activation function consistently performs well across different models and optimizers in most cases, whereas the Softmax activation function consistently performs poorly in all cases. Finally, this study also contributes to the understanding of how different optimizers handle the challenge of determining the best and most suitable training parameters utilizing accuracy and training duration as performance metrics. The results provide valuable insights for researchers and practitioners in the field of DL and optimization.

ACKNOWLEDGMENTS

The author sincerely thanks Assoc. Prof. Ts. Dr. Khairul Najmy Rani and Assoc. Prof. Ts. Dr. Amiza Amir for all the insights and suggestions in realizing this paper.

REFERENCES

Adem, K., & Kiliçarslan, S. (2019). Performance analysis of optimization algorithms on stacked autoencoder. In *3rd International Symposium on Multidisciplinary Studies and Innovative Technologies* (pp. 1-4). IEEE. https://doi.org/10.1109/ISMSIT.2019.8932880

Alzubaidi, L., Zhang, J., Humaidi, A. J., Al-Dujaili, A., Duan, Y., Al-Shamma, O., Santamaría, J., Fadhel, M. A., Al-Amidie, M., & Farhan, L. (2021). Review of deep learning: Concepts, CNN architectures, challenges, applications, future directions. *Journal of Big Data*, *8*, 53. https://doi.org/10.1186/s40537-021-00444-8

Banos, O., Garcia, R., Holgado-Terriza, J. A., Damas, M., Pomares, H., Rojas, I., Saez, A., & Villalonga, C. (2014). mHealthDroid: A novel framework for agile development of mobile health applications. In L. Pecchia, L. L. Chen, C. Nugent, & J. Bravo (Eds.), *Ambient assisted living and daily activities* (pp. 91–98). Springer. https://doi.org/10.1007/978-3-319-13105-4_14

Chandra, K., Xie, A., Ragan-Kelley, J., & Meijer, E. (2022). Gradient descent: The ultimate optimizer. In *NIPS'22: Proceedings of the 36th International Conference on Neural Information Processing Systems* (pp. 8214-8225). Associaton for Computing Machinery.

Chen, W., Zheng, F., Gao, S., & Hu, K. (2022). An LSTM with differential structure and its application in action recognition. *Mathematical Problems in Engineering*, *2022*(1), 7316396. https://doi.org/https://doi.org/10.1155/2022/7316396

Dogo, E. M., Afolabi, O. J., Nwulu, N. I., Twala, B., & Aigbavboa, C. O. (2018). A comparative analysis of gradient descent-based optimization algorithms on convolutional neural networks. In *2018 International Conference on Computational Techniques, Electronics and Mechanical Systems* (pp. 92-99). IEEE. https://doi.org/10.1109/CTEMS.2018.8769211

Duchi, J., Hazan, E., & Singer, Y. (2011). Adaptive subgradient methods for online learning and stochastic optimization. *Journal of Machine Learning Research*, *12*, 2121-2159.

Ethem, A. (2020). *Introduction to machine learning* (4th ed.). The MIT Press.

Fatima, N. (2020). Enhancing performance of a deep neural network: A comparative analysis of optimization algorithms. *Advances in Distributed Computing and Artificial Intelligence Journal*, *9*(2), 79–90. https://doi.org/10.14201/adcaij2020927990

Goodfellow, I., Bengio, Y., & Courville, A. (2016). *Deep learning*. The MIT Press.

Haji, S. H., & Abdulazeez, A. M. (2021). Comparison of optimization techniques based on gradient descent algorithm: A review. *PalArch's Journal of Archaeology of Egypt / Egyptology*, *18*(4), 2715–2743.

Hallén, R. (2017). *A study of gradient-based algorithms*. http://lup.lub.lu.se/luur/download?func=downloadFile&recordOId=8904399&fileOId=8904400

Hinton, G., & Tieleman, T. (2012). Lecture 6.5 - Rmsprop: Divide the gradient by a running average of its recent magnitude. *Neural Networks for Machine Learning*, *4*, 26-31.

Hochreiter, S., & Schmidhuber, J. (1997). Long short-term memory. *Neural Computation*, *9*(8), 1735-1780. https://doi.org/10.1162/neco.1997.9.8.1735

Karna, V. V. R., Karna, V. R., Janamala, V., Devana, V. N. K. R., Ch, V. R. S., & Tummala, A. B. (2024). A comprehensive review on heart disease risk prediction using machine learning and deep learning algorithms. *Archives of Computational Methods in Engineering*, *32*, 1763-1795. https://doi.org/10.1007/s11831-024-10194-4

Kingma, D. P., & Ba, J. L. (2015). *ADAM: A method for stochastic optimization*. arXiv. https://doi.org/10.48550/arXiv.1412.6980

Lv, K., Jiang, S., & Li, J. (2017). *Learning gradient descent: Better generalization and longer horizons*. arXiv. https://doi.org/10.48550/arXiv.1703.03633

Mehmood, F., Ahmad, S., & Whangbo, T. K. (2023). An efficient optimization technique for training deep neural networks. *Mathematics*, *11*(6), 1360. https://doi.org/10.3390/math11061360

Miljanovic, M. (2012). Comparative analysis of recurrent and finite impulse response neural networks in time series prediction. *Indian Journal of Computer Science and Engineering*, *3*(1), 180–191.

Papamakarios, G. (2014). *Comparison of modern stochastic optimization algorithms*. University of Edinburgh.

Ruder, S. (2016). *An overview of gradient descent optimization algorithms*. arXiv. https://doi.org/10.48550/arXiv.1609.04747

Schaul, T., Antonoglou, I., & Silver, D. (2013). *Unit tests for stochastic optimization*. arXiv. https://doi.org/10.48550/arXiv.1312.6055

Seeli, D. J. J., & Thanammal, K. K. (2024). Quantitative analysis of gradient descent algorithm using scaling methods for improving the prediction process based on Artificial Neural Network. *Multimedia Tools and Applications*, *83*, 15677–15691. https://doi.org/10.1007/s11042-023-16136-9

Shalev-Shwartz, S., Shamir, O., & Shammah, S. (2017). *Failures of gradient-based deep learning*. arXiv. https://doi.org/10.48550/arXiv.1703.07950

Shen, K., Guo, J., Tan, X., Tang, S., Wang, R., & Bian, J. (2023). *A study on ReLU and Softmax in Transformer*. arXiv. https://doi.org/10.48550/arXiv.2302.06461

Sherstinsky, A. (2020). Fundamentals of Recurrent Neural Network (RNN) and Long Short-Term Memory (LSTM) network. *Physica D: Nonlinear Phenomena*, *404*, 132306. https://doi.org/10.1016/j.physd.2019.132306

Solanke, A. V., & Patnaik, G. K. (2020). Intrusion detection using deep learning approach with different optimization. *International Journal for Research in Applied Science and Engineering Technology*, *8*(5), 128–134. https://doi.org/10.22214/ijraset.2020.5022

Sun, R. (2019). *Optimization for deep learning: Theory and algorithms*. arXiv. https://doi.org/10.48550/arXiv.1912.08957

Sutskever, I., Martens, J., Dahl, G., & Hinton, G. (2013). On the importance of initialization and momentum in deep learning. *Proceedings of the 30th International Conference on Machine Learning*, *28*(3), 1139-1147.

Szandała, T. (2020). Review and comparison of commonly used activation functions for deep neural networks. In A. K. Bhoi, P. K. Mallick, C.-M. Liu, & V. E. Balas (Eds.), *Bio-inspired neurocomputinge* (Vol. 903, pp. 203-224). Springer. https://doi.org/10.1007/978-981-15-5495-7_11

Van Houdt, G., Mosquera, C., & Nápoles, G. (2020). A review on the long short-term memory model. *Artificial Intelligence Review*, *53*, 5929–5955. https://doi.org/10.1007/s10462-020-09838-1

Yazan, E., & Talu, M. F. (2017). *Comparison of the stochastic gradient descent based optimization techniques*. In *2017 International Artificial Intelligence and Data Processing Symposium (pp. 1-5). IEEE.* https://doi.org/10.1109/idap.2017.8090299

Yi, D., Ahn, J., & Ji, S. (2020). An effective optimization method for machine learning based on ADAM. *Applied Sciences*, *10*(3), 1073. https://doi.org/10.3390/app10031073

Zeiler, M. D. (2012). *ADADELTA: An adaptive learning rate method*. arXiv. https://doi.org/10.48550/arXiv.1212.5701

Zou, F., Shen, L., Jie, Z., Zhang, W., & Liu, W. (2019). A sufficient condition for convergences of ADAM and RMSProp. In *2019 Proceedings of the IEEE/CVF Conference on Computer Vision and Pattern Recognition* (pp. 11119–11127). IEEE. https://doi.org/10.1109/CVPR.2019.01138

Pertanika J. Sci. & Technol. 33 (4): 1971 - 2000 (2025)

PERTANIKA JOURNALS

SCIENCE & TECHNOLOGY

Journal homepage: http://www.pertanika.upm.edu.my/

Reduction of Transport Carbon Emissions of India by the Implementation of Strategies Based on IoT-Enabled Intelligent Transportation System: A System Dynamics Approach

Aditi Rajput* and Madhuri Jain

Department of Mathematics and Statistics, Banasthali Vidyapith, Rajasthan-304022, India

ABSTRACT

India is the third-largest carbon emitter in the world. In this paper, a Synergistic System Dynamics Simulation (SSDS) model is developed to reduce the Total Transport Carbon Emissions (TTCE) and Total Transport Energy Consumptions (TTEC) in million-plus cities of India by the implementation of strategies based on Internet of Things-enabled Intelligent Transportation System (IoT-ITS). Intelligent Transportation System (ITS) refers to the interconnection of an adaptive and intelligent integration of vehicles, drivers, and the transportation system. The SSDS model consists of four subsystems: total population, Gross Domestic Product (GDP), carbon emission, and four sub-models enabled IoT-ITS-based road transportation subsystem and provides the interrelation between parameters, which plays an important role in altering the TTCE and TTEC of the road transportation network. The model is validated, and a sensitivity test is used for the optimum management of the system. Six strategies based on IoT-enabled ITS: Traffic and transportation demand management (TTDM), Bus transport (BT), Rules and regulations management (RRM), Technology upgradation (TU), No implementation (No-IMP), and All integrated (AIN), are also formulated based on derived crucial parameters. The simulation of the model indicates that, despite the high cost of IoT-enabled ITS

ARTICLE INFO

Article history:
Received: 29 November 2024
Accepted: 08 April 2025
Published: 23 July 2025

DOI: https://doi.org/10.47836/pjst.33.4.14

E-mail addresses:
aditirajput0106@gmail.com; abrma20116_aditi@banasthali.in (Aditi Rajput)
madhurijain@banasthali.in (Madhuri Jain)

e-ISSN: 2231-8526

© Universiti Putra Malaysia Press

implementation, AIN is best suited, while RRM is the fastest for reducing TTCE. TTDM is highly useful in a short span, while TU gives a very high reduction of TTCE.

Keywords: Internet of Things, Intelligent Transportation System, strategies analysis, system dynamics, Total Transport Carbon Emissions, Total Transport Energy Consumptions

INTRODUCTION

India is the third highest emitter of carbon dioxide (CO_2) in the world (Timperley, 2019), with annual emissions totaling 3.6 gigatons and a trajectory that could reach 7.3 gigatons per year by 2050 (Hossain et al., 2023) and has a vision to reduce CO_2 emissions from industries, waste, forest, energy sector, and transportation sector by the end of 2030 (Welle, 2020). India also announced a carbon neutrality commitment by 2070 at the 26th Conference of the Parties (COP26) (World Economic Forum, 2021). In order to fulfil such an ambitious climate target, stricter policies and longer-term decarbonization strategies are needed for carbon-intensive transportation sector. Road transportation is main culprit for the major global transportation pollution due to high vehicular carbon emissions and is the main driving force for the economic development and creation of the well beings of the modern societies. The Indian road traffic and transportation system, which is governed by different modes of mobility- public transport, tempo and auto-rickshaws, taxis and jeeps, motorcycles-scooters-scooty, cars, and bicycles, is a critical life support system of our major population but is a substantial CO_2 emitter source. The dominance of internal combustion engines based four and two wheelers is leading to surge in CO_2 emissions. Due to change in buying habits and high living standard of majority of Indians living in million plus cities of India, the CO_2 emissions of road transportation sector will reach to danger level very soon and every Indian transportation system expert and decision maker will be responsible for this.

The road transportation sector of India accounts for approximately 56% of our country's transportation system emissions (O'Rourke et al., 2021). The decarbonation of transportation system to achieve net zero emissions will play a negative effect on roads. Roads are the backbone for the survival of society. Hence the main goal shift is now to develop a different line of action for the utilization of roads to strengthen the mobility as well as to achieve net zero emissions. Thus, this research work is an innovative step in this direction to implement strategies based on IoT-enabled ITS for Indian road traffic and transportation system.

ITS can easily create this opportunity by revolutionizing the Indian road network, reducing traffic congestion and emissions of greenhouse gases, making smooth flow of traffic, encouraging green safer mobility, and finally zooming to main goal of achieving net zero emissions. ITS is a holistic system using synergistic approach of people, processes,

places, data, technology, and vehicles and will lead to regular carbon reduction role in the Indian transportation system. ITS is a technological platform that offers hi-tech systems to meet future demands of transportation decision makers, traffic policy makers, and commuters, attains other technology outcomes based on different applications that monitor, manage, and improve the quality and efficiency of transportation system.

The IoT is the network of interconnected web based smart devices which uses embedded technology (smart sensors, processors, actuators, software, communication hardware), connectivity technologies (LoRaWan, Zigbee, message queuing telemetry transport [MQTT], cellular, wi-fi, bluetooth), data processing, data security, big data analytics, security and privacy technologies, cameras, and network that enable them to collect, exchange and act on data. The goal of IoT is to create a smart, connected world where devices can communicate and interact with each other to make intelligent decisions and improve efficiency.

System dynamics (SD) modelling technique is an innovative interdisciplinary effective research tool based on feedback of system information to study the dynamic systems and to solve real world very complex social and technical system integrated problems. SD cross fertilizes three background threads, the elements of traditional management, feedback control theory, and the technique of computer simulation, which allows one to determine the time varying behavior implicit in the complex structure of a system. SD focuses on dynamic approach and generates scenarios for real world problems by employing synergistic approach of qualitative and quantitative technique and integrated system reasoning.

In this paper, a SSDS model is designed and developed to reduce the TTCE and TTEC of the road transportation system in Million-plus Cities of India (MCI) by the implementation of strategies based on IoT-ITS. The model generates six critical strategies based on IoT-ITS and policy implementation recommendations on the basis of model simulation, validation, and sensitivity analysis and also delivers a wide range of additional paybacks. The work's architecture is depicted in Figure 1. The contribution of the proposed work is to offer a synergistic SD-based framework, which can study key influencing sub-systems, sub-models, and predict the impact of implementations of critical strategies based on IoT-ITS to reduce the TTCE and TTEC in MCI. The implementation of strategies based on IoT-ITS in Indian road traffic and transportation system, transport infrastructure as well as in green transport solutions like electrification of road traffic and transportation system including e-vehicles and e-public transport buses will definitely reduce TTCE and TTEC by approximately 33-35% upto 2030 and 70-75% upto 2050 and this road map of aggressive and high ambition implementation of strategies based on IoT-ITS finally zoom to main goal of achieving net zero emissions. The model guides the future low carbon transition and serves as an open platform which can be easily adjusted according to the requirements of transportation system decision makers and can be easily applied to any part of world.

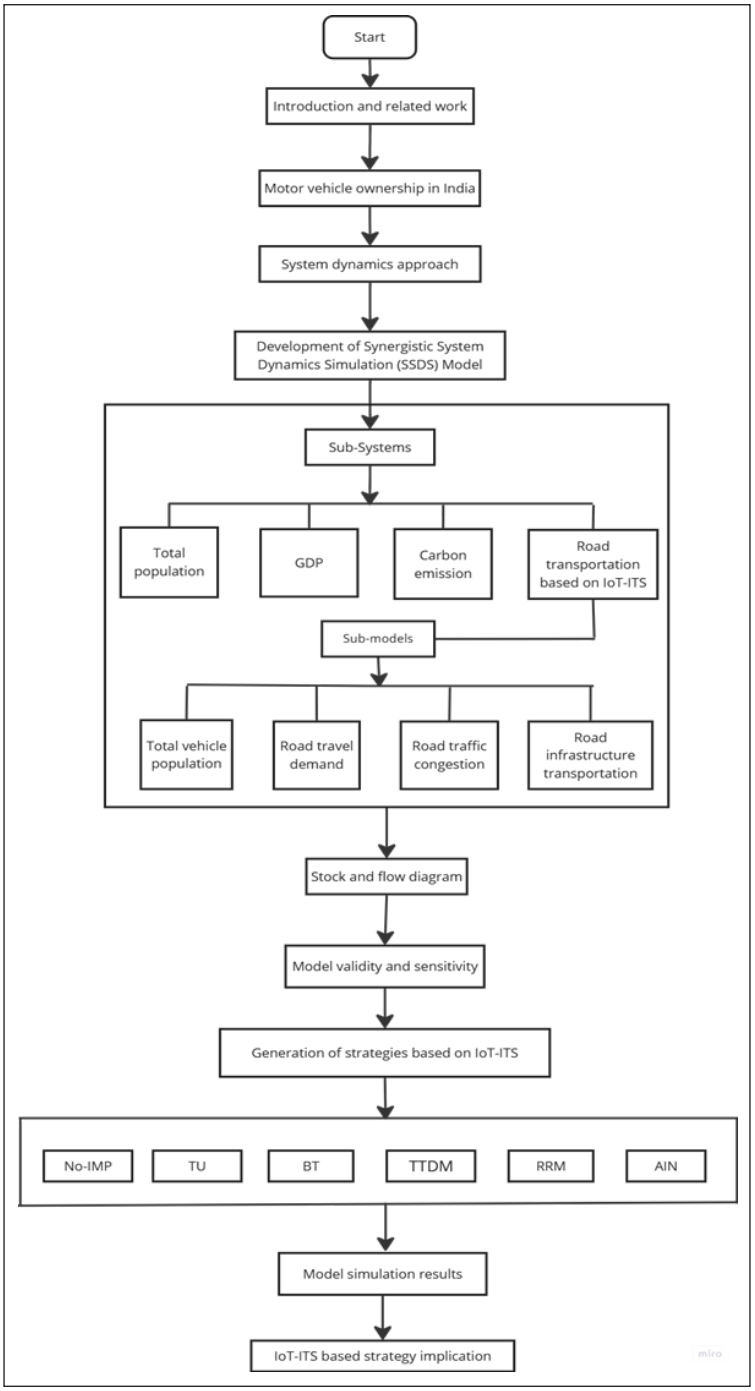

Figure 1. Work's architecture

Note. GDP = Gross Domestic Product; IoT-ITS = Internet of Things-enabled Intelligent Transportation System; No-IMP = No implementation; TU = Technology upgradation; BT = Bus transport; TTDM = Traffic and transportation demand management; RRM = Rules and regulations management; AIN = All integrated

RELATED WORK

Dong and Ullah (2023) provided empirical evidence for the positive effect of IoT, environmental regulations, and related factors on green growth. Bautista and Mester (2023) discussed the impact of IoT on the development of self-driving cars to focus on the broader implications for the development of intelligent cities. Upadhyay et al. (2024) proposed a comprehensive multi-layered framework for V-IoT systems, addressing challenges related to security, scalability, and efficient communication. Al-Mayouf et al. (2018) developed an accident management system that utilized vehicular ad hoc networks in conjunction with cellular technology for public transport. Mahdi et al. (2024) developed an IoT emergency services system based on a real-time node rank index algorithm to determine the optimal route with the dynamic traffic conditions for ambulance to reach the patient quickly and deliver necessary medical services during emergencies. Mahdi et al. (2021) proposed an innovative strategy void-hole aware and reliable data forwarding strategy. This strategy was used to help each cluster head node to know its neighbor's performance ranking index to conduct a reliable packet transmission to the sink via the most energy-efficient route.

Iliopoulou and Kepaptsoglou (2019) discussed the potential of using ITS data to optimize public transportation planning and operations. Gao et al. (2022) proposed an ITS-based vehicle consensus scheme for management of traffic and selection of infrastructure for users. Dasgupta et al. (2022) proposed a fusion model to detect pedestrian in dim light driving during night hours. Alkinani et al. (2022) developed a neural network-based model to make intelligent decisions for public transportation. Ramesh et al. (2022) developed a model to enhance safety on road and to reduce accidents due to traffic jams. Lin et al. (2019) developed measurement and evaluation models for ITS products to provide technological means. Yuan et al. (2022) discussed about machine learning for next generation of ITS.

Chen et al. (2022) developed a system dynamics model for urban pollution to evaluate the impact of various policies and benefits of synergistic approach for addressing environmental problems and traffic congestion. Gupta et al. (2019) used a system dynamics approach to measure the effectiveness of carbon tax on Indian road passenger transport. Wang et al. (2021) developed a system dynamics model to capture feedback processes and to interact between different sectors and various population, water quality, and resources factors. Shahsavari-Pour et al. (2022) developed a simulated model using system dynamics technique to analyze the pollution level taking into consideration its sources and outcomes. Norouzian-Maleki et al. (2022) presented a new framework as a combination of system dynamics approach and data envelopment analysis technique. Nunes et al. (2021) developed a system dynamics approach-based smart city using modern technologies. Ding et al. (2022) developed a perimeter control method for a congested urban road network with dynamic and variable ranges.

It is very interesting to note that very limited literature is available on the reduction of the carbon emissions and energy consumptions of Indian road transportation system using SD modelling technique but the literature related to development of SD simulation model to reduce the total transport carbon emissions and total transport energy consumptions of the road transportation system in million plus cities of India by the implementation of six strategies based on IoT-ITS simultaneously are almost negligible. Therefore, to fill this vast research gap in Indian literature, an innovative first-time effort is being made in this research work.

MOTOR VEHICLE OWNERSHIP IN INDIA

The Indian road transportation system is home to a dynamic blend of everything from luxury petrol cars, sport utility vehicles (SUVs), electric vehicles (EVs), diesel taxis, to the humble two-wheelers, e-bikes, e-autos, and bicycles. There is tremendous change in motor vehicle ownership in India as the auto industry is transitioning from vehicle manufacturing to providing mobility solutions. The advanced technologies—electrification, vehicle intelligence, autonomous driving, and connected features are gaining traction at a very fast pace. The adoption of environment-friendly vehicles is slated to make significant strides. The motor vehicle ownership is gearing up to foray into the battery EVs segment and EVs will be at the sweet spot and forefront of the journey towards sustainable mobility, but its penetration in the freight sector is not gaining traction in India. Table 1 shows the number of EVs from 2019 to 2023 having all types of e-vehicles (AutoInsurance.com, 2025). There is no EV data from 2011 to 2018. The passenger vehicles segment of auto industry is observing louder calls for backing other advanced technologies—biofuels, biogas, strong hybrids besides compressed natural gas (CNG). Table 2 shows the number of traditional internal combustion engine vehicles from 2011 to 2019.

Table 1
Number of electric vehicles (EVs)

Year	EVs
2019	687
2020	3,143
2021	12,050
2022	48,023
2023	82,270

Table 2
Number of traditional internal combustion engine vehicles

Year	Two wheelers (thousand)	Cars, jeeps and taxis (thousand)	Buses (thousand)	Goods vehicles (thousand)
2011	101,865	19,231	1,604	7,064
2012	115,419	21,568	1,677	7,658
2013	127,830	24,056	1,814	8,307
2014	139,410	25,998	1,887	8,698

Table 2 *(continue)*

Year	Two wheelers (thousand)	Cars, jeeps and taxis (thousand)	Buses (thousand)	Goods vehicles (thousand)
2015	154,298	28,611	1,971	9,344
2016	168,975	30,242	1,757	10,516
2017	187,091	33,688	1,864	12,256
2018	202,755	36,453	1,943	12,773
2019	221,270	38,433	2,049	13,766

Source: Ministry of Road Transport and Highways (MoRTH) (2023)

ITS are revolutionizing India's road transportation landscape by integrating advanced ITS technologies to enhance road traffic management, public transit, transportation efficiency, road safety and sustainability. Here is a brief look at the following key ITS technologies being implemented across the country:

Advanced Public Transport Systems (APTS)

Implementation. Indian cities are adopting Global Positioning System (GPS)-based bus tracking, electronic ticketing, and real-time passenger information systems to improve public transportation efficiency.

Examples:

1. Bengaluru Metropolitan Transport Corporation (BMTC): Launched the "Namma BMTC" app, offering real-time bus tracking, route planning, and fare calculation. The app also includes a Save Our Soul (SOS) feature for emergencies.
2. Delhi Integrated Multi-Modal Transit System (DIMTS): Operates the "My Bus" app, providing real-time bus tracking and electronic ticketing.

Advanced Traveller Information Systems (ATIS)

Implementation. Deployment of digital signage, mobile applications, and websites to deliver real-time traffic updates, public transport schedules, and route optimization information.

Examples:

1. Delhi traffic police app: Offers live traffic updates, route planning, and alerts on road closures.
2. Google Maps and other navigation services: Integrated with real-time traffic data to assist commuters in route planning.

Automated Vehicle Control Systems (AVCS)

Implementation. Utilization of AI-driven traffic signal automation, automatic number plate recognition (ANPR), and red-light violation detection to enhance traffic flow and safety.

Examples:

1. AI-based traffic management: Cities like Mumbai, Bengaluru, and Hyderabad have implemented AI-driven traffic management systems to optimize signal timings and reduce congestion.
2. Automatic speed enforcement: Installation of speed cameras on highways to monitor and enforce speed limits.

Electric Vehicle Systems (EVS)

Implementation. Government initiatives such as the Faster Adoption and Manufacturing of (Hybrid) and Electric Vehicles (FAME) India scheme promote EV adoption through incentives and infrastructure development.

Examples:

1. Ola Electric and Tata EVs: Companies like Ola Electric and Tata Motors are expanding the EV market with a wide range of electric vehicles.
2. Charging Infrastructure: Installation of charging stations by entities like Energy Efficiency Services Limited (EESL) and Tata Power across major cities.

There are some major challenges like infrastructure constraints, public awareness, 5th Generation (5G) integration, use of AI and machine learning, expansion of tier-2 and tier-3 cities, and financial limitations in implementing ITS in India. While challenges remain, ongoing efforts and future technological advancements hold promise for a more intelligent and connected transportation ecosystem. ITS offers great opportunity to revolutionize Indian road network system by using transformative approach and can easily provide a better solution to the problems of traffic congestion and total carbon emissions caused by the rapid increase in the motor vehicle ownership/number of vehicles and paves the way for greener mobility, leading to attainment of global net zero ambitions. Table 3 shows the trend for total carbon emissions from the transport sector from 2011 to 2023 (Statista, 2025).

Table 3
Trend for total carbon emissions from transportation sector from 2011 to 2023

Year	Total carbon emissions from transportation sector (million metric tons)
2011	209
2012	222
2013	226

Table 3 *(continue)*

Year	Total carbon emissions from transportation sector (million metric tons)
2014	236
2015	258
2016	269
2017	291
2018	306
2019	308
2020	269
2021	295
2022	324
2023	340

Note. Source = Statista (2025)

MATERIALS AND METHODS

SSDS Model

SSDS model is developed to reduce the total transport carbon emissions and total transport energy consumptions of the road traffic and transportation system in MCI by the implementation of strategies based on IoT-ITS. The model also generates six critical strategies based on IoT-ITS and policy implementation recommendations on the basis of validation and sensitivity analysis to reduce the TTCE and TTEC, and also delivers a wide range of additional paybacks. Figure 2 shows the flowchart of the SSDS model. In this model, the relationship of critical variables affecting the TTCE and TTEC of the road traffic and transportation system in MCI is depicted in the designed and developed SSDS model.

The structure of the model is based on four main sub systems: GDP Sub-System (GDP-SS), Total Population Sub-System (ToPoP-SS), Carbon Emission Sub-System (CaEm-SS) and Road Transportation Sub-System (RoTr-SS) based on IoT-ITS. RoTr-SS based on IoT-ITS consists of four sub-models: total vehicle population sub-model, road travel demand sub-model, road traffic congestion sub-model, and road transportation infrastructure sub-model and all these four sub-models of RoTr-SS are totally linked with GDP-SS, ToPoP-SS, and CaEm-SS. The relation between four sub systems: GDP-SS, ToPoP-SS, CaEm-SS, and four sub-models based RoTr-SS of SSDS model are shown in Figure 3. Figure 4 depicts stock flow diagram of SSDS model.

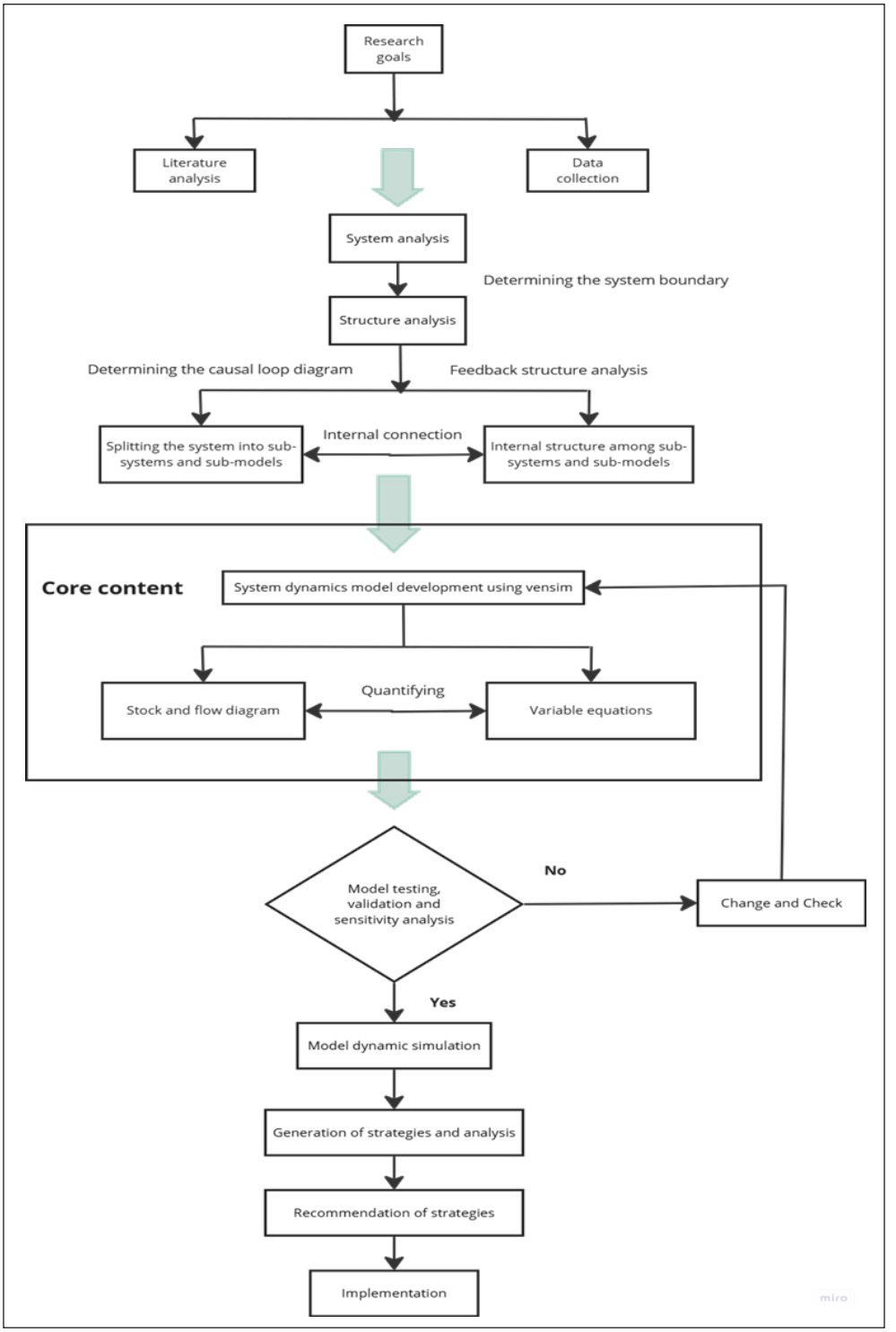

Figure 2. Flow chart of the Synergistic System Dynamics Simulation (SSDS) model

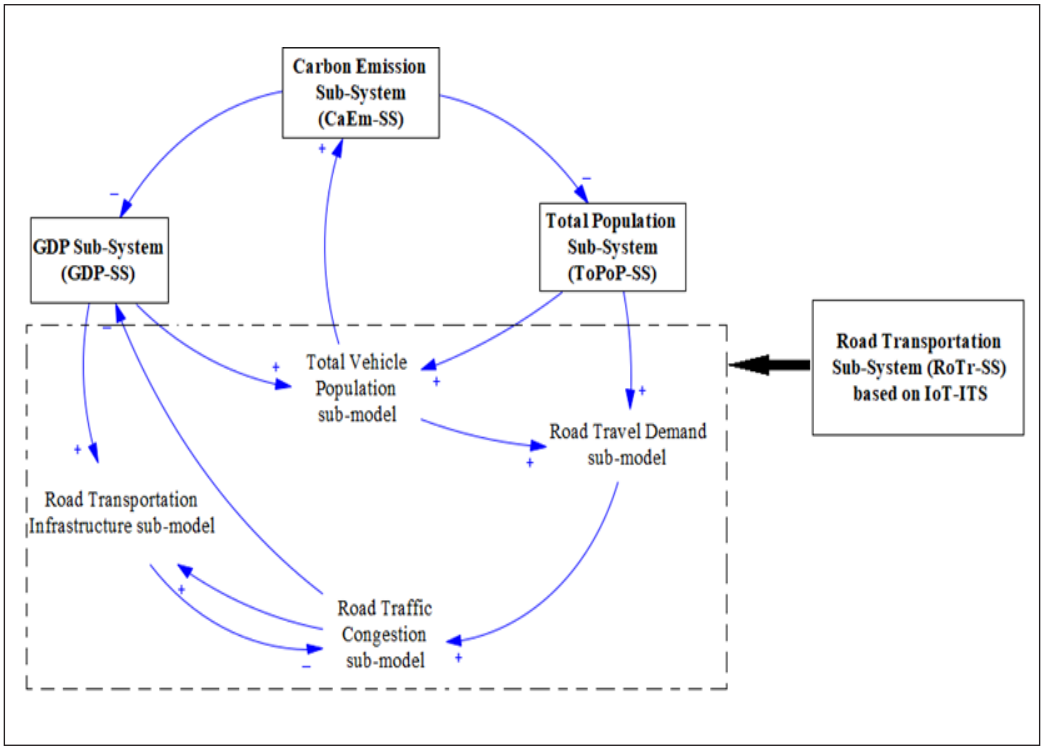

Figure 3. Relation between sub-systems of the Synergistic System Dynamics Simulation (SSDS) model
Note. GDP-SS = GDP Sub-System; CaEm-SS = Carbon Emission Sub-System; ToPoP-SS = Total Population Sub-System; RoTr-SS = Road Transportation Sub-System; IoT-ITS = Internet of Things-enabled Intelligent Transportation System

ToPoP-SS

The road transportation sector of MCI is mainly affected by the structural pattern and magnitude of the total population. Due to expansion in cities of India, the total floating population phenomenon plays an important role in the total population and is slightly different from the other natural displacements of the total population. This population is basically a group of people who reside in the border area of the cities but study or work in a different place, thus affecting both the origin cities as well as destination cities, and is one of the major problems in the road transportation system of MCI. The rise in this total floating population is bound to drastically affect the road transportation system of these cities. The total floating population is treated like an incremental parameter of the GDP/capita and its effect on the total floating population is evaluated. The stock variable total local population and the stock variable total floating population will synergistically affect the total population of the cities.

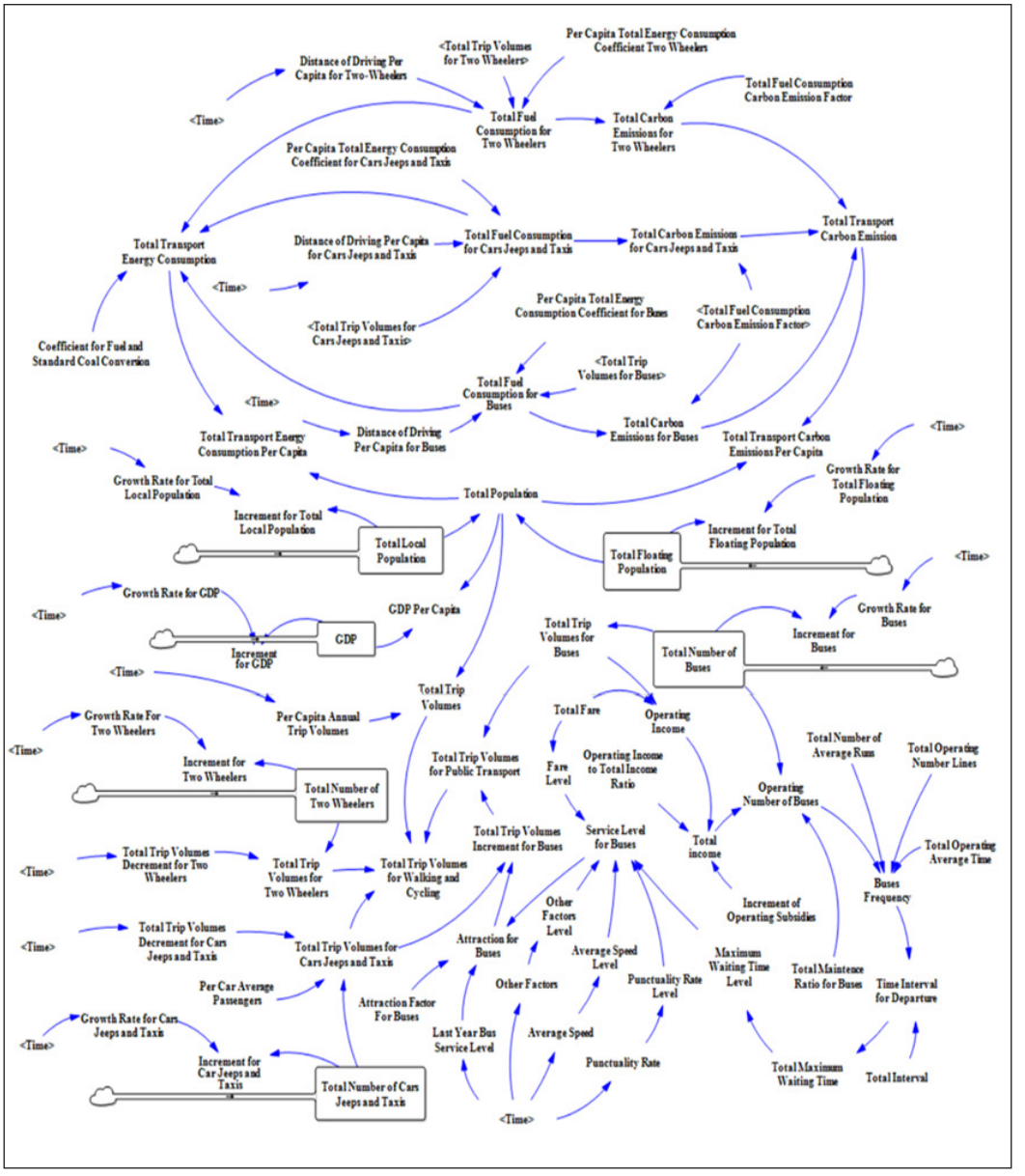

Figure 4. Stock flow diagram of the Synergistic System Dynamics Simulation (SSDS) model

GDP-SS

Due to rise in GDP/capita, the total population of MCI can easily afford to buy motorized vehicles like cars, scooters, and motor bikes, for driving or movement purpose and this will result in shift from non-motorized modes to motorized transport modes. Thus, there is one to one relation between the growth of GDP/capita and the road transportation system of MCI.

RoTr-SS Based on IoT-ITS

The RoTr-SS based on IoT-ITS consists of four sub-models: total vehicle population sub-model, road travel demand sub-model, road traffic congestion sub-model, and road transportation infrastructure sub-model. The residents of MCI are changing their mode of road transportation due to their high living standard from non-motorized to motorized and using two wheelers, cars, taxies, jeeps, and public transport. The segment rate of cycling and walking is decreasing continuously, and segment rate of motorization is rising with a tremendous pace. The segment rate of cars, jeeps and taxies is continuously increasing at a very fast pace and plays an important role in the road traffic congestion, accidents, and rise in TTCE and TTEC. Due to improvement of punctuality, travel time and comfort, reduction in waiting time and cheaper mode of transportation in comparison to cars, jeeps and taxies, the majority of commuters are slowly switching over and using the bus transportation system in Indian cities. The important parameters like quantity of vehicles - two wheelers, cars, taxies, jeeps, and buses; vehicles mileage driven, and vehicles energy efficiency are directly affecting the TTEC. The fuel consumption is increasing with a fast pace inspite of price rise and the demand of private jeeps and cars is also continuously growing due to rise in people living standards and growth in economy. The promotion of the usage of IoT-ITS based new energy efficient vehicles and development of IoT-ITS based green bus transport are very strong measures for reduction of TTCE.

CaEm-SS

Reduction of TTEC and TTCE of road traffic and transportation system in MCI is the major goal of SSDS model. Table 4 depicts the notations for equations. The TTEC and TTCE can be calculated from the following equations:

$$\mathrm{TTEC_{m,n}} = \mathrm{TTECC_{m,n}} \times \mathrm{DD_m} \times \mathrm{TV_m} \quad [1]$$

$$\mathrm{TTCE_{m,n}} = \mathrm{TTECC_{m,n}} \times \mathrm{DD_m} \times \mathrm{TV_m} \times \mathrm{Ef_n} \quad [2]$$

$$\mathrm{TTEC} = \sum_{m,n} \mathrm{TTECC_{m,n}} \times \mathrm{DD_m} \times \mathrm{TV_m} \times \mathrm{ECC_n} \quad [3]$$

$$\mathrm{PCTEC} = \frac{\sum_{m,n} \mathrm{TTECC_{m,n}} \times \mathrm{DD_m} \times \mathrm{TV_m} \times \mathrm{ECC_n}}{\mathrm{TP}} \quad [4]$$

$$\mathrm{TTCE} = \sum_{m,n} \mathrm{TTECC_{m,n}} \times \mathrm{DD_m} \times \mathrm{TV_m} \times \mathrm{Ef_n} \quad [5]$$

$$\mathrm{PCTCE} = \frac{\sum_{m,n} \mathrm{TTECC_{m,n}} \times \mathrm{DD_m} \times \mathrm{TV_m} \times \mathrm{Ef_n}}{\mathrm{TP}} \quad [6]$$

Table 4
Table of notations

Notations	Description
$TTCE$	Total Transport Carbon Emissions
$TTEC$	Total Transport Energy Consumption
$TTEC_{m,n}$	Total Transport Energy Consumption due to particular modes of transport *m* for different types of total transport energy consumption *n*
$TTECC_{m,n}$	Total Transport Energy Consumption Coefficient per Capita
DD_m	Distance of Driving per capita for particular modes of transport *m*
TV_m	Trip Volumes per year for particular modes of transport *m*
$TTCE_{m,n}$	Total Transport Carbon Emissions due to particular modes of transport *m* for different types of total transport energy consumption *n*
Ef_n	Emission factor from total transport energy consumption *n*
ECC_n	Energy Conservation Coefficient from energy type n
$PCTEC$	Per Capita Transport Energy Consumption
TP	Total Population
$PCTCE$	Per Capita Transport Carbon Emission

SSDS Model Validity and Sensitivity

The parameters of SSDS model are continuously modified and adjusted during the course of development of interrelation between different parameters to reduce the error between actual historical and simulated data, and ultimately to improve the reliability of the model. Table 5 presents the historical data and simulated data for key parameters from 2011 to 2019.

The error rate (ER), error variance (EV), mean absolute percentage error (MAPE), and root mean square percentage error (RMSPE) of the key parameters are calculated using the following equations, respectively:

$$ER = \frac{|\text{Simulated Value} - \text{Absolute Value}|}{\text{Absolute Value}} \times 100\% \quad [7]$$

$$EV = \frac{|\text{Average Rate of Simulated Value} - \text{Average Rate of Absolute Value}|}{\text{Average Rate of Absolute Value}} \times 100\% \quad [8]$$

$$MAPE = \frac{1}{n}\sum_{i=1}^{n}\left|\frac{\text{Simulated Value} - \text{Absolute Value}}{\text{Absolute Value}}\right| \times 100\% \quad [9]$$

$$RMSPE = \sqrt{\frac{1}{n}\sum_{i=1}^{n}\left|\frac{\text{Simulated Value} - \text{Absolute Value}}{\text{Absolute Value}}\right|^2} \times 100\% \quad [10]$$

Table 5
Comparison between historical data and simulated data of key parameters

Year	Total population			GDP			Total number of two wheelers			Total number of cars jeeps and taxis			Total number of buses		
	Simulated data	Historical data	Error %	Simulated data	Historical data	Error %	Simulated data	Historical data	Error %	Simulated data	Historical data	Error %	Simulated data	Historical data	Error %
2011	1.25	1.25	0.00	8,736,330	8,736,329	0.00	101,865	101,865	0.00	19,231	19,231	0.00	1,604	1,604	0.00
2012	1.28	1.27	0.01	9,190,620	9,213,017	0.00	113,274	115,419	0.02	21,616.2	21,568	0.00	1,684.89	1,677	0.00
2013	1.31	1.28	0.02	9,686,910	9,801,370	0.01	128,340	127,830	0.00	24,243.1	24,056	0.01	1,761.62	1,814	0.03
2014	1.33	1.32	0.01	10,297,200	10,527,675	0.02	142,072	139,410	0.02	27,039.6	25,998	0.04	1,905.61	1,887	0.01
2015	1.36	1.35	0.01	11,059,200	11,369,493	0.03	154,859	154,298	0.00	29,222.3	28,611	0.02	1,982.33	1,971	0.01
2016	1.39	1.37	0.01	11,932,900	12,308,193	0.03	171,274	168,975	0.01	32,159.3	30,242	0.06	1,737.61	1,757	0.01
2017	1.41	1.43	0.01	12,911,400	13,144,582	0.02	187,545	187,091	0.00	33,992.4	33,688	0.01	1,845.69	1,864	0.01
2018	1.44	1.45	0.01	13,776,400	14,003,316	0.02	207,612	202,755	0.02	37,864.3	36,453	0.04	1,958.15	1,943	0.01
2019	1.46	1.47	0.00	14,671,900	14,569,268	0.01	224,844	221,270	0.02	40,971.9	38,433	0.07	2,041.18	2,049	0.00

Note. GDP = Gross Domestic Product

Table 6 depicts the values of ER, EV, MAPE, and RMSPE for total population; GDP; total number of two wheelers; total number of cars, jeeps and taxis; and total number of buses, respectively.

Table 6
Values of ER, EV, MAPE, and RMSPE in percentage

	ER	**EV**	**MAPE**	**RMSE**
Total population	0.4266	10.3593	0.4635	1.0767
GDP	1.3604	0.8505	1.3409	1.8021
Total number of two wheelers	0.9001	3.9265	0.7141	1.4003
Total number of cars, jeeps and taxis	3.1206	10.6186	2.7628	3.6653
Total number of buses	0.2711	3.3509	0.2826	1.1925

Note. ER = Error rate; EV = Error variance; MAPE = Mean Absolute Percentage Error; RMSPE = Root Mean Square Percentage Error

The developed SSDS model is totally effective, valid, and generating reliable simulated results because the values of ER and EV of key parameters are less than or equal to 5% and 30% respectively, while MAPE and RMSPE are also very close to zero which clearly shows that error is very low and SSDS model's prediction ability is best. Using 2011 as the base year, the historical data from 2011 to 2019 (Economic Survey, n.d.; MoRTH, 2023; Office of the Registrar General and Census Commissioner, India & Ministry of Home Affairs, Government of India, n.d.) are utilized to verify the validity of the model. The key parameters fully satisfy the validity for future projections, and Figures 5(a) to 5(e) depict the comparison graph between simulated data and actual data of key parameters.

The sensitivity test of developed SSDS model was also conducted to examine how much sensitive the model is due to alterations in the different values of the selected parameters and due to changes in the basic structure of the developed SSDS model. The results of the sensitivity analysis showed that the total population and per capita annual trip volumes had larger impact on total trip volumes. The total trip volume, per capita total energy consumption coefficient, and distance of driving per capita for cars jeeps and taxis had major impact while total trip volume and per capita total energy consumption coefficient for buses had minor impact on TTCE and TTEC. This clearly proved that the developed SSDS model is totally under control and is totally fit for simulation to generate strategies based on IoT-ITS.

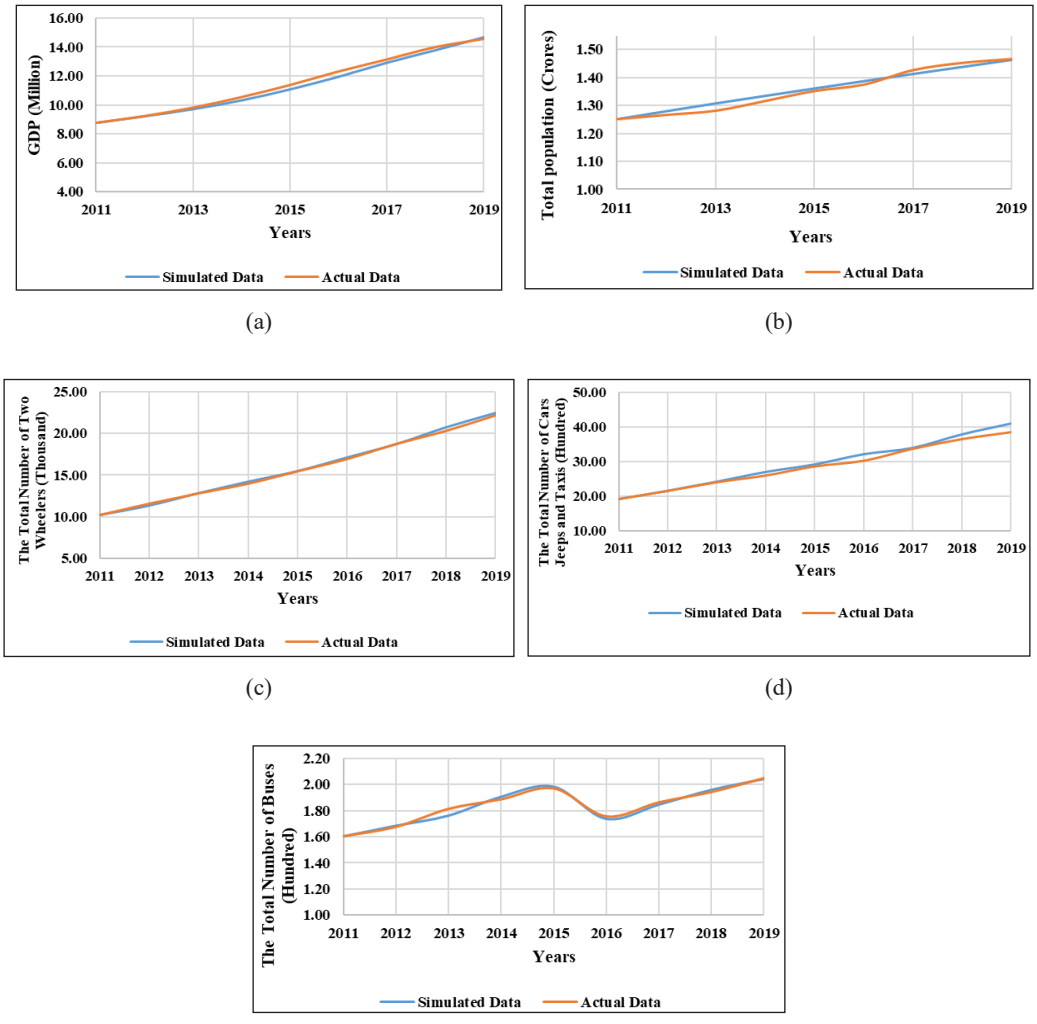

Figure 5. Comparison graph between simulated and actual data of (a) gross domestic product (GDP), (b) total population, (c) total number of two wheelers, (d) total number of cars jeeps and taxis, and (e) total number of buses, respectively

Generation of Strategies Based on IoT-Enabled ITS

The ITS uses integration of information technologies- cloud computing, mobile internet, IoT and big data technology with communication technologies, and by effectively utilizing the present transportation infrastructure can drastically reduce TTCE and TTEC, road accidents, traffic congestions, and improve traffic and transportation services. Thus, ITS reinforces the synergistic relation between environment, vehicles, roads and the commuters, and its demand is increasing day by day and is a future market.

APTS, ATIS, Advanced Traffic Management Systems (ATMS), AVCS, Emergency Vehicle Services (EVS), and Commercial Vehicle Operations (CVO) are major functional areas of ITS. APTS increases the efficiency of public transportation network and APTS solutions include smart bus core (networking devices on the bus), smart bus camera (help passenger counting and analysis), driver status monitoring, blind spot detection, ultrasonic sensors and smart card integrated circuit scanners while ATIS is the most extensively used ITS application area that provides real time information to the travelers to enhance their mobility.

ATMS is another ITS application platform that covers monitoring, controlling and safety on roads and highways. ATMS solutions include signal optimization and innovative ramp metering, real time traffic information, incident detection and rapid accident response, signalized arterial networks, highway advisory radio, adaptive signal control, real time decision support. In contrast, advanced vehicle control systems solution include longitudinal assistance systems preventing rear-end and front-end collisions, dedicated short range communication radios to enable vehicle-to-vehicle, vehicle-to-infrastructure, and infrastructure-to-vehicle to improve safety. Emergency vehicle services solutions include drones and unmanned aerial vehicles, green wave system, visual roadside units, and emergency vehicle lighting and sirens, while commercial vehicle operations application area of ITS deals in regulating and transporting freight in commercial vehicles and includes fleet administration, freight administration, electronic clearance, and commercial vehicle administrative processes.

A total of six strategies based on IoT-ITS: TTDM strategy, BT strategy, RRM strategy, TU strategy, No-IMP strategy and AIN strategy, are formulated and generated to monitor TTCE and TTEC, in MCI using the output of sensitivity test of the key parameters of SSDS model. The developed robust SSDS model is simulated for generated strategies based on IoT-ITS to reduce TTCE and TTEC. The outcome pattern of TTCE and TTEC is analyzed and simulated from 2011-2020 (pre COVID-19 period), during COVID-19 period, and post COVID-19 time period from 2022 to 2030 to observe the effect of generated strategies based on IoT-ITS.

No-IMP Strategy Based on IoT-ITS

In No-IMP strategy, there is no change in TTCE and TTEC pattern in MCI because it follows the current national developmental trend. Also, there is no implementation of IoT-ITS, as well as no addition of any new policy to the four main sub-systems and four sub-models of RoTr-SS. Thus, TTCE and TTEC will continuously increase in the near future and reach a new height.

BT Strategy Based on IoT-ITS

The basic aim of BT strategy is to provide the intelligent and innovative services to enhance the mobility, safety, efficiency, and environment of public bus transport of MCI. BT strategy cannot cover all the dense points of cities, but can only cover all the major and important locations. It will definitely play an attention mode to reduce the TTCE and TTEC. The share of public bus transport equipped with IoT-ITS must increase by 60% while a serious effort should be made to reduce the personal motorized four and two wheelers to reduce TTCE.

TTDM Strategy Based on IoT-ITS

The TTDM strategy aims to establish IoT-ITS-based guidelines for managing road traffic and transportation in MCI to reduce total traffic congestion and emissions. It includes implementing IoT-ITS rules to control vehicle population growth, balancing infrastructure between cities and smaller towns, and supporting scrappage policies for outdated vehicles to achieve net-zero emissions. Additionally, IoT-ITS vehicle fitness testing and automated testing stations are recommended for all vehicles. Policies like an odd-even traffic rule and congestion fees at peak hours would help manage congestion and emissions by tracking vehicle numbers and encouraging eco-friendly vehicle use.

TU Strategy Based on IoT-ITS

The role of TU strategy in MCI will play a very important role in reducing TTCE and TTEC by eliminating the use of very high pollution generation vehicles, and very old two and four wheelers, and introducing IoT-ITS-based hi-tech vehicles. The health of children and adults are slowly coming in danger zone in MCI due to very heavy polluted traffic and transport environment. The only solution to prevent the escalating environmental pollution is the introduction of IoT-ITS-based hi-tech e-vehicles. Road transportation is mainly governed by diesel and petrol-based vehicles. The introduction of IoT-ITS-based hi-tech e-vehicles will improve the quality, efficiency, performance and reduce the fuel consumptions and carbon emissions.

RRM Strategy Based on IoT-ITS

The RRM strategy aims to establish IoT-based guidelines to manage traffic and transportation in MCI, reducing traffic congestion and emissions. Key actions include implementing IoT-driven rules to regulate new vehicle purchases and control population inflow by balancing infrastructure between cities and smaller areas. Government-supported scrappage policies will help phase out old, polluting vehicles, promoting eco-friendly and high-tech e-vehicles. IoT-based vehicle fitness testing stations and odd-even traffic rules will further reduce congestion, while peak-hour congestion fees will manage traffic flow and emissions effectively, moving towards to reduce TTCE and TTEC.

AIN Strategy

AIN strategy is basically a synergistic approach of TTDM, BT, RRM, and TU, with all their restrictions and due to these multiple effects of all these four strategies, an accumulated decreasing pattern of TTCE and TTEC is observed in MCI.

RESULTS AND DISCUSSION

The simulation results of SSDS model for generated strategies based on IoT-ITS to reduce TTCE and TTEC of road traffic and transportation system in MCI are shown in Figures 6 and 7, respectively. Figure 6 (a) depicts TTEC pattern in MCI for different strategies based on IoT-ITS. The value of TTEC under AIN is minimum in base year 2011 and has the lowest rising outcome pattern of all six strategies upto COVID-19 period and after the aggressive implementation of IoT-ITS from the post-COVID-19 time period 2023 to 2030, it has the highest continuous decline pattern of all six strategies. The output pattern of AIN is the most effective strategy pattern among all six strategies in reducing TTEC in both long and short period. In RRM, the value of TTEC has one of the lowest rising patterns of all of five separate strategies upto the COVID-19 period but after the aggressive implementation of RRM from the post-COVID-19 period 2023 to 2030, has the second highest continuous decline pattern and thus very realistic strategy for the short duration reduction of TTEC. In No-IMP, there is minimum decline pattern in comparison to all other strategies and in TU, there is second minimum decline in TTEC before and after the COVID-19 period. Before COVID-19 period, there is less rising pattern in TTEC due to BT and TTDM in comparison of No-IMP and TU but after COVID-19 period there is comparatively further less rising pattern in TTEC due to BT and TTDM. The TTDM looks very realistic strategy for the short duration reduction of TTEC.

Figure 6 (b) depicts the variations in TTEC per capita in MCI for different strategies based on IoT-ITS. There is very minor decline pattern in TTEC per capita under TU primarily due to less short duration progress in energy consumption economy of urban transportation in India mainly due to constraint of advanced technology and finance before COVID-19 period. There is also very slow paced decline pattern in TTEC per capita under TTDM before COVID-19 period. During COVID-19 period, there is a very sharp decline but after COVID-19 period there is a faster decline pattern in TTEC per capita. In BT, the pattern of TTEC per capita depicts a bit sharp decline behavior before COVID-19 period but after COVID-19 period, the decline pattern depicts a gradual slow pace of decline. In RRM, TTEC per capita has the lowermost value of all the specific strategies. In RRM and TTDM before the COVID-19 period in comparison to all other strategies have a tremendous initial decline pattern in TTEC per capita but BT depicts a drastic decline pattern in totality in TTEC per capita not only before COVID-19 period but also in the post-COVID-19 period. The model simulation clearly shows that BT is the best suited strategy for reduction of TTEC from public bus transport. The TTEC per capita depicts the lowest level value in

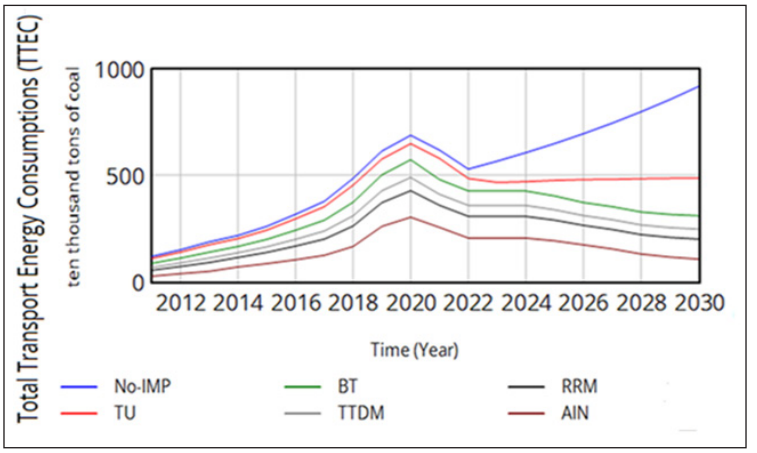

(a)

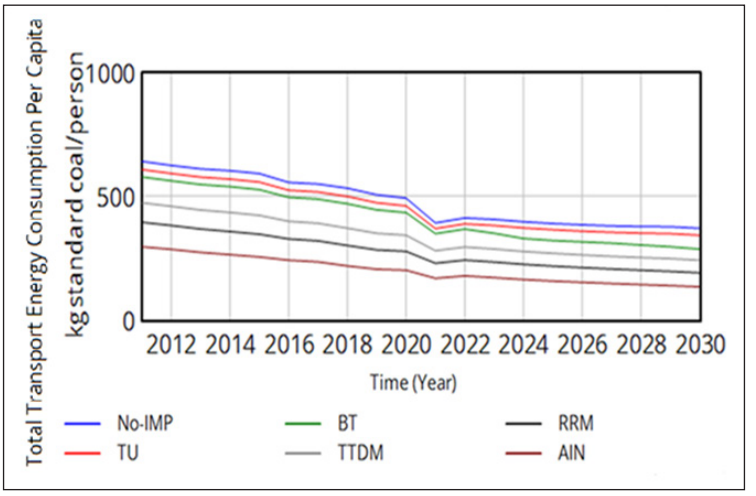

(b)

Figure 6. (a) Total Transport Energy Consumptions (TTEC) and (b) TTEC per capita pattern in Million-plus Cities of India (MCI) for different strategies based on Internet of Things-enabled Intelligent Transportation System (IoT-ITS)

Note. No-IMP = No implementation; TU = Technology upgradation; BT = Bus transport; TTDM = Traffic and transportation demand management; RRM = Rules and regulations management; AIN = All integrated

the start for AIN and there is continuous fall in its values before and after the COVID-19 period. It is interesting to note that decline of TTEC per capita under AIN is very fast in the beginning but after a passage of time slows down.

TTCE pattern in MCI for six different strategies based on IoT-ITS is shown in Figure 7(a). The value of TTCE under AIN has the lowest rising pattern of all of six strategies upto the COVID-19 period and after the aggressive implementation of IoT-ITS from 2023

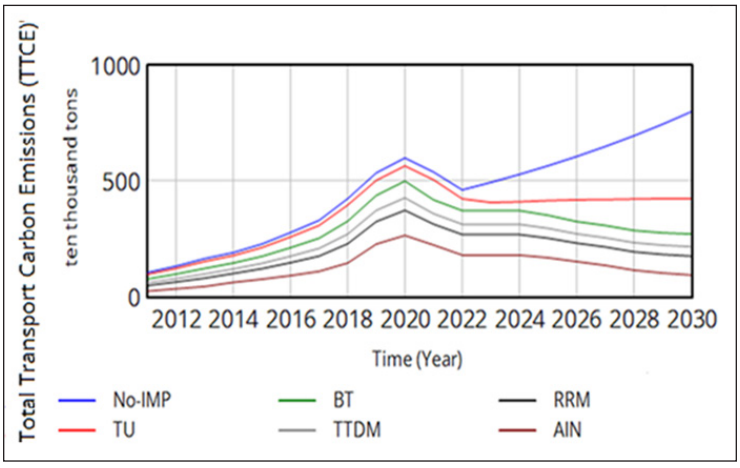

(a)

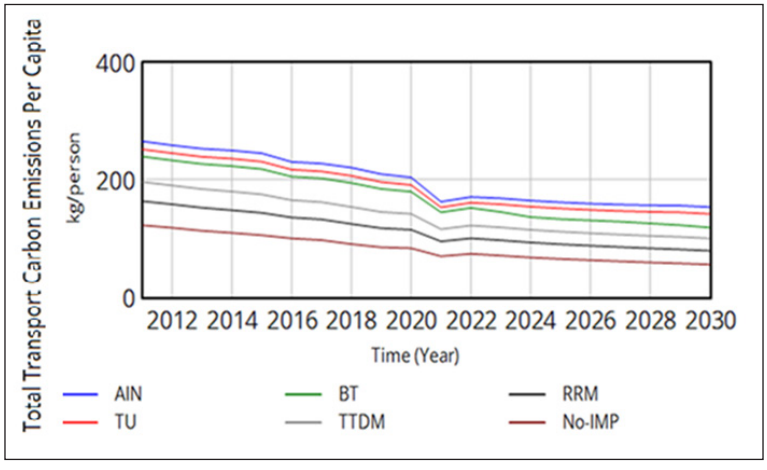

(b)

Figure 7. (a) Total Transport Carbon Emissions (TTCE) and (b) TTCE per capita pattern in Million-plus Cities of India (MCI) for different strategies based on Internet of Things-enabled Intelligent Transportation System (IoT-ITS)
Note. No-IMP = No implementation; TU = Technology upgradation; BT = Bus transport; TTDM = Traffic and transportation demand management; RRM = Rules and regulations management; AIN = All integrated

to 2030, again has the highest continuous decline pattern of all six strategies based on IoT-ITS. Under RRM, the TTCE pattern after the aggressive implementation of RRM from the post-COVID-19 period, has the second highest continuous steady decline and thus again highly realistic strategy for the short duration reduction of TTCE. Due to tremendous rise in travel pattern of target population, the value of TTCE is still rising, but not with great pace due to implementation of strategies based on IoT-ITS. Variations in TTCE per capita in MCI for the six different strategies based on IoT-ITS are shown in Figure 7(b). The

simulation patterns for TTEC per capita and TTCE per capita are very similar for TTDM, BT, RRM, and AIN. The TTCE per capita due to TU depicts overall greater changes.

Discussion and IoT-ITS Based Strategy Implications

It is interesting to note that RRM has the extreme result in reduction of TTEC and TTCE. Secondly, the role of TU is better in reduction of TTCE to the reduction of TTEC. The implementation of AIN is always most authentic in the reduction of TTEC and TTCE in comparison to the implementation of any particular strategy. Figure 8 (a) depicts the outcome changing pattern in reduction of TTCE due to implementation of BT under different strategy combinations. Now the combinations are: BT– (No-IMP) = ΔBT; BT– TTDM = Δ[BT + TTDM] – ΔTTDM; BT–TU = Δ[BT + TU]– ΔTU; BT– RRM = Δ[BT + RRM] – ΔRRM; BT – [TTDM + TU] = Δ[BT + TTDM + TU] – Δ[TTDM + TU]; BT – [TTDM + RRM] =Δ[BT + TTDM + RRM] – Δ[TTDM + RRM]; BT – [TU + RRM] = Δ[BT + TU + RRM] – Δ[TU + RRM)]; BT– [TTDM + TU + RRM)] = ΔAIN – Δ[TTDM + TU + RRM].

Here BT – [TTDM + TU] represents the outcome pattern in reduction of TTCE due to implementation of BT after the prior implementation of TTDM and TU. Now the outcome pattern BT – [TTDM + TU] is prominent in all and depicts that the outcome pattern of BT is superb but only after the implementation of TTDM and TU. Now comparison of three pairs BT – TU; BT – TTDM; and BT – RRM, clearly shows that BT is most effective after the implementation of TU. Now BT – [TTDM + TU + RRM] has always outcome pattern positive while BT – [TU +RRM] and BT – TU has always outcome pattern negative. These conflicting patterns clearly indicate that RRM has a very strong effect on the implementation behavior of BT. Hence, the correct order is first of all implement BT and then RRM. So now the best order to capitalize the maximum effect of BT is TU > TTDM > BT > RRM.

Figure 8 (b) depicts the outcome changing pattern in reduction of TTCE due to implementation of TU under different strategy combinations. Now the combinations are: TU – (No-IMP) = ΔTU; TU – BT = Δ[BT + TU] – ΔBT; TU – TTDM = Δ[TTDM + TU] – ΔTTDM; TU – RRM = Δ[TU + RRM] – ΔRRM; TU – [BT + TTDM] = Δ[BT + TTDM + TU] – Δ[BT + TTDM]; TU – [BT + RRM] = Δ[BT + TU + RRM] – Δ[BT + RRM]; TU – [TTDM + RRM] = Δ[TTDM + TU + RRM] – Δ[TTDM + RRM]; TU – [BT + TTDM + RRM)] = ΔAIN – Δ[BT + TTDM + RRM]. Now the outcome pattern of TU – [BT + TTDM] is prominent in all and clearly recommends that TU should be implemented first and then RRM should be implemented to give us most effective results. Now comparison of three pairs TU – BT; TU – TTDM; and TU – RRM, clearly shows the best order of implementation: BT followed by TTDM and then in the last RRM. So now to capitalize the maximum effect of TU, the best sequence is BT > TTDM > TU > RRM.

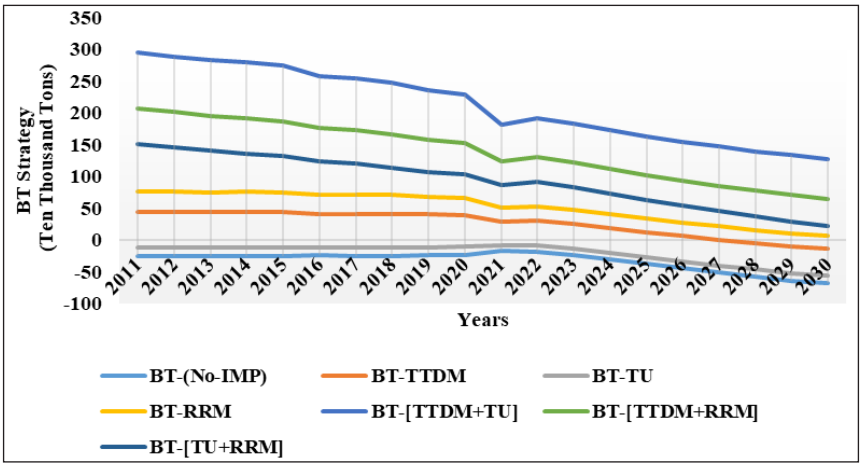

(a)

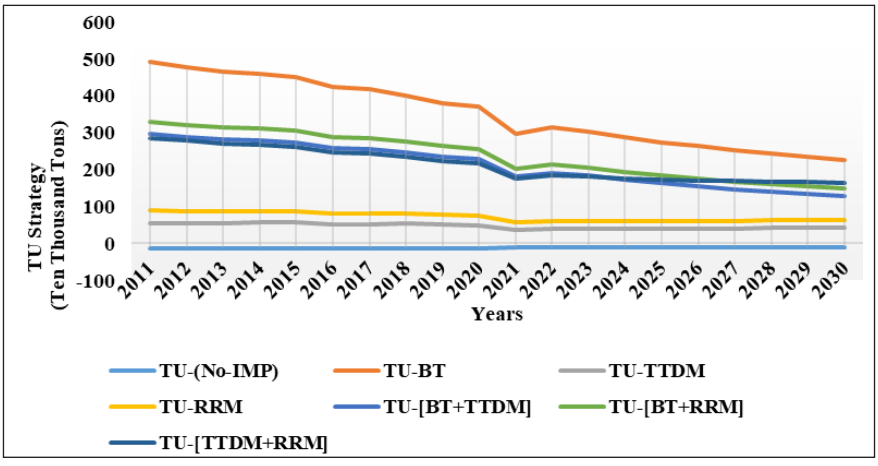

(b)

Figure 8. Outcome changing pattern in reduction of Total Transport Carbon Emissions (TTCE) due to implementation of (a) Bus transport (BT) Strategy and (b) Technology upgradation (TU) Strategy
Note. TU–(No-IMP) = Technology upgradation–(No implementation); TU–BT = Technology upgradation–Bus transport; TU–TTDM = Technology upgradation–Traffic and transportation demand management; TU–RRM = Technology upgradation–Rules and regulations management; TU–[BT+TTDM] = Technology upgradation–[Bus transport + Traffic and transportation demand management]; TU–[BT+RRM] = Technology upgradation–[Bus transport + Rules and regulations management]; TU–[TTDM + RRM] = Technology upgradation–[Traffic and transportation demand management + Rules and regulations management]

Figure 9 (a) depicts the outcome changing pattern in reduction of TTCE due to implementation of TTDM under different strategy combinations. Now the combinations are: TTDM – (No-IMP) = ΔTTDM; TTDM –BT = Δ[BT + TTDM] – ΔBT; TTDM – TU = Δ[TTDM + TU] – ΔTU; TTDM –RRM = Δ[TTDM + RRM] – ΔRRM; TTDM – [BT

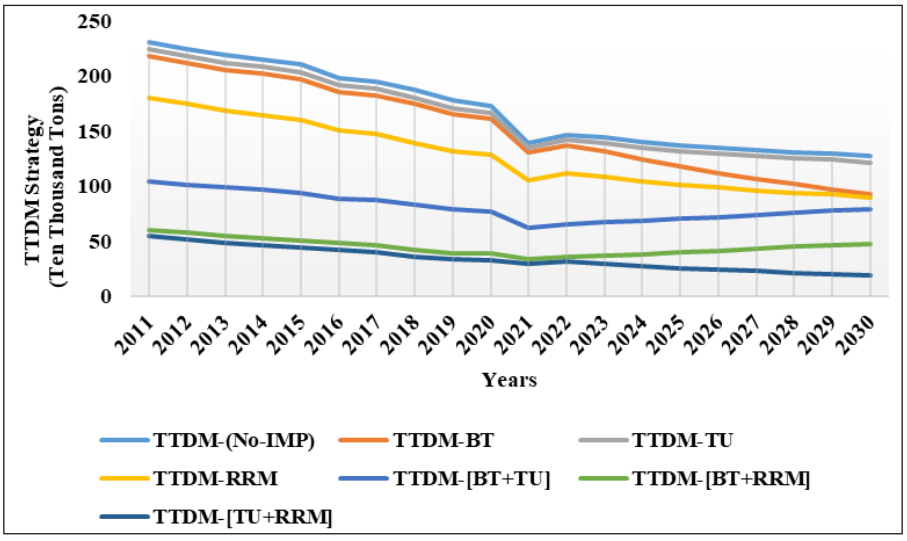

(a)

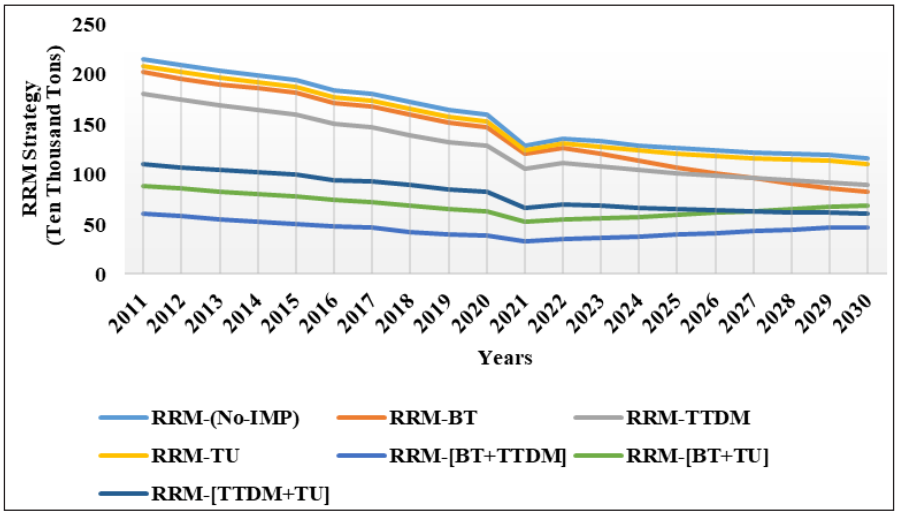

(b)

Figure 9. Outcome changing pattern in reduction of Total Transport Carbon Emissions (TTCE) due to implementation of (a) Traffic and transportation demand management (TTDM) Strategy and (b) Rules and regulations management (RRM) Strategy

Note. RRM–(No-IMP) = Rules and regulations management–(No implementation); RRM–BT = Rules and regulations management–Bus transportation; RRM–TTDM = Rules and regulations management–Traffic and transportation demand management; RRM–TU = Rules and regulations management–Technology upgradation; RRM–[BT+TTDM] = Rules and regulations management–[Bus transportation + Traffic and transportation demand management]; RRM–[BT+TU] = Rules and regulations management–[Bus transportation + Technology upgradation]; RRM–[TTDM+TU] = Rules and regulations management–[Traffic and transportation demand management + Technology upgradation]

+ TU] = Δ[BT + TTDM + TU] – Δ[BT + TU]; TTDM – [BT + RRM] = Δ[BT + TTDM + RRM] – Δ[BT + RRM]; TTDM – [TU + RRM] = Δ[TTDM + TU + RRM] – Δ[TU + RRM); TTDM – [BT + TU + RRM] = ΔAIN – Δ[BT + TU + RRM]. Here the TTDM – [BT + TU] represents the outcome pattern in reduction of TTCE due to TTDM after the prior implementation of BT and TU. Now the outcome pattern of TTDM – [BT + TU] is best in all and indicates that outcome pattern of TTDM is most realistic when this is implemented after the implementation of BT and TU. Now comparison of three pairs TTDM – BT; TTDM – TU; and TTDM – RRM, shows that the outcome pattern of TTDM is weak after the implementation of RRM but is strong after the implementation of TU. Now the outcome pattern of TTDM – [BT + TU + RRM] is noticeable which clearly indicates that TTDM always gives realistic pattern to resolve the problems at any stage of time and hence it should be used continuously. So now the best order to capitalize the maximum effect of TTDM is TU > BT > TTDM > RRM.

Figure 9 (b) depicts the outcome changing pattern in reduction of TTCE due to implementation of RRM under different strategy combinations. Now the combinations are: RRM – (No-IMP) = ΔRRM; RRM – BT = Δ[BT + RRM] – ΔBT; RRM – TTDM = Δ[TTDM + RRM] – ΔTTDM; RRM – TU = Δ[RRM + TU] – ΔTU; RRM – [BT + TTDM] = Δ[BT + TTDM + RRM] – Δ[BT + TTDM]; RRM – [BT + TU] = Δ[BT + TU + RRM] – Δ[BT + TU]; RRM – [TTDM + TU] = Δ[TTDM + TU + RRM] – Δ[TTDM + TU]; RRM – [BT + TTDM + TU] = ΔAIN– Δ[BT + TTDM + TU]. The implementation of RRM has a powerful decreasing pattern tendency on implementation of TTDM, BT and TU and should be executed latter. Now to get the best outcome pattern of RRM – No-IMP, the RRM should be executed initially. The outcome pattern of RRM – TU is the next noticeable and therefore TU should be executed first. The comparison of RRM – TTDM with RRM – BT clearly indicates that in the early stages, the outcome pattern of RRM – BT is more significant than RRM – TTDM but in the post Covid-19 period the outcome pattern is worst. The implementation of TTDM need good condition of public transportation as an essential requirement while implementation of BT need a particular time lag. So now the best order to capitalize the maximum effect of RRM is TU > BT > TTDM > RRM.

Similarly, the best order to capitalize the maximum effect of all separate strategy in AIN is TU > BT > TTDM > RRM.

CONCLUSION

A SSDS model was designed in four stages to reduce TTEC and TTCE of road traffic and transportation system in MCI by the implementation of strategies based on IoT-ITS. Total six strategies based on IoT-ITS were formulated and generated to monitor TTEC and TTCE in MCI. The outcome pattern was analyzed and simulated. The implementation of BT has an optimistic outcome pattern but implementation of BT needs a particular time lag and

hence the output pattern will only be effective slowly after a passage of time, whereas the implementation of TTDM has a quick favorable outcome pattern and is very effective for short duration. When both BT and TTDM are implemented jointly, then TTDM can easily take care of time lag due to BT. The TU plays a very important role in reduction of TTCE than savings of TTEC, while implementation of RRM can play an important role in attaining the targets very quickly than others. The implementation of AIN is very expensive in reducing TTCE and TTEC but its overall outcome pattern is excellent in comparison of implementation of each specific strategy individually.

For the generation of IoT-ITS-based total low carbon emission transportation modes in the near future and for achieving the target goal of reducing TTCE and TTEC, BT is a very realistic and sound to manage and reduce the road traffic accidents and collisions, road traffic congestions and consumption of fuels. There is also an urgent need to promote the dedicated cycling zones, dedicated e-vehicle lanes, and safe walking zones by developing IoT-ITS-based driveways and promoting e-vehicles. The sophisticated structure of TTDM can play a very important role in managing the traffic and transportation system. The transport strategic planners and administrators are supposed to carefully examine the possible bottlenecks in this strategy, and should diagnose and predict the future line of action to avoid the eleventh-hour crisis and should study in advance the effect of IoT-ITS-based infrastructure development on the travel pattern due to TTDM.

The TU has a lot of hidden merits and should be thoroughly explored. TU has a better role in reducing TTCE than the savings in total transport energy. IoT-ITS-based research has a very long duration investment remuneration system, and has a good potential for a variety of different high-tech inputs from the practical point of view. The majority of energy workers and two or four-wheelers manufacturers generally have less drive for technology research. Hence, it is necessary for the Government of India to strictly introduce and implement very severe technical guidelines immediately to avoid an explosive disaster due to carbon emissions. The provision of exemption from taxes and such other incentives can also play a significant role in the realization of target goals.

The RRM is totally based on the strong discretion of the Government of India. Hence it is very necessary for the government machinery to strictly impose the RRM with full boldness and fairness. The police and Regional Transport Office (RTO) officials must circulate as well as announce detailed explanations on a regular basis about different RRM to the residents to get back their full cooperation and to minimize the rebound behavior. A safe exit process and controlling behavior are main tools for different RRM. The overall effect of different RRM is definitely very optimistic. It is very interesting to note that though implementation of AIN is highly expensive, but it is the best golden strategy in all the strategies. Hence, the optimal order of strategy implementation in AIN is TU > BT > TTDM > RRM.

The traffic and transportation system at present globally contributes approximately 26% of total energy-based emissions, and this will rise to approximately 55 to 60% in the year 2050. Similarly, the contribution of freight road transportation-based energy emissions will rise to approximately 80% in the year 2050, which is at present around 42%. The aggressive and high ambition implementation of strategies based on IoT-ITS using SSDS model in Indian road traffic and transportation system, total infrastructure as well as in electrification of road traffic and transportation system including electric vehicles and e-public transport buses will definitely reduce TTCE by approximately 33-35% upto 2030 and 70-75% upto 2050 and this road map of aggressive and high ambition implementation of strategies based on IoT-ITS finally zoom to main goal of achieving net zero emissions.

ACKNOWLEDGEMENTS

The authors extend their gratitude to the referees for their constructive comments and suggestions, which significantly enhanced the quality and depth of this research work.

REFERENCES

Alkinani, M. H., Almazroi, A. A., Adhikari, M., & Menon, V. G. (2022). Design and analysis of logistic agent-based swarm-neural network for intelligent transportation system. *Alexandria Engineering Journal*, *61*(10), 8325–8334. https://doi.org/10.1016/j.aej.2022.01.046

Al-Mayouf, Y. R. B., Mahdi, O. A., Taha, N. A., Abdullah, N. F., Khan, S., & Alam, M. (2018). Accident management system based on vehicular network for an intelligent transportation system in urban environments. *Journal of Advanced Transportation*, *2018*(15), 1-11. https://doi.org/10.1155/2018/6168981

AutoInsurance.com. (2025). *2025 Electric vehicle statistics*. https://www.autoinsurance.com/research/electric-vehicle-statistics/?utm_source=chatgpt.com

Bautista, C., & Mester, G. (2023). Internet of Things in self-driving cars environment. *Interdisciplinary Description of Complex Systems*, *21*(2), 188–198. https://doi.org/10.7906/indecs.21.2.8

Chen, Z., Zan, Z., & Jia, S. (2022). Effect of urban traffic-restriction policy on improving air quality based on system dynamics and a non-homogeneous discrete grey model. *Clean Technologies and Environmental Policy*, *24*, 2365–2384. https://doi.org/10.1007/s10098-022-02319-9

Dasgupta, K., Das, A., Das, S., Bhattacharya, U., & Yogamani, S. (2022). Spatio-contextual deep network-based multimodal pedestrian detection for autonomous driving. *IEEE Transactions on Intelligent Transportation Systems*, *23*(9), 15940–15950. https://doi.org/10.1109/TITS.2022.3146575

Ding, H., Di, Y., Feng, Z., Zhang, W., Zheng, X., & Yang, T. (2022). A perimeter control method for a congested urban road network with dynamic and variable ranges. *Transportation Research Part B: Methodological*, *155*, 160–187. https://doi.org/10.1016/j.trb.2021.11.008

Dong, Z., & Ullah, S. (2023). Towards a green economy in China? Examining the impact of the Internet of Things and environmental regulation on green growth. *Sustainability*, *15*(16), 12528. https://doi.org/10.3390/su151612528

Economic Survey. (n.d.). *Economy survey 2024-2025*. https://www.indiabudget.gov.in/economicsurvey/

Gao, J., Manogaran, G., Nguyen, T. N., Kadry, S., Hsu, C.-H., & Kumar, P. M. (2022). A vehicle-consensus information exchange scheme for traffic management in vehicular ad-hoc networks. *IEEE Transactions on Intelligent Transportation Systems*, *23*(10), 19602–19612. https://doi.org/10.1109/TITS.2021.3130087

Gupta, M., Bandyopadhyay, K. R., & Singh, S. K. (2019). Measuring effectiveness of carbon tax on Indian road passenger transport: A system dynamics approach. *Energy Economics*, *81*, 341–354. https://doi.org/10.1016/j.eneco.2019.03.013

Hossain, M. S., Fang, Y. R., Ma, T., Huang, C., Peng, W., Urpelainen, J., Hebbale, C., & Dai, H. (2023). Narrowing fossil fuel consumption in the Indian road transport sector towards reaching carbon neutrality. *Energy Policy*, *172*, 113330. https://doi.org/10.1016/j.enpol.2022.113330

Iliopoulou, C., & Kepaptsoglou, K. (2019). Combining ITS and optimization in public transportation planning: State of the art and future research paths. *European Transport Research Review*, *11*, 27. https://doi.org/10.1186/s12544-019-0365-5

Lin, C., Zhou, X., & Gong, B. (2019). Trusted measurement and evaluation for intelligent transportation system products: A case study for traffic signal controller. *Advances in Mechanical Engineering*, *11*(3). https://doi.org/10.1177/1687814019829597

Mahdi, O. A., Eleiwy, J. A., Al-Mayouf, Y. R. B., & AL-Attar, B. (2024). An efficient node selection algorithm in the context of IoT-based vehicular ad hoc network for emergency service. *Journal of Intelligent Systems*, *33*(1), 20240208. https://doi.org/10.1515/jisys-2024-0208

Mahdi, O. A., Ghazi, A. B., & Al-Mayouf, Y. R. B. (2021). Void-hole aware and reliable data forwarding strategy for underwater wireless sensor networks. *Journal of Intelligent Systems*, *30*(1), 564-577. https://doi.org/10.1515/jisys-2020-0137

Ministry of Road Transport and Highways. (2023). *Road transport yearbook 2019-20*. MoRTH. https://morth.nic.in/sites/default/files/RTYB_Publication_2019_20%20(1).pdf

Norouzian-Maleki, P., Izadbakhsh, H., Saberi, M., Hussain, O., Rezaee, M. J., & GanbarTehrani, N. (2022). An integrated approach to system dynamics and data envelopment analysis for determining efficient policies and forecasting travel demand in an urban transport system. *Transportation Letters*, *14*(2), 157–173. https://doi.org/10.1080/19427867.2020.1839716

Nunes, S. A. S., Ferreira, F. A. F., Govindan, K., & Pereira, L. F. (2021). "Cities go smart!": A system dynamics-based approach to smart city conceptualization. *Journal of Cleaner Production*, *313*, 127683. https://doi.org/10.1016/j.jclepro.2021.127683

Office of the Registrar General and Census Commissioner, India., & Ministry of Home Affairs, Government of India. (n.d.). *Census division*. https://censusindia.gov.in/census.website/node/378

O'Rourke, P. R., Smith, S. J., Mott, A., & Ahsan, H., McDuffie, E. E., Crippa, M., Klimont, Z., Mc Donald, B., Wang, S., Nicholson, M. B., Feng, L., & Hosely, R. M. (2021). *CEDS v_2021_02_05 release emission data*. https://zenodo.org/record/4509372#.YgtLXt9BxnI

Ramesh, T. R., Vijayaragavan, M., Poongodi, M., Hamdi, M., Wang, H., & Boutouis, S. (2022). Peer-to-peer trust management in intelligent transportation system: An Aumann's agreement theorem-based approach. *ICT Express*, *8*(3), 340–346. https://doi.org/10.1016/j.icte.2022.02.004

Shahsavari-Pour, N., Bahador, S., Heydari, A., & Fekih, A. (2022). Analyzing Tehran's air pollution using system dynamics approach. *Sustainability*, *14*(3), 1181. https://doi.org/10.3390/su14031181

Statista. (2025). *Carbon dioxide emissions from the transportation sector worldwide from 1990 to 2023, by country or region*. https://www.statista.com/statistics/1200787/carbon-dioxide-emissions-transport-sector-worldwide-by-country/

Timperley, J. (2019). *The carbon brief profile: India*. Carbon Brief. https://www.carbonbrief.org/the-carbon-brief-profile-india

Upadhyay, P., Goyal, S. J., Marriboyina, V., & Kumar, M. (2024). Securing vehicular Internet of Things (V-IoT) communication in smart VANET infrastructure using a multi-layered communication framework and a novel threat detection algorithm. *International Journal of Intelligent Systems and Applications in Engineering*, *12*(6s), 789–803.

Wang, L., Wang, R., & Yan, H. (2021). System-dynamics modeling for exploring the impact of industrial-structure adjustment on the water quality of the river network in the Yangtze Delta area. *Sustainability*, *13*(14), 7696. https://doi.org/10.3390/su13147696

Welle, D. (2020). *India only G20 nation doing its 'fair share' to meet 2-degree goal, says report*. The Indian Express. https://www.dw.com/en/india-only-g20-nation-doing-its-fair-share-to-meet-2-degree-goal-report/a-55657420

World Economic Forum. (2021). *Mission 2070: A Green New Deal for a Net Zero India*. https://www3.weforum.org/docs/WEF_Mission_2070_A_Green_New_Deal_for_a_Net_Zero_India_2021.pdf

Yuan, T., Da Rocha Neto, W., Rothenberg, C. E., Obraczka, K., Barakat, C., & Turletti, T. (2022). Machine learning for next-generation intelligent transportation systems: A survey. *Transactions on Emerging Telecommunications Technologies*, *33*(4), e4427. https://doi.org/10.1002/ett.4427

Pertanika J. Sci. & Technol. 33 (4): 2001 - 2025 (2025)

PERTANIKA JOURNALS

SCIENCE & TECHNOLOGY

Journal homepage: http://www.pertanika.upm.edu.my/

Comparison of Crystal Structure, Surface Morphology Structure, and Energy Band Gap of Thin Films of Zinc Oxide, Tin(IV) Oxide, and Titanium Dioxide

Teguh Ardianto[1]*, Aris Doyan[2], Susilawati[2], Dedi Riyan Rizaldi[3], Ziadatul Fatimah[4], Muhammad Ikhsan[5] and Nuraini Rachma Ardianti[5]

[1]Physics, Faculty of Mathematics and Science, University of Mataram, Jl. Majapahit No. 62 Mataram 83125, Indonesia
[2]Physics Education, Faculty of Teacher Training and Education, University of Mataram, Jl. Majapahit No. 62 Mataram 83125, Indonesia
[3]MA Plus Nurul Islam Sekarbela, Jl. Swasembada No. IX Karang Pule Mataram 83115, Indonesia
[4]SMA NW Mataram, Jl. Kaktus No. 1-3 Mataram 83126, Indonesia
[5]Balai Publikasi Indonesia, Jl. Pendidikan No. 37 Mataram 83125, Indonesia

ABSTRACT

This study was conducted with the aim of analyzing the crystal structure, surface morphology structure, and energy band gap values in zinc oxide (ZnO), tin(IV) oxide (SnO_2), and titanium dioxide (TiO_2) thin films. This study uses an experimental research type that goes through two stages of work, namely synthesis and characterization of thin films. The synthesis stage is through the process of making sol-gel solutions, depositing solutions on substrate media, and heating thin film samples. While the characterization stage is carried out through three testing processes using X-ray diffraction (XRD), scanning electron microscopy (SEM), and UV-Vis spectrophotometry. The research data obtained were analyzed descriptively and presented in the form of images, tables, and graphs to see the quality and characteristics of the test samples. Based on the results of the analysis, it is known that the crystal structure of the ZnO thin film is hexagonal while SnO_2 and TiO_2 are tetragonal. The surface morphology of the SnO_2 and TiO_2 thin films is granular, while the ZnO thin film is a nanorod. The smallest energy band gap value is found in the ZnO thin film with a value of 2.00 eV. There are four factors that affect the energy band gap value in thin films, namely precursor material, deposition method, substrate media, and dopant material.

Keywords: Crystal structure, energy band gap, morphological structure, thin film, tin(IV)oxide, titanium dioxide, zinc oxide

ARTICLE INFO

Article history:
Received: 15 December 2024
Accepted: 17 March 2025
Published: 23 July 2025

DOI: https://doi.org/10.47836/pjst.33.4.15

E-mail addresses:
teguhardianto@unram.ac.id (Teguh Ardianto)
aris_doyan@unram.ac.id (Aris Doyan)
susilawatihambali@unram.ac.id (Susilawati)
dedi0313@gmail.com (Dedi Riyan Rizaldi)
ziadatulfatimah96@gmail.com (Ziadatul Fatimah)
muhammadikhsan99.mi@gmail.com (Muhammad Ikhsan)
nurainirachmaa@gmail.com (Nuraini Rachma Ardianti)
* Corresponding author

e-ISSN: 2231-8526

© Universiti Putra Malaysia Press

INTRODUCTION

Researchers worldwide have paid considerable attention to the development of technology in the field of materials. Various studies have been conducted with the aim of producing materials that have good characteristics and are in accordance with human needs. One way that can be done to produce materials that are in accordance with what is desired is by using the material coating technique process (Butt, 2022). In today's conditions, various material coating sciences and technologies play a very important role in the electronics industry. One of the main objectives of this development process is to be able to meet the various needs for a circuit that is integrated and often used in the electronics industry process (McIvor & Humphreys, 2004). Research on material coatings that is often carried out today is the process of forming thin layers.

A thin layer is a layer on a material that has a thickness ranging from nanometers (single layer) to micrometers (Koziej et al., 2014). This thickness condition when compared to the substrate used is included in the very thin category. Currently, thin films are of interest to develop because they can impart new properties to materials. Thin films have characteristics such as a uniform surface (coating the substrate evenly without defects), stable surface temperature and high precision, strong intermolecular adhesion, and crystal structure (Zhao et al., 2008). Thin layers can be developed by carrying out a deposition process of a material which can be organic, non-organic, metal, or a mixture of the three materials on a substrate in the form of a plate, thus producing a new property. The application of thin layers for semiconductors is developed in the form of transparent conductive oxide (TCO), sensors, capacitors, diodes, transistors, touch screens, solar cells, and various other forms of technology that are useful for human life today (Imawanti et al., 2017; Paul David et al., 2021).

However, in general, the materials that are often used by researchers in developing thin layers are materials that are included in the metal oxide group. Some examples of these metals include ZnO, SnO_2, and TiO_2. The selection of metal oxides as one of the good materials in the development of thin films is because these materials have the characteristics of high optical transparency at visible light waves and are transparent to light. Various previous studies have proven that the above materials are good precursors in the process of developing various thin layers that have characteristic values according to the needs of various industries, especially those related to electronics. According to Nunes et al. (2002), because of its optical and electrical qualities, high chemical and mechanical stability, and natural availability, ZnO has become one of the most promising materials. ZnO is also used as a base material for thin films because it is readily available, non-toxic, and efficient to produce (Vyas, 2020). The physical properties of ZnO nanostructures: it is important to note that the size of semiconductor materials is continuously decreasing towards the nanometer scale or even smaller, and some of their physical properties undergo changes

known as quantum size effects (Doyan & Humaini, 2017). Understanding the basic physical properties is important for the design of functional devices (Xin et al., 2019).

The next material in the group of oxidation metals that is often used is SnO_2. Of the many constituent elements, titanium (Ti) and zinc (Zn) have the greatest abundance compared to other elements. However, tin (Sn) is a good alternative as a base material for thin layers because it has advantages over other metals, namely it is one of the good electrical conductors with a low electrical resistivity of 4.60 μΩ.cm, easy to form, resistant to corrosion, lightweight, non-flammable, and durable (Doyan et al., 2017, 2021). One of the nanoscale materials, which includes semiconductor materials, is SnO_2. Tin (IV) oxide finds extensive use in sensor gases, solar cells, TCO, and optoelectronic devices (Muliyadi et al., 2019). Furthermore, tin (IV) oxide has a number of benefits, including low resistivity, excellent transparency, good chemical stability, and a band gap width of about 3.6 eV (Schell et al., 2017). Additionally, the tin (IV) oxide is highly sensitive to the atmosphere surrounding it, which makes it useful as a sensor gas (Pandit & Ahmad, 2022).

The last material that is often used in the development of thin films is titanium dioxide. Titanium dioxide, or chemically written as TiO_2, is a semiconductor material with a band gap of 3-4 eV, so it will only absorb light with wavelengths in the ultraviolet color region and is transparent to visible light (Bedghiou et al., 2019; Rizaldi et al., 2022). In addition, physically, titanium dioxide has a low density of 4.23 g/cc, a molecular weight of 79.886 g/mol, a high level of stability, corrosion resistance, a white crystal form, and is acidic, so it does not dissolve in water (Khasanah et al., 2019; Prastiwi et al., 2017).

The three materials above certainly have characteristics that allow them to be used as basic materials or precursors in developing thin films. However, of course, each of these materials still has characteristics that cannot be used optimally in various industries. These characteristics need to be modified in order to adjust the inherent characteristics of each metal material so that it can be used in various technologies. One way that can be done to change the characteristics of the material is by carrying out a doping process (Norris et al., 2008). Some doping that has been used in this study to improve the capabilities of the three precursors above are aluminum, fluorine, indium, and cobalt.

In this study, two methods of thin layer sample preparation processes were used, namely the sol-gel spin coating and dip coating methods. The use of the sol-gel method is certainly due to several advantages, including being able to produce products with low synthesis temperatures, high purity and structural homogeneity, as well as producing electrochemical properties in the form of good conductivity compared to other methods. According to Costa et al. (2025), the sol-gel method allows the manufacture of SiO_2 glass at a relatively lower temperature (~1,000 °C) without significant loss of phosphate because it is immobilized in aluminum-phosphate units. This method allows the preparation of homogeneous aluminophosphosilicate (APS) samples, which cannot be achieved using the melt-quenching

method. Meanwhile, according to Zhang et al. (2025), compared to other methods, powders prepared by the sol-gel method offer advantages such as fine particle size (Najafi, et al., 2022; Sharifi et al., 2023) and easy stoichiometry control (Khalaj et al., 2023). In its implementation, the sol-gel method can be combined with spin coating and dip coating techniques. Both techniques are used by researchers because they have their respective advantages.

Spin coating is a popular and rapid method for coating thin films on substrates. The main advantage of this method is the ease of producing a highly uniform coating. Centripetal force and surface tension of the liquid work together to coat the substrate evenly when a solution of a particular substance is spun at high speed. After excess solvent is removed, spin coating produces a thin film with a thickness ranging from a few nanometers to a few microns (Butt, 2022). The spin coating process is used to coat small materials with diameters ranging from a few square millimeters to a meter or more. One of the main advantages of the spin coating technique is the relative ease and simplicity of the process setup, as well as the thinness and homogeneity (Atay, 2020). Meanwhile, dip coating technique is often used for optical coatings, including wide-area antireflective coatings for sun visors and vehicle rear view mirrors; it is a fast, easy, affordable, and high-quality method used in industrial and laboratory applications (Butt, 2022; Jafri & Jaafar, 2024; Tang & Yan, 2017). During the dip coating process, the substrate is immersed in a solution containing the coating components before the solution is dried (Y. Yang et al., 2018). This method can be described as the deposition of an air-based liquid phase onto the substrate surface.

Research on the synthesis and characterization of thin films has always attracted the attention of scientists because of its wide application in everyday life, both in the fields of decoration, construction, and electronics. In the field of electronics, thin films are used to make semiconductors (Rahmawati & Agustina, 2018). The three precursors used by researchers are certainly expected to have semiconductor material characteristics that are in accordance with several technologies that support human life, such as touch screens, gas sensors, and, of course, solar cells. Solar cell technology is one of the main objectives of thin film development carried out by researchers by applying various precursors and dopant materials to find the best and most efficient characteristic values for the advancement of material research in the future. Based on the problems above, the purpose of this study is to determine and compare the energy band gap values of the precursor materials, namely ZnO, SnO_2, and TiO_2, after being added by various dopants such as zinc, aluminum, fluorine, indium, and cobalt.

METHODS AND MATERIALS

This research is experimental research. This research goes through two main stages, namely the formation of thin layer samples and thin layer characterization tests. The synthesis process itself goes through several stages, including:

(1) Preparation of research materials, including precursors consisting of zinc acetate dihydrate (Zn $(CH_3COO)_2H_2O$), tin (II) chloride dihydrate ($SnCl_2 \cdot 2H_2O$), and others, titanium dioxide (TiO_2); solvents consisting of ethanol (C_2H_5OH), hydrochloric acid (HCl), and aquades; while the dopant materials used include zinc dichloride ($ZnCl_2$), aluminum chloride ($AlCl_3$), indium (III) chloride tetrahydrate ($InCl_3 \cdot 4H_2O$), ammonium fluoride (NH_4F), and cobalt (II) chloride ($CoCl_2 \cdot 6H_2O$). The media used in the material coating process are glass and quartz substrates.

(2) Making a sol-gel solution by mixing precursors, solvents, and doping materials into the same container and then stirring using a magnetic stirrer for 30-60 min until the mixture looks homogeneous.

   (a) ZnO sol-gel solution
   $Zn(CH_3COO)_2 2H_2O$ was dissolved into ethanol solution (C_2H_6O), and mono ethanolamine (MEA:C_2H_7NO) at room temperature with a molar ratio of MEA and ZnAc of 1:1. Then the solution was stirred using a magnetic stirrer at a temperature of ±70°C for 30 min until a homogeneous solution was obtained.

   (b) SnO_2 sol-gel solution
   $SnCl_2.2H_2O$ as much as 0.902 g in powder form is dissolved in 40 ml of ethanol. The process of dissolving $SnCl_2.2H_2O$ in ethanol using a hot plate and stirring using a magnetic stirrer until it reaches a temperature of 80°C for 30 minutes or until the solution is homogeneous. Then dopant materials are added according to the variables used, namely aluminum, indium, and fluorine, and then stirred again until all mixtures look homogeneous.

   (c) TiO_2 sol-gel solution
   The preparation of TiO_2 sol-gel solution uses 20 ml of ethanol solvent with a fixed concentration of 1 M. After the process of making the precursor solution in the form of TiO_2, then the addition of NH_4F, Indium(III)Chloride ($InCl_3$), and cobalt(II)chloride ($CoCl_2$) doping is carried out according to the mass calculation of each research material. Specifically for the use of $CoCl_2$ doping, it is necessary to add hydrochloric acid (HCl) solution. This needs to be done so that the $CoCl_2$ material can be mixed homogeneously with the precursor used.

(3) The process of depositing sol-gel solution on the substrate, where this stage is the process of coating the substrate material using a previously prepared solution. The deposition process uses aids in the form of a dip coater and a modified centrifuge with the aim that the deposited solution can be evenly distributed over the substrate used (glass or quartz).

(4) The process of heating thin layer samples using an oven or furnace, which aims to dry and remove other solutions that are still on the surface of the substrate.

In this study, it has been developed into several types of research samples with different treatments. To facilitate the analysis process, the researcher provides categorization or codes (Table 1).

The second stage after the thin film synthesis process is carried out is to conduct a thin film characterization test. In this study, three analysis test processes were carried out, namely 1) using XRD to measure the crystal structure of thin film samples, 2) using a scanning electron microscope (SEM) to determine the morphological structure of the surface of the thin film sample, and 3) using a UV-Vis spectrophotometry tool to determine the distribution of absorbance values of the thin film sample. The data from the UV-Vis spectrophotometry test results were used by researchers to determine the energy band gap value of each thin film sample.

The energy band gap value can be determined using the Tauc plot graphic method, which describes the relationship between hv and $(ahv)^n$ (Efelina, 2017). The value of n = ½ for the direct energy gap and n = 2 for the indirect energy gap (Susilawati et al., 2009). The Tauc determination of the energy band gap from the relationship graph between hv and $(ahv)^n$ until it intersects the hv axis. The method process uses absorbance value data that has been obtained and analyzed using Microsoft Excel 2010. Determination of the energy band gap from the relationship graph between hv and $(ahv)^n$ until it intersects the hv axis. To make it easier to understand the procedure in this study, it can be seen in the following chart (Figure 1).

Table 1
Thin film research samples

No.	Sample	Method	Substrate	Sample code
1	Zinc oxide	Sol-gel dip-coating	Glass	ZnO type A
2	Zinc oxide	Sol-gel spin-coating	Glass	ZnO type B
3	Tin(IV) oxide doping aluminum	Sol-gel spin-coating	Quartz	SnO_2:Al type A
4	Tin(IV) oxide doping aluminum	Sol-gel spin-coating	Glass	SnO_2:Al type B
5	Tin(IV) oxide doping indium	Sol-gel spin-coating	Glass	SnO_2:In
6	Tin(IV) oxide doping fluorine	Sol-gel spin-coating	Glass	SnO_2:F
7	Tin(IV) oxide doping aluminum and fluorine	Sol-gel spin-coating	Glass	SnO_2:(Al+F)
8	Tin(IV) oxide doping aluminum and indium	Sol-gel spin-coating	Glass	SnO_2:(Al+In)
9	Tin(IV) oxide doping aluminum, fluorine, and indium	Sol-gel spin-coating	Glass	SnO_2:(Al+F+In)
10	Titanium dioxide doping fluorine and indium	Sol-gel spin-coating	Glass	TiO_2:(F+In)
11	Titanium dioxide doping cobalt	Sol-gel spin-coating	Glass	TiO_2:Co

Note. ZnO = Zinc oxide; SnO_2:Al = Tin(IV) oxide doped with aluminum; SnO_2:In = Tin(IV) oxide doped with indium; SnO_2:F = Tin(IV) oxide doped fluorine; SnO_2:(Al+F) = Tin(IV) oxide is doped with a mixture of aluminum and fluorine; SnO_2:(Al+In) = Tin(IV) oxide is doped with a mixture of aluminum and indium; SnO_2:(Al+F+In) = Tin(IV) oxide is doped with a mixture of aluminum, fluorine, and indium; TiO_2:(F+In) = Titanium dioxide doped with mixture fluorine and indium; TiO_2:Co = Titanium dioxide doped with cobalt

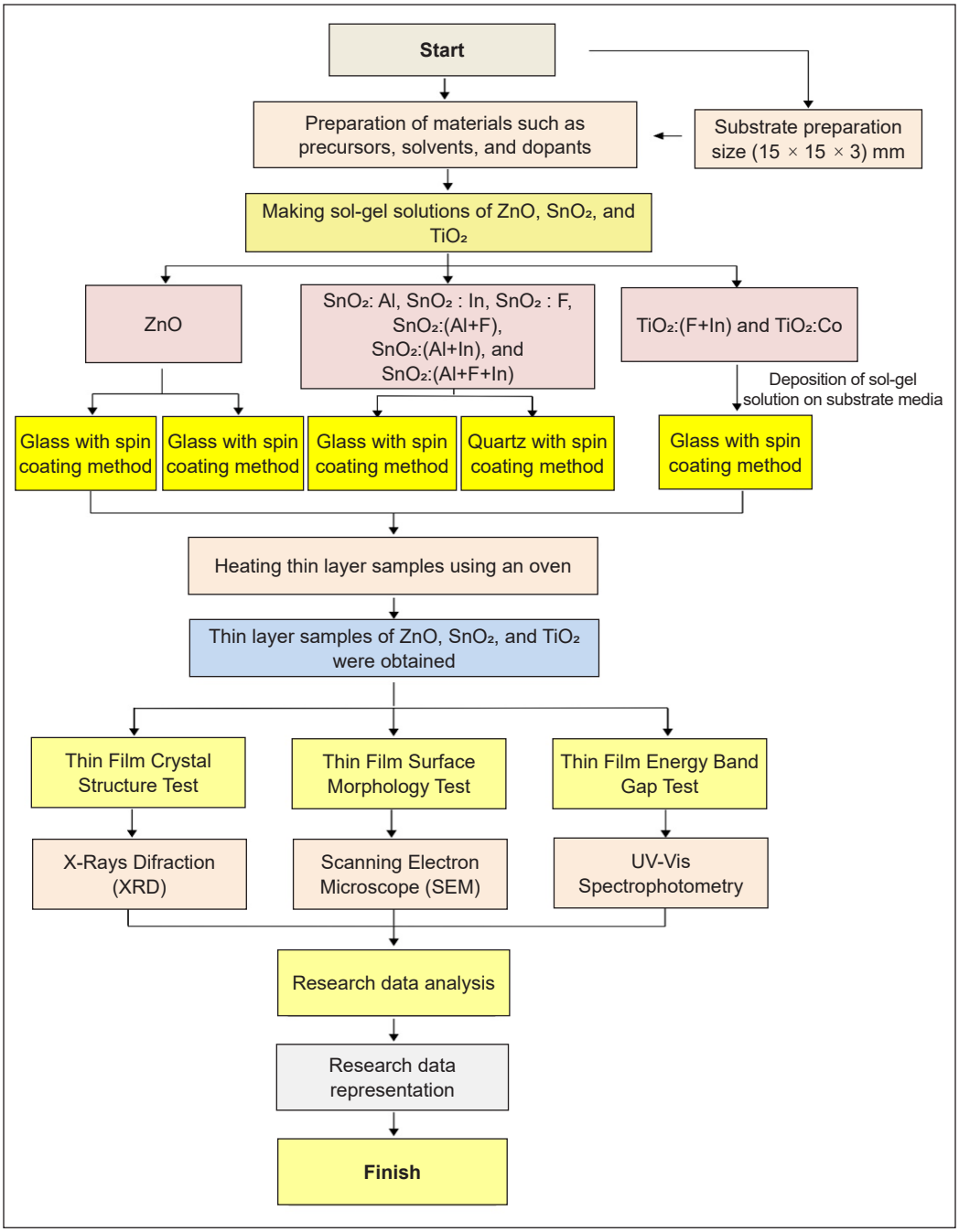

Figure 1. Research stages of ZnO, SnO_2, and TiO_2 thin films

Note. ZnO = Zinc oxide; SnO_2:Al = Tin(IV) oxide doped with aluminum; SnO_2:In = Tin(IV) oxide doped with indium; SnO_2:F = Tin(IV) oxide doped fluorine; SnO_2:(Al+F) = Tin(IV) oxide is doped with a mixture of aluminum and fluorine; SnO_2:(Al+In) = Tin(IV) oxide is doped with a mixture of aluminum and indium; SnO_2:(Al+F+In) = Tin(IV) oxide is doped with a mixture of aluminum, fluorine, and indium; TiO_2:(F+In) = Titanium dioxide doped with mixture fluorine and indium; TiO_2:Co = Titanium dioxide doped with cobalt

RESULTS AND DISCUSSION

Thin Film Synthesis

This study was conducted with the aim of determining the surface morphology structure and energy band gap value of thin films with ZnO, SnO_2, and TiO_2 precursor materials. The process of making thin layer samples begins with the process of determining the mass of each material used in the study, such as precursors and dopants. This is very important to ensure that the mass ratio between precursors and dopants is appropriate so that it can produce a homogeneous solution when mixed. The equation that can be used to determine the total mass of precursors and dopants in the study is as follows.

$$M = \frac{m_t}{m_r} \times \frac{1000}{V} \qquad [1]$$

After the total mass of the precursor and dopant materials is obtained, the precursor mass calculation process is carried out according to the concentration used in the study by referring to the following equation.

$$(100 - n)\% = \frac{m_x Prekursor \times \frac{1}{m_{r\ Prekursor}})}{m_t Dopant \times \frac{1}{M_{r\ Dopant}}} \qquad [2]$$

Where M = molarity; m_t = Total mass of the sample; m_r = Relative molecular mass; V = Volume of solution; n = Concentration; and m_x = Mass of materials used

After carrying out the material calculation process, the solution-making process is carried out by mixing the precursor and dopant with the solvent used. This process aims to ensure that all research materials used can be mixed evenly or homogeneously and produce a sol-gel solution made from ZnO, SnO_2, and TiO_2. The sol-gel solution that has been produced is then subjected to a deposition process using either the dip-coating or spin-coating method on the substrate media. The results of this deposition process are then heated using an oven, and several displays of thin layer samples with ZnO, SnO_2, and TiO_2 precursor materials are obtained as follows in Figure 2.

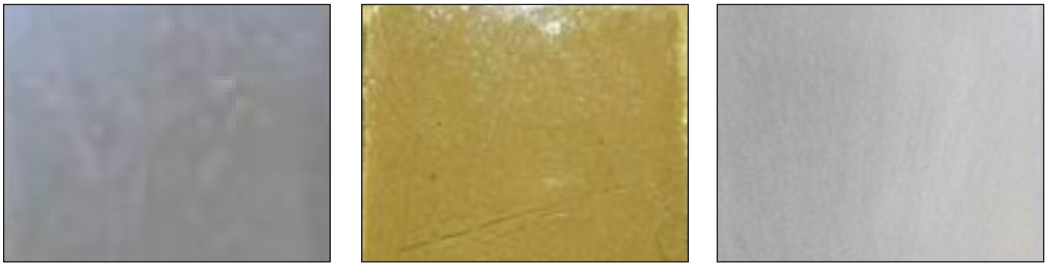

(a) (b) (c)

Figure 2. Thin film samples: (a) Zinc oxide, (b) Tin(IV) oxide, and (c) Titanium dioxide

Thin Film Characterization

Characterization is a test process to determine the extent of the character or nature of the research sample that has been carried out. Characterization in this study measures two properties of thin layer samples, namely the surface morphological structure and the energy band gap value.

Thin Film Crystal Structure

The crystal structure of the thin film was tested using XRD data with the aim of determining the crystal orientation phase and crystal size formed in the thin film sample. The measurement uses an angle range of 10° to 90° on the grounds that the crystals will be detected at a diffraction source wavelength of 1.5406 Å from the CuKa source (Ramesh et al., 2023; X. Yang et al., 2022). The measurement produces data in the form of a diffraction pattern of the relationship between intensity (y-axis) and scattering angle or 2θ (x-axis). Based on the test results, the diffraction pattern of the thin layer sample can be seen in the following Figure 3.

The differences in diffraction patterns are found in thin film samples made from ZnO, SnO_2, and TiO_2 precursors. Of course, each precursor has special characteristics that describe the characteristics of the compound. The diffraction pattern of ZnO crystal planes is (101) and hexagonal ZnO crystal. SnO_2 thin film samples generally have three highest trend peaks, which indicates that the crystal form is tetragonal. This is supported by the results of research conducted by Zaini et al. (2018), which found that the lattice parameters of the synthesized SnO_2 are almost the same as SnO_2 no. COD 969007534 in the form of a

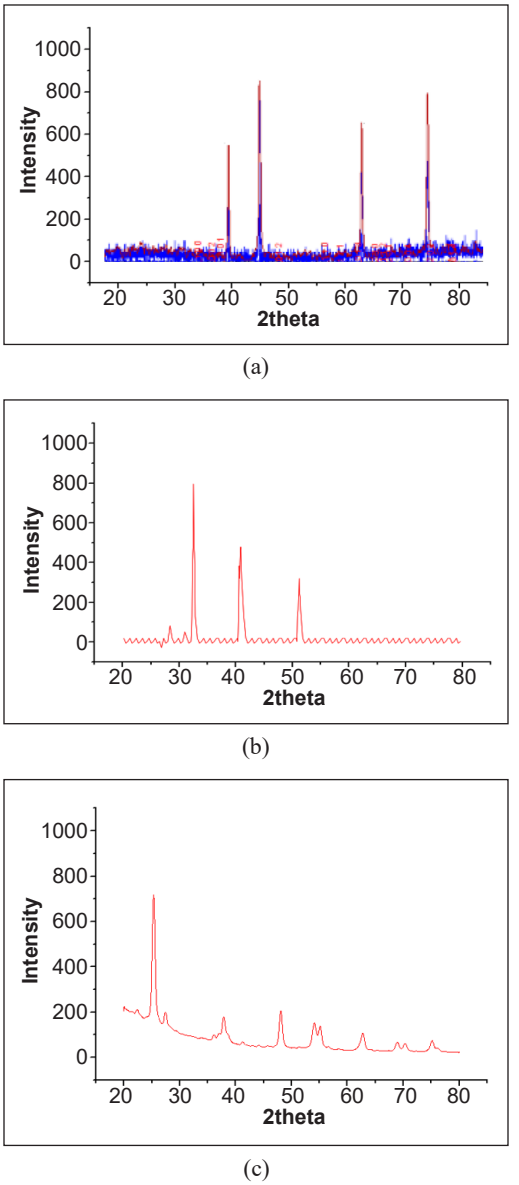

(a)

(b)

(c)

Figure 3. Diffraction patterns of thin film samples: (a) Zinc oxide, (b) Tin(IV) oxide, and (c) Titanium dioxide

tetragonal crystal structure with a space group. Meanwhile, in the TiO_2 sample, it can be seen that the highest intensity is seen, especially in the (101) plane, with the maximum intensity value produced for the highest peak in the TiO_2 sample at the 2θ value of 25°, which is in accordance with the main peak typical of the TiO_2 anatase phase (tetragonal) (Khan et al., 2020; Preeti & Rohilla, 2020). The intensity value obtained from the XRD measurement results illustrates the proportionality to the level of crystallinity of a material, where the higher the intensity of the diffractogram peak, the more perfect the crystal shape formed in the material (Khan et al., 2020; Tjahjanti, 2019).

In addition to determining the phase and form of the crystal structure, XRD test data can be used to determine the crystal grain size of thin film samples. To determine the size of the crystal particles that make up the thin film, it can be calculated by utilizing the XRD test results using the Debye-Scherrer equation (Khan et al., 2020), namely:

$$D = \frac{k\lambda}{\beta cos\theta} \qquad [3]$$

Where D = Crystal size; k = Material constant (usually 0.9); θ = Diffraction angle; λ= The wavelength of the X-ray source used; and β = Full width at half maximum (FWHM) value

Based on the results of the crystal size calculations obtained in the ZnO, SnO_2, and TiO_2 samples, they can be seen in Table 2.

Based on Table 2, it can be seen that the thin film sample with ZnO material has the smallest crystal grain size compared to the other two precursors. The width of the XRD spectrum, specifically the FWHM value, influences the value of the crystal grain size. If the FWHM value is small, the crystal grain size is large, and vice versa. Data related to crystal grain size can be used as an indicator to explain the catalytic ability of a thin film, where the smaller the crystal grain size, the larger the particle surface area so that the catalytic power will be better (Putra Parmita et al., 2023; Xian et al., 2019). According to research conducted by Li et al. (2020), photocatalysts with nano sizes ranging from 1 to 100 nm will provide high catalytic activity.

Table 2
Comparison of crystal grain size of thin film samples

Sample	Scattering angle (2θ) (deg)	Miller index (hkl)	FWHM (deg)	Crystalline grain size (D) (nm)
ZnO	44.48	101	0.2086	14.45
SnO_2	26.60	110	0.0028	43.43
TiO_2	27.44	101	0.1882	15.16

Note. ZnO = Zinc oxide; SnO_2 = Tin(IV) oxide; TiO_2 = Titanium dioxide; FWHM = Full width at half maximum

Thin Layer Surface Morphology Structure

The morphological structure of the layer can be seen using a SEM. The test method with this tool uses a high-energy beam of electrons to scan the object to produce an image and sample composition (Sahdiah & Kurniawan, 2023). The images produced by this method have better resolution and image detail than an optical microscope because the electron beam used as a source has a wavelength tens of thousands of times shorter than the wavelength of light.

The three precursors used illustrate that the surface appearance of the TiO_2 thin film has a more regular and symmetrical distribution when compared to other materials, as seen in Figure 4. Each material has its own characteristics; this can be seen in that the ZnO precursor has an appearance like a root distribution along the surface of the thin layer. This is in line with the results of research conducted by Ridhuan et al. (2012), which showed that the agglomeration process still occurs, causing the surface morphology of the particles to be larger and in the form of nanorods. This is possible because the calcination process is not yet perfect so that there is still a part of the extract that coats the particles. However, if referring to its performance, the surface conditions of this ZnO have quite high potential related to the energy band gap value. Due to lower grain boundaries, surface defects, interference, and discontinuous interfaces, one-dimensional ZnO nanostructures, such as nanorods, nanowires, and nanotubes, allow for more efficient carrier transport (Chowdhury & Bhowmik, 2021; Dutta et al., 2023).

The morphology of the sample using SnO_2 looks almost even, but there are still many cracks or boundaries along the surface of the thin layer. These cracks indicate that the deposition process of the SnO_2 solution on the substrate media is still not evenly distributed so that when the sample goes through the heating process, there is a part of the substrate surface that is only coated by the solvent used. When the heating process is carried out, of course the goal is to remove the solvent that is still present during the deposition process so that there are parts of the thin layer surface that do not contain SnO_2. To find out more specifically the inner structure of the thin layer with ZnO, SnO_2, and TiO_2 precursors, an

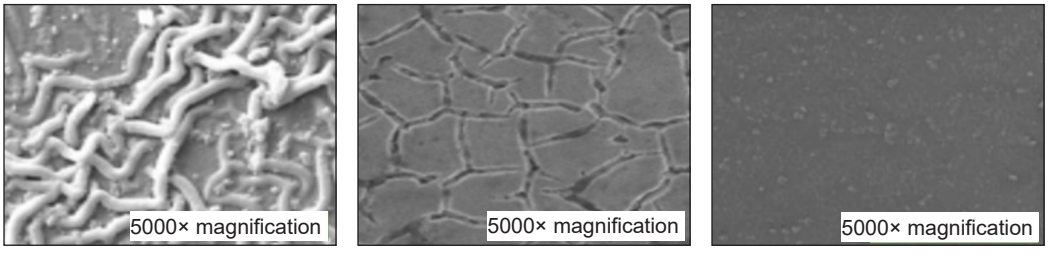

(a) (b) (c)

Figure 4. Morphological structure of surface part of thin film with precursors at 5,000× magnification : (a) Zinc oxide, (b) Tin(IV) oxide, and (c) Titanium dioxide

observation enlargement process is carried out so that researchers can watch in detail the inside of the sample, as seen in Figure 5.

TiO_2 thin film sample has a denser structure compared to the ZnO and SnO_2 samples. The size of the constituent particles also looks almost the same, namely in the form of round particles that have denser cavities, indicating that the distribution of the sol-gel solution is evenly distributed throughout the surface of the substrate used. There is agglomeration between neighboring particles, so that the particle size increases again due to the merging of neighboring particles. The shape of the TiO_2 sample particles tends to resemble balls, where the particle size is large and agglomeration occurs in the sample (Listanti et al., 2018). This condition allows the formation of denser crystal particles and increases the ability of TiO_2 in the absorption process. This is what makes TiO_2 one of the precursors that is often used in developing solar cell nanoparticle technology.

In the three results, it can be seen that SnO_2 and TiO_2 have almost the same crystal structure. Both precursors have a round shape that forms the surface of the thin film. This is supported by the results of research conducted by Firooz et al. (2009), where in their research one of the forms of the structure of the thin layer made from SnO_2 is granules apart from the flower and sheet forms. This is different from ZnO, which has a structure resembling a tube or is often called nanorods. The nanostructures of ZnO are very diverse, such as nanobelts, nanoplatelets, nanowires, and nanorods (Novitasari et al., 2022; Raub et al., 2024).

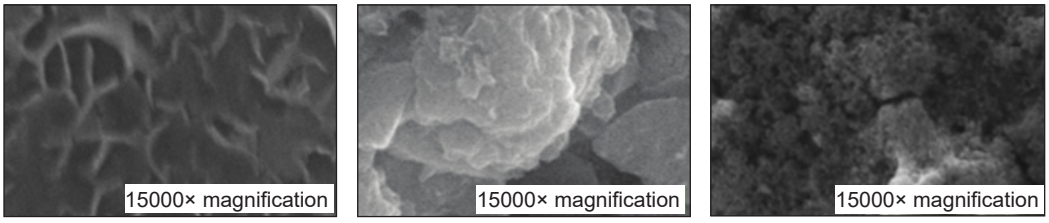

(a) (b) (c)

Figure 5. Morphological form of the inner structure of thin layers with precursors at 15,000× magnification: (a) Zinc oxide, (b) Tin(IV) oxide, and (c) Titanium dioxide

Thin Film Energy Band Gap

The energy band gap is the most important part or one of the indicators that need to be considered in the development process of various nanoparticle technologies. The energy band gap value describes the ability of a material to conduct electricity (Bouzidi et al., 2024). So that good materials in thin film technology must be able to enter the semiconductor material category. Semiconductors are materials that have electrical conductivity between conductors and insulators, or materials that have resistivity between conductors and insulators, namely 10^{-2}-10^{-9} Ωm (Maslakah, 2015). In semiconductor materials, the valence

band condition is almost full, and the conduction band is almost empty with a very small forbidden band width (Eg) (±1 to 2 eV) (Tjahjanti, 2019; Woods-Robinson et al., 2020). It is necessary to know the measurement of the energy band gap of a semiconductor material because the nature of the energy band gap has implications for the differences in the nature of the dependence of the absorbance coefficient on the photon frequency (Mikrajudin, 2010, as cited in Doyan & Humaini, 2017, p. 38). The process of calculating the energy band gap using the absorption value data of the thin layer sample analyzed using the Tauc Plot approach to obtain a slope that describes the relationship between $(ahv)^n$ and photon energy (hv). The Tauc Plot graph that represents the energy band gap value of the thin layer sample can be seen in the following image.

The energy band gap value in each thin layer can be determined by extrapolating from the relationship graph (hv) as the abscissa and $(ahv)^n$ as the ordinate until it intersects the energy axis (the resulting slope graph) and the optical band gap value is obtained. Of course, by using this approach, we obtain energy band gap values that are easier to represent, as seen in Figure 6. By using the same approach and method, then in this study, there are at least 11 research samples derived from three precursor materials, namely ZnO, SnO_2, and TiO_2, and using 4 dopant materials, namely indium (In), aluminum (Al), fluorine (F), and cobalt (Co). To facilitate the discussion process, all samples and the energy band gap value for each thin film sample in this study have been recorded (Table 3).

To analyse in depth the various factors that affect the energy band gap value, the use of the solution deposition method, the use of substrates, and the influence of dopants can be seen in the following description.

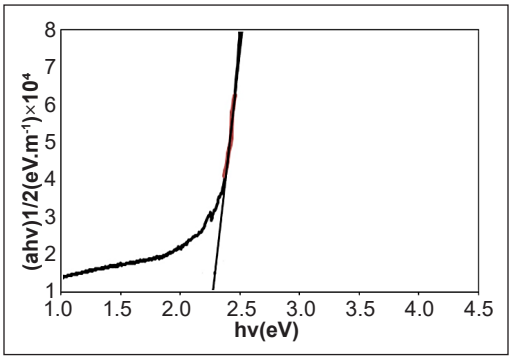

(a)

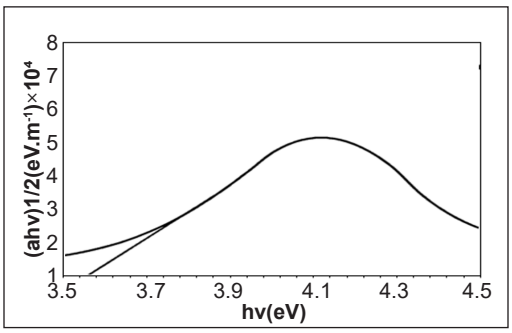

(b)

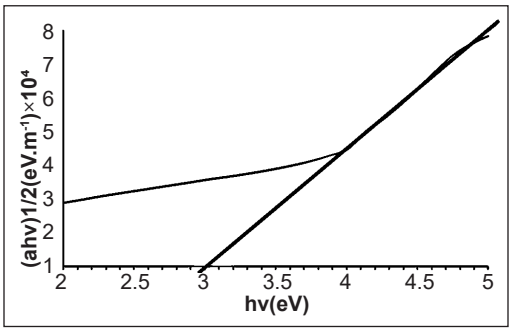

(c)

Figure 6. Comparison of Tauc Plot graphs of energy band gap of thin films: (a) Zinc oxide, (b) Tin(IV) oxide, and (c) Titanium dioxide

Table 3
Thin film energy band gap

No.	Sample	Sample code	Energy band gap value (eV)
1	Zinc oxide	ZnO type A	2.00 – 2.10
2	Zinc oxide	ZnO type B	2.03 – 2.98
3	Tin(IV) oxide doping aluminum	SnO_2:Al type A	3.24 – 3.30
4	Tin(IV) oxide doping aluminum	SnO_2:Al type B	3.50 – 3.57
5	Tin(IV) oxide doping indium	SnO_2:In	3.55 – 3.62
6	Tin(IV) oxide doping fluorine	SnO_2:F	3.53 – 3.59
7	Tin(IV) oxide doping aluminum and fluorine	SnO_2:(Al+F)	3.47 – 3.56
8	Tin(IV) oxide doping aluminum and indium	SnO_2:(Al+In)	3.45 – 3.51
9	Tin(IV) oxide doping aluminum, fluorine, and indium	SnO_2:(Al+F+In)	3.36 – 3.50
10	Titanium dioxide doping fluorine and indium	TiO_2:(F+In)	2.97 – 3.23
11	Titanium dioxide doping cobalt	TiO_2:Co	3.22 – 3.44

Note. ZnO = Zinc oxide; SnO_2:Al = Tin(IV) oxide doped with aluminum; SnO_2:In = Tin(IV) oxide doped with indium; SnO_2:F = Tin(IV) oxide doped fluorine; SnO_2:(Al+F) = Tin(IV) oxide is doped with a mixture of aluminum and fluorine; SnO_2:(Al+In) = Tin(IV) oxide is doped with a mixture of aluminum and indium; SnO_2:(Al+F+In) = Tin(IV) oxide is doped with a mixture of aluminum, fluorine, and indium; TiO_2:(F+In) = Titanium dioxide doped with mixture fluorine and indium; TiO_2:Co = Titanium dioxide doped with cobal

The Effect of Using Prekursor

Referring to the energy band gap value in Table 3, it can be seen that the ZnO thin film has the smallest energy band gap value compared to other thin film samples using SnO_2 and TiO_2 precursor materials. Both ZnO thin film samples using the dip-coating and spin-coating methods have the lowest energy band gap, reaching a value of 2.00. This condition certainly allows for easy electron transfer from the valence band to the conduction band. If the width of the energy gap decreases, it allows more electrons to undergo electronic transitions from the valence band to the conduction band so that the thin film becomes more conductive (Klein et al., 2010).

In general conditions, ZnO already has an energy band gap value of 3.37 eV and a binding energy of 60 MeV (Tarwal & Patil, 2011). ZnO and TiO_2 are two types of materials that have good energy band gap values in the process of developing solar cell technology when compared to SnO_2. In optimizing the efficiency of perovskite solar cells, one of the materials that plays an important role is the electron transport material (electron transport material [ETM]) made of metal oxide semiconductors such as TiO_2 and ZnO (Yurestira et al., 2021).

In addition to its energy band gap value, ZnO is considered a basic material for the development of various nanoparticle technologies because this material can be developed using various methods, not only focusing on dip-coating and spin-coating.

ZnO nanomaterials can be synthesized using several methods, including vapor-liquid-solid (VLS), aqueous chemical growth (ACG), chemical vapor deposition (CVD), electrochemical deposition (ECD), physical vapor deposition (PVD), metal-organic chemical vapor deposition (MOCVD), and chemical vapor transport and condensation (CVTC) (Maddu et al., 2023; Santibenchakul et al., 2018; Silva et al., 2022; Veerabhadraiah et al., 2022).

Referring to the size of the crystal structure of each precursor component as seen in Table 2, the smaller the energy band gap value produced, the smaller the crystal grain size value. ZnO with the smallest crystal size has an average energy band gap value lower than the precursors SnO_2 and TiO_2. Of the three precursors, it can be seen that ZnO and TiO_2 tend to have the same energy band gap crystal grain size. This is because both materials have almost the same physical and chemical properties as precursor materials in the development of thin film research. In other studies, it was found that these two precursors can be used as materials that are paired and formed into multi-layers (Bhatti et al., 2019; Boukerche et al., 2019; Rad et al., 2023). According to Hakim and Haris (2016), small crystal sizes can expand the catalyst surface so that the catalyst performance becomes more effective, which indicates that the energy band gap value will also decrease, thus increasing the catalyst performance in thin layers.

The Effect of Using the Solution Deposition Method

In this study, to see the extent to which the use of variations in solution deposition methods differs, two methods most often used by researchers are used, namely, dip-coating and spin-coating. The use of these two methods can be seen in thin layers of ZnO precursor material with sample codes ZnO type A for the sol-gel dip-coating method and ZnO type B for the sol-gel spin-coating method. Based on the data in Table 3, it can be seen that the two ZnO samples have energy band gap values that are not much different. The ZnO sample with the dip coating method has a lower energy band gap value with the smallest value at 2.00 eV and the highest at 2.10 eV. A comparison of the lowest and highest energy band gap values between the two samples can be seen in Figure 7.

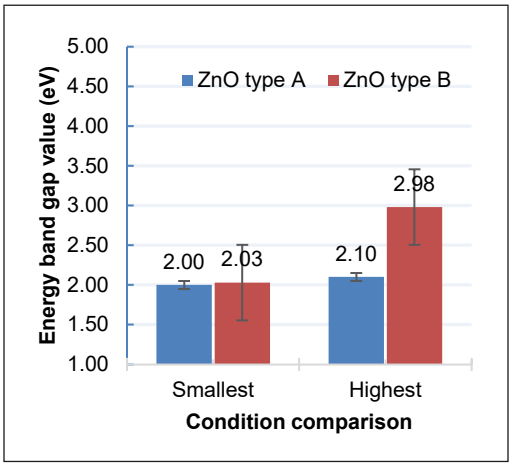

Figure 7. Comparison of energy band gap values of zinc oxide (ZnO) thin films based on the layer deposition method

The energy band gap value in the thin film sample has a significant difference at the highest value. Referring to the results

above, the ZnO type A thin film has a much better value because the range of its values is in the range of 2.00 - 2.10 eV, while in the ZnO type B thin film sample, the range of energy band gap values is 2.03 - 2.98 eV. In thin film development research, the slightest difference in the energy band gap value greatly affects the performance of the device. The use of the dip-coating method provides better energy band gap values compared to using the spin-coating method.

The dip-coating method is a process where a substrate is dipped into a solution and then lifted vertically at a constant speed (Tang & Yan, 2017). The precursor solution that sticks to the substrate and forms a thin layer because the solvent will evaporate and some of the solution will fall due to gravity (Brinker, 2013). The thickness of the solution can be adjusted according to the speed of the substrate withdrawal. This method has been successfully used to create a thin layer of ferroelectric and electronic semiconductor materials (Mukhsinin et al., 2019). This method is widely in demand because the process is simple and does not require expensive costs; besides, it does not damage the environment, and the equipment used is not so complex (Djarwanti & Syahrono, 2014; Patil et al., 2023).

The Effect of Using Substrate Media

The substrate media used in this study consisted of two types, namely glass and quartz. Both of these materials generally have almost the same characteristics because they are included in TCO materials; only for quartz, it is composed of minerals formed from silicon and oxygen chemical compounds with the chemical composition SiO_2 (Imawanti et al., 2017). The selection of media use needs to be considered by researchers; the orientation of the substrate material affects the characteristics of nucleation and growth that dominate the microstructural properties and physical properties of thin films (Mousa et al., 2015).

To determine the effect of using substrate media in this study, we refer to the sample code SnO_2:Al type A using quartz media and the sample code SnO_2:Al type B using glass media as seen in Figure 8. The difference in energy band gap values in the two types of media can be seen in the following graph.

The SnO_2 type A thin film sample using quartz as a substrate produces a smaller energy band gap value compared to using glass. This difference is seen both in the smallest and largest values. This certainly

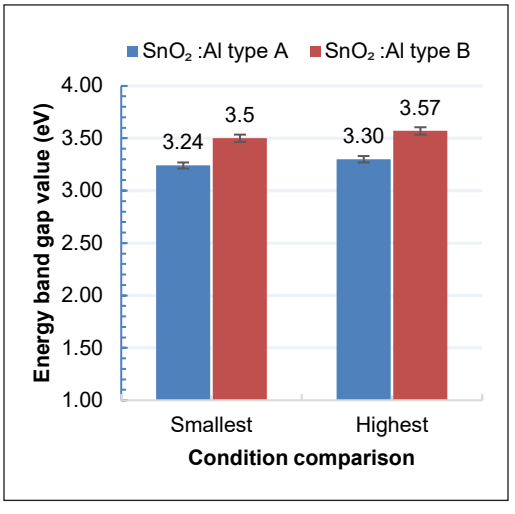

Figure 8. Comparison of energy band gap values of tin(IV) oxide (SnO_2) thin films based on substrate media

indicates that the use of media has an effect on the energy band gap value produced in the thin film sample. An important difference between quartz glass and ordinary glass is its good transmittance across the spectrum, especially in the ultraviolet and deep ultraviolet spectra, which are not available in ordinary optical glass (Ehrt, 2018; Khashan & Nassif, 2001).

Quartz is the most important polymorph of the silica group (SiO_2) and one of the purest minerals in the earth's crust. The SiO_2 system is quite intricate. Despite having the straightforward chemical formula SiO_2, it has at least 15 known variations or polymorphs, or mineral phases with distinct crystal shapes but the identical stoichiometric composition (Götze et al., 2021). As a major component of sedimentary, metamorphic, and magmatic rocks, quartz is the most significant silica polymorph found in nature. Furthermore, one silica raw material that is economically significant is quartz. Single crystals and polycrystalline quartz are both utilized in industry, for instance, as silicon metal ore, refractory materials, or high-purity quartz crystals or sands (Götze et al., 2021).

The Effect of Using Dopan

Doping is a process that aims to change the characteristics of a material so that it can achieve certain conditions and according to the needs required by researchers. The use of various dopants is certainly one of the alternative variables that are often used by researchers to determine the extent of the properties produced in thin layers. In this study, of course, the main purpose of using dopant variations is to obtain thin layer samples with the smallest energy band gap values. Research data related to the effect of dopant use can be observed in samples with SnO_2 and TiO_2 precursor materials, where both precursors are treated with cross-sections of various types of dopants such as aluminum, indium, fluorine, and cobalt. Data related to the comparison of energy band gap values in thin layers made of SnO_2 and TiO_2 (Figures 9 and 10).

The dopant incorporation process gives a better effect on the process of reducing the energy band gap in both SnO_2 and TiO_2 precursors. This can be seen from the results of the values of each sample, namely SnO_2: (Al+ F+In) and TiO_2: (F+In), which have the smallest energy band gap values with values of 3.36 and 2.97 eV, respectively. If researchers look at the overall results of the energy band gap values of thin film samples, it can be seen that the use of various dopants gives varying results. This is certainly because the characteristics of each element are different from one another.

Various studies have shown that the use of two or more dopants in one deposition process has a better impact on changing the properties or characteristics of thin film samples. Research conducted by Han et al. (2018) proved that tridoping has higher photocatalytic activity compared to pure SnO_2, SnO_2-ZnO, or mono- or di-doped SnO_2-ZnO thin films. SnO_2-ZnO tridoped B/Ag/F composite thin films have the highest photocatalytic

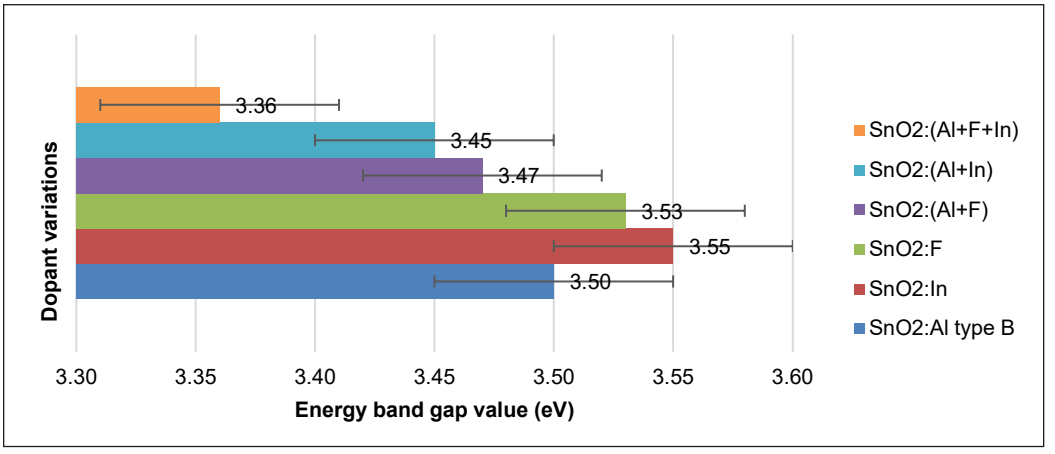

Figure 9. Comparison of Tin(IV) oxide (SnO_2) energy band gap values based on dopant variables
Note. SnO_2:(Al+F+In) = Tin(IV) oxide is doped with a mixture of aluminum, fluorine, and indium; SnO_2:(Al+In) = Tin(IV) oxide is doped with a mixture of aluminum and indium; SnO_2:(Al+F) = Tin(IV) oxide is doped with a mixture of aluminum and fluorine; SnO_2:F = Tin(IV) oxide doped fluorine; SnO_2:In = Tin(IV) oxide doped with indium; SnO_2:Al = Tin(IV) oxide doped with aluminum

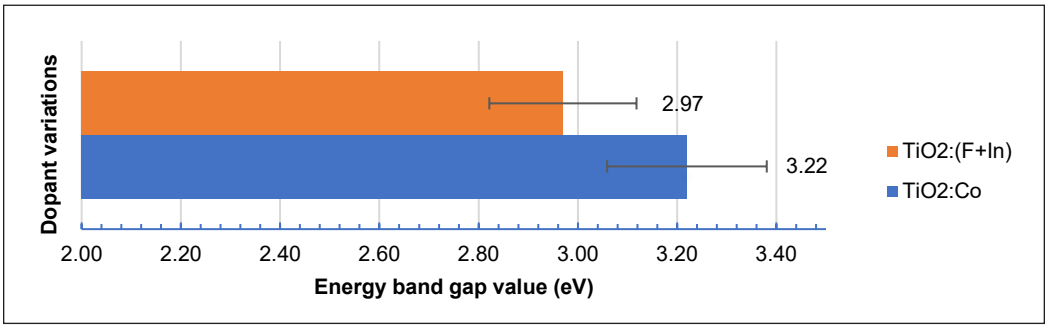

Figure 10. Comparison of Titanium dioxide (TiO_2) energy band gap values based on dopant variables
Note. TiO_2:(F+In) = Titanium dioxide doped with mixture fluorine and indium; TiO_2:Co = Titanium dioxide doped with cobalt

activity. The composition of SnO_2-ZnO and tridoping B/Ag/F are very important for the photocatalytic activity of thin films. The low electron-hole pair recombination rate and strong light absorption appear to be correlated with the increased activity of SnO_2-ZnO tridoped B/Ag/F thin films.

The same condition also occurs in the thin layer of TiO_2 that the provision of double doping is able to produce better characteristics compared to the use of single doping. This is supported by research conducted by Ashkarran et al. (2014), which obtained the results that after optimizing the dopant concentration, the research findings showed that TiO_2 nanoparticles (NPs) with double doping had the highest photocatalytic and antibacterial activities when compared to TiO_2 NPs with single doping. In contrast, TiO_2 NPs with silver

and nitrogen doping expanded the light absorption spectrum towards the visible region and significantly increased the photodegradation of model dyes and inactivation of bacteria under visible light irradiation. When TiO_2 is exposed to visible light, two different electronic states capture its inner electrons and narrow the band gap. This changes the optical response from the ultraviolet region to the visible light region, which is responsible for the better photocatalytic activity and antibacterial quality of TiO_2 NPs with double doping.

CONCLUSION

Based on the results of data analysis and discussion, it can be concluded that 1) the crystal structure of ZnO thin films is hexagonal while SnO_2 and TiO_2 are tetragonal, 2) the surface morphology of SnO_2 and TiO_2 thin films is granular, while ZnO thin films are nanorod, and 3) the smallest energy band gap value is found in ZnO thin films with a value of 2.00 eV. There are four factors that affect the energy band gap value in thin films, namely precursor materials, deposition methods, substrate media, and dopant materials. Each variable that produces the smallest energy band gap value in this study is the ZnO precursor, dip-coating method, quartz substrate media, and the use of double or triple dopants in one deposition treatment.

ACKNOWLEDGEMENTS

The author would like to thank those who have helped in making this article, especially the Laboratory Analytical Chemistry and Basic Chemistry Laboratory of the Faculty of Mathematics and Natural Sciences at Mataram University, the Integrated Science Laboratory of Mataram State Islamic University, the Laboratory Physics Department Institute Technology Bandung, and the Integrated Laboratory of Diponegoro University.

REFERENCES

Ashkarran, A. A., Hamidinezhad, H., Haddadi, H., & Mahmoudi, M. (2014). Double-doped TiO_2 nanoparticles as an efficient visible-light-active photocatalyst and antibacterial agent under solar simulated light. *Applied Surface Science*, *301*, 338-345. https://doi.org/10.1016/j.apsusc.2014.02.074

Atay, H. Y. (2020). Fabrication methods for polymer coatings. In Inamuddin., R. Boddula, M. I. Ahamed, & A. M. Asiri (Eds.), *Polymer coatings: Technology and applications* (pp. 1-20). Scrivener Publishing. https://doi.org/10.1002/9781119655145.ch1

Bedghiou, D., Reguig, F. H., & Boumaza, A. (2019). Novel high/ultrahigh pressure structures of TiO_2 with low band gaps. *Computational Materials Science*, *166*, 303-310. https://doi.org/10.1016/j.commatsci.2019.05.016

Bhatti, K. A., Khan, M. I., Saleem, M., Alvi, F., Raza, R., & Rehman, S. (2019). Analysis of multilayer based TiO_2 and ZnO photoanodes for dye-sensitized solar cells. In *Materials Research Express* (Vol. 6, No. 7, p. 075902). IOP Publishing. https://doi.org/10.1088/2053-1591/ab11e8

Boukerche, S., Himour, A., Bououdina, M., Bensouici, F., & Ouchenane, S. (2019). Multilayered ZnO/TiO_2 nanostructures as efficient corrosion protection for stainless steel 304. In *Materials Research Express* (Vol. 6, No. 5, p. 055052). IOP Publishing. https://doi.org/10.1088/2053-1591/ab042f

Bouzidi, M., Bechir, M. B., Almalawi, D. R., Smaili, I. H., & Aljuaid, F. (2024). From molecular salt to layered network: cation-driven tuning of band gap, structure, and charge transport in $A_3Bi_2I_9$ (A= Cs, Rb) perovskites. *RSC Advances*, *14*(32), 23058-23072. https://doi.org/10.1039/D4RA04464A

Brinker, C. J. (2013). Dip coating. In T. Schneller, R. Waser, M. Kosec, & D. Payne (Eds.), *Chemical solution deposition of functional oxide thin films* (pp. 233-261). Springer. https://doi.org/10.1007/978-3-211-99311-8_10

Butt, M. A. (2022). Thin-film coating methods: A successful marriage of high-quality and cost-effectiveness - A brief exploration. *Coatings*, *12*(8), 1115. https://doi.org/10.3390/coatings12081115

Chowdhury, N. K., & Bhowmik, B. (2021). Micro/nanostructured gas sensors: The physics behind the nanostructure growth, sensing and selectivity mechanisms. *Nanoscale Advances*, *3*(1), 73-93. https://doi.org/10.1039/D0NA00552E

Costa, B. H., Tayama, G. T., Rivera, V. A. G., Messaddeq, Y., & Santagneli, S. H. (2025). Effects of the thermal treatment on structural and luminescence properties of Er^{3+}-doped aluminophosphosilicate glasses obtained by the sol-gel method. *Journal of Alloys and Compounds*, *1010*, 177112. https://doi.org/10.1016/j.jallcom.2024.177112

Djarwanti, D., & Syahroni, C. (2014). Pengaruh H_2O_2, pH dan sumber sinar pada degradasi air limbah pewarna indigo menggunakan katalis TiO_2 [Influence of H_2O_2, pH, and light source on the degradation of indigo dye wastewater using TiO_2 catalyst]. *Jurnal Riset Teknologi Pencegahan Pencemaran Industri*, *5*(1), 7-14. https://doi.org/10.21771/jrtppi.2014.v5.no1.p7-14

Doyan, A., & Humaini, H. (2017). Sifat optik lapisan tipis ZnO [Optical properties of ZnO thin layers]. *Jurnal Pendidikan Fisika dan Teknologi*, *3*(1), 34-39. https://doi.org/10.29303/jpft.v3i1.321

Doyan, A., Susilawati, & Imawanti, Y. D. (2017). Synthesis and characterization of SnO_2 thin layer with a doping aluminum is deposited on quartz substrates. In *AIP Conference Proceedings* (Vol. 1801, No. 1, p. 020005). AIP Publishing. https://doi.org/10.1063/1.4973083

Doyan, A., Susilawati. & Munandar, H. (2021). Optical characteristics of tin oxide thin films doped with indium and aluminum using the sol-gel spin coating technique. In *Proceedings of the 7th International Conference on Research, Implementation, and Education of Mathematics and Sciences* (pp. 396-403). Atlantis Press. https://doi.org/10.2991/assehr.k.210305.057

Dutta, T., Noushin, T., Tabassum, S., & Mishra, S. K. (2023). Road map of semiconductor metal-oxide-based sensors: A review. *Sensors*, *23*(15), 6849. https://doi.org/10.3390/s23156849

Efelina, V. (2017). Preparasi dan penentuan energi gap film tipis TiO_2:Cu yang ditumbuhkan menggunakan *spin coating* [Preparation and determination of gap energy of TiO_2:Cu thin films grown using spin coating]. *Jurnal Pendidikan Fisikadan Keilmuan*, *3*(1), 19-27. https://doi.org/10.25273/jpfk.v3i1.941

Ehrt, D. (2018). Deep-UV materials. *Advanced Optical Technologies*, *7*(4), 225-242. https://doi.org/10.1515/aot-2018-0023

Firooz, A. A., Mahjoub, A. R., & Khodadadi, A. A. (2009). Effects of flower-like, sheet-like and granular SnO_2 nanostructures prepared by solid-state reactions on CO sensing. *Materials Chemistry and Physics*, *115*(1), 196-199. https://doi.org/10.1016/j.matchemphys.2008.11.028

Götze, J., Pan, Y., & Müller, A. (2021). Mineralogy and mineral chemistry of quartz: A review. *Mineralogical Magazine*, *85*(5), 639-664. https://doi.org/10.1180/mgm.2021.72

Hakim, A. R., & Haris, A. (2016). Sintesis fotokatalis ZnO-Al dan aplikasinya pada degradasi fenol dan reduksi Cd(II) secara simultan [Synthesis of ZnO-Al photocatalyst and its application in simultaneous phenol degradation and Cd(II) reduction]. *Jurnal Kimia Sains dan Aplikasi*, *19*(1), 7-10. https://doi.org/10.14710/jksa.19.1.7-10

Han, K., Peng, X.-L., Li, F., & Yao, M.-M. (2018). SnO_2 composite films for enhanced photocatalytic activities. *Catalysts*, *8*(10), 453. https://doi.org/10.3390/catal8100453

Imawanti, Y. D., Doyan, A., & Gunawan, E. R. (2017). Sintesis lapisan tipis (thin film) SnO_2 dan SnO_2: Al menggunakan teknik sol-gel spin coating pada substrat kaca dan quartz [Thin film synthesis of SnO_2 and SnO_2: Al using sol-gel spin coating techniques on glass and quartz substrates]. *Jurnal Penelitian Pendidikan IPA*, *3*(1). https://doi.org/10.29303/jppipa.v3i1.49

Jafri, N. N. M., & Jaafar, J. (2024). Dip coating technique. In M. H. D. Othman, M. A. Rahman, T. Matsuura, M. R. Adam, & S. N. N. M. Makhtar (Eds.), *Advanced ceramics for photocatalytic membranes* (pp. 101-127). Elsevier. https://doi.org/10.1016/B978-0-323-95418-1.00016-1

Khalaj, G., Soleymani, F., Sharifi, F., & Najafi, A. (2023). Evaluation of APC impact on controlling precursors properties in the sol for synthesizing meso porous ZrC nanopowder through sol-gel process. *Journal of Materials Research and Technology*, *26*, 6182-6192. https://doi.org/10.1016/j.jmrt.2023.08.287

Khan, H., Yerramilli, A. S., D'Oliveira, A., Alford, T. L., Boffito, D. C., & Patience, G. S. (2020). Experimental methods in chemical engineering: X-ray diffraction spectroscopy - XRD. *The Canadian Journal of Chemical Engineering*, *98*(6), 1255-1266. https://doi.org/10.1002/cjce.23747

Khasanah, J. U., Mukaromah, A. H., & Dewi, S. S. (2019). Penurunan jumlah bakteri *Eschercherichia coli* dengan penyaringan membran zeolit ZSM-5/TiO_2 [Decreasing the number of *Eschercherichia coli* bacteria by ZSM-5/TiO_2 zeolite membrane filtering]. *Prosiding Seminar Nasional Mahasiswa Unimus*, *2*, 271-276.

Khashan, M. A., & Nassif, A. Y. (2001). Dispersion of the optical constants of quartz and polymethyl methacrylate glasses in a wide spectral range: 0.2–3 μm. *Optics Communications*, *188*(1-4), 129-139. https://doi.org/10.1016/S0030-4018(00)01152-4

Klein, A., Körber, C., Wachau, A., Säuberlich, F., Gassenbauer, Y., Harvey, S. P., Harvey, S. P., Proffit, D. E., & Mason, T. O. (2010). Transparent conducting oxides for photovoltaics: Manipulation of fermi level, work function and energy band alignment. *Materials*, *3*(11), 4892-4914. https://doi.org/10.3390/ma3114892

Koziej, D., Lauria, A., & Niederberger, M. (2014). 25th anniversary article: Metal oxide particles in materials science: Addressing all length scales. *Advanced Materials*, *26*(2), 235-257. https://doi.org/10.1002/adma.201303161

Li, D., Song, H., Meng, X., Shen, T., Sun, J., Han, W., & Wang, X. (2020). Effects of particle size on the structure and photocatalytic performance by alkali-treated TiO_2. *Nanomaterials*, *10*(3), 546. https://doi.org/10.3390/nano10030546

Listanti, A., Taufiq, A., Hidayat, A., & Sunaryono, S. (2018). Investigasi struktur dan energi band gap partikel nano TiO_2 hasil sintesis menggunakan metode sol-gel [Investigation of the structure and band gap energy of TiO_2 nanoparticles synthesized using the sol-gel method]. *Journal of Physical Science and Engineering*, *3*(1), 8-15. https://doi.org/10.17977/um024v3i12018p008

Maddu, A., Zikri, Z., & Irzaman, I. (2023). Structure and morphology of ZnO nanoparticles prepared by sonochemical method. *TIME in Physics*, *1*(2), 51-58. https://doi.org/10.11594/timeinphys.2023.v1i2p51-58

Maslakah, U. (2015). *Analisis lebar celah pita energi dan ikatan molekul lapisan tipis a-Si:H yang ditumbuhkan dengan metode PECVD* [Analysis of energy band gap and molecular bonding of a-Si:H thin films deposited by PECVD method] [Bachelor's thesis, Institut Teknologi Sepuluh Nopember]. ITS Repository. https://repository.its.ac.id/51894/1/1110100030-Undergraduate%20Thesis.pdf

McIvor, R., & Humphreys, P. (2004). Early supplier involvement in the design process: Lessons from the electronics industry. *Omega*, *32*(3), 179-199. https://doi.org/10.1016/j.omega.2003.09.005

Mousa, A. O., Habubi, N. F., & Nema, N. A. (2015). Substrate effects on structural and optical properties of ZnO thin films deposited by chemical spray pyrolysis. *International Letters of Chemistry, Physics and Astronomy*, *51*, 69-77. https://doi.org/10.56431/p-gcf022

Mukhsinin, A., Nehru, N., & Afrianto, M. F. (2019). Rancang bangun alat pembuat lapisan tipis metode dip coating berbasis arduino uno [Design and build a thin layer maker using the arduino uno based dip coating method]. *Jurnal Ilmu Fisika dan Pembelajarannya*, *3*(2), 76-83. https://doi.org/10.19109/jifp.v3i2.4117

Muliyadi, L., Doyan, A., Susilawati, S., & Hakim, S. (2019). Synthesis of SnO_2 thin layer with a doping fluorine by sol-gel spin coating method. *Jurnal Penelitian Pendidikan IPA*, *5*(2), 175-178. https://doi.org/10.29303/jppipa.v5i2.257

Najafi, A., Sharifi, F., Mesgari-Abbasi, S., & Khalaj, G. (2022). Influence of pH and temperature parameters on the sol-gel synthesis process of meso porous ZrC nanopowder. *Ceramics International*, *48*(18), 26725-26731. https://doi.org/10.1016/j.ceramint.2022.05.367

Norris, D. J., Efros, A. L., & Erwin, S. C. (2008). Doped nanocrystals. *Science*, *319*(5871), 1776-1779. https://doi.org/10.1126/science.1143802

Novitasari, D., Lusiana, L. A., Sembiring, S., & Junaidi. (2022). Studi pendahuluan penentuan nilai energi band gap komposit perak silika (Ag/SiO_2) berbasis sekam padi [A preliminary study to determine the band gap energy value of silica silver composite (Ag/SiO_2) based on rice husk]. *Jurnal Teori dan Aplikasi Fisika*, *10*(1), 36-40. https://doi.org/10.23960/jtaf.v10i1.2892

Nunes, P., Fortunato, E., Tonello, P., Fernandes, F. B., Vilarinho, P., & Martins, R. (2002). Effect of different dopant elements on the properties of ZnO thin films. *Vacuum*, *64*(3-4), 281-285. https://doi.org/10.1016/S0042-207X(01)00322-0

Pandit, N. A., & Ahmad, T. (2022). Tin oxide based hybrid nanostructures for efficient gas sensing. *Molecules*, *27*(20), 7038. https://doi.org/10.3390/molecules27207038

Patil, S. L., Sankapal, S. R., & Almuntaser, F. M. A. (2023). Dip coating: Simple way of coating thin films. In B. R. Sankapal, A. Ennaoui, R. B. Gupta, & C. D. Lokhande (Eds.), *Simple chemical methods for thin film deposition: Synthesis and applications* (pp. 425-447). Springer. https://doi.org/10.1007/978-981-99-0961-2_10

Paul David, S., Soosaimanickam, A., Sakthivel, T., Sambandam, B., & Sivaramalingam, A. (2021). Thin film metal oxides for displays and other optoelectronic applications. In S. Rajendran, J. Qin, F. Gracia, & E. Lichtfouse (Eds.), *Metal and metal oxides for energy and electronics* (pp. 185-250). Springer. https://doi.org/10.1007/978-3-030-53065-5_6

Prastiwi, W. D., Maulana, K. D., Wibowo, E. A. P., Aji, N. R., & Setyani, A. (2017). Sintesis dan karakteristik TiO_2 dan SiO_2 serta aplikasinya terhadap kadar Fe dalam air sumur [Synthesis and characteristics of TiO_2 and SiO_2 and its application to Fe levels in well water]. *Jurnal Ilmiah Sains*, *17*(1), 30-34. https://doi.org/10.35799/jis.17.1.2017.15220

Preeti., & Rohilla, S. (2020). Rietveld refinement and structural characterization of $TiO_2/CoFe_2O_4$ nanocomposites. In *IOP Conference Series: Materials Science and Engineering* (Vol. 872, No. 1, p. 012171). IOP Publishing. https://doi.org/10.1088/1757-899X/872/1/012171

Putra Parmita, A. W. Y. P., Panji., Sasongko, A., Qulub, F., & Triana, Y. (2023). Studi pengaruh temperatur kalsinasi dalam pembentukan nanomagnetite dengan metode green synthesis ekstrak daun nanas [Study of the influence of calcination temperature on the formation of nanomagnetite using the green synthesis method of pineapple leaf extract]. *SPECTA Journal of Technology*, *7*(2), 584-592. https://doi.org/10.35718/specta.v7i2.940

Rad, A. S., Afshar, A., & Azadeh, M. (2023). Antireflection and photocatalytic single layer and double layer ZnO and ZnO-TiO_2 thin films. *Optical Materials*, *136*, 113501. https://doi.org/10.1016/j.optmat.2023.113501

Rahmawati, E., & Agustina, S. (2018). Rekayasa permukaan lapisan tipis kitosan sebagai dasar pengembangan teknologi *self cleaning* [Surface engineering of a thin layer of chitosan as a basis for the development of self-cleaning technology]. *Gravity Edu: Jurnal Pembelajaran dan Pengajaran Fisika*, *1*(2), 16-19. https://doi.org/10.33627/ge.v2i2.95

Ramesh, K. S., Saravanabhavan, M., Muhammad, S., Edison, D., Ho, M.-S., Sekar, M., & Al-Sehemi, A. G. (2023). Synthesis, physico-chemical characterization and quantum chemical studies of 2, 3-dimethyl quinoxalinium-5-sulphosalicylate crystal. *Journal of Molecular Structure*, *1285*, 135425. https://doi.org/10.1016/j.molstruc.2023.135425

Raub, A. A. M., Bahru, R., Nashruddin, S. N. A. M., & Yunas, J. (2024). A review on vertical aligned zinc oxide nanorods: Synthesis methods, properties, and applications. *Journal of Nanoparticle Research*, *26*, 186. https://doi.org/10.1007/s11051-024-06098-w

Ridhuan, N. S., Abdul Razak, K., Lockman, Z., & Abdul Aziz, A. (2012). Structural and morphology of ZnO nanorods synthesized using ZnO seeded growth hydrothermal method and its properties as UV sensing. *PLOS One*, *7*(11), e50405. https://doi.org/10.1371/journal.pone.0050405

Rizaldi, D. R., Doyan, A., & Susilawati, S. (2022). Sintesis lapisan tipis TiO2:(F + In) pada substrat kaca dengan metode spin-coating sebagai bahan sel surya [Synthesis of a thin layer of TiO_2:(F + In) on a glass substrate using the spin-coating method as a solar cell material]. *ORBITA: Jurnal Pendidikan dan Ilmu Fisika*, *7*(1), 219-224.

Sahdiah, H., & Kurniawan, R. (2023). Optimasi tegangan akselerasi pada scanning electron microscope–energy dispersive X-ray spectroscopy (SEM-EDX) untuk pengamatan morfologi sampel biologi [Optimization of acceleration voltage on scanning electron microscope–energy dispersive X-ray spectroscopy (SEM-EDX) for observing the morphology of biological samples]. *Jurnal Sains dan Edukasi Sains*, *6*(2), 117-123. https://doi.org/10.24246/juses.v6i2p117-123

Santibenchakul, S., Sirijaturaporn, P., Mekprasart, W., & Pechrapa, W. (2018). Ga-doped ZnO nanoparticles synthesized by sonochemical-assisted process. *Materials Today: Proceedings*, *5*(6), 13865-13869. https://doi.org/10.1016/j.matpr.2018.02.030

Schell, J., Lupascu, D. C., Carbonari, A. W., Mansano, R. D., Dang, T. T., & Vianden, R. (2017). Implantation of cobalt in SnO_2 thin films studied by TDPAC. In *AIP Advances* (Vol. 7, No. 5, p. 055304). AIP Publishing. https://doi.org/10.1063/1.4983270

Sharifi, F., Mahmoodi, Z., Abbasi, S. M., Najafi, A., & Khalaj, G. (2023). Synthesis and characterization of mesoporous TiC nanopowder/nanowhisker with low residual carbon processed by sol-gel method. *Journal of Materials Research and Technology*, *22*, 2462-2472. https://doi.org/10.1016/j.jmrt.2022.12.097

Silva, D. J., Barbosa, R. F. S., Souza, A. G., Ferreira, R. R., Camani, P. H., & Rosa, D. S. (2022). Morphological, UV blocking, and antimicrobial features of multifunctional cotton fibers coated with ZnO/Cu via sonochemistry. *Materials Chemistry and Physics*, *286*, 126210. https://doi.org/10.1016/j.matchemphys.2022.126210

Susilawati., & Doyan, A. (2009). Dose response and optical properties of dyed poly vinyl alcohol-trichloroacetic acid polymeric blends irradiated with gamma-rays. *American Journal of Applied Sciences*, *6*(12), 2071-2077. https://doi.org/10.3844/ajassp.2009.2071.2077

Tang, X., & Yan, X. (2017). Dip-coating for fibrous materials: Mechanism, methods and applications. *Journal of Sol-Gel Science and Technology*, *81*, 378-404. https://doi.org/10.1007/s10971-016-4197-7

Tarwal, N. L., & Patil, P. S. (2011). Enhanced photoelectrochemical performance of Ag–ZnO thin films synthesized by spray pyrolysis technique. *Electrochimica Acta*, *56*(18), 6510-6516. https://doi.org/10.1016/j.electacta.2011.05.001

Tjahjanti, P. H. (2019). *Pengetahuan bahan teknik* [Knowledge of technical materials]. Umsida Press. https://doi.org/10.21070/2019/978-602-5914-85-0

Veerabhadraiah, S. R., Maji, S., & Panneerselvam, A. (2022). Solvent influence on the formation of ZnO nanoparticles by sonochemical technique and evaluation of UV-blocking efficiency. *Journal of Crystal Growth*, *579*, 126430. https://doi.org/10.1016/j.jcrysgro.2021.126430

Vyas, S. (2020). A short review on properties and applications of zinc oxide based thin films and devices: ZnO as a promising material for applications in electronics, optoelectronics, biomedical and sensors. *Johnson Matthey Technology Review*, *64*(2), 202-218. https://doi.org/10.1595/205651320X15694993568524

Woods-Robinson, R., Han, Y., Zhang, H., Ablekim, T., Khan, I., Persson, K. A., & Zakutayev, A. (2020). Wide band gap chalcogenide semiconductors. *Chemical Reviews*, *120*(9), 4007-4055. https://doi.org/10.1021/acs.chemrev.9b00600

Xian, G., Zhang, G., Chang, H., Zhang, Y., Zou, Z., & Li, X. (2019). Heterogeneous activation of persulfate by Co_3O_4-CeO_2 catalyst for diclofenac removal. *Journal of Environmental Management*, *234*, 265-272. https://doi.org/10.1016/j.jenvman.2019.01.013

Xin, N., Guan, J., Zhou, C., Chen, X., Gu, C., Li, Y., Ratner, M. A., Nitzan, A., Stoddart, J. F., & Guo, X. (2019). Concepts in the design and engineering of single-molecule electronic devices. *Nature Reviews Physics*, *1*, 211-230. https://doi.org/10.1038/s42254-019-0022-x

Yang, X., Yokokura, S., Nagahama, T., Yamaguchi, M., & Shimada, T. (2022). Molecular Dynamics simulation of poly (ether ether ketone) (PEEK) polymer to analyze intermolecular ordering by low wavenumber Raman spectroscopy and X-ray diffraction. *Polymers*, *14*(24), 5406. https://doi.org/10.3390/polym14245406

Yang, Y., Shen, L., Yuan, F., Fu, H., & Shan, W. (2018). Preparation of sustained release capsules by electrostatic dry powder coating, using traditional dip coating as reference. *International Journal of Pharmaceutics*, *543*(1-2), 345-351. https://doi.org/10.1016/j.ijpharm.2018.03.047

Yurestira, I., Aji, A. P., Desfri, M. F., Rini, A. S., & Rati, Y. (2021). Potensi ZnO/ZnS sebagai electron transport material pada sel surya perovskit [Potential of ZnO/ZnS as electron transport materials on perovskite solar cells]. *Journal of Aceh Physics Society*, *10*(2), 41-47.

Zaini, M. B., Maryam, S., Suryani, S. E. I., Himmah, S. W., Nurdiana, Z., Solehudin, S., Suprayogi, T., Sunaryono, S., & Diantoro, M. (2018). Pengaruh fraksi nano (TiO_2: SnO_2) terhadap struktur dan efisiensi DSSC TiO_2: SnO_2/β-karoten/FTO [The effect of nano fraction (TiO_2: SnO_2) on the structure and efficiency of DSSC TiO_2: SnO_2/β-carotene/FTO]. *Journal of Physical Science and Engineering*, *3*(2), 63-69. https://doi.org/10.17977/um024v3i22018p063

Zhang, Q., Zhang, J., Cao, Y., Jiang, F., Feng, G., Liu, J., Liang, J., Li, H., Hu, Q., & Xu, Z. (2025). Low-temperature preparation of nano-sized Al_2TiO_5 powder via non-hydrolytic sol-gel route with Al metal as the aluminum source. *Journal of Alloys and Compounds*, *1010*, 177716. https://doi.org/10.1016/j.jallcom.2024.177716

Zhao, L., Jiang, Q., & Lian, J. (2008). Visible-light photocatalytic activity of nitrogen-doped TiO_2 thin film prepared by pulsed laser deposition. *Applied Surface Science*, *254*(15), 4620-4625. https://doi.org/10.1016/j.apsusc.2008.01.069

REFEREES FOR THE PERTANIKA
JOURNAL OF SCIENCE & TECHNOLOGY

Vol. 33 (4) Jul. 2025

The Editorial Board of the Pertanika Journal of Science and Technology wishes to thank the following:

Ab Rahman Ab Al Hadi
(UTM, Malaysia)

Abdul Halin Alfian
(UPM, Malaysia)

Abdullah Goktas
(HU, Turkey)

Abu Arpah
(UM, Malaysia)

Ahmed Abtan Al-Jumaili
(TU, Iraq)

Ahmed Abtan Al-Jumaili
(TU, Iraq)

Alexander Cimprich
(UWaterloo, Canada)

Ali Kadhum M. Al-Qurabat
(UOB, Iraq)

Ali Salem
(ZNU, China)

Amy J. Davis
(USDA, USA)

Armstrong Ighodalo Omoregie
(UTS, Malaysia)

Aykut Fatih Guven
(YU, Turkey)

Bahman Arasteh
(Istinye, Turkey)

Chua Han Bing
(Curtin, Malaysia)

Dayang Azra Awang Mat
(UNIMAS, Malaysia)

Dele Afolabi
(UNITEN, Malaysia)

Dericks Praise Shukla
(IIT Mandi, India)

Farhad Soleimanian Gharehchopogh
(IAU, Iran)

Fazidah Wahit
(UNITAR, Malaysia)

Firas Salim
(UOB, Iraq)

Fuat Kara
(DU, Turkey)

Gbenga Festus Akomolafe
(Fulafia, Nigeria)

Hasanul Fahmi
(UNITAR, Malaysia)

Hasfalina Che Man
(UPM, Malaysia)

Hesam Kamyab
(SIMTS, India)

Jafar A. Alzubi
(BAU, Jordan)

Jiban Shrestha
(NARC, Nepal)

Kek Sie Long
(UTHM, Malaysia)

Leonardo Jose Agamez Polo
(UNISINÚ, Colombia)

Masoomeh Mirrashid
(ADU, United Arab Emirates)

Michaelraj Kingston Roberts
(SECE, India)

Mohd. Dawood Mahadimenakbar
(UMS, Malaysia)

Muditha K. Meegahakumbura
(UWU, Sri Lanka)

Nasrul Ilminnafik
(UNEJ, Indonesia)

Nazarudin
(UNJA, Indonesia)

Ng Choy Peng Jocelyn
(UPNM, Malaysia)

Ngiam Robin Wen Jiang
(Singapore)

Nur Azida Che Lah
(UniKL, Malaysia)

Osman Saliza Azlina
(UTHM, Malaysia)

Padmanabhan
(VIT Chennai, India)

Parodi-Camaño Tobias
(Uniremington, Colombia)

Saeid Amini
(UI, Iran)

Saleha Shamsudin
(UniMAP, Malaysia)

Seyed Mehdi Talebi
(AU, Iran)

Shalyda Md Shaarani
(UMPSA, Malaysia)

Siti Ujila Masuri
(UPM, Malaysia)

Xiong You-Cai
(LZU, China)

Yusor Rafid Bahar Al-Mayouf
(UOB, Iraq)

ADU - *Abu Dhabi University*
AU - *Arak University*
BAU - *Al-Balqa' Applied University*
Curtin - *Curtin University Malaysia*
DU - *Düzce Üniversitesi*
Fulafia - *Federal University of Lafia*
HU - *Harran Üniversitesi*
IAU - *Islamic Azad University*
IIT Mandi - *Indian Institute of Technology Mandi*
Istinye - *İstinye Üniversitesi*
LZU - *Lanzhou University*
NARC - *Nepal Agricultural Research Council*
SECE - *Sri Eshwar College of Engineering*
SIMTS - *Saveetha Institute of Medical And Technical Sciences*
TU - *Tikrit University*
UI - *University of Isfahan*
UM - *Universiti Malaya*
UMPSA - *Universiti Malaysia Pahang Al-Sultan Abdullah*
UMS - *Universiti Malaysia Sabah*
UNEJ - *Universitas Jember*
UniKL - *Universiti Kuala Lumpur*
UniMAP - *Universiti Malaysia Perlis*
UNIMAS - *Universiti Malaysia Sarawak*
Uniremington - *Corporación Universitaria Remington*
UNISINÚ - *Universidad del Sinú*
UNITAR - *UNITAR International University*
UNITEN - *Universiti Tenaga Nasional*
UNJA - *Universitas Jambi*
UOB - *University of Babylon*
UOB - *University of Baghdad*
UPM – *Universiti Putra Malaysia*
UPNM - *Universiti Pertahanan Nasional Malaysia*
USDA - *United States Department of Agriculture*
UTHM - *Universiti Tun Hussein Onn Malaysia*
UTM - *Universiti Teknologi Malaysia*
UTS - *University of Technology Sarawak*
UWaterloo - *University of Waterloo*
UWU - *Uva Wellassa University*
VIT Chennai - *Vellore Institute of Technology, Chennai Campus*
YU - *Yalova Üniversitesi*
ZNU - *Zhoukou Normal University*

While every effort has been made to include a complete list of referees for the period stated above, however if any name(s) have been omitted unintentionally or spelt incorrectly, please notify the Chief Executive Editor, *Pertanika* Journals at executive_editor.pertanika@upm.edu.my

Any inclusion or exclusion of name(s) on this page does not commit the *Pertanika* Editorial Office, nor the UPM Press or the university to provide any liability for whatsoever reason.

Morphological and Genetic Relationship of Ancient Shan Tea Tree *(Camellia sinensis* var. *assamica)* from Ecogeographical Regions in Northern Vietnam 1849
Lien Thuy Bui, Phong Xuan Ong, Thiep Van Nguyen, Khang Tan Do, Huy Gia Tran, Phi Bang Cao, Ha Duc Chu, Dung Phuong Le and Hong Viet La

Growth and Productivity of Maize *(Zea mays)* Using Gibberellic Acid 3 (GA3) with Different Planting Distances in a Clay Condition at Cabagan, Isabela, Philippines 1869
Darwin Marzan Cacal, Janet Paday-os Pablo, Leila Mary Alipio Ayban, Esther Josephine Daoal Sagalla and Darwin Aldas Basquial

Analysis of Phased Array Corrosion Mapping Data Using Probabilistic Detection (POD) Method 1887
Jan Lean Tai, Mohamed Thariq Hameed Sultan and Farah Syazwani Shahar

Stochastic Distribution of Channel Allocation Algorithm for 5G and Future Generation Ultra-Dense Networks Applications 1907
Joseph Sunday Ojo, Olalekan Lawrence Ojo and Stephen Adebayo Olu-Ojo

Distribution and Population Abundance of Odonates in Relation to Abiotic Factors in an Urbanized Freshwater Ecosystem: A Case Study from Universiti Sains Malaysia 1923
Nur Aina Alisa Adnan, Azimah Abd Rahman, Nur Faeza Abu Kassim and Nurhafizul Abu Seri

A Comparative Study of Gradient Descent Methods in Deep Learning Using Body Motion Dataset 1943
Zulfikar Sembiring, Khairul Najmy Abdul Rani and Amiza Amir

Reduction of Transport Carbon Emissions of India by the Implementation of Strategies Based on IoT-Enabled Intelligent Transportation System: A System Dynamics Approach 1971
Aditi Rajput and Madhuri Jai

Comparison of Crystal Structure, Surface Morphology Structure, and Energy Band Gap of Thin Films of Zinc Oxide, Tin(IV) Oxide, and Titanium Dioxide 2001
Teguh Ardianto, Aris Doyan, Susilawati, Dedi Riyan Rizaldi, Ziadatul Fatimah, Muhammad Ikhsan and Nuraini Rachma Ardianti

Pertanika Journal of Science & Technology
Vol. 33 (4) Jul. 2025

Content

Foreword i
Luqman Chuah Abdullah

Efficiency of Self-Healing Microcapsules in Concrete Slabs Subjected to Low Velocity Impact Force 1683
Salima Al Badi, Zarina Itam, Wong Leong Sing, Muhammad Imran Najeeb, Nazirul Mubin Zahari, Afeeq Haiqal Mohd Hafiez, Shaikh Muhammad Mubin Shaik Ahmad Fadzil, Mohd Meer Saddiq Mohd Sabee and Zuratul Ain Abdul Hamid

Review Article 1707
MXene as a Microstructural Modifier in Solar Thermal Absorber: A Review
Mannir Ibrahim Tarno, Azmah Hanim Mohamed Ariff, Suraya Mohd Tahir and Che Nor Aiza Jaafar

Tailored Cognitive Interventions for Aging Populations: Development and Analysis of a Machine Learning-Driven Web Platform 1743
Mario Macea-Anaya, Rubén Baena-Navarro, Yulieth Carriazo-Regino, Ober Primera-Correa and Juan Pérez-Díaz

Influence of Pyrolysis Temperature on the Composition of Bio-Oil Derived from *Cerbera odollam* as a Raw Material 1765
Muhammad Fathuddin Noor, Sumardi Hadi Sumarlan, Bambang Dwi Argo and Yusuf Hendrawan

Development of Machine Learning Wildlife Camera Using ESP32 CAM for Small Mammals 1783
Leu Mei Xin and Nik Fadzly N Rosely

Analysis and Simulation of Temperature Reduction and Cooling Rate in Precooling Process Using Compressive Force Plate Cooler 1809
Surya Abdul Muttalib, Nursigit Bintoro, Joko Nugroho Wahyu Karyadi and Arifin Dwi Saputro

A Novel Multifaceted Approach to the Detection and Analysis of Formalin's Effect on Enhancing the Shelf Life of Apples 1829
Shahed Alam, Md Saif Kabir, Md. Minhazul Islam Royel and Md. Rakibul Islam

Pertanika Editorial Office, Journal Division,
Putra Science Park,
1st Floor, IDEA Tower II,
UPM-MTDC Center,
Universiti Putra Malaysia,
43400 UPM Serdang,
Selangor Darul Ehsan
Malaysia

http://www.pertanika.upm.edu.my
Email: executive_editor.pertanika@upm.edu.my
Tel. No.: +603- 9769 1622

PENERBIT UPM UNIVERSITI PUTRA MALAYSIA PRESS

http://penerbit.upm.edu.my
Email: penerbit@upm.edu.my
Tel. No.: +603- 9769 8855

e-ISSN 2231-8526